Ceramic coatings for Cervical Total Disc Replacement

Kinga Marta Pasko

Submitted in accordance with the requirements for the degree of Doctor of Philosophy

The University of Leeds

School of Mechanical Engineering

August 2017

The candidate confirms that the work submitted is her own and that appropriate credit has been given where reference has been made to the work of others.

This copy has been supplied on the understanding that it is copyright material and that no quotation from the thesis may be published without proper acknowledgement.

The right of Kinga Marta Pasko to be identified as Author of this work has been asserted by her in accordance with the Copyright, Designs and Patents Act 1988.

© 2017 The University of Leeds and Kinga Marta Pasko

Acknowledgements

I would like to acknowledge and thank my supervisors Professor Joanne Tipper, Professor Richard Hall and Professor Anne Neville for their guidance and help throughout the project. All three provided me with invaluable motivation and ideas, as well as patience in the ups and downs of the project.

This research would not have been possible without the support and collaboration of researches from the institutions involved in the Life Long Joints project, particularly Dr Cecilia Persson from University of Uppsala, who allowed me to visit and carry out experiments and training in her labs, and Dr Peter Hatto from IonBond, who provided me with coated samples used in this project.

Special regards to the technical staff in the Institute of Medical and Biological Engineering across the School of Mechanical Engineering and School of Biology, who have helped me tremendously with the practical aspects of the work carried out in this thesis. Your technical support, understanding and patience has been invaluable.

Many thanks to my office crew, for their help and countless hours of discussions, often on the most random subjects. I am glad we have clarified the definition of a sandwich. I will truly miss every single one of you and wish you all the best.

Outside of University, thanks to all my family and friends for your words of encouragement. Dorota, you always knew what was up and had my corner.

I would like to say thank you to Jamie, for showing endless patience, understanding, support and love thought the highs and lows of the journey this PhD has been. Thank you for not letting me give up.

Finally, I would like to dedicate this thesis to my parents. I would not be who and where I am without your love, encouragement and support. I will be forever grateful.

Abstract

Surgical interventions for the treatment of chronic neck pain, which affects 330 million people globally, include fusion and cervical total disc replacement (CTDR). Most of the currently clinically available CTDRs designs include a metal-on-polymer (MoP) bearing. Numerous studies suggest that MoP CTDRs are associated with issues similar to those affecting other MoP joint replacement devices, including excessive wear and wear particle-related inflammation and osteolysis.

The aim of this study was to investigate the biotribology of a novel metal-on-metal (MoM) design of cervical total disc replacement device in its pristine form and coated with chromium nitride or silicon nitride, in order to understand the influence of loading conditions upon the tribological performance of the implant, and to investigate biological effects of the wear debris produced by the implants. To achieve this, a series of studies were carried out.

Chromium nitride and silicon nitride coatings have been characterised for their mechanical properties, chemical composition and surface finish. Whilst some of the experiments showed minor differences between the mechanical properties and adhesion of the coatings, there was no indication of significant differences between the chromium nitride and silicon nitride coated samples.

Functional testing in the six-station spine wear simulator showed that MoM CTDRs produced wear volumes significantly lower than those of the commercially available MoP devices. The wear volumes were reduced further by three-fold, following testing under altered ISO-18192-1:2011 kinematics, whereby, reduced ranges of motions were applied. Whilst the silicon nitride coated CTDRs failed catastrophically early in the test, chromium nitride coated CTDRs produced an eight-fold reduction in wear volumes, when compared to the pristine devices tested under the same conditions.

Investigation of potential biological effects of the particles generated in wear testing showed that that high concentrations (5-50μm^3 per cell) of CoCrMo particles resulted in significant reduction of cell viability of the L929 fibroblast cells, but not the dural fibroblasts, which were used in this study. No ceramic coating particles, at any concentrations, caused significant reduction of cell viability.

In summary, results presented in this thesis showed that whilst the MoM CTDR device exhibited significantly lower wear rates than those of the commercially available MoP devices, the cytotoxic wear particles could potentially lead to adverse biological reactions, particularly in patients with metal hypersensitivity, and lead to devastating consequences similar to those of failed MoM THRs. Currently, the consequences of similar failure, leading to metalosis or pseudotumour formation in the vicinity of the spinal cord are unknown. During the investigation of the ceramic coatings, it was also found that chromium nitride ceramic coating could not only lower wear rates further, but it also has the potential to reduce the cytotoxic potential of the wear particles.

Table of Contents

Acknowledgements iii
Abstract iv
Table of figures xii
List of Tables xxiii

Chapter 1 : Background and literature review i

1.1 Introduction 26
1.2 The spine 28
  1.2.1 The vertebral column 28
  1.2.2 The cervical spine 30
  1.2.3 Cervical vertebrae 30
  1.2.4 Musculature and ligaments of the cervical spine 34
  1.2.5 The spinal cord 36
  1.2.6 The intervertebral disc 36
  1.2.7 Spine biomechanics 39
  1.2.8 Spine kinematics 40
1.3 Causes of neck pain 41
  1.3.1 Pathways of treatment of neck pain 43
  1.3.2 Non-surgical approaches 43
  1.3.3 Surgical approaches 43
1.4 Tribology theory 47
1.5 Biotribology in Total Joint Replacement 48
1.6 Lubrication regimes 49
  1.6.1 Hydrodynamic lubrication 50
  1.6.2 Boundary lubrication 51
  1.6.3 Mixed lubrication 51
1.7 Friction 51
1.8 Wear 52
  1.8.1 Fatigue wear 53
  1.8.2 Corrosive wear 54
  1.8.3 Adhesive wear 54
  1.8.4 Abrasive wear 55
1.9 Cervical Total Disc Replacement 56
  1.9.1 Materials design considerations 57
  1.9.2 Biomechanical design considerations 58

1.9.3 Clinical results 60
1.9.4 Wear in total disc replacement 63
1.10 Wear testing of CTDRs 66
1.11 Tribological coatings 69
1.11.1 Deposition processes 70
1.11.2 Tribological coatings for biomedical applications 73
1.12 Aims and Objectives 78
Chapter 2 : Design of a generic cervical metal-on-metal Total Disc Replacement 81
2.1 Rationale and aims 81
2.1.1 Material selection 81
2.1.2 Endplate size and shape 83
2.1.3 Fixation 83
2.1.4 Bearing surface 83
2.1.5 Radial clearance and bearing radius 85
2.1.6 Contact stress analysis 85
2.2 Materials 86
2.2.1 Machining and component inspection 86
2.2.2 Contact stress analysis 89
2.3 Methods 90
2.3.1 Component inspection 90
2.3.2 Contact stress analysis and lubrication regime prediction 91
2.4 Results 94
2.4.1 Component inspection 94
2.4.2 Contact stress analysis 98
2.5 Discussion 105
2.5.1 Design of the CTDR device 105
2.5.2 Contact stress analysis and lubrication regime prediction 105
2.6 Conclusions 109
Chapter 3 : Coating characterisation 111
3.1 Introduction 111
3.2 Materials 113
3.2.1 Test samples 113
3.2.2 Equipment for coating characterisation 114
3.2.3 General lab consumables 114
3.2.4 Computer Software 115

3.2.5 Statistical analysis 115
3.3 Methods 115
3.3.1 Sample allocation 115
3.3.2 X-ray photoelectron spectroscopy (XPS) 116
3.3.3 Surface roughness 117
3.3.4 Coating thickness 119
3.3.5 Nanoindentation 122
3.3.6 Scratch testing 126
3.4 Results 128
3.4.1 X-ray photoelectron spectroscopy (XPS) analysis 128
3.4.2 Surface roughness 135
3.4.3 Coating thickness 136
3.4.4 Nanoindentation 143
3.4.5 Scratch testing 146
3.5 Discussion 149
3.5.1 X-ray photoelectron spectroscopy 150
3.5.2 Surface characterisation 151
3.5.3 Coating thickness 152
3.5.4 Mechanical properties of coatings 153
3.6 Conclusions 156
Chapter 4 : Wear assessment of CTDR 157
4.1 Introduction to spine simulator testing 157
4.1.1 Leeds six-station spine simulator 157
4.1.2 Testing protocol 159
4.2 Materials 161
4.2.1 CTDR samples 161
4.2.2 Wear testing lubricant 161
4.2.3 Laboratory consumables and chemicals 161
4.2.4 Gravimetric analysis 162
4.2.5 Surface topography analysis 162
4.2.6 Post-test dimensional inspection 162
4.2.7 Microscopy 162
4.2.8 Scanning Electron Microscopy 162
4.3 Methods 163
4.3.1 Spine simulator calibration 163

4.3.2 Altered testing conditions ... 167
4.3.3 Standard ISO simulator testing conditions ... 168
4.3.4 Spine simulator testing ... 170
4.3.5 Gravimetric analysis ... 172
4.3.6 Surface profile analysis ... 172
4.3.7 Post-test component dimensional inspection ... 174
4.3.8 Light microscopy of CTDR components ... 174
4.3.9 Scanning Electron Microscopy analysis of CTDR components 175
4.3.10 Statistical analysis ... 175
4.4 Results ... 175
4.4.1 Pristine CoCr-CoCr CTDRs ... 175
4.4.2 Coated CTDRs ... 196
4.5 Discussion ... 212
4.5.1 Wear assessment ... 213
4.5.2 Surface topography ... 217
4.5.3 Ceramic coatings in CTDR applications ... 218
4.6 Conclusion ... 222
Chapter 5 : Biological effects of wear particles generated in wear simulation ... 224
5.1 Introduction ... 224
5.2 Materials ... 226
5.2.1 Cobalt-chromium pins and plates ... 226
5.2.2 Cobalt chromium CTDRs ... 227
5.2.3 Coated CTDRs ... 227
5.2.4 Model silicon nitride (Si_3N_4) particles ... 228
5.2.5 Fibroblast cell line ... 228
5.2.6 Primary fibroblast cells ... 228
5.2.7 Cell culture medium and supplements ... 228
5.2.8 Carbon dioxide and liquid nitrogen ... 228
5.2.9 ATP-Lite luminescence assay detection kit ... 228
5.2.10 Chemicals ... 229
5.2.11 Laboratory consumables and glassware ... 229
5.2.12 Equipment for particle characterisation ... 230
5.2.13 Equipment for cell culture maintenance and cell viability assays 230

5.2.14 Equipment for particle isolation 230
5.2.15 Computer software 231
5.3 Methods 231
5.3.1 Particle generation using six-station pin-on-plate wear rig ..231
5.3.2 Particle generation using a six-station spine simulator........233
5.3.3 Particle isolation 235
5.3.4 Freeze drying of water generated particle solution..............240
5.3.5 Preparation of endotoxin-free wear particles and model silicon nitride particles for cell culture experiments 240
5.3.6 Characterisation of cobalt chromium, chromium nitride and silicon nitride wear particles and silicon nitride model particles 240
5.3.7 Cell resurrection and cell culture 242
5.3.8 Cell count using the trypan blue exclusion assay................243
5.3.9 Growth curves for L929 murine fibroblasts and primary porcine dural fibroblasts..244
5.3.10 Culture of L929 and primary dural fibroblasts cells with cobalt chromium wear particles 246
5.3.11 Culture of L929 and primary dural fibroblasts cells with model silicon nitride particles and chromium nitride and silicon nitride wear particles 248
5.3.12 Determining changes in cell viability using the ATP-Lite assay 251
5.4 Results 251
5.4.1 Particle generation using a six-station pin-on-plate wear rig 251
5.4.2 Particle generation using a six-station spine simulator........254
5.4.3 Characterisation of cobalt chromium wear particles............254
5.4.4 Characterisation of ceramic coating wear particles generated in the six-station spine simulator 260
5.4.5 Characterisation of model silicon nitride particles 263
5.4.6 Growth curve of L929 murine fibroblasts and primary porcine dural fibroblasts..267
5.4.7 Investigation of the cytotoxic effects of cobalt chromium wear particles on L929 murine fibroblasts and primary porcine dural fibroblasts...269
5.4.8 Investigation of the cytotoxic effects of model silicon nitride particles (submicron and nanoscale) on L929 murine fibroblasts and primary porcine dural fibroblasts 275

5.4.9 Investigation of the cytotoxic effects of ceramic coatings wear particles (chromium nitride and silicon nitride) on L929 murine fibroblasts and primary porcine dural fibroblasts 279

5.5 Discussion 283

5.6 Conclusions 290

Chapter 6 : Summary review 291

6.1 Overall discussion and main findings 291

6.2 Limitations of studies 297

6.3 Future work 299

6.4 Conclusions 301

Chapter 7 : Appendices 303

7.1.1 Appendix I - Summary of the main design features of the CTDR devices cleared by the FDA 303

7.1.2 Appendix II – Leeds Spine Simulator 306

7.1.3 Appendix III – Spine simulator CTDR component fixtures ..309

7.1.4 Appendix IV - Talysurf CTDR component fixture.................311

7.1.5 Appendix V - SOP 01.03 rev. 6 312

Chapter 8 : References 303

Table of figures

Figure 1.1: Lateral view of the macroscopic bony anatomy of the vertebral column with cervical, thoracic, lumbar, sacral and coccygeal sections and the spinal curvatures indicated [20]. 29

Figure 1.2: Typical cervical vertebra, A – cranial view, B – lateral view [23]. 31

Figure 1.3: Anatomy of C1 (atlas) and C2 (axis) vertebrae; A- Cranial view of the atlas, B – Caudal view of the atlas; C – Cranial view of the axis, D – Anterior view of the axis [23]...32

Figure 1.4: Uncovertebral joints (joints of Luschka) in the cervical spine are formed largely by the lateral uncinate processes which prevent posterolateral disc protrusions [23]..33

Figure 1.5: Saddle shape of cervical intervertebral joints in the sagittal plane (s). The vertebral body forms a lip; the superior surface of the lower vertebral body is concave upwards in the transverse plane (t) [28]. 33

Figure 1.6: A - Anterior and lateral vertebral muscles; B – Deep layer of deep dorsal cervical muscles [30]..35

Figure 1.7:Anatomy of the intervertebral disc and its position between vertebrae [39]..38

Figure 1.8: Fusion restricts motion at the affected level, which results in greater strains being exerted on the adjacent segments. 45

Figure 1.9: Idealised Stribeck curve. Coefficient of friction (μ), Sommerfeld number (z). 49

Figure 1.10: Edge view of an ultra-high molecular weight polyethylene (UHMWPE) core from a lumbar total disc replacement component. Radial cracks of the rim were caused by fatigue [86]..........................53

Figure 1.11: Schematic representation of adhesive wear [90]. 55

Figure 1.12: Differences between two- and three-body abrasive wear [91]. 56

Figure 1.13: A - Mean instantaneous axes of rotation for each motion segment of the cervical spine depicted with a dot. Two standard deviation range of distribution is located within the enclosed circles shown. B - The position of IAR can change position during motion and can be determined by superimposing tracing of a vertebrae in full ROM [28]. 60

Figure 1.14: Basic concept of a magnetron; S and N relate to the South and North poles of the magnets, respectively...72

Figure 1.15: Schematic diagram of a simple HiPIMS deposition chamber (adapted from [150]). 73

Figure 1.16: Summary of the studies performed in each chapter. The experimental work has been divided into 4 parts which investigated coating properties, theoretical analysis of maximum stress and lubrication regime, in vitro wear performance and potential biological consequences of wear. 80

Figure 2.1: Dimensions and geometrical tolerances speficied for the concave components of the CTDR device. 87

Figure 2.2: Dimensions and geometrical tolerances speficied for the convex components of the CTDR device. 88

Figure 2.3: A: Five, approximately equally spaced points (marked red) were used to create XY planes. In addition, four points, taken on the superior flat surface of each endplate, were used to create the Z plane. B: Twenty-five measurement points were taken on each component, one point on the pole, followed by 3 sets of 8 equally spaced points at 1/4, 1/2 and 3/4 of the bearing height. 91

Figure 2.4: Schematic diagraph showing the geometry of the ball-and-socket joint 92

Figure 2.5: Variation of maximum contact pressure depending on radial clearance, under loads ranging from 0 to 150 N. The worst-case clearance (c=0.17mm) resulted in maximum contact pressure of 189MPa, 205MPa and 177MPa for CoCr-CoCr, Si_3N_4-Si_3N_4 and CrN-CrN bearing combinations, respectively. 98

Figure 2.6: Variation of minimum film thickness with angular velocity for different radial clearances and different bearing material combinations. The figure shows prediction for a CDTR under 150 N load. 101

Figure 2.7: Variation of lambda ratio with angular velocity for different radial clearances and different bearing material combinations. The figure shows prediction for a CDTR under 150 N load...............................102

Figure 2.8: Variation of minimum film thickness under load range 0-150 N and for different angular velocities for different bearing combinations. A constant radial clearance of c=0.15 mm was used. 103

Figure 2.9: Variation of lambda ratio under load range 0-150N and for different angular velocities for different bearing combinations. A constant radial clearance of c=0.15 mm was used. At lower loads and higher entraining velocities the λ ratio for each bearing combination can reach approximately λ=3...104

Figure 3.1: Method of wire cutting and fracturing of the coated samples. The cuts were made through the mid-section of the sample, leaving approximately 0.5 mm of the material uncut. The sample was subsequently fractured inwards in order to avoid buckling and delamination of the coating. 114

Figure 3.2: Schematic representation of the two traces taken across the surface of each coated coupon. 118

Figure 3.3: Typical projection seen on a surface following coating abrasion in Calo test...119

Figure 3.4: Schematic representation of the Calo test and dimensions used in calculating coating thickness. 120

Figure 3.5: Fractured silicon nitride-coated sample embedded in the Bakelite resin. 122

Figure 3.6: Typical load-displacement curve (indentation depth) obtained from the nanoindentation measurements. 123

Figure 3.7: Schematic representation of the section through an indentation; A_c is the projected contact area. Reproduced based on Oliver and Pharr [253]. 124

Figure 3.8: Schematic representation of a scratch produced on a surface of a coated sample. Position of the L_1 is associated with chevron-line cracks at the edges of the scratch; L_2 associated with spallation of the coating at the edges of the scratch and L_3 with complete failure of the coating, whereby the tip penetrates through the coating in the middle of the scratch [256]. 127

Figure 3.9: Cascaded views of survey spectra of coupons 1 (top), 2 (middle) and 3 (bottom) at different sputtering times, as indicated on the right side of each graph. The locations of peaks corresponding with different elements are the same for spectra obtained following sputtering. Only small variations in peak presence were noted for spectra obtained following no sputtering. 129

Figure 3.10: Overlaid survey spectra of three CrN coated coupons, with peaks correlating with specific elements identified. Carbon C1s and oxygen O1s peaks were stronger in samples that did not undergo any Ar^+ ion sputtering (red spectra line), whilst signals of chromium Cr2p and nitrogen N1s were stronger once the samples were sputtered with argon ions for at least 100s (other colours). 131

Figure 3.11: Cascaded views of survey spectra of coupons 1 (top), 2 (middle) and 3 (bottom) at different sputtering times, as indicated on the right side of each graph. The locations of peaks corresponding with different elements are the same for spectra obtained following sputtering. Only small variations in peak presence were noted for spectra obtained following no-sputtering. 132

Figure 3.12: Overlaid survey spectra of three Si_3N_4 coated coupons, with peaks correlating with specific elements identified. Red survey line – non-sputtered, remaining colours – post sputtering. 133

Figure 3.13: Projection on the surface of silicon nitride-coated coupon. For each sample, the x and y dimensions were measured using the Leica microscope software. Data was collated in a spreadsheet and coating thickness was determined. 137

Figure 3.14 SEM image of a cross section of a silicon nitride-coated coupon. Clear layers of the substrate, coating and Bakelite resin can be distinguished. 139

Figure 3.15: EDX analysis of a chromium nitride coated sample. The SEM image (A) was used to visually identify, whilst the EDX was employed to confirm regions of substrate (B) and coating (C) locations. 140

Figure 3.16: EDX analysis of a silicon nitride coated sample. The SEM image (A) was used to visually identify, whilst the EDX was employed to confirm regions of substrate (B) and coating (C) locations. 141

Figure 3.17: Indentation depth-loading hystereses for chromium nitride coated coupons. Each of 10 indentations has been recorded. 144

Figure 3.18: Indentation depth-loading hystereses for silicon nitride coated coupons. Each of 10 indentations has been recorded. 145

Figure 3.19: A silicon nitride coated coupon following scratch testing; five scratches were made on each coupon, which were subsequently analysed using a light microscope to identify locations of failures associated with critical loads...146

Figure 3.20: Micrograph of scratches generated with the scratch testing on coupons coated with CrN (left) and Si_3N_4 (right) coatings..................147

Figure 4.1: Leeds Spine Simulator A showing Banks 1 and 2 with stations 1-6 and a soak station...158

Figure 4.2: Fully assembled test cell. The axial force and rotations are applied to the inferior fixture, whilst the anterior shear, flexion/extension and lateral bending motions are applied to the superior fixture. 159

Figure 4.3: Set up for axial loading calibration using an independent load cell and bespoke jig..163

Figure 4.4: Set up for flexion-extension calibration using a digital inclinometer. 165

Figure 4.5: Revised phasing of the displacement and load curves applied in Test 2. The frequencies of all motions and AF (axial loading) remained at 1 Hz; ROMs are reduced to ±3°, ±2° and ±2° for FE (flexion/extension), LB (lateral bending) and AR (axial rotation), respectively. 168

Figure 4.6: Phasing of the displacement and load curves for CTDRs specified by ISO-18192-1:2011; AF- axial force, LB – lateral bending, FE – flexion/extension, AR – axial rotation...169

Figure 4.7: Fully assembled test cell showing the superior and inferior fixtures and placement of a sample in an enclosed gaiter.............................171

Figure 4.8: A: top view showing the schematic representation of six traces taken across the surface of each CTDR component for the measurement of surface roughness; B: side view showing the measured area included only the bearing surface and excluded the flat endplate areas. 173

Figure 4.9: Example of wear area measurement using ImageJ software. .175

Figure 4.10: Cumulative volume loss from CoCr-CoCr CTDR components tested under the ISO-18192-1:2011 protocol. There was no significant difference in convex and concave component volume loss across 4MC of simulator testing. Error bars represent 95% confidence limits. 176

Figure 4.11: Station variability in volume loss across 4MC of testing under ISO-18192-1:2011 protocol of CoCr-CoCr CTDR devices................177

Figure 4.12: High magnification light micrograph depicting the noticeable discolouration of the surface area, associated with wear. Multidirectional, criss-crossing scratches were also present (convex component, 3MC under ISO-18192-1:2011 conditions). 181

Figure 4.13: Deep wear marks found on some surfaces (concave component, 2MC under ISO-18192-1:2011 conditions). 181

Figure 4.14: Example of deposit build-up on the surfaces at the edges of the wear area (concave component, 4MC under ISO-18192-1:2011 conditions). 182

Figure 4.15: Example of surface damage at the pole of a convex component, at 4MC under ISO-18192-1:2011 conditions, showing signs of micropitting. 182

Figure 4.16: SEM micrographs of multidirectional and criss-crossing scratches on the surface of a CoCr CTDR component (convex component, 3MC under ISO-18192-1:2011 conditions)...183

Figure 4.17: SEM micrograph of morphological difference between worn (right) and unworn (left) surface (convex component, 3MC under ISO-18192-1:2011 conditions). 184

Figure 4.18: SEM micrographs of deposit found surfaces, most commonly found on the outside edges of the wear area (top), as well as in deeper wear scratches (bottom) (concave component, 2MC under ISO-18192-1:2011 conditions..185

Figure 4.19: Example of micro-pits found on the surfaces of uncoated, metal CTDR components, following 2MC of standard ISO testing. 186

Figure 4.20: Cumulative volume loss of CTDR components following 4MC of standard ISO testing protocol and 2MC of modified ISO testing protocol. There was a significant reduction in mass loss i.e. wear in the second phase of the testing whereby the modified ISO testing protocol was employed (4-6MC). Error bars represent 95% confidence limits........189

Figure 4.21: Example of high magnification micrograph showing the noticeable discolouration of the surface area, associated with wear. Multidirectional, criss-crossing scratches were also present. (convex component, 5MC i.e. 4MC ISO-18192-1:2011 + 1MC altered ISO)...192

Figure 4.22: High magnification image of deep wear marks found on some surfaces (concave component, 5CM i.e. 4MC ISO-18192-1:2011 + 1MC altered ISO). Some deposit build-up around the scratches were also observed...192

Figure 4.23: Surface damage at the pole of a convex component, at 5MC (4MC ISO-18192-1:2011 + 1MC altered ISO), showing signs of micropitting. 193

Figure 4.24: High magnification, high resolution image of multidirectional and criss-crossing scratches on the surface of a metal CTDR component. 194

Figure 4.25: Deposit found inside the grooves of the wear scratches of CoCr CTDRs tested under altered ISO-18192-1:2011 protocol. 194

Figure 4.26: SEM micrograph (mag=1.66K) of micro-pits found on the surfaces of CoCr CTDR components, following 2MC of standard ISO testing. 195

Figure 4.27: SEM image of silicon nitride-coated CTDR device. A large hole in the coating was observed – substrate material, with polishing marks visible, was seen. Moreover, small splashing defect (marked with an arrow) was found. 197

Figure 4.28: SEM image of chromium nitride-coated CTDR device. Portion of coating was missing from the surface, substrate material with polishing marks was observed underneath. Numerous holes/pits, as well as portions of coating protruding out of the coating were observed....197

Figure 4.29: Cumulative volume loss from CrN-CrN CTDR components tested under the ISO-18192-1:2011 protocol. There was no significant difference in convex and concave component volume loss across 2MC of simulator testing. Error bars represent 95% confidence interval limits. 199

Figure 4.30: Cumulative volume loss from Si_3N_4-Si_3N_4 CTDR components tested under the ISO-18192-1:2011 protocol. Following coating failure and delamination at 71,000 cycles, the data was linearly extrapolated to 1MC. There was no significant difference in convex and concave component volume loss across 4MC of simulator testing. Error bars represent 95% confidence interval limits. 200

Figure 4.31: Silicon nitride-coated concave component showing catastrophic damage and delamination of the coating following 71,000 cycles under the standard ISO-18192-1:2011 protocol. Substrate material showing through(indicated by the arrows) and multidirectional scratches were discovered on the surface....205

Figure 4.32: Higher magnification image of a convex component, showing damage of the silicon nitride coating sustained following 71,000 cycles of the standard ISO-18192-1:2011 testing protocol. Multidirectional scratches and substrate material (coating delamination) were observed on the surface. 206

Figure 4.33: High magnification, high resolution SEM image of the silicon nitride coating delamination damage. 206

Figure 4.34: EDX of the area of suspected silicon nitride coating delamination, confirming the catastrophic damage of the coating. Spectrum 3 (A), taken from the area where the coating remained intact confirmed the chemical composition of the coating (strong silicon and nitride peaks). Spectrum 5 (B), taken from the area where the coating appeared delaminated, confirmed the chemical composition of the substrate material, showing strong peaks of cobalt (Co), chromium (Cr) and molybdenum (Mo). .207

Figure 4.35: Light micrograph showing a CrN-coated concave component following 2MC of standard ISO-18192-1:2011 testing protocol. Polished area at the pole of the component was observed, with a dark deposit collected at the edge of this area. The un-worn area appeared rougher with some micropitting present. 208

Figure 4.36: Higher magnification light micrograph of the bearing surface of a CrN-coated convex component tested for 2MC under the standard ISO-18192-1:2011 protocol. Highly polished, wear area at the pole of the component was observed. Unworn area appeared rougher and polishing marks were observed. 209

Figure 4.37: SEM image of the un-worn area of the chromium-nitride coated CTDR component following 2MC of standard ISO-18192-1:2011 protocol testing. Numerous coating defects (micropits and protrusions) and rough appearance of the coating were observed. 210

Figure 4.38: SEM image of the worn area of the chromium-nitride coated CTDR component following 2MC of standard ISO-18192-1:2011 protocol testing. Smoother appearance, larger micropits and lack of protrusions were observed. 210

Figure 4.39: SEM image of the bearing surface of a chromium nitride-coated CTDR component following 2MC of standard ISO-18192-1:2011 testing protocol. Relatively large portions of the coating appeared to have worn out/flaked off from the surface, however, no coating delamination was observed. Some micropitting on the surface was noted. 211

Figure 5.1 Schematic of a wear pin (A) and plate (B) used in the six-station pin-on-plate wear test. 227

Figure 5.2: Six-station pin-on-plate wear rig components, prior to assembly: 1 – bridges securing pin holders, 2 – racks, 3 – outer baths, 4 - miscellaneous screws, 5 – ball bearings, 6 – connecting rods, 7 – pin holders, 8 – inner baths, 9 – plastic covers, 10 – pin holder bore, 11 – pinions and ratchets...232

Figure 5.3: Calibration set-up of the six-station pin-on-plate wear simulator, as per SOP 01.03, Appendix V. 233

Figure 5.4: Particle isolation process used in this study, based on Lal et al. [353]. 239

Figure 5.5: Schematic representation of a magnified view the Neubauer haemocytometer grid used in cell counting. At least 100 cells within all 25 squares (selected in red) had to be counted per cell suspension sample. Cells on the left and bottom edge of the grid were not counted; cells on the top and right edge of the grid were counted. 244

Figure 5.6: Layout of the 96-well plate used in the growth curve studies of L929 murine fibroblasts and primary porcine dural fibroblasts. 245

Figure 5.7: Layout of 96-well plates used for culturing cells with the cobalt chromium wear particles. Plate A (top) included particles generated in the six-station pin-on-plate wear simulator and the six-station spine simulator in water. Plate B (bottom) included particles generated in the six-station spine simulator in foetal bovine serum. The same plate layouts were used for both L929 and primary dural fibroblasts cells..248

Figure 5.8: Layout of a 96-well plate used for culturing the L929 cells with the submicron- and nanoscale silicon nitride powder particles. 250

Figure 5.9: Layout of a 96-well plate used for culturing cells with the chromium nitride and silicon nitride coating particles generated in six-station spine simulator. The same plate layout was used for L929 murine fibroblasts and primary porcine dural fibroblasts. 251

Figure 5.10: Cobalt chrome plates (left) and pins (right) components following 613,615 cycles of testing on the six-station pin-on-plate wear rig. The components shown are arranged in order corresponding to stations 6-1, respectively. 252

Figure 5.11: Wear factors produced by the cobalt chromium pin and plate by each station, 1-6. Across all the stations, both pins and plates produced relatively similar wear factors, with only station 3 components resulting in a slightly lower wear factors. Identification numbers of pins and plates are marked in each stacked bar. 253

Figure 5.12: Cobalt chromium particles generated in the six-station pin-on-plate wear rig in water. The submicron sized particles showed a tendency to agglomerate. 255

Figure 5.13: Particle volume distribution of cobalt chromium particles generated in a six-station pin-on-plate wear rig in water. The mean particle size was 51nm. 255

Figure 5.14: EDX spectra of cobalt chromium particles generated in the six-station pin-on-plate wear rig in sterile water. Chromium (Cr) and cobalt (Co) were confirmed in the spectroscopy. Iridium peaks were detected due to the iridium coating the samples were coated with prior to observation. 256

Figure 5.15: Cobalt chromium particles generated in a six-station spine simulator in foetal bovine serum. 257

Figure 5.16: EDX spectra of an agglomerate of cobalt chromium wear particles. Only chromium (Cr) was detected (11.5%wt), alongside a similar amount of tungsten (W) (13.9%wt), which was likely to be a residue from the isolation process. High amounts of carbon (C) and oxygen (O) (46.9%wt and 19.6%wt) suggest protein contamination around the particles. 257

Figure 5.17: Cobalt chromium particles generated in a six-station spine simulator in sterile water. 258

Figure 5.18: Particle volume distribution of cobalt chromium particles generated in a six-station spine simulator in sterile water. The mean particle size was 154nm...259

Figure 5.19: EDX spectra of cobalt chromium particles generated in the six-station spine simulator in sterile water. Chromium (Cr), cobalt (Co) and molybdenum (Mo) were confirmed in the spectroscopy. Iridium peaks were detected due to the iridium coating samples were coated with. 259

Figure 5.20: A chromium nitride coating particle generated in a six-station spine simulator in sterile water, filtered through a 0.015µm polycarbonate filter membrane. The particles were relatively large with sharp edges and flake-like morphology. Some pitting observed on the surface of the flake-like particles was observed, as indicated by the arrows. 260

Figure 5.21: EDX spectra of chromium nitride particle generated in the six-station spine simulator in sterile water. Strong peaks and a large quantity (44.3%) of Chromium (Cr) were confirmed in the spectroscopy. 261

Figure 5.22: Silicon nitride coating particle generated in a six-station spine simulator in sterile water, filtered through a 0.1µm polycarbonate filter membrane. The particles were relatively large with sharp edges and flake-like morphology. Some nano-sized particles can also be observed, however it was not possible to confirm their origin with EDX. 262

Figure 5.23: EDX spectra of a silicon nitride coating particle generated in the six-station spine simulator in sterile water. Strong peaks and large quantity (30%) of Silicon (Si) were confirmed in the spectroscopy. 262

Figure 5.24: Submicron silicon nitride particles aggregated together. The particles were mostly irregular in shape, with some round particles also observed. 263

Figure 5.25: Particle size distribution of model silicon nitride particles of submicron size. The mean particle size was 138nm. 264

Figure 5.26: EDX spectra of the commercially available submicron silicon nitride particles. Strong Silicon (Si) and Nitrogen (N) peaks were detected in the analysis. Iridium peaks were detected due to the iridium coating samples were coated with. 264

Figure 5.27: Nanoscale silicon nitride model particles agglomerated together. High magnification (x150k) images revealed that the particles were predominantly round and had smooth edges. 265

Figure 5.28: Particle size distribution of model silicon nitride particles of nanoscale size. The mean particle size was 43nm. 266

Figure 5.29: EDX spectra of the commercially available nanoscale silicon nitride particles. Strong Silicon (Si) and Nitrogen (N) peaks were detected in the analysis. Iridium peaks were detected due to the iridium coating samples were coated with. 266

Figure 5.30: Cell viability of L929 murine fibroblasts seeded at different cell seeding densities determined using the ATPLite assay. The error bars represent 95% confidence limits. 267

Figure 5.31: Cell viability of primary porcine dural fibroblasts seeded at different cell seeding densities determined using the ATPLite assay. The error bars represent 95% confidence limits. 268

Figure 5.32: Effects of cobalt chromium wear particles generated in the six-station pin-on-plate wear rig on L929 murine fibroblasts cell viability. Data was analysed using ANOVA test (α=0.05) and the T-method. Significantly (p<0.05) reduced cell viability was indicated with an asterisk (*)......270

Figure 5.33: Effects of cobalt chromium wear particles generated in the six-station spine simulator in water on L929 murine fibroblasts cell viability. Data was analysed using ANOVA test (α=0.05) and the T-method. Significantly (p<0.05) reduced cell viability was indicated with an asterisk (*)......271

Figure 5.34: Effects of cobalt chromium wear particles generated in the six-station spine simulator in foetal bovine serum on L929 murine fibroblasts cell viability. Data was analysed using ANOVA test (α=0.05) and T-method. Significantly (p<0.05) reduced cell viability was indicated with an asterisk (*)......272

Figure 5.35: Effects of cobalt chromium wear particles generated in sterile water in six-station pin-on-plate wear rig on primary porcine dural fibroblasts cell viability. Data was analysed using ANOVA test (α=0.05) and the T-method. Significantly (p<0.05) reduced cell viability was indicated with an asterisk (*)......273

Figure 5.36: Effects of cobalt chromium wear particles generated in sterile water in six-station spine simulator on primary porcine dural fibroblasts cell viability. Data was analysed using ANOVA test (α=0.05) and the T-method. Significantly (p<0.05) reduced cell viability was indicated with an asterisk (*)......274

Figure 5.37: Effects of cobalt chromium wear particles generated in foetal bovine serum in the six-station spine simulator on primary porcine dural fibroblasts cell viability. Data was analysed using ANOVA test (α=0.05) and the T-method. Significantly (p<0.05) reduced cell viability was indicated with an asterisk (*)......275

Figure 5.38: Effects of commercially available submicron silicon nitride particles on L929 murine fibroblasts. Data was analysed using ANOVA test (α=0.05) and the T-method. Significantly (p<0.05) reduced cell viability was indicated with an asterisk (*)......276

Figure 5.39: Effects of commercially available nanoscale silicon nitride particles on L929 murine fibroblasts. Data was analysed using ANOVA test (α=0.05) the T-method. Significantly (p<0.05) reduced cell viability was indicated with an asterisk (*)......277

Figure 5.40: Effects of commercially available submicron silicon nitride particles on primary porcine dural fibroblasts. Data was analysed using ANOVA test (α=0.05) and T-method. Significantly (p<0.05) reduced cell viability was indicated with an asterisk (*)......278

Figure 5.41: Effects of commercially available nanoscale silicon nitride particles on primary porcine dural fibroblasts. Data was analysed using ANOVA test (α=0.05) and the T-method. Significantly (p<0.05) reduced cell viability was indicated with an asterisk (*)......279

Figure 5.42: Effects of chromium nitride coating particles generated in sterile water in the six-station spine simulator on L929 murine fibroblasts. Data was analysed using ANOVA test (α=0.05) and the T-method. Significantly (p<0.05) reduced cell viability was indicated with an asterisk (*). 280

Figure 5.43: Effects of silicon nitride coating particles generated in sterile water in the six-station spine simulator on L929 murine fibroblasts. Data was analysed using ANOVA test (α=0.05) and the T-method. Significantly (p<0.05) reduced cell viability was indicated with an asterisk (*). 280

Figure 5.44: Effects of chromium nitride coating particles generated in sterile water in the six-station spine simulator on primary porcine dural fibroblasts. Data was analysed using ANOVA test (α=0.05) and the T-method. Significantly (p<0.05) reduced cell viability was indicated with an asterisk (*). 282

Figure 5.45: Effects of silicon nitride coating particles generated in sterile water in the six-station spine simulator on primary porcine dural fibroblasts. Data was analysed using ANOVA test (α=0.05) and the T-method. Significantly (p<0.05) reduced cell viability was indicated with an asterisk (*). 282

Figure 6.1: Pubmed literature search results for ‘cervical total disc replacement’ or ‘cervical total disc arthroplasty’ showing the limited numbers of publications around CTDR technology. 292

Figure 6.2: Load and displacement profile for lumbar spine extension impingement wear test, as per ISO-18192-3:2017 [406]. 301

Figure 7.1: Axial loading mechanism showing how the cam compresses the spring, and the load is applied to the sample. 306

Figure 7.2: Anterior-posterior shear mechanism, showing the connection of the motor to the individual station, and how this transfers movement to the sample 307

Figure 7.3: Flexion-extension mechanism for one group of three stations, showing application of Flexion (F) and Extension (E) 307

Figure 7.4: Lateral bending mechanism showing the lateral bending motor and gearbox, the linkages that attach to the gimbal and the counter-weight needed to stabilise the motion, applying left (L) and right (R) lateral bending 308

Figure 7.5: Axial rotation mechanism showing right (R) and left (L) axial rotation applied to one group of three stations via linkages 308

List of Tables

Table 1.1: Passive ROMs measured at different levels of the cervical spine; AOJ – atlantooccipital joint; AAJ- atlantoaxial joint. 41

Table 1.2: A summary of main outcome characteristics of the 7 FDA-approved CTDR devices for a single-level treatment compared to ACDF control groups; NDI – neck disability index; RCT – randomised controlled trial 63

Table 1.3: Range of motion and total excursion after 10^6 cycles as specified per the ISO 18192-1 and ASTM F2423-11. 67

Table 2.1: Main design characteristics, including sizes and range of motion of the currently FDA-approved CTDR devices. 84

Table 2.2: Parameters used in the Hertzian theoretical contact stress prediction model. 90

Table 2.3: Radial clearances of paired uncoated devices measured using the CMM. 94

Table 2.4: Dimensional inspection of the bearing surface radii and endplates of the uncoated CTDRs. 95

Table 2.5: Radial clearances of paired coated components measured using the CMM. Devices corresponding with Stations 1, 3 and 5 were coated with chromium nitride, whilst devices from stations 2, 4 and 6 were coated with silicon nitride. The additional six sets of components were also inspected and are detailed here with the annotation ‘a’. 96

Table 2.6: Dimensional inspection of the bearing surface radii and endplates. Additional components were annotated with ‘a’...................................97

Table 2.7: Results of minimum film thickness prediction for different bearing materials, at maximum angular velocities and a constant load of 150 N. 100

Table 2.8: Results of lambda ratio for different bearing materials, at maximum angular velocities and a constant load of 150N 100

Table 3.1: Allocation of ceramic coating test coupons for coating characterisation testing. 115

Table 3.2: Values of cut-off depending on R_a values as stipulated by ISO-4288-1996. Relationship of λ_c/ λ_s i.e. bandwidth is based on ISO-3247:1998..119

Table 3.3: Chemical composition of the surface region of Cr–N films deposited on three coupons, represented in atomic percent (at.%). 130

Table 3.4: Chemical composition of the surface region of Si_3N_4 films deposited on three coupons, represented in atomic percent (at.%). 134

Table 3.5: Summary of surface roughness results of chromium nitride coated coupons. 135

Table 3.6: Summary of surface roughness results of silicon nitride coated coupons. 136

Table 3.7: Summary of chromium nitride coating thickness results, as obtained with a Calo tester. The average coating thickness of chromium nitride was found to be 4.9±0.8µm..137

Table 3.8: Summary of silicon nitride coating thickness results, as obtained with Calo tester. The average coating thickness of silicon nitride was found to be 5.1±0.3µm. 138

Table 3.9: Summary of coating thickness of chromium nitride coated coupons, as measured in ImageJ using images obtained from SEM. 142

Table 3.10: Summary of coating thickness of silicon nitride coated coupons, as measured in ImageJ using images obtained from SEM. 142

Table 3.11: Summary of the nanoindentation results of chromium nitride coated coupons, showing average hardness and Young's modulus of the coating. 144

Table 3.12: Summary of nanoindentation results of silicon nitride coated coupons, showing average hardness and Young's modulus of the coating. 145

Table 3.13: Summary of values of critical loads measured during scratch testing of chromium nitride coated coupons. The average load at which the scratch tip penetrated through the chromium nitride coating was 73.92±3.56 N. 148

Table 3.14: Summary of values of critical loads measured during scratch testing of silicon nitride coated coupons. The average load at which the scratch tip penetrated through the silicon nitride coating was 63.06±6.40 N. 148

Table 4.1: Standard ISO-18192-1:2011 testing inputs and error margins..169

Table 4.2: Testing protocol inputs for spine simulator test under altered ISO-18192-1:2011 protocol, changes to the protocol were highlighted. Range of all motions were decreased, loads and phasing of the motions remained in line with the ISO standard. 167

Table 4.3: Values of cut-off depending on R_a values as stipulated by ISO-4288-1998. Relationship of λ_c/ λ_s i.e. bandwidth is based on ISO-3247-1998...174

Table 4.4: Mean pre-test R_a, R_p, R_v and R_{sk} values for different traces taken across the surfaces of convex and concave components of CoCr-CoCr CTDR devices; the traces with lowest values are highlighted in green. One-way ANOVA analysis of the pre-test surface finish parameters showed that the R_a, R_p and R_{sk} of concave components were significantly lower ($p<0.05$) than those of the convex components. Values of the R_v parameter were not found to be significantly different between the two component groups. 178

Table 4.5 Mean Ra, Rp, Rv and Rsk values of CoCr-CoCr CTDRs following 4MC of ISO-18192-1:2011 testing for different traces taken across the surfaces of convex and concave components; the traces with lowest values are highlighted in green. One-way ANOVA analysis of the post-test results showed that the changes in parameters following the testing were statistically significant ($p<0.05$) only in convex components. 179

Table 4.6: Summary of mean values of the visible wear area on the CoCr CTDR components, measured throughout the 4MC of standard ISO testing (ISO-18192-1:2011). 187

Table 4.7: Summary of pre- and post-test values of radial clearances of each test station. 187

Table 4.8: Summary of contact profilometry results of the CTDR components following 2MC of altered ISO testing protocol. Mean R_a, R_p, R_v and R_{sk} values different traces taken across the surfaces of convex and concave components; highlighted in green are the traces with lowest values. One-way ANOVA analysis of the results showed that the changes in all parameters, in comparison to the pre-test condition, were not statistically significant ($p>0.05$). 190

Table 4.9: Summary of pre- and post-test values of radial clearances of each test station i.e. prior to and following 2MC of testing following the altered ISO protocol...196

Table 4.10: Mean pre-test R_a, R_p, R_v and R_{sk} values for different traces taken across the surfaces of convex and concave components of CrN-CrN CTDR devices; the traces with lowest values are highlighted in green. One-way ANOVA analysis of the pre-test surface finish parameters showed that the R_a, R_p and R_{sk} of convex components were significantly lower ($p<0.05$) than those of the convex components. Values of the R_v parameter were not found to be significantly different between the two component groups. 202

Table 4.11: Mean R_a, R_p, R_v and R_{sk} values of CrN-CrN CTDRs following 2MC of ISO-18192-1:2011 testing for different traces taken across the surfaces of convex and concave components; the traces with lowest values are highlighted in green. One-way ANOVA analysis of the post-test results showed that only the changes in R_p and R_v of the concave components were statistically significant ($p<0.05$). 203

Table 4.12: Mean pre-test R_a, R_p, R_v and R_{sk} values of Si_3N_4- Si_3N_4 CTDRs for different traces taken across the surfaces of convex and concave components; the traces with lowest values are highlighted in green. One-way ANOVA analysis of the pre-test surface finish parameters showed that the R_p and R_{sk} of convex components were significantly lower ($p<0.05$) than those of the concave components. Values of the R_a and R_v parameter were not found to be significantly different between the two component groups. 204

Table 5.1: Summary of materials, generation and preparation methods for all particles used...242

Table 5.2: Summary of wear volumes and factors produced in the 6 station pin on plate wear simulator fitted with cobalt chromium wear test components. Red and black colours distinguish between the pins (red) and plates (black). 253

Table 5.3: Summary of wear rates exhibited by different bearing materials of CTDRs tested in the current study. 254

Chapter 1 : Background and literature review

1.1 Introduction

There is extensive variation in the anatomical definition of ‘neck pain’ in the literature, with over 300 case definitions used [1]. Typically, the definition of ‘neck pain’ includes or excludes the shoulder. Similarly, there are a plethora of potential causes, determinants and risk factors related to neck pain. The following sections will introduce the most common causes of neck pain, incidence and prevalence, risk and prognostic factors, and finally, the global impact of neck pain.

Neck pain is a common health problem and most people will experience some degree of neck pain in their lifetime. Vos *et al*. [2] estimated that in 2010 about 330 million people globally (4.9% of the population) were affected by neck pain. The overall one year prevalence ranged from 4.8% to 79.5% in studies documented by Hoy *et al*. [3]. While in many cases the episodes of pain are acute in nature, most run a chronic and impairing episodic course and 50% to 85% of patients will report recurring neck pain in the period of 1 to 5 years [4]. A study by Hill *et al*. [5] found that 48% of the general population who experienced neck pain at some point, reported pain of at least the same frequency one year later. Similar findings were reported by Côté *et al*. [6], whereby 37.4% of their cohort of patients experienced no change in pain over a 12 month period. It is important to highlight, that it is almost impossible to determine the proportion of patients who experienced persistent vs. recurrent neck pain, due to variable pain levels and patient perception of pain. Additionally, it is extremely challenging to compare prevalence between populations and time due to the heterogeneity of methodologies applied in studies.

There is a common agreement that many factors can influence the onset and course of neck pain. Both risk and prognostic factors can be environmental and personal in nature. There is a widespread consensus about the risk of neck pain being increased with age, with the number of incidents reported peaking at ages 35 to 49 years old [7]. Additionally, there is also consistent evidence that a younger age is prognostic for a better recovery. Results regarding gender as a risk factor often vary, however some studies suggest that men are more likely to have complete resolution of neck pain than women [8]. History of prior pain, its intensity and duration [9], prior neck injury [5], predominantly whiplash injury [10], co-morbid low back pain and other musculoskeletal problems, chronic headaches and general self-assessed poor health [11] have also been found to increase the risk of neck pain onset. A study by Kelsey *et al*. [12] suggested that smoking may also increase the risk of neck pain. Consistent evidence shows that occupation may play an important role in the likelihood of neck pain onset. Computer and office workers have the highest incidence of neck disorders with an annual prevalence of neck pain of 57% in the US, 36% in Sweden and 34% in Finland [6]. However, relatively high prevalence was also found among construction workers, nurses and armed services members in the UK [13].

Neck pain has a substantial personal and societal impact on affected individuals, their families, carers, the healthcare systems and businesses [14]. The pain can often limit the ability to perform many activities, which can result in their reduced ability to participate at work and in social endeavours [15]. With relatively high percentages of prevalence and recurrence, neck pain is one of the most common causes of work absenteeism [6,13]. Martin *et al*. [16] reported that the annual costs of healthcare related to spine problems increased between the years 1997 and 2005, however this was not reflected in improvements in health. Similarly to low back pain, chronic neck pain is often unresponsive to treatment and patients repeatedly receive inappropriate or ineffective care, which results in high direct and indirect costs of the burden of disability related to neck pain [17]. The annual direct costs of spine related problems in the US were estimated to be 193.9 billion USD between 2002 and 2004 [18]. However, neck pain was also associated with additional annual indirect costs of lost earnings (14 billion USD) [18] and worker insurance compensation claims (7 billion USD) [19].

The majority of the direct costs are related to treatment and patient aftercare. Currently, pathways of treatment include conservative methods (analgesics, physical therapy etc.) and surgical interventions (fusion, cervical total disc replacement). While fusion is the current gold standard, the cervical total disc replacement (CTDR) becomes a more popular approach in managing neck pain, which is otherwise non-responsive to conservative methods. Cervical TDR show promising short-term clinical performance results; however, long-term safety and efficacy of the technology is yet to be determined. Cervical TDR, its performance, tribology and wear in particular, will be the focus of this research.

The following sections ahead will guide the reader through the anatomy of spine, neck pain and currently available treatments, introduce CTDR, examine the biotribological considerations of such devices and introduce surface coating technologies in biomedical applications.

1.2 The spine

1.2.1 The vertebral column

The human spine is a complex mechanical structure which serves three main biomechanical functions. It protects the spinal cord and nerve roots from potential damaging forces resulting from physiological motions and trauma. Secondly, it has a weight bearing function; it transmits weight of the upper body to the pelvis. Moreover, it delivers a stable, upright torso. Additionally, it allows motion between the head, trunk and pelvis.

The vertebral column (Figure 1.1) is made up of 33 vertebrae, where 9 of the vertebrae are fused together forming a solid base in the pelvic region. The five regions of the spine and the vertebrae numbers in each of the regions are:

1. Seven cervical
2. Twelve thoracic
3. Five lumbar
4. Five fused sacral
5. Three to four fused coccyx

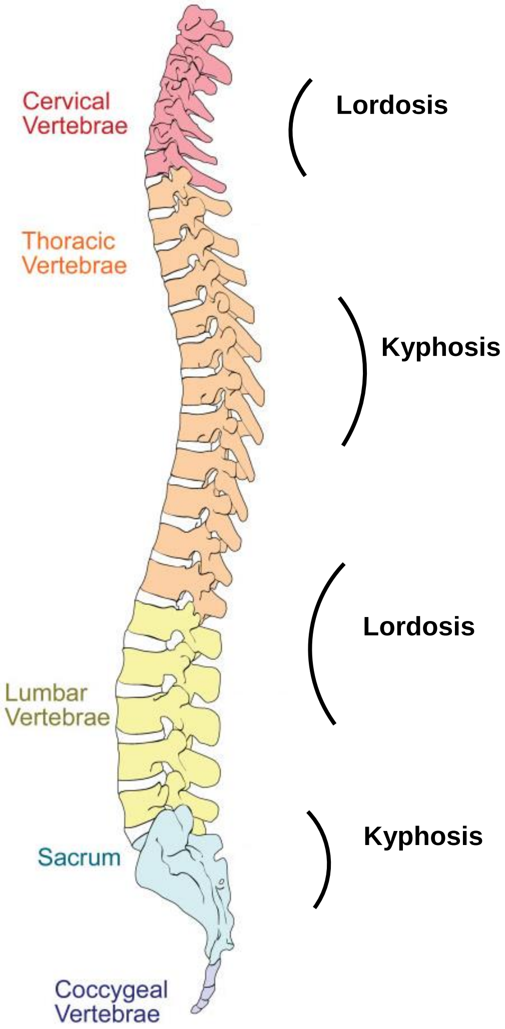
Cervical Vertebrae
Lordosis
Thoracic Vertebrae
Kyphosis
Lordosis
Lumbar Vertebrae
Sacrum
Kyphosis
Coccygeal Vertebrae

Figure 1.1: Lateral view of the macroscopic bony anatomy of the vertebral column with cervical, thoracic, lumbar, sacral and coccygeal sections and the spinal curvatures indicated [20].

Each section consists of vertebrae which are joined by ligaments, controlled by muscles and separated by intervertebral discs, and articulating (facet) joints. The spine has four curves (in the sagittal plane); the cervical and lumbar regions are convex anteriorly (lordotic), and the thoracic and sacral regions are convex posteriorly (kyphotic). The junctions between adjacent spinal regions are often sites of degeneration, due to the changes in the curvature of the spine, and high stresses being exerted at these junctions [21]. The spine can be divided into smaller motion units - functional spinal units (FSU), which consist of two adjacent vertebrae, the intervertebral disc between them, plus the adjoining ligaments but are devoid of the musculature.

1.2.2 The cervical spine

The cervical spine comprises of 7 vertebrae which begin at the base of the skull and connect to the thoracic vertebra T1. The cervical vertebrae, together with the ligaments, muscles, tendons and joints are responsible for the structure, support and stabilisation of the neck. The cervical spine maintains several crucial roles:

- Protects the spinal cord
- Provides stable support of the head
- Allows rotational and flexion/extension movements of the head
- Facilitates brain blood flow

1.2.3 Cervical vertebrae

Each of the vertebrae have similar morphologic characteristics, except for the two upper vertebrae - the atlas (C1) and axis (C2) which exhibit different morphology due to their specific function. Each vertebra consists of the anterior vertebral body (centrum) and the posterior arch (neural arch) (**Figure 1.2**). The neural arch consists of a pair of pedicles, a pair of laminae, and supports seven processes: four articular processes, which fit with adjacent vertebrae creating articular facets (facet joints), two transverse processes, which serve as the attachment site for muscles and ligaments, and one spinous process that also serves as a muscle and ligaments attachment site. The facet joints are synovial joints which during motion guide and limit motion of a FSU, in order to protect the segment from excessive flexion, extension or rotation, as well as anterior shear forces [22]. The vertebral body is the primary weight bearing area and provides the attachment site to the intervertebral disc. The facet joints allow and limit motion between adjacent vertebrae, and transmit compressive stresses resulting from bending and rotating motions.

Although the general morphology of the vertebrae is similar across the spinal column (with the exception of C1 and C2, Figure 1.3) there are regional differences with respect to the shape and size of the vertebra. Cervical vertebrae have large spinal canals, oval shaped vertebral bodies, obliquely orientated articular facets, and bifid spinous processes (with an exception of C7, which has a long spinous process similar to thoracic vertebrae, which does not bifurcate).

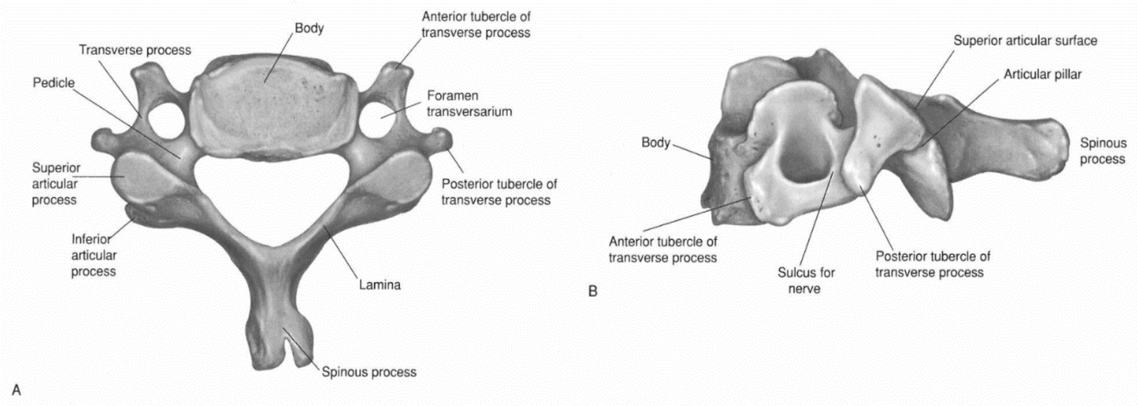
Body
Anterior tubercle of transverse process
Transverse process
Pedicle
Foramen transversarium
Superior articular process
Posterior tubercle of transverse process
Inferior articular process
Lamina
Spinous process
A
Superior articular surface
Articular pillar
Body
Spinous process
Anterior tubercle of transverse process
Sulcus for nerve
Posterior tubercle of transverse process
B

Figure 1.2: Typical cervical vertebra, A – cranial view, B – lateral view [23].

Additionally, the lower cervical vertebrae have uncinate processes, which are upward projections of the lateral edges of the vertebral body on each side. These processes create a unique connection between the vertebrae, whereby the uncinate processes contact the disc and bevelled inferolateral surface of the superior vertebra and are called uncovertebral joints or joints of Luschka (Figure 1.4). These joints can undergo degeneration and hypertrophy, which often can cause nerve root impingement [24] .The uncinate processes may or may not be removed during a total disc replacement procedure [25] (uncinatectomy). However, both finite element analysis [26] and cadaveric [27] studies showed that unilateral or bilateral uncinatectomy substantially increase level motion, load and ligament strain, especially in extension, therefore it is beneficial to preserve the uncinate joints. The vertebral bodies of cervical vertebrae are not flat; rather they form a lip that hangs downwards and forwards (Figure 1.5) in the sagittal plane. Consequently, the plane of the intervertebral discs of the cervical spine is positioned somewhat oblique to the long axis of the vertebral bodies [28].

The two most cranial vertebrae, C1 (atlas) and C2 (axis), both shown in Figure 1.3, have a unique structure and role in articulation between the head and the cervical spine. The C1 vertebra, together with the occipital bone of the skull forms the atlanto-occipital joint (AOJ) and is an additional functional part of the cervical spine. The entire occiput-C1-C2 complex is responsible for approximately 40% of cervical flexion and 60% of cervical rotation [21].

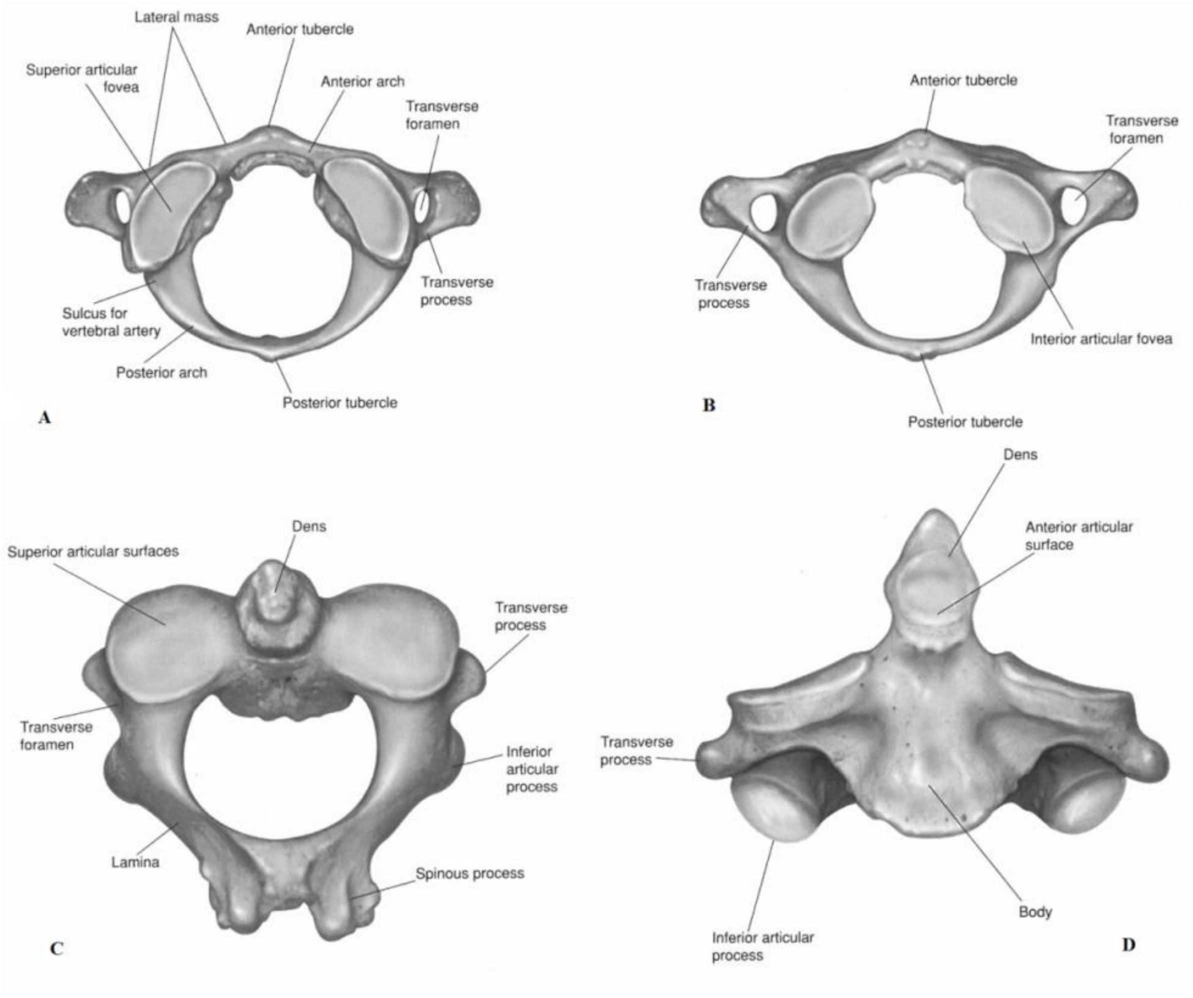
Lateral mass
Anterior tubercle
Superior articular fovea
Anterior arch
Transverse foramen
Transverse process
Sulcus for vertebral artery
Posterior arch
Posterior tubercle
A
Anterior tubercle
Transverse foramen
Transverse process
Interior articular fovea
B
Posterior tubercle
Dens
Superior articular surfaces
Dens
Transverse process
Transverse foramen
Inferior articular process
Lamina
Spinous process
C
Anterior articular surface
Transverse process
Body
Inferior articular process
D

Figure 1.3: Anatomy of C1 (atlas) and C2 (axis) vertebrae; A- Cranial view of the atlas, B – Caudal view of the atlas; C – Cranial view of the axis, D – Anterior view of the axis [23].

The outside layer of bone tissue of the vertebral body – the vertebral shell, surrounds the cancellous bone found inside of a vertebra. The inferior and superior surfaces of a vertebral body create an endplate which creates a junction with an intervertebral disc. There are substantial regional differences in mineralisation of endplates, which result in variations of their mechanical properties [29].

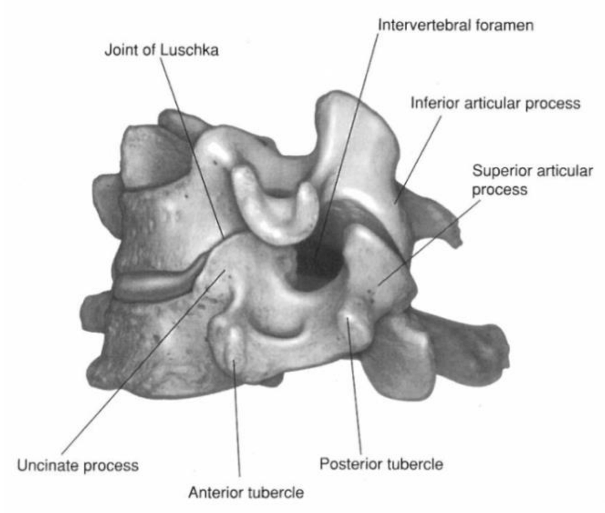
Intervertebral foramen
Joint of Luschka
Inferior articular process
Superior articular process
Uncinate process
Anterior tubercle
Posterior tubercle

Figure 1.4: Uncovertebral joints (joints of Luschka) in the cervical spine are formed largely by the lateral uncinate processes which prevent posterolateral disc protrusions [23].

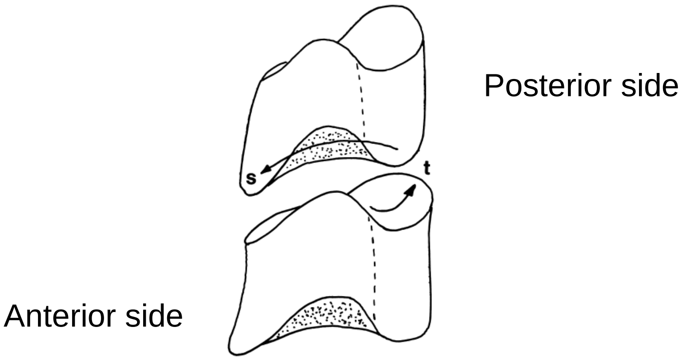
Posterior side
s
t
Anterior side

Figure 1.5: Saddle shape of cervical intervertebral joints in the sagittal plane (s). The vertebral body forms a lip; the superior surface of the lower vertebral body is concave upwards in the transverse plane (t) [28].

1.2.4 Musculature and ligaments of the cervical spine

The muscular system of the spine is complex, and its primary function is to support and stabilise the spine as well as provide movement. The muscles associated with the cervical and upper thoracic spine support movements and stability of the neck and head, allowing for all rotational and translational movement to be executed. Spinal muscles can often be a source of pain, however; muscles spasms can occur secondary to inflammation of other tissues in close vicinity, e.g. facet joints. There are 3 major groups of muscles affecting the vertebral column: a group of muscles in the anterior aspect of the torso; muscles in the posterior aspect of the torso; and the psoas and iliacus muscles, which are joined together and often called the iliopsoas muscle. In the head and neck area there are 4 major groups of muscles (some shown in Figure 1.6).

- **Cervical**– responsible for the movement of the hyoid bone and larynx during swallowing and speech
- **Vertebral, attaching to the skull** – the group comprises of several muscles responsible for the motion and stability of the head i.e. flexion, extension, rotation and bending
- **Vertebral, attaching adjacent vertebrae** – (obliquus capitis inferior muscle) connects C1 and C2 vertebrae and allows rotational movement of the head
- **Vertebral, attaching to ribs/scapula** – groups of muscles originating mainly at the lower cervical vertebrae, which help with elevating the scapula or the first and second ribs to aid breathing

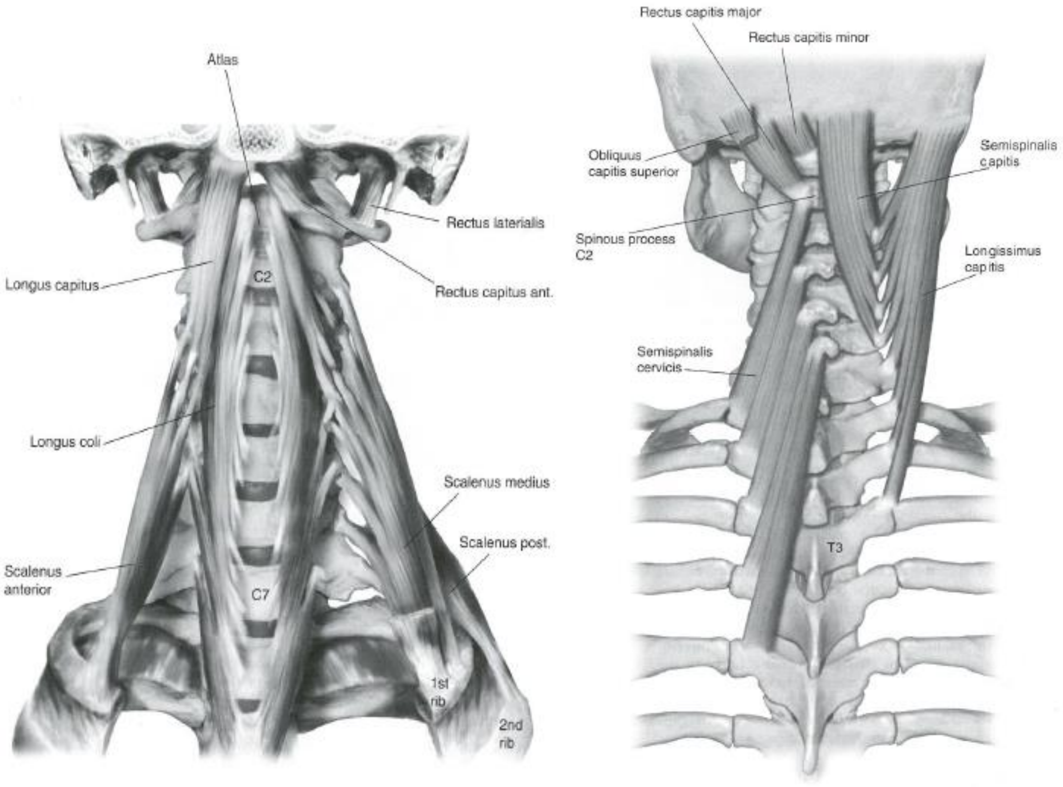
Atlas
Rectus laterialis
Longus capitus
C2
Rectus capitus ant.
Longus coli
Scalenus medius
Scalenus post.
Scalenus anterior
C7
1st rib
2nd rib
Rectus capitis major
Rectus capitis minor
Obliquus capitis superior
Semispinalis capitis
Spinous process C2
Longissimus capitis
Semispinalis cervicis
T3

Figure 1.6: A - Anterior and lateral vertebral muscles; B – Deep layer of deep dorsal cervical muscles [30].

Each FSU in the spine (including the lower cervical spine) is connected by spinal ligaments which provide structural stability and protect the neural structures through motion restriction. Additionally, the ligaments absorb energy and thus prevent injury. The ligaments are mainly made of collagen fibres, with an exception of the ligamentum flavum (LF), which is primarily comprised of elastin, which prevents buckling of the ligament into the spinal canal during extension, which could result in canal compression. Spinal ligaments are viscoelastic and exhibit non-linear elastic responses. There are two main systems of ligaments in the spine: the intrasegmental and the intersegmental. The role of the intrasegmental ligaments is to connect individual vertebrae together. The intrasegmental system includes the ligamentum flavum, interspinous (ISL) and intertransverse (ITL) ligaments. The intersegmental system connects and holds together several vertebrae, and includes the anterior (ALL) and posterior (PLL) longitudinal ligaments and the supraspinous ligaments (SSL). Additionally, each facet joint is surrounded by the capsular ligaments (CL). Ivancic *et al*. [31] measured dynamic mechanical properties of cervical spine ligaments. Peak forces at high elongation rates (723 mm/s) of the following ligaments were found to be: ALL (138 N), PLL (163N), CL (220 N), LF (244N), ISS+SSL (85N).

1.2.5 The spinal cord

The spinal cord is a long, thin bundle of nervous tissue and support cells that extends from the medulla oblongata (lower part of the brainstem) to the vertebral foramina. The lower end of the spinal cord (*conus medullaris*) is located at levels L1-L2. Morphology of the spinal cord changes at different levels; it enlarges at the cervical and lumbar levels, mainly due to the increased number of exiting nerves at these levels supplying the regions and limbs of the respective levels [32]. The spinal cord and the exiting nerve roots are covered in 3 layers (meninges) – the dura mater, the arachnoid mater and the pia mater. The most superficial layer, the dura mater extends from the foramen magnum to the S2 vertebra and has tubular prolongations along the nerve roots and the spinal nerves as they pass through the intervertebral foramina to leave the spine. The space between the dura and the periosteum (epidural space) contains veins, loose fat and areolar tissue. Beneath the dura is the arachnoid which is connected to the dura and surrounds the entering and exiting nerves and blood vessels. The most intrinsic layer, the pia mater envelops the spinal cord and the spinal nerve roots. The space between the arachnoid and pia mater – the subarachnoid space, contains cerebrospinal fluid.

1.2.6 The intervertebral disc

The intervertebral discs (IVDs) lie between two adjacent vertebrae linking their vertebral bodies together (with the exception of C1/C2 joint, as due to atypical anatomy of atlas there is no IVD between the two vertebrae). The main role of a disc is to transmit loads which arise in the spinal column through body weight and muscle activity. The intervertebral discs allow flexion, bending and torsion of the spinal column. It is commonly believed that IVDs have shock absorption abilities coming from their viscoelastic structure. However, limited numbers of experimental studies support the idea that these shock absorption capabilities exist. Combined with vertebrae and facet joints, each FSU has 6 degrees of freedom and can undergo translational and rotational motion. Size and thickness of the intervertebral discs varies depending on the location – they are approximately 3mm thick in the cervical spine and approximately 7-10mm thick in the lumbar spine [33,34]. There are three main anatomic zones in each of the intervertebral discs: the outer annulus fibrosus, the central nucleus pulposus, and the cartilage endplates located inferiorly and superiorly to the annulus and nucleus (Figure 1.7).

The annulus forms the outer boundary of the discs and consists of two regions: the outer collagenous area and the inner transitional area and there are gradual changes in composition between the two areas. The annulus consists of a series of 15 to 25 concentric lamellae [34] with collagen fibres highly orientated into parallel bundles within each lamella. The outer area comprises mainly collagen type I, while the inner area is a mixture of collagen type I and II. With disc degeneration, collagen type II will disappear in the nucleus and be gradually replaced with collagen type I [30,35] .

The nucleus pulposus is located in the centre the disc. Its extracellular matrix comprises randomly orientated collagen type II fibres [35], elastin fibres which are arranged radially [36], a proteoglycan-water gel, and some non-collagenous proteins. High concentrations of proteoglycans (which are hydrophilic) attract water and result in the swelling capacity of the nucleus [37]. The nucleus consists of 70%-90% water and the percentage decreases with age [38]. The collagen fibres are interconnected with the inner annulus fibre network, as well as the endplate.

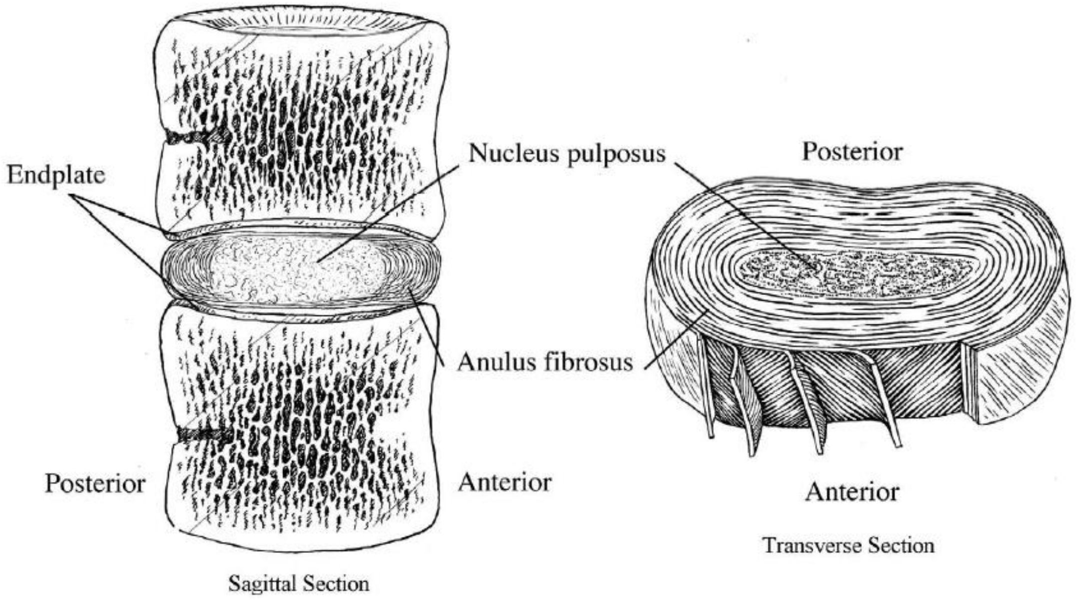

Figure 1.7:Anatomy of the intervertebral disc and its position between vertebrae [39]**.**

The endplates are located on the superior and inferior aspect of each intervertebral disc. The endplates are cartilaginous and comprise mainly hyaline cartilage which is about 1mm thick and interfaces with the disc and vertebral body. The collagen fibres in the endplates are organised horizontally and parallel to the disc and vertebral body, and some of the fibres are interconnected with the disc. The endplates serve as a semipermeable membrane, which plays a role in the diffusion of nutrients from the vertebral body to the disc, prevent bulging of the nucleus into the adjacent vertebral body as well as absorbing the hydrostatic pressure present in the spine. Moreover, it has been shown that bony part of the endplates can resist substantial axial loading [40,41], up to 1550 N [40] and its mechanical properties depend on the loading rate [42]. The intervertebral disc has few blood vessels which branch from the longitudinal ligaments adjacent to the disc. Such poor vascularisation of the disc results in poor nutrient supply to the cells present in the disc, which subsequently results in the low regenerative capabilities of the disc.

Some of the nerves present in the spinal column branch and innervate the disc. The nerves are mainly restricted to the outer lamellae of the annulus fibrosus.

It has been found that branches of the sinuvertebral nerve (branch of the spinal nerve) enter the annulus fibrosus [43].

1.2.7 Spine biomechanics

The spine is subjected to large compressive forces which can be of internal and external origin. The loads in the cervical spine are typically 3 times the weight of the head and associated soft tissues – approximately 200 N, however, depending on activity these loads can reach up to 1200 N [44]. The static loads exerted on the cervical spine arise mainly from the weight of the head and associated soft tissues, which is approximately 4.5-5 kg (~7% of body weight). The strength and load carrying capacity of the cervical spine comes only partially from the mechanical strength of the vertebrae, intervertebral discs and it is largely determined and supported by the mechanical properties of the ligaments and muscles. The weight of the body segment carried by the cervical spine is approximately 50 N [45]. In their study, Panjabi *et al.* [46] found that the average critical axial loading of the osteoligamentous cervical spine (C1-T1) was 10.5 N. It was therefore shown, that the osteoligamentous spine contributes approximately 20% of the mechanical stability, while the remaining 80% is provided by the neck muscles.

The spine is under constant compression, even in the supine position. The intervertebral disc exhibits viscoelastic behaviour, similar to many other biological tissues. The disc’s response to loading is dependent on the rate of loading and its time history. Any vertical load exerted on the FSU is distributed horizontally from one vertebra to the next through the intervertebral discs. Applied compressive loads create intradiscal pressure inside the nucleus. This hydrostatic pressure is distributed evenly in all directions across the nucleus which subsequently pushes on the surrounding annulus. As a result, the laminae of the annulus are under tensile stress. Due to disc degeneration, stress distribution in the disc changes [47]; as the hydration of the disc decreases the stresses in the collagen fibres on the annulus become compressive.

1.2.8 Spine kinematics

Each spinal unit has 6 degrees of freedom and can undergo axial, lateral and sagittal rotations, and translations. The spine can perform movements of flexion/extension, lateral bending and axial rotation (torsion). Another parameter which can characterise the kinematics is the instantaneous axis of rotation (IAR). It is an axis about which a vertebra rotates at some instance of time. In a healthy spinal unit the IAR is confined to a small area within the spinal unit. In degenerated spines the locations of the IAR can shift outside the physical space, and thus alter the biomechanics of the unit. The overall range of motion (ROM) of the cervical spine is 120° in flexion/extension, 80° in lateral bending and 140° in axial rotation [48]. While these values represent passive ROM of the segments, Cobian *et al*. [49] estimated that the majority of movements during daily activities are between 5° and 15° in flexion-extension, and less than 3% and 15% of movements exceed 50° in lateral bending, and axial rotation, respectively. Similar findings were reported by Bennet *et al.* [50], who measured active ROM during daily activities. The majority of the activities resulted in an average active ROM of 4.2°, 16.5° and 19.5° in the lateral bending, axial rotation and flexion-extension, respectively. It was also found that the majority of the tasks required a combination of movements, which shows the multidirectional nature of motions in the cervical spine. A summary of passive ROMs measured at different levels of the cervical spine is shown in Table 1.1. All the investigators works in this table analysed a single FSU or joint (AOJ or AAJ), whereas Lysell *et al.* [51] studied the entire cervical spine, hence the substantial difference in ROM reported.

The cervical spine has a unique anatomy and provides a highly mobile, functional support to the skull, while protecting the spinal cord. The vertebral motions are capable of up to six degrees freedom and their patterns are often a combination of flexion-extension, bending and axial rotation. The mechanical strength of the cervical spine comes from a combination of mechanical strength of the vertebrae, intervertebral discs and associated ligaments and musculature. Appreciation of the biomechanics and kinematics of the cervical spine is important in understanding injury and degeneration mechanisms occurring in that region of the spine. Moreover, one of the primary aims of neck pain treatments is not only to reduce the pain, but to maintain or restore the normal biomechanics and kinematics of the neck.

Table 1.1: Passive ROMs measured at different levels of the cervical spine; AOJ – atlantooccipital joint; AAJ- atlantoaxial joint.

Author	Level	ROM		
		Flexion/Extension	Axial Rotation	Lateral Bending
Panjabi et al. [52]	AOJ	23°	7°	-
Steinmetz et al. [53]	AOJ	27°	7°	-
	AAJ	10°-22°	23°-38°	-
Lysell et al. [51]	C2-C7	64°	90° ±45°	-
Goel et al. [54]	C4/C5	7.3°	3.6°	5.4°
	C5/C6	10.1°	2.8°	4.6°

1.3 Causes of neck pain

The perception of pain in the spine is related to the stimulation of pain-sensitive tissues i.e. nerves and nerve roots. However, it is often extremely difficult to clearly determine the exact origin of pain, especially with the presence of radicular pain. Additionally, many problems can manifest similar symptoms. For example, numbness in hands can be caused by both carpal tunnel syndrome, as well as cervical myelopathy [55]. The majority of pain causes are related to congenital or acquired conditions, which affect the vertebrae, intervertebral discs, ligaments, joints and paraspinal muscles. Most of the problems in the cervical spine are caused by wear and degeneration of tissues, broadly defined as spondylosis. The condition often affects the intervertebral discs, facet joints and uncovertebral joints. While the exact pathogenesis of such degeneration is still unknown, it has been suggested that it occurs due to aging or is caused by abnormal loading conditions (overloading and immobilisation).

Degeneration of the intervertebral disc is a cascade process which causes changes in the composition of the tissue, and thus its mechanical properties. The annulus can develop tears, fissures, clefts and bulges. Degeneration of the nucleus occurs due to water loss, change of structure into more collagenous and shrinkage, which in turn results in changes to the elastic modulus of the nucleus and thus altered ability to absorb and transmit posture-related changes in the pressure. Disc tears accompanied by localised displacement of disc material, which occurs beyond the limits of the intervertebral disc space are termed as disc herniation and can often cause nerve root compression and result in pain.

Degenerative changes at the intervertebral disc can also affect bones and joints. As an effect of disc bulging, the vertebrae can develop bony spurs on both superior and inferior aspects as well as on the sides. The zygapophyseal (facet) and uncovertebral joints can undergo arthritic degeneration and well as hypertrophic changes, which result in a nerve impingement. Moreover, facet joints can be affected by rheumatoid arthritis (RA), which is the most common inflammatory disorder of the cervical spine [56], and osteoarthritis (OA), which causes degeneration of the affected bones and joints.

Often whiplash injury can lead to chronic neck pain. The definition of whiplash was coined by the 1995 Quebec Task Force on Whiplash Associated Disorders (an international team of whiplash experts consisting of 18 members) as an ‘acceleration-deceleration mechanism of energy transfer to the neck which often results from rear-end or side-impact motor vehicle collision’ [57]. The impact can often result in bony or soft tissue injuries (whiplash associated disorder – WAD) with clinical manifestations including acute neck pain and stiffness, but may also encompass various neurological deficits and chronic problems such as disc protrusions and nerve root impingement [58].

1.3.1 Pathways of treatment of neck pain

1.3.2 Non-surgical approaches

Most patients with acute neck pain show improvement following a course of comfort control treatment i.e. over-the-counter analgesics, heat, cold, muscle relaxants and prescription analgesics. Patients with chronic and recurrent pain which may be caused by spondylosis should initially be considered for on-going physical therapy. Pharmacology treatments of chronic neck pain include non-steroidal anti-inflammatory drugs (NSAIDs), and neuromodulating medications. Injection therapies, including epidural corticosteroid injections provide little or no benefit to most patients, as the pain is mostly myofascial in nature. However, injections directed at the facet joints can provide both short and long term improvements. Another non-invasive method, associated with relatively good outcomes and low complication rates, is radiofrequency lesioning of nerves. The procedure interrupts nerve conduction on a semi-permanent basis. For some patients with chronic pain and pain associated problems, a combination of different therapies is more likely to be effective than one. In cases where the conservative treatment options have been exhausted, or the type and duration of symptoms match indications for surgery, such treatment routes should be followed.

1.3.3 Surgical approaches

Surgical procedures are rarely performed for neck pain alone. The pain itself results from radiculopathy, where the nerves are compressed, or myelopathy, where the spinal cord is impeded by the narrowing of the spinal canal, spondylosis or disc herniation. There are several different surgical procedures that can be performed, depending on the cause and location of the source of the pain. Based on these factors, the procedure can be performed using either on anterior or posterior approach. The posterior techniques include foraminotomy (removal of bone tissue from the intervertebral foramina), discectomy (removal of the IVD), decompressive laminectomy (removal of the disc and/or a bony spur without fusion) and fusion with various grafting materials and instrumentation. The anterior techniques include corpectomy (removal of part of the vertebral body), discectomy and fusion with bone grafting and instrumentation. One of the most common and successful surgical procedures performed in the cervical spine is anterior cervical discectomy and fusion (ACDF) [59,60], which removes a herniated or degenerated intervertebral disc and fuses the segment, restricting the motion at the affected level.

1.3.3.1 Anterior Cervical Discectomy and Fusion (ACDF)

Anterior cervical discectomy and fusion Is the current ‘gold standard’ in surgical treatments of cervical spine disorders. It is typically performed in conjunction with instrumentation systems (screws, plates, rods) and grafting materials (bone graft, bone substitute graft, cages), used to improve to the stability of the segment. The main goal of ACDF is to maintain disc height and to restrict motion by fusing the affected level, without creating further deformities. When cages, fusion plates and screws are used in conjunction with ACDF, there is a risk of stress shielding of the bone, caused by an inadequate loading of the bone required to assure bone healing (Wolff’s Law). Stress shielding may result in bone resorption causing poor bone healing at the fusion site, leading to non-union and onset of pseudo-arthrosis [61]. In order to compensate for eliminated motion at one segment, increased motions are transferred through the adjacent levels. These motions exerted on adjacent spinal units are hypothesised to accelerate the onset of degeneration in other spinal units. The phenomenon is known as adjacent segment degeneration (ASD) and can affect IVDs, facet and uncovertebral joints (Figure 1.8).

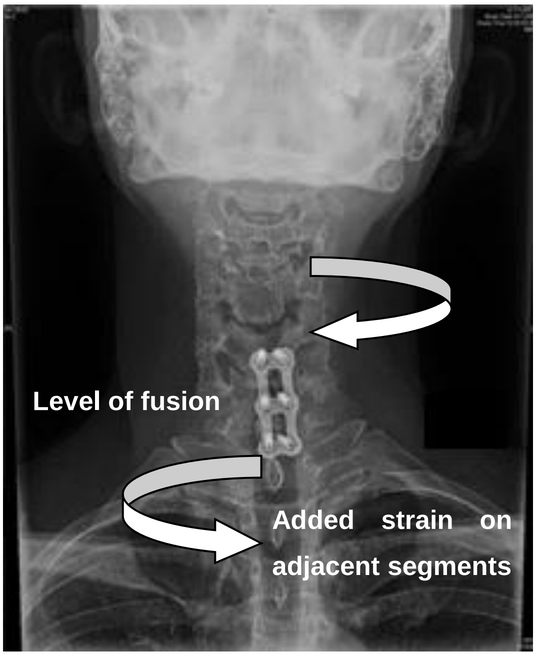

Figure 1.8: Fusion restricts motion at the affected level, which results in greater strains being exerted on the adjacent segments.

There are three distinct causes of ASD identified in the literature: the natural history and progression of the disease; altered biomechanical stresses on the adjacent level caused by fusion; and disruption of the anatomy of the adjacent level during surgery[62,63]. Goffin *et al*. [64] reported that at >5 year follow up, ASD was found in 92% of their 180 cohort patients who were treated by ACDF. The study has also shown that similar rates of degeneration were found in younger trauma-related and older non-trauma-related patients, suggesting that biomechanical impact of the interbody and the natural progression of the pre-existing degeneration may act as triggering factors [64]. While ACDF is claimed to be one of the most successful surgical procedures performed in the cervical spine [59], Hillibrand *et al.* [65] reported that in a span of 10 years, 25.6% of patients treated with ACDF developed new symptoms at the index level, and approximately 2.9% of annual reoperation rates are due to ASD. Other authors reported a 32.6% pseudoarthritis occurrence rate 1 year post operatively following treatment with an ACDF device [66].

The potential complications and the difficulties associated with the surgical procedure alone, were the primary reasons for developing an alternative treatment to ACDF. Driven by the success in motion restoration observed in total hip replacement (THR) and total knee replacement (TKR), spinal motion-retaining technologies began to emerge. The main goal of the alternative device was to maintain kinematics of the normal FSU as closely as possible, and thus to avoid the risk of adjacent level degeneration.

1.3.3.2 Total Disc Replacement

Total disc replacement (TDR) is an alternative surgical treatment to the anterior discectomy and fusion, and it is available for both the lumbar (LTDR) and cervical (CTDR) levels. The procedure removes the diseased disc and replaces it with an artificial device. TDR devices are designed to retain disc height and maintain physiological segment motion and kinematics. Currently, TDR devices, especially for use in the cervical spine, are still evolving, and therefore, the indications and contradictions for their use are not clearly defined. To date, it has been suggested that patients with radiographic instabilities, rheumatoid arthritis, osteoporosis and recent infections or osteomyelitis, should not be treated with CTDR [67]. CTDR is recommended for single level treatment at levels C3-C7. Indications for surgery are broad in the cervical spine, mainly because access is the same as with ACDF, and the procedure is considered to be less risky than at the lumbar level. However, complications, due to close the proximity of the spinal cord and oesophagus, may be of higher impact.

The surgical procedure involves a removal of the degenerated disc through a small incision in patient’s neck. Once the disc material has been removed, the intervertebral space is prepared by milling or shaping the endplates to incorporate the CTDR device. It must be ensured that as much of the disc tissue as possible is removed and the endplates are prepared in such way that the metal endplates of the disc replacement device have as much contact with the bone as possible. Once the device is placed in the disc space the otherwise retracted vertebral bodies are released, so that the disc can be firmly held in place. Improper endplate preparation, alongside poor bone quality or inadequate load distribution, can be a cause of device subsidence, which occurs in 3-10% of the cases [68]. It is also crucial that the device used has a matching endplate footprint, as under-sizing of prosthetic device may cause subsidence, loosening, heterotopic ossification and biomechanical failure resulting from an incorrect centre of rotation and load distribution [68,69].

TDR devices do not provide a shock absorbing role and introduce articulating surfaces to the spinal unit. Moreover, the natural disc exhibits non-linear resistance to torque, which depends on the angle of rotation. Such non-linear resistance to rotation is not provided by the articulating disc. It has been suggested that viscoelastic devices may replicate the natural behaviour of the disc and retain physiologic kinematics of the FSU. However, to date only two viscoelastic TDR devices have been approved for use in the European Union. The Cervical and Lumbar Freedom® Discs received their CE mark in 2009 and 2012, respectively; however the clinical outcomes evidence data is currently limited. The majority of currently approved TDRs are of the articulating bearing type, and rely on a technology based on the total hip and knee replacement, and are subject to tribological problems.

1.4 Tribology theory

Tribology is defined as the study of friction, wear and lubrication of interacting surfaces in relative motion. Friction is the resisting force to the relative motion of two surfaces which arises from fundamental electromagnetic forces between the charged particles constituting the two contacting surfaces. In all bearing systems, including total joint replacement devices, friction is undesirable as it may be indicative of wear, which results in material removal. The vast majority of problems encountered in the TJR design are tribological in nature. The design of a TJR must ensure sufficiently low wear to enable the prosthesis to operate safely and efficiently. Moreover, the friction force between the articulating surfaces should be minimised to limit potential implant fixation problems [70]. Friction and wear can be reduced by introducing a lubricant into the bearing system; however, under *in vivo* conditions the supply of the lubricant, i.e., the synovial fluid is limited.

In the natural spine, the joint connection between two vertebrae and the intervertebral disc is not a synovial joint (unlike the facet joints, which are synovial joints). There are no bearing surfaces articulating against each other enclosed within a synovial capsule. However, the design of an artificial disc replacement introduces such articulating surfaces (one or two, depending on the design) and the artificial disc is assumed to be lubricated by interstitial fluid [71,72]; therefore the following sections on biotribology, lubrication regimes, friction and wear are relevant to this research. Moreover, the TDR uses materials of much higher hardness than the natural tissues, which has an effect on the biotribology, lubrication and wear of the vertebra-disc connection.

1.5 Biotribology in Total Joint Replacement

The term biotribology was first used in 1973 by Dowson and Wright and refers to tribological phenomena occurring in the human body [73]. It encompasses the tribological processes occurring naturally in the tissues and organs, as well as the processes that may occur following implantation of an artificial device such as an orthopaedic implant. An important part of biotribology in total joint replacement relates to wear debris - their generation mechanisms, potential negative effects on an implant performance due to changes in surface morphology, and potential adverse biological reactions to wear debris and/or released ions [74,75].

Natural synovial joints are contained within a synovial membrane and the bearing surfaces (cartilage) are lubricated by synovial fluid. Following an implantation of a joint replacement blood and interstitial fluids act as a lubricant and are later replaced by synovial fluid if the synovial membrane is intact. Total joint replacement devices are passive, i.e,. there are no additional components which pump the lubricant into the system. Therefore, the bearing design of a device must allow the lubricant to freely entrain between the bearing surfaces in order to separate the surfaces, reduce asperity contact and thus reduce wear.

1.6 Lubrication regimes

Lubrication is a technique seeking to reduce wear between two surfaces sliding against each other in close proximity, by introducing a lubricant between the surfaces. The lubricant separates the materials and helps carrying load generated at the interface of two surfaces. The ratio (λ ratio) between the film thickness (h_{min}) and average surface roughness (R_a) helps to determine lubrication regime. There are three main regimes of lubrication upon which an engineering system can work: boundary, mixed and hydrodynamic (fluid film). A graphical representation characterising different lubrication regimes was introduced in the first half of the 20th century by Richard Stribeck. The plot (shown in Figure 1.9) is defined as the relationship (in logarithmic scale) between the coefficient of friction (μ) and so-called Sommerfeld number (z), which is defined as (Equation1.1):

$$z = \frac{\eta u R}{W}$$

Equation1.1

where:

η – lubricant viscosity R – radius

u – entraining speed W - load

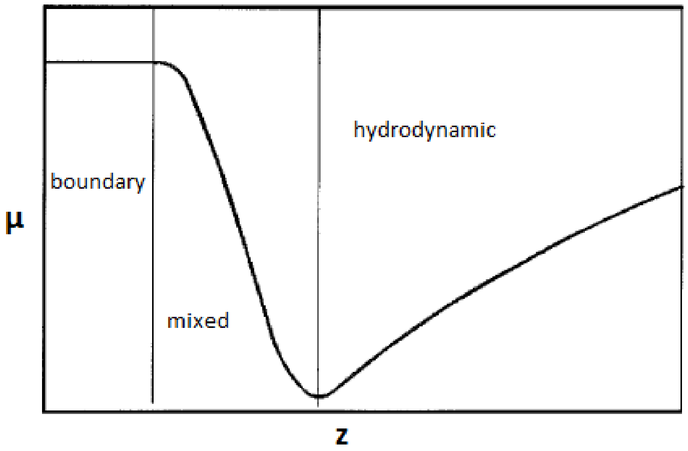

Figure 1.9: Idealised Stribeck curve. Coefficient of friction (μ), Sommerfeld number (z).

There is still no clear agreement on which mechanism is the primary one within natural synovial joints. It has been suggested that modifications or combinations of the main three regimes take place.

1.6.1 Hydrodynamic lubrication

In hydrodynamic (fluid film) lubrication regimes, the fluid film fully separates two surfaces and the λ ratio values are higher than 3. Usually a thick and continuous film is observed and the friction is determined by the rheological properties of the lubricant. The relative motion of two surfaces causes the lubricant to enter into the space between them and keeps them apart, by generating a sufficient amount of pressure within the fluid in order to sustain the load across the bearing.

Elastohydrodynamic Lubrication (EHL)

Elastohydrodynamic lubrication (EHL) is a modification of the fluid film lubrication regime which occurs in bearings of low geometrical conformities and materials which deform elastically. Due to high local pressure of the fluid, one or two of the surfaces deform, thus increasing conformity and resulting in a localised fluid film separation of the surfaces. The EHL lubrication regime has been theorised in order to explain the very low friction and wear of articular cartilage [76].

Micro Elastohydrodynamic Lubrication (mEHL)

The micro EHL lubrication model was theorised to exist in the natural articular cartilage [77]. It has been proposed that the mEHL lubrication results in the smoothing of relatively rough cartilage surfaces allowing a sufficiently thick fluid film separation.

Squeeze Film Lubrication

It has been postulated that the natural synovial joints are lubricated with the squeeze film which is replenished by the hydrodynamic action [78]. A temporary increase in pressure in the lubricant generated by two approaching surfaces, keeps the two surfaces apart. Artificial joints may also operate under squeeze-film lubrication, where a finite amount of time is required to expel fluid from between the two bearings [79].

Boosted Lubrication

The boosted lubrication mechanism, first suggested by Walker *et al*. [80] occurs when a low molecular fraction of the synovial fluid is forced into the cartilage, leaving a highly viscous, high molecular weight protein gel which protects the surfaces and is capable of carrying greater loads for a longer period of time than normal synovial fluid.

Weeping Lubrication

Investigations by Lewis and McCutchen [81] suggest that natural joints may operate under so called weeping lubrication regime, where the synovial fluid is squeezed in and out of the articular cartilage during a load bearing activity.

1.6.2 Boundary lubrication

In boundary lubrication, the film thickness is similar to the height of asperities within the surfaces which causes direct contact between the two materials. It is characterised by the absence of hydrodynamic pressure or fluid pressure. The λ ratio in the boundary regime is smaller than 1. Generally high friction and wear rates are produced under boundary lubrication conditions.

1.6.3 Mixed lubrication

The mixed lubrication regime promotes a thin and discontinuous lubrication film. Both boundary and hydrodynamic conditions may be present i.e. both direct contact and full fluid film separation of the surfaces may occur. The λ ratio values are between 1 and 3 in the mixed lubrication conditions.

1.7 Friction

The first experimental work around friction was conducted by Leonardo da Vinci in 16th century, who observed that friction is not a function of the contact area and that it is proportional to object weight. The first two laws of friction, however, were enunciated by Amonton in 1699, and eighty two years later in 1781, Coulomb proposed the third law:

1. The force of friction is directly proportional to the applied load (Amonton’s 1st Law).
2. The force of friction is independent of the apparent area of contact (Amonton’s 2nd Law).
3. Kinetic friction is independent of the sliding velocity (Coulomb's Law).

The three laws are attributed to dry or boundary lubricated conditions with low relative motion speeds. While it has been well known since ancient times that introduction of a lubricant can significantly alter the tribological properties of a relative motion of two objects, it was not studied pragmatically until the later years of 19th century.

1.8 Wear

Wear is outlined as a progressive loss of material from the articulating surface of a body occurring as a result of relative motion of the surfaces. It is a consequence of two sliding surfaces under an applied load. Archard’s wear equation [82]) shows the proportional relationship between the sliding distance (x), the load (W), the wear factor (K) and the produced wear volume (V) (Equation 1.2). The wear factor K is an experimental constant related to the hardness of the surfaces and other tribological factors such as surface roughness and type of lubricant used.

$$\boldsymbol{V = KWx}$$

Equation 1.2

Wear is a complex mechanism which can be dependent on chemical, thermal, mechanical and physical properties of materials. Useful trends with toughness, ductility, modulus, strength properties, and hardness of material have been discovered [83]. Wear tends to decrease with increased hardness of a material. Wear is a critical issue in medical implantable devices, as it leads to a significant loss of material. Moreover, produced debris may cause adverse tissue reaction around the implant, followed by osteolysis, which in turn will lead to failure of the device through loosening [84].

There are several classifications of wear mechanisms. These are based on the physical mechanism of damage, the appearance of the damage and the conditions surrounding the damage process, such as presence of lubrication, temperature etc. [83]. In many implantable devices damage occurs mainly by means of adhesive wear, abrasive wear, corrosive wear, and fatigue wear [85].

1.8.1 Fatigue wear

Fatigue wear occurs under conditions of repeated, cyclic loading and unloading. High stresses cause particles to be removed from the surface as a result of formation of surface or sub-surface cracks. These cracks are formed at weak and imperfect areas of the surface, where the shear stresses are at their highest, depending upon the geometry of the materials. As the cyclic motion continues, cracks grow and propagate through the material, causing it to fracture and wear debris to be formed. Fatigue wear can be a serious problem in polymer components used in total joint replacement [86].

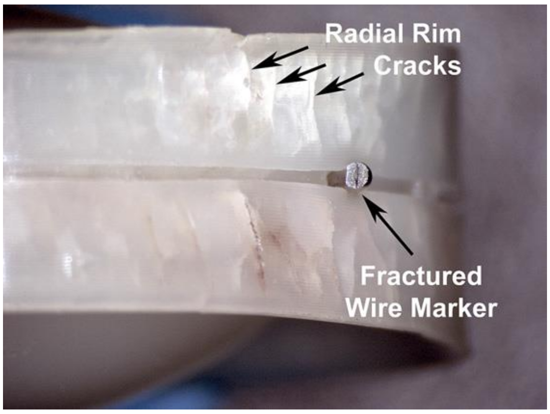

Figure 1.10: Edge view of an ultra-high molecular weight polyethylene (UHMWPE) core from a lumbar total disc replacement component. Radial cracks of the rim were caused by fatigue [86].

1.8.2 Corrosive wear

Corrosive wear is observed when chemical or electrochemical interaction occurs between the environment and one or both of the surfaces. The wear rate depends upon the environmental conditions affecting the chemical reactivity of the surfaces [87,88]. This type of wear is important for biomaterials and the extremely harsh environment of the human body in which they are functioning. Surface oxidation is the most common corrosion process. This type of wear can be reduced by decreasing the oxidation rate, increasing the critical oxide thickness, raising the fracture toughness and microhardness of the oxide, or by coating a metal with an inert substance that does not undergo oxidation.

1.8.3 Adhesive wear

Adhesive wear occurs when two surfaces are brought together and slide against each other under a load. During the relative movement asperities of the two surfaces are in contact and undergo deformation. The number of such asperity-to-asperity junctions is determined by the surface roughness of both surfaces. A bond may be formed between the surfaces in contact, which is stronger than the intrinsic strength of the weaker material. When the relative motion between two surfaces continues, the weaker of the materials fails and material is transferred to the contacting surface. It is recognised that this occurs due to a fatigue process on a microscopic scale. During the relative motion the deformation of asperities goes from elastic to plastic when the shear stress exceeds the yield strength of the asperities. Adhesive wear damage is mainly caused by the fracture transfer of material at the asperitiy contact junctions (Figure 1.11). When two dissimilar materials (with regards to hardness) are in contact, it is usually the material of lower hardness which generates wear debris – in total joint replacement, adhesive wear debris is generated mainly from polyethylene bearings [89]. Adhesive wear can be reduced by increasing hardness or work hardenability, introducing a low coefficient of friction coating, reducing the tendency of the surfaces to cold weld, providing sufficient lubrication, or by providing a smoother surface finish.

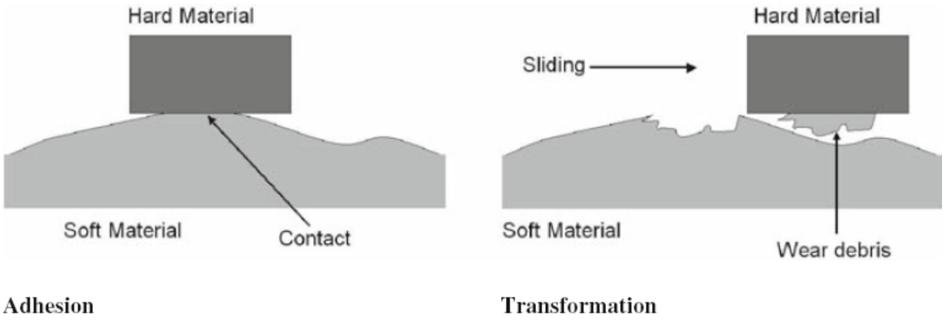

Figure 1.11: Schematic representation of adhesive wear [90]**.**

1.8.4 Abrasive wear

Abrasive wear is result of hard particles and protuberances indenting or cutting a groove in a softer material. Abrasive wear can be divided into two-body and three-body wear mechanisms. In two-body wear asperities or particles which are attached to one of mating surfaces are the source of wear damage. Three-body wear is caused by hard particles that can freely move between two mating surfaces, as they are not fixed on to either of the surfaces. Differences between the two and three body wear is shown in Figure 1.12. In total joint replacement, surgery generated particles of bone, bone cement or metal, can be a source of three-body wear.

Abrasive wear can be subdivided into low and high stress. Low-stress abrasion occurs due to relatively light rubbing of abrasive particles on the surface of the material. The criterion for low-stress abrasion is that the forces must not exhibit the level in which the abradant particles are damaged. Wear scars will show scratches and a minimal deformation of the subsurface. High-stress abrasion occurs under a level of stress that is high enough to crush the abrasive. Another type of abrasive wear is polishing wear. This form of abrasion is extremely mild and surfaces which have been subjected to polishing are usually smoothed and brightened. The hardness of the material is one of the major factors in the resistance to abrasive wear; however, other properties such as yield strength, elastic modulus, fracture toughness, composition and microstructure play an important role in improving abrasive wear resistance.

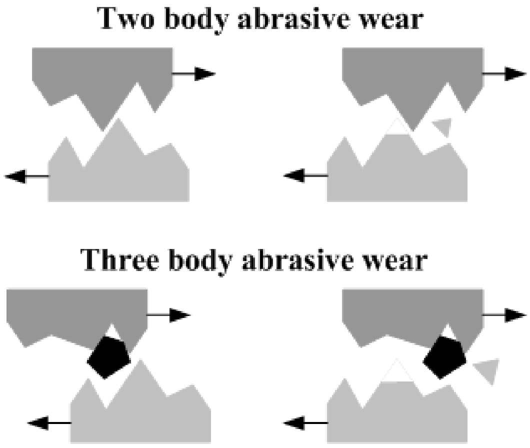

Figure 1.12: Differences between two- and three-body abrasive wear [91]**.**

1.9 Cervical Total Disc Replacement

The success of total joint arthroplasty and complications associated with the ACDF, such as adjacent segment degeneration, has led to research and development of an alternative surgical treatment for degeneration in the cervical spine, which preserves motion in the affected segment – cervical total disc replacement (CTDR). The first ball-in-socket CTDR device was designed in 1980s by Cummins *et al.* [92]. Since then, a number of devices have evolved and undergone several design iterations. The cervical disc replacement is a relatively new technology; constant progress is being made in an effort to improve the safety and efficacy of the new devices. At the time of writing, seven CTDR devices have received approval by the Food and Drug Administration (FDA) for marketing in the U.S in one-level applications. A summary of the main design features and characteristics of the FDA approved CTDRs can be found in Appendix I. While the Bryan (Medtronic Sofamor Danek USA Inc.), Mobi-C (LDR Spine USA Inc.), PCM (NuVasive Inc.), Prestige LP and Prestige ST cervical discs (Medtronic Sofamor Danek), ProDisc-C total disc replacement device (Synthes Spine), and Secure-C (Globus Medical Inc) have been approved for single-level arthroplasty, the Prestige LP and Mobi-C have also gained approval for use at 2 levels.

1.9.1 Materials design considerations

The main goal of the CTDR is to retain disc height and to maintain motion in the FSU as close as possible to that observed in the natural joint. Hallab *et al.* [93] identified material optimisation criteria for use in CTDRs. These included preservation of kinematics and biomechanics, disc height retention, biocompatibility, reliability and durability of the materials.

Stainless steel is the most inexpensive and readily available biomaterial. Medical grade stainless steel (316L) has a long, successful record of use in a variety of orthopaedic implants. While its ductility is superior to other metals used in orthopaedic instrumentation, stainless steel is less corrosion resistant than comparative metals, which has a negative impact on the overall biocompatibility of the material [94]. The Prestige ST device is constructed of two articulating stainless steel components.

Cobalt-chromium medical alloy (CoCr) is one of the most commonly used biomaterial in total joint replacement, due to its superior mechanical properties. Wear properties of cobalt-chrome are superior to those of both titanium and stainless steel, however it has been shown that the wear particles generated by cobalt-chrome bearings can have cytotoxic effects on cells in the tissues in close proximity to the implant [95]. Cobalt chrome endplates, coated with titanium porous coatings, are used in the ProDisc-C total disc replacement device.

Titanium alloys are prominent as dental and orthopaedic materials due to their strength-to-weight ratio, relatively low elastic modulus, excellent corrosion and fatigue resistance and biocompatibility. The major drawback of titanium alloys is their poor wear resistance; therefore, they are not widely used as bearing components. Titanium ceramic composites (Ti_6Al_4V + 10% TiC), were introduced as bearing materials in the design of the Prestige-LP. Moreover, titanium has been widely used as a porous coating, as it promotes bone ingrowth (e.g. the Bryan, Prodisc-C, Prestige LP and Secure-C discs). Titanium endplates are also used in the Bryan cervical disc prosthesis implants.

Ultra-high molecular weight polyethylene (UHMWPE) is broadly used in total joint arthroplasty as a bearing material. It exhibits low friction when coupled with suitable metal alloy and can be easily machined or moulded into desirable shapes. There are major concerns associated with the use of UHMWPE bearings related to relatively high concentrations of wear particles produced by the material. Wear debris generated by UHMWPE is considered to be the main cause of osteolysis-induced implant loosening [96]. The design of the ProDisc-C, PCM, Secure-C and Mobi-C devices include a UHMWPE core, which allows articulation of the CoCr endplates. The Bryan cervical prosthesis design incorporates a polycarbonate-polyurethane (PCU) core articulating against titanium endplates. PCU is widely used in medical applications and has excellent biocompatibility. Its viscoelastic properties are superior to those of UHMWPE, and for this reason, it is used in lumbar dynamic pedicle screw devices, as well as in cervical arthroplasty.

1.9.2 Biomechanical design considerations

The biomechanics of CTDR devices are complex due to the multidirectional nature of the motions in the cervical spine, 6 degrees of freedom motion and the interaction between other spinal level via the muscular, facet and ligamentous systems. The main goal of a CTDR device is to preserve motion at the index level, and prevent the development of ASD. Critical design factors, such as the position of the centre of rotation, level of constraint and bearing surface geometry, must be taken into consideration during the design and development of a CTDR implant.

The instantaneous axis of rotation (IAR) is not a fixed point, rather its position changes throughout the physiologic range of motion (ROM). In the lower cervical spine (C5-7) the position of the IAR can be estimated to lie just posterior and inferior to the centre of the caudal vertebral end plate. In the middle cervical segments (C4-5), however, the mean IAR deviates more posteriorly and caudally, relative to the disc space (Figure 1.13-A). This is caused by more variable physiologic characteristics of the facets in the upper cervical spine. While the segmental arc of motion in the upper cervical spine is flatter, due to the facets being positioned more horizontally, in the lower cervical segments the more vertical nature of the facets results in a sharper arc of motion. By superimposing radiographic tracings of a vertebra moving from full extension to full flexion the position of the IAR can be determined (Figure 1.13-B). Restoring the centre of rotation is extremely important in maintaining natural joint kinematics. It has been found that abnormal positioning of the IAR following the lumbar TDR, may result in increased stress exerted on the ligaments and facet joints, which in turn can cause pain and degeneration of said joints [97].

Constraint in the CTDRs can be defined as the limitation of pure A-P or lateral translational intervertebral motion [98]. While an unconstrained device allows for unrestricted multidirectional motions, a fully constrained device permits purely uniplanar motions (i.e. rotation), without any translation. Less constrained devices (e.g. the Bryan cervical disc) result in the restoration of the position of the natural IAR during motion and thus closely mimic physiologic motion. On the other hand, more constrained designs (e.g. the ProDisc-C and PrestigeST) were found to reduce shear strain transmission to the facets, which is hypothesised to reduce or even prevent the development of ASD [98].

The geometry design of the articulating surfaces determines the degree of constraint and centre of rotation of the device. The ball-and-socket designs (e.g. the ProDisc-C) have a predetermined centre of rotation, positioned at the centre of the conceptual sphere of the convex surface. Designs incorporating a mobile core (e.g. the Bryan cervical disc) have a variable position of the centre of rotation. The latter are considered to be more forgiving of surgical errors and less precision in the placement of the device is necessary, in order to replicate the physiologic centre of rotation. A ball-and-trough design (e.g. the PrestigeST) features a greater radius of curvature in the sagittal place and thus allows for some translational motion during the extremes of flexion and extension.

Figure 1.13: A - Mean instantaneous axes of rotation for each motion segment of the cervical spine depicted with a dot. Two standard deviation range of distribution is located within the enclosed circles shown. B - The position of IAR can change position during motion and can be determined by superimposing tracing of a vertebrae in full ROM [28].

1.9.3 Clinical results

A review of reports of FDA IDE trials for each of 7 available devices, showed that CTDRs are becoming a safe and effective alternative to ACDF in selected patients [99–116]. Each study followed strict inclusion and exclusion criteria and was based on the primary hypothesis of noninferiority, i.e., that the overall success rate of the investigated device was statistically noninferior to the rate of the control group (ACDF). The secondary hypothesis investigated superiority, i.e., that the overall success rate of the investigational group was statistically superior when compared to the ACDF group. A summary of the results can be found in Table 1.2. Overall, the results of the trials were assessed based on the improvement of the neck disability index (NDI); neurological success, defined as a maintenance or improvement of 3 neurological parameters – motor, sensory and reflexes, rate of secondary surgeries; and overall success, defined as absence of adverse events related to the treatment, improvement of NDI by at least 20% or 15 points; improvement or maintenance of neurological parameters; and no removals, reoperations or additional fixation required to modify the implant.

The Prestige-ST cervical disc system was the first CTDR implant to be approved by the FDA (July 2007), and it is also marketed in Europe via a CE

Mark (approved since 2006). The design of the device comprises a stainless-steel metal-on-metal (MoM) bearing couple. A prospective, randomised, nonblinded study was conducted under an approved IDE trial [99–101]. Additionally, a multicentre, randomised trial was carried out across 4 sites in Europe and Australia [102]. The most recently published, 7 year follow-up results of the FDA IDE trial reported by Burkus *et al.* [101], which was conducted at 32 investigational sites and involved 541 patients randomly assigned to CTDR group (276 patients) and ACDF (265 patients), showed that the NDI scores were noninferior, when compared to the control group, whilst the remainder of the parameters showed superiority of the investigational group.

The ProDisc-C, comprising of a metal-on-polyethylene (MoP) bearing (CoCr and UHMWPE), received its FDA approval for marketing in the U.S in 2007. In 2005 the implant was also cleared for marketing in Europe, after receiving the CE Mark. The device has undergone a randomised, multicentre IDE trial [103–105] prior to FDA approval, in which the clinical outcomes were compared against the ACDF control. Patients in the study were randomised and blinded to the treatment they received, until shortly after the surgery. A total of 209 patients (103 ProDisc-C and 106 ACDF) were enrolled at 13 investigational sites. Only the occurrence rate of secondary surgeries was found to be significantly lower than in the ACDF group, whilst the remaining outcomes – NDI score, neurological success and overall success were found to be noninferior in the CTDR patient group.

The Bryan cervical disc obtaine the CE mark registration in September 2000 and was later approved by the FDA for marketing in the U.S in May 2009. The device is made from a titanium endplates and polycarbonate uretahne nucleus. A prospective, randomised, multicentre study of surgical treatment with the Bryan and ACDF was conducted under an approved IDE trial [106,107,117]. A total of 263 patients (242 patients treated with Bryan disc and 221 with ACDF) treated at 30 investigational centres were assessed. The IDE study was initially designed to last 48 months (however additional follow up was requested by the FDA); as a result, not all centres participated in the 4 year follow up. Patients were nonblinded and randomised prior to the surgery, which resulted in several patients withdrawing from the study, mainly in the ACDF group.

The Secure-C MoP (CoCr and UHMWPE) cervical disc obtained FDA Premarket Approval (PMA) in 2012, following a successful IDE clinical trial [108,109], which included 380 patients from 18 investigational sites. Of the cohort, 89 nonrandomised and 151 randomised patients were treated with Secure-C disc and 140 patients received an ACDF device.

The Porous Coated Motion (PCM) received the CE Mark in 2002 and was also approved by the FDA in 2012. The device design incorporates a MoP (CoCr and UHMWPE) bearing. A total of 416 patients were recruited for a prospective, randomised, multicentre study conducted under an IDE trial [110,111], however only 403 were treated (218 patients received the PCM disc and 185 were treated with ACDF). The 5-year follow up study reported on 163 PCM-treated and 130 ACDF-treated patients.

The Mobi-C is the first device to receive CE Mark (in 2004) and FDA market approval (in 2013) for two-level treatment of radiculopathy or myeloradiculpathy that is unresponsive to non-surgical treatment. The device incorporates a mobile, MoP (CoCr and UHMWPE) bearing. A controlled, randomised FDA IDE trial was conducted across 23 clinical sites and involved 245 patients, who were randomised into two treatment groups and remained blinded to the treatment until after the surgery [112–114]. At the five year follow up the results of 164 patients who received the Mobi-C disc and 81who were treated with an ACDF device, were reported.

The Prestige LP device consists of a MoM (titanium ceramic composite). It received its FDA approval in 2014. A prospective multicentre, nonrandomised IDE trial [115,116] followed 280 patients who were treated with the Prestige LP disc and 265 control patients, who received ACDF treatment. The treatment group achieved superior neurological and overall success scores and noninferior NDI scores.

Table 1.2: A summary of main outcome characteristics of the 7 FDA-approved CTDR devices for a single-level treatment compared to ACDF control groups; NDI – neck disability index; RCT – randomised controlled trial

Device (approved in)	Study design	NDI	Neurological success	Secondary surgery	Overall success
Prestige ST (2007)	RCT	Noninferior	Superior	Superior	Superior
ProDisc-C (2007)	RCT	Noninferior	Noninferior	Superior	Noninferior
Bryan (2009)	RCT	Superior	Noninferior	Noninferior	Superior
Secure-C (2012)	RCT	Noninferior	Noninferior	Superior	Superior
PCM (2012)	RCT	Superior	Noninferior	Noninferior	Noninferior
Mobi-C (2013)	RCT	Noninferior	Noninferior	Superior	Noninferior
Prestige LP (2014)	Non-RCT	Noninferior	Superior	Noninferior	Superior

1.9.4 Wear in total disc replacement

Similarly to total hip and knee replacements [118], wear and wear debris are hypothsised to play a key role in the long term success outcomes of TDR. The numbers of long term outcome reports and studies documenting wear characteristics of the CTDRs (*in vivo)* are limited. For this reason, cases and studies covering wear in lumbar TDR will also be included in this section.

A number of studies have conducted analyses of failed devices retrieved from patients, in effort to study potential reasons of failure. Seven explanted lumbar MoM (CoCr) devices (Maverick™) examined by Kurtz *et al*. [119] were found with scratches; however no macroscopic evidence of plastic deformation, 3rd body wear, burnishing, pitting or fracture was found. The primary wear mechanism was microabrasion. Consistely across all 7 devices, smokey, hazy discolouration, which was determined to be carbo- and oxygen-rich films, were noted. Similar discolourations have been found previously in CoCr MoM hip implants [120]. Tissue analysis found no tissue discolouration; however necrotic bone, bone marrow and dense fibrous connective tissues were found. Focal microscopic metallic debris was infrequently observed. Metallic debris was not found in a uniform distribution throughout the samples, unlike in the Prestige-ST CTDRs, which are made from stainless steel [121].

Similar surface damage on disc replacement devices were reported by other authors [122,123]. Out of 29 analysed ProDisc-C implants (MoP), 96% had signs of impingement, 86% burnishing of the CoCr endplate and 17% on the UHMWPE insert. Mild burnishing, scratching and pitting of the insert were also reported. Wear patterns on the insert were asymmetrical; dome regions of the inserts showed some wear and slight deformation, while the rims were largerly unremarkable. Out of all investigated devices, 21% of the implants had signs of 3rd body wear. Twenty Prestige-ST explants were examined by Kurtz *et al*. [119] and found to have signs of microabrasion on their surface. Slight discolouration and evidence of anterior impingement were found in 69% of the examined samples, which despite different device design, is similar to the findings reported by Lebl *et al.* [122,123].

In THR and TKR it is not uncommon for wear and wear debris to induce osteolytic processes of the bone in the vicitnity of the implant [84]. Despite limited numbers of long-term results of the TDR devices, several cases and studies report similar reactions. A case of cervical osteolysis following implantation of the ProDisc-C, revised at 15 months postoperatively, was documented by Tumialan *et al.* [124]. Signs of progressive osteolysis around the keel of the superior endplate were found. Product examination did not show implant damage. The osteolytic processes were stopped after explantation, and the authors hypothesised that an immune-mediated osteolytic process was the most likely cause. Additional case studies of wear-related osteolysis found in the lumbar TDR are reported in the literature [125,126]. A study by Cunningham *et al.*[127], which included an animal model and some retrievals, showed that very small quantities of titanium wear particles (comercially available titanium powder, 1-5µm dia.) elicted osteolytic type responses in the vicinity of the implant. Following the experience of THR and TKR technologies, it can be expected that as more patients receive treatment involving TDR devices and the currently existing data will become of long-term significance, more cases of osteolysis will be reported.

Several reports documented abnormal inflammatory reactions and pseudotumours formations due to reactions to metal on metal (MoM) TDR. Guyer *et al.* [128] reported on three case reports and one case series involving one CTDR and three LTDR devices. Upon revision, thick soft tissue extending into epidural space was found. Histology revealed avascular hyaline tissue with lymphocytes and macrophages and eosinophilic granules. The cervical device was found with visible blackening of the tissue; however no third-body metal debris were observed on the surfaces of the implant. Similar findings were reported by Cavanaugh *et al.* [129]. Upon revision of a failed cervical MoM deivce, a large, yellowish necrotic tissue, extending into the epidural space was found. Histology revealed necrotic hyaline tissue with lymphatic predominant chronic inflammation. No intra- or extracellular metal wear debris found despite electron microscopy used in the analysis; nonetheless cellular patterns were found to be similar to those surrounding failed MoM hip devices. Kurtz et al. [119] have also found characteristics of inflammatory respose in their histological analysis of tissue samples found around failed cervical MoM devices. Lagier *et al.* [130] reported a case of delayed hypersensitivity and allergic reaction in an individual implated with a Mobi-C device, however no detailed histology analysis was performed.

Further issues with MoM TDR devices (Maverick) were reported by Berry *et al.* [131]. A case of an iliac vein occlusion and epidural cauda equina compression was documented. Histology revealed a granulomatous mass with diffuse metallic wear debris particles. Another failed Maverick device reported by Francois *et al.* [132] caused gross metalosis. The device was removed 12 months postoperatively due to persistent pain. Presence of metal debris in the periprosthetic tissue generated by a cervical MoM device was also reported by

Kurtz *et al.* [119]. Additionally, focal metalosis, uniform tissue discolouration and fibrous tissue were found.

To date the numbers of case reports documenting *in vivo* wear, and wear-related failures are limited. However, it is expected that as the number of patients treated with CTDRs will continuously increase and more long-term studies will be published over time. Longer term follow up of TJR has highlighted the role of wear particles in the failure process of both metal-on-polyethylene [133] and metal-on-metal prostheses [74,134]. Therefore, it is necessary to assess the wear of TDR devices *in vitro* in order to compare wear rates and the volume of debris to those found in the clinical setting.

1.10 Wear testing of CTDRs

Two internationally recognised testing protocols have emerged for wear assessment of cervical disc replacement: ISO 18192-1 [135] and ASTM F2423-11 [136]. The kinetic motions adopted by both the ISO and ASTM standards are a sinusoidal approximation of the loads exerted in the spine. The ISO 18192-1 input motions run concurrently, those in the ASTM standard allow the user to input the test motions sequentially, or in any chosen combination.

The two standards specify suggested ROM and total annual excursion to be applied during testing. A summary of those inputs is shown in Table 1.3. The motions defined by the ISO standard lead to cross-path motion for both lumbar and cervical test conditions [137]. Both standards recommend regular assessment of the bearing surfaces and produced wear debris at each million cycle over a continued testing period of $10x10^6$ cycles. It is believed that 10^6 cycles are an equivalent of one year *in vivo* wear [49], and similar conversion is widely used in THR wear assessment testing.

Table 1.3: Range of motion and total excursion after 10^6 cycles as specified per the ISO 18192-1 and ASTM F2423-11.

Standard		Flexion-extension (FE)	Lateral bending (LB)	Axial rotation (AR)	Load (N)
ISO 18192-1	ROM (°)	±7.5	±6.0	±4.0	±150
	Annual excursion (x10^6 cycles)	30	24	16	
ASTM F2423-11	ROM (°)	±7.5	±6.0	±6.0	+150/-50
	Annual excursion (x10^6 cycles)	30	24	24	

A comparative study of the ISO 18192-1, ASTM F2423-11 and observed daily motions in the cervical spine [49] determined that the annual excursion was higher than those specified in the ISO standard; the observed-to-standard ratios were 1.22, 1.09 and 1.04 for the FE, LB and AR respectively. Motions are more frequent than the million cycles per year specified. The amplitudes of motions were smaller than specified in the ISO standard. *In vivo* movements were found to be more frequent but of lower amplitude. It has been suggested that for the wear assessment in the cervical spine to be clinically relevant, the number of cycles should be $3x10^6$ to $5x10^6$ times per year in each axis [49]. Simulator tests of the Bryan cervical disc [121] produced significantly more wear; the reported wear rate of 0.57mm^3/million cycles was approximately 5 to 10 fold higher than those found in explants. Such differences are likely to be caused by differences in the implantation time of the retrieved components. Kurtz *et al.* compared Prestige-ST components tested in the spine simulator (non-standard test protocol) to retrievals [138]. The main wear mechanism *in vivo* was found to be abrasive wear, with components worn more posteriorly than anteriorly. Wear scars and mechanisms were similar to those tested in the simulator; however, retrieval wear was not as severe as *in vitro* tested samples. The average surface roughness for *in vivo* components was measured to be 0.12±0.1µm, whereas in the simulator tested samples it was 1.4±1.0µm. Similarly, the waviness within the wear scar was significantly greater in the simulator tested components. Higher wear rates were reported during the coupled AR/LB sequence of the test. It was hypothesised that due to the ball-in-trough design of the bearing, which is more conforming in the coronal plane than in the sagittal plane, higher wear rates during the AR/LB coupled motions are due to the predominance of sliding, whereas during the FE motion rolling contact dominates. Anderson *et al.* [121] who also tested the Prestige-ST implant reported the wear rate of 0.18mm^3/million cycles. Additionally, they found that components tested for only 0.3 million cycles produced much higher wear than in a device explanted from a patient after 39 months i.e. an equivalent of 3.25 million cycles of simulator tests. Such findings are consistent with those reported on the Bryan cervical disc device [121], despite minor differences in test conditions. The loads and ROMs applied in the testing of both of the devices were within the range specified by both ISO 18192-1 and ASTM F2423-11, which may suggest that such test inputs are not clinically relevant, probably significantly overestimate wear *in vivo* and require further investigation and possible revision.

Comparison between *in vitro* simulator studies and retrievals [139,140] found that abrasion on the simulator tested samples was more severe than those observed *in vivo*. Like Anderson *et al*. [121] Kurtz *et al.*[139] and Siskey *et al.* [140] hypothesised this was due to short implantation times. Siskey *et al.* [140] tested metal-on-metal Prestige-ST devices only over 1 million cycles, and found that the wear results were very similar to those found *in vivo*. Surface roughness of simulator tested samples was also comparable to those of explants i.e. 0.16±0.07µm and 0.12±0.08µm, respectively. The wear scar area was greater in the simulator tested components, which suggested that the ROMs applied in the ISO standard are more extensive than those experienced *in vivo*. The wear tracks on the PrestigeST implants suggested a curvilinear motion pattern, unlike the asymmetrical pattern found in the ball in socket design of the ProDisc-C [141].

To date, there are a few reports in the literature investigating the size of UHMWPE particles produced in simulator-tested TDR device and no studies report on the characteristics generated from MoM TDRs. ProDisc-C implants tested for 10 million cycles and under conditions specified by ISO 18192-1 were found to produce particles of mean particle size ranging between 0.17 and 0.35 µm [142]. Similar findings were reported by Bushelow *et al.* [143], whereby 90%

of the particles generated by simulator-tested ProDisc-C devices were of submicron size and the mean size ranged from 0.22 to 0.37µm. Hyde *et al*. [144] found that all UHMWPE particles generated from a lumbar disc replacement device, (Prodisc-L) tested under the ISO protocol, were submicron in size. These particles were of similar size to those previously found in THR and TKR [145] and within the range of 0.1-1.0µm, which are the most biologically active, in terms of production osteolytic cytokines [133,146].

In vitro simulator studies published in the literature often do not use testing protocols that comply with the ISO or ASTM standards. This may be due to questionable clinical relevance of the test parameters specified by the standards. Increased guidance on testing protocols is required; these include standard and adverse conditions. It is important to validate clinical relevancy of the testing protocols against *in vivo* evidence. So far, some discrepancies between *in vivo* and *in vitro* results have been reported. These differences may be caused by selection bias, in that the explanted devices are from failed arthroplasties which display features such as high wear that form a part of the failure scenario.

1.11 Tribological coatings

Tribological coatings are defined as coatings of sufficiently thin thickness, so that the properties of the substrate material play a role in the tribological and friction performance. Typical thickness of tribological coatings ranges between 0.1 and 10 µm [147]. Tribological coatings are used to modify the physical and chemical properties and morphology of a surface, and are used in diverse technological applications, orthopaedic implants being one of them. Surface properties of biomedical implants are critical not only to the lifetime, but most importantly, to the safety, efficacy and biocompatibility of a medical device. As a result, biocompatible coatings of high hardness, resulting in low friction, improved wear and corrosion resistance have obvious applications in orthopaedics.

A tribological coating is expected to meet certain design requirements, including the following:

1) The lifetime of the coating must be longer than the required implant lifetime and estimated with certain probability.
2) The wear of the coated surface and the counterface must not exceed certain values specified by the design.
3) The initial coefficient of friction, steady-state coefficient of friction and the friction instability must not exceed certain values specified by the design.

1.11.1 Deposition processes

A wide variety of deposition techniques are currently available and used across different industries, however, there are many that are at a developmental stage and not available commercially. Matthews [148] proposed a general classification of deposition techniques, dividing the processes into four categories, depending on the state of the depositing phase:

1) Gaseous state processes
2) Solution state processes
3) Molten or semi-molten state processes
4) Solid state processes

The gaseous state processes include techniques in which the target material passes through a gaseous or vapour phase prior to being deposited on to the substrate. The main generic classification of gaseous state processes include ion implantation (II) and beam assisted deposition (BAD), which by applying a high-energy beam energy the ions to a sufficient energy level to become embedded within the surface; chemical vapour deposition (CVD), in which the source of coating species comes from gaseous reagents; and physical vapour deposition (PVD), whereby at least one of the coating species is evaporated from a solid target within the coating chamber. The PVD process is often utilised to deposit coatings used in orthopaedic applications, therefore the following sections will cover this subject in more detail.

1.11.1.1 Physical Vapour Deposition

Physical vapour deposition (PVD) processes form coatings through evaporation or atomisation of a material from a solid source. Historically PVD was used for metallic coatings only; however, with technology developments, ceramic materials can also now be deposited by using ceramic sources or a combination of metal sources and reactive gases in the deposition chambers. In general, PVD methods are categorised into three groups, based on whether the target material is removed through the transfer of kinetic energy (sputtering group), by input of thermal energy (evaporation group) or in a hybrid process of thermal evaporation and sputtering (ion plating group). Several different variants of the three methods of atomisation methods exist. The various PVD techniques can be altered by the addition of plasma within the deposition chamber, which results in improved film nucleation and growth kinetics of the process.

The basic plasma assisted (PA) PVD processes include reactive sputtering (RS) and activated reactive evaporation (ARE). In the ARE technique the metal ions are produced when the source evaporates after being heated up by thermionic electron beam, a plasma electron beam, resistance heating or arc heating. Rapid development of plasma-assisted thin film coatings in recent years has been caused largely due to the availability of new deposition methods and processes, which can provide enhancements to morphology, structure, composition, adhesion, and cohesion of a coating. Several new or advanced PVD technologies have emerged in recent years, including atomic layer deposition (ALD), glancing angle deposition (GLAD), filtered cathodic arc deposition, vacuum polymer deposition (VPD) and high-power impulse magnetron sputtering (HiPIMS). While the principles of most of these processes have been known for over 70 years, their development and scaling up have been limited and delayed, due to slow advances of technologies involved in the processes, such as high-current and high-voltage power supply technology, process control and related electronic technologies, plasma physics and chemistry and vacuum technology.

1.11.1.2 High Power Impulse Magnetron Sputtering

Magnetron sputtering, a type of PVD deposition method, is a plasma based technique, in which a magnetic field is applied to trap electrons in the vicinity of the target, in order to increase the degree of ionisation. The number of sputtered atoms depends upon the amount of inert gas ions which bombard the target surface. The supply of the inert gas can be increased by increasing ionising collisions of neutral gas atoms with electrons. Such increased ionisation confined within the region near the target surface can be promoted using the magnetic field. The concept of a magnetron is shown in Figure 1.14, while a schematic diagram of a HiPIMS deposition chamber is shown in Figure 1.15. The confined electrons continually create ions out of the inert gas, and subsequently bombard the target surface, consequently increasing the sputtering rate. In magnetron sputtering the degree of ionisation of the plasma particles is relatively low [149], which results in a low total flux of ions involved in film growth on the substrate. The degree of ionisation can be increased by applying high bias voltage (up to the magnitude of several thousands of volts).

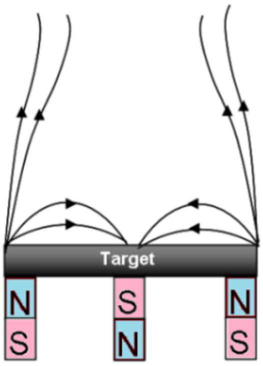

Figure 1.14: Basic concept of a magnetron; S and N relate to the South and North poles of the magnets, respectively.

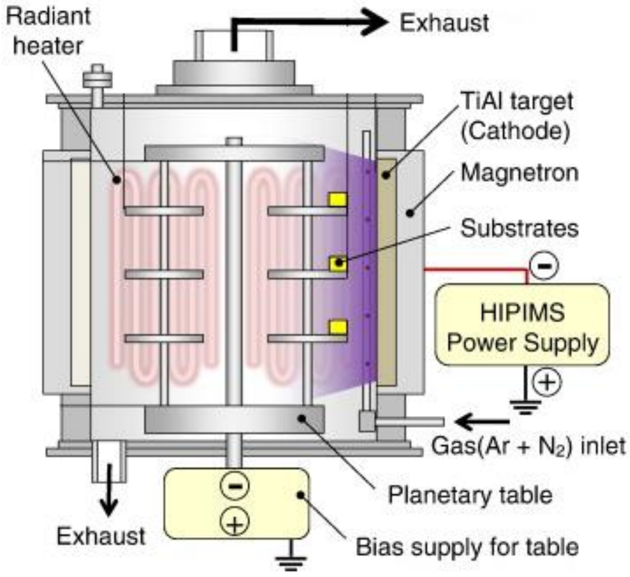

Figure 1.15: Schematic diagram of a simple HiPIMS deposition chamber (adapted from [150]).

In 1999 Kouznetsov *et al*. [151] proposed a high power pulsed operation of the sputtered target, showing an increased total ion flux and a sputtered material ionisation of approximately 70%. The new deposition method was called High-Power Impulse Magnetron Sputtering (HiPIMS) and was patented in the US in 2001. The HiPIMS method utilises high power density (500 – 2000 W/cm^2), short impulses (in the order of microseconds) at low duty cycles (0.5 – 5%) [152], which allows the target material to cool down during the ‘off’ period and for the process to maintain stability. The plasma in HiPIMS is generated by glow discharge, while the discharge voltage is maintained at several hundred volts. The main advantages of HiPIMS are high density plasma and high ionisation fraction of the sputtered vapour, which results in better control of film growth. The coating deposited by HiPIMS has high density morphology, has a potential to produce defect-free films and has an increased ratio of hardness to Young’s modulus, which is a measure of the toughness properties of the coating.

1.11.2 Tribological coatings for biomedical applications

In vivo wear performance of medical implantable devices is paramount to their longevity. Wear particles generated *in vivo* may cause an adverse tissue reaction around the implant, followed by osteolysis, which in turn will lead to failure of the device through loosening. Wear and wear related damage is a common failure cause of total joint replacement prostheses [153,154].Therefore, low friction and wear rates are desirable for articulating surfaces for load-bearing implants. With the decrease of popularity of MoM devices, tribological coatings may provide favourable combination of material durability and wear performance and without having a negative impact on the biocompatibility of the device. The tribological performance of medical alloys can be improved using surface engineering treatments such as nitrogen ion implantation, ceramic coating deposition or diamond-like carbon film formation. Moreover, delamination resistance and coating adhesion of the tribological coatings are very important. The following section will give a brief overview of several tribological coatings proposed for joint replacement implant applications.

Diamond-like Carbon coatings

Diamond-like carbon (DLC) coatings can consist of different forms of amorphous carbon, which display some of the characteristics of diamond. They can be deposited by using different coating technologies and various process parameters can be optimised in order to produce the most suitable coating for a given application. The coating can be deposited with and without hydrogen, alloyed and doped with additional compounds, and with a variable sp^2/sp^3 ratio (ratio of different types of atoms hybridisation). It has been shown that properties like electrical conductivity [155,156]; mechanical hardness and ductility, surface energy [157] and bacterial suppression [158] of the coating, can be altered by alloying or doping with various elements. As a result of its improved tribological and mechanical properties [159], good corrosion resistance, bio- and haemocompatibility [160,161], DLC coatings have emerged as a promising material for medical applications. To date, several cardiovascular, dental and orthopaedic devices coated with DLC are available on the market. The load bearing joint replacement devices include hip, knee, metatarsophalangeal, and spinal disc (both lumbar and cervical) implants. The *in vitro* simulator tests of the hip, knee and spinal disc implants have shown promising, significant decrease in wear volumes, when compared to other, commercially available material combinations, such as uncoated CoCr and alumina[158,162–167]. Although the tests showed superior tribological performance of the DLC coated implants, the test approaches and protocols applied in the studies differ from one another, and rarely comply with any of the internationally recognised standards (ISO, ASTM). Additionally, any *in vitro* results require *in vivo* validation, which, particularly for the orthopaedic devices, are sparse. A limited number of publications on *in vivo* performance of DLC coated implants are available. Maestretti *et al.* [168] and Benmekhbi *et al.* [169] published studies on the development of cervical disc replacement devices (BAGUERA® and DiscMaxxC®, respectively), both coated with commercially available coating - Diamolith™. Nonetheless, no detailed medical follow-up studies involving these implants are available in the literature. A series of DLC coated titanium femoral heads articulating against UHMWPE cups [170], and DLC coated CoCrMo metatarsophalangeal prostheses [171] were found to have high failure rates. The failure of both devices was associated with delayed delamination of the coating caused by crevice corrosion of the silicon interlayer [172,173].

Ceramic coatings

Titanium nitride (TiN) ceramic coatings are extremely hard and often used to harden and protect cutting and sliding surfaces. In the biomedical industry, TiN coatings are often deposited on medical grade titanium alloy (Ti6Al4V), in attempt to improve its poor wear performance, which is the major disadvantage of the material. Another common ceramic coating used in biomedical applications is chromium nitride (CrN), which is extremely hard and corrosion resistant. Both coatings are typically deposited by various PVD techniques. Titanium nitride achieved promising results in *in vitro* tests, including hip simulator tests when articulating against UHMWPE inserts [174], however some *in vivo* failures occurred [175]. Explant analyses of failed TiN coated femoral heads showed discolouration and delamination of the coating [175,176]. Moreover, voids in the coating and TiN wear fragments in the periprosthetic tissues were found. Clinical studies conducted by Massoud *et al.* [177] showed increased numbers of femoral head loosening in the TiN-coated group than in the CoCr control group at a 26 months follow-up.

Commercially, CrN coatings deposited via PVD are used to enhance the mechanical and tribological properties of forming and machining tools made from high speed steels and cemented tungsten carbide [178] . When CrN was compared with TiN and DLC coatings, it was shown that the CrN and DLC coatings had superior tribological properties and exhibited significantly lower wear rates [179–181]. Application of CrN coatings for carpometacarpal joint replacement application showed significant reduction of mean volumetric wear, as well as the amount of metallic debris produced [182]. Moreover, it was shown that CrN-coated THR implants exhibited superior wear properties when compared to uncoated devices [183]. However, it was noted that adverse testing conditions (edge loading) of MoM implants, as well as insufficient adhesion and coating defects, such as droplets, can affect the performance of ceramic coatings [184]. When CrN was used in MoP hip design, significant reduction of volumetric wear and metal ion release was shown [185], under both standard and adverse conditions where 3rd body wear particles were introduced.

Recently a new ceramic material (in both bulk and coating form) has been proposed for load bearing joint implants. Owning to its superior mechanical properties, excellent biocompatibility and low wear rates, silicon nitride has recently been introduced into the biomedical field. Synthetic silicon nitride (Si_3N_4) was first developed in 1895; however it was not used commercially until the 1980’s, when it was introduced for use in internal combustion engines and high-temperature gas turbines. Current uses of Si_3N_4 include high-performance bearings, turbine blades, ball bearings and glow plugs; these applications require a material with a high fracture toughness, strength and low wear properties. The Si_3N_4 ceramics present a favourable combination of mechanical, tribological, chemical and thermal properties that make them suitable for components requiring high performance in severe environments. As a consequence, silicon nitride ceramics have been proposed as an alternative structural material [186,187] or as tribological coatings [188–190] for joint replacement load bearing components. Furthermore, silicon nitride and its particles have been shown to dissolve in polar solvents, such as water [191,192], phosphate buffered saline, blood, serum [193] and gastric acid [194]. As a result, it has been suggested that wear debris produced by Si_3N_4 bearings may dissolve over time *in vivo*, and thus reduce the adverse biological responses in periprosthetic tissues, and consequently increase longevity of implants. Recent assessments of the tribological properties of silicon nitride coatings resulted in similar to bulk Si_3N_4 coefficients of friction. Ball on disc testing of different silicon nitride coatings [188,190] resulted in a coefficient of friction which ranges between 0.12 and 0.22, as reported by Olofsson *et al*. [188] and 0.1 and 0.3 as reported by Pettersson *et al.*[190]. One of the coatings tested by Olofsson *et al.* [188] demonstrated coefficient of friction of 0.45; however the sample had high surface roughness, which, most likely, was a result of high target power used in the deposition process of this sample. Olofsson *et al*. [188] also assessed the coating adhesion properties, utilising scratch testing. The results showed poor coating adhesion, with all but one samples failing upon the tip engagement, resulting in zero coating adhesion results were found by Pettersson *et al.* [190]; all the coating samples delaminated during friction testing. Low wear rates and coefficients of friction demonstrated by both bulk and coating forms of silicon nitride, among other favourable features of the material, such as mechanical properties and biocompatibility, suggest the potential of the material for use in bearing surfaces of total joint replacements. Current biomedical applications of bulk Si_3N_4 include cervical spacers and spinal fusion devices, which achieve successful short-term results [195]. Moreover, silicon nitride fixation plates and screws, as well as bearings for spine disc surgery, total hip and knee replacement have also been developed [196,197].

Clearly, biotribological performance of cervical total disc replacement devices is still not fully understood. Moreover, the wear debris produced by the devices has not been fully characterised and biological responses to the debris has not been studied in detail. With early reports on wear-induced inflammatory responses and metalosis [119,121,128,132], there is a clear need for further investigations. Additionally, as new biomaterials and coatings become available, and their potential for improving tribological performance and biocompatibility of the wear require further studies. This literature review has provided the background for the studies performed within this thesis.

1.12 Aims and Objectives

In total joint replacement, the assessment and understanding of the biotribological performance of a device can help predict and gain insight into its performance *in vivo*. In the current work, a MoM CTDR design was developed and tested *in vitro.* Both chromium nitride and silicon nitride coatings were proposed for CTDRs applications, as an alternative to the currently available MoP devices and as a comparison group to the MoM design.

The primary aim of this study was to investigate the biotribology of a novel design of cervical total disc replacement device in its pristine form and coated with chromium nitride or silicon nitride, in order to understand the influence of loading conditions upon the tribological performance of the implant, and to investigate biological effects of the wear debris produced by the implants. These aims will be achieved via a number of objectives:

- To investigate the effect of disc design on the theoretical maximum pressure and predicated lubrication regime of CTDRs, by applying the Hertzian contact model. All theoretical calculations and subsequent physical testing to be conducted based on and using a generic CTDR device designed by the author.

- To investigate the mechanical properties of the chromium nitride and silicon nitride coatings deposited on flat coupons through series of bench tests evaluating Young’s modulus, hardness, surface roughness, scratch resistance, chemical composition and thickness of the coatings.

- To determine the effect of bearing material on the tribological performance of coated and uncoated CTDR devices by performing an *in vitro* wear study in the six-station spine simulator and assessing wear rates produced by pristine and coated CTDRs.

- To investigate the effect of loading and kinematic conditions applied on the tribological performance and wear modes and patterns exhibited by the CTDR devices through application of different loading regimes used in simulator testing: as per standard ISO-18192-1:2011 [135] and a modified version of the standard protocol.

- To characterise the wear debris and to determine the biological responses of primary porcine dural fibroblasts and murine fibroblast cell lines to the wear debris generated from uncoated and coated devices, and assess the dose-dependent effects on the cell viability to the debris, by co-culturing cells and wear particles and employing ATP Lite assays over a period of 6 days to evaluate cell viability.

The following chapters of this thesis will take the reader through the work undertaken by the author in order to fulfil the aims outlined above. The studies (as shown in Figure 1.16) were divided into themes: theoretical prediction of maximum contact stress and lubrication regime; coating characterisation; wear performance; and biological consequences of wear. It was considered that potential clinical success of the device proposed in this study would be multifactorial and mainly comprise of these four aspects.

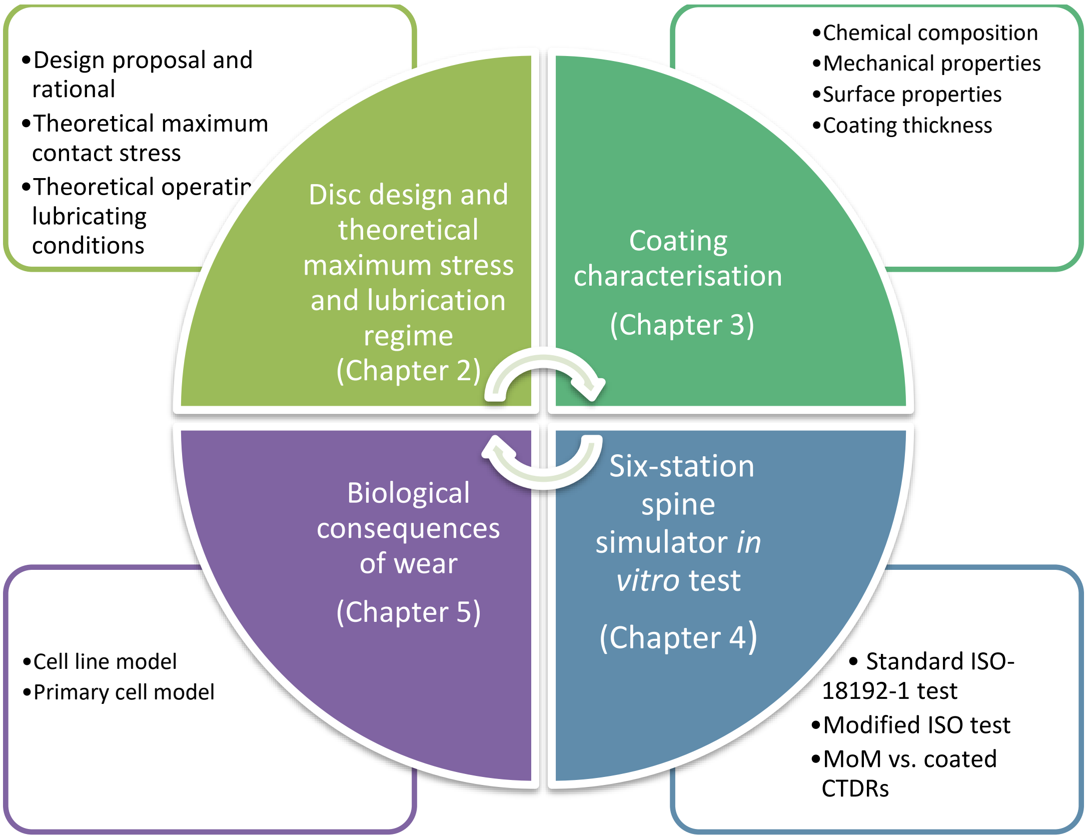
•Design proposal and rational
•Theoretical maximum contact stress
•Theoretical operatir lubricating conditions
Disc design and theoretical maximum stress and lubrication regime (Chapter 2)
•Chemical composition
•Mechanical properties
•Surface properties
•Coating thickness
Coating characterisation (Chapter 3)
Six-station spine simulator in vitro test (Chapter 4)
• Standard ISO-18192-1 test
•Modified ISO test
•MoM vs. coated CTDRs
Biological consequences of wear (Chapter 5)
•Cell line model
•Primary cell model

Figure 1.16: Summary of the studies performed in each chapter. The experimental work has been divided into 4 parts which investigated coating properties, theoretical analysis of maximum stress and lubrication regime, *in vitro* wear performance and potential biological consequences of wear.

Chapter 2 : Design of a generic cervical metal-on-metal Total Disc Replacement

2.1 Rationale and aims

One of the aims of this project was to investigate wear and wear debris produced by metal-on-metal (MoM) and ceramic-coated (silicon nitride and chromium nitride) cervical disc replacement systems. To ensure a high level of validity and comparable results, it was deemed necessary to design a generic CTDR device that could be used across all tribological testing methodologies.

Overall, the design of the generic CTDR device was based on other implants available commercially (Appendix 1). Ranges of sizes, bearing geometries and clearances have been reviewed and considered by the author (Chapter 1, section 1.9). The final geometry design has been closely based on a mid-size ProDisc-C device, which has shown successful clinical performance. The MoP bearing has been replaced by a MoM bearing or a ceramic-coated surface.

All devices were designed and manufactured to ensure identical size, shape and surface finish. The first section of this chapter will guide the reader through the design of the novel MoM CTDR, the initial inspection of the machined devices. The following sections will investigate the design and bearing material implications on the theoretical lubrication regime and theoretical maximum contact stress exhibited by the device.

2.1.1 Material selection

The main goal of the CTDR is to retain disc height and to maintain motion in the affected segment as closely as possible to the natural joint. Hallab *et al.* [93] identified materials optimisation criteria for use in CTDR design. These included the ability to preserve kinematics, biomechanics and height of the disc, biocompatibility, reliability and durability of the materials. The majority of the currently available CTDRs are based on metal-on-polyethylene bearing material combination, with the metal components primarily being made of cobalt-chromium alloys, while the polymeric portion is made of ultra-high molecular weight polyethylene (UHMWPE). While such a combination exhibits low friction [93] there are major concerns associated with the use of UHMWPE, which are related to relatively high concentrations of wear particles produced by the material. Wear debris generated by UHMWPE is considered to be the main cause of osteolysis-induced implant loosening [198]. Recent studies, including CTDR [124] and LTDR [125,126] devices have reported signs of osteolysis following implantation of metal-on-polyethylene artificial disc devices. While to date the number of similar reports documenting *in vivo* wear, and wear-related failures are limited, it is expected that as the number of patients treated with CTDRs continues to increase, more long-term studies will be published over time.

Cobalt chromium molybdenum (CoCrMo) alloy is one of the most commonly used biomaterials in TJR, due to its superior mechanical properties [199]. Wear properties of CoCr are superior to those of other metal biomaterials (stainless steel and titanium) [199], however, a growing body of evidence suggests that wear particles and ions generated by cobalt chromium bearings can have cytotoxic effects on cells in tissues in close proximity to the implants, which can lead to hypersensitivity and pseudotumour formation [95].

While excessive wear can be prevented with adequate material selection and operating lubrication regime, another method of decreasing wear is the use of tribological coatings. In the past, CoCr substrates, used in TJR applications, have been successfully coated with DLC, CrN as well as Si_3N_4 and have shown superior tribological properties, when compared to uncoated controls or the same coatings deposited on titanium substrates [180,181,187,200].

The current study investigated an all metal CTDR device comprised of two cobalt chromium endplates; two variants of the device were investigated – pristine and coated with one of two tribological coatings – chromium nitride or silicon nitride. For the purpose of tribological assessment, two sets of components were manufactured – uncoated cobalt chromium components acting as control group and coated components acting as the investigative group. Both coated and uncoated components were based on the same generic CTDR design.

2.1.2 Endplate size and shape

The endplate shape and size were considered not to be an important factor in the design in this study, as this was not expected to have an effect on the wear performance of the device. While the effects of mismatch in endplate footprint and vertebral body size have been previously highlighted in the literature [68,201], investigation of potential subsidence or fixation issues were not considered as objectives of this project. For this reason, the endplates were designed to have a simple rectangular shape. The endplate dimensions and bearing radius chosen for the device used in this study were based on medium/large size equivalents of other CTDR devices currently approved by the FDA. The comparison of the main design features of the FDA approved devices and the one designed for the purpose of this study is shown in Table 2.1.

2.1.3 Fixation

The fixation method was not considered an important factor of the design as component fixation was not part of any of the investigations conducted in this study. The primary investigations revolved around the bearing surfaces and their tribological performance. For this reason, a simple tapered keel has been designed to assist in device fixation and removal (for measurements timepoints) from fixtures made from Erthacetal®H resin.

2.1.4 Bearing surface

The bearing surfaces of the device were designed as a simple ball-in-cup type of articulation, similar to the one seen in ProDisc-C device. The convex side of the bearing was placed on the caudal endplate, while the concave on the cranial endplate. The radii used in the design were selected such that the height of the device was similar to those found in other CTDR devices (Table 2.1). The design of bearing surfaces of the device specified a surface finish of R_a 0.01-0.05μm. Such surface roughness is in accordance with requirements for metal-on-metal hip replacement implants specified by ISO-7206-2:2011 – '*Implants for surgery -- Partial and total hip joint prostheses -- Part 2: Articulating surfaces made of metallic, ceramic and plastics materials'* [202] .

Table 2.1: Main design characteristics, including sizes and range of motion of the currently FDA-approved CTDR devices.

Brand name	Endplate size	Disc height	Range of motion		
			Flexion/Extension	Lateral Bending	Axial rotation
Bryan	14-18mm dia	6mm	±11°	±11°	7°
PrestigeST	12x17.8mm	6mm	±10°	±10°	Unconstrained
ProDisc-C	12x15mm,14x15mm, 14x17mm,16x17mm, 16x19mm,18x19mm	5-7mm	±20°	±20°	Unconstrained
Secure-C	11x12mm,13x14mm, 14x16mm,15x18mm	6-11mm anterior side 7-12mm posterior side	±15°	±10°	Unconstrained
Mobi-C	13x15mm,13x17mm,14x15mm,14x17mm,15x15mm,15x17mm	5-7mm	Information unavailable	Information unavailable	Unconstrained
Generic CTDR design (this study)	14x17mm	7mm	±17°	±17°	Unconstrained

2.1.5 Radial clearance and bearing radius

The radii of the convex and concave components were chosen such that the radial clearance was in the range of 0.150 and 0.175 mm. The radii of the convex and concave components were design to be 6.45 and 6.30 mm, respectively. Clearances ranging between 0.05 mm and 0.2 mm have previously been used in studies investigating lumbar total disc replacement devices, such as ProDisc-L [71,203,204]. Moreover, clearances of 0.1 mm and 0.15 mm have been used for hip and wrist implants [205,206].

2.1.6 Contact stress analysis

Investigation of the maximum contact stress and lubrication regimes for MoM and ceramic-coated CoCr cervical total disc replacement devices was carried out. The analyses provided an additional rationale for the design of the device, as well as determined likely lubrication operation conditions of the devices. Additional insight into how the theoretical lubrication regime and maximum contact stress can be affected by changes in the radial clearance and type of the surface material, was investigated.

Contact mechanics investigates deformation of solid bodies, which contact each other at one or more points. The theoretical calculations allow determining stress-strain state near the contact region, which depends upon the shape of the body, material properties and loading conditions applied.

The Hertzian theory, used in the current analysis, focuses mainly on non-adhesive, fully elastic sphere-sphere contact geometry and its main assumptions were:

- Each body can be considered an elastic half-space
- The surfaces are frictionless
- The contacting bodies are made of isotropic and homogenous materials
- The strains are small and within the elastic limit
- The surfaces are continuous and non-conforming i.e. the contact radius is significantly smaller than the radii of curvature of the contacting bodies

The theoretical lubrication regime prediction used in this chapter was based on the determination of the lambda ratio (λ ratio), which is based upon the relationship between the film thickness and the average surface roughness. There are three main regimes of lubrication upon which an engineering system can work: boundary (indicated by $\lambda<1$), mixed (true for $1<\lambda<3$) and hydrodynamic (determined by $\lambda<3$) (see section 1.6).

2.2 Materials

2.2.1 Machining and component inspection

Total disc replacement components, convex and concave plates, were machined from a low carbon < 0.14% (w/w) CoCr alloy (ASTM-F1537) supplied by Peter Brehm GmbH (Weisendorf, Germany). Eighteen convex and eighteen concave parts were machined. The dimensions and geometrical tolerances of the components are shown in Figure 2.1 and Figure 2.2. All components were later polished by Mrs. Jane Cardie (Technician, School of Mechanical Engineering) and finished to an R_a of <0.05µm. Once polished, 12 convex and 12 concave components were shipped to IonBond Ltd. (Olten, Switzerland), where they have undergone physical vapour deposition (PVD) coating process; six were coated with silicon nitride (using HiPIMS PVD) and the other six with chromium nitride (n=6). Following the coating process, samples were re-polished manually at IonBond.

All components (coated and uncoated) were inspected for their geometry, bearing surface radius, radial clearance and surface roughness. The bearing radii, as well as the width and length of the endplates, of both convex and concave components were determined using Legex 322 Coordinate-Measuring Machine (CMM) (Mituyoto, Andover, UK). The CMM was fitted with PH6M probe head (Mituyoto, Andover, UK) and TP7M probe module (Mituyoto, Andover, UK). Measurements were taken using a 1mm diameter stylus (A-5000-3551) (Mituyoto, Andover, UK). A two-dimensional contacting profilometer, (Talysurf PGI 800) used in surface roughness assessment was supplied by Taylor Hobson (Leicester, UK). The methodology and results of the surface roughness inspection of the pristine and coated CTDRs is presented in Chapter 4.

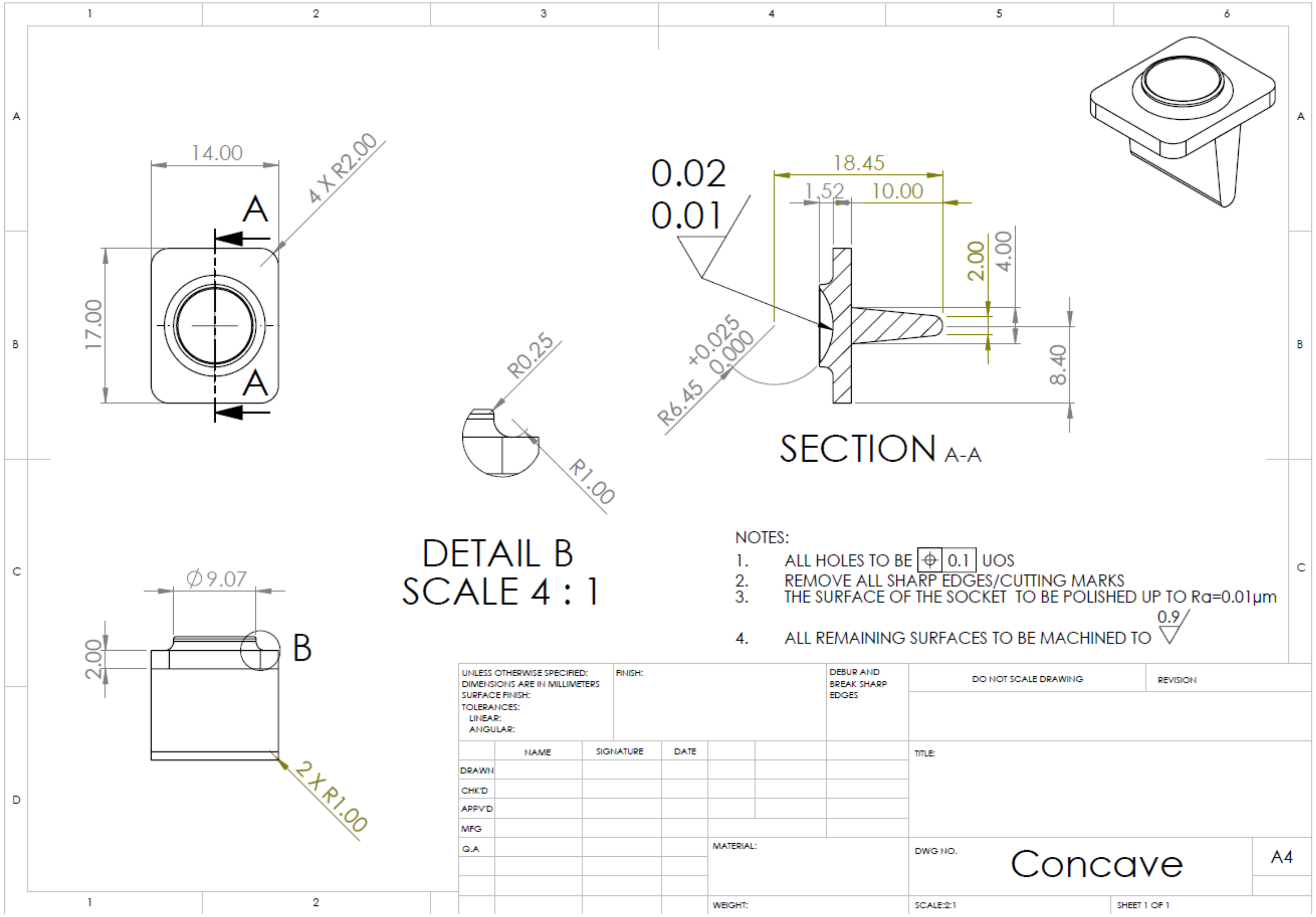
14.00
4 X R2.00
A
A
17.00
R0.25
R1.00
DETAIL B
SCALE 4 : 1
0.02
0.01
18.45
1.52
10.00
2.00
4.00
+0.025
0.000
R6.45
8.40
SECTION A-A
Ø9.07
2.00
B
2 X R1.00
NOTES:
1. ALL HOLES TO BE ⌖ 0.1 UOS
2. REMOVE ALL SHARP EDGES/CUTTING MARKS
3. THE SURFACE OF THE SOCKET TO BE POLISHED UP TO Ra=0.01µm
4. ALL REMAINING SURFACES TO BE MACHINED TO 0.9
UNLESS OTHERWISE SPECIFIED:
DIMENSIONS ARE IN MILLIMETERS
SURFACE FINISH:
TOLERANCES:
LINEAR:
ANGULAR:
FINISH:
DEBUR AND BREAK SHARP EDGES
DO NOT SCALE DRAWING
REVISION
NAME
SIGNATURE
DATE
DRAWN
CHK'D
APPV'D
MFG
Q.A
MATERIAL:
WEIGHT:
TITLE:
DWG NO.
Concave
A4
SCALE:2:1
SHEET 1 OF 1

Figure 2.1: Dimensions and geometrical tolerances speficied for the concave components of the CTDR device.

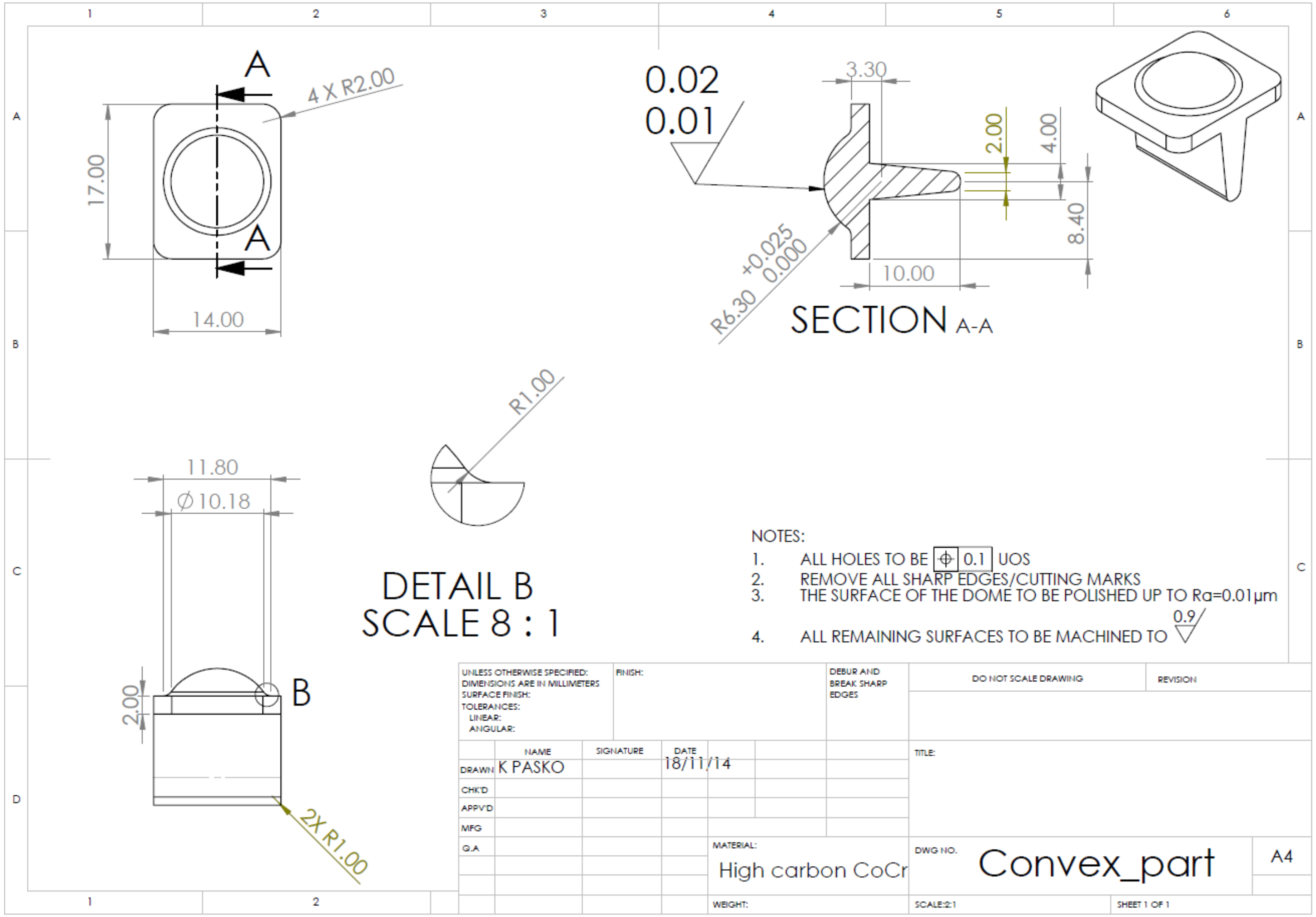
A
4 X R2.00
17.00
A
14.00
0.02
0.01
3.30
2.00
4.00
8.40
+0.025
0.000
R6.30
10.00
SECTION A-A
R1.00
DETAIL B
SCALE 8 : 1
11.80
Ø10.18
2.00
B
2X R1.00
UNLESS OTHERWISE SPECIFIED:
DIMENSIONS ARE IN MILLIMETERS
SURFACE FINISH:
TOLERANCES:
LINEAR:
ANGULAR:
FINISH:
DEBUR AND BREAK SHARP EDGES
DO NOT SCALE DRAWING
REVISION
NAME
SIGNATURE
DATE
DRAWN
K PASKO
18/11/14
CHK'D
APPV'D
MFG
Q.A
MATERIAL:
High carbon CoCr
WEIGHT:
TITLE:
DWG NO.
Convex_part
A4
SCALE:2:1
SHEET 1 OF 1

NOTES:
1. ALL HOLES TO BE ⌖ 0.1 UOS
2. REMOVE ALL SHARP EDGES/CUTTING MARKS
3. THE SURFACE OF THE DOME TO BE POLISHED UP TO Ra=0.01μm
4. ALL REMAINING SURFACES TO BE MACHINED TO 0.9

Figure 2.2: Dimensions and geometrical tolerances speficied for the convex components of the CTDR device.

2.2.2 Contact stress analysis

The analyses investigated a range of different parameters (Table 2.2), which allowed assessment of the potential effects of the radial clearance (i.e. dimensional deviations from the design) on the maximum contact pressure and determination of the theoretical lubrication regime under which the CTDR components may operate.

The baseline radius used in the analysis remained as specified by the design – 6.3 mm, however, a range of radial clearances were analysed, in order to include those measured during component inspection. For uncoated CoCr, the Young's modulus and Poisson's ratio were chosen to be 210 GPa and 0.3, respectively (as per datasheet supplied by the manufacturer, which met the ASTM-1537-11 requirements) [207]. For the coated devices, Young's moduli and Poisson's ratios of a bulk material were used – for silicon nitride 250GPa and 0.2 [208], and for chromium nitride 201GPa and 0.2 [209]. However, it must be pointed out, that the values of Young's modulus and Poisson's ratio of coatings reported in the literature vary with coating deposition parameters and deposition methods. The maximum load used in the analysis corresponds to the maximum load used in the standard spine simulator testing protocol for cervical components, as per ISO-18192-1:2001. Similarly, the angular velocity corresponds to the flexion/extension motion used in the standard ISO protocol i.e. ±7.5° at 1Hz. The viscosity used in the analysis corresponded to that of 25% (v/v) foetal bovine serum, which was used as a lubricant in spine simulator 37±0.1° [210–212]. Average surface roughness values measured in the pre-test component inspection have been used in the analysis (reported in Chapter 4 Section 4.5.1.1.2).

Table 2.2: Parameters used in the Hertzian theoretical contact stress prediction model.

Parameter	Constant	Variable
Radius [mm]	6.30	
Clearance [mm]		0.13; 0.15; 0.17;
Elastic modulus [GPa]		210, 250, 200
Poisson’s ratio		0.3, 0.2, 0.2
Load [N]		0-150
Angular velocity [rad/s]		0-0.3
Viscosity [mPas]		0.9*
Surface roughness [µm]	0.025; 0.015	

*25% (v/v) bovine serum at 37±0.1° [210–212]

2.3 Methods

2.3.1 Component inspection

A coordinate measuring machine was used to determine the critical dimensions of the cervical disc components – the length and width of the endplates, as well as the radii of the concave and convex bearing surfaces.

Five measurement points were taken on two edges of each endplate and used to create the X and the Y planes. An additional 4 points were taken on each corner of the superior flat surface of each endplate (Figure 2.3) and these were used to create the Z plane. Distances between those points in the X and Y direction were assumed to be equal to the length and width of each endplate.

Twenty-five measurement points were taken on convex or concave surface of each component. One point was taken at the pole, following by 3 rings of 8 equally spaced points (intervals of 45°) at approximately ¼, ½, and ¾ of the convex/concave bearing height. The clearances were determined by subtracting the diameter of the convex surface from the diameter of the concave surface. All measurements were repeated three times on the same component and average values were presented in this work.

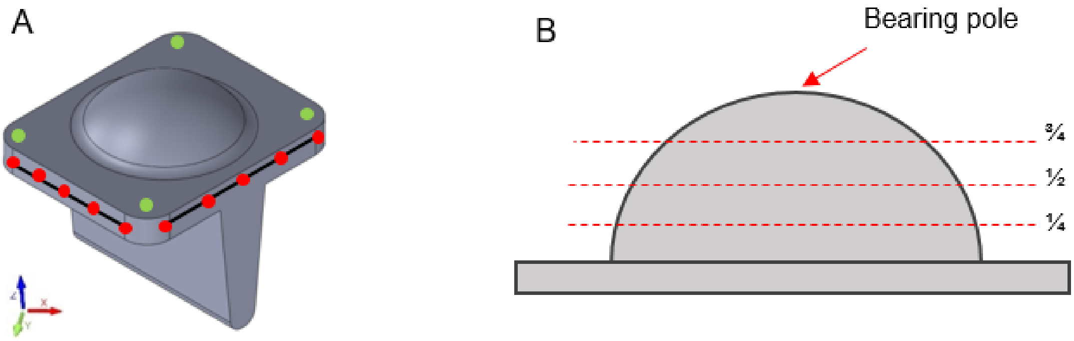

Figure 2.3: A: Five, approximately equally spaced points (marked red) were used to create XY planes. In addition, four points, taken on the superior flat surface of each endplate, were used to create the Z plane. B: Twenty-five measurement points were taken on each component, one point on the pole, followed by 3 sets of 8 equally spaced points at 1/4, 1/2 and 3/4 of the bearing height.

2.3.2 Contact stress analysis and lubrication regime prediction

2.3.2.1 Maximum contact stress

The cervical disc replacement is a semi-constrained design, which attempts to retain motion of the disease-affected spinal segment by adopting a ball-on-socket articulation. It is equivalent to a ball-and-socket joint, with the ball having a radius R_1 and socket having a radius of R_2 (as shown in Figure 2.4). The Young's modulus and Poisson's ratio for both the ball and socket were E and v, respectively. The radial clearance c between the ball and socket was defined as:

$$\boldsymbol{c = R_2 - R_1}$$

Equation 2.1

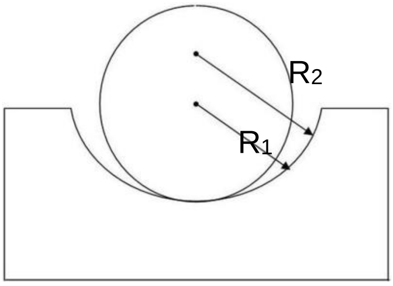

Figure 2.4: Schematic diagraph showing the geometry of the ball-and-socket joint

The Hertzian contact model was employed to analyse the surface contact stresses between the bearing surfaces. The maximum contact stress ($P_{\max}$) was determined from [203,213,214]:

$$\boldsymbol{P_{max}} = \left[\frac{\boldsymbol{6FE'^2}}{\boldsymbol{\pi^3 R'^2}}\right]^{\frac{1}{3}}$$

Equation 2.2

where F is the applied force, E' is the equivalent elastic modulus for the two bearing materials and R' is the equivalent radius for the ball and socket. These two parameters were calculated from:

$$\boldsymbol{E'} = \frac{\boldsymbol{E}}{\boldsymbol{2(1-\nu^2)}}$$

Equation 2.3

and

$$\boldsymbol{R'} = \frac{\boldsymbol{R_1(R_1+c)}}{\boldsymbol{c}}$$

Equation 2.4

2.3.2.2 Lubrication

The lubrication regime was predicted by calculating the corresponding lambda ratio (λ) and given as:

$$\boldsymbol{\lambda} = \frac{\boldsymbol{h_{min}}}{\boldsymbol{\sigma}}$$

Equation 2.5

where h_{min} is the minimum effective film thickness and σ is the compound surface roughness given by:

$$\boldsymbol{\sigma = \sqrt{R_{a1}^2 + R_{a2}^2}}$$

Equation 2.6

where R_{a1} and R_{a2} are the mean surface roughness of the bearing surfaces for the ball and socket, respectively. These were measured during component inspection and were R_{a1}=0.015±0.02μm and R_{a2}= 0.023±0.03μm.

2.3.2.3 Minimum effective film thickness

The minimum film thickness between the bearing surfaces was calculated using the formula below, proposed by Hamrock & Dowson [215]. This equation has been used by in many studies of joint replacement, such as hip joint [210] and lumbar TDR [71].

$$\boldsymbol{h_{min} = 2.8R'\left(\frac{\eta u}{E'R'}\right)^{0.65}\left(\frac{F}{E'R'^2}\right)^{-0.21}}$$

Equation 2.7

where, η is the lubricant viscosity, E' is the equivalent modulus of elasticity and u is the entraining velocity. The latter two parameters were calculated from:

$$\boldsymbol{E' = \frac{E}{(1-\nu^2)}}$$

Equation 2.8

and

$$\boldsymbol{u = \frac{\omega R_1}{2}}$$

Equation 2.9

where ω is the angular velocity in radians per second.

2.4 Results

2.4.1 Component inspection

2.4.1.1 Uncoated CTDRs

Data gathered during the component dimensional inspection of the uncoated CTDRs is shown in Table 2.3 and Table 2.4. The dimensional inspection showed that the control of width and length of the endplates, which were machined on a CNC machine, was better, when compared to the bearing radius, which has undergone manual polishing process. Following the radius inspection, the components were paired, so that the radial clearance remained as consistent as possible across all pairs. Subsequently, the paired components were numbered 1-6, correlating with the station number of the spine simulator they were to be fitted in. The resultant radial clearances of all pairs are shown in Table 2.3. The endplate and bearing radii dimensions as well as assigned station IDs are listed in Table 2.4.

Table 2.3: Radial clearances of paired uncoated devices measured using the CMM.

Component ID	Radial clearance [mm]
1	0.157
2	0.162
3	0.162
4	0.166
5	0.166
6	0.163
Mean±SD	**0.163±0.003**

Table 2.4: Dimensional inspection of the bearing surface radii and endplates of the uncoated CTDRs.

Station ID		Radius±SD [mm]	Width±SD [mm]	Length±SD [mm]
1	Concave	6.430±0.002	14.03±0.01	17.00±0.02
	Convex	6.273±0.001	14.06±0.01	17.00±0.01
2	Concave	6.447±0.001	14.02±0.02	17.00±0.03
	Convex	6.285±0.001	14.03±0.01	17.00±0.01
3	Concave	6.455±0.001	14.02±0.03	17.00±0.04
	Convex	6.292±0.002	14.06±0.01	16.99±0.02
4	Concave	6.440±0.003	14.01±0.03	17.00±0.03
	Convex	6.278±0.001	14.06±0.03	16.99±0.01
5	Concave	6.452±0.001	14.02±0.02	17.00±0.01
	Convex	6.286±0.004	14.05±0.03	16.99±0.02
6	Concave	6.455±0.001	14.03±0.01	16.99±0.03
	Convex	6.298±0.001	14.04±0.03	16.99±0.04

2.4.1.2 Coated CTDRs

Data gathered during the component dimensional inspection of the coated CTDRs is shown in Table 2.5 and Table 2.6. Similarly, to the uncoated parts, following the radius inspection, the components were paired so that the radial clearance remained as consistent as possible across all pairs. Subsequently, the paired components were numbered 1-6, correlating with the station number of the spine simulator they were to be fitted in. To address the possibility of the coatings were inability to withstand the initial testing and becoming damaged, spare six devices were also prepared. Inspection results of these additional components are also included in Table 2.5 and Table 2.6. The resultant radial clearances of all pairs are shown in Table 2.5. The endplate and bearing radii dimensions, as well as assigned station IDs are listed in Table 2.6.

Table 2.5: Radial clearances of paired coated components measured using the CMM. Devices corresponding with Stations 1, 3 and 5 were coated with chromium nitride, whilst devices from stations 2, 4 and 6 were coated with silicon nitride. The additional six sets of components were also inspected and are detailed here with the annotation '$_a$'.

Station ID (coating)	Radial clearance [mm]
1 (CrN)	0.128
2 (Si_3N_4)	0.135
3 (CrN)	0.130
4 (Si_3N_4)	0.135
5 (CrN)	0.129
6 (Si_3N_4)	0.126
1_a (CrN)	0.124
2_a (Si_3N_4)	0.159
3_a (CrN)	0.124
4_a (Si_3N_4)	0.100
5_a (CrN)	0.116
6_a (Si_3N_4)	0.100
Mean±SD	**0.125±0.016**

Table 2.6: Dimensional inspection of the bearing surface radii and endplates. Additional components were annotated with ‘$_a$’.

Station ID		Radius±SD [mm]	Width±SD [mm]	Length±SD [mm]
1	Concave	6.430±0.003	14.03±0.01	17.00±0.03
	Convex	6.302±0.001	14.06±0.02	17.00±0.01
2	Concave	6.437±0.002	14.02±0.02	17.00±0.03
	Convex	6.304±0.001	14.06±0.01	17.00±0.01
3	Concave	6.432±0.001	14.02±0.02	17.00±0.03
	Convex	6.302±0.003	14.06±0.01	16.99±0.01
4	Concave	6.438±0.001	14.03±0.01	17.01±0.01
	Convex	6.303±0.001	14.03±0.01	16.99±0.04
5	Concave	6.433±0.002	14.03±0.01	17.00±0.02
	Convex	6.304±0.005	14.04±0.01	17.00±0.01
6	Concave	6.424±0.001	14.02±0.03	17.00±0.04
	Convex	6.304±0.003	14.06±0.01	16.99±0.02
1_a	Concave	6.421±0.002	14.01±0.02	17.00±0.02
	Convex	6.297±0.004	14.02±0.01	17.00±0.01
2_a	Concave	6.457±0.002	14.03±0.03	17.00±0.01
	Convex	6.300±0.003	14.06±0.03	16.99±0.02
3_a	Concave	6.421±0.003	14.02±0.02	17.01±0.01
	Convex	6.297±0.003	14.01±0.03	16.99±0.02
4_a	Concave	6.396±0.004	14.03±0.01	16.99±0.03
	Convex	6.300±0.001	14.06±0.03	16.99±0.04
5_a	Concave	6.425±0.002	14.03±0.01	17.00±0.02
	Convex	6.309±0.001	14.03±0.01	17.00±0.01
6_a	Concave	6.390±0.002	14.03±0.03	17.00±0.03
	Convex	6.293±0.005	14.05±0.03	16.99±0.01

2.4.2 Contact stress analysis

2.4.2.1 Maximum contact pressure

The relationship between radial clearance and maximum contact pressure is shown inFigure 2.5. For the MoM combination, under a load of 150 N the maximum contact pressure was found to be 159 MPa, 174 MPa and 189 MPa for clearances of 0.13 mm, 0.15 mm and 0.17 mm, respectively. Under the same conditions, the maximum contact pressure for silicon nitride-coated devices was found to be 172 MPa, 189 MPa and 205 MPa for clearances of 0.13 mm, 0.15 mm and 0.17 mm, respectively. Chromium nitride-coated devices were found to produce maximum contact pressures of 149 MPa, 163 MPa and 177 MPa, for clearances 0.13 mm, 0.15 mm and 0.17 mm, respectively.

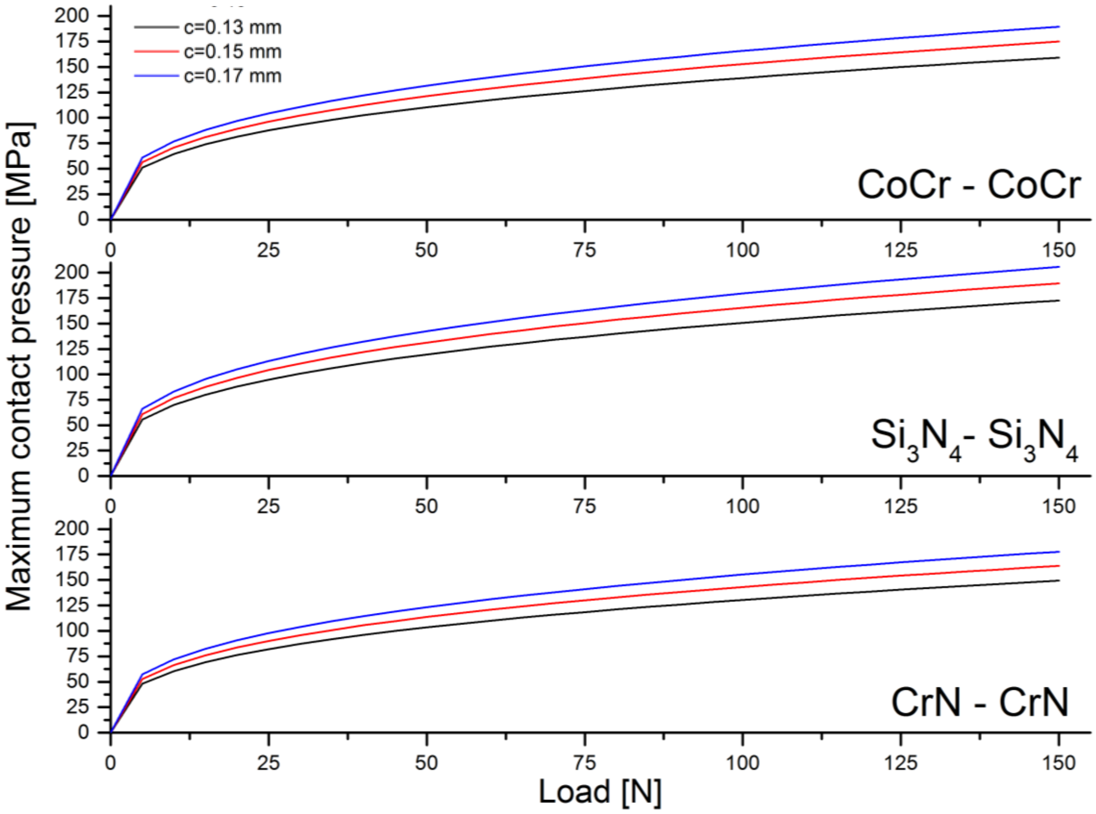

Figure 2.5: Variation of maximum contact pressure depending on radial clearance, under loads ranging from 0 to 150 N. The worst-case clearance (c=0.17mm) resulted in maximum contact pressure of 189MPa, 205MPa and 177MPa for CoCr-CoCr, Si_3N_4-Si_3N_4 and CrN-CrN bearing combinations, respectively.

2.4.2.2 Lubrication

The effect of radial clearance on predicted minimum film thickness and lambda ratio are shown in Figure 2.6 and Figure 2.7, respectively. For the same angular velocities, the theoretical minimum film thickness and lambda ratio were increasing with smaller radial clearances. At the same time, higher values of the minimum film thickness and lambda ratio were observed at for higher angular velocities. The same relationship between the angular velocities, radial clearance and minimum film thickness, and lambda ratio were found for all three bearing material combinations.

Results of the minimum film predictions at the highest angular velocities at constant load of 150N (Table 2.7) show that chromium nitride bearing combination resulted in the highest minimum film thickness values, for all bearing clearances investigated. Predictions of the lambda ratio at the highest angular velocities at a constant load are shown in Table 2.8. These results show that for each clearance tested, chromium nitride achieved the highest values of lambda ratio. Changes in minimum film thickness and λ ratio under changing loads for different bearing combinations are shown Figure 2.8 and Figure 2.9, respectively. There results show that both minimum film thickness and lambda ratio had the highest values at lower loads and highest entraining velocities. The same relationship between the load, entraining velocity and minimum film thickness, and lambda ration were found for all bearing material combination investigated. However, it was found that when tested with the same loads and entraining velocities chromium nitride bearing material achieved the highest values of minimum film thickness and lambda ratio.

Table 2.7: Results of minimum film thickness prediction for different bearing materials, at maximum angular velocities and a constant load of 150 N.

Bearing	Minimum film thickness [µm]		
	c = 0.13 mm	**c = 0.15 mm**	**c = 0.17 mm**
CoCr	0.055	0.048	0.043
Si_3N_4	0.053	0.047	0.042
CrN	0.058	0.051	0.045

Table 2.8: Results of lambda ratio for different bearing materials, at maximum angular velocities and a constant load of 150N

Bearing	Lambda ratio		
	c = 0.13 mm	**c = 0.15 mm**	**c = 0.17 mm**
CoCr	1.89	1.69	1.49
Si_3N_4	1.82	1.63	1.44
CrN	2.00	1.74	1.54

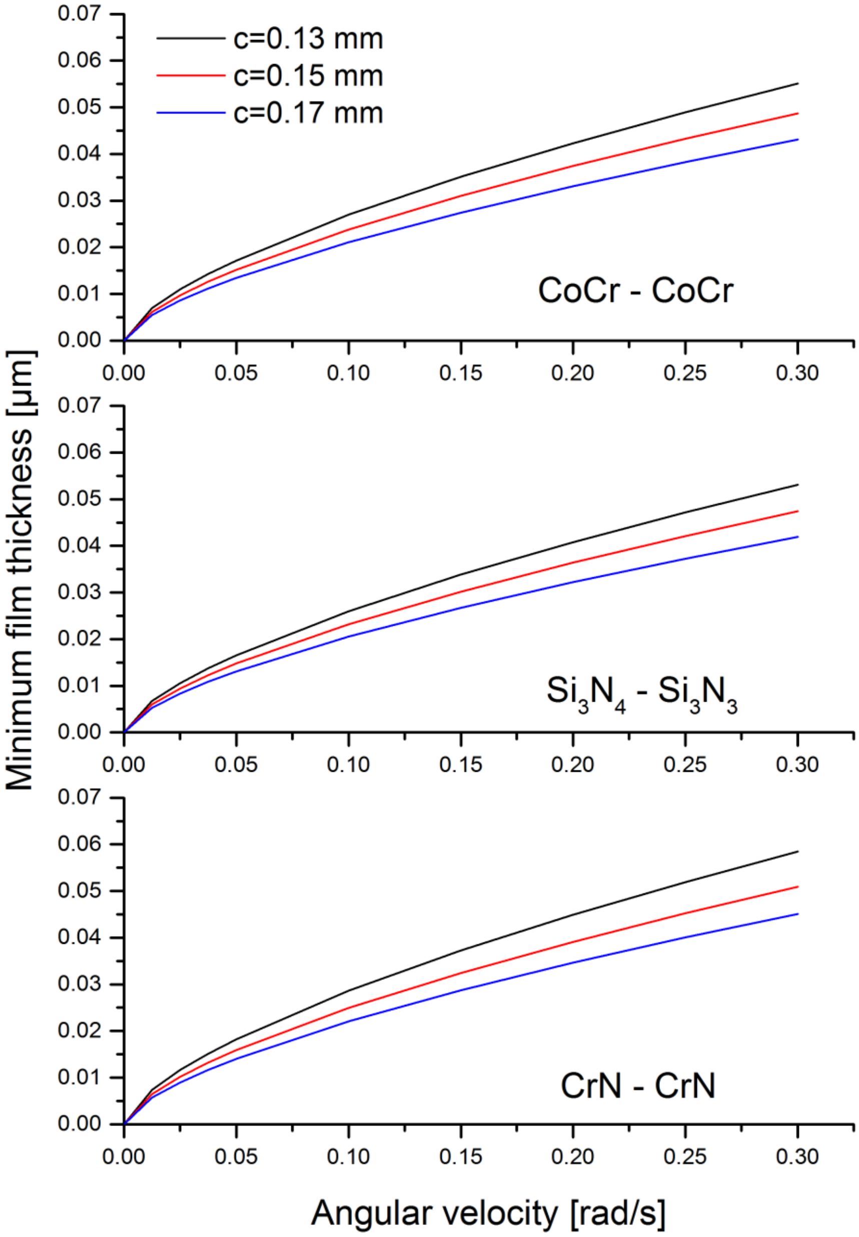

Figure 2.6: Variation of minimum film thickness with angular velocity for different radial clearances and different bearing material combinations. The figure shows prediction for a CDTR under 150 N load.

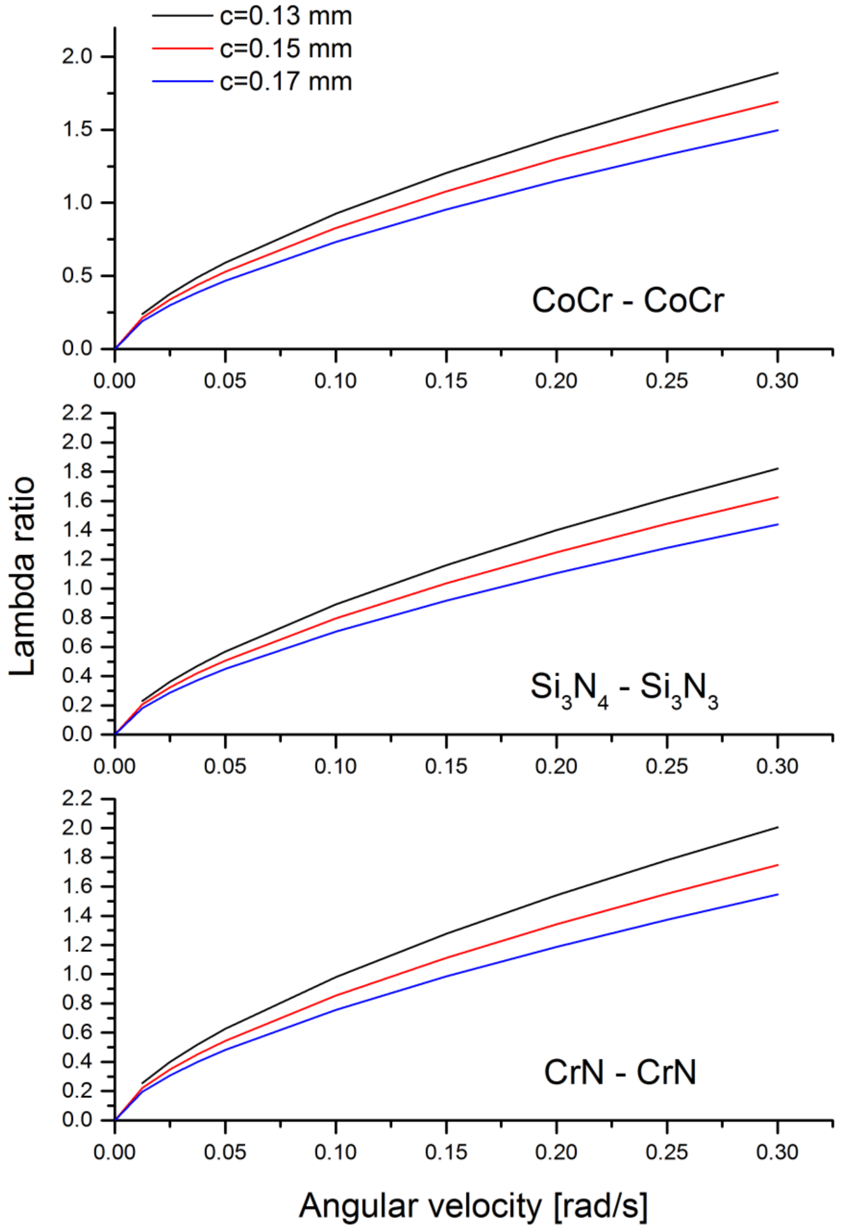

Figure 2.7: Variation of lambda ratio with angular velocity for different radial clearances and different bearing material combinations. The figure shows prediction for a CDTR under 150 N load.

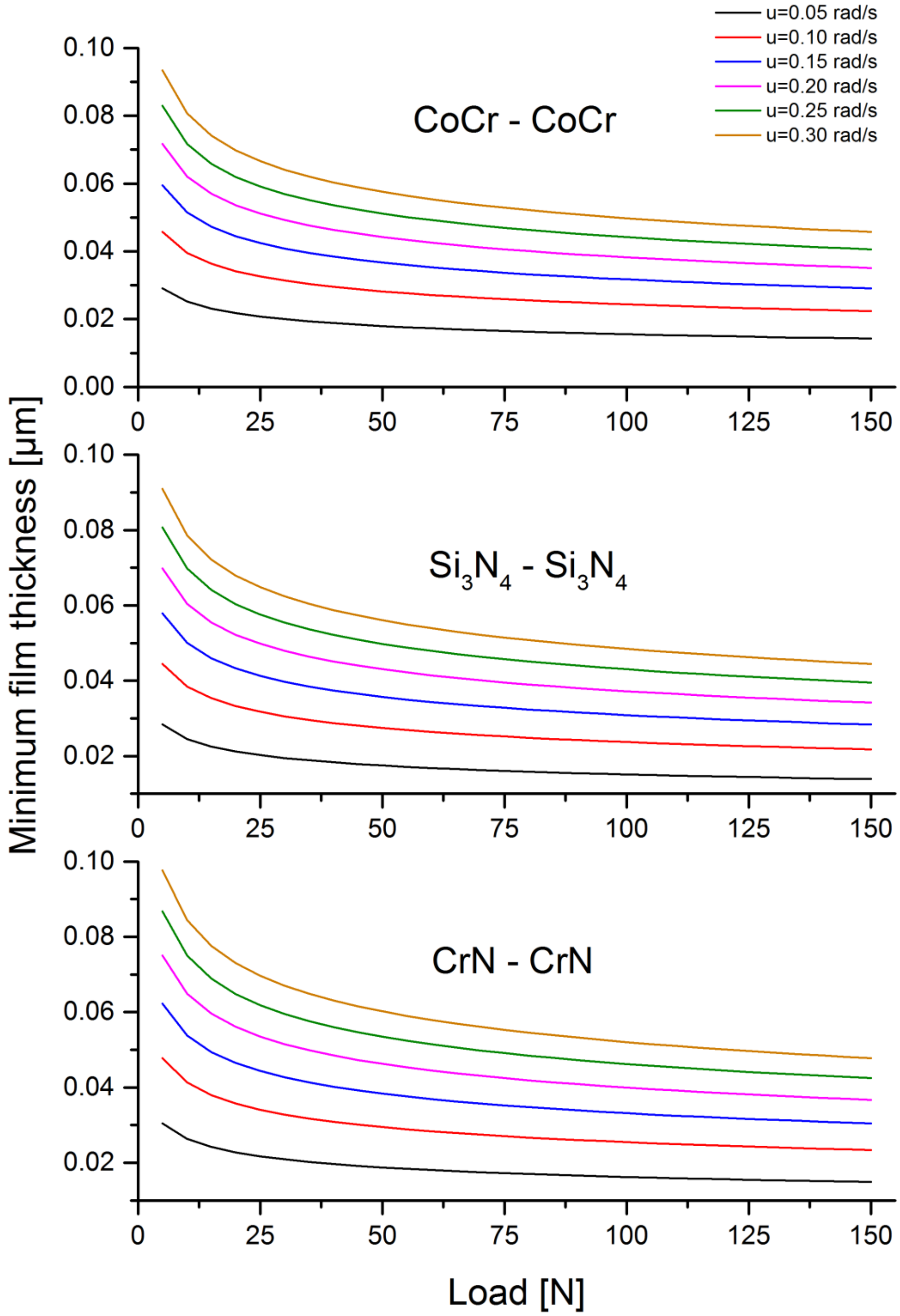

Figure 2.8: Variation of minimum film thickness under load range 0-150 N and for different angular velocities for different bearing combinations. A constant radial clearance of c=0.15 mm was used.

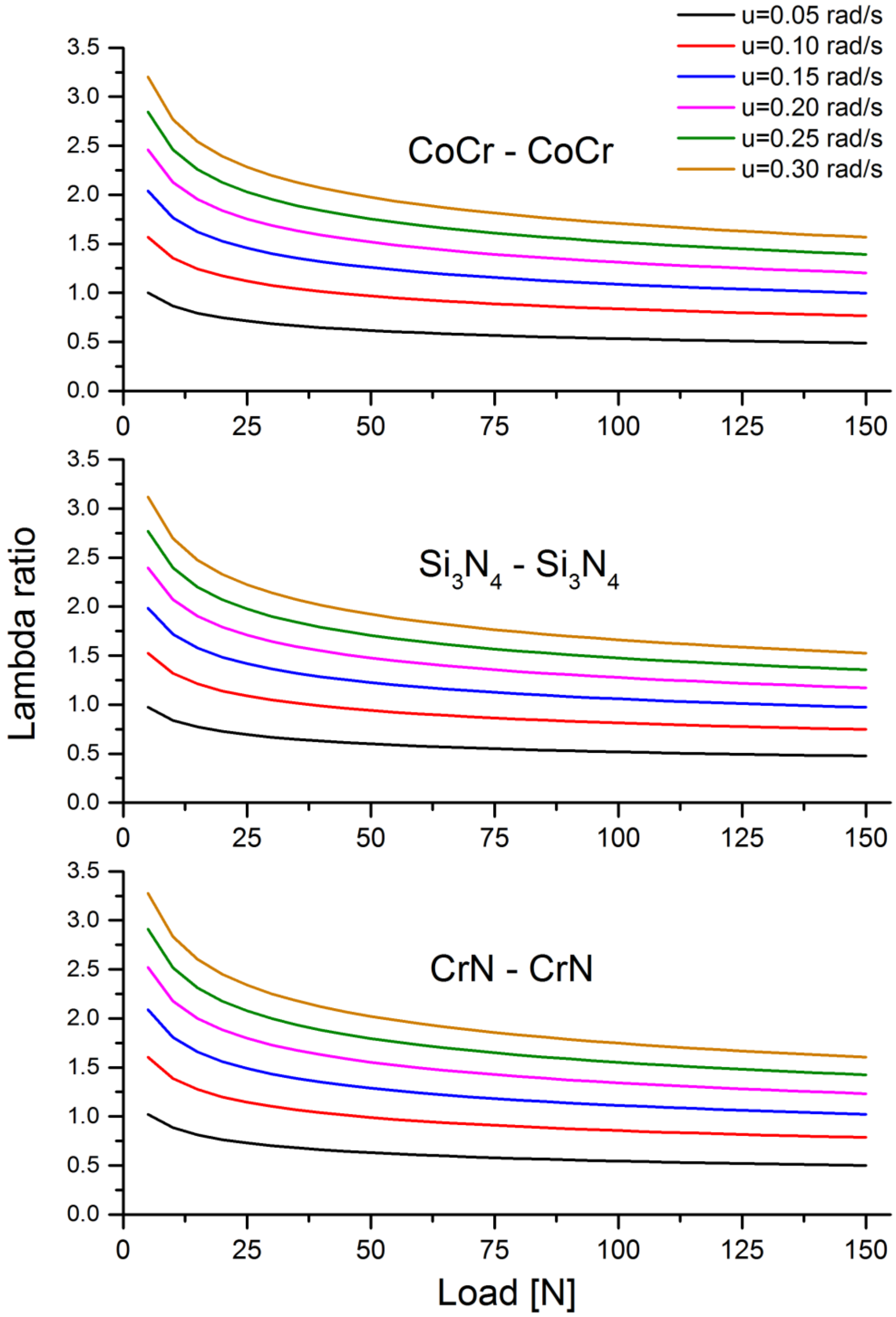

Figure 2.9: Variation of lambda ratio under load range 0-150N and for different angular velocities for different bearing combinations. A constant radial clearance of c=0.15 mm was used. At lower loads and higher entraining velocities the λ ratio for each bearing combination can reach approximately λ=3.

2.5 Discussion

2.5.1 Design of the CTDR device

The concave and convex radii were (per design) 6.45mm (+0.025/-0.00) and 6.30mm (+0.025/-0.000), respectively. The radial clearance was therefore designed to be in the range between 0.150 and 0.175mm. The component dimensional inspection has showed that some of the components did not meet the dimensional design specification. The dimensional deviations of the bearing radii were most likely caused by the manual polishing process, during which the control over material removal across the surface was limited and depended on the user's experience. Despite these small dimensional deviations, the radial clearances of the MoM CTDRs remained within the specified range. The average clearance of the uncoated components was 0.163±0.003mm, whilst the average clearance of the coated components was 0.126±0.016mm, which was significantly lower ($p<0.05$, CI 95%). Such average clearances were outside (lower) the design specification. The main reason for this difference was the additional layer of coating added to the coated components. At the CTDR design stage of the project, the exact thickness of the coating was unknown and yet to be determined. It was later found that each coating was approximately 5µm, and thus the coating layer resulted in a decrease in the radial clearance of approximately 10µm. Additionally, the CTDRs components, which subsequently coated, were polished at a different timepoint in the project, at which stage the process of manual polishing may have been improved with time, with improved user experience. The importance and effect of radial clearance on maximum contact pressure and relationship between operating lubrication regime and surface roughness are discussed in the following section. Moreover, a difference in the predicted maximum contract pressure between coated and uncoated components was investigated.

2.5.2 Contact stress analysis and lubrication regime prediction

The Hertzian contact model for cobalt-chromium on cobalt-chromium cervical total disc replacement predicted the maximum contact pressure, under a 150 N load, to be in the range of 159-189 MPa, depending on the radial clearance used in the prediction model. The same model applied to ceramic-coated devices predicted that for the chromium nitride coated devices the maximum contact pressure was in the range of 149-177 MPa, whilst for silicon nitride coated devices the maximum contact pressure was in the range of 172-205 MPa. Based on the results of the model, it can be concluded that under the same testing conditions and the same radial clearance chromium nitride has the most favourable mechanical properties, which, under those particular conditions, results in the lowest contact pressure.

In their study, Xin, Shepherd and Dearn [216], found that the maximum contact pressure of a PEEK CTDR, under a load of 150 N, was in the range of 5.9-32.1 MPa. Such difference is a result of a different material combination and much lower contact pressures found in materials with lower elastic moduli. Similarly, applying a Hertzian model to lumbar TDRs, the maximum contact pressure was found to be in the range of 3-6 MPa and 63-130 MPa for metal-on-polyethylene and metal-on-metal combinations, respectively [203]. However, it must be pointed out that lumbar TDR devices have larger bearing radii, which results in lower values of maximum contact pressure. Despite relatively high values of the maximum contact pressure found for the metal-on-metal CTDR device in this study, as compared to other joint replacement devices, the theoretical maximum contact stress was below the fatigue strength of CoCr alloy – reported as 610MPa at $>10^6$ cycles [217]. Similarly, the maximum contact pressure for both coatings was found to be below the fatigue strength of the CrN coating – reported as 750MPa at 10^7 cycles [218] and silicon nitride 600MPa at 10^5 cycles [219]. However, the results of the CrN coating fatigue strength presented by Costa *et al.* [218] were based on the coating deposited on Ti_6Al_4V substrate.

The operating lubrication regime prediction model showed the λ ratio for MoM bearings to be in the range of 1.49-1.89, for different clearances. The chromium nitride coated CTDRs were found to generate a λ ratio range of 1.54 to 2.0, whilst the silicon nitride coated CTDRs 1.44-1.82. These are also reflected by the minimum film thicknesses achieved by different bearings – at the smallest tested clearance (0.13mm), the results were 0.055mm, 0.053mm and 0.058mm for MoM, silicon nitride and chromium nitride, respectively. For all bearing combinations, the λ ratio indicated that devices would operate in a mixed lubrication regime. Whilst, under lower loads (<50N) and higher angular velocities, the λ ratio achieved by all bearings were as high as 3.2, indicating full film separation between the concave and convex components, such conditions are unlikely *in vivo*. To the author's knowledge, at the time of writing, no studies on lubrication regime of MoM or ceramic-coated CTDRs have been published. Xin, Shepherd and Dearn [216] predicted PEEK-PEEK CTDR devices to operate under boundary conditions. Similarly, Shaheen and Shepherd, as well as *Bushelow et al.* predicted MoP and MoM lumbar TDRs to operate under boundary conditions [71,220]. While direct comparison between the lumbar and cervical TDRs cannot be made, due to differences in material combination, motions and loads, it can be speculated that similar lubrication conditions can be found in MoM hip implants.

It has previously been shown, both theoretically [221] and experimentally [222], that MoM hip implants operate in mixed elastohydrodynamic lubrication (EHL) regime. Under this lubrication regime a large portion of the applied load is supported by films created through an elastohydrodynamic action [223]. During dynamic loading pressure in the converging film between two surfaces is produced. This pressure is sufficient to cause a local elastic deformation of either of the surfaces and keep them separated. Additionally, Dowson [224] reported on a localised micro-elastohydrodynamic effect occurring in MoM hip implants, where pressure perturbations in the film can cause a substantial flattening of surface asperities. This flattening increases conformity of two surfaces and assists in maintaining the lubrication film.

When investigated, ceramic-on-ceramic (CoC) hip implants were found to operate in mixed-to-fluid film lubrication regime, depending on the exact conditions [210,225]. This is somewhat in line with the current study, whereby particularly the chromium nitride-coated devices were found to have higher predicted film thicknesses and lambda ratios compared to the other bearings tested. High Young's modulus of silicon nitride meant that the predicted film thickness and lambda ratio were the lowest out of all bearing combinations investigated.

While the method of predicting lubrication regime is widely used in the literature, it has some limitations. The prediction model assumes that the lubricant used is Newtonian. In case of simulator testing, foetal bovine serum is used, which is a non-Newtonian fluid and shows shear thinning characteristics under relatively low shear rates [226]. Moreover, the analysis is limited to steady-state motion, which is not likely to be clinically relevant. In order to produce more clinically relevant prediction of the lubrication regime, experimental measurements of the frictional torque and plotting the Stribeck curve are necessary. The application of this simplified model, however, can be justified in the current study, where it was used merely to highlight the effect of radial clearance, material selection, loading on the operating lubricating regime. Observations made by Jin, Dowson and Fisher [223] and Dowson [227] advocated the importance of the clearance in the design of joint replacement implants. These authors stated that while the diameter of the bearing should be as large as possible, it is important for the radial clearance to be as small as practicable. Another important factor, which can have an effect on the lubrication regime, is surface roughness. It has been reported that alongside the radial clearance, the surface finish is the most important factor in lubrication mode determination [221]. Surface roughness is extremely important for maximising the λ ratio, especially during the running-in phase of wear. During the running-in phase, the implant operates in the boundary lubrication regime, the entire applied load is carried directly by the bearing interface and wear rates are up to 20 times higher as compared to the steady state wear phase operated in the mixed EHL [228].

By applying the Hamrock-Dawson elasto-hydrodynamic lubrication theory to a cervical total disc replacement and modelling *in vivo* operating conditions (loading, surface finish, motion profile and lubricant viscosity), it was shown that formation of a full film separation between the two CTDR components is unlikely. In fact, the lubrication was shown to be mainly governed by mixed or boundary lubrication, which indicates potential direct contact between the bearing surfaces.

The Hertzian contact model, used in this thesis, assumes that the contact surface is smooth and frictionless and adhesion forces between the two contacting surfaces are not considered. Other elastic-smooth contact models, such as Johnson-Kandall-Roberts (JKR), take adhesion forces into consideration. Whereas in the work by Xin, Shepherd and Dearn [216], the two contact models were compared and no difference in the maximum contact stress exhibited by PEEK-PEEK interface was found, this was mainly due to the relatively low surface energy of PEEK (0.044 $J.m^{-2}$) [229]. Surface energy of CrN coating was found to be close to this of PEEK (0.045 $J.m^{-2}$) [230]; however silicon nitride surface energy can be as low as 0.008 $J.m^{-2}$, when unoxidized [231], and thus surface adhesion of the two ceramic coatings would be assumed to be negligible. Moreover, the lambda ratio for the two coatings found in this thesis, was between 1 and 2, which suggested that, theoretically, mixed operating lubrication condition can be found in the CDTRs. Consequently, this suggested that the two bearing surfaces would often be separated by the lubricant, minimising the potential for adhesion and adhesive wear. CoCrMo alloy has much higher surface energy (56 $J.m^{-2}$) [232] and therefore could (potentially) result in increased potential for adhesion between the two surfaces. Moreover, the theoretical lubrication operating conditions for MoM CTDRs was found to be ranging from boundary to mixed, and thus potential of direct contact between the two CoCr surfaces could be assumed. On the other hand, JKR contact model assumes that the two surfaces in contact are pristine and clean, which is not the case in neither the *in vitro* testing, as confirmed by the findings in this thesis i.e. presence of deposit on the surface of tested CTDRs, nor *in vivo,* where formation of tribofilm on MoM explants has been reported [138,233].

2.6 Conclusions

A novel MoM CTDR device was designed for the purpose of this thesis. The design comprised of two CoCrMo endplates, sizes of which were based on other devices currently available clinically. Pristine and ceramic-coated variants were produced for further tribological investigations. The inspection of the components found that the radial clearance of the components varied between the components, particularly between the pristine and coated CTDRs, which were found to have smaller radial clearance, due to the additional 5µm of coating on each of the convex and concave components. Some variation of the bearing radii was likely to have been caused during the manual polishing process the components underwent.

The maximum contact stress exerted on the CTDR devices was calculated using the Hertzian model. It was found that, in comparison to MoP bearings, MoM and ceramic-coated devices would exhibit significantly higher contact stress, due to the mechanical properties of the materials. However, it was found that these stresses would not exceed fatigue strength of the raw materials used in the prediction model. The theoretical operating lubrication regime was also calculated, it was predicted that the CTDRs would operate mainly in the mixed conditions, however a variation of all three regimes could be observed, depending on the bearing material, radial clearance, load and entraining velocity of the lubricant. Whilst the results obtained in the current study are theoretical, it is known that lubrication regime can significantly influence wear performance of an artificial joint device, and thus MoM CTDR implant design parameters must be optimised in order, to achieve improved wear behaviour, similar to those seen in total hip replacement. *In vitro* investigation of the tribological performance of the uncoated and ceramic-coated CTDRs is reported in the next chapter.

Chapter 3 : Coating characterisation

3.1 Introduction

The biomedical sector is one example of an industry, where surface properties of an implant are critical to their lifetime, safety, efficacy and biocompatibility. As such, one of the main requirements of a biomaterial is its resistance to the environment found in the human body. Corrosion resistance is one of the crucial design considerations of any implantable material. Body fluids consist of inorganic ions (Na^+ , Cl^- , Ca^{2+}, $H_xPO_4^{n-}$ etc.), aminoacids, proteins and organic acids, and are essentially oxygenated saline solutions with a salt content of about 0.9% (w/v), pH of 7.4 and temperature of 37±1 °C, which together generate a relatively harsh operating environment. High corrosion resistance, resulting in low or negligible ion release, is a requirement for metal implants. Whilst cobalt-chromium based alloys have excellent corrosion resistance [234], biocorrosion of modular junctions and wear particles generated from the orthopaedic implants manufactured out of this alloy has been one of the major issues dealt with in the orthopaedic industry in recent years [235–238]. Corrosion of metal implants and nano-sized wear particles generated in those devices [239] may cause ion release into the body and result in local cytotoxity, genotoxicity and hypersensitivity, which affect the morphology and structure of the tissue, and may lead to systemic cytotoxity, carcinogenesis [240], allergic reactions, and even pseudotumour formation [241]. Wear is another critical issue in medical implantable devices often determining the longevity of the implant. Micron-sized wear particles, mainly of polyethylene origin, generated *in vivo* may cause adverse tissue reactions around the implant, followed by osteolysis, which in turn will lead to failure of the device through loosening [242,243]. Wear and wear-related damage is a common cause of failure of total joint replacement prostheses [131,154].Therefore, corrosion resistance and low wear rates are desirable for articulating surfaces for load bearing implants. The tribological performance of medical alloys can be improved using surface engineering treatments such as nitrogen ion implantation, ceramic coating deposition or diamond-like carbon film formation.

Ceramic coatings, such as titanium nitride (TiN), chromium nitride (CrN) and silicon nitride (Si_3N_4), are often used to harden, and protect cutting and sliding surfaces, such as cutting tools. They also have wide range of applications in the biomedical sector - TiN coatings are often deposited on medical grade titanium alloy (Ti6Al4V), in attempt to improve the poor wear performance of the latter, which is the major disadvantage of this material. Whilst TiN was found to have favourable effect on the biocompatibility and tribological properties of surfaces, reports of third body wear, pitting, delamination, fretting and coating breakthrough have been reported in the literature [244]. Another common ceramic coating used in biomedical applications is chromium nitride (CrN), which is extremely hard and corrosion resistant, often used in metal forming and on surgical tools. When THR application of TiN was compared with CrN, it was shown that the CrN coating had superior tribological properties and exhibited significantly lower wear rates [179–181]. However, in all the cases insufficient adhesion and coating artefacts, such as droplets, were reported as major concerns for these coatings. Recently a new ceramic material (in both bulk and coating form) has been proposed for load bearing joint implants. Silicon nitride exhibits superior mechanical properties, excellent biocompatibility and low wear rates and has recently been introduced into the biomedical field. First developed in 1895, when it was introduced for use in internal combustion engines and high-temperature gas turbines. Current uses of bulk Si_3N_4 include high-performance bearings, turbine blades, ball bearings and glow plugs; these applications require a material with a high fracture toughness, strength and low wear properties. The Si_3N_4 ceramics present a favourable combination of mechanical, tribological, chemical and thermal properties that make them suitable for components requiring high performance in severe environments. Consequently, silicon nitride ceramics have been proposed as an alternative structural material [186,187] or as tribological coatings [189,190,245] for joint replacement load bearing components. Current biomedical applications of bulk Si_3N_4 include cervical spacers and spinal fusion devices, which have achieved successful short-term results [195]. Moreover, silicon nitride fixation plates and screws, as well as bearings for spine disc surgery, total hip and knee replacements have also been developed [197,246,247]. In 2011, the first silicon nitride femoral head was implanted [248]; however, to date, no clinical follow up data has been published.

In the current study, two ceramic coatings were investigated for their potential to improve the tribological and biocompatibility performance of MoM CTDRs. Chromium nitride and silicon nitride coatings were deposited on coupons, and their mechanical properties and chemical composition were investigated. The following section will describe the samples and methods used in these investigations, as well as report and discuss the results obtained.

3.2 Materials

3.2.1 Test samples

Eighteen disc coupons were machined from a low carbon <0.05 (w/w) CoCr alloy (ASTM-F1537) supplied by Peter Brehm GmbH (Weisendorf, Germany). The discs were polished by Mrs. Jane Cardie (technician, School of Mechanical Engineering) and finished to a Ra of <0.01µm. The discs had a radius of 16mm and thickness of 3mm. Once polished, the coupons were shipped to IonBond (Olten, Switzerland), where they were subjected to a physical vapour deposition (PVD) coating process; nine coupons were coated with a chromium nitride coating (via PVD) and the remaining nine coupons were coated with a silicon nitride coating (via HiPIMS). Following the coating process, the coupons were cleaned and re-polished at IonBond. Samples to be used in SEM coating thickness evaluation were partially wire eroded in the mid-section) and fractured inwards (as shown in Figure 3.1).

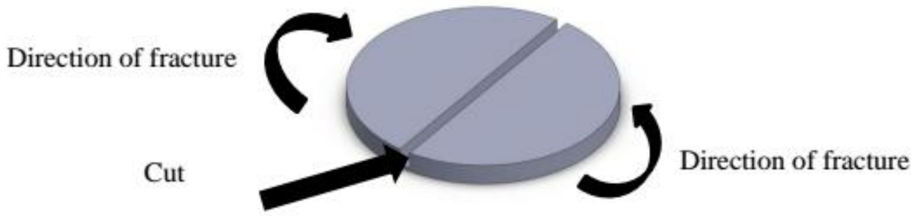

Figure 3.1: Method of wire cutting and fracturing of the coated samples. The cuts were made through the mid-section of the sample, leaving approximately 0.5 mm of the material uncut. The sample was subsequently fractured inwards in order to avoid buckling and delamination of the coating.

3.2.2 Equipment for coating characterisation

The coated coupons were polished using a Forcipool polishing system, supplied by Kemet International (Maidstone, UK). A Calotester and a scratch-tester (Millennium 200), used for measuring coating thickness and coating adhesion measurements, respectively, were purchased from Tribotechnic (Clichy, France). The scratch-tester was fitted with a Rockwell type C diamond tip (r=0.2mm). Coating nano-hardness and Young’s modulus were evaluated using a NanoTest nanoindenter manufactured by NTX Micromaterials (Wrexam, UK), fitted with a Berkovich diamond tip. A two-dimensional contacting profilometer, used for surface roughness measurements, (Talysurf PGI 800) was supplied by Taylor Hobson (Leicester, UK). Al k-alpha XPS system was manufactured by ThermoScientific (Loughborough, UK). Microscopic evaluation of samples was conducted using a Leica DM 6000M optical microscope, supplied by Leica Microsystems Inc. (Buffalo Grove, IL, USA), as well as Carl Zeiss EVO MA15 Scanning Electron Microscope (SEM) in conjunction with the Oxford Instruments AZtecEnergy EDX analysis system (Oxford, UK). An automatic mounting press SimipliMet™ 3000 was supplied by Buehler (Coventry, UK).

3.2.3 General lab consumables

Ethanol and isopropanol, at a concentration of 99.8+% (v/v) were supplied by Fisher Scientific UK (Leicestershire, UK), diamond paste and waterproof abrasive discs were supplied by Kemet International (Maidstone, UK), hot mounting compound was supplied by MetPrep (Coventry, UK).

3.2.4 Computer Software

Numerical data collected in the coating characterisation investigations was collated in Excel v.2013 (Microsoft Office). Coating cross-section thickness was measured digitally in ImageJ v.1.48 software (National Institutes of Health). Raw XPS data was exported and analysed in CasaXPS v.2.3.16 software (Casa Software Ltd.). The EDX spectra were acquired using AZtec computer software, purchased from Oxford Instruments AZtecEnergy EDX system (Oxford, UK).

3.2.5 Statistical analysis

All statistical analysis of data was performed using SPSS for Windows (v.21.0, SPSS Inc., Chicago, IL, USA). One-way analysis of variance (ANOVA) was used to analyse obtained data with $\alpha=0.05$ for differences between data sets obtained from different coating characterisation experiments.

3.3 Methods

3.3.1 Sample allocation

Eighteen metal coupons were machined and coated with ceramic coatings either chromium nitride or silicon nitride, 9 of each coating. The coupons were marked with an ID number and coating type, and allocated for coating characterisation tests, as shown in Table 3.1. Where possible, i.e. where non-destructive methods were applied or where only a small surface area was used, the same samples were used in multiple investigations.

Table 3.1: Allocation of ceramic coating test coupons for coating characterisation testing.

Characterisation test	Chromium nitride sample ID	Silicon nitride sample ID
XPS	1,2,3	1,2,3
Surface roughness	4,5,6,7	4,5,6,7
Calo test	4,5,6	4,5,6
Cross-section SEM	4,5,6	4,5,6
Nanoindentation	7,8,9	7,8,9
Scratch test	7,8,9	7,8,9

3.3.2 X-ray photoelectron spectroscopy (XPS)

X-ray photoelectron spectroscopy (XPS) is a quantitative technique widely used in surface analysis of the elemental composition of surfaces. The method is based on photo-ionisation and analysis of the kinetic energy spectrum of the emitted photoelectrons. In principle, XPS utilises photons of a known energy typically to excite and eject atoms below the surface of a sample, a process during which energy is created, all within the boundaries of the conservation of energy requirements (Equation 3.1). Energy created by emitted photoelectrons is filtered via a hemispherical analyser (HSA), before the intensity is recorded by a detector.

$$KE = h\nu - BE$$

Equation 3.1

where:

KE – kinetic energy of electrons

h – Planck's conststnt

v– frequency of the radiation

BE – binding energy of photoelectrons

The binding energy of emitted photoelectrons represents the difference in energy between the ionised and neutral atoms. Each element has a characteristic binding energy, which is used to characterise surface chemical composition; as a result, the presence of peaks in the spectrum at particular energies indicates the presence of a specific element in the surface of a test sample. Moreover, since the number of electrons recorded by the detector is proportional to the numbers of atoms present in the surface, the intensity of those peaks represents the concentration of elements within the sample. The most commonly used source of electrons are mono-energetic Al K_α (*h*v=1486.6 eV) x-rays. Kα x-rays which are generated when an electron transitions to the innermost 'K' shell from a 2p orbital of the second or 'L' shell and typically generate the strongest x-rays. Al Kα x-rays are produced by diffracting and focussing a beam of non-monochromatic x-rays off of a thin disc of natural, crystalline quartz.

In the current study, the XPS analysis was performed at the National EPSRC XPS User's Service (NEXUS) at Newcastle University (Newcastle, UK). The chemical composition and bonding within coatings were determined using XPS with a monochromatic Al-Kα source, applying electron and ion neutraliser during measurements. Three samples of each coating were investigated using this analysis. Each coupon was subjected to survey spectrum analysis combined with a depth profile. During such analysis, the surface of a sample is sputtered with 4keV Ar^+ ions for different time durations and at each specified timepoint, a full spectrum of elements present on the sample was obtained. In this analysis, survey spectra were obtained after 0, 100, 200, 300, 400, 500 and 600 seconds of Ar^+ ion sputtering. In this way, any potential changes in chemical composition of the coating with depth were detected. Data analysis was performed using CasaXPS software. All spectra were referenced to the C1s line of hydrocarbon-type carbon. The most common position of the C1s line found in the literature value was 284.8 eV [18].

3.3.3 Surface roughness

A two-dimensional contacting profilometer fitted with a diamond tip was used to assess the surface roughness of coated coupons. In contact profilometry, the diamond tip is traced across the surface of a sample; any small deviations of the surface are projected by a laser onto a sensitive screen and converted into a mathematical value. Different algorithms can be used by the software to generate values of surface parameters, such as average roughness (R_a). R_a is universally recognised parameter for surface roughness and it is the arithmetic average of the absolute deviations of the roughness profile from the mean line. It does not differentiate between peaks and valleys and therefore does not provide much information about the surface profile as a standalone parameter. R_{sk} values give information on the morphology of the surface texture and the symmetry of the profile. R_p and R_v are measures of height of the highest peaks and deepest valleys, respectively. High values of those two parameters indicate the presence of deep scratches in investigated surface.

Four samples of each coating were used in this investigation. On each component, two 10 mm long traces were taken across the surface, as shown in Figure 3.2. The traces were positioned approximately at the equators of each coupon, in order to collect the greatest amount of data as was feasibly possible, in a repeatable manner. Parameters such as surface roughness (R_a), skewness (R_{sk}), maximum peak height (R_p) and maximum valley depth (R_v) were recorded.

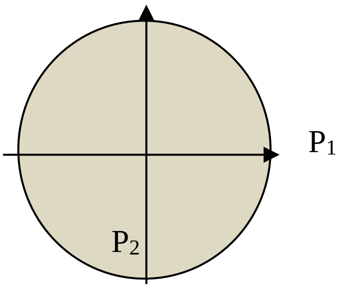

Figure 3.2: Schematic representation of the two traces taken across the surface of each coated coupon.

Collected data was analysed using least squares line with a Gaussian filter and appropriate cut-off, which uses a mathematical or electronic means to reduce or remove unwanted data, in order to focus on the wavelength in the region of interest. An appropriate long-wave cut-off wavelength, dependent on the R_a values and an appropriate bandwidth, based on the long-wave to short-wave cut off wavelength ratio (λ_c/ λ_s), were used, as shown in Table 3.2. The cut off values and bandwidth ratios were specified by ISO-4288:1996 (‘*Geometric product specification (GPS). Surface texture. Profile method: Rules and procedures for the assessment of surface texture’)* [249] and ISO-3274:1998 (‘*Geometrical Product Specifications (GPS) -- Surface texture: Profile method -- Nominal characteristics of contact (stylus) instruments’*) [250], respectively.

Table 3.2: Values of cut-off depending on R_a values as stipulated by ISO-4288-1996. Relationship of λ_c / λ_s i.e. bandwidth is based on ISO-3247:1998

R_a (µm)	Cut off λ_s (mm)	Cut off λ_c (mm)	Bandwidth (λ_c / λ_s)
≤ 0.02	2.5	0.08	30
$0.02 < R_a \leq 0.1$	2.5	0.25	100
$0.1 < R_a \leq 2$	2.5	0.8	300
$2 < R_a \leq 10$	8	2.5	300
$10 < R_a \leq 80$	25	8	300

3.3.4 Coating thickness

The coating thickness of the silicon nitride and chromium nitride coatings was assessed using two methods – a Calo test and SEM analysis of a cross-section of each sample.

3.3.4.1 Calo test

A Calo test was used determine coating thickness. In principle, a hardened steel ball was placed against the surface of a sample and rotated on a spindle. A diamond paste suspension was added between the two surfaces, to aid abrasion of the coating. Once the film layer was abraded off, the surface of each sample was evaluated, as shown in Figure 3.3.

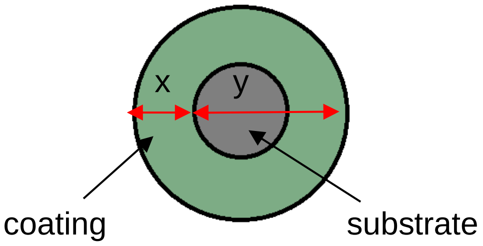

Figure 3.3: Typical projection seen on a surface following coating abrasion in Calo test.

Three samples of each coating were analysed using the Calo test, with three measurements taken from each sample. The hardened steel ball had a diameter of 25mm was rotated at a speed of 250rad/s for a duration of 240s.

Following coating abrasion using the Calo tester, a Leica microscope and its integrated software were used to take x and y measurements, which were collated in an Excel spreadsheet; the coating thickness was calculated using Equation 1.2. The calculation method for a flat sample (ball/plane model) was based on the BS EN ISO-26423:2016 standard [251] and shown in Figure 3.4 and was derived as:

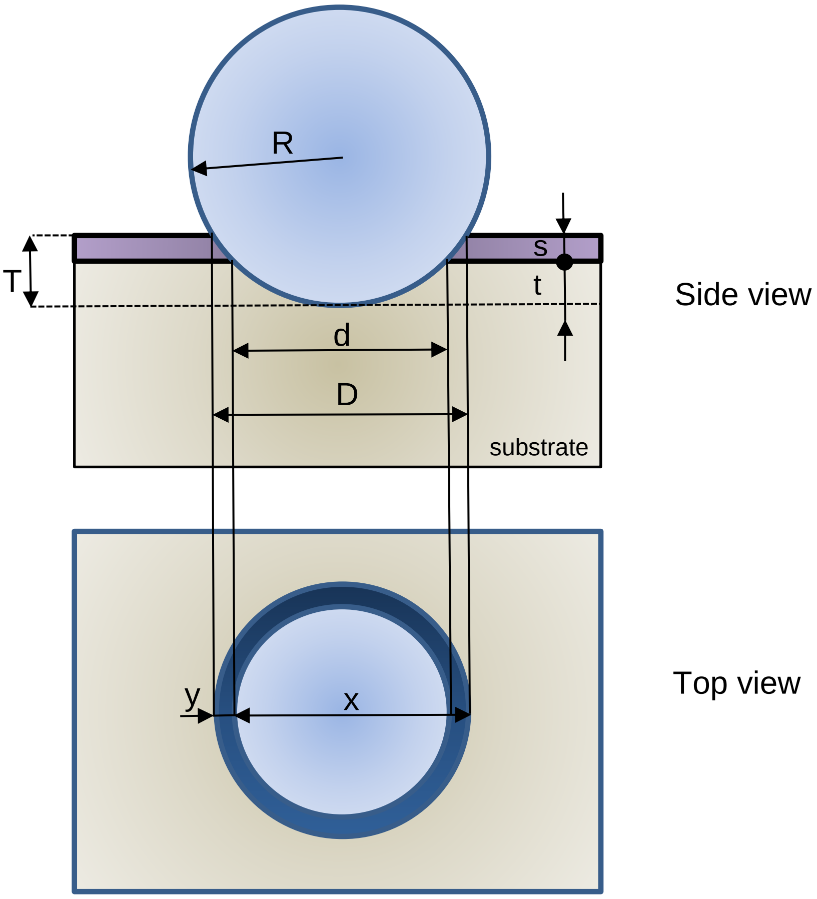

Figure 3.4: Schematic representation of the Calo test and dimensions used in calculating coating thickness.

where ***s*** is the thickness of the coating:

$$s = T - t$$

Equation 3.2

and ***T*** is the total depth of penetration:

$$T = R - (1/_2\sqrt{4R^2 - D^2})$$

Equation 3.3

and ***t*** is the depth of penetration in the substrate, given by:

$$T = R - (1/_2\sqrt{4R^2 - d^2})$$

Equation 3.4

Thus, Equation 3.2 becomes:

$$s = 1/_2 - (\sqrt{4R^2 - d^2 - }\sqrt{4R^2 - D^2})$$

Equation 3.5

For thin films, the penetration depth is small in comparison to the radius ***R*** of the ball. Therefore, Equation 3.5 can be simplified to:

$$S = \frac{D^2 - d^2}{8R}$$

Equation 3.6

Assuming that $D = x + y$ and $d = x - y$, the measurements of x and y were used to calculate the coating thicknesses.

3.3.4.2 SEM cross-section analysis

Three samples of each coating were prepared by wire cutting and fracturing, as described in Section 3.2.1. The samples were fractured in a particular direction (inwards, as shown in Figure 3.1), in order to avoid coating buckling and delamination, as well as avoiding any potential heat damage from wire cutting directly through the coating layer. The fractured components were embedded in Bakelite resin, so that the fracture site was facing up, as shown in Figure 3.5. Samples were then polished manually using grit polishing paper in grades of

1200, 800, 400, 200 and 100. Subsequently, the samples were polished to a mirror finish using a cloth and diamond paste. Samples were then analysed using SEM at 20kV with the electron backscatter function on, and images of the coating cross-sections were taken (1-5 kX magnification range); the coating thickness was measured at 18 different locations (from a multiple number of images) using ImageJ software. Additionally, EDX analysis was used to confirm chemical spectra of the coating and the substrate.

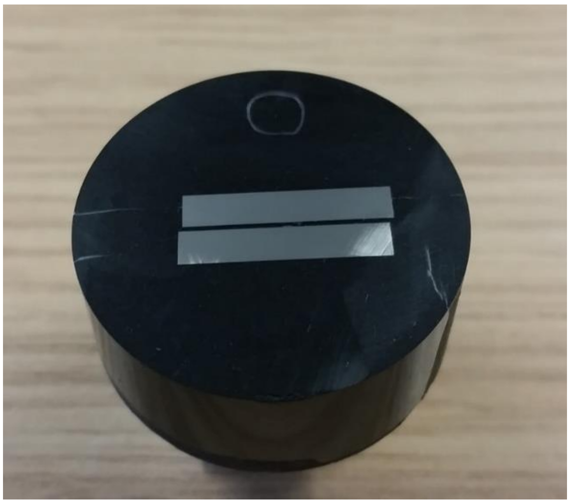

Figure 3.5: Fractured silicon nitride-coated sample embedded in the Bakelite resin.

3.3.5 Nanoindentation

In a nanoindentation test, a hard tip of known shape and mechanical properties is pressed onto a surface of a test sample, allowing the tip to penetrate the surface. Throughout the test, the load and tip displacement (i.e. depth) were reordered and the area of the indent is determined using the known geometry of the tip. During each measurement, a complete track of deformations occurring during the test was recorded and represented in a load (P) – displacement (h) curve (Figure 3.6). Such load-displacement curves consist of a loading and unloading curve; the loading curve is a representation of a material resistance against tip penetration and reflects the elastic and plastic properties of material. The unloading curve represents elastic recovery of the indented material.

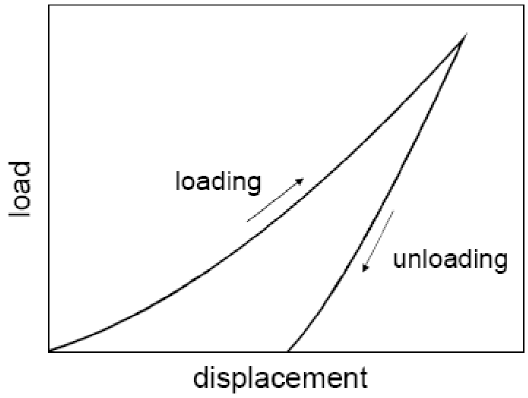

Figure 3.6: Typical load-displacement curve (indentation depth) obtained from the nanoindentation measurements.

Using the Oliver-Pharr method (built into the software) nanohardness of the ceramic coatings was determined. The method was originally derived from Sneddon's work, who established the relationship between load, displacement and contact area [252]. The Oliver-Pharr method determines contact stiffness and projected contact area at the maximum load from the unloading curve (obtained during the nanoindentation test). The contact stiffness was determined in two steps:

1) Fraction of the unloading curve was fitted with Equation 3.7.

$$P = \alpha(h - h_f)^m$$

Equation 3.7

Where:

P – applied force [N]

$(h - h_f)$ – elastic displacement of the indenter

m, α – fitting parameters

2) The unloading curve fit was differentiated to determine the slope at maximum load.

The projected contact area at maximum load was determined by the depth of contact (h_c). From Sneddon's analysis, the depth of contact was given by Equation 3.8:

$$h_c = h_{max} - \varepsilon(h_{max} - h_i)$$

Equation 3.8

where:

ε - an indenter geometry factor (0.75 for a Berkovich indenter)
h_i - an intercept of the initial unloading slope with displacement axis.

The relationship between depth of contact (h_c), residual contact depth (h_f), and the maximum displacement (h_{max}) is shown in Figure 3.7.

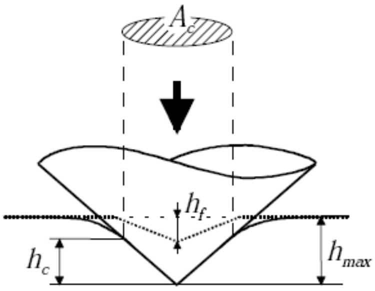

Figure 3.7: Schematic representation of the section through an indentation; A_c is the projected contact area. Reproduced based on Oliver and Pharr [253]**.**

The relationship between contact depth and projected contact area was given by tip shape area function $A_c = f(h_c)$. It should be noted that the measured contact displacement consists of three factors:

1) Elastic and/or plastic deformation of a sample;
2) Elastic deformation of the indenter;
3) Elastic deformation of the measuring frame.

The elastic deformation of the indenter has been accounted for by introducing a reduced Young's modulus E_r. This reduced modulus accounted for the fact that the indenter was not ideally rigid and this assumption was especially useful when measuring stiff materials (e.g. ceramics). The elastic deformation of the measuring frame i.e. compliance of the frame was determined by modelling the sample/loading frame as a system of two springs in series, and determined in several calculation steps. Once the loading frame compliance was determined, the tip shape/area function was calculated. To do so, several indents under different loads were made on fused quartz. The projected contact areas for each indentation was determined by Equation 3.9.

$$A_c = \frac{\pi}{4} \times \frac{1}{E_r^2 \times (c_t - c_f)^2}$$

Equation 3.9

where:

E_r – reduced Young's modulus
c_t – total compliance
c_f – loading frame compliance

Once determined, the projected contact areas were plotted against the contact depth. Finally, the tip shape area function was obtained by fitting A_c and h_c data to a polynomial equation:

$$A_c = a_0 h_c^2 + a_1 h_c + a_2 h_c^{1/2} + a_3 h_c^{1/4} + a_4 h_c^{1/8} + a_5 h_c^{1/16}$$

Equation 3.10

where:

a_i - fitting constants.

Such tip shape area function can be used for any particular indentation by inserting h_c of a measurement. Finally, to determine hardness, the contact area value of an indent was fitted into Equation 3.10.

$$H = \frac{P_{max}}{A_c}$$

Equation 3.11

where:

H – material hardness
P_{max} – applied force
A_c – projected contact area

The nanoindentation equipment used in this test applied an electromagnetic force application and capacitive depth measurement to determine elastic and plastic properties of the ceramic coatings. The testing instrument incorporated a three-plate capacitive force/displacement transducer, which assured high sensitivity and a linear force/displacement output. Three coupons of each coating were subjected to this analysis; each sample underwent 10 indentations. The indentations were made at 10 random locations across the surface of each sample. The measurements were made at a constant maximum load of 20mN and at a loading/unloading rate of 1000μN/ minute. Results were collated in Excel. Statistical analysis of the results was determined using one-way ANOVA ($\alpha=0.05$) in SPSS for Windows software.

3.3.6 Scratch testing

The scratch test for coating adhesion evaluation was first developed in 1950 by Heavens [254]. Later, Benjamin and Weaver have proposed the critical load (L_c) as a quantitative value to evaluate coating adhesion [255]. In this test, a sphero-conical diamond tip was pressed against the surface of a sample and drawn across the surface at a constant speed and with a progressive load applied at a constant loading rate. The current study followed BS EN 1071-3:2005 standard (‘*Advanced technical ceramics – Methods of test for ceramic coatings – Part 3: Determination of adhesion and other mechanical failure modes by a scratch test’)* [256]. During scratching, the critical loads were detected as acoustic emissions. The acoustic sensor elastic waves were generated as a result of formation and propagation of microcracks. Typically, three critical loads were detected - Lc_1 – where the first plastic deformation cracking occurred, Lc_2 – where spallation occurred (i.e. the coating started to flake off the substrate, typically at the edges on the scratch) and Lc_3 – where the tip penetrated the coating through to the substrate at the centre of the crack (as show in Figure 3.8). Additionally, the scratches were inspected visually under a light microscope and coating failures characteristics along with critical load characteristics were detected. The critical loads depend on the mechanical strength (cohesion and adhesion) of a coating-substrate composite.

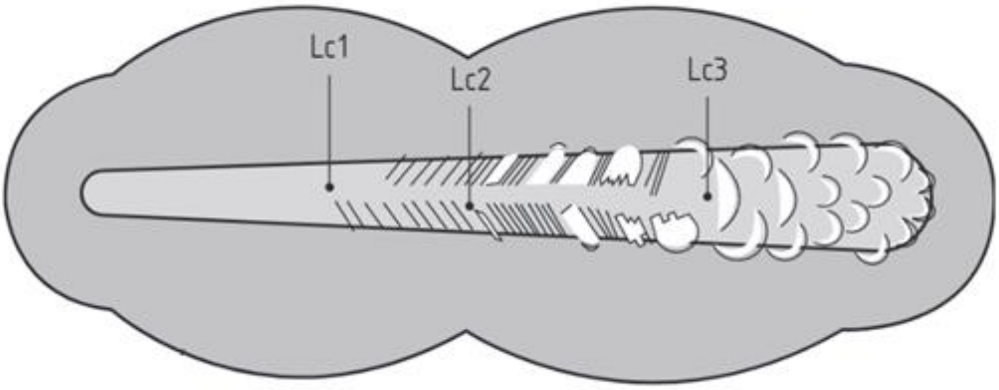

Figure 3.8: Schematic representation of a scratch produced on a surface of a coated sample. Position of the L_1 is associated with chevron-line cracks at the edges of the scratch; L_2 associated with spallation of the coating at the edges of the scratch and L_3 with complete failure of the coating, whereby the tip penetrates through the coating in the middle of the scratch [256]**.**

Three samples of each coating were subjected to this investigation; five scratches were made on the surface of each coupon. A Rockwell type C diamond tip with a radius of r=0.2mm was used in the test. Each scratch yielded a maximum tip load of 100N at a loading rate of 200N/min, resulting in 5mm long scratches. While the machine used in this test was fitted with acoustic emission detector, it was found that the values of critical loads recorded as acoustic emissions were not accurate, and the signal often carried signal noise artefacts. As a result, following the scratch testing, each scratch was inspected using a light microscope and positions of coating mechanical failures, which can be associated with each critical load, were marked and used to calculate the critical load values in Excel. As the scratch distance and loading rates were known, it was possible to calculate the load (in this case the critical load) at any particular position within the scratch.

3.4 Results

3.4.1 X-ray photoelectron spectroscopy (XPS) analysis

3.4.1.1 Chromium nitride coated coupons

The surfaces of three chromium nitride coated coupons were analysed using XPS. Survey spectra were obtained following Ar^+ ion sputtering for different times (0-600s), thus a depth profile of the coating was obtained. The effects of sputtering time on the peaks detected from survey spectra are shown in Figure 3.9; the cascaded view of the spectra revealed that sputtering with Ar^+ ions resulted in additional elements being detected in the spectra. For all three coupons, an overlaid view of the same spectra, showing labels of peak position correlated with particular elements (Figure 3.10), revealed that in spectra obtained without Ar^+ ion sputtering peaks correlating with carbon C1s (~284.8 eV) and oxygen O1s (~532 eV) were smaller than those from the post-sputtering spectra peaks. Conversely, peaks correlating with N1s (~399 eV) and Cr 2p1/2, Cr2p and Cr2p3/2 (~584 eV), whilst present, were smaller in the spectra obtained without sputtering. The overlaid view (Figure 3.10) also revealed that the length of the sputtering process did not make a substantial difference to the signal strengths obtained from the survey spectra, as long as the sample had been sputtered for at least 100s.

These results are supported by the chemical composition, calculated from the obtained survey spectra, depending on the sputtering time, as shown in Table 3.3. Once a sample had undergone at least 100s of Ar^+ ion sputtering, the chemical composition of the chromium nitride coating did not change significantly.

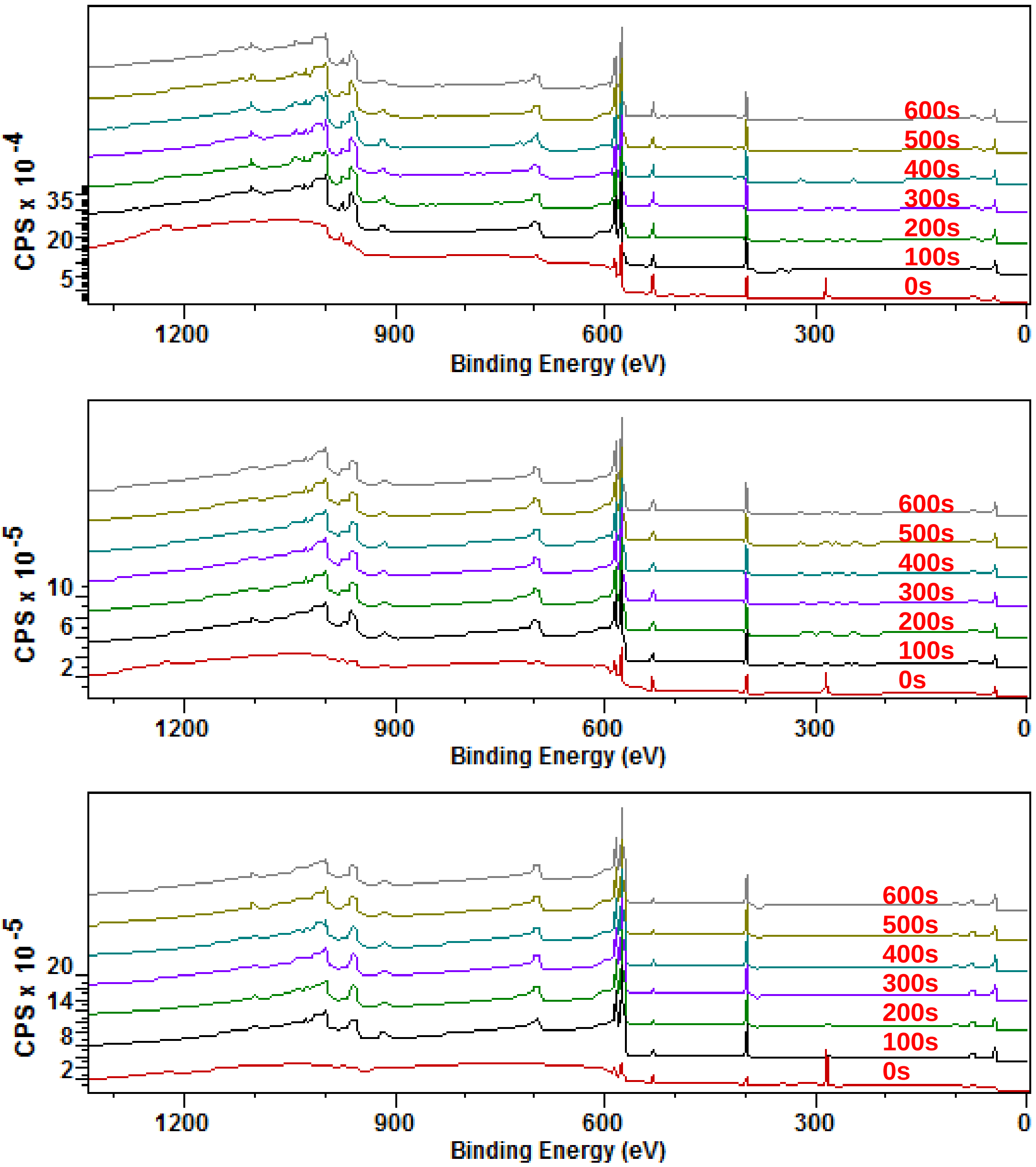

Figure 3.9: Cascaded views of survey spectra of coupons 1 (top), 2 (middle) and 3 (bottom) at different sputtering times, as indicated on the right side of each graph. The locations of peaks corresponding with different elements are the same for spectra obtained following sputtering. Only small variations in peak presence were noted for spectra obtained following no sputtering.

Table 3.3: Chemical composition of the surface region of CrN films deposited on three coupons, represented in atomic percent (at.%).

	Sputtering time						
Spectra	Pristine	100s	200s	300s	400s	500s	600s
Coupon 1							
C1s	41.6	3.3	2.2	1.6	1.2	1.6	1.0
O1s	22.2	16.8	15.7	15.7	16.3	15.9	16.4
N1s	18.8	34.7	35.4	35.0	35.4	36.1	34.5
Cr2p	17.5	45.2	46.7	47.7	47.1	46.4	48.1
Coupon 2							
C1s	47.6	4.2	3.3	2.7	2.2	2.2	2.0
O1s	16.7	12.4	12.7	13.0	12.9	13.2	13.3
N1s	20.3	38.4	37.8	37.7	37.8	37.7	37.5
Cr2p	15.4	45.1	46.2	46.7	47.1	47.0	47.3
Coupon 3							
C1s	68.2	7.7	5.2	7.2	7.2	7.1	7.0
O1s	12.0	7.2	7.1	3.7	3.3	2.4	2.0
N1s	12.8	31.5	32.1	32.5	33.2	33.0	32.9
Cr2p	6.9	53.6	55.6	56.7	56.3	57.5	58.2

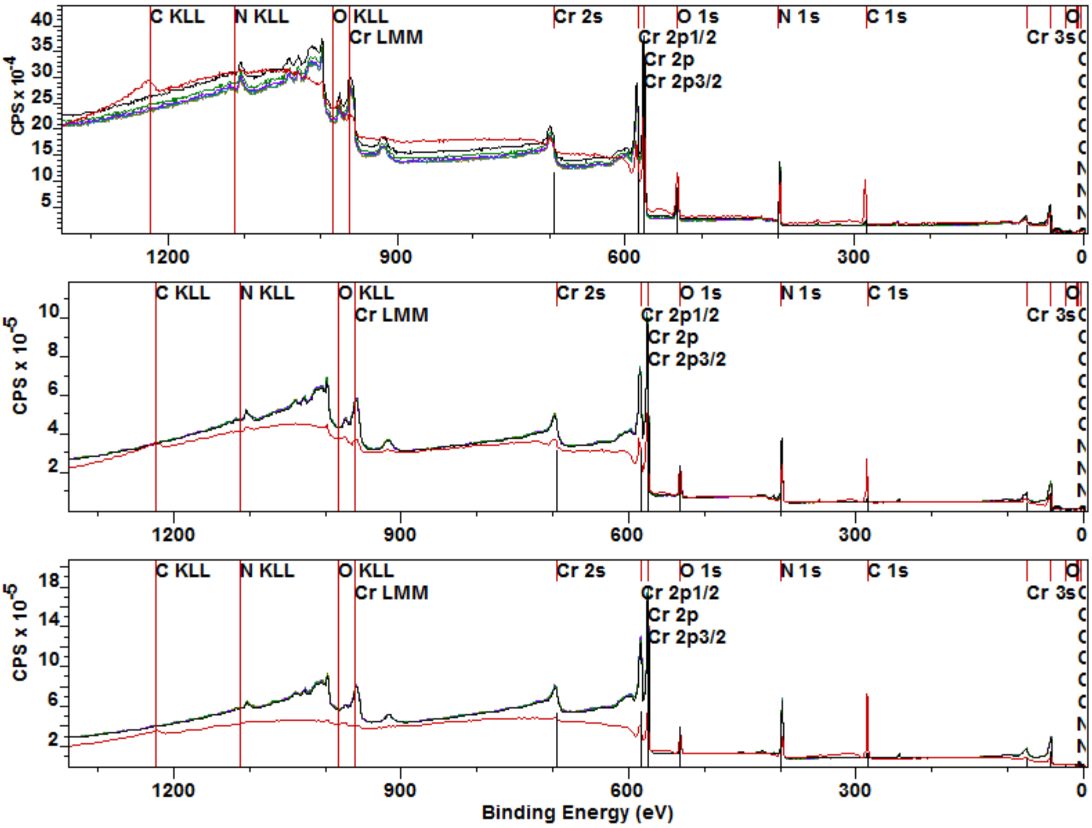

Figure 3.10: Overlaid survey spectra of three CrN coated coupons, with peaks correlating with specific elements identified. Carbon C1s and oxygen O1s peaks were stronger in samples that did not undergo any Ar$^+$ ion sputtering (red spectra line), whilst signals of chromium Cr2p and nitrogen N1s were stronger once the samples were sputtered with argon ions for at least 100s (other colours).

3.4.1.2 Silicon nitride coated coupons

The surfaces of three silicon nitride coated coupons were analysed using XPS. Survey spectra were obtained following sputtering for different times i.e. 0-600s. The effects of the sputtering on peaks detected from survey spectra can be seen in Figure 3.11; the cascaded view of the spectra reveals that those obtained with no Ar$^+$ ion sputtering had a slightly different shape i.e. the same peaks were not detected in the non-sputtered spectra.

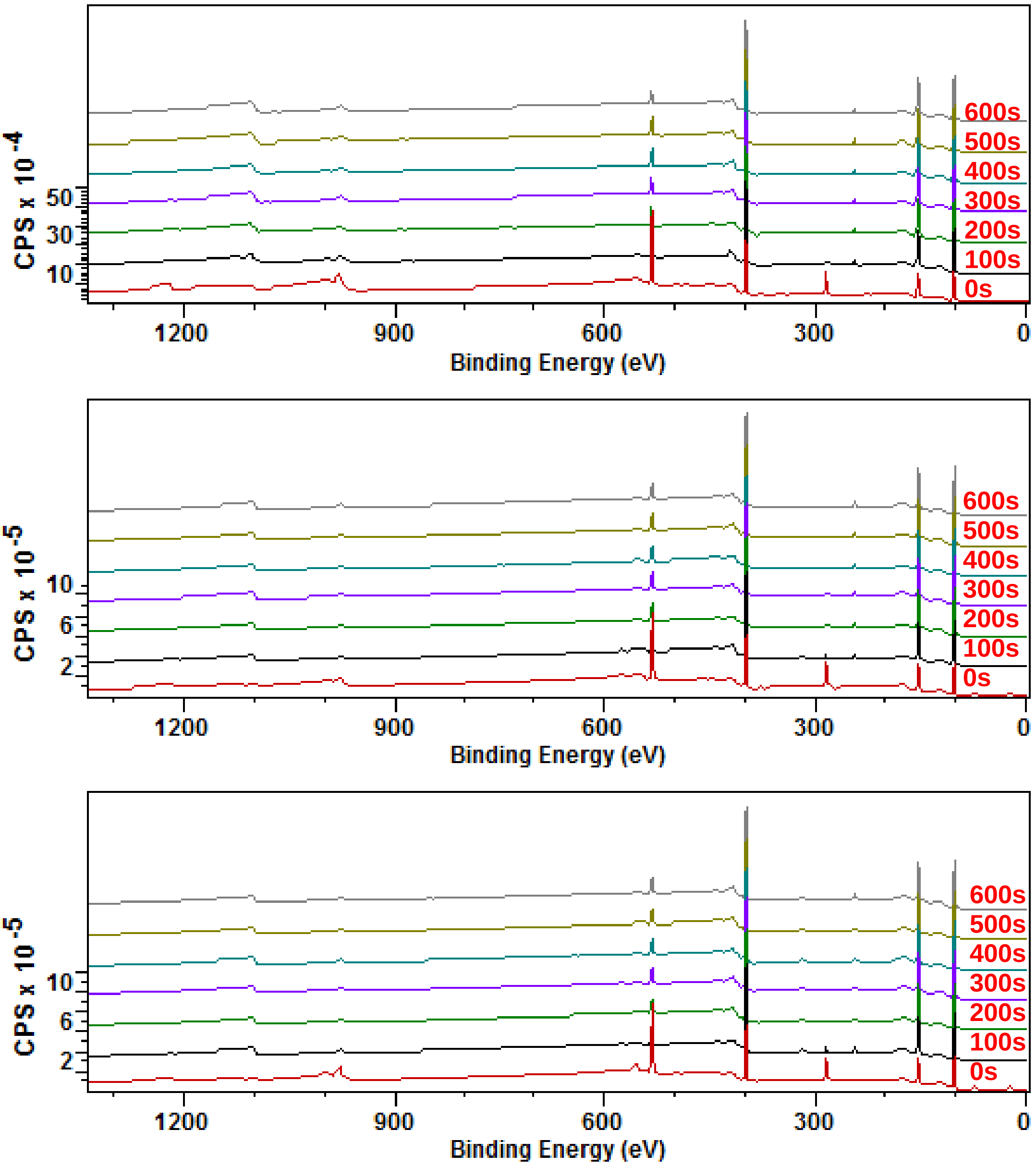

Figure 3.11: Cascaded views of survey spectra of coupons 1 (top), 2 (middle) and 3 (bottom) at different sputtering times, as indicated on the right side of each graph. The locations of peaks corresponding with different elements are the same for spectra obtained following sputtering. Only small variations in peak presence were noted for spectra obtained following no-sputtering.

For instance, the non-sputtered spectra show much stronger C1s (~284 eV) and O1s (~532 eV) peaks, whilst the survey spectra of samples which had undergone sputtering show these peaks were of much lower intensity (as also shown in Figure 3.12). Conversely, peaks correlating with N1s (~399 eV) and Si2p (~100 eV), whilst present, were smaller in the spectra obtained without sputtering. The overlaid view shown in Figure 3.12 also revealed that the length of the sputtering process did not make a substantial difference in signal strengths obtained from the survey spectra, as long as the sample has been sputtered for at least 100s. Those findings were supported by the chemical composition, calculated from the obtained survey spectra, depending on the sputtering time, as shown in Table 3.4. Once a sample has undergone at least 100s of Ar^+ ion sputtering, chemical composition of the silicon nitride coated samples did not change substantially.

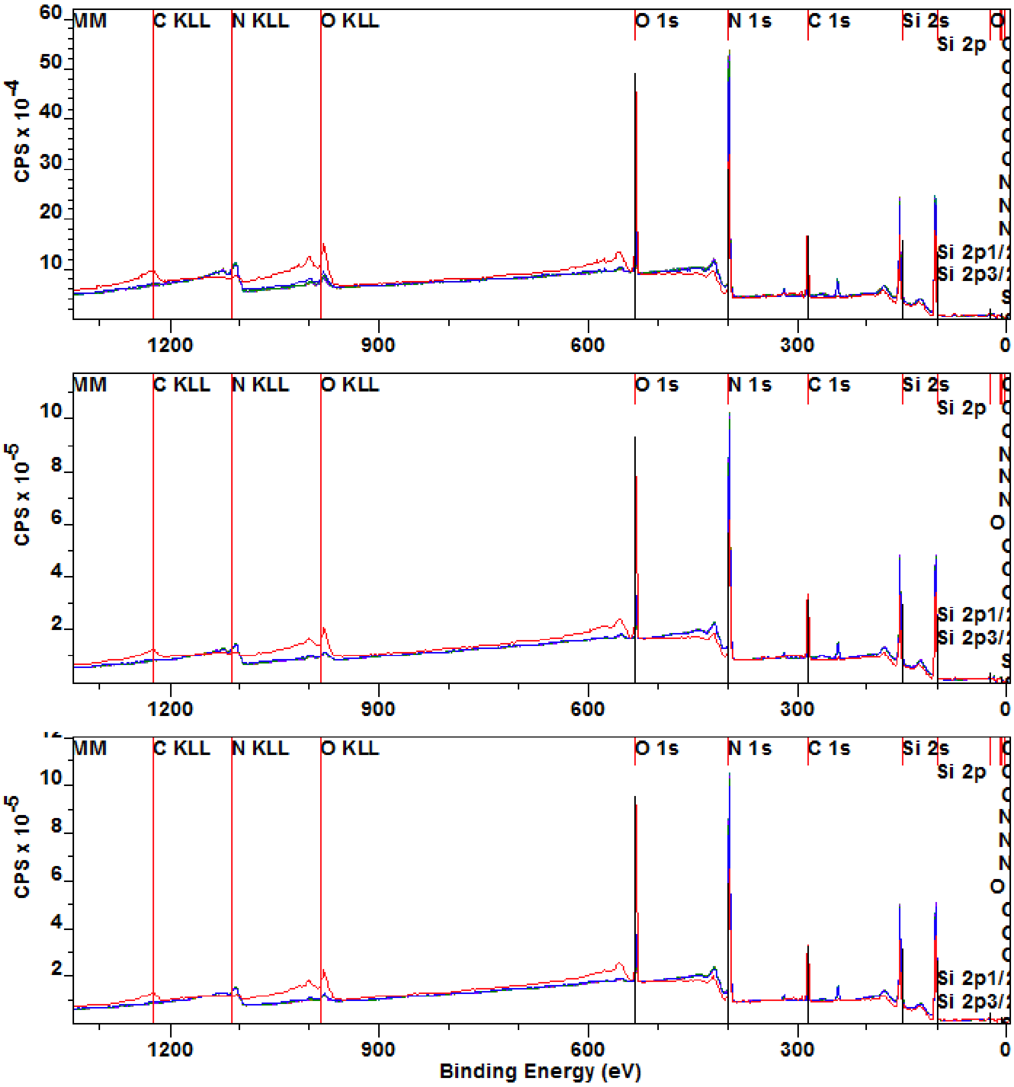

Figure 3.12: Overlaid survey spectra of three Si_3N_4 coated coupons, with peaks correlating with specific elements identified. Red survey line – non-sputtered, remaining colours – post sputtering.

Table 3.4: Chemical composition of the surface region of Si_3N_4 films deposited on three coupons, represented in atomic percent (at.%).

	Sputtering time						
Spectra	Pristine	100s	200s	300s	400s	500s	600s
Coupon 1							
C1s	19.3	3.3	2.1	1.5	1.25	0.9	0.9
O1s	25.4	9.5	7.2	6.5	6.0	5.8	5.6
N1s	24.0	39.5	41.3	42.1	42.5	43.1	43.0
Si2p	31.3	47.7	49.5	49.4	50.2	50.2	50.5
Coupon 2							
C1s	22.2	4.3	2.4	1.6	1.3	1.4	1.0
O1s	22.6	5.9	5.3	5.1	5.34	5.2	5.3
N1s	23.6	39.8	41.2	47.7	41.8	41.7	41.8
Si2p	31.5	49.9	51.0	51.5	51.6	51.7	51.9
Coupon 3							
C1s	19.3	3.8	2.2	1.3	1.4	1.0	0.9
O1s	23.8	6.4	5.6	5.5	5.4	5.5	5.6
N1s	24.0	39.8	41.0	41.5	41.5	41.7	41.6
SI2p	32.9	50.0	51.2	51.7	51.7	51.8	51.9

3.4.2 Surface roughness

The surface roughness of coated coupons was measured using contacting profilometry; R_a, R_p, R_v and R_{sk} parameters were recorded. A summary of the surface roughness of chromium nitride coupons can be found in Table 3.5, whilst the results for silicon nitride coated coupons are summarised in Table 3.6. Statistical analysis of the results (one-way ANOVA, α=0.05) did not show statistical differences in R_a, R_p or R_v ($p>0.05$, CI 95%) values of the two coatings. Only the skewness was found to be statistically different ($p<0.05$, CI 95%) between the two coatings; the average skewness of the silicon nitride coatings was R_{sk} = 3.3113 whilst the average surface skewness of the chromium nitride coatings was R_{sk} = 0.6236.

Table 3.5: Summary of surface roughness results of chromium nitride coated coupons.

	Trace	R_a [µm]	R_p [µm]	R_v [µm]	R_{sk}
Coupon 4	P_1	0.0196	0.0540	0.0585	-0.4530
	P_2	0.0190	0.0531	0.0554	0.5308
Coupon 5	P_1	0.0571	0.2802	0.1326	1.6390
	P_2	0.0621	0.2779	0.1397	1.3782
Coupon 6	P_1	0.0261	0.1233	0.0875	0.8581
	P_2	0.0322	0.1626	0.1138	1.0899
Coupon 7	P_1	0.0257	0.1025	0.0973	-0.0613
	P_2	0.0252	0.1008	0.0948	0.0071
Average		0.0334	0.1443	0.0975	0.6236
St-dev		0.0166	0.0904	0.0309	0.7454

Table 3.6: Summary of surface roughness results of silicon nitride coated coupons.

	R_a [µm]	R_p [µm]	R_v [µm]	R_{sk}
Coupon 4	0.0242	0.1183	0.0756	3.4570
	0.0263	0.1182	0.0916	4.8350
Coupon 5	0.0251	0.1459	0.0861	6.7027
	0.0203	0.0866	0.0799	2.5632
Coupon 6	0.0288	0.1496	0.1283	-3.7067
	0.0269	0.1452	0.0817	5.4169
Coupon 7	0.0235	0.0865	0.0932	2.4577
	0.0259	0.1196	0.0882	4.7649
Average	0.0251	0.1212	0.0906	3.3113
St-dev	0.0026	0.0251	0.0164	3.1833

3.4.3 Coating thickness

3.4.3.1 Calo test

A calo test was employed to assess the thickness of the coatings on the coupons. Once craters were abraded by the Calo tester, the surfaces were analysed using a light microscope and the sizes of the abraded crater scars were measured and fitted into Equation 1.2. As such, coating thicknesses were calculated. An example of a sample measurement is shown in Figure 3.13. The results of chromium nitride coating thicknesses are summarised in Table 3.7, while the results for the silicon nitride coating are summarised in Table 3.8. The average thickness of chromium nitride coatings was found to be 4.9±0.8µm, while the average thickness of silicon nitride coating was 5.1±0.3µm. Statistical analysis of the results (one-way ANOVA, $\alpha=0.05$) did not show statistical differences in coating thickness between the two ceramic coatings ($p>0.05$, CI 95%).

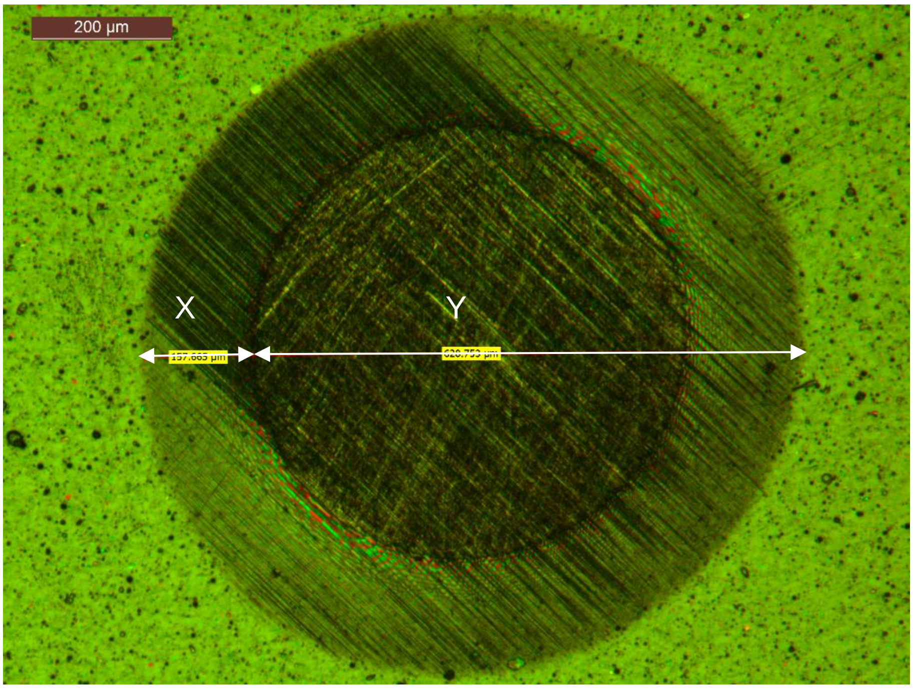

Figure 3.13: Projection on the surface of silicon nitride-coated coupon. For each sample, the x and y dimensions were measured using the Leica microscope software. Data was collated in a spreadsheet and coating thickness was determined.

Table 3.7: Summary of chromium nitride coating thickness results, as obtained with a Calo tester. The average coating thickness of chromium nitride was found to be 4.9±0.8µm.

Sample	Scratch	x [µm]	y [µm]	Coating thickness [µm]
Coupon 4	a	612.5	240.4	5.9
	b	641.8	237.2	6.1
	c	637.1	238.6	6.1
Coupon 5	a	672.7	149.5	4.0
	b	674.3	164.1	4.4
	c	732.8	149.5	4.4
Coupon 6	a	825.3	133.2	4.4
	b	773.3	151.1	4.7
	c	830.2	136.5	4.5
Average		711.1	533.3	4.9
St-dev.		82.5	123.8	0.8

Table 3.8: Summary of silicon nitride coating thickness results, as obtained with Calo tester. The average coating thickness of silicon nitride was found to be 5.1±0.3μm.

Sample	Scratch	x [μm]	y [μm]	Coating thickness [μm]
Coupon 4	a	646.6	194.9	5.1
	b	500.4	256.7	5.1
	c	458.2	313.6	5.7
Coupon 5	a	697	164.1	4.6
	b	802.6	149.5	4.8
	c	567	220.9	5.0
Coupon 6	a	786.5	157.7	4.9
	b	651.7	187	4.9
	c	643.4	203.1	5.2
Average		639.3	205.3	5.1
St-dev.		116.8	52.6	0.3

3.4.3.2 SEM cross-section analysis

Cross sections of coupons coated with ceramic coatings, fixed in Bakelite resin, were analysed under SEM; EDX analysis was used to confirm the location of the coating and substrate. Example of an SEM image of coating cross-section is shown in Figure 3.14. Examples of EDX analysis of sample cross sections are shown in Figure 3.15 and Figure 3.16.Coating thicknesses were measured using SEM-obtained images and ImageJ software. The summary of coating thickness results for chromium nitride coatings can be found in Table 3.9, while the results for silicon nitride coatings are summarised in Table 3.10. The average coating thicknesses were found to be 4.6±0.4μm and 5.1±0.3μm for the chromium nitride and silicon nitride coatings, respectively. Statistical analysis of the results (one-way ANOVA, $\alpha=0.05$) showed significant differences in thickness between the two ceramic coatings ($p<0.05$, CI 95%).

When the two methods were compared, no statistical difference was found in the thickness of the chromium nitride ($p>0.05$, CI 95%) or silicon nitride coatings ($p>0.05$, CI 95%).

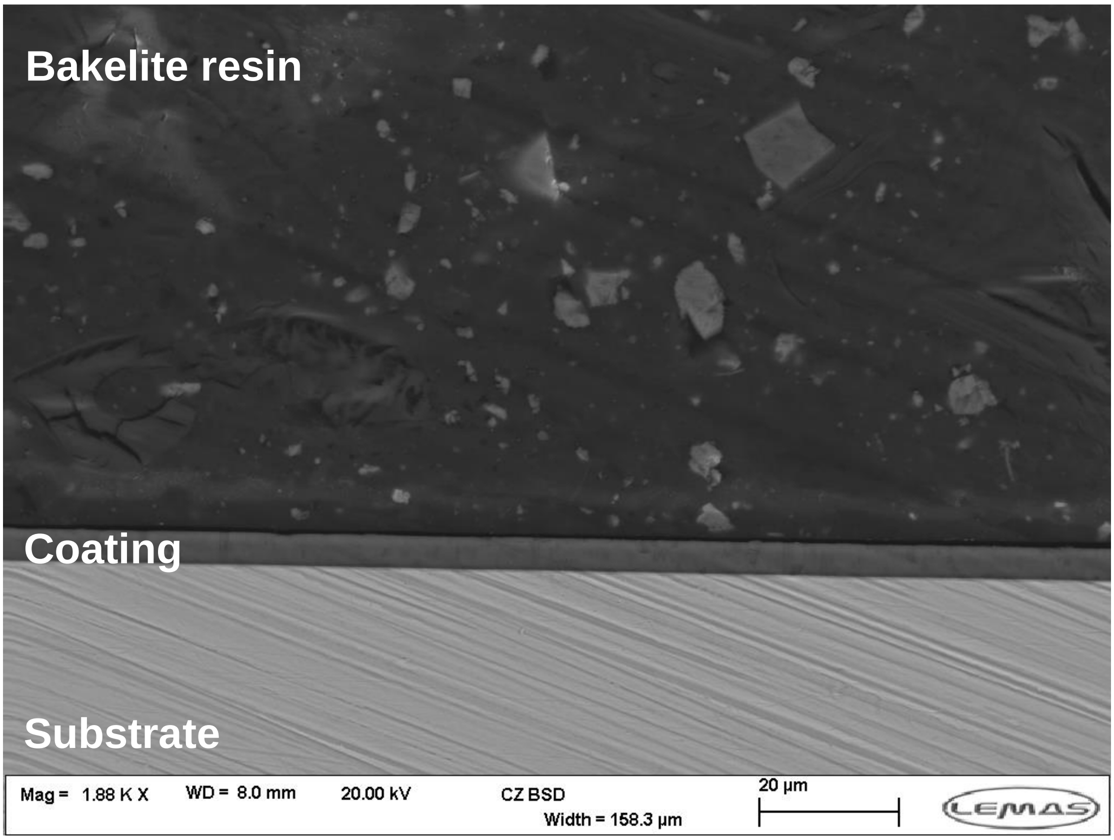
Bakelite resin
Coating
Substrate
Mag = 1.88 K X
WD = 8.0 mm
20.00 kV
CZ BSD
Width = 158.3 µm
20 µm
LEMAS

Figure 3.14 SEM image of a cross section of a silicon nitride-coated coupon. Clear layers of the substrate, coating and Bakelite resin can be distinguished.

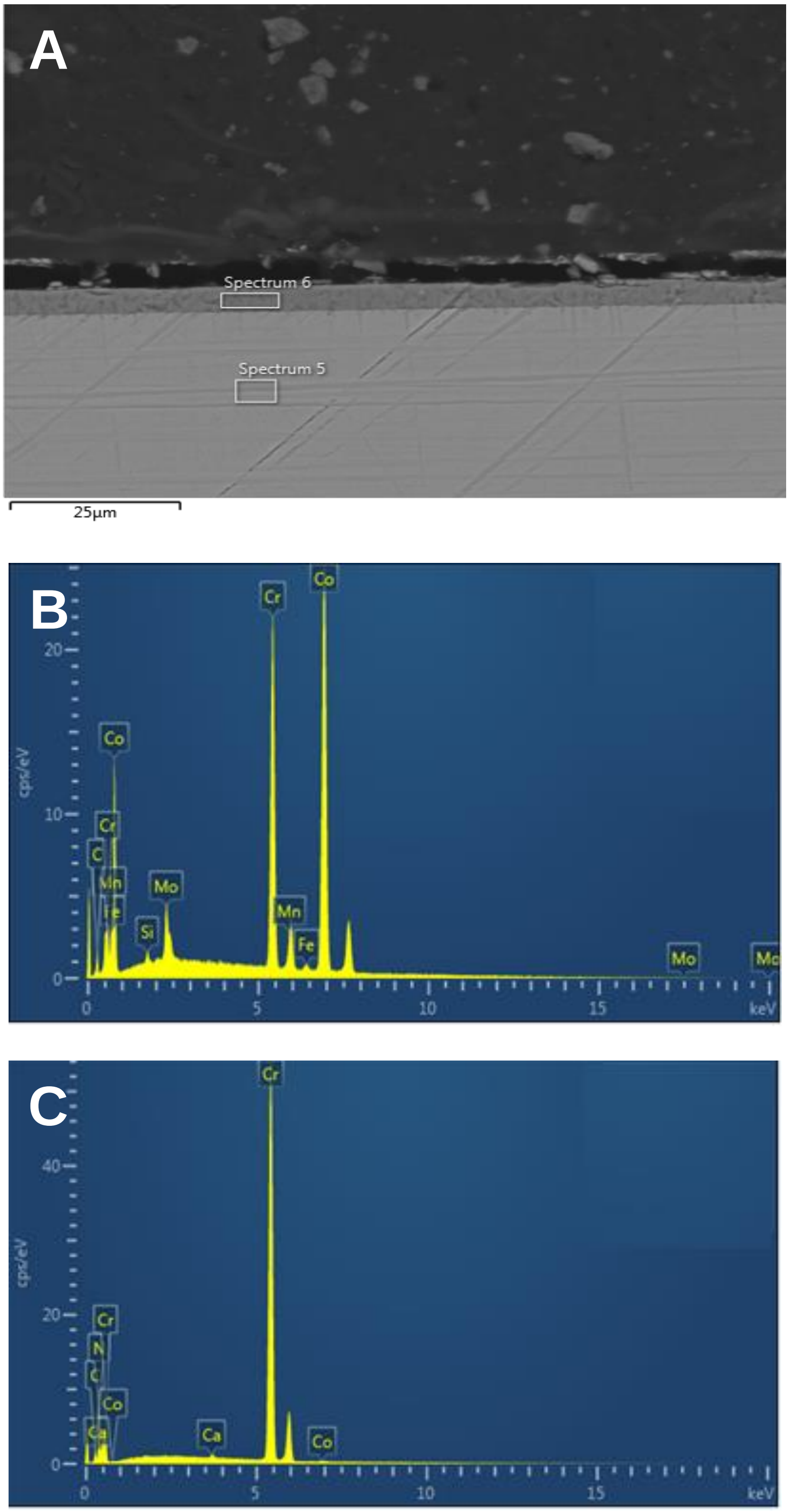

Figure 3.15: EDX analysis of a chromium nitride coated sample. The SEM image (A) was used to visually identify, whilst the EDX was employed to confirm regions of substrate (B) and coating (C) locations.

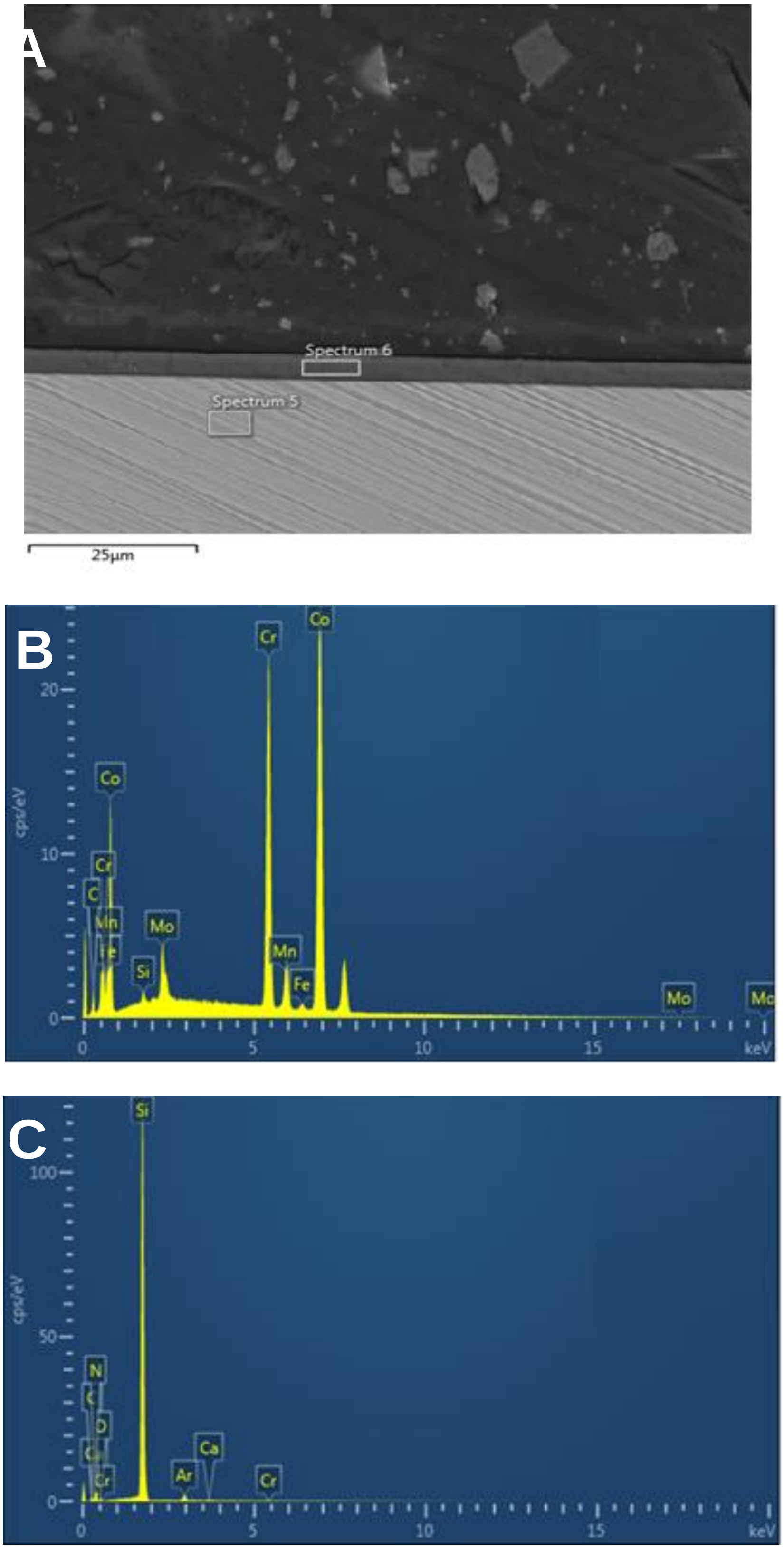

Figure 3.16: EDX analysis of a silicon nitride coated sample. The SEM image (A) was used to visually identify, whilst the EDX was employed to confirm regions of substrate (B) and coating (C) locations.

Table 3.9: Summary of coating thickness of chromium nitride coated coupons, as measured in ImageJ using images obtained from SEM.

	Coating thickness [µm]	Average [µm]	St-dev. [µm]
Coupon 4	4.349, 4.270, 4.430, 3.795, 4.348, 4.428, 4.357, 4.461, 4.476, 4.402, 4.417, 4.188, 4.224, 4.301, 4.167, 4.834, 5.037, 4.839	4.407	0.279
Coupon 5	4.356, 4.237, 4.148, 4.150, 4.000, 4.030, 4.474, 4.572, 4.803, 4.704, 4.639, 4.441, 4.507, 4.441, 4.638, 4.628, 4.592, 4.555	4.440	0.237
Coupon 6	4.532, 4.606, 4.082, 4.284, 5.833, 4.103, 5.781, 5.893, 5.939, 4.780, 4.650, 4.393, 4.589, 4.523, 4.841, 4.268, 4.523, 4.902	4.807	0.622
Average		4.551	0.448

Table 3.10: Summary of coating thickness of silicon nitride coated coupons, as measured in ImageJ using images obtained from SEM.

	Coating thickness [µm]	Average [µm]	St-dev. [µm]
Coupon 4	5.000, 4.871, 4.978, 5.210, 4.832, 4.935, 5.091, 4.944, 4.814, 4.878, 4.644, 4.814, 4.972, 4.917, 5.011, 5.020, 4.994, 5.134	4.976	0.147
Coupon 5	4.888, 4.826, 4.862, 4.857, 4.961, 4.834, 4.708, 4.933, 4.834, 5.245, 5.182, 5.888, 5.616, 4.887, 5.766, 5.645, 5.391, 5.258	5.118	0.361
Coupon 6	5.194, 5.175, 5.133, 5.215, 5.133, 5.429, 5.337, 5.271, 5.111, 5.143, 5.048, 5.398, 5.529, 5.575, 5.297, 5.227, 5.296, 5.251	5.250	0.169
Average		5.115	0.267

3.4.4 Nanoindentation

Three coupons coated with each coating – chromium nitride and silicon nitride, were analysed using nanoindentation. Each was subjected to 10 indentations, during which load and displacement were recorded. Indentation load-depth hystereses for each chromium nitride coated coupon are shown in Figure 3.17. The resulting hardness and Young's moduli of the chromium nitride coating are listed in Table 3.11. The average hardness and Young's modulus of chromium nitride coatings were found to be 23.69±1.18 GPa and 247.51±40.09 GPa, respectively. Similarly, the indentation load-depth hystereses for each silicon nitride sample are shown in Figure 3.18, while the hardness and Young's modulus values of the silicon nitride coatings are summarised in Table 3.12. The average hardness and Young's modulus of silicon nitride coating were found to be 19.07±0.68GPa and 213.39±6.83 GPa, respectively. Statistical analysis of the results (one-way ANOVA, $\alpha=0.05$) showed that the chromium nitride coatings had a significantly higher hardness ($p<0.05$, CI 95%) and Young's modulus ($p<0.05$, CI 95%) than the silicon nitride coatings. Both of the coatings showed a substantially higher hardness than the substrate material (CoCr), which under its ASTM-F1537-11 specification has a hardness of 1.1GPa [207]. The mean H/E ratio of the chromium nitride coating was significantly higher ($p<0.05$, CI 95%) than these of silicon nitride coated samples; 0.10±0.02 and 0.09±0.01, respectively. The H/E ratio of the CoCr substrate, assuming E=210GPa, was 0.01.

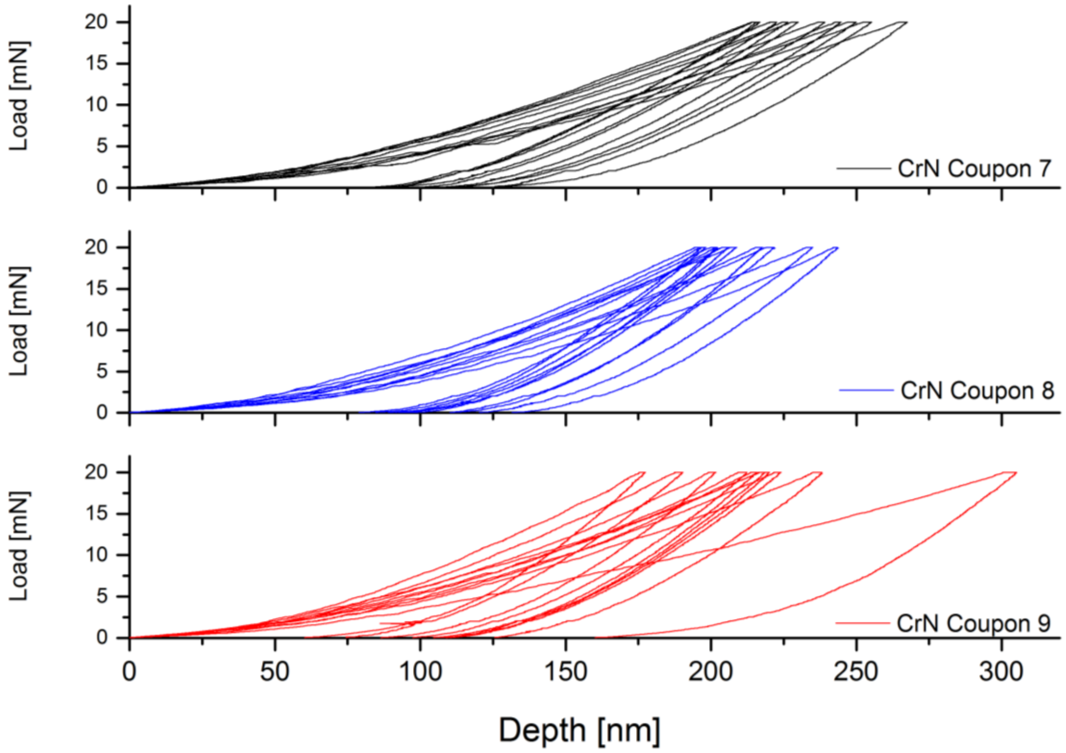

Figure 3.17: Indentation depth-loading hystereses for chromium nitride coated coupons. Each of 10 indentations has been recorded.

Table 3.11: Summary of the nanoindentation results of chromium nitride coated coupons, showing average hardness and Young's modulus of the coating.

		Hardness [GPa]	**Young's modulus [GPa]**	**H/E ratio**
Coupon	7	22.47	201.24	0.11
	8	24.83	272.07	0.09
	9	23.78	269.20	0.09
Average		23.69	247.51	0.10
St-dev.		1.18	40.09	0.02

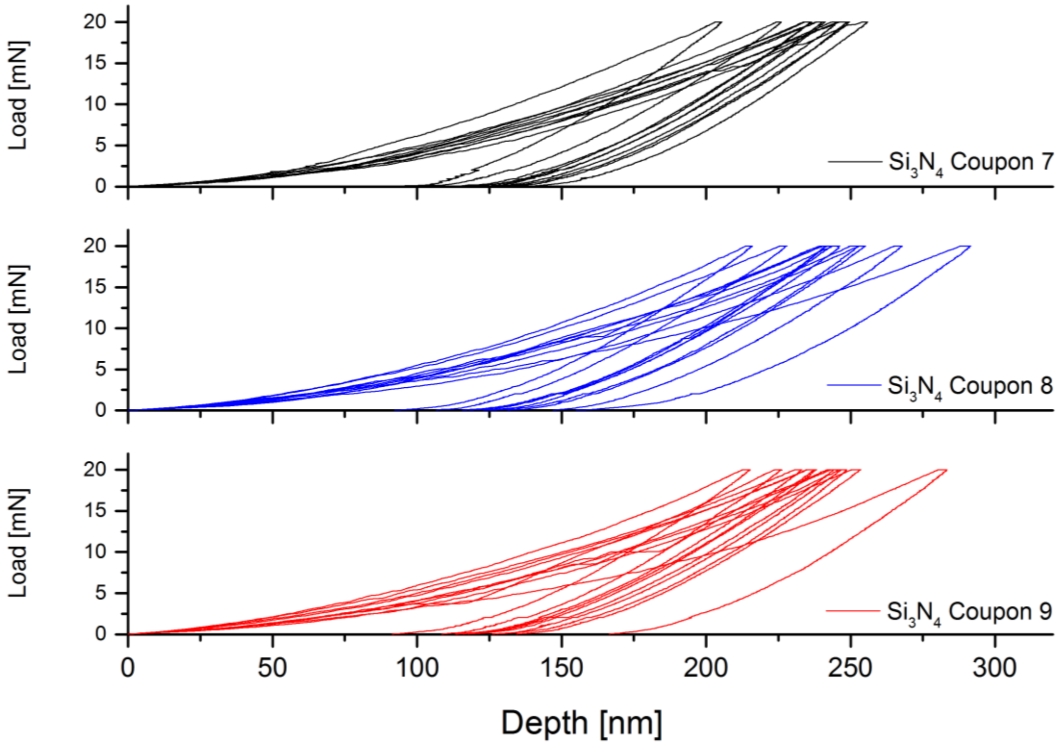

Figure 3.18: Indentation depth-loading hystereses for silicon nitride coated coupons. Each of 10 indentations has been recorded.

Table 3.12: Summary of nanoindentation results of silicon nitride coated coupons, showing average hardness and Young’s modulus of the coating.

		Hardness [GPa]	Young's modulus [GPa]	H/E ratio
Coupon	7	19.63	220.42	0.09
	8	18.32	206.79	0.09
	9	19.27	212.96	0.09
Average		19.07	213.39	0.09
St-dev.		0.68	6.83	0.01

3.4.5 Scratch testing

Three coupons coated with either chromium nitride or silicon nitride were subjected to scratch tests; each sample was scratched 5 times (Figure 3.19). Scratches were inspected under using the light microscope (Figure 3.20) and visually, locations of the critical failures were marked. From known scratch lengths and loading rates, the loads applied at these locations were calculated. A summary of critical load calculations for chromium nitride and silicon nitride coatings can be found in Table 3.13 and Table 3.14, respectively. The average critical loads L_{c1}, L_{c2} and L_{c3} for chromium nitride coatings were 10.42±0.74 N, 16.24±0.7 4N and 73.92±3.56 N, respectively. The same critical load values for the silicon nitride coatings were 4.48±0.80 N, 22.85±2.70 N and 63.06±6.40 N. Statistical analysis of the results (ANOVA, α=0.05) showed significant differences in the values of all three L_c ($p<0.05$, CI 95%) critical loads between the two coatings. It was found that the L_{c1} and L_{c3} values were higher for the chromium nitride coating, whilst the L_{c2} value was higher for the silicon nitride-coated samples.

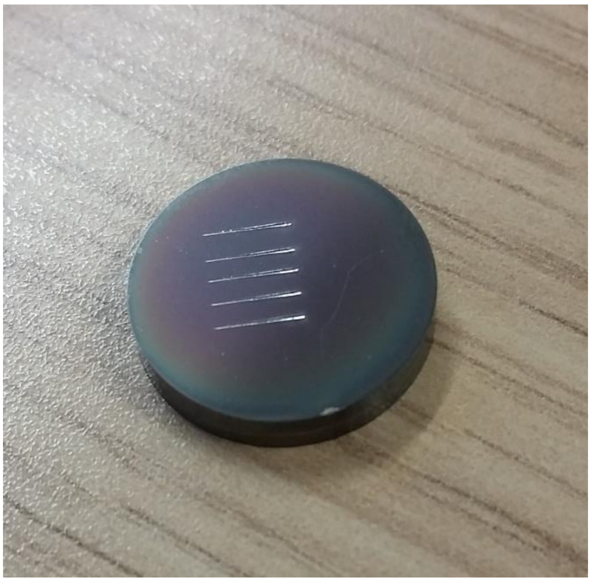

Figure 3.19: A silicon nitride coated coupon following scratch testing; five scratches were made on each coupon, which were subsequently analysed using a light microscope to identify locations of failures associated with critical loads.

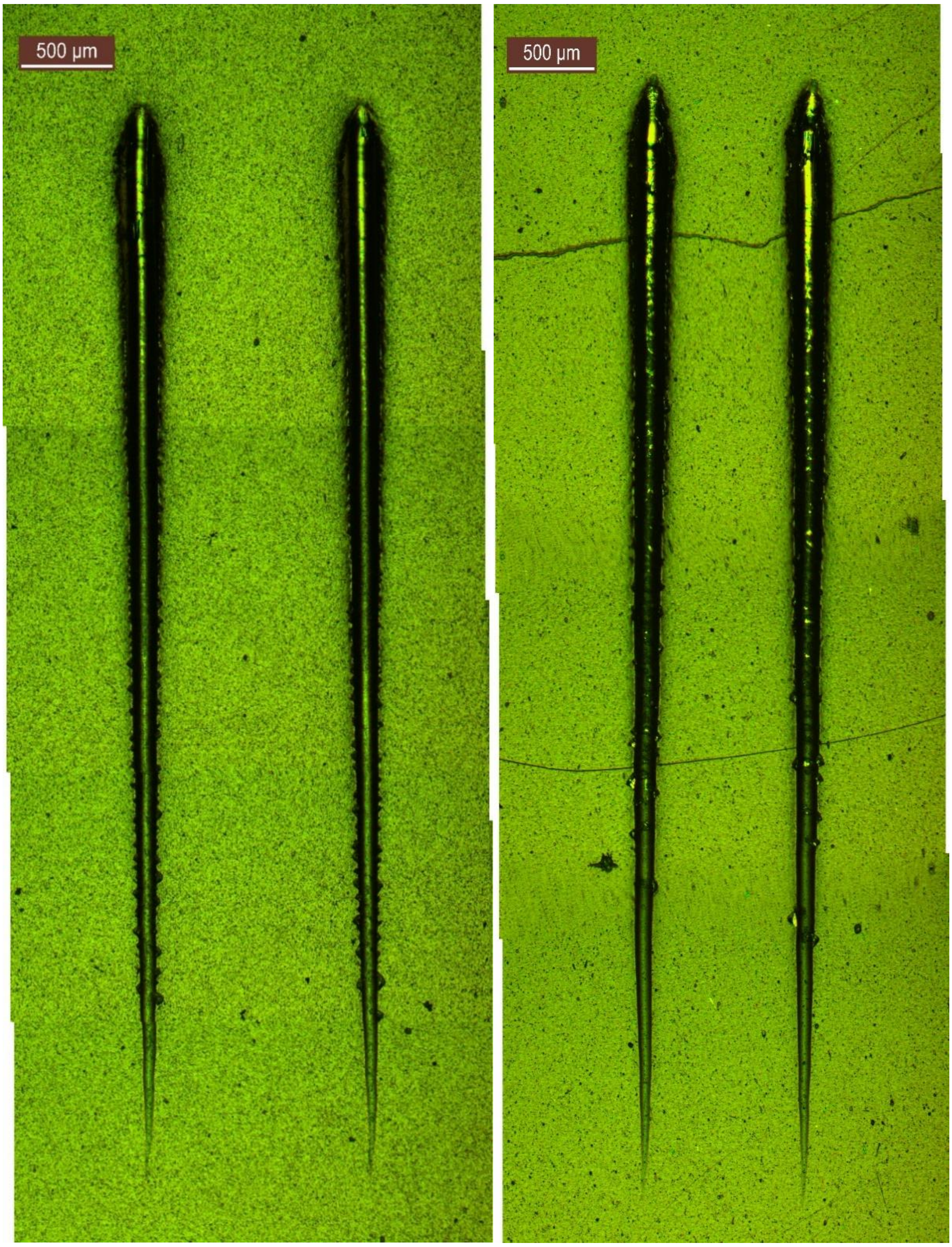

Figure 3.20: Micrograph of scratches generated with the scratch testing on coupons coated with CrN (left) and Si_3N_4 (right) coatings.

Table 3.13: Summary of values of critical loads measured during scratch testing of chromium nitride coated coupons. The average load at which the scratch tip penetrated through the chromium nitride coating was 73.92±3.56 N.

Coupon	Scratch	Lc_1 [N]	Lc_2 [N]	Lc_3 [N]
7	1	11.87	16.65	80.56
	2	9.75	17.40	74.51
	3	10.77	14.92	78.78
	4	10.61	16.34	77.01
	5	9.91	15.95	77.05
8	1	10.35	17.20	71.64
	2	9.59	16.08	70.23
	3	9.34	17.55	69.57
	4	9.47	16.47	70.31
	5	11.71	15.92	68.38
9	1	11.09	15.84	76.68
	2	10.61	15.12	74.53
	3	10.00	16.67	72.76
	4	10.37	15.76	71.01
	5	10.83	15.66	75.70
Average		10.42	16.24	73.92
St-dev.		0.74	0.74	3.56

Table 3.14: Summary of values of critical loads measured during scratch testing of silicon nitride coated coupons. The average load at which the scratch tip penetrated through the silicon nitride coating was 63.06±6.40 N.

Coupon	Scratch	Lc_1 [N]	Lc_2 [N]	Lc_3 [N]
7	1	4.95	21.24	69.00
	2	4.18	21.94	49.89
	3	3.37	19.96	53.48
	4	5.09	24.91	58.83
	5	4.19	18.08	60.11
8	1	3.74	20.96	70.45
	2	4.27	20.49	67.81
	3	4.59	23.83	68.52
	4	4.71	26.39	62.90
	5	4.27	21.56	63.70
9	1	4.97	27.36	72.42
	2	3.16	20.79	67.08
	3	6.68	23.37	64.21
	4	4.65	25.02	54.43
	5	4.40	26.92	63.03
Average		4.48	22.85	63.06
St-dev.		0.80	2.70	6.40

3.5 Discussion

Historically, surgical interventions involving total joint replacement were aimed at older and less active individuals. Currently, the recipients of artificial joints are younger and more active, thus longevity of such devices is paramount. Ceramic coatings have the potential to reduce the risks associated with wear-related implant failure by improving surface properties of the bearings. The optimal ceramic coating for total joint applications must have appropriate mechanical properties (hardness, elastic modulus), adhesion to the substrate, smooth surface, high resistance to wear as well as be biocompatible [257]. The work presented in this chapter aimed to characterise two coatings proposed for the improvement of the tribological performance of total disc replacements – chromium nitride and silicon nitride. The coatings were deposited on CoCr coupons and their surface roughness, coating thickness, adhesion, composition, hardness and Young's modulus were assessed. These analyses were considered as a simple comparison assessment between the two coatings, as well as an indication of their fitness for purpose for use in CTDR applications. All the coating characterisation investigations in this chapter were conducted on flat samples and some differences in coating quality and thickness may have taken place in the CTDR components, as PVD is a line-of-sight deposition technique. The chromium nitride coatings were deposited using PVD method, whilst the silicon nitride coatings were deposited via HiPIMS. The samples tested in the current study were coated by an industrial collaborator (IonBond) and thus the exact deposition parameters and coating formulae were proprietary. Therefore, it was not possible to discuss the potential relationships between the coatings characterisation results and deposition method and parameters. Moreover, this study did not investigate different batches of the coatings, rather established the chemical composition, mechanical and surface properties of the available samples. Direct comparison of the two coatings was somewhat limited, as the methods of coating deposition were different to one another. It has been previously shown that coatings deposited via HiPIMS deposition can exhibit superior hardness, microstructure, droplet and defect-free, low-friction surfaces [258–260]. It has been recognised that any differences between the two coatings' characteristics may have been a result of the different deposition methods.

3.5.1 X-ray photoelectron spectroscopy

The X-ray photoelectron spectroscopy analysis of the silicon nitride and chromium nitride coatings was used to confirm chemical composition of the coatings and to establish potential depth profiles of the deposited coatings. This method confirmed that pristine samples i.e. not pre-sputtered with Ar^+ ions had a high concentration of oxygen and carbon contamination; the chromium nitride coated samples showed an average content of C1s, O1s, N1s and Cr2p as 53%, 17% 17% and 13%, respectively, while the pristine silicon nitride coated samples had a composition of C1s, O1s, N1s and Si2p of 20%, 24%, 24% and 32%, respectively. Once sputtered for at least 100s the composition of the chromium nitride coating changed to C1s (3%), O1s (11%), N1s (35%) and Cr2p (51%), which indicated that the coating was likely to be composed mainly of Cr_2N (575.3-576.1 eV) [20],. The relatively high oxygen content and 3% carbon content were a likely result of a presence of chromium oxides and carbides in the coating. This hypothesis was also supported by the hardness values of the chromium nitride coatings measured in the current study (H= 23.7 GPa), which was similar to those measured by Hones *et al.* [261]. Their study found that stoichiometric Cr_2N films exhibited a hardness of 29GPa, whilst bulk CrN had a hardness of 11GPa. Varying compositions of chromium nitride coatings i.e. mixtures of CrN and Cr_2N are dependent on the nitrogen content and pressure in the deposition chamber, as well as the substrate temperature [261–263]. The silicon nitride coatings, once sputtered with Ar^+ ions, had a composition of C1s (1%), O1s (6%), N1s (42%) and Si2p (51%), which indicated that the coating was composed mainly of Si_3N_4 (397.4 eV) [30-32] and a small proportion of silicon oxides (532.8 eV) [35, 36]. Similar composition i.e. a mixture of Si_3N_4 and SiO_2 of silicon nitride coatings were observed by Diéguez *et al.* [264], however the coatings in their study were deposited by r.f. magnetron sputtering. The N/Si in the current study was 1.24 compared to stoichiometric Si_3N_4 (1.33). The N/Si ratio can be controlled by Si target power and deposition temperature [189]. It was found that higher N/Si ratios, along with increased numbers of Si-N and decreased numbers of Si-Si bonds yield higher hardness of the coating [190]. Moreover, work by Pettersson *et al.* [190] found that coating composition, controlled by deposition parameters, affects the structure and mechanical properties of silicon nitride coatings.

3.5.2 Surface characterisation

The surface of the coatings was analysed using contacting profilometry, a method which is widely used by many industries. Contact profilometry is generally recognised for its ease of use and capability of application on a range of materials, including reflective and opaque materials. Contact profilometry can be affected by the stylus wear, however this can be avoided by performing a thorough inspection of the stylus prior to taking measurements. Moreover, contact profilometry only provides information gathered from the traces used in the measurements, which, depending on the condition of the surface, may not be representative of the whole surface. In the present study, the coated coupons were in pristine state, therefore it was assumed that the characteristics of the surface will be the same across the whole sample. In the present study, the coupons were polished both prior to and following coating deposition. In total joint replacement, surface roughness influences tribological performance and operating lubrication conditions [226], thus it was important for the coatings to be as smooth as possible. It was found that the chromium nitride and silicon nitride coatings had an average surface roughness (R_a) of 0.03±0.02μm and 0.03±0.01μm, respectively, and were not statistically significantly different from each other ($p>0.05$, CI 95%). Significant differences in surface skewness (R_{sk}) ($p<0.05$, CI 95%), whereby the skewness of the chromium nitride and silicon nitride were found to be $R_{sk}=0.62\pm0.74$ and $R_{sk}=3.31\pm3.18$, respectively, indicated that the overall topography of the silicon nitride coating consisted predominantly of peaks and asperities, which were significantly larger than those found on the surface of chromium nitride coated coupons. Surfaces, that are predominantly made of peaks and asperities may have a negative influence on the wear performance, as they may result in direct contact of the asperities of the articulating surfaces and thus increased wear rates, particularly in hard-on-hard bearing combinations used in total joint replacement [227]. The surface roughness of both coatings was within the range specified for metal-on-metal THR devices (<0.05µm) [265], however it was above the required value for ceramic-on-ceramic devices (<0.02 µm) [265], which indicated sufficient surface finish of the coatings for potential total joint applications. Similar surface roughness of both coatings were previously reported in the literature [178,184,200,266], however, in general, surface characteristics are highly dependent on the coating deposition method and parameters, as well as the substrate material used [178,267].

3.5.3 Coating thickness

The thickness of the coatings was assessed using the Calo test and by measuring SEM images of the cross-sections of the coated samples. Both methods rely on manual measurements of microscopic images (light and scanning electron microscopy), which may lead to a level of user error and bias in the results. The average coating thickness of the chromium nitride coatings and silicon nitride coatings measured by the Calo test was 4.9±0.8µm and 5.1±0.3µm, respectively. Similar average coating thickness was found by measuring cross-sections of the samples by using SEM; the average thickness of chromium nitride and silicon nitride coatings was 4.6±0.4µm and 5.1±0.3µm, respectively. Statistical analysis of the thickness results (one-way ANOVA, $\alpha=0.05$) obtained from the Calo test did not show statistically significant differences between the two coatings ($p>0.05$, CI 95%). On the contrary, thickness results from the analysis of the SEM images of the cross-sections of the coupons showed that the silicon nitride coatings were significantly thicker than chromium nitride ($p<0.05$, CI 95%). This difference was most likely caused by high variability in chromium nitride coating thickness measurements taken using the Calo test. It appeared that the chromium nitride coating on one of the three coupons used in the analysis was thicker that the others. This may have been a result of varying position of the coupons in the coater chamber during the coating deposition process [268]. Whilst appropriate coating properties, such as hardness and adhesion, tend to prevent excessive wear and coating delamination, some degree of wear will always occur in TJR bearings. When considered for CTDR applications, coating thickness, in isolation, must be sufficient to prevent wearing through of the coating. Typically, in clinical applications ceramic coating thicknesses of 3.5-6µm have been used [164,269,270]. This design input i.e. appropriate coating thickness, is particularly important in the case of the silicon nitride coating, since particles have been reported to be soluble in polar solvents [193,245]. Whist this property of the silicon nitride coating may have positive implications in the aspect of biocompatibility and harmful ion release prevention from cobalt chromium, it must be assured that appropriate coating thickness can be sustained throughout the *in vivo* implantation time.

3.5.4 Mechanical properties of coatings

High hardness of ceramic coatings used in TJR application is a desirable property due to the risk of potential third body wear. Bone, porous coating and cement particles may become entrapped in the bearing causing abrasion [271,272]. The chromium nitride and silicon nitride coatings were assessed for their hardness and Young's modulus using nanoindentation. The results showed that the chromium nitride coatings were significantly harder ($p<0.05$, CI 95%) (H=23.7±1.2 GPa) and stiffer (E=247.5±40.1 GPa) than silicon nitride coatings (H=19.1±0.7; E=213.4±6.8 GPa). This indicated that, when subjected to third-body wear, the chromium nitride coating was expected to present higher resistance to abrasion. The silicon nitride coating hardness was similar to that of its bulk, sintered form (~16GPa) [273]. Elastic modulus of both coatings was close to that of the cobalt chromium substrate (~200GPa) [207]. Similar mechanical properties of both coatings were previously reported in the literature [3,190,245,274,275], however, as with other coating properties, the hardness and Young's modulus are often highly dependent on the coating deposition method, parameters and substrate material the coatings are applied on. Moreover, the hardness-to-Young's modulus (H/E) ratios of the chromium nitride-coated samples (H/E= 0.1±0.02) were found to be significantly higher ($p<0.05$, CI 95%) than those of the silicon nitride coating (H/E=0.09±0.01) and the substrate material (H/E=0.01) [207]. Leyland and Matthews [276] highlighted the importance of the H/E ratio, relating elastic strain to fracture, and fracture toughness in predicting the wear performance of materials, including coatings, than hardness and Young's modulus alone. Their work suggested that high H/E ratio of a coating was often an indicator of good wear resistance. Further, work conducted by Recco *et al.* [277] suggested that coating adhesion may be improved by optimising and matching H/E ratios of the coating and substrate, they found that adhesion of the film to the substrate was greater when the *H*/*E* ratio of the film and of the substrate were similar. However, this work was conducted on titanium films and steel substrates, thus such conclusion may not be relevant to the current work.

To date, successful coating adhesion has been one of the most challenging coating characteristics to be achieved in total joint replacement applications [278] and has frequently been a cause of failure of coated devices [167,170,279,280]. The current study investigated coating adhesion using scratch testing. The method, combined with visual assessment of the scratches generated during testing, established three critical loads. On average, the L_{c1} values, i.e. load at which the initial plastic deformation occurred, were higher for the chromium nitride coating (10.4±0.7N) than for the silicon nitride coatings (4.5±0.8N). This is likely a result of significantly higher hardness of the chromium nitride coatings. At these lower loads both coatings showed brittle tensile cracking – chevron cracking opening in the direction of scratch. The initial plastic deformation of the coatings was followed by cohesive failure demonstrated by chipping and spallation on the edges of the scratches, initial occurrence of which defined the values of L_{c2}. The L_{c2} critical load was found to be higher in the silicon nitride coatings (22.9±2.7N), when compared to the chromium nitride coatings (16.24±0.7N), which suggested higher cohesive strength of the silicon nitride coatings. On the other hand, L_{c3} critical loads, which were determined by locations at which the coatings were fully penetrated by the stylus, were significantly higher for the chromium nitride coatings (73.9±3.6N) than the silicon nitride coatings (63.1±6.4N). Overall, the results presented in the current study indicated relatively good adhesion of both coatings. The results of the chromium nitride coated samples were in line with previously published results [178,281]. Results of the silicon nitride coatings investigated in the current study were significantly better than those previously reported by Olofsson *et al.* [245] whereby the majority of the coatings failed at the tip engagement step. Similar results were reported by Pettersson *et al.,* where all the coating samples delaminated during friction testing, indicating insufficient adhesion [190]. It has previously been found that coating adhesion is highly dependent on coating deposition methods and parameters [178], as well as coating thickness [281,282]. Fuentes *et al.* found that cathodic arc deposition resulted in more adherent coating [178] when compared to other PVD methods (electron beam, or magnetron sputtering). Heinke *et al*. [281], as well as Ollendorf and Schneider [282] reported that coatings deposited via PVD (titanium nitride and chromium nitride) exhibited improved adhesion with increasing coating thickness. However, it has been shown in the past that different adhesion measuring methods do not yield consistent results and often the same samples evaluated by different methods can lead to contradictory results [282]. For that reason, it was difficult, if not impossible to directly compare the current results to the present literature. Some methods of improving coating adhesion of PVD coatings have been proposed and application of interlayers have shown promising results; improved coating adhesion and corrosion resistance of CrN coatings with Al_2O_3 or Cr interlayers, deposited via HiPIMS PVD, were reported in the literature [283,284], however it was found that the effectiveness of interlayer application depended of the substrate surface roughness and interlayer thickness [284]. Moreover, it has been shown that substrates with rougher surfaces yield superior coating adhesion [285]. Ollendorf and Schneider [282] reported that pre-sputtering of substrate material, prior to coating, can result in improved coating adhesion by removing any potential contaminants on the surface which may affect the coating adhesion [286]. The test coupons, as well as the pristine CTDR devices described in Chapter 3, were polished to mirror finish (~Ra=0.02µm), which may have potentially reduced the coating adhesion of the chromium nitride and silicon nitride. Moreover, introduction of sample pre-coating sputtering could potentially improve the adhesion further.

3.6 Conclusions

Characterisation of the silicon nitride and chromium nitride coatings showed their surface and mechanical properties were adequate for total joint replacement applications. The surface roughness of both coatings was within the ISO specification for MoM THR (ISO-7206–2:2011) [265], the hardness of both coatings was superior to the substrate material and the adhesion of the coatings was found to be good overall. The thickness of both coatings was found to be similar (~5µm). All studies carried out in this chapter were indicative that the chromium nitride coating exhibited superior mechanical and adhesion properties to those of the silicon nitride coating. Such coating characterisation tests are a useful tool in assessing the initial differences between the coatings. However, functional testing, such as simulator wear testing is required, particularly when investigating coatings for specific applications, in order to test the coated devices under relevant operating loads, motions and environmental conditions. For that reason, CTDR devices were coated with the chromium nitride and silicon nitride coatings and tested in six-station spine simulator.

Chapter 4 : Wear assessment of CTDR

In total joint replacement, the assessment and understanding of the biotribological performance of a device can help predict and gain insight into its performance *in vivo.* To date, *in vitro* testing of other total joint replacement implants, such as hip or knee, is at a mature level, where the ISO standards and a large body of evidence have been produced, particularly for hip and knee replacement devices. Recently total disc replacement testing also achieved standardisation of testing input parameters, however, extensive practical experience of its application, expected wear performance of devices and clinical relevancy of the standard are yet to be established.

This chapter gives an overview of the testing methodologies used in this thesis for *in vitro* wear testing of metal-on-metal and ceramic-coated cervical disc replacement devices. Both variants of devices (coated or uncoated) were tested in six-station spine simulator under standard ISO-18192-1:2011 conditions for a duration of 4 million cycles. Further, the testing protocol was altered, whereby the applied ranges of motion were reduced, whilst the load and frequency remained the same as the standard protocol. This chapter outlines the wear performance of metal-on-metal and ceramic coated CTDRs tested under the standard and altered testing conditions.

4.1 Introduction to spine simulator testing

4.1.1 Leeds six-station spine simulator

The spine simulator was developed as part of collaboration between the Institute of Medical and Biological Engineering (IMBE), University of Leeds and Simulation Solutions Ltd (SimSol), Manchester, UK. The technical specification of the simulator was drawn up by IMBE and the subsequent simulator design and manufacture was undertaken by SimSol. The specification took many of its key points from ISO 18192-1:2008 – ‘*Wear of total intervertebral spinal disc prostheses -- Part 1: Loading and displacement parameters for wear testing and corresponding environmental conditions for test’* [135], with additional features that allow for more demanding and physiologically representative simulation. Moreover, at the time of development, the simulator was new in concept, applying five active degrees of freedom (rotation in three planes, translation in anterior-posterior plane and axial loading) in contrast to other spine wear simulators which applied only four active degrees of freedom and did not incorporate translation motion. In addition, all loads and motions are applied exclusively by electro-mechanical actuators, as opposed to hydraulics or pneumatics, which improves the accuracy and control of the loads and motions. The simulator contains two banks of three stations (Figure 4.1), allowing six stations to be tested with one additional soak control station, which can apply cyclic axial loading. Axial loading (AF) and axial rotation (AR) are applied to the inferior fixture, whilst flexion-extension (FE), lateral bending (LB) and anterior-posterior shear (AP) (under load or displacement control) are applied to the superior fixture (Figure 4.2). The details of how different loads and motions were applied in the simulator can be found in Appendix II.

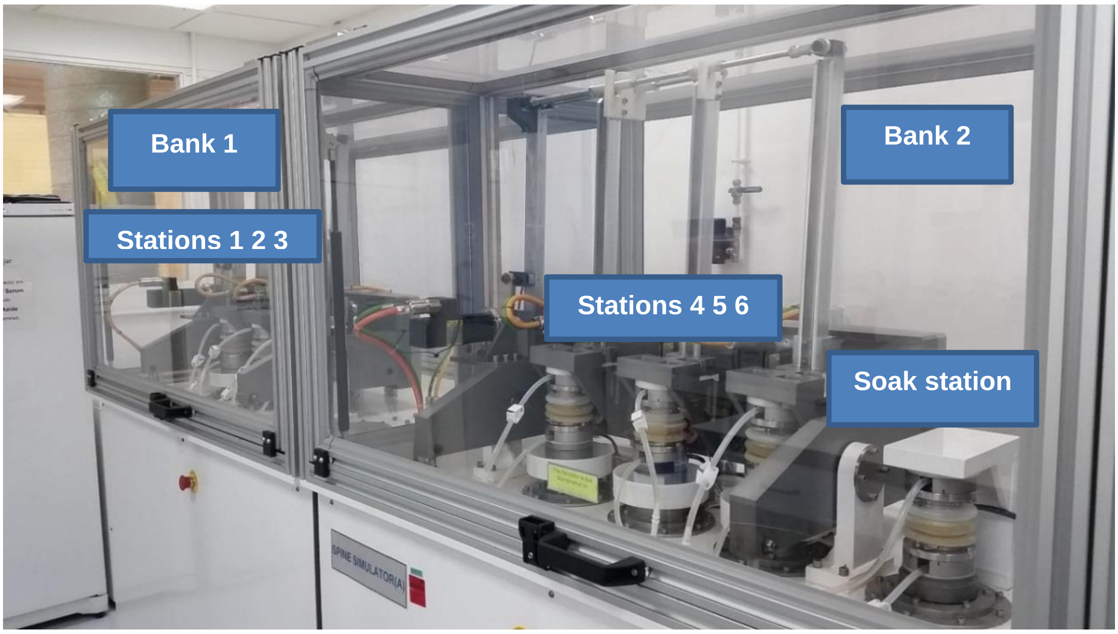

Figure 4.1: Leeds Spine Simulator A showing Banks 1 and 2 with stations 1-6 and a soak station

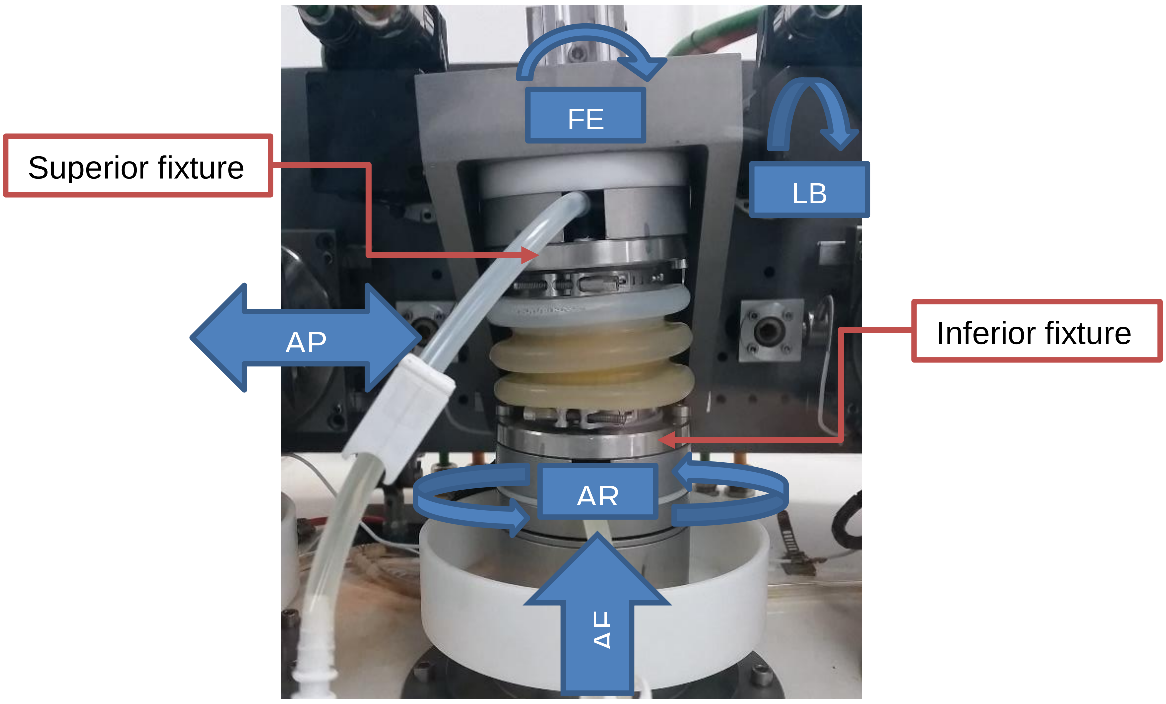

Figure 4.2: Fully assembled test cell. The axial force and rotations are applied to the inferior fixture, whilst the anterior shear, flexion/extension and lateral bending motions are applied to the superior fixture.

4.1.2 Testing protocol

There are two internationally recognised documents prescribing methods of *in vitro* wear simulation of cervical total disc replacement devices - ISO-18192-1, and ASTM F2423-11. A comparison study of the ISO-18192-1, ASTM F2423-11 and observed daily motions in the cervical spine found that motions in the cervical spine are more frequent than the million cycles per year specified by standards [49]. Moreover, the authors have suggested that the amplitudes of motions were much smaller than those stipulated by the ISO-18192-1:2011; most daily activities investigated by the study resulted in ROMs of 2-3°, compared to the 4-7.5° specified by the ISO standard.

Simulator testing of the Bryan cervical disc (CTDR, MoP bearing, titanium and polyurethane) [121] produced significantly more wear when compared to retrieved devices; the reported wear rate of 0.57mm^3/million cycles was higher by approximately 5 to 10 fold than those found in explants.

Kurtz *et al.* [138] compared Prestige-ST (CTDR, MoM bearing, stainless steel) components tested in a spine simulator to retrievals. However, the *in vitro* testing was conducted under a non-standard test protocol: coupled lateral bending (±4.7°) and axial rotation (±3.8°) with a 49N axial load for 5 million cycles followed by 10 million cycles of flexion-extension (±9.7°) with 148N axial load. It was not possible to establish the exact wear rates of the explants and compare them directly to the *in vitro* test results (range of 0.03 - 0.74mm^3/MC, depending on testing conditions). Wear scars and mechanisms of explants were similar to those found in samples tested in the simulator; however, retrieval wear was not as severe as *in vitro* tested samples. It was observed that the simulator tested samples had deeper scratches and higher surface roughness, when compared to explanted devices. Anderson *et al.* [121], who also tested Prestige-ST implant, reported a wear rate of 0.18mm^3/million cycles. Additionally, those authors found that components tested for only 0.3 million cycles produced much higher wear than in a device explanted from a patient after 39 months *in vivo* i.e. an equivalent of 3.25 million cycles of simulator tests. Findings suggesting exaggeration of wear rates found in *in vitro* studies are consistent with those reported for the Bryan cervical disc device [121], even though there were minor differences in test conditions (ranges of motion, loads and duration) and fundamental differences in device designs (bearing type and material combination). Comparison between *in vitro* simulator studies and retrievals, [139,140] found that abrasion found in the simulator tested samples was more severe than that observed *in vivo*. Similarly to Anderson *et al*. [121] these authors hypothesised this was due to short implantation times. Siskey *et al.* [140] tested metal-on-metal Prestige-ST devices and found that the wear scar area was greater in the simulator tested components, which suggested that the ROMs applied in the ISO standard are more extensive than those experienced *in vivo*.

The loads and ROMs applied in the testing of both of the Bryan and Prestige-ST devices were within the range specified by ISO 18192-1, which may suggest that such test inputs are not fully representative of conditions *in vivo* and significantly overestimate wear rates, and thus require further investigation and possible revision. For that reason, a variant of the standard testing protocol, whereby the ranges of motion were decreased, has been investigated in this thesis. The choice of the altered ROMs (±2-3°), whilst higher than those suggested by Cobian *et al.*, [49], was rationalised by the feasibility of the error margins used in the testing. Decreasing ROMs further would result in the tolerances accounting for a larger proportion of the ROM applied. The frequency of all motions remained at 1Hz.

4.2 Materials

4.2.1 CTDR samples

For all testing conducted in this thesis, generic CTDR devices were designed and manufactured. A detailed rationale, materials and methods used in disc design, manufacturing and inspection are provided in Chapter 3.

Six pristine (un-coated) MoM devices as well as 12 coated devices (six coated with silicon nitride and six coated with chromium nitride coatings) were used in simulator testing. The convex and concave components were paired based on their radial clearance, to ensure clearance was similar and close to the specified 0.15 mm, across all devices.

Samples were securely mounted in the simulator fixtures using bespoke holders made from Erthacetal®H resin (Quadrant EPP UK Ltd., Todmorden, UK) (Appendix III). The design assured interference fit between the holders and CTDR components, which provided a secure fit without the necessity of using PMMA cement.

4.2.2 Wear testing lubricant

Newborn bovine serum (Sera Labs, Loughborough, United Kingdom) was used as a lubricant, diluted to 25% (v/v) using de-ionised water and supplemented with 0.03% (w/v) Sodium Azide solution (Sigma-Aldrich, Gillingham, Dorset, UK) to minimise bacterial growth, resulting in a protein content in the lubricant of approximately 15 g/L.

4.2.3 Laboratory consumables and chemicals

Fairy soap detergent (Procter & Gamble, London UK) was used in the cleaning protocol of the CTDR components, as well as the spine simulator stations and fixtures. Trigene disinfectant solution was supplied by Scientific Laboratory Supplies Ltd. (Nottingham, UK). Isopropanol, at a concentration of 99.8+% (v/v) (10090320) was supplied by Fisher Scientific UK (Leicestershire, UK).

4.2.4 Gravimetric analysis

Each component, convex and concave parts separately, were weighed prior to wear testing, as well as at each measurement timepoint of $1x10^6$ cycles, using a Mettler Toledo XP26 microbalance (Mettler-Toledo Safeline, Salford, UK).

4.2.5 Surface topography analysis

A two-dimensional contacting profilometer, (Talysurf PGI 800) was supplied by Taylor Hobson (Leicester, UK). Components were mounted in a specially designed fixture made from Erthacetal®H resin (Quadrant EPP UK Ltd., Todmorden, UK), which ensured repeatability of sample fixation and measurements at each timepoint (Appendix IV).

4.2.6 Post-test dimensional inspection

The radii of the convex and concave components, and the resultant radial clearances, were measured using a Legex 322 CMM (Mituyoto, Andover, UK) fitted with a PH6M probe head (Mituyoto, Andover, UK) and a TP7M probe module (Mituyoto, Andover, UK). Measurements were taken using a 1mm diameter stylus (A-5000-3551) (Mituyoto, Andover, UK).

4.2.7 Microscopy

Micrographs of each component were taken at each measurement timepoint of $1x10^6$ cycles using the Nikon SMZ800 microscope (Nikon Instruments, Amesterdam, Netherlands) fitted with a Pixelink camera (Pixelink Ottawa, Canada) in conjunction with a Photonic PL 2000 light source (Photonic, Vienna, Austria). The size of wear area was measured using ImageJ software (National Instruments of Health, Bethesdam Naryland, USA).

4.2.8 Scanning Electron Microscopy

Detailed images of the component surfaces were taken using a Carl Zeiss EVO MA15 Scanning Electron Microscope (SEM), fitted with EDX system, in conjunction with an Oxford Instruments AZtecEnergy system (Oxford, UK).

4.3 Methods

4.3.1 Spine simulator calibration

4.3.1.1 Axial load verification

The axial loading of the spine simulator was calibrated using an external load cell (Sensotec 4.5kN, Honeywell International Inc., Columbus, OH, USA) mounted in a bespoke fixture allowing stable positioning of the load cell in the horizontal and vertical plane, perpendicular to the applied force (Figure 4.3).

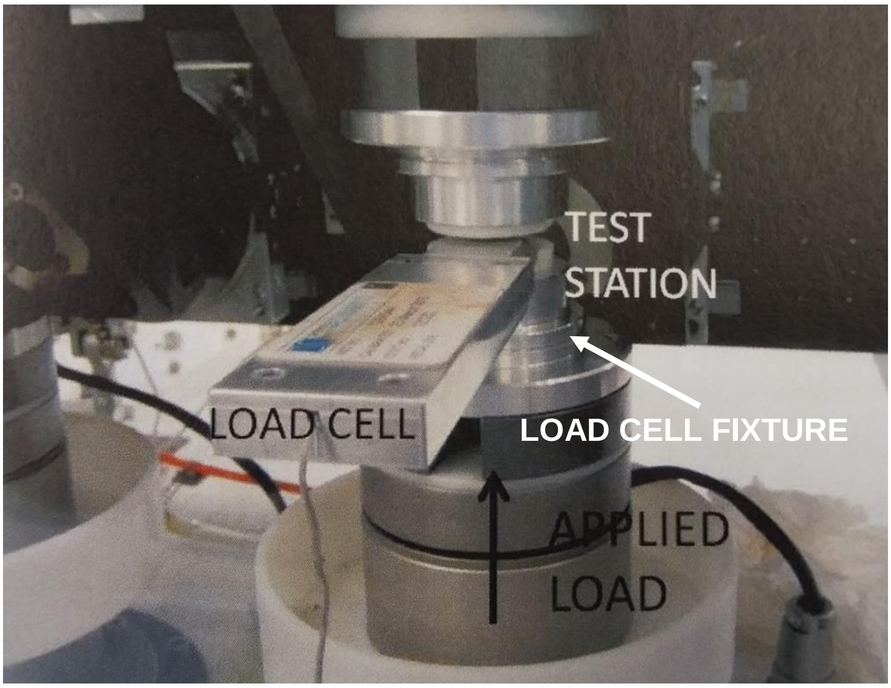

Figure 4.3: Set up for axial loading calibration using an independent load cell and bespoke jig.

Software controlling the simulator, allowing independent motor control, was used to move the axial force motor in incremental positions of 5°. The resulting loading at each station load cell was recorded and compared with readings from the external load cell.

Values of the simulator and external load cells were compared in a specially designed spreadsheet, which was used to calculate the correction factors of the axial load motors. In an ideal case, where the recorded values were identical, a plot of those values would show a gradient equal to the current gain and intercept at zero. Stations where this was not the case were recalibrated.

To recalibrate, values of offset and gain of the axial load motor had to be calculated using an Equation 4.1.

$$F = CG + O$$

Equation 4.1

where:

F - axial force

C – motor count (feature of the motor control unit)

G – gain (amplification of the motor input signal)

O – offset (nominal position control)

The values of gain and offset, as well as the recorded values of axial loading from the external and simulator load cells were used in re-calibration of the simulator axial loading. To achieve this, the gain and offset parameters were adjusted so that the load output values were within the tolerance bands specified by the ISO standard (±5% of the maximum load).

The revised gain and offset values were inputted in the source file (_default.ssp) controlling the axial loading motors. The loads were checked again and results plotted. The revised plot should be within the tolerance bands. Other outcomes indicated potential external errors such as operator error, incorrect placement of the external load cell or non-zero positions of flexion-extension or lateral bending inputs. The calibration process was applied to each station (1-7). As a standard operating procedure, the calibration process is repeated every 6 months or before each test. The load cell was calibrated to within ±5% of the applied load.

4.3.1.2 Flexion-extension

The motors controlling flexion-extension (FE) inputs do not have encoders built in and thus a table of motor positions and corresponding outputs must be completed. The simulator software uses a calibration table to compute a linear motor input table, so that the FE motion is accurate and linear.

The spine simulator has two motors controlling FE motion – one responsible for stations 1-3 and a second for stations 4-6. Station 7 is a soak station and has no kinematic input or output. Each motor controlling FE is connected to its 3 corresponding stations via connecting bars. As a result of this linkage, the FE motion has to only be calibrated for one station per bank. However, the other two stations should be checked for congruity with the calibrated station. For this purpose, a measurement error of ±0.1° was chosen as the smallest practicable tolerance.

The FE input angles of motions were measured using an independent digital inclinometer (Pro 360 digital inclinometer, SmartTool Tech Inc., Oklahoma City, OK, USA) with a resolution of 0.1° placed on one station and fixed using tape (Figure 4.4). Software controlling the simulator, allowing independent motor control, was used to move the FE motors in incremental positions of ±2° within the range of ±10°. The resulting angle of motion was measured, recorded and compared with the current output of the simulator. If the values specified by the simulator were different to those measured by the inclinometer, recalibration was required. This was achieved by simply readjusting the linearisation table. In order, to check if the recalibration was successful, the software had to be restarted and the calibration procedure repeated.

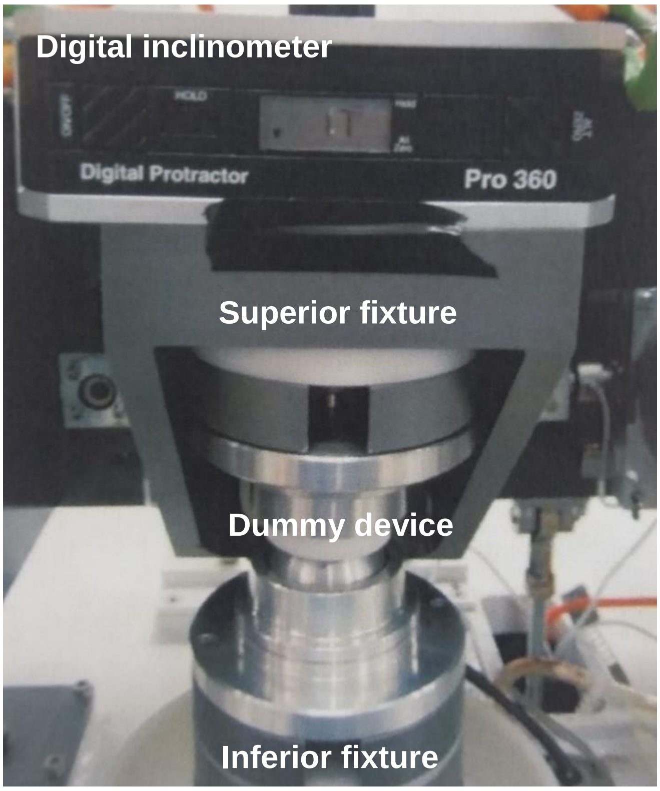

Figure 4.4: Set up for flexion-extension calibration using a digital inclinometer.

4.3.1.3 Lateral bending

The lateral bending (LB) motion of the spine simulator is controlled by two independent motors, which control stations 1-3 and 4-6 separately. The connection between the motors and its corresponding stations is achieved via a gimbal system, which provides a rigid connection. As a result, only one calibration procedure for each motor had to be carried out and it was not necessary to check each separate station for congruity.

The calibration process was similar to the procedure applied for the calibration of flexion-extension motions. An independent digital inclinometer was used to measure the motion angle corresponding with the motor angle controlled by the simulator software. Incremental positions of ±2° within the range of ±10° were used. If the values specified by the simulator were different to those measured by the inclinometer, recalibration was required. This was achieved by simply readjusting the linearisation table. In order, to check if the recalibration was successful, the software had to be restarted and the calibration procedure repeated.

4.3.1.4 Axial rotation

The calibration process of the motor controlling the axial rotation (AR) was similar to the one for FE and LB calibration. However, the AR motor angle corresponds directly to the specimen angle and thus no calibration table was required. To verify the motor accuracy the use of a rotational scale was required. For that purpose, the angular increments of 2° were converted into a distance using the formula for an arc length of a circle ($S=r\theta$). The radius of the test station was 45 mm; therefore, the corresponding rotation distance was 1.57mm. Software controlling the simulator, allowing independent motor control, was used to move the AR motors in incremental positions of ±2° within the range of ±10°. The resulting angle of motion was measured, recorded, compared with the motor position and adjusted if necessary by editing the calibration file.

4.3.1.5 Phase calibration

The frequency of motions performed by the simulator was checked with a stop watch; the number of cycles performed within a given time duration was recorded. Such checks were carried out periodically throughout the tests. The phases between the demand and output profiles were checked at the start of each test.

4.3.1.6 Temperature calibration

As per ISO 18192:1, the test cells were heated to body temperature (37±2ºC) in order to produce clinically relevant conditions. The spine simulator was fitted with heating elements and thermocouples at each station. Calibration of the temperature was conducted using an independent thermocouple (Fluke 51 K/J, John Fluke Manufacturing Co. Inc, Everett, WA, USA). The temperature of each station was measured using the independent thermocouple and if necessary, the simulator thermocouples were adjusted accordingly.

4.3.2 Altered testing conditions

With findings in the literature suggesting that the testing protocol specified by ISO-18192-1 may result in overestimated wear rates, additional test with altered parameters (range of motion) was conducted in the present study. The amended inputs (highlighted) of the test are listed in Table 4.1. The revised input curves for load and displacement are shown in Figure 4.5. No changes were made to relative phasing of the inputs and these remained in line with ISO-18192-1:2011. This altered testing protocol was used in testing for a duration of $2x10^6$ cycles.

Table 4.1: Testing protocol inputs for spine simulator test under altered ISO-18192-1:2011 protocol, changes to the protocol were highlighted. Range of all motions were decreased, loads and phasing of the motions remained in line with the ISO standard.

Test ID	Duration	Input	Value	Tolerance
2	$2x10^6$ cycles	Load	50-150 N	±5% of maximum load
		Flexion/Extension	±3.0°	±0.5°
		Lateral bending	±2.0°	±0.5°
		Axial rotation	±2.0°	±0.5°
		Frequency	1 Hz	2% of cycle time

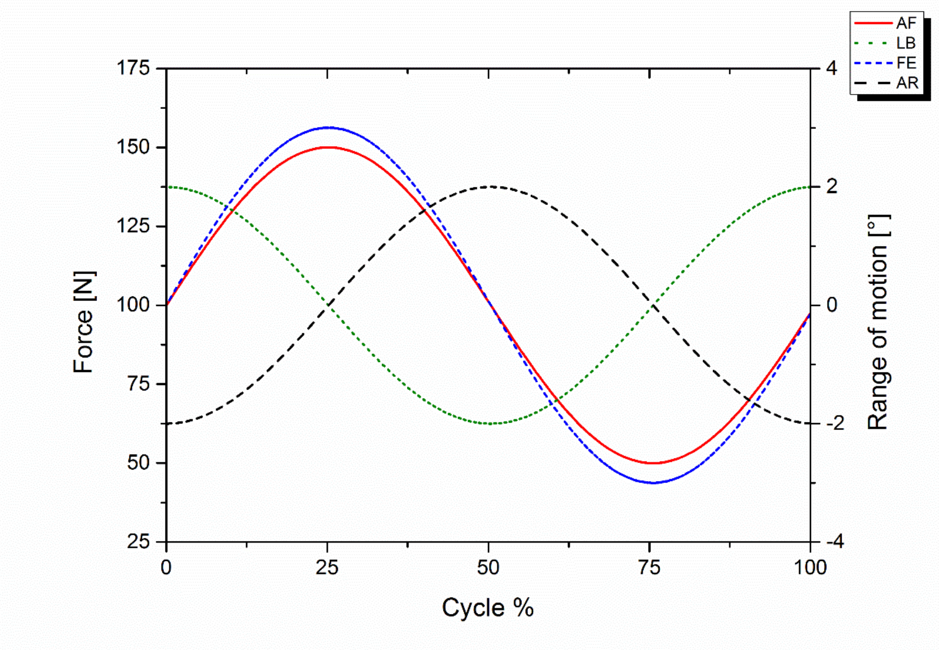

Figure 4.5: Revised phasing of the displacement and load curves applied in Test 2. The frequencies of all motions and AF (axial loading) remained at 1 Hz; ROMs are reduced to ±3°, ±2° and ±2° for FE (flexion/extension), LB (lateral bending) and AR (axial rotation), respectively.

4.3.3 Standard ISO simulator testing conditions

The initial simulator testing of CTDR components was conducted under conditions adhering to ISO 18192-1:2011. The kinetic inputs and tolerances applied in the standard tests are listed in Table 4.2, below. While the Leeds Spine Simulator (A) has the capability to apply AP shear in force and displacement control, it was not required by the ISO 18192-1:2011 testing protocol and was therefore not used in the testing.

The kinetic inputs of the ISO standard are a sinusoidal approximation of the loads exerted in the spine, running concurrently, as shown in Figure 4.6. The axial force input stipulated by ISO-18192-1 ranged between 50 and 150 N, which aimed to represent *in vivo* conditions. It is believed that the cervical spine is subjected to loads equal to 3 times the weight of the head and associated soft tissues – approximately 200 N [44].

Table 4.2: Standard ISO-18192-1:2011 testing inputs and error margins

Test ID	Duration	Input	Value	Tolerance
1	$4x10^6$ cycles	Load	50-150 N	±5% of maximum load
		Flexion/Extension	±7.5°	±0.5°
		Lateral bending	±6.0°	±0.5°
		Axial rotation	±4.0°	±0.5°
		Frequency	1 Hz	2% of cycle time

The static loads exerted on the cervical spine arise mainly from the weight of the head and associated soft tissues, which are approximately 4.5-5 kg (~7% of body weight). The strength and load carrying capacity of the cervical spine comes only partially from the mechanical strength of vertebrae and intervertebral discs and it is largely determined and supported by the mechanical properties of the ligaments and muscles. The weight of the body segment carried by the cervical spine is approximately 50N [45].

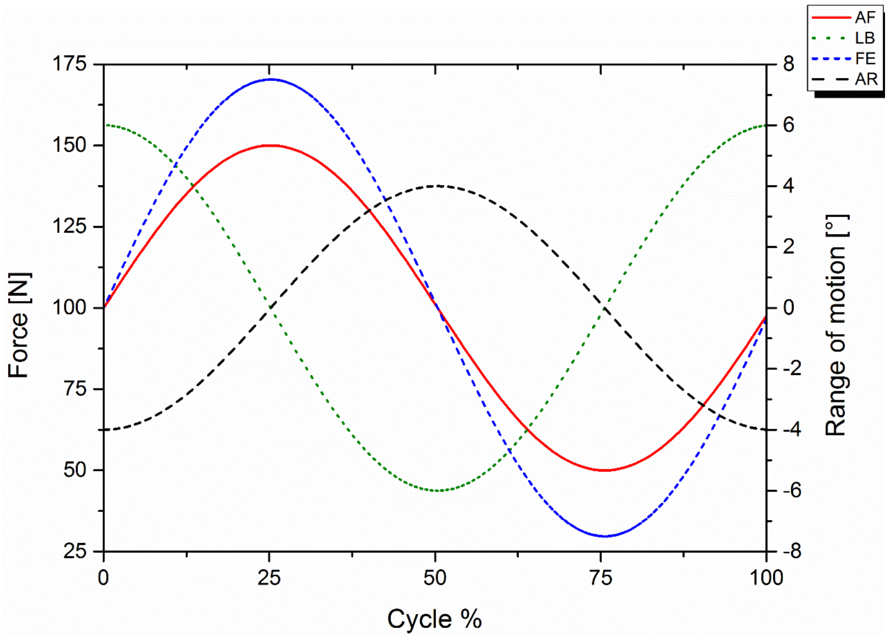

Figure 4.6: Phasing of the displacement and load curves for CTDRs specified by ISO-18192-1:2011; AF- axial force, LB – lateral bending, FE – flexion/extension, AR – axial rotation.

The kinematic inputs specified by ISO-18192-1:2011 lie within the typical ranges of *in vivo* motions of the neck found in the literature [49,50,52], however, they are unlikely to represent single index level motion, as the range of motion of the neck is a combination of a motion occurring at several segments at the same time. Thus, it can be argued that the current ISO standard requirements may exaggerate the conditions found *in vivo*; and such extended motions can lead to overestimated wear rates. For that reason, additional test applying alternative testing conditions was carried out. This further testing investigated altered ranges of motion applied during wear testing.

4.3.4 Spine simulator testing

Prior to testing, components were thoroughly cleaned with detergent and ethanol (as described below) and all pre-test measurements (surface profilometry and weighing) were performed (sections 4.2.4 and 4.2.5). Components were then mounted in bespoke resin fixtures, which subsequently were placed in the lower and upper holders and secured with screws. The resin fixtures were designed such, that the height at which the superior and inferior components were placed at, and the resultant centre of rotation (CoR), matched the CoR of the simulator. Once assembled into a test cell (Figure 4.7) components were securely enclosed in a silicon gaiter, allowing full submersion in the lubricant.

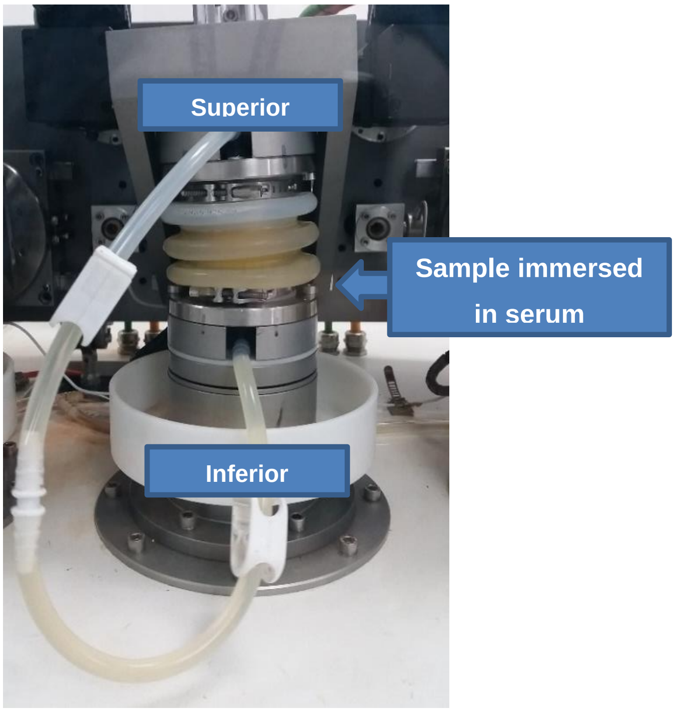

Figure 4.7: Fully assembled test cell showing the superior and inferior fixtures and placement of a sample in an enclosed gaiter.

Two silicone tubes were connected to the upper and lower holder, allowing lubricant filling and draining. The two pipes were then connected creating a sealed environment for each test cell, which reduced the potential of airborne contamination of the lubricant. Following each 3.3x10^{5} cycles, the lubricant was drained and stored at -20°C for further particle characterisation and cytotxicity analyses (Chapter 5). Each station was then rinsed out with diluted soap detergent, soaked in the Trigene disinfectant solution for 20 minutes at room temperature, after which each station was rinsed out twice with tap water and once with deionised water. The waste liquid generated during the cleaning was discarded and cleaned, empty station gaiters were refilled with fresh lubricant.

At measurement points, i.e., following every 1x10^{6} cycles of testing, the test cells were disassembled and components removed from the resin fixtures. The components of test cells (resin fixtures, holders, jubilee clips, silicon gaiters and tubes) were scrubbed and washed with soap detergent, soaked in the Trigene disinfectant solution for 20 minutes in room temperature and rinsed with tap and deionised water, as described above. The components were gently cleaned (avoiding any abrasion to the articulating surfaces) with soap detergent and a sponge, sonicated in ultrasonication bath soap detergent dilute for 15 minutes, rinsed with tap and deionised water, sonicated in 70% (v/v) isopropanol for 15 minutes and left to dry in air for 10 minutes. Prior to any measurements, the components were placed in a temperature and humidity controlled room for 24 hours.

4.3.5 Gravimetric analysis

Each component, convex and concave parts separately, were weighed prior to the wear testing, as well as at each measurement timepoint of $1x10^6$ cycles to determine mass loss. Subsequently, volume loss was calculated using the material density (CoCr=8.3g/cm^3, Si_3N_4=3.44g/cm^3 and CrN=5.9g/cm^3). Before taking measurements, it was ensured that the balance was stable and read zero. At least 5 measurements of each component were completed, ensuring that all the readings for each component were within ±0.01 mg of each other.

4.3.6 Surface profile analysis

A two-dimensional contacting profilometer fitted with a diamond tip was used to assess bearing surfaces of the cervical disc components, prior to wear testing, as well as at each measurement timepoint of $1x10^6$ cycles. Detailed methodology of surface profilometry has previously been discussed in Chapter 2 section 2.3.2.

On each component, six 11 mm long traces across the bearing surface were taken, as shown in Figure 4.8A. The traces were positioned in order to collect the greatest amount of data as possible. Parameters such as surface roughness ($R_{a)}$, skweness ($R_{sk)}$, maximum peak height ($R_{p)}$ and maximum valley depth ($R_{v)}$ were recorded. Traces P_2 and P_5 were normal to each other and passed through the pole. In order to find the pole (highest point of the convex surface and lowest point of the concave surface) the stylus was crested before each measurement i.e. adjusted in the horizontal plane until the maximum (convex surface) or a minimum (concave surface) vertical values were reached.

Traces P_1 and P_2 were approximately 3 mm away from the position of the P_1 trace, while traces P_5 and P_6 were 3 mm away from the position of the P_4 trace. In instances where the traces included the flat portion of the endplate, those areas were excluded from the analyses, as shown in Figure 4.8B.

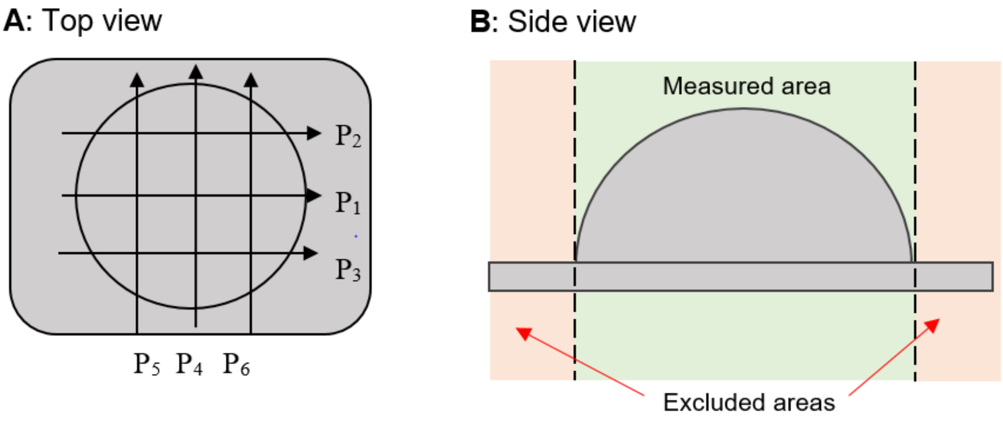

Figure 4.8: A: top view showing the schematic representation of six traces taken across the surface of each CTDR component for the measurement of surface roughness; B: side view showing the measured area included only the bearing surface and excluded the flat endplate areas.

Collected data was analysed using least squares arc with a Gaussian filter and appropriate cut-off, which uses mathematical or electronic means to reduce or remove unwanted data, in order, to focus on wavelength in the region of interest. An appropriate long-wave cut-off wavelength, dependent on the R_a values and an appropriate bandwidth, based on the long-wave to short-wave cut off wavelength ratio (λ_c / λ_s), were used, as shown in Table 4.3 The cut off values and bandwidth ratios are specified by ISO-4288:1998 ('*Geometric product specification (GPS). Surface texture. Profile method: Rules and procedures for the assessment of surface texture'*) and ISO-3274:1996 ('*Geometrical Product Specifications (GPS) -- Surface texture: Profile method -- Nominal characteristics of contact (stylus) instruments'*), respectively.

Table 4.3: Values of cut-off depending on R_a values as stipulated by ISO-4288-1998. Relationship of λ_c / λ_s i.e. bandwidth is based on ISO-3247-1998

R_a (µm)	Cut off λ_s (mm)	Cut off λ_c (mm)	Bandwidth (λ_c / λ_s)
≤ 0.02	2.5	0.08	30
$0.02 < R_a \leq 0.1$	2.5	0.25	100
$0.1 < R_a \leq 2$	2.5	0.8	300
$2 < R_a \leq 10$	8	2.5	300
$10 < R_a \leq 80$	25	8	300

4.3.7 Post-test component dimensional inspection

After completion of each spine simulator test, radial clearance of the components was measured. In order, to measure the radial clearance, radii of the convex and concave components were measured using the CMM and the method described in Chapter 2 Section 2.2.2.

4.3.8 Light microscopy of CTDR components

At each measurement timepoint, micrographs of all components were taken. The images were taken at x1 magnification, allowing the entire articulating surface to be viewed and analysed. The scale of all images was set using a calibrated graticule. The set scale (170.71px/mm) was later used in ImageJ image processing software. The wear scar on the CTDRs appeared to be darker and using the freehand selection tool in ImageJ, the size of the area was measured, as shown in Figure 4.9. Further images at higher magnifications were taken to assess wear tracks and surface damage of the components.

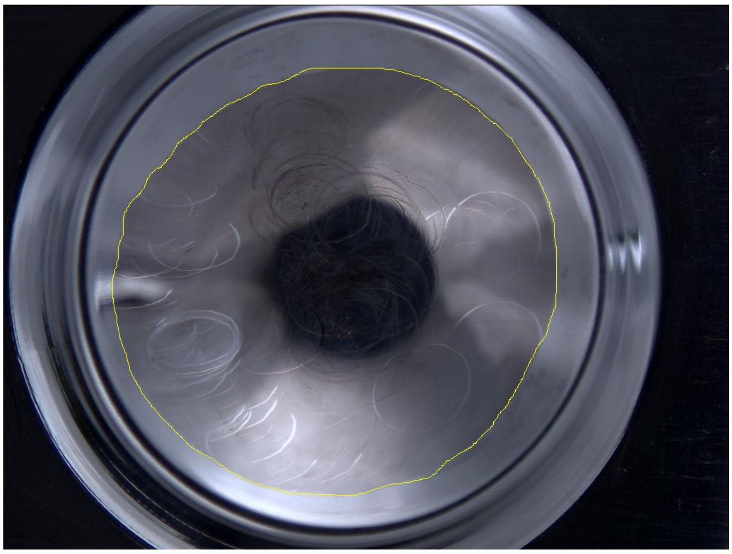

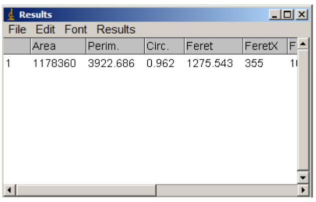

```
     Area     Perim.    Circ.  Feret     FeretX  F
1    1178360  3922.686  0.962  1275.543  355     1
```

Figure 4.9: Example of wear area measurement using ImageJ software.

4.3.9 Scanning Electron Microscopy analysis of CTDR components

A Carl Zeiss EVO MA15 SEM fitted with an EDX system was used for all SEM image capture. Components were fixed in a specially made fixture (Appendix IV) mounted on stubs using a carbon sticker. Carbon paint was used around the edges of components and the fixture to ensure sufficient conductivity and reduce chances of static surface charge accumulation. Images were taken at a range of magnitfications and working distances, at 20kV accelerating voltages. Images of components were taken prior to testing and at each measurement timepoint.

4.3.10 Statistical analysis

All statistical analysis of data was performed using SPPS for Windows (v.21.0, SPSS Inc., Chicago, IL, USA). One-way analysis of variance (ANOVA) was used to analyse obtained data with α=0.05 for difference between data sets.

4.4 Results

4.4.1 Pristine CoCr-CoCr CTDRs

4.4.1.1 Standard ISO simulator testing conditions

The initial test consisted of 4MC of standard ISO-18192:2011 input. This test (referred to as Phase 1 testing) was to act as a benchmark for further testing of altered ISO inputs (Phase 2 testing) as well as the same ISO testing of CTDR components coated with CrN and Si_3N_4.

4.4.1.1.1 Wear rates

The overall mean volume loss was 0.98±0.1mm^3 over 4MC, ranging from 0.81mm^3 (Stn.3) to 1.08mm^3 (Stn.6). The mean volumetric wear rate was 0.24mm^3/MC, ranging from 0.20mm^3/MC (Stn.3) to 0.27mm^3/MC (Stn.6). On average, the volume loss from the convex components was 0.12mm^3/MC and 0.13mm^3/MC from concave components, as shown in Figure 4.10 . No significant differences between the mass loss from the two component groups was found ($p>0.05$, CI 95%, convex vs. concave components). Throughout the test, the volumetric wear was linear; no significant bedding-in period was observed. Therefore, at 4MC it was decided that further testing was unlikely to show dramatic changes in wear rates and patterns and thus further testing was conducted under the altered ISO-18192-1:2011 testing protocol (section 4.3.2).

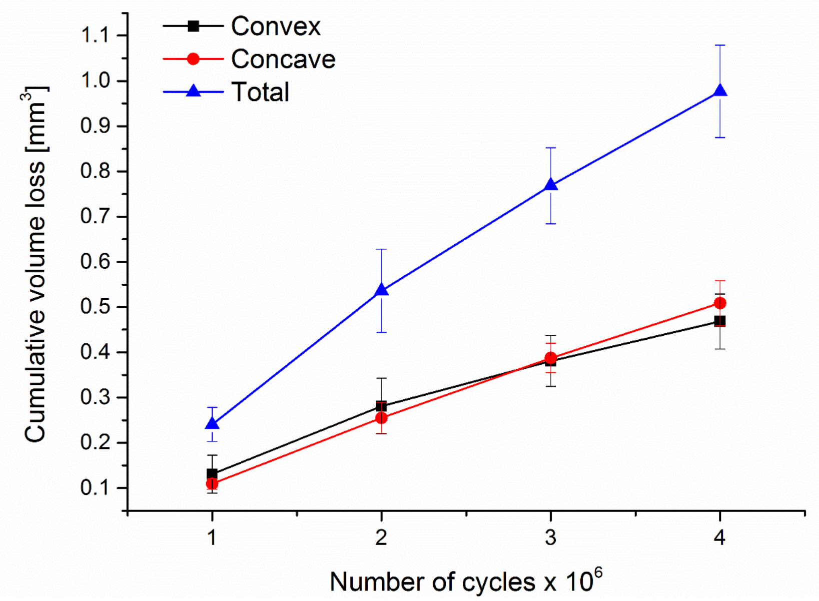

Figure 4.10: Cumulative volume loss from CoCr-CoCr CTDR components tested under the ISO-18192-1:2011 protocol. There was no significant difference in convex and concave component volume loss across 4MC of simulator testing. Error bars represent 95% confidence limits.

There was some inter-station variability across the duration of the test, as shown in Figure 4.11. Station 3 produced the lowest volume losses from 2MC until the end of the Phase 1 testing. At 4MC station 6 produced the highest volume loss. For the first 3MC of the test, station 2 produced the highest volume loss.

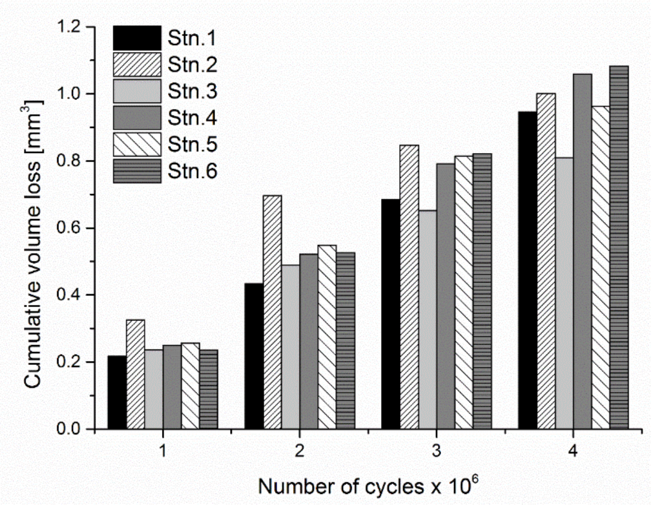

Figure 4.11: Station variability in volume loss across 4MC of testing under ISO-18192-1:2011 protocol of CoCr-CoCr CTDR devices.

4.4.1.1.2 Surface roughness

Prior to testing, the convex and concave components had mean R_a values of 0.023±0.003µm (SD) and 0.015±0.002µm (SD), respectively. These were calculated as an average value of all 6 traces across the surface of each component. It has been noted in the pre-test measurements that the traces taken across the pole of each component (traces P_1 and P_4) showed lower R_a values, as shown in Table 4.4. After 4MC of standard ISO testing (Test 1) surfaces of all components were analysed using the same method. Following testing the mean R_a values of convex and concave components were 0.012±0.002µm and 0.012±0.002µm, respectively. This reduction in the R_a parameters was found statistically significant for both the convex ($p<0.05$, CI 95%) and concave ($p<0.05$, CI 95%) components. As with the pre-test results, measurements taken across the pole of each component (traces P_1 and P_4) showed the lowest values of R_a, as summarised in Table 4.5. Following the 4CM of standard ISO-18192-1:2011 protocol testing, the mean R_a values for the convex and concave components decreased by 48% and 14%, respectively. The most notable decrease in R_a values was seen in the off-pole traces (P_2, P_3, P_5 and P_6) of the convex components, which decreased by 60%, 46%, 53% and 51%, respectively.

Table 4.4: Mean pre-test R_a, R_p, R_v and R_{sk} values for different traces taken across the surfaces of convex and concave components of CoCr-CoCr CTDR devices; the traces with lowest values are highlighted in green. One-way ANOVA analysis (α0.05) of the pre-test surface finish parameters showed that the R_a, R_p and R_{sk} of concave components were significantly lower ($p<0.05$) than those of the convex components. Values of the R_v parameter were not found to be significantly different between the two component groups.

Component	Trace number							
	P_1	P_2	P_3	P_4	P_5	P_6	Average(SD)	p-value*
	R_a [μm]							
Convex	0.019	0.026	0.026	0.014	0.026	0.030	0.023(0.003)	<0.05
Concave	0.011	0.015	0.016	0.011	0.015	0.017	0.015(0.002)	
	Trace R_p [μm]							
Convex	0.046	0.063	0.072	0.032	0.068	0.078	0.060(0.005)	<0.05
Concave	0.027	0.043	0.040	0.026	0.040	0.043	0.036(0.004)	
	Trace R_v [μm]							
Convex	0.076	0.113	0.106	0.063	0.101	0.077	0.089(0.007)	>0.05
Concave	0.046	0.075	0.085	0.044	0.071	0.091	0.069(0.012)	
	Trace R_{sk} [μm]							
Convex	-1.026	-1.319	-1.079	-1.109	-1.108	-1.108	-1.108(0.111)	<0.05
Concave	-1.683	-1.715	-2.247	-1.550	-2.068	-1.957	-1.870(0.265)	

*comparison between convex and concave components

A similar trend was observed for R_p and R_v parameters, where values decreased following testing, with the lowest values found for traces P_1 and P_4. Prior to testing the mean R_p values were 0.060±0.005μm (SD) and 0.036±0.004μm (SD) for the convex and concave components, respectively (Table 4.4). After 4MC of standard ISO testing the mean R_p values decreased to 0.032±0.006μm (SD) and 0.035±0.004μm (SD), for convex and concave components, respectively, which was statistically significant for the convex ($p<0.05$, CI 95%) but not for the concave components ($p>0.05$, CI 95%) (Table

4.5). Prior to testing, the mean R_v values were 0.090±0.007µm (SD) and 0.067±0.012µm (SD) for the convex and concave components, respectively (Table 4.4). Following 4MC of standard ISO testing the mean R_v values decreased to 0.056±0.037µm (SD) and 0.050±0.010µm (SD), for convex and concave components, respectively (Table 4.5). Such reduction in the Rv parameter was found significant ($p<0.05$, CI 95%) for both component groups.

Table 4.5 Mean Ra, Rp, Rv and Rsk values of CoCr-CoCr CTDRs following 4MC of ISO-18192-1:2011 testing for different traces taken across the surfaces of convex and concave components; the traces with lowest values are highlighted in green. One-way ANOVA analysis (α=0.05) of the post-test results showed that the changes in parameters following the testing were statistically significant (p<0.05) only in convex components.

Component	**Trace**							
	P_1	**P_2**	**P_3**	**P_4**	**P_5**	**P_6**	**Average(SD)**	**p-value***
	R_a [µm]							
Convex	0.010	0.011	0.014	0.010	0.012	0.015	0.012(0.002)	<0.05
Concave	0.010	0.015	0.011	0.010	0.015	0.012	0.012(0.002)	>0.05
	R_p [µm]							
Convex	0.026	0.029	0.038	0.028	0.031	0.041	0.032(0.006)	<0.05
Concave	0.028	0.041	0.033	0.027	0.044	0.034	0.035(0.004)	>0.05
	R_v [µm]							
Convex	0.045	0.048	0.066	0.050	0.062	0.066	0.056(0.037)	<0.05
Concave	0.039	0.060	0.046	0.040	0.059	0.056	0.050(0.010)	>0.05
	R_{sk} [µm]							
Convex	-4.039	-2.879	-1.974	-3.129	-3.886	-2.109	-3.000(0.865)	<0.05
Concave	-4.489	-1.439	-2.274	-3.139	-1.664	-3.592	-2.766(1.183)	>0.05

*comparison between the pre- and post-test data, standard ISO-18192-1 protocol

The mean values of the skewness parameter (R_{sk}) before testing were -1.108±0.111µm (SD) and -1.870±0.265 (SD) for convex and concave components, respectively (Table 4.4). Following the testing, the values have decreased significantly to -3.000±0.865µm (SD) ($p<0.05$, CI 95%) and -2.766±1.183µm ($p>0.05$, CI 95%) for convex and concave components, respectively (Table 4.5). Only the R_v parameter was not found significantly different ($p>0.05$, CI 95%) between the two component groups (Table 4.4). It may indicate that the manual polishing method applied in the preparation method of the CTDR devices, did not achieve the same surface finish results for the different components.

4.4.1.1.3 Surface damage

At each measurement timepoint light micrographs of the surfaces of all components were captured, to inspect the changes of the surfaces and in an attempt to identify wear modes, mechanisms, types of damage and any surface features. Moreover, ImageJ software was used in order to track changes in the size of the wear area.

Damage to the surface was similar across all stations at each measurement timepoint. There was evidence of surface discolouration on all the components, which appeared to be related to the main wear area; there was a clear difference between the discoloured (worn) and un-worn area (Figure 4.12). Multidirectional, criss-crossing scratches on the wear surfaces were observed (Figure 4.12). In some cases, deep, circular wear scars were observed, as shown in Figure 4.13.

Despite the cleaning protocol being followed diligently at every 1MC measurement timepoint, some components showed evidence of a dark brown deposit build-up on the surfaces (Figure 4.14). With additional scrubbing with acetone-soaked tissue, it was possible to remove some of these deposits. However, in the case of the concave components, this remained difficult to achieve.

High magnification images showed evidence of micropitting, particularly in the pole areas of the concave and convex components (Figure 4.15).

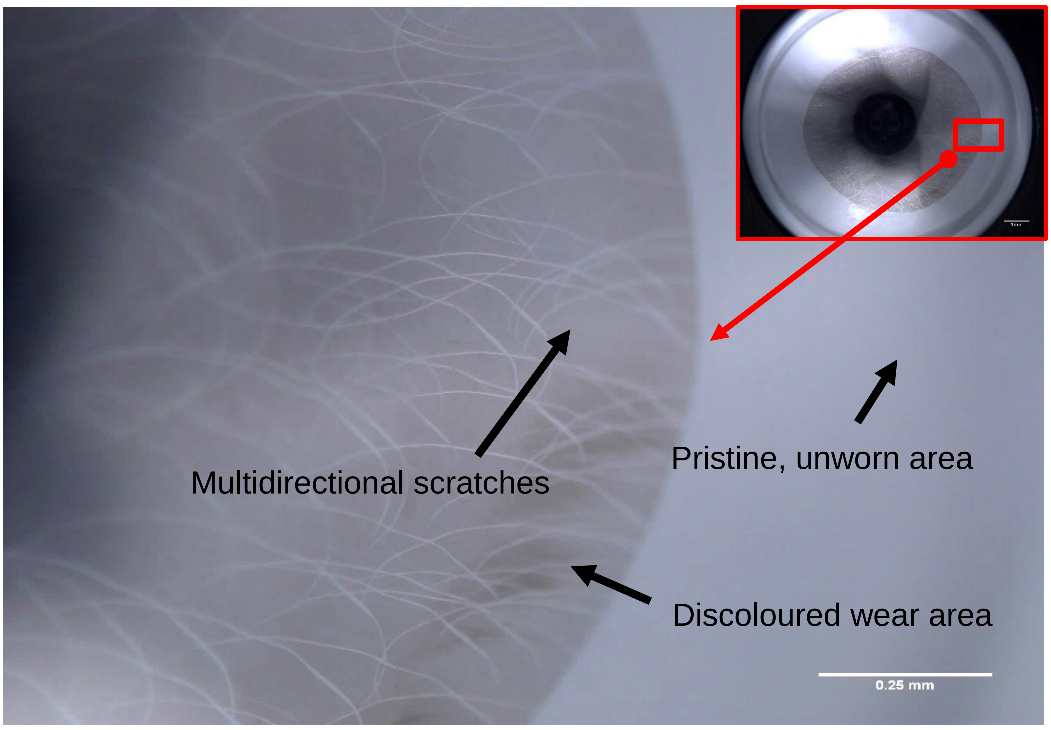
Multidirectional scratches
Pristine, unworn area
Discoloured wear area
0.25 mm

Figure 4.12: High magnification light micrograph depicting the noticeable discolouration of the surface area, associated with wear. Multidirectional, criss-crossing scratches were also present (convex component, 3MC under ISO-18192-1:2011 conditions).

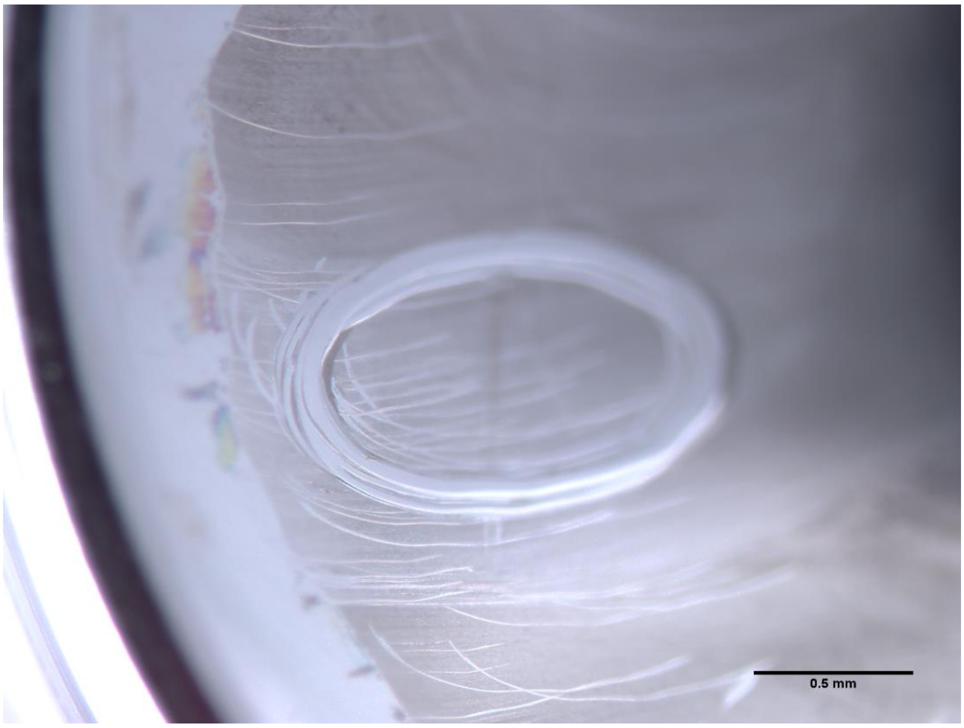

Figure 4.13: Deep wear marks found on some surfaces (concave component, 2MC under ISO-18192-1:2011 conditions).

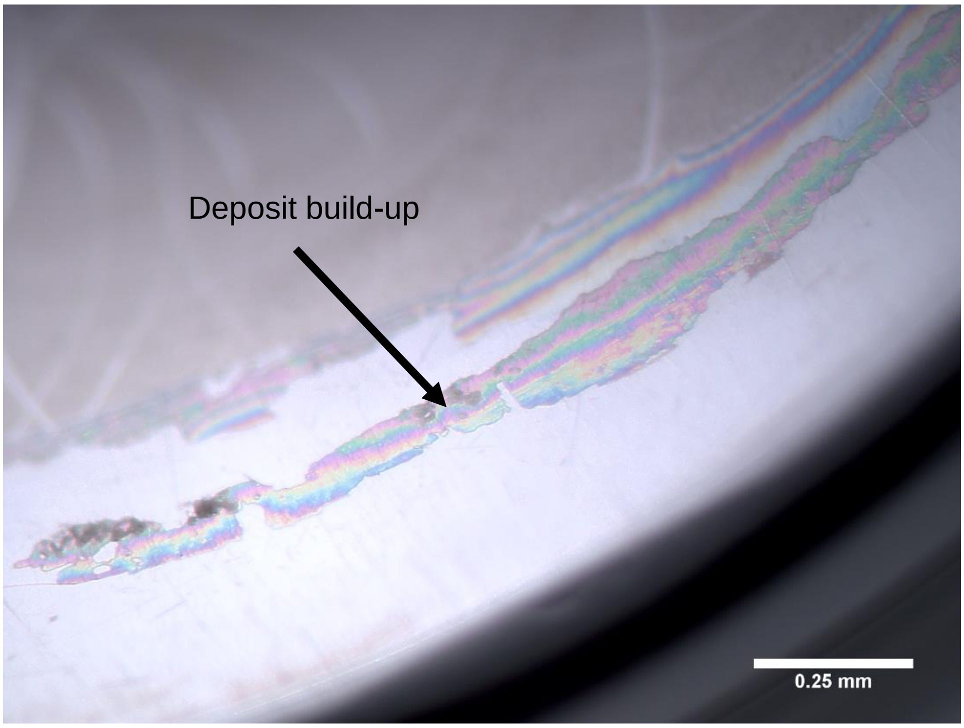
Deposit build-up
0.25 mm

Figure 4.14: Example of deposit build-up on the surfaces at the edges of the wear area (concave component, 4MC under ISO-18192-1:2011 conditions).

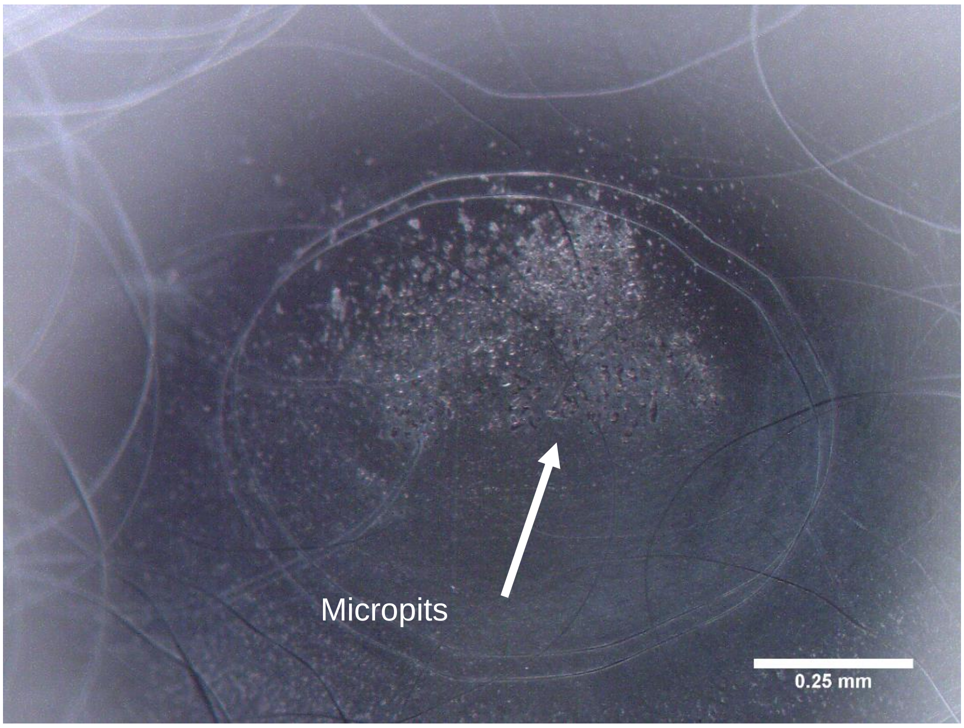
Micropits
0.25 mm

Figure 4.15: Example of surface damage at the pole of a convex component, at 4MC under ISO-18192-1:2011 conditions, showing signs of micropitting.

High resolution, high magnification images captured using SEM showed similar findings to the light micrographs. Surface damage characteristics were similar across all components. Evidence of multidirectional and criss-crossing scratches in the wear area was found (Figure 4.16) along with clear difference in the surface morphology in the wear area, when compared to the unworn surface (Figure 4.17). In some cases, components were present with a layer of deposit, which most commonly occurred at the outside edges of the wear area as well as in deep wear scars (Figure 4.18). Evidence of micropitting was also observed using the SEM (Figure 4.19).

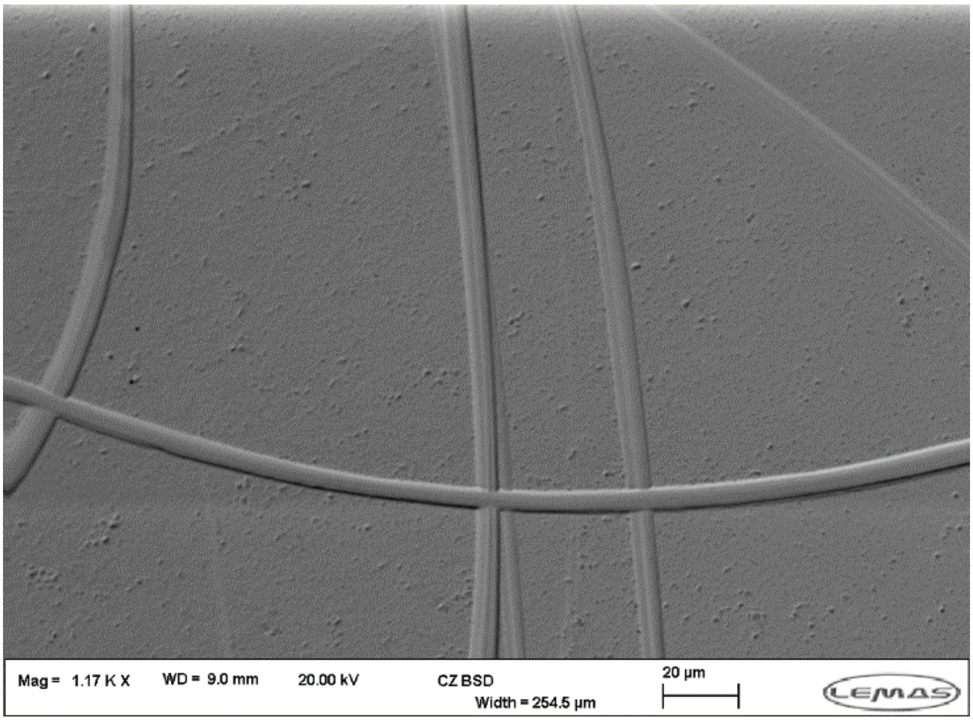

Figure 4.16: SEM micrographs of multidirectional and criss-crossing scratches on the surface of a CoCr CTDR component (convex component, 3MC under ISO-18192-1:2011 conditions)

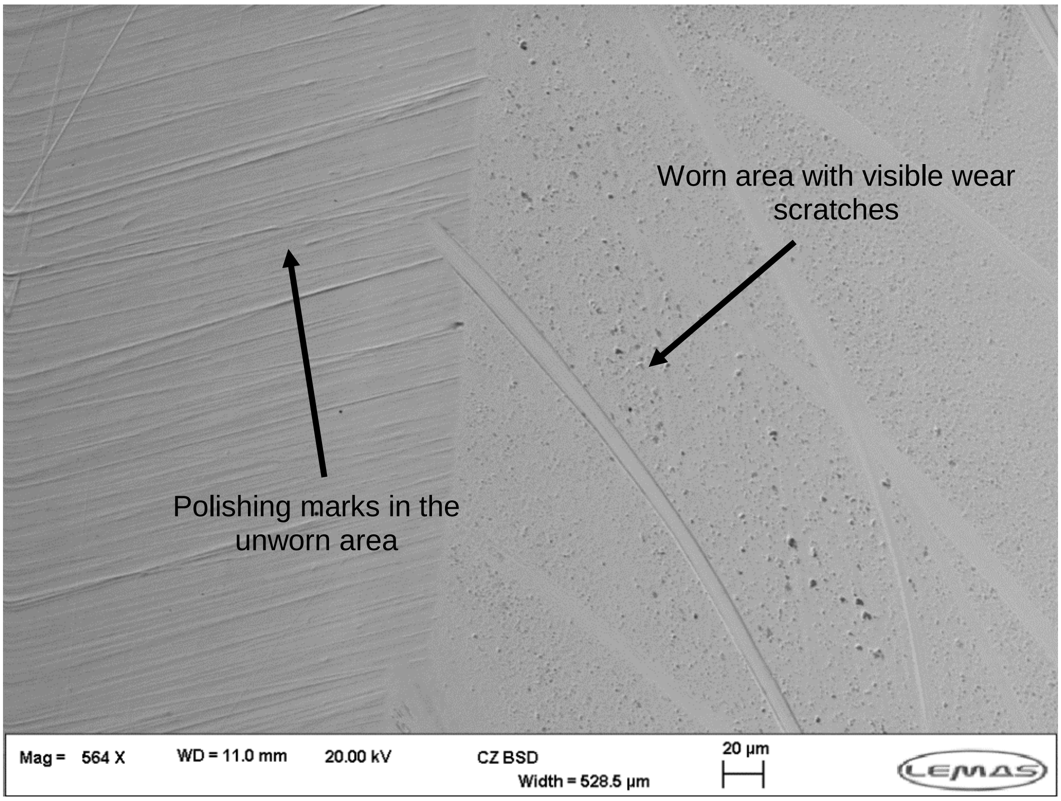
Worn area with visible wear scratches
Polishing marks in the unworn area
Mag = 564 X
WD = 11.0 mm
20.00 kV
CZ BSD
Width = 528.5 µm
20 µm
LEMAS

Figure 4.17: SEM micrograph of morphological difference between worn (right) and unworn (left) surface (convex component, 3MC under ISO-18192-1:2011 conditions).

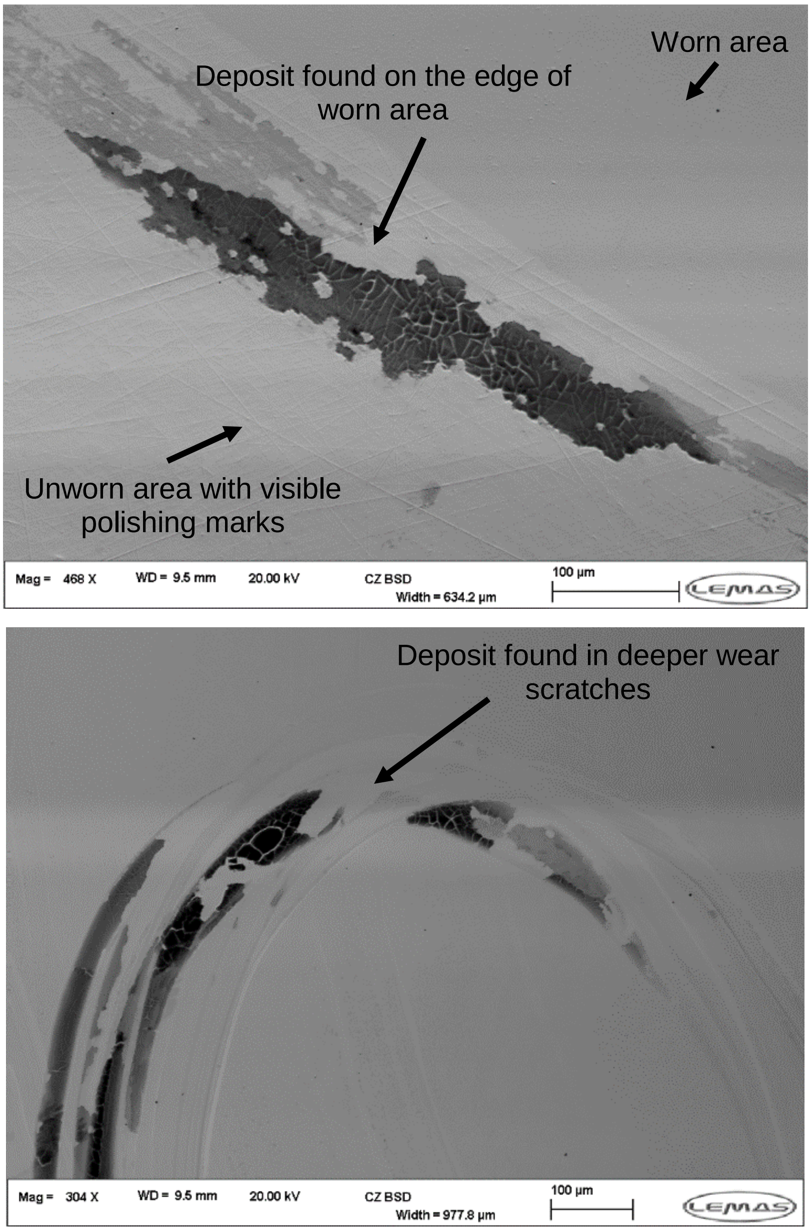
Worn area
Deposit found on the edge of worn area
Unworn area with visible polishing marks
Mag = 468 X
WD = 9.5 mm
20.00 kV
CZ BSD
Width = 634.2 µm
100 µm
LEMAS
Deposit found in deeper wear scratches
Mag = 304 X
WD = 9.5 mm
20.00 kV
CZ BSD
Width = 977.8 µm
100 µm
LEMAS

Figure 4.18: SEM micrographs of deposit found surfaces, most commonly found on the outside edges of the wear area (top), as well as in deeper wear scratches (bottom) (concave component, 2MC under ISO-18192-1:2011 conditions

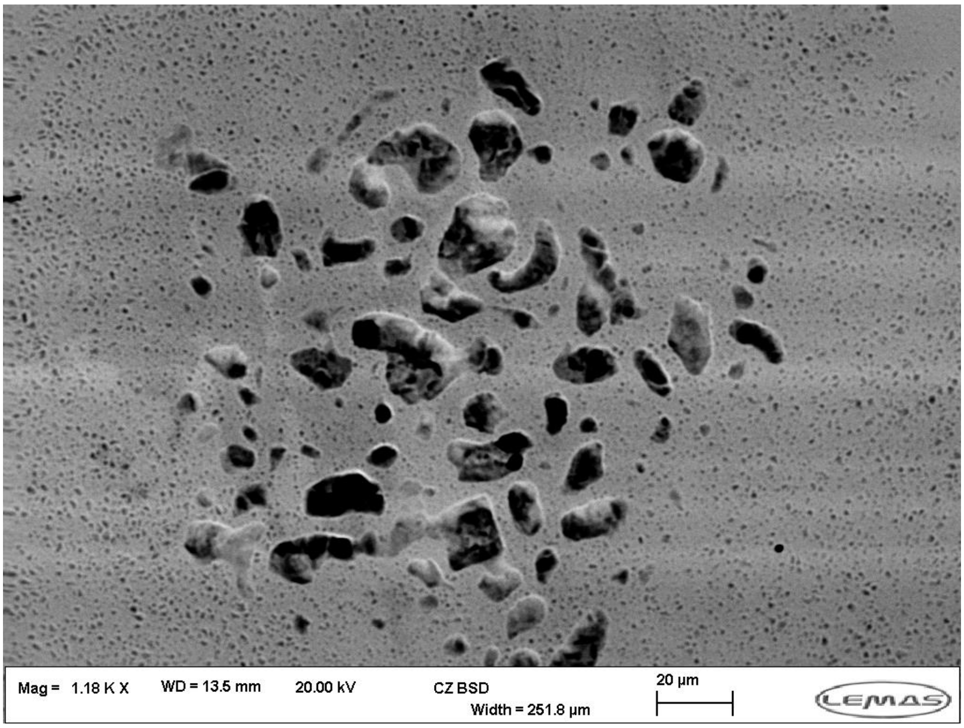

Figure 4.19: Example of micro-pits found on the surfaces of uncoated, metal CTDR components, following 2MC of standard ISO testing.

The size of the visible wear area was assessed at each measurement timepoint using the light micrographs and ImageJ software. A summary of the results is shown in Table 4.6. The mean value of the visible wear area for convex components increased from 22.1±2.9mm^2 at the 1MC timepoint, to 35.1±1.0mm^2 at the 4MC timepoint. Similarly, the mean value for concave components increased from 27.8±2.3mm^2 at 1MC timepoint to 43.1±1.1mm^2 at 4MC timepoint. Throughout the entire duration of standard ISO-18192-1:2011 protocol, the visible wear area was larger on the concave components. Assuming, that the bearing area was flat (i.e. as observed through the light microscope), the bearing surface of the convex and concave components were 76.4mm^2 and 57.2mm^2, respectively. Thus, the wear area observed at the convex components increased from 38.6% of the total bearing surface at 1MC to 45.9% at 4MC. Similarly, the wear area on the concave components progressed from 48.6% of the total bearing area at 1MC to 75.3% at 4MC. At each timepoint the wear scars observed on the concave components were significantly larger ($p<0.05$, CI 95%) and accounted for a larger proportion of the total bearing area, than those observed on the convex components.

Table 4.6: Summary of mean values of the visible wear area on the CoCr CTDR components, measured throughout the 4MC of standard ISO testing (ISO-18192-1:2011). One-way ANOVA (α=0.05) was used to calculate p-values.

Visible wear area ± SD [mm²]					
No. of cycles	1	2	3	4	Mean
Convex	22.1±2.9	31.0±1.8	33.4±1.4	35.1±1.0	30.4±5.5
Concave	27.8±2.3	34.8±2.5	36.6±1.8	43.1±1.1	36.2±6.3
p-value	$p<0.05$	$p<0.05$	$p<0.05$	$p<0.05$	$p<0.05$

4.4.1.1.4 Post-test dimensional inspection

The radius of each component was measured as described in Chapter 3 section 1.2.2 and the resulting radial clearance of each test station was calculated. The same process was repeated after the completion of Test 1 i.e. after 4MC of standard ISO-18192-1:2011 testing conditions (Table 4.7). The mean value of the radial clearance prior to testing (0.162±0.004mm) decreased, following 4MC of standard ISO testing conditions, to 0.048±0.019mm, which was statistically significantly lower ($p<0.05$, CI 95%).

Table 4.7: Summary of pre- and post-test values of radial clearances of each test station.

Station ID	Pre-test radial clearance ±SD [mm]	Post-test radial clearance ±SD [mm]
1	0.157±0.014	0.043±0.026
2	0.162±0.011	0.058±0.019
3	0.163±0.014	0.070±0.012
4	0.162±0.016	0.049±0.013
5	0.162±0.013	0.055±0.006
6	0.157±0.011	0.013±0.023
Mean	0.162±0.004	0.048±0.019

4.4.1.2 Altered ISO simulator testing conditions

Since the pristine CoCr-CoCr CTDRs did not sustain significant surface damage following the 4MC of standard ISO-18192-1:2011 testing protocol, it was decided continue wear testing under the altered ISO protocol (section 4.3.2) with the same CTDR devices.

4.4.1.2.1 Wear rates

The initial test consisted of 4MC of standard ISO-18192-1:2011 input (Test 1). Subsequently, 2MC of altered ISO inputs (Test 2) were applied. The overall mean volume loss in Test 2 was 0.08±0.0.06mm^3 following 2MC of testing, ranging from 0.05mm^3 (Stn.1) to 0.14mm^3 (Stn.4). The mean volumetric wear rate was 0.039mm^3/MC, ranging from 0.02mm^3/MC (Stn.1) to 0.07mm^3/MC (Stn.4). On average, the volume loss was 0.03mm^3/MC and 0.05mm^3/MC for the convex and concave components, respectively (Figure 4.20). No significant difference between the volume loss of the two component groups was found ($p>0.05$, CI 95%). The altered ISO testing showed a linear wear behaviour, same as in Phase 1 testing. However, there was a significant ($p<0.05$, CI 95%) reduction in wear of CTDRs when tested under the altered ISO conditions, showing that tribological performance of CTDRs was strongly influenced by the reduction in ROMs used in the testing protocol.

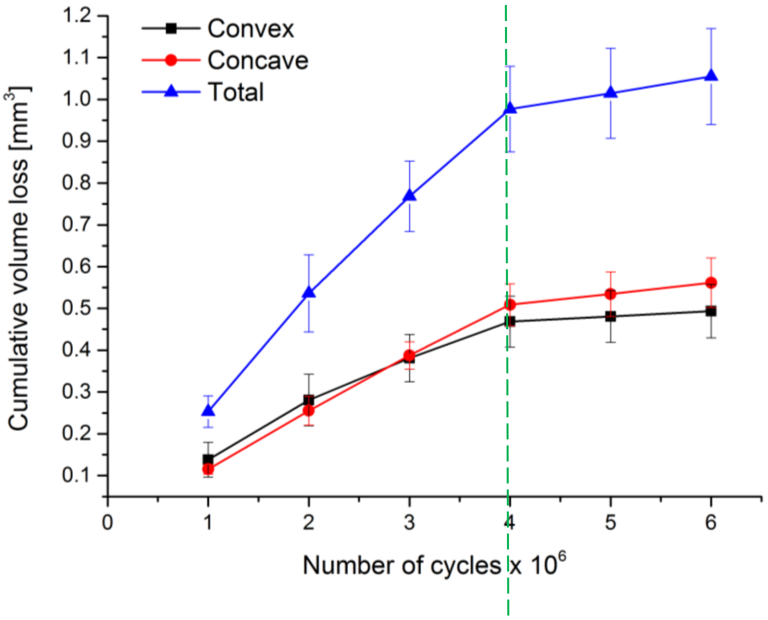

Figure 4.20: Cumulative volume loss of CTDR components following 4MC of standard ISO testing protocol and 2MC of modified ISO testing protocol. There was a significant reduction in mass loss i.e. wear in the second phase of the testing whereby the modified ISO testing protocol was employed (4-6MC). Error bars represent 95% confidence limits.

4.4.1.2.2 Surface roughness

The surface topography parameters measured following 4MC of standard ISO protocol were now considered as pre-test values of the non-ISO protocol test. These have previously been reported in Section 4.4.1.1.2,Table 4.5.

Following 2MC of altered ISO testing, the surface topography of the MoM components was measured again. A summary of those measurements is listed in Table 4.8.

Prior to the Test 2 part of the study, the convex and concave components had mean R_a values 0.012±0.002µm and 0.012±0.002µm (±SD), for the convex and concave components, respectively (Table 4.5). These were calculated as an average value of all 6 traces across the surface of each component. Following 2MC of the altered ISO testing protocol, the mean values of R_a changed to 0.015±0.001µm and 0.018±0.001µm for convex and concave components, respectively. The increase of surface roughness (R_a) following the altered ISO testing, was not statistically significant for either the convex ($p>0.05$, CI 95%) or the concave components ($p>0.05$, CI 95%).

Measurements taken across the pole of each component (traces P_1 and P_4), following 2 MC of the altered ISO test protocol, showed the lowest values of R_a, as summarised in Table 4.8. Some changes in the R_p, R_v and R_{sk} was also noted, following the 2MC of the altered protocol testing. In most cases the mean values increased following the altered testing, however, none of the changes were statistically significant. A summary of the one-way ANOVA tests (p-values) are listed in Table 4.8.

Table 4.8: Summary of contact profilometry results of the CTDR components following 2MC of altered ISO testing protocol. Mean R_a, R_p, R_v and R_{sk} values different traces taken across the surfaces of convex and concave components; highlighted in green are the traces with lowest values. One-way ANOVA analysis (α=0.05) of the results showed that the changes in all parameters, in comparison to the pre-test condition, were not statistically significant.

Component	Trace							
	P_1	P_2	P_3	P_4	P_5	P_6	Average	p-value*
	R_a [µm]							
Convex	0.009	0.014	0.017	0.010	0.016	0.022	0.015	>0.05
Concave	0.009	0.045	0.012	0.011	0.018	0.015	0.018	>0.05
	R_p [µm]							
Convex	0.022	0.037	0.048	0.027	0.042	0.063	0.046	>0.05
Concave	0.025	0.048	0.033	0.030	0.044	0.034	0.035	>0.05
	R_v [µm]							
Convex	0.04	0.059	0.081	0.079	0.083	0.131	0.092	>0.05
Concave	0.033	0.063	0.053	0.044	0.081	0.060	0.056	>0.05
	R_{sk} [µm]							
Convex	-3.085	-1.454	-1.914	-4.936	-2.568	-1.539	-3.012	>0.05
Concave	-2.203	-1.880	-1.519	-3.472	-1.997	-1.784	-2.142	>0.05

*comparison of pre- and post-test data, altered ISO-18192-1 testing protocol

4.4.1.2.3 Surface damage

At each measurement timepoint light micrographs of the surfaces of all components were captured, in order, to inspect the changes of the surfaces and in an attempt to identify wear modes, mechanisms, types damage and any surface features. Moreover, ImageJ software was used in order, to track changes in the size of the wear area.

Similarly, to the components tested under the ISO protocol, damage to the surface was similar across all stations at each measurement timepoint. There was evidence of surface discolouration on all the components, which appeared to be related to the main wear area; there was a clear difference between the discoloured (worn) and un-worn area (Figure 4.21). Multidirectional, criss-crossing scratches on the wear surfaces were observed (Figure 4.12), some of which were generated in the first phase of testing (ISO protocol) and some when components were tested under the altered ISO testing protocol. Significant difference in wear marks (scratches) size was observed – the wear marks generated following the altered ISO testing protocol were smaller, when compared to those generated under the ISO-18192-1:2011 protocol. In some cases, deep, circular wear scars were found, as shown in Figure 4.13.

Despite the cleaning protocol that was followed diligently at each measurement timepoint, some components showed evidence of dark brown deposit build-up on the surfaces (Figure 4.22). With additional scrubbing with acetone-soaked tissue, it was possible to remove some of these deposits. High magnification images showed evidence of micropitting, particularly in the pole areas of the concave and convex components (Figure 4.23), however, some of this damage might have occurred during the ISO protocol testing.

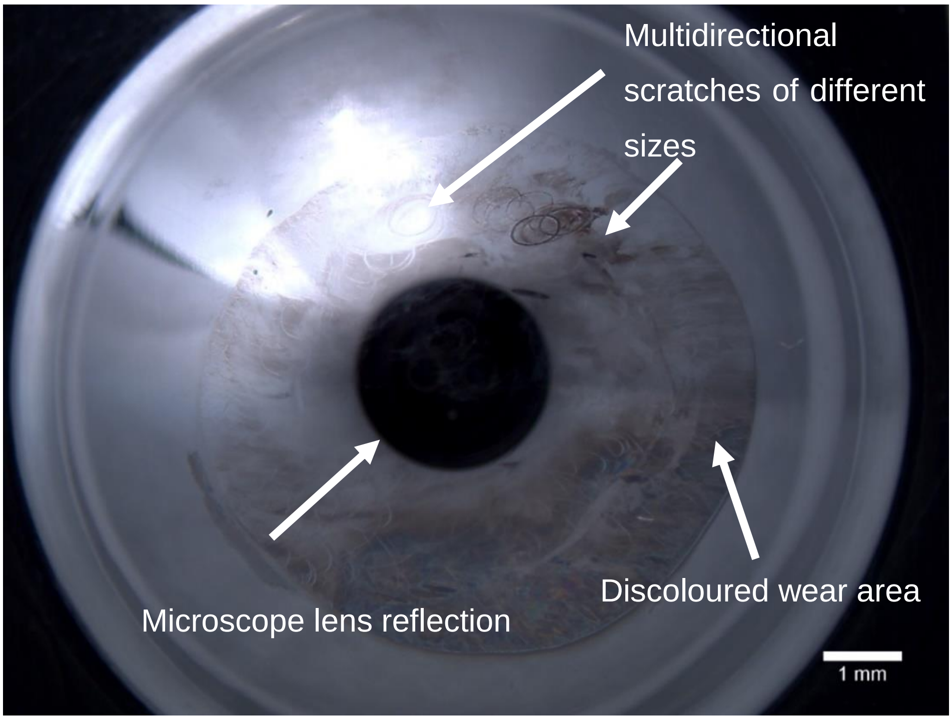
Multidirectional scratches of different sizes
Microscope lens reflection
Discoloured wear area
1 mm

Figure 4.21: Example of high magnification micrograph showing the noticeable discolouration of the surface area, associated with wear. Multidirectional, criss-crossing scratches were also present. (convex component, 5MC i.e. 4MC ISO-18192-1:2011 + 1MC altered ISO).

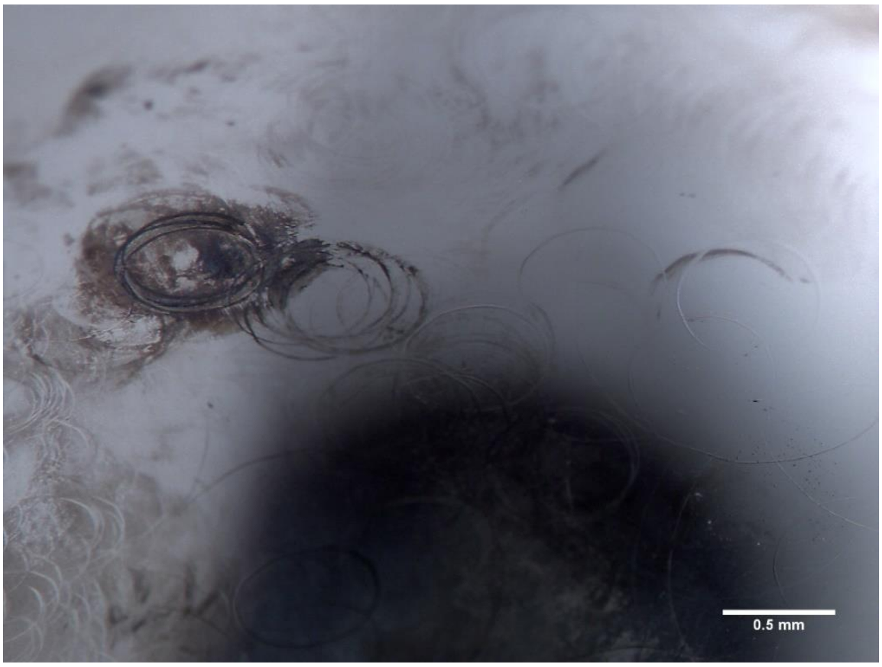

Figure 4.22: High magnification image of deep wear marks found on some surfaces (concave component, 5CM i.e. 4MC ISO-18192-1:2011 + 1MC altered ISO). Some deposit build-up around the scratches were also observed.

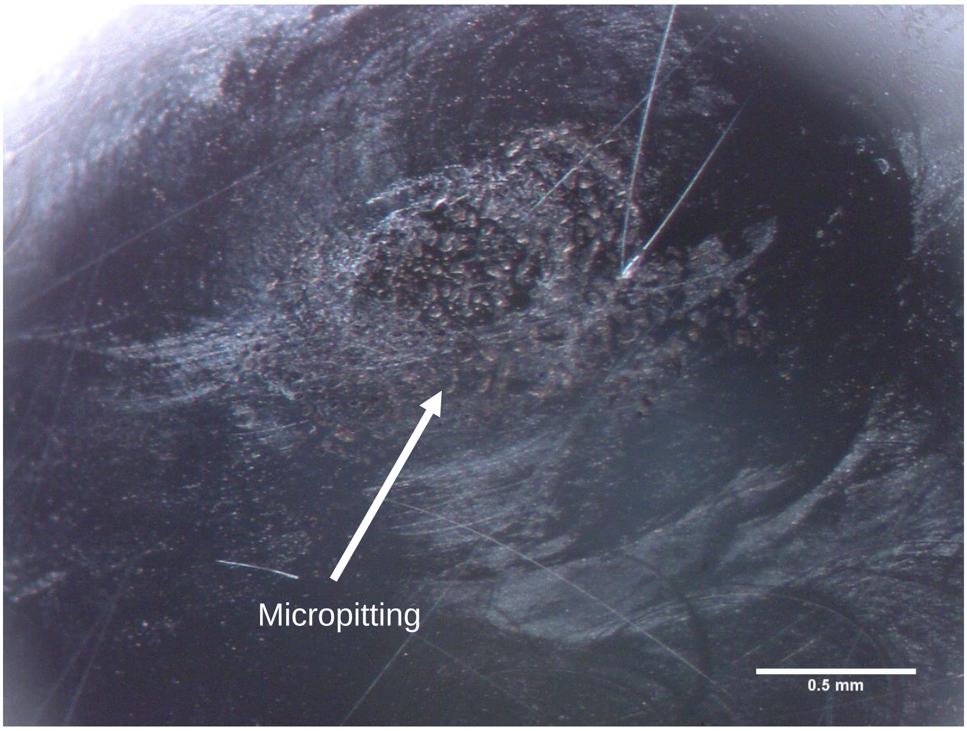

Figure 4.23: Surface damage at the pole of a convex component, at 5MC (4MC ISO-18192-1:2011 + 1MC altered ISO), showing signs of micropitting.

Following 6MC of testing, which included 4MC of ISO-18192-1:2011 protocol testing and 2MC of altered ISO testing, high resolution, high magnification images were captured using SEM. The images showed similar type of damage as those observed in the light micrographs. Surface damage characteristics were similar across all components. Evidence of multidirectional and criss-crossing scratches in the wear area was found (Figure 4.24); some of the scars were larger – generated under the ISO-protocol testing conditions, and some were smaller – generated under the ISO-altered testing protocol. Some evidence of deposits (Figure 4.25) and micropitting (Figure 4.26) was also observed on the surfaces, following 6CM of testing. It was not possible to determine at which point of testing i.e. under which testing conditions the micropitting occurred.

No assessment of the visible wear area was performed following the 2MC of altered ISO protocol, as it was not possible to establish the exact area of wear, which was generated during the second phase of testing (altered ISO protocol).

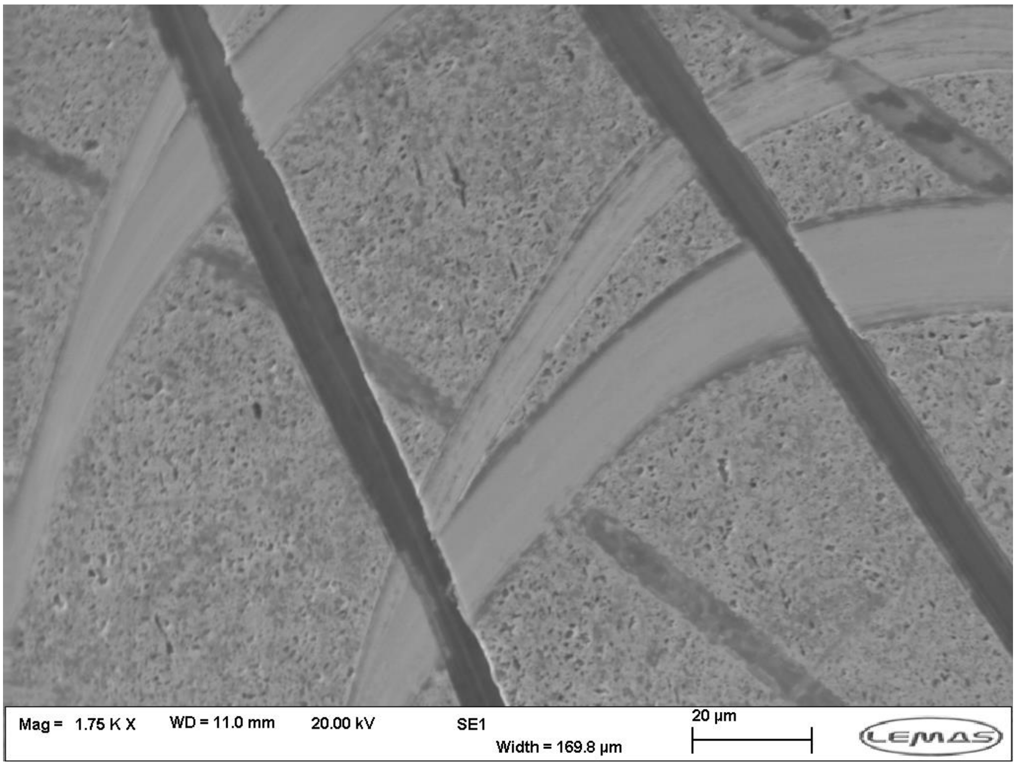
Mag = 1.75 K X
WD = 11.0 mm
20.00 kV
SE1
Width = 169.8 µm
20 µm
LEMAS

Figure 4.24: High magnification, high resolution image of multidirectional and criss-crossing scratches on the surface of a metal CTDR component.

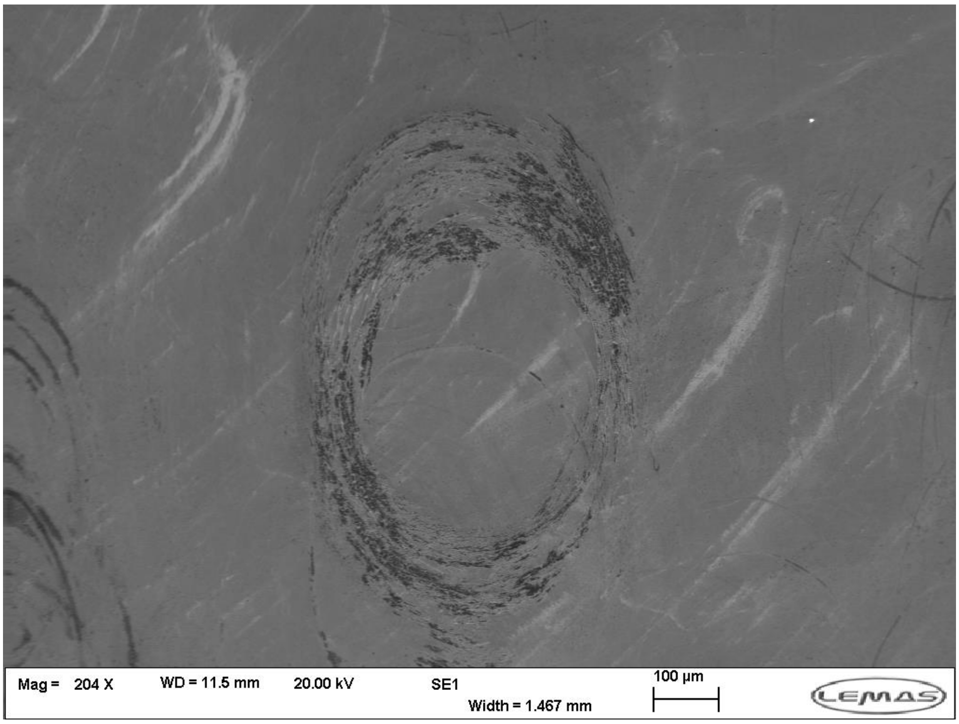
Mag = 204 X
WD = 11.5 mm
20.00 kV
SE1
Width = 1.467 mm
100 µm
LEMAS

Figure 4.25: Deposit found inside the grooves of the wear scratches of CoCr CTDRs tested under altered ISO-18192-1:2011 protocol.

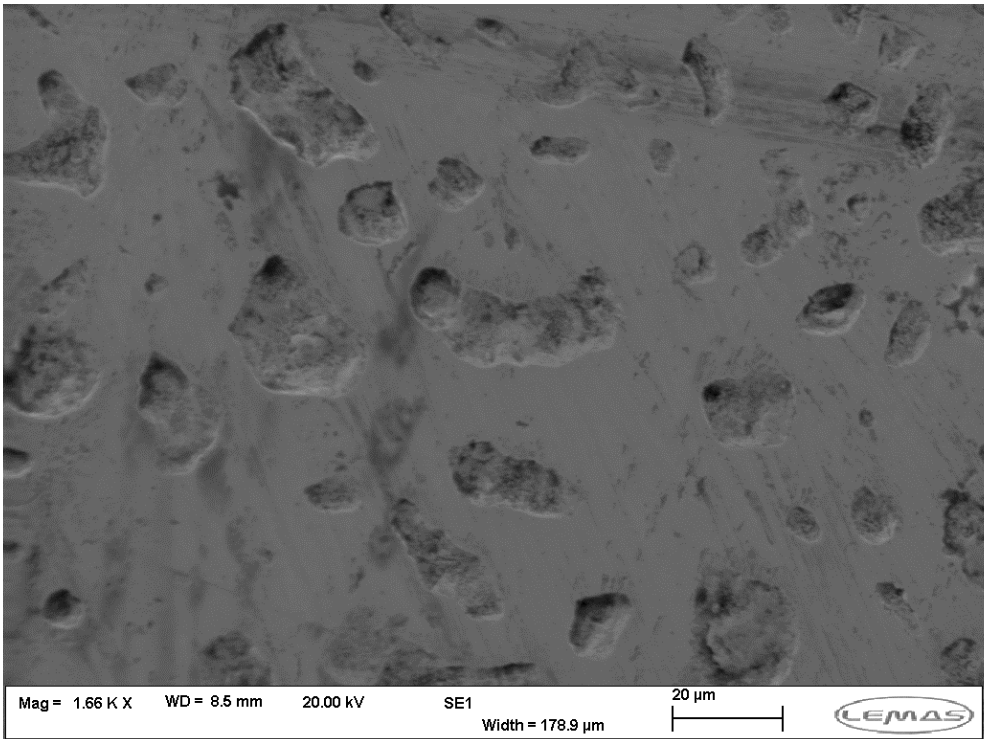

Figure 4.26: SEM micrograph (mag=1.66K) of micro-pits found on the surfaces of CoCr CTDR components, following 2MC of standard ISO testing.

4.4.1.2.4 Post-test dimensional inspection

The radius of each component was measured as described in Chapter 3 section 1.2.2 and the resulting radial clearance of each test station was calculated. The same process was repeated after the completion of Test 2 i.e. the 2MC of altered ISO-18192-1:2011 testing protocol (section 4.3.2). A summary of the measurements and a comparison to thee pre-test (as of 4MC) radial clearance is shown in Table 4.9 . The mean value of radial clearance prior to testing of 0.048±0.019mm has decreased, following 2MC of the altered ISO testing conditions to 0.028±0.010mm, which was statistically significant ($p<0.05$, CI 95%).

Table 4.9: Summary of pre- and post-test values of radial clearances of each test station i.e. prior to and following 2MC of testing following the altered ISO protocol.

Station ID	Pre-test radial clearance ±SD [mm]	Post-test radial clearance ±SD [mm]
1	0.043±0.026	0.024±0.003
2	0.058±0.019	0.034±0.007
3	0.070±0.012	0.034±0.007
4	0.049±0.013	0.030±0.008
5	0.055±0.006	0.037±0.009
6	0.013±0.023	0.010±0.016
Average	0.048±0.019	0.028±0.010

4.4.2 Coated CTDRs

4.4.2.1 Pre-test coating inspection

Prior to *in vitro* wear testing, SEM images of the silicon nitride and chromium nitride-coated CTDRs were taken, in order, to inspect the quality of the coatings. Some coating defects – holes, pits and splashing defects were observed on the surfaces, as shown in Figure 4.27 and Figure 4.28.

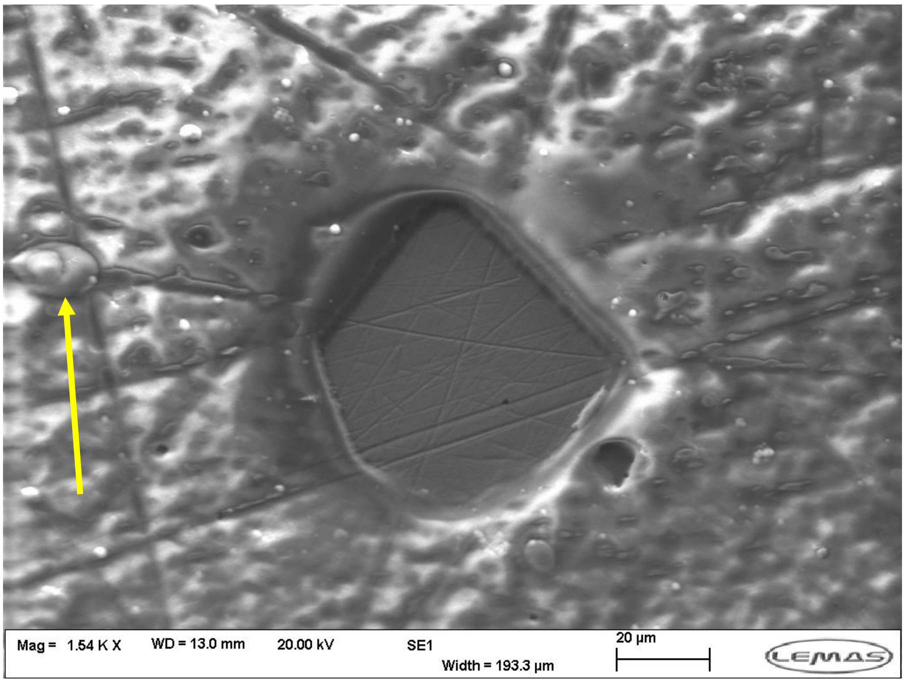
Mag = 1.54 K X
WD = 13.0 mm
20.00 kV
SE1
Width = 193.3 µm
20 µm
LEMAS

Figure 4.27: SEM image of silicon nitride-coated CTDR device. A large hole in the coating was observed – substrate material, with polishing marks visible, was seen. Moreover, small splashing defect (marked with an arrow) was found.

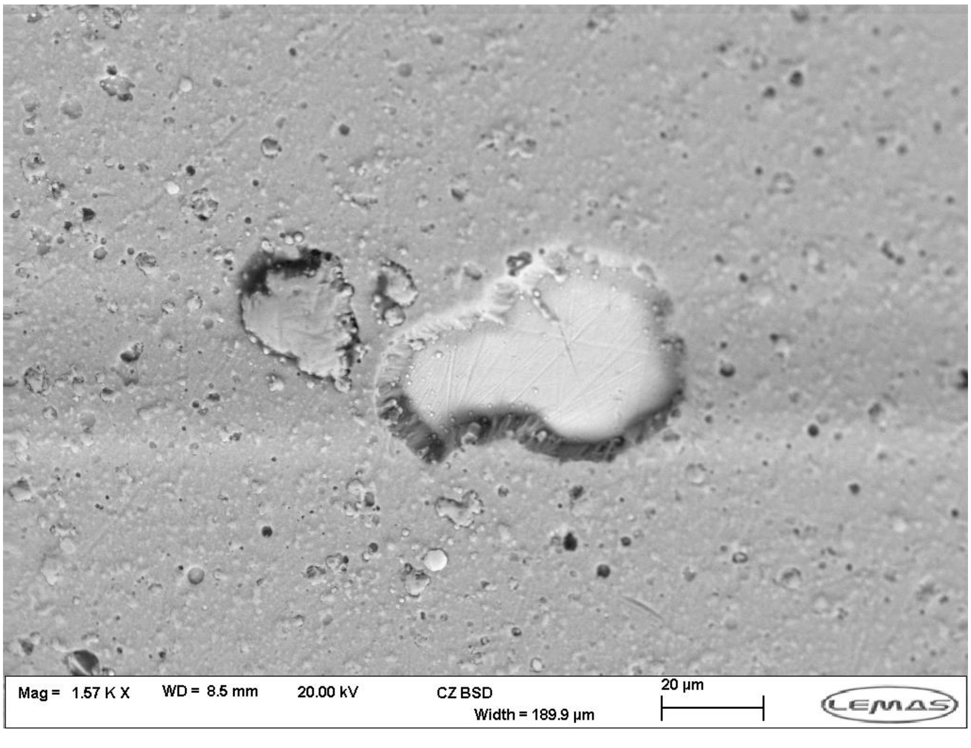
Mag = 1.57 K X
WD = 8.5 mm
20.00 kV
CZ BSD
Width = 189.9 µm
20 µm
LEMAS

Figure 4.28: SEM image of chromium nitride-coated CTDR device. Portion of coating was missing from the surface, substrate material with polishing marks was observed underneath. Numerous holes/pits, as well as portions of coating protruding out of the coating were observed.

4.4.2.2 Standard simulator testing conditions

Silicon nitride- and chromium nitride-coated CTDRs were fitted into the six-station spine simulator and tested under standard ISO-18192-1:2011 testing conditions. The aim of this study was to assess the wear performance of the coated devices, in comparison to the pristine (MoM) CTDRs, which were tested under the same testing conditions for 4×10^6 cycles and exhibited an average wear rate of $0.24 mm^3/MC$ (4.4.1.1.1).

Following 71,000 cycles, it was noted that the silicon nitride-coated components had sustained damage and delamination of the coating. Thus, the testing of those components was not continued further. At the same number of cycles, the chromium nitride coating remained intact, and thus the testing under the standard ISO-18192-1:2011 testing conditions was continued. The chromium nitride-coated components were inspected for coating failure following 1×10^6 cycles, when no coating delamination was discovered. Testing of CrN CTDRs was continued for further 1×10^6 cycles, until 2×10^6 cycles was reached.

4.4.2.2.1 Wear rates

The preliminary results of the wear performance of chromium nitride-coated CTDRs, following 2MC of testing in the six-station spine simulator, under the standard ISO-18192-1:2011 showed an overall mean volume loss of $0.06 \pm 0.02 mm^3$ over 2MC of testing, ranging from $0.034 mm^3$ (Stn.1) to $0.07 mm^3$ (Stn.2). The mean volumetric wear rate was $0.03 \pm 0.01 mm^3/MC$, ranging from $0.02 mm^3/MC$ (Stn.1) to $0.04 mm^3/MC$ (Stn.3) On average, the overall volume loss from the convex components was $0.05 \pm 0.01 mm^3$ and $0.06 \pm 0.03 mm^3$ from the concave components, as shown in Figure 4.29. No significant differences between the two component groups was found ($p > 0.05$, CI 95%).

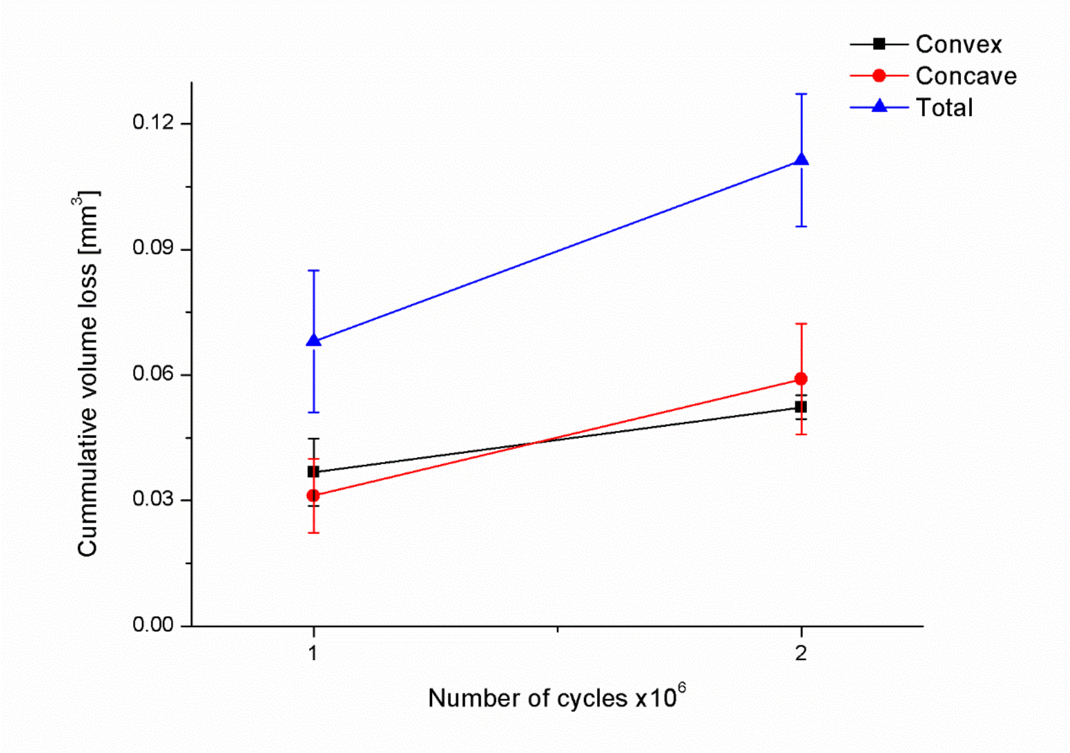

Figure 4.29: Cumulative volume loss from CrN-CrN CTDR components tested under the ISO-18192-1:2011 protocol. There was no significant difference in convex and concave component volume loss across 2MC of simulator testing. Error bars represent 95% confidence interval limits.

The silicon nitride coated components did not reach 1MC of testing. The overall mean volume loss at 71, 000 cycles was 0.21±0.06mm^3, ranging from 0.14mm^3 (Stn. 6) to 0.25mm^3 (Stn.2). By linearly extrapolating the data, the theoretical mean volumetric wear rate of the silicon nitride-coated components was 2.92±0.88mm^3/MC. On average, at 71,000 cycles, the volume loss from the convex components was 0.10mm^3 and 0.11mm^3 from the concave components, as shown in Figure 4.30. There was no statistically significant difference between the volume loss exhibited by the convex and concave components ($p>0.05$, CI 95%).

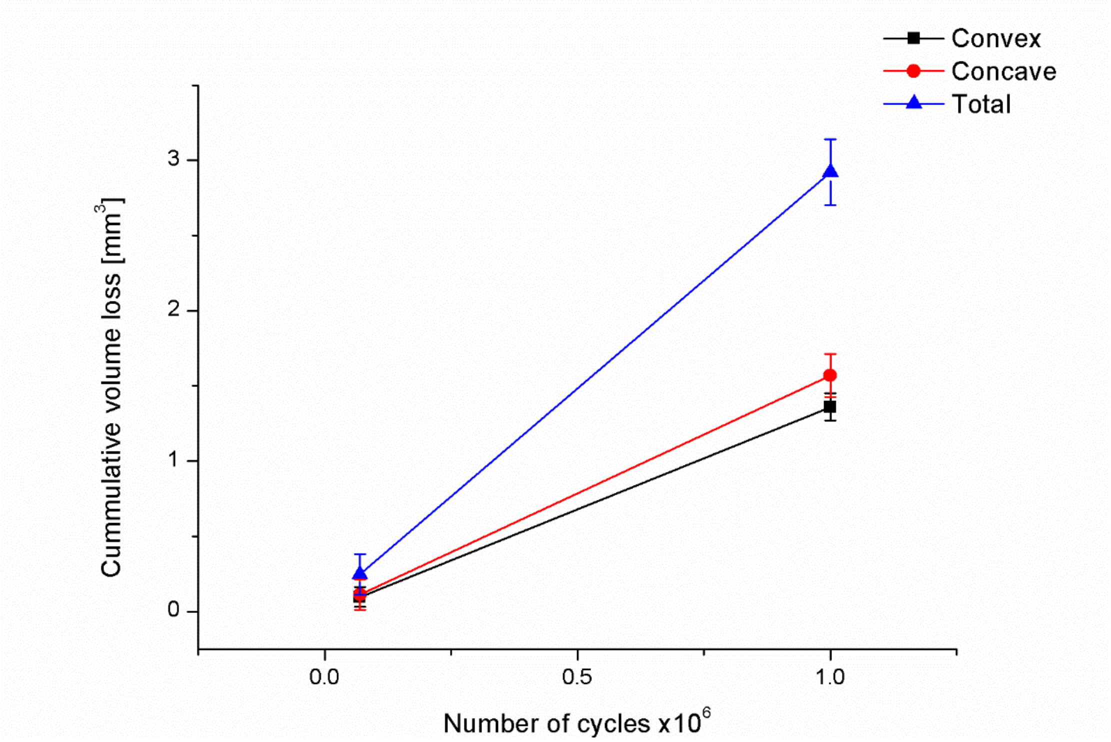

Figure 4.30: Cumulative volume loss from Si_3N_4-Si_3N_4 CTDR components tested under the ISO-18192-1:2011 protocol. Following coating failure and delamination at 71,000 cycles, the data was linearly extrapolated to 1MC. There was no significant difference in convex and concave component volume loss across 4MC of simulator testing. Error bars represent 95% confidence interval limits.

Using the linearly extrapolated data for Si_3N_4 coating, the difference in volumetric wear rates between the silicon nitride- (2.92±0.88mm^3/MC) and chromium nitride-coated CTDRs (0.03±0.01mm^3/MC) was found to be statistically significant ($p<0.05$, CI 95%).

4.4.2.2.2 Surface roughness

Prior to testing, surface roughness of the convex and concave components of both silicon nitride- and chromium nitride-coated devices was measured. The results of the pre-test surface measurements of the chromium nitride-coated components are summarised in Table 4.10. The mean R_a values of the convex and concave components were 0.065±0.023µm (SD) and 0.087±0.012µm (SD), respectively. These were calculated as an average value of all six traces across the surface of each component. It was observed that in the pre-test measurements the traces taken across the pole of each component (traces P_1 and P_4) showed lower R_a values. As shown in Table 4.10, convex components exhibited significantly lower values of the R_a, R_p and R_{sk} values, when compared to the concave components ($p<0.05$, CI 95%). There were no significant differences of the R_v parameter between the two component groups ($p>0.05$, CI 95%). Following 2MC of standard ISO testing surfaces of all chromium nitride-coated components were analysed using the same method. Following the wear testing the mean R_a values of the convex and concave components decreased by 56% to a value of 0.037±0.024µm (SD) and by 62% to a value of 0.054±0.035µm (SD), respectively (Table 4.11). The predominant reduction of the R_a parameter occurred at the pole area of the components, correlating with P_1 and P_4 traces, which value were reduced by 8-fold on average following the *in vitro* wear testing under the ISO-18192-1:2011 testing protocol. There were no statistically significant differences between the convex and concave component surface profile parameters following the wear testing. The results obtained after the wear testing showed that the R_a, R_v and R_p parameters decreased significantly ($p<0.05$, CI 95%) after 2MC of wear testing under the ISO-18192-1:2011 protocol. The R_{sk} parameter did not change significantly ($p>0.05$, CI 95%).

Table 4.10: Mean pre-test R_a, R_p, R_v and R_{sk} values for different traces taken across the surfaces of convex and concave components of CrN-CrN CTDR devices; the traces with lowest values are highlighted in green. One-way ANOVA analysis (α=0.05) of the pre-test surface finish parameters showed that the R_a, R_p and R_{sk} of convex components were significantly lower ($p<0.05$) than those of the convex components. Values of the R_v parameter were not found to be significantly different between the two component groups.

Component	Trace							
	P_1	P_2	P_3	P_4	P_5	P_6	Average(SD)	p-value*
	R_a [µm]							
Convex	0.045	0.062	0.091	0.049	0.056	0.088	0.065(0.023)	<0.05
Concave	0.083	0.104	0.077	0.081	0.086	0.088	0.087(0.012)	
	Trace R_p [µm]							
Convex	0.110	0.173	0.233	0.117	0.152	0.267	0.175(0.065)	<0.05
Concave	0.489	0.672	0.536	0.488	0.598	0.557	0.554(0.106)	
	Trace R_v [µm]							
Convex	0.225	0.287	0.437	0.208	0.235	0.407	0.299(0.118)	>0.05
Concave	0.278	0.390	0.295	0.255	0.345	0.278	0.307(0.056)	
	Trace R_{sk} [µm]							
Convex	-1.738	-0.928	-1.092	-1.599	-0.625	-0.681	-1.111(0.566)	<0.05
Concave	1.6814	1.493	1.967	2.755	0.964	2.579	1.907(0.923)	

*comparison between convex and concave data

Table 4.11: Mean R_a, R_p, R_v and R_{sk} values of CrN-CrN CTDRs following 2MC of ISO-18192-1:2011 testing for different traces taken across the surfaces of convex and concave components; the traces with lowest values are highlighted in green. One-way ANOVA analysis ($\alpha=0.05$) of the post-test results showed that only the changes in R_p and R_v of the concave components were statistically significant ($p<0.05$).

Component	Trace							
	P_1	P_2	P_3	P_4	P_5	P_6	Average(SD)	p-value*
	R_a [µm]							
Convex	0.008	0.051	0.058	0.005	0.053	0.055	0.037(0.024)	>0.05
Concave	0.010	0.094	0.072	0.011	0.077	0.062	0.054(0.035)	>0.05
	R_p [µm]							
Convex	0.012	0.138	0.142	0.010	0.145	0.131	0.093(0.063)	>0.05
Concave	0.018	0.294	0.384	0.203	0.335	0.315	0.228(0.190)	<0.05
	R_v [µm]							
Convex	0.046	0.259	0.168	0.011	0.287	0.231	0.167(0.119)	>0.05
Concave	0.061	0.157	0.208	0.067	0.261	0.179	0.156(0.897)	<0.05
	R_{sk} [µm]							
Convex	-5.448	-1.663	-1.114	-1.979	-1.370	-0.936	-1.962(2.864)	>0.05
Concave	-1.939	1.309	3.100	-3.206	0.495	2.569	0.388(2.679)	>0.05

*comparison of pre- and post-test data, standard ISO-18192-1

The results of the pre-test surface measurements of the silicon nitride-coated components were summarised in Table 4.12. The mean R_a values of the convex and concave components were 0.030±0.008 (SD) and 0.037±0.005 (SD), respectively. These were calculated as an average value of all six traces across the surface of each component. It was noted in the pre-test measurements that the traces taken across the pole of each component (traces P_1 and P_4) showed lower R_a values, as shown in Table 4.12. Convex components exhibited significantly lower values of R_p and R_{sk} parameters ($p<0.05$, CI 95%), whilst R_a and R_v parameters were not statistically different ($p>0.05$, CI 95%). The pre-test results showed that silicon nitride coating was significantly smoother (R_a) than chromium nitride ($p<0.05$, 95%). Due to substantial coating damage and delamination sustained following 71,000 cycles of the standard ISO-18192-1:2011, no post-test surface roughness measurements of the silicon nitride-coated devices were obtained.

Table 4.12: Mean pre-test R_a, R_p, R_v and R_{sk} values of Si_3N_4- Si_3N_4 CTDRs for different traces taken across the surfaces of convex and concave components; the traces with lowest values are highlighted in green. One-way ANOVA analysis ($\alpha=0.05$) of the pre-test surface finish parameters showed that the R_p and R_{sk} of convex components were significantly lower ($p<0.05$) than those of the concave components. Values of the R_a and R_v parameter were not found to be significantly different between the two component groups.

Component	**Trace**							
	P_1	**P_2**	**P_3**	**P_4**	**P_5**	**P_6**	**Average(SD)**	**p-value***
	R_a [μm]							
Convex	0.025	0.031	0.029	0.019	0.038	0.039	0.030(0.008)	>0.05
Concave	0.034	0.036	0.038	0.032	0.046	0.033	0.037(0.005)	
	Trace R_p [μm]							
Convex	0.066	0.068	0.105	0.049	0.135	0.124	0.091(0.035)	<0.05
Concave	0.342	0.416	0.415	0.423	0.509	0.514	0.437(0.065)	
	Trace R_v [μm]							
Convex	0.171	0.255	0.195	0.269	0.313	0.377	0.263(0.076)	>0.05
Concave	0.217	0.218	0.238	0.194	0.256	0.219	0.224(0.021)	
	Trace R_{sk} [μm]							
Convex	-13.913	-7.467	-1.916	-8.049	-5.856	-2.877	-6.679(4.304)	<0.05
Concave	-0.379	3.889	3.136	0.657	4.359	3.239	2.483(1.898)	

*comparison between concave and convex components

4.4.2.2.3 Surface damage

Following 71,000 cycles of the ISO-18192-1:2011 testing protocol, all three, silicon nitride-coated CTDRs sustained catastrophic coating damage and delamination. Light micrographs of the damage surfaces (Figure 4.31 and Figure 4.32) showed multidirectional scratches on the surfaces and delamination of the coating (substrate material showing through). No further wear testing of the silicon nitride-coated CTDRs was conducted.

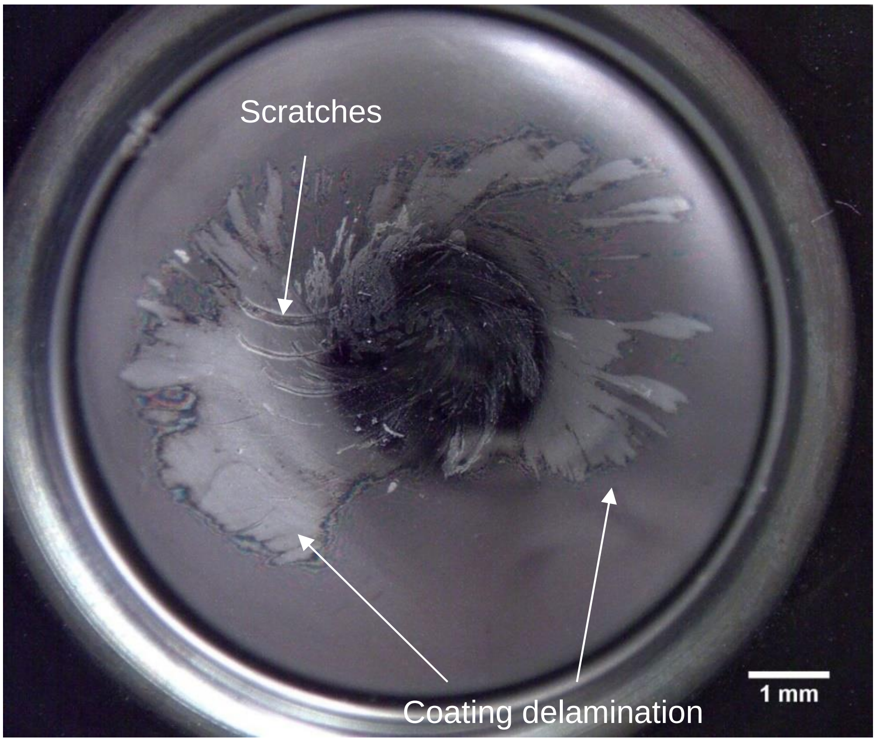

Figure 4.31: Silicon nitride-coated concave component showing catastrophic damage and delamination of the coating following 71,000 cycles under the standard ISO-18192-1:2011 protocol. Substrate material showing through(indicated by the arrows) and multidirectional scratches were discovered on the surface.

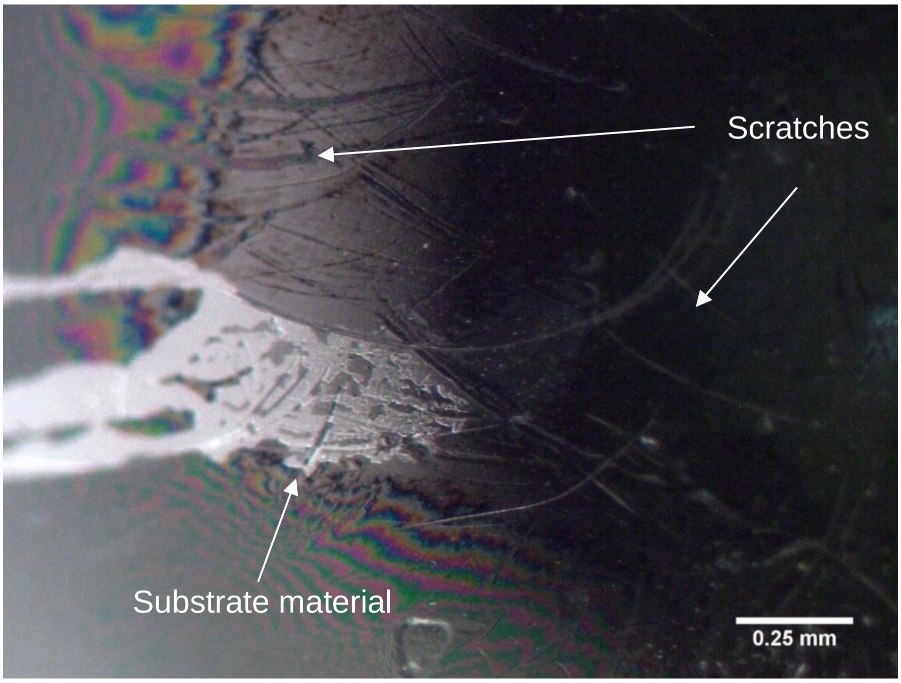
Scratches
Substrate material
0.25 mm

Figure 4.32: Higher magnification image of a convex component, showing damage of the silicon nitride coating sustained following 71,000 cycles of the standard ISO-18192-1:2011 testing protocol. Multidirectional scratches and substrate material (coating delamination) were observed on the surface.

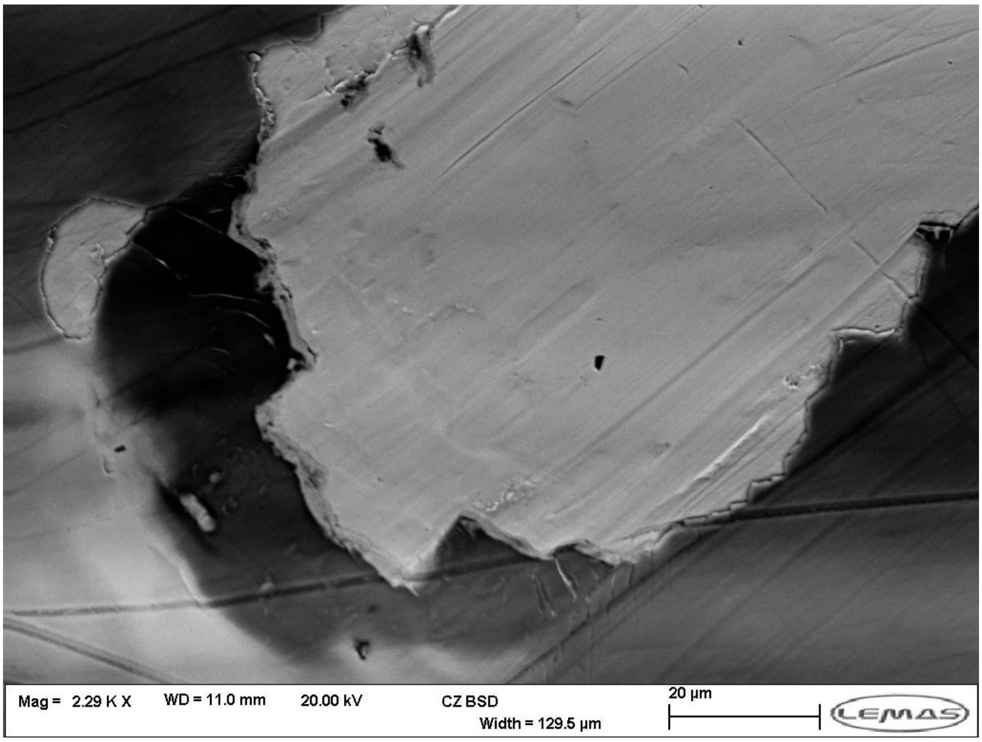
Mag = 2.29 K X
WD = 11.0 mm
20.00 kV
CZ BSD
Width = 129.5 µm
20 µm
LEMAS

Figure 4.33: High magnification, high resolution SEM image of the silicon nitride coating delamination damage.

High resolution, high magnification images of the silicon nitride-coated CTDRs, taken using the cold field emission SEM, showed similar findings to the light micrographs. Catastrophic damage of the silicon nitride coating was observed, as shown in Figure 4.33. Through-wear (delamination of the coating) was confirmed by EDX spectra (Figure 4.34), the area of coating delamination showed strong peaks of cobalt (Co), chromium (Cr) and molybdenum (Mo).

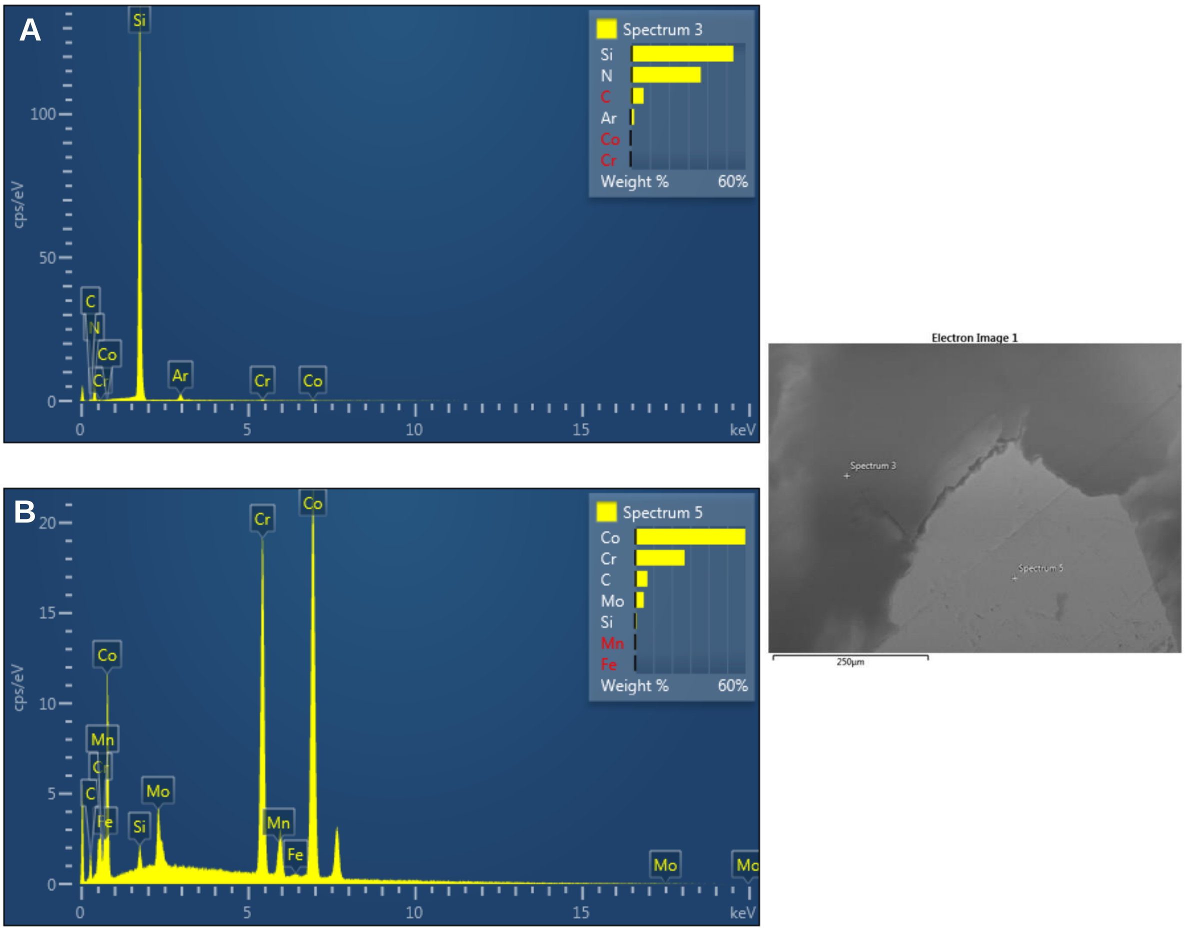

Figure 4.34: EDX of the area of suspected silicon nitride coating delamination, confirming the catastrophic damage of the coating. Spectrum 3 (A), taken from the area where the coating remained intact confirmed the chemical composition of the coating (strong silicon and nitride peaks). Spectrum 5 (B), taken from the area where the coating appeared delaminated, confirmed the chemical composition of the substrate material, showing strong peaks of cobalt (Co), chromium (Cr) and molybdenum (Mo).

The chromium nitride-coated CTDRs did not sustain significant coating damage following 71,000 cycles and were thus tested for a total of 2MC, under the standard ISO-18192-1:2011 testing protocol. Light micrographs of the surfaces were completed following each 10^6 cycles, to inspect the changes of the surfaces and in an attempt to identify wear modes, mechanisms, types of damage and any surface features.

The pole areas of the bearing surfaces of the components appeared more polished than the outside areas of the bearing surfaces, as shown in Figure 4.35 and Figure 4.36. It is most likely that those polished areas represented the main contact area and the wear area of the devices. Some dark deposits on the border between the worn and un-worn areas were noted. The surfaces of the un-worn areas appeared rough, were not reflecting light well, and some micro-pitting was apparent. These micropits were most likely coating defects introduced during the coating deposition process. Unlike the CoCr CTDRs, no apparent circular wear tracks were observed on the bearing surfaces.

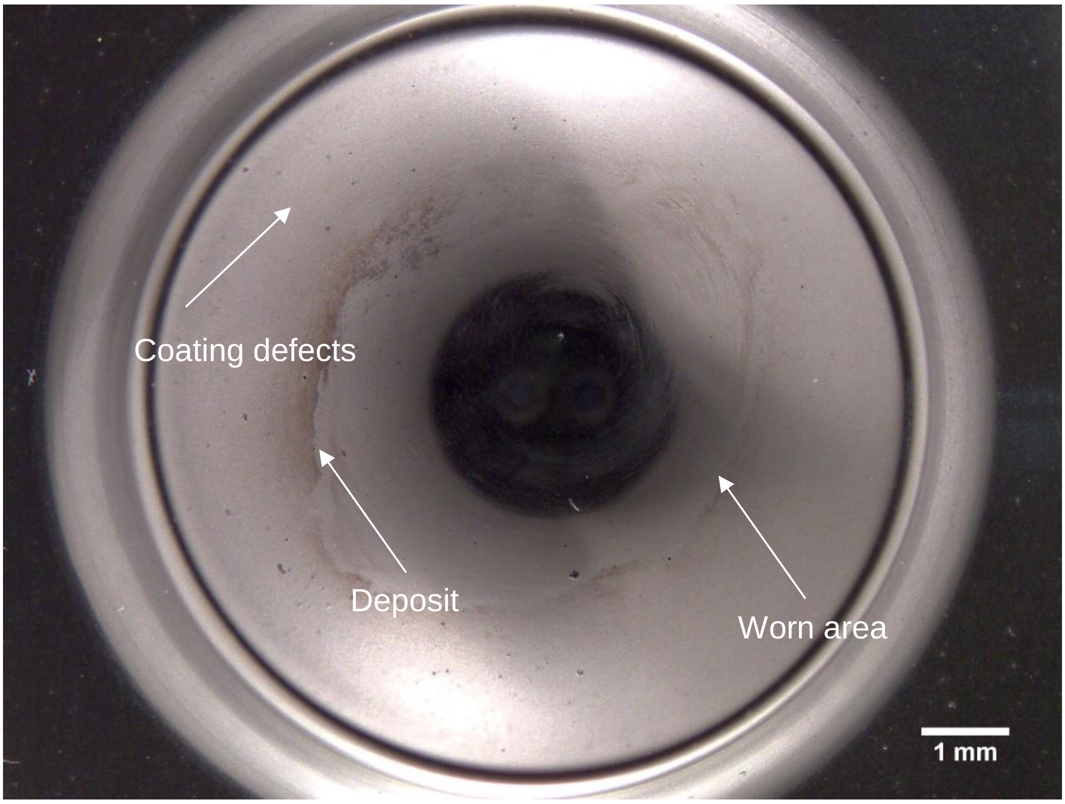

Figure 4.35: Light micrograph showing a CrN-coated concave component following 2MC of standard ISO-18192-1:2011 testing protocol. Polished area at the pole of the component was observed, with a dark deposit collected at the edge of this area. The un-worn area appeared rougher with some micropitting present.

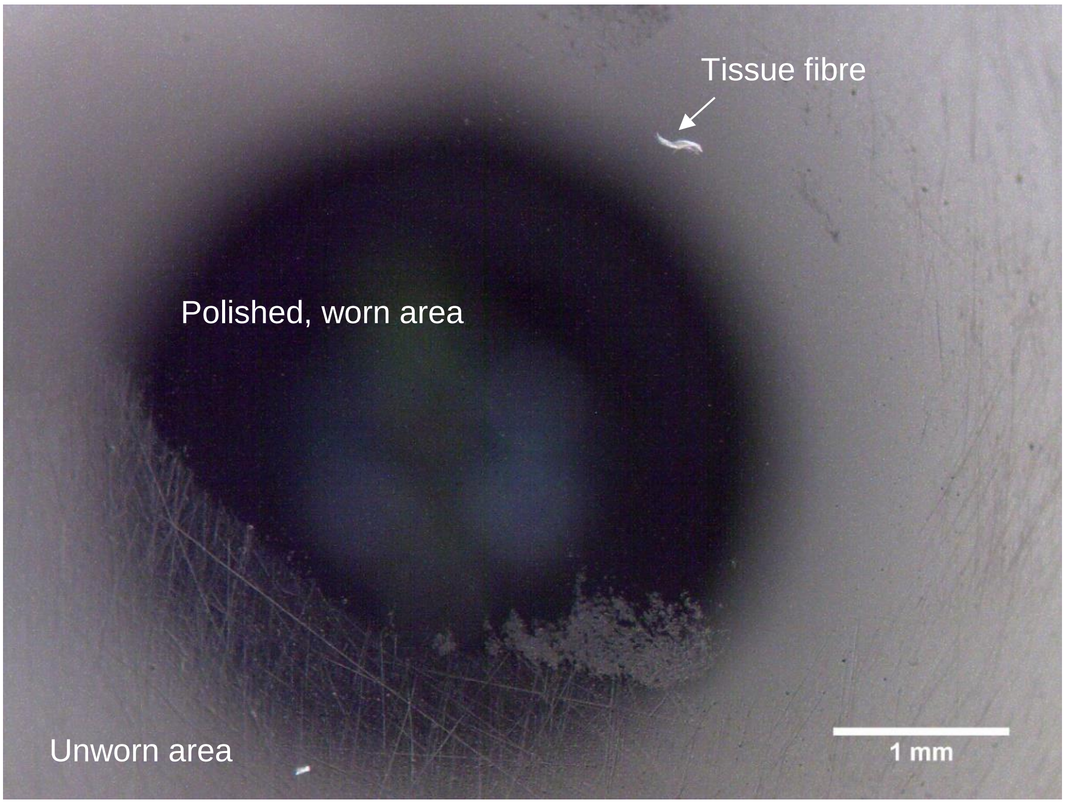

Figure 4.36: Higher magnification light micrograph of the bearing surface of a CrN-coated convex component tested for 2MC under the standard ISO-18192-1:2011 protocol. Highly polished, wear area at the pole of the component was observed. Unworn area appeared rougher and polishing marks were observed.

The high magnification, high resolution images, captured using cold field emission SEM, taken in the areas which appeared unworn and rough in the light micrographs showed numerous micropits and defects protruding out of the coating surface, as shown in Figure 4.37. On the other hand, as shown in Figure 4.38, SEM images taken in the areas which, under the light microscope, appeared polished and worn, showed much smoother surfaces than that shown in Figure 4.37. Moreover, it appeared that the micropits were larger in the worn area, suggesting that some of the defects protruding from the bearing surface were removed during the wear test. Some post-testing images of the chromium nitride-coated components (Figure 4.39) showed relatively large portions of the coating missing from the surface, which may indicate cohesive defects of the coating. No through-wear or coating, however, was observed.

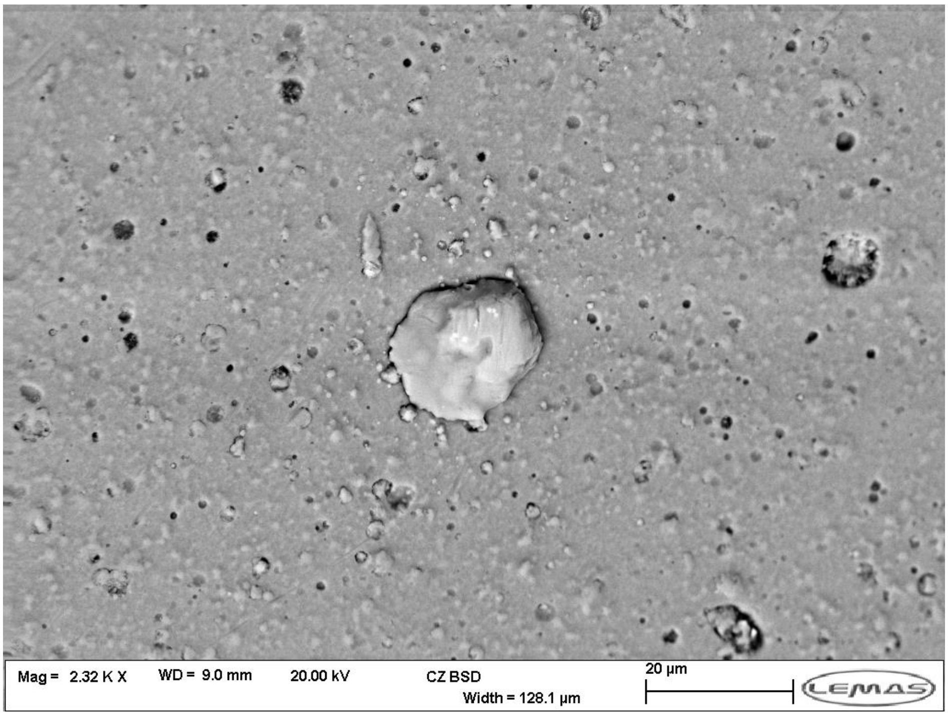
Mag = 2.32 K X
WD = 9.0 mm
20.00 kV
CZ BSD
Width = 128.1 µm
20 µm
LEMAS

Figure 4.37: SEM image of the un-worn area of the chromium-nitride coated CTDR component following 2MC of standard ISO-18192-1:2011 protocol testing. Numerous coating defects (micropits and protrusions) and rough appearance of the coating were observed.

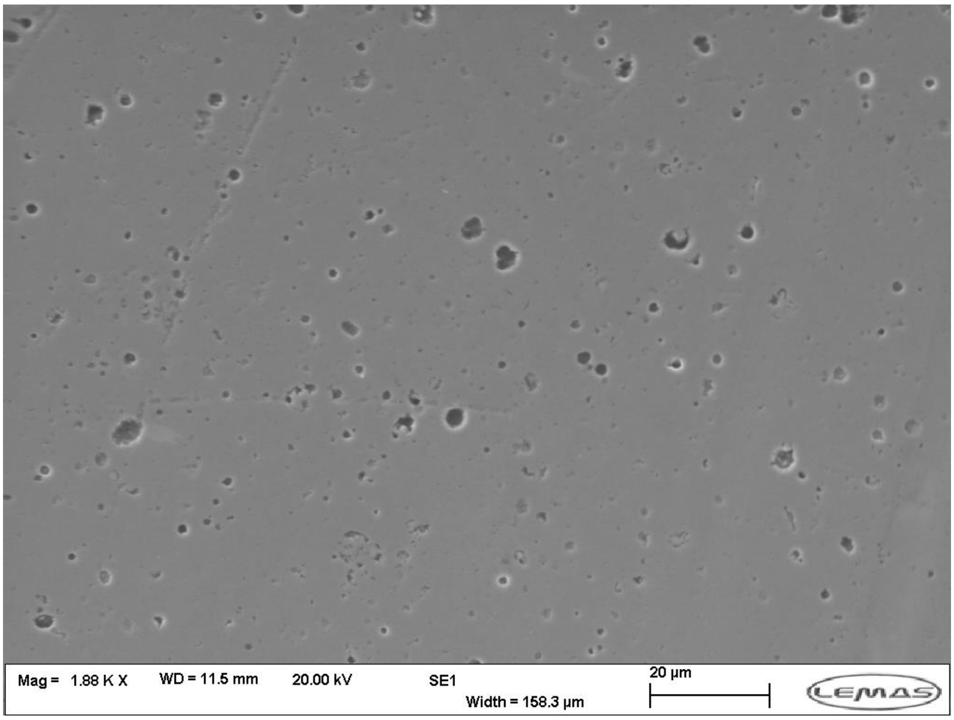
Mag = 1.88 K X
WD = 11.5 mm
20.00 kV
SE1
Width = 158.3 µm
20 µm
LEMAS

Figure 4.38: SEM image of the worn area of the chromium-nitride coated CTDR component following 2MC of standard ISO-18192-1:2011 protocol testing. Smoother appearance, larger micropits and lack of protrusions were observed.

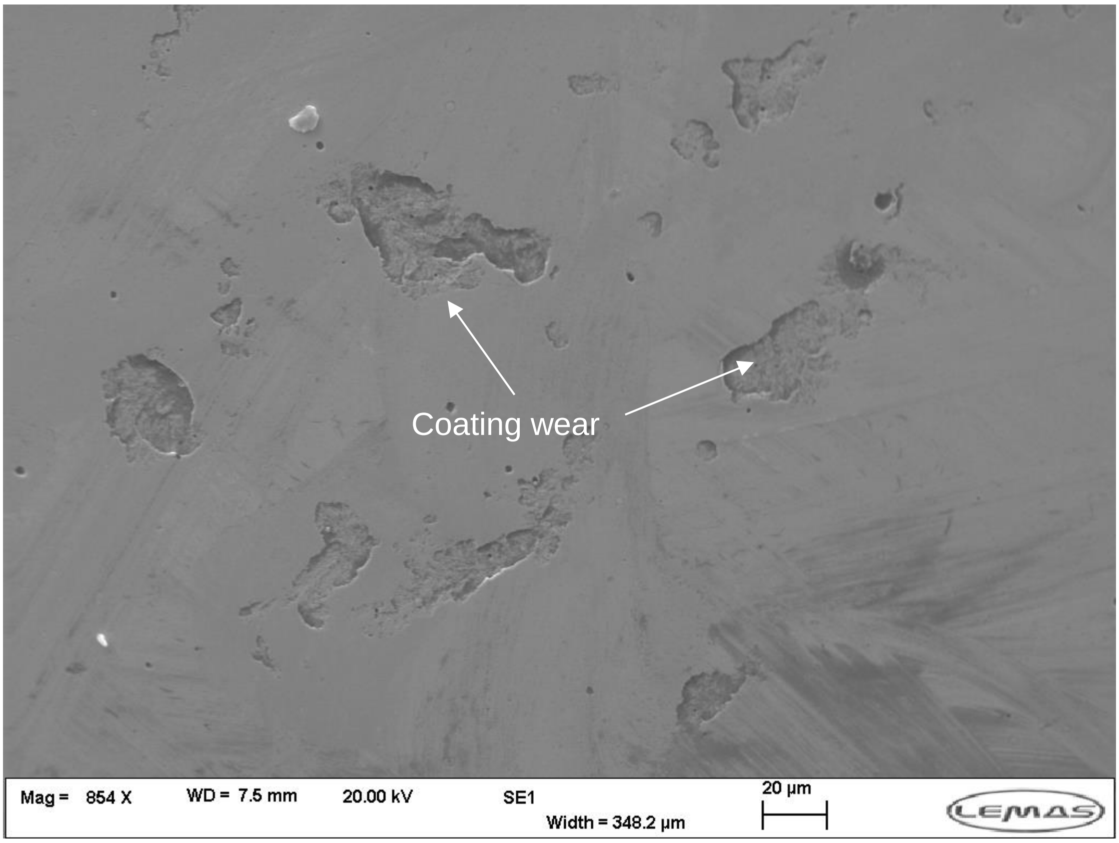

Figure 4.39: SEM image of the bearing surface of a chromium nitride-coated CTDR component following 2MC of standard ISO-18192-1:2011 testing protocol. Relatively large portions of the coating appeared to have worn out/flaked off from the surface, however, no coating delamination was observed. Some micropitting on the surface was noted.

Due to extensive damage sustained by the silicon nitride-coated devices and substantially low wear rates generated by the chromium nitride-coated CTDRs during the 2MC of standard ISO-18192-1:2011 testing, it was decided not to conduct any further testing of the coated CTDR devices under the standard ISO-18192-1:2011 testing protocol (section 4.3.3) or the modified ISO testing protocol (section 4.3.2). It was determined that silicon nitride coating sustained adhesive failure and thus, at the time of writing, the coating was deemed unsuitable for use in MoM CoCr CTDR devices.

The aim of altering the ISO-18192-1:2011 protocol, by reducing applied ROMs, was to study the effects of the testing method on wear rates of the MoM CTDRs (section 0) and to investigate potential higher clinical relevance of sucha protocol, when compared to the ISO predicate, as previously discussed in section 4.3.2. The wear rates generated by CoCr CTDRs tested under the altered protocol were reduced by three-fold, when compared to those generated under the standard ISO-18192-1:2011. It was thus hypothesised that the chromium nitride-coated CTDRs will follow the same pattern and the wear rates generated under the altered ISO protocol will be reduced in comparison to those generated under the standard ISO-18192-1:2011 protocol. However, under the standard ISO protocol, chromium nitride-coated CTDRs generated wear rates reduced by six-fold to those of CoCr devices tested under the same conditions. With the possibility of further reduction of wear rates generated by chromium nitride-coated devices, it was decided not to carry out further *in vitro* wear testing of these devices under the altered ISO-18192-1:2011 protocol due to the limitation of the measuring capacity of the microbalance used in the gravimetric analysis.

4.5 Discussion

Cervical total disc replacement is becoming an increasingly popular alternative treatment to anterior cervical discectomy and fusion - the current gold standard procedure used in late stages of degenerative disc disease requiring surgical intervention. To date, a limited number of *in vitro* wear studies on CTDRs have been conducted and the published literature predominantly concerns designs utilising metal-on-polymer bearings. At the time of writing, limited number of studies on the wear performance and wear rates of metal-on-metal CTDRs have been published. Concerns remain regarding long-term wear and potential effects of wear products generated by CTDRs, particularly in light of the evidence of devastating effects of excessive wear and wear products released from MoM THR, such as pseudotumour formation, hypersensitivity or metalosis and tissue necrosis [241,287,288]. A number of studies of surface engineered total joint replacement devices showed promising results and potential improvement of wear performance and biocompatibility of coated MoM TJR, when compared to un-coated devices [200,289,290]. The present study investigated the wear of pristine MoM and coated (silicon nitride and chromium nitride) CTDRs, in order, to establish short-to-mid-term wear performance of such devices. Furthermore, changes to surface topography were studied.

Moreover, the effect of different testing protocols on wear performance of MoM CTDRs has been investigated.

Employment of *in vitro* wear simulation has been well established in THRs and TKRs, as a valid method of generating clinically relevant wear rates [291,292] and particles [145,293,294]. As the CTDR technology is relatively novel, in comparison to THR and TKR, so is the application of *in vitro* wear simulation of such devices. Thus, there is a sparse number of published studies reporting on *in vitro* wear rates generated by CTDR devices. Most the published wear data reports wear performance of metal-on-polyethylene bearing cervical devices.

4.5.1 Wear assessment

The current study, which tested MoM bearings, showed a linear wear rate (no bedding-in period was observed) of 0.24±0.03mm^3/MC for CoCr-CoCr CTDR devices tested under the standard ISO-18192-1:2011 testing protocol. The current study applied one deviation from the standard, whereby the protein content of the lubricant was lower than that prescribed by ISO. Whilst the protein content specified by ISO 18192-1:2011 (20g/L) is higher than the one used here in the tests described in this thesis, the 15g/L protein content was within the range of concentrations used in studies showing clinically relevant wear data in total hip replacement [295]. The choice of lubricant protein concentration followed the Standard Operating Procedures used for Spine Wear Simulator Studies, which allowed direct comparison of results from previous total disc replacement studies conducted at University of Leeds. Whilst reduction of the protein content was shown to affect the viscosity of the lubricant [296–298] and thus results in harsher wear environment, this in turn provided more stringent testing conditions and it can be argued that the nature and composition of interstitial fluid, providing lubrication *in vivo* [299] is different to the natural lubricant (synovial fluid) found in articulating joints such as hip or knee [299].

To date, only one group of authors have investigated *in vitro* wear performance of a MoM CTDR – the PrestigeST, which is made from stainless steel. Kurtz *et al.* [138] tested the device under varying testing conditions, whereby the first phase of testing included lateral bending (±4.7°) and axial rotation (±3.8°) motions coupled with a static load of 49N for 5MC and this was followed by

10MC of flexion-extension motion (±9.7°), axially loaded at 148N. The first phase of testing generated a wear rate of 0.74±0.3mm^3/MC, whilst the second phase of testing a wear rate of 0.03±0.03mm^3/MC. Whilst the approach of testing applied by Kurtz *et al.*, i.e. separating motions, may be crucial in identifying of the motions which contribute to the wear performance the most, it may not fully represent *in vivo* conditions, as most of the clinical MoM retrievals (both cervical and lumbar) showed multidirectional abrasive wear, strongly suggesting that simultaneous motions and loading take place *in vivo*. Furthermore, one study, which tested a generic MoM lumbar TDR device (CoCr-CoCr) under the standard ISO-18192-1:2011 testing protocol (for lumbar devices), reported a wear rate of 0.76±0.02mm^3/MC [300]. Predictably, this wear rate was higher than the one reported in the current study, as the devices were tested under different loading and motion conditions. Whilst the ISO-18192-1:2011 testing protocol suggests axial loading range of 50-150N, the standard for lumbar devices prescribes loads of 600-2000N. Similarly, the ROMs in the protocol for the cervical devices are much smaller when compared to the lumbar protocol [135].

Wear rates generated by MoP CTDRs reported in the literature varied slightly depending on the testing protocol and device design used in the investigations. Devices with MoP bearings made from UHMWPE, tested under the standard ISO-18192-1:2011 testing protocol, were reported to generate wear rates of 1.07±0.01mm^3/MC, 2.53±0.7mm^3/MC, 2.13±0.16mm^3/MC, 1.95±0.18mm^3/MC and 2.1±0.2mm^3/MC [142,143,301,302]. Even higher mean volumetric wear rates of UHMWPE-on-metal bearings were reported by authors conducting wear tests of lumbar TDRs tested under the ISO-18192-1:2011 conditions. The Charité LTDR generated mean volumetric wear rates of 13.1±1.1mm^3/MC, 12.8±1.2mm^3/MC and 12.9±2.5mm^3/MC, as reported by Vicars *et al.* [303], Mohgadas *et al*. [304] and Prokopovich *et al*. [305], respectively. A different LTDR device (ProDisc-L), with a semi-constrained, UHMWPE-on-metal bearing design, was reported to generate a mean volumetric wear rate of 17.2±1.5mm^3/MC, when tested under the standard ISO-18192-1:2011 lumbar protocol. Both cervical and lumbar TDR devices with MoP bearing design produce significantly higher wear rates than those reported in the current study, as well as those of other MoM CTDR [138] and LTDR [300] reported in the literature. Similar findings were reported in THR, whereby the MoM bearings produce significantly lower volumetric wear rates (0.1-0.5mm^3/MC) than those of MoP designs (36-180mm^3/MC) [293,306–308].

The comparison of *in vitro* and *in vivo* wear measurements should be performed with caution. Firstly, the *in vitro* reports, such as the current study, use gravimetric wear analysis as a method of estimating wear rates generated by CTDRs, while the retrieval studies lack the *zero-reference* point, which makes accurate wear rate assessment impossible. Moreover, the *in vitro* studies apply testing methods that utilise pre-set, repetitive motions of the same magnitude. As such, the clinical relevance of these testing methods may be questioned, due to more varied sets of motions and combination of motions executed by individuals during day-to-day activities [49,121,138,139,309]. Indeed, it has been reported that the surface damage (i.e. surface roughness, wear area and depth of scratches) sustained by retrieved CTDRs were less severe (approximately 5-10 fold), when compared to devices tested in spine simulators [119,121,138]. Additionally, it has been reported that components tested for only 0.3 million cycles produced much higher wear than in device explanted from a patient after 39 months *in vivo* i.e. an equivalent of 3.25 million cycles of simulator tests [121]. Another study suggested that the current testing protocol prescribed by ISO-18192-1:2011 may only be relevant for predicting short-term wear performance (up to 1MC) [140]. Siskey *et al.* [140] found that implants explanted shortly after the surgery (approximately 12 months post-op) carried similar signs of wear and tear to those tested for 1MC. At the same time devices which were explanted following a longer period of time *in situ* showed less severe surface damage than the devices tested *in vitro* for an equivalent period of time. Based on these findings and hypotheses reported in the literature, the current study investigated the role of reduced ROMs applied in *in vitro* simulation and the potentially higher clinical relevance of the wear rates generated by MoM devices tested under such a regime. The mean volumetric wear rate produced by the CTDRs tested under the altered ISO-18192-1:2011 conditions was significantly lower than that produced by the same devices tested under the standard ISO conditions ($p<0.05$, CI 95%). A three-fold reduction of the mean volumetric wear rate ($0.08\pm0.06mm^3$/MC) was in line with the predictions published by other authors [121]. It is possible, that the current ISO protocol for CTDR wear testing (ISO-18192-1:2011) may require further development to include a wider range of more clinically relevant physiological conditions and motions, in order to achieve longer lasting implants that meet the demands of patients. The wear areas observed on the components tested in this study, which appeared as a dark/hazy discolouration of the bearing surface, were measured following each $1x10^6$ of *in vitro* testing, using ImageJ software. Wear scars observed on the concave components were significantly larger ($p<0.05$, CI 95%), and accounted for a larger proportion of the total bearing area, than those observed on the convex components. Similar progressive increases in the wear area, though measured over a shorter testing period (up to 1MC), were observed by Siskey *et al.* [140]. The progressive increase of the wear areas observed on the components of the CoCr-CoCr CTDRs can be correlated with the progressive material loss sustained by the CTDRs.

The types of surface damage following 4MC of standard ISO-18192-1:2011 testing and 2MC of the altered testing protocol of MoM CTDR observed in the current study, were similar to those previously reported in the literature. Damage found on the surfaces of the CTDR devices tested in the current study was consistent with characteristics of abrasive wear i.e. wear tracks and microabrasive scratches were noted. The curvilinear shape of the wear tracks as well as microabrasion of the bearing surfaces has previously been observed in explanted metal-on-metal CTDR [119,138,140] devices and *in vitro* tested metal-on-metal [138,140] and metal-on-polyethylene CTDRs [119,301]. Moreover, component discolouration and surface film formation reported in this study, has also been observed by other authors in both *in vitro* tested and explanted MoM CTDRs [119,138,140]. Similar material deposit formation has previously been observed in MoM hip replacement devices [120]. Micropitting damage observed in some of the CTDRs in the current study has previously been found in MoM THR devices [310,311]. Micropitting originates from the local contact of asperities and is produced by insufficient lubrication. Wang *et al.* [312] have also shown that the occurrence of micropitting in CoCr alloys used in THRs may be related the pre-existing carbides in the surfaces and sub-surfaces of the bearings. Moreover, as with to the current study, Wang *et al*. [312] observed the micropitting to be confined mainly to the apex of the implants, where the contact stress was the greatest. These authors also hypothesised that the generation of micropitting, more prominent in the later stages of their study (6MC) was a result of a fatigue mechanism, resulting from cyclic loading of the CoCr implants.

4.5.2 Surface topography

The surface roughness of the CoCr devices changed significantly following the initial 4MC of testing under the standard ISO-18192-1:2011 protocol. The mean R_a parameter of the devices decreased significantly from 0.019±0.007μm to 0.012±0.002μm following the testing ($p<0.05$, CI 95%) indicating smoothing of the surface in the worn areas. Moreover, the average skewness of the surface profiles decreased significantly from -1.49±0.43 to -2.88±0.99 ($p<0.05$, CI 95%), indicating more pronounced domination of *valleys* over *peaks* in the surface structure. It is thought that the change of surface skewness may play a role in the reduction of wear and a level of improvement of lubrication regime in the steady-state wear. The change of those two parameters strongly suggests that the surfaces of the MoM CTDRs have undergone a ‘self-polishing’ phenomenon, which has previously been observed in MoM THRSs and reported by numerous authors [236,307,313–315]. The self-polishing has been attributed with the running-in period observed in MoM THRs, whereby during the initial million cycles of *in vitro* testing (and years *in vivo*), asperities are worn and removed, resulting in smoother and more conforming surfaces [316]. The self-polishing of MoM bearings has also been hypothesised to be a result of nanoscale particles generated during motions acting as a polishing or solid phase self-lubricating mechanism [317]. As observed in the current study, the clearance of CTDRs indeed decreased following the *in vitro* testing, resulting in more conforming bearings. Whilst an obvious running-in period was not observed in the current study, it may be possible that due to overall low volumetric wear rates and small wear areas, the running-in period took place in the first million of cycles, when the gravimetric analysis was not conducted. Furthermore, the light micrographs and SEM images of the CoCr bearing surfaces showed a distinguishable difference between the worn and un-worn areas; particularly the SEM images revealed a difference in surface appearance between the two areas – the un-worn parts were still carrying polishing marks, whilst the worn parts appeared smooth.

4.5.3 Ceramic coatings in CTDR applications

Application of surface engineering solutions, such as ceramic coatings, has been proposed by numerous authors as a method of improving wear performance and biocompatibility of TJR devices. The current study investigated two ceramic coatings, developed and deposited by IonBond Ltd. (Olten, Switzerland). The CrN coatings were deposited using a PVD method, whilst the Si_3N_4 coatings were deposited utilising the HiPIMS method. Both types of coatings were deposited on CoCr CTDR substrates, which subsequently were tested in the six-station spine simulator, under the standard ISO-18192-1:2011 testing regime. Following the initial 71,000 cycles of the testing, the silicon nitride coating sustained a catastrophic damage and delamination of portions of the coating was observed on all three silicon nitride-coated devices tested. Complete delamination of coating, where the coating separated from the substrate material, was indicative of adhesive failure of the coating. A total volume of 0.207±0.06mm^3 of material was lost from the surface of the silicon nitride-coated devices. It was assumed that 100% of the mass loss which occurred at 71,000 cycles constituted of the silicon nitride coating, however this could not be confirmed. By linearly extrapolating the wear data obtained at 71,000 cycles, it was estimated that a mean volumetric wear rate for the silicon nitride-coated components was 2.922±0.884mm^3/MC. The theoretical mean volumetric wear rate of silicon nitride-coated CTRDs was significantly lower than the CoCr-CoCr CTDRs, however, functionally the silicon nitride coating failed in this application. At the time of writing, no direct comparisons for Si_3N_4-coated, or CTDRs and LTDRs coated by a ceramic coating were available in the literature.

Two other investigational assessments of tribological properties of silicon nitride coatings reported in the literature, resulted in coefficients of friction similar to those of bulk Si_3N_4. Ball on disc testing of different silicon nitride coatings, as per ASTM-F732-00:2006, resulted in a coefficient of friction ranging between 0.12 and 0.22, as reported by Olofsson *et al.*, [245] and 0.1 and 0.3, as reported by Pettersson *et al.* [190]. One of the coatings tested by Olofsson *et al.* demonstrated a coefficient of friction of 0.45; however, the sample had high surface roughness, which, most likely, was a result of high target power used in the deposition process of this sample. Olofsson *et al.* [245] also assessed the coating adhesion properties, utilising scratch testing. The results showed poor coating adhesion, with all, but one of the samples failing upon the tip engagement, resulting from coating adhesion of 0N. Similar results were found by Pettersson *et al.* [190], where all the coating samples delaminated during friction testing. Both studies highlighted low coefficients of friction exhibited by silicon nitride coating, however silicon nitride coating adhesion required further development, which was in line with the results obtained from the current study. Whilst the scratch testing of the silicon nitride coatings investigated in this work showed superior adhesion to the CoCr substrate, in comparison to the published reports, the functional testing i.e. spine wear simulator testing, revealed adhesive failure and coating delamination.

Several publications investigated the wear properties of bulk Si_3N_4 and reported low coefficients of friction and extremely low wear rates. However, none of the publications investigated CTDR applications. Mazzocchi *et al,* [186,187] investigated the friction of bulk silicon nitride, using a ball-on-disc tribometer. Very low and constant friction coefficients (~0.1) were found. Other authors reported friction coefficient of bulk Si_3N_4 articulating against itself to be 0.002 [318], 0.005 [319], 0.6 [320] and 0.8 [321]. Olofsson *et al.* [245] investigated the coefficient of friction of Si_3N_4- Si_3N_4 in both PBS and serum, obtaining results of 0.01 and 0.2, respectively. Such wide ranges of coefficient of friction results can be related to different specimen preparation and testing protocols used in studies. Bal *et al.* [208, 218] investigated the tribological behaviour of 28mm Si_3N_4 femoral heads articulating against Si_3N_4 and CoCr cups. The components were tested in a hip simulator for duration of 1 million cycles, under standard gait cycle conditions (ISO-14242-1). The Si_3N_4-Si_3N_4 and Si_3N_4-CoCr couples produced wear volumes of 0.2 mm^3 and 0.18 mm^3, respectively. The results were then extrapolated to 10 million cycles, on the assumption that hard-on-hard bearings follow a biphasic pattern with high wear in the early run-in period (to approximately 0.5 million cycles), followed by a lower, linear wear pattern [322–324]. This extrapolation resulted in wear rates approximation of 0.47 mm^3 and 0.65 mm^3 for the Si_3N_4-Si_3N_4 and Si_3N_4-CoCr bearings, respectively. In comparison to results obtained for Al_2O_3-Al_2O_3 (0.35-0.6 mm^3) and CoCr-CoCr bearings (6.5 mm^3) [323], silicon nitride bearings demonstrated significantly lower wear rates. Moreover, McEntire *et al.* [325] tested 28mm Si_3N_4 and CoCr femoral heads under the standard gait cycle (ISO-14242-1, 5MC), articulating against UHMWPE liners. Further, self-mated Si_3N_4 and Al_2O_3 bearings were tested under the standard gait cycle (ISO-14242-3, 3MC) followed by *stop-dwell-start* protocol (2MC). The authors found that self-mated bulk silicon nitride hip replacement generated ultra-low, near zero wear rates under the standard walking cycle testing protocol; these wear rates and were comparable to those of alumina bearings tested under the same conditions (ISO-14242-3). Introduction of the *stop-dwell-start* protocol resulted in wear rates of 7.99mm^3/MC generated by the Si_3N_4 bearings, whilst the wear rates of the alumina remained near-zero [325].

There is a general consensus, that Si_3N_4 demonstrates friction properties required for self-articulation, even when water is the only lubricant [186,325,326]. This has been related to the presence of two wear modes Si_3N_4 can undergo: mechanical and tribochemical. Mechanical wear is exhibited under high loads, low speeds and stop-start conditions, while tribochemical wear occurs through the dissolution of the Si_3N_4, and is operative at lower loads, higher speeds and continuous motion [321,325]. Silicon nitride can react with water, resulting in the creation of a silicon oxide lubricated film between the articulating surfaces. The predominance of the tribochemical wear mode may be the main reason for the extremely low wear volumes and coefficient of friction obtained in in vitro tests of Si_3N_4, tested both as a bulk and coating material [186,187,196,325,326]. The interruption of the high-speed/low-load continuous motion pattern can result in higher wear rates exhibited by Si_3N_4-Si_3N_4 bearings, as reported by McEntire *et al.,* [325]. In their hip simulator studies, the silicon nitride bearings tested under standard ISO-14242-3 gait cycle testing protocol showed extremely low wear rates, and were found to be comparable to those generated by alumina ceramics. However, introduction of a *stop-dwell-start* protocol, which caused disruption of the gelatinous silicic acid tribochemical film, resulted in wear rate increases.

At 71,000 and further timepoints no adhesive failure of the CrN coating was observed, thus 2×10^6 cycles, under the standard ISO-18192-1:2011 protocol, were completed for the CrN-coated devices. Following 2MC of wear testing, the CrN-coated CTDRs generated a mean volumetric wear rate of $0.03\pm0.01mm^3$/MC, which was significantly lower than the wear rate of CoCr-CoCr CTDR bearing combination tested under the same test conditions. The superior (to MoM) wear performance of CrN CTDR bearings was most likely an effect of increased H/E ratio, mainly a result of increased hardness (23GPa compared to 2.1GPa of CoCr), which in turn increased resistance to abrasive wear. In agreement with the CoCr CTDR devices, signs of abrasive wear were observed on the surfaces of the CrN-coated devices, however, they were not as severe. Surface roughness (R_a) of the CrN-CrN CTDRs reduced significantly from 0.076µm to 0.045µm ($p<0.05$, CI 95%) following the 2MC of altered ISO testing protocol, showing a degree of self-polishing exhibited by the coated devices.

The *in vitro* testing of the CrN-coated CTDRs employed in the current study could be considered as short-term (2MC). It has been shown by another author [184] that bedding-in period of CrN coatings may be as long as 3MC. It was suggested that due to low bedding-in wear rates, longer periods of time may be required to achieve component conformity required to reduce the contact pressure and allow improved lubrication [327]. No literature on the wear of CrN coated CTDR devices was available at the time of writing. Whilst no direct comparison could be made, several authors have reported significantly lower wear rates of *in vitro* tested CrN-coated hip replacement devices, in comparison to their CoCr-CoCr equivalents [179,180,184]. Tested under the standard walking cycle protocol (ISO-14242-1), mean volumetric wear rates of CrN-CrN hips were reported to be $0.02mm^3$/MC for 28mm bearings (compared to $0.05mm^3$/MC generated by CoCr-CoCr bearings) [179,180], $0.09mm^3$/MC and

0.12mm^3/MC for 39mm and 55mm bearings, respectively (in comparison to 5.2mm^3/MC and 2.8mm^3/MC, respectively) [184]

The application of surface coatings in total joint replacement has been a research subject for several years. A number of studies have shown different levels of success of *in vitro* performance of titanium nitride [174,179], titanium niobium nitride [269], DLC [164] and chromium nitride [179,180,185,289,328,329] ceramic coatings deposited on total hip devices. However, limited number of coated devices have been used in patients. Whilst insightful, reports of explant analyses of such devices are sparse and limited to failed devices [175,279,330–333]. The majority of the studies, *in vitro* or *in vivo*, investigated metal-coated on polyethylene bearings, in which the polyethylene surface was expected to be the main source of wear. The chief problem associated with unsuccessful application of ceramic coatings in TJR was through wear and adhesive failure of the coatings. Coating impurities and defects, such as those observed in the SEM images taken prior to *in vitro* testing, were often associated with poor coating adhesion. Moreover, is has been suggested that better adhesion can be achieved by coatings deposited on rougher substrates [334–336], as well as on those of similar H/E ratios [277] as the coating.

4.6 Conclusion

Standard protocol (ISO-18192-1:2011) of *in vitro* wear testing was used in the wear assessment of MoM CTDR devices and showed low volumetric wear rate of 0.24±0.03mm^3/MC following 4MC of testing. This wear rate was lower than previously reported wear rates of MoP CTDRs and LTDRs tested under the same ISO conditions. Self-polishing of the metal components and predominance of abrasive wear were observed. Alteration of the ISO-18192-1:2011 testing protocol, by reducing the ROMs applied during testing, showed significant, 3-fold reduction of volumetric wear generated by MoM CTDRs (0.08±0.06mm^3/MC), which supported the hypothesis that the testing parameters currently prescribed by the ISO protocol, may be exaggerated. Application of chromium nitride coatings on CoCr CTDRs showed significant reduction of volumetric wear rate. When tested under the standard testing protocol (ISO-18192-1:2011), the wear rate generated by the coated devices was reduced 10-fold compared to MoM bearings. Further long-term testing of CrN-CrN CTDR bearings is required to fully assess wear performance and their potential use in CTDR applications.

Silicon nitride coating deposited on CTDRs and tested *in vitro* showed catastrophic delamination and failure at early stages of testing. At the current stage of development, the silicon nitride coating was not suitable for the CTDR application.

Long term clinical success of TJR is a synergy of several factors, and favourable wear performance of a device is only one of its aspects. Often devices which performed well in *in vitro* setting, failed clinically due to local and systemic responses to wear and wear products. Therefore, characterisation of wear particles generated by MoM and coated CTDRs, as well as potential biological responses elicited by those wear particles require further investigation.

Chapter 5 : Biological effects of wear particles generated in wear simulation

5.1 Introduction

While most total joint replacements perform well, up to 10% of the devices require revision after 10 years *in vivo* [337]. In their most recently published yearly reports (2011-2016), the National Joint Registry (NJR) for England, Wales, Northern Ireland and the Isle of Man showed a consistent trend of aseptic loosening being the chief contributor to implant failure, followed by dislocation and infection. It has been shown that wear and biological responses to wear products can lead to osteolysis and aseptic loosening of total joint replacement., particularly in devises with MoP bearings [74,84,338,339]. Moreover, there is gross evidence suggesting that the volume of wear produced, as well as particle size and morphology (of both polyethylene and metal origin) can affect the inflammatory responses elicited [74,340–342]. It is generally accepted that the majority of UHMWPE particles generated in total joint replacements range between 0.1 and 10µm, whilst the particles between 0.1 and 1µm are considered the most biologically active [89,145]. These particles are phagocytosed by macrophages, which unable to digest the particles, release inflammatory cytokines and chemokines, including tumour necrosis factor alpha (TNF-α), interleukin-1beta (IL-1β), IL-6, and IL-8. In turn, these cytokines stimulate the release of other mediators, which lead to an inflammatory cascade and a periprosthetic granulomatous tissue reaction, resulting in bone resorption and implant loosening [343].

Metal wear particles generated in total joint replacements are reported to be in the size range of 10 – 400nm, with the majority of produced particles in the range of 15-25nm [236]. Although wear volumes produced by MoM implants are generally lower than MoP, it cannot be assumed that numbers of biologically active particles produced are low, due to the reactive size of the metal wear debris. The small size of metal wear debris sustains formation of particle agglomerates. Once released to the joint space, singular and accumulated metal wear particles attract macrophages to the site, which attempt to digest the wear debris and this can lead to a similar responses to these elicited by polyethylene particles, as well as aseptic lymphocyte-dominated vasculitis-associated lesions (ALVAL), hypersensitivity, genotoxicity or pseudotumour formation [74,241,287,344–347].

In this study, the *in vitro* wear results of CTDRs (Chapter 4) have shown MoM and ceramic-coated CTDRs to produce lower wear rates than MoP devices of similar design. However, it is important to establish and understand particle characteristics and to investigate potential biological consequences of wear particles produced by these devices. From clinical experience, large diameter MoM hips (36-54mm), despite their favourable tribological performance *in vitro*, were associated with severe patient complications, including pseudotumour formation, hypersensitivity reactions and metallosis [241,348]. In addition, aside a number of isolated incidences of ceramic wear-induced osteolysis reported, failure of such devices was mainl associated with severe implant malpositioning, leading to high wear [134,349].

Similarly to total hip and knee replacements, wear and wear debris are hypothesised to play the key role in successful long term outcomes of CTDRs. However, currently the number of long term outcome reports and studies documenting wear and wear debris produced by CTDRs *in vivo* are limited. There have, however, been a small number of studies reporting on wear induced osteolysis, pseudotumour formation and implant failure in patients implanted with a CTDR device [124,128,129,350]. Consequently, despite enhanced tribological *in vitro* performance of MoM and ceramic coated CTDRs over MoP designs, the potential biological responses of wear and wear debris must be studied.

The aim of this chapter was to investigate the biological effects of wear particles generated by metal-on-metal CTDRs, as well as wear particles generated by CTDRs coated with ceramic coatings – chromium nitride and silicon nitride. The studies presented here investigated metal (CoCr) wear particles generated in a six-station pin-on-plate wear rig, by evaluating biological responses of primary cells and cell lines elicited by the wear particles. The pin-on-plate method has previously been validated to produce clinically relevant wear particles [228,293,317,351], and thus was used as a baseline in this study. Further, particles (both of metal and ceramic origin) generated in a six-station spine simulator were investigated in the same manner, by evaluating potential cytotoxic effects of the wear particles on primary dural fibroblasts and L929 murine fibroblasts cell line. The L929 murine fibroblasts cell line has been suggested by ISO-10993-5:2009 *'Biological evaluation of medical devices -- Part 5: Tests for in vitro cytotoxicity'* for *in vitro* cytotoxicity testing [352]. Primary dural fibroblasts, isolated from meningeal membranes, were considered as clinically relevant in testing cytotoxic potential of CDTR-generated wear particles, due to the close vicinity of the meninges to the spinal discs, which may have undergone replacement. In the experiments, both sterile water and foetal bovine serum were used as lubricants; particles generated in foetal bovine serum were isolated from the lubricant using an adaptation of a novel particle isolation method [353]. The particle morphology and size distribution of metal and ceramic coating particles was determined. Investigations into the effects of these particles on cell viability of L929 murine fibroblasts and primary porcine dural fibroblasts were performed. The role of particle size, origin and dose, generation method, as well as use of different lubricants in particle generation, on cell viability was determined.

5.2 Materials

5.2.1 Cobalt-chromium pins and plates

Six CoCr pins were machined in house from a low carbon <0.05% (w/w) CoCr alloy (ASTM F1537) [207] bar stock supplied by Peter Brehm GmbH (Weisendorf, Germany). The pins were polished in house by Mrs. Jane Cardie (Technician, School of Mechanical Engineering) to have a radius of 100° and were finished to a R_a of 0.02 – 0.04µm. Six smooth CoCr plates were also machined from the same bar stock supplied by Peter Brehm GmbH (Weisendorf, Germany), and polished to have R_a of <0.01µm. The dimensions and geometrical tolerances of the pins and plates are shown in Figure 5.1.

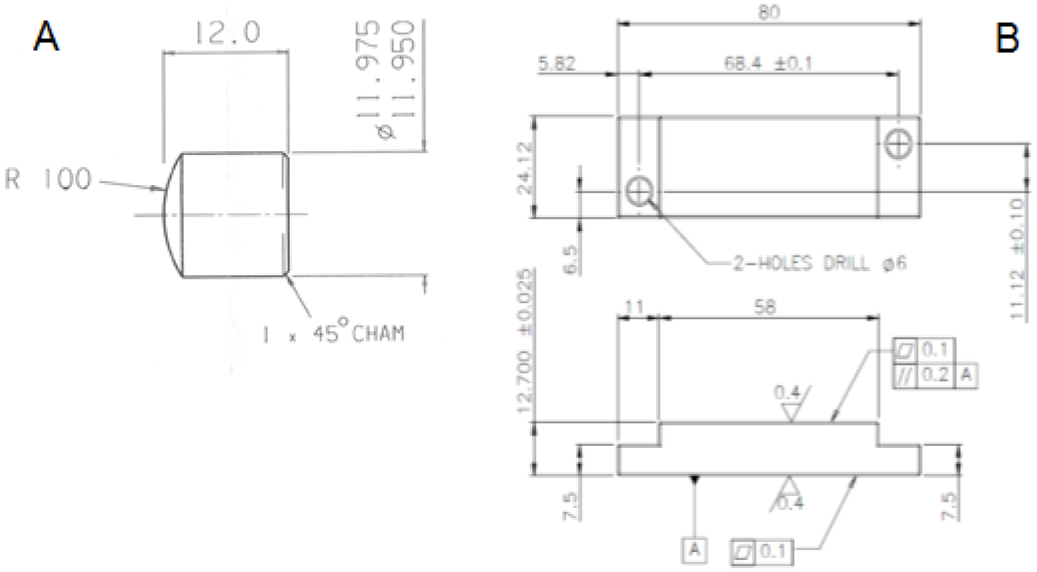

Figure 5.1 Schematic of a wear pin (A) and plate (B) used in the six-station pin-on-plate wear test.

5.2.2 Cobalt chromium CTDRs

Six CoCr CTDRs machined from low carbon <0.05% (w/w) CoCr alloy (ASTM F1537) [207] bar stock supplied by Peter Brehm GmbH (Weisendorf, Germany), were used in CoCr particle generation in the spine simulator. The CTDRs were polished in house by Mrs. Jane Cardie (Technician, School of Mechanical Engineering) to have an R_a of 0.02 – 0.04µm. Detailed design specifications for the CTDRs were included in Chapter 3.

5.2.3 Coated CTDRs

Six CoCr CTDRs machined from low carbon <0.05% (w/w) CoCr alloy (ASTM F1537) [207] bar stock supplied by Peter Brehm GmbH (Weisendorf, Germany), were used in CoCr particle generation in the spine simulator. The CTDRs were polished in house by Mrs. Jane Cardie (Technician, School of Mechanical Engineering) to have an R_a of 0.02 – 0.04µm. The CTDRs were then coated with ceramic coatings – chromium nitride (CrN) and silicon nitride (Si_3N_4) by IonBond (Olten, Switzerland), three devices of each coating. Detailed information on the composition of ceramic coatings is included in Chapter 2.

5.2.4 Model silicon nitride (Si_3N_4) particles

Submicron silicon nitride powder (<1µm) (33410-3) and nano-sized (<50nm) silicon nitride powder (636703), were supplied by Sigma-Aldrich (Irvine, UK).

5.2.5 Fibroblast cell line

The L929 murine fibroblast cell line (ECACC 85011425) was supplied by the European Collection of Animal Cell Culture, Porton Down (Salisbury, U.K).

5.2.6 Primary fibroblast cells

Primary porcine fibroblast cells were isolated from porcine dural membrane by explant culture by Dr Iraklis Papageorgiou [354].

5.2.7 Cell culture medium and supplements

Dulbecco’s modified Eagles medium (DMEM), without L-glutamine (D6546) was supplied by Sigma-Aldrich (Irvine, UK). The DMEM was stored at 4°C until required. Penicillin (5000 U) and streptomycin (5000 U) (DE17-603E) were supplied by Lonza Biologics (Cambridge, UK) and stored at -20°C until required. L-glutamine at a concentration of 200mM in 0.85% (w/v) of sodium chloride (NaCl) (25030-024) was purchased from Invitrogen Ltd. (Paisley, UK) and stored at -20°C. Foetal Calf Serum (FCS) (A101112-2177) was purchased from GE Healthcare (Buckinghamshire, UK) and stored at -20°C.

5.2.8 Carbon dioxide and liquid nitrogen

Carbon dioxide (CO_2) in air (5% v/v) and liquid nitrogen were supplied by the British Oxygen Company Ltd. (Manchester, UK).

5.2.9 ATP-Lite luminescence assay detection kit

Cell viability was measured using adenosine triphosphate (ATP) luminescence detection kit (ATP Lite) supplied by Perkin-Elmer (Cambridge, UK). The contents of the kit (mammalian cell lysis solution, buffer and lyophilised substrate) were stored at 4°C until required. The reconstituted lyophilised substrate was stored at -20°C.

5.2.10 Chemicals

Trypsin-ethylenediaminetetraacetic (EDTA) (T3924), Dulbecco's phosphate buffered saline (DPBS) without calcium chloride ($CaCl_2$) and magnesium chloride ($MgCl_2$) (D8537), Camptothecin powder and Trypan Blue solution (0.4%) (T8154) were supplied by Sigma-Aldrich (Irvine, UK). Sterile, distilled water (UKF7114) was purchased from Baxter (Newbury, UK). Ethanol, at a concentration of 96% (v/v) was supplied by Fisher Scientific (Loughborough, UK). Trigene disinfectant solution was supplied by Scientific Laboratory Supplies Ltd. (Nottingham, UK). Isopropanol, at a concentration of 99.8+% (v/v) (10090320) was supplied by Fisher Scientific UK (Leicestershire, UK). Surfasil™ siliconizing fluid was supplied by ThermoScientific (Loughborough, UK). Methanol was supplied by Atom Scientific LTD (Manchester, UK). Proteinase-K powder was supplied by Fisher Scientific (Loughborough, UK). HEPES (acid free), at a concentration of >99.5% was purchased from Melford Laboratories Ltd. (Ipswich, UK). Sodium dodecyl sulphate (SDS), sodium polytungstate solution (85% w/v), Lysozyme powder (from chicken egg white), Trizma® hydrochloride (Tris-HCl) and calcium chloride were supplied by Sigma-Aldrich (Irvine, UK). Sodium chloride-TRIS-EDTA-Triton (STET) buffer was purchased from Alfa Aesar (Heysham, UK). Fairy soap detergent was supplied by Proctor&Gamble (London, UK).

5.2.11 Laboratory consumables and glassware

Filter pipette tips were purchased from Starlab (Helsinki, Finland). Individually wrapped, sterile pipettes and cryovials were supplied by Sarstedt Ltd. (Leicester, UK). Disposable, plastic syringes were purchased from Terumo® (Leuven, Belgium). White 96-well Opti-Plates® and transparent seals were purchased from Perkin-Elmer (Cambridge, UK). Tissue culture flasks and 96-well plates plus lids (167008) were supplied by Fisher Scientific UK (Leicestershire, UK). Sterile universal containers and bijous were purchased from Bibby Sterilin (Staffordshire, UK). Millipore glass filtration unit with stainless steel support was supplied by Milipore (Consett, UK). Nucleopore polycarbonate filter membranes (0.015µm and 0.02µm pore size) were purchased from Whatman (Maidstone, UK). Polypropylene centrifuge tubes (14ml and 32ml) were supplied by Beckman Coulter Ltd. (High Wycombe, UK).

5.2.12 Equipment for particle characterisation

A microbalance (XP26) was purchased from Mettler Toledo (Leicester, UK). Polycarbonate filter membranes were coated with a High-Resolution Sputter coater with a carbon target, manufactured by Agar Scientific (Stansted, Essex, UK). Filtered particles were analysed using a Hitachi SU8230 cold field emission (CFE) scanning electron microscope (SEM) (Hitachi, Maidenhead, UK), fitted with an Oxford Instruments Aztec Energy EDX system (AZtecEnergy, Oxford, UK). SEM specimen stubs, carbon adhesive discs and conducting carbon cement (Leit-C) were purchased from Agar Scientific (Stanstead, UK)

5.2.13 Equipment for cell culture maintenance and cell viability assays

The light microscope in the Faculty of Biological Sciences (University of Leeds, UK) (CK40) was supplied by the Olympus Optical Company (London, UK). The plate shaker (Vari-Shaker®) was supplied by Dynatech Ltd. (Billinghurst, UK). The Chameleon™V luminescence plate reader was manufactured by Hidex (Turku, Finalnd). The Multiscan Spectrum plate reader used for the MTT assay was manufactured by Thermo Labsystems (Helsinki, Finland). The class II cell culture hood (Herasafe) was purchased from Heraeus Instruments (Hanau, Germany), The 37°C, 5% (v/v) CO_2 incubator (MCO0-20AIC) was supplied by Sanyo (Watford, UK).

5.2.14 Equipment for particle isolation

Ultracentrifuge Optima L80, rotors SW40Ti and SW32Ti with their corresponding swing buckets were supplied by Beckman Coulter Ltd. (High Wycombe, UK). The 37° incubator (MIR262) was purchased from Panasonic Healthcare Co., Ltd. (Gunma, Japan). The balance (GR-200) was supplied by A&D Jencons Plc. (Bedfodshire, UK). Lint free cotton wipes were purchased from RS Components (Corby, UK). The class I cabinet (Airone-R) was purchased from SafeLab (Weston-super-Mare, UK). The vortex mixer (SA8) was supplied by Bibby Scientific Ltd. (Staffordshire, UK) The Ika orbital shaker was supplied by Sigma Aldrich (Irvine, UK). The ultrasonic water bath was purchased from VWR International Ltd. (Leicestershire, UK). A freeze dryer (Savant™ ModulyoD) was supplied by ThermoScientific (Loughborough, UK)

5.2.15 Computer software

Computer software, MikroWin used to measure luminescence readings from the ATP assay was purchased from MikroTek Laborsysteme GmbH. The EDX spectra were acquired using AZtec computer software, purchased from Oxford Instruments AZtecEnergy EDX system (Oxford, UK). ImageJ software (National Instruments of Health, Bethesdam Naryland, USA) was used in particle sizing.

5.3 Methods

5.3.1 Particle generation using six-station pin-on-plate wear rig

Cobalt chromium wear particles were generated using a six-station pin-on-plate wear rig, which was designed and manufactured in house by the School of Mechanical Engineering, University of Leeds. Smooth (Ra <0.04µm) cobalt chromium pins and plates were machined and polished as described in section 5.2.1. All test components were cleaned following the protocol in accordance with the SOP.01.3 rev.6 (Appendix V). All the test components were sonicated in a household detergent solution for 5 minutes. The components were then rinsed with tap water and deionised water, sonicated for 10 minutes in 70% (v/v) isopropanol solution and left to dry in air for 15 minutes. All rig components (Figure 5.2) were washed in a soap detergent solution and soaked in 1% (v/v) Trigene solution for twenty minutes. Subsequently, all the parts were rinsed in tap and deionised water, and dried for use. All rig components were then assembled appropriately, following the instructions listed in SOP.01.03 rev.6 (Appendix V).

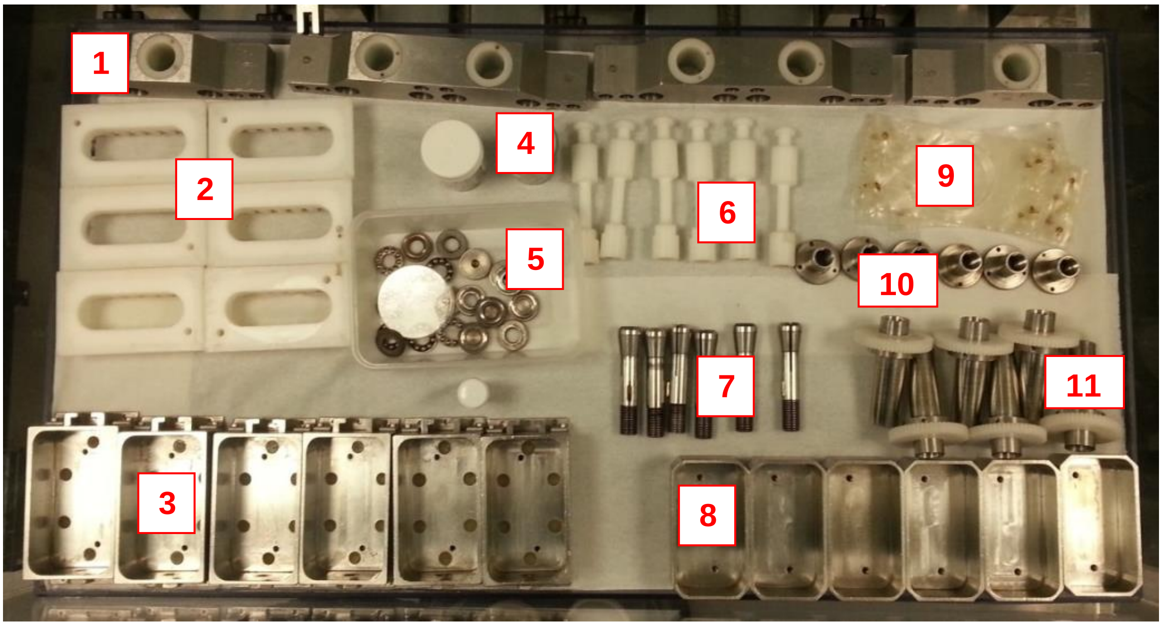

Figure 5.2: Six-station pin-on-plate wear rig components, prior to assembly: 1 – bridges securing pin holders, 2 – racks, 3 – outer baths, 4 - miscellaneous screws, 5 – ball bearings, 6 – connecting rods, 7 – pin holders, 8 – inner baths, 9 – plastic covers, 10 – pin holder bore, 11 – pinions and ratchets

Prior to the start of the test the rig was calibrated – the positions of the weights on the cantilever arms were set to exert load of 80N. The calibration setup is shown below (Figure 5.3) and the calibration protocol followed was specified in the SOP.01.03 rev.6 (Appendix V). The calibration process ensured that the loads applied by the weights placed on the cantilever matched the desired specification. Using an external load cell (Sensotec 4.5kN, Honeywell International Inc., Columbus, OH, USA), the position of the weights was adjusted accordingly.

The test was conducted at a frequency of 1Hz. The cantilever arm was loaded to generate a load of 80N and the stroke length was set to 28mm (±30° rotation). Deionised water was used as a lubricant. The cobalt chromium test components were labelled with numbers, which corresponded with the number of the station they were fitted into. This arrangement was constant over the entire duration of the test. The orientation of the plate in the bath also remained constant. Prior to the start, approximately 30 ml of lubricant was added to each bath. The cycle counter was set to zero and the motor was turned on. The speed was gradually increased and adjusted so that the frequency of the stroke was 1Hz (60 cycles per minute). Once the speed was adjusted, the weights were placed on the cantilever arms, at positions corresponding to 80N.

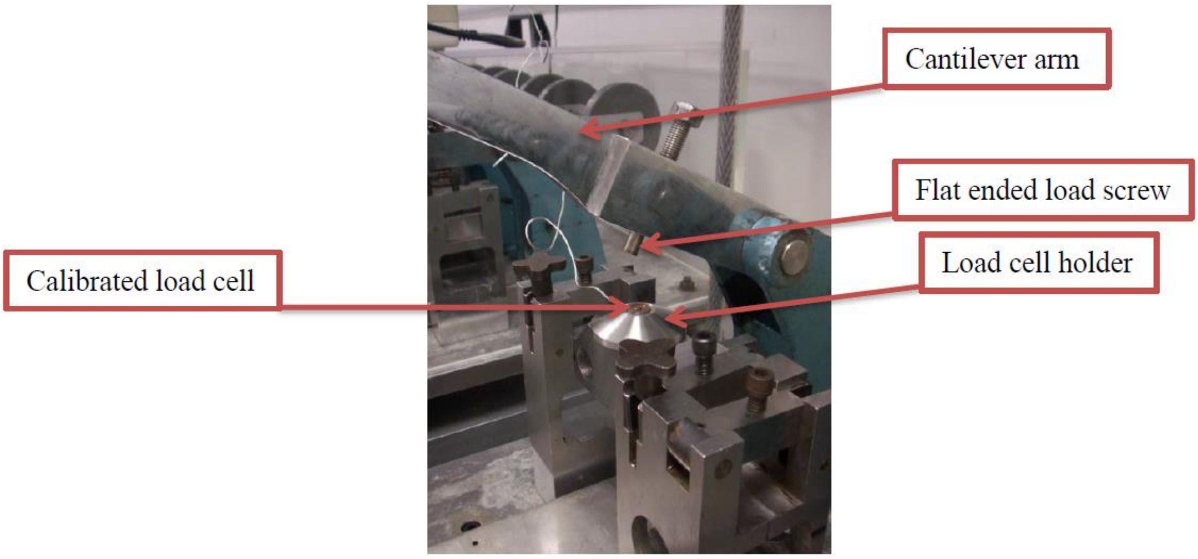

Figure 5.3: Calibration set-up of the six-station pin-on-plate wear simulator, as per SOP 01.03, Appendix V.

The rig was inspected and the lubricant was topped up twice each day. The test was stopped for weekends, when the rig was disassembled and cleaned. Upon the completion of each week of testing, the number of cycles was recorded and the test components were cleaned, following the same protocol described earlier in this section. The lubricant containing the debris from each station was collected into appropriately labelled plastic containers (test number, material, station number, date) and stored at -20°C. The rig operated for 2 weeks, 5 days a week.

5.3.2 Particle generation using a six-station spine simulator

Clinically-relevant particles were generated using a six-station spine simulator. A standard ISO protocol (ISO-18192-1:2011) was applied. Detailed methodology applied in the particle generation has previously been described in Chapter 3 section 3.4.1.

5.3.2.1 Cobalt chromium particles

5.3.2.1.1 Particle generation in foetal bovine serum

Six cobalt chromium CTDR devices were fitted in the spine simulator and tested under standard testing conditions, as per ISO-18192-1:2011. The devices were tested for a total of $4x10^6$ cycles. Foetal bovine serum (25% v/v) was used as the lubricant, which was collected and stored at-20°C, until required, at every $3.3x10^5$ cycles of the first $1x10^6$ cycles, and at every $1x10^6$ cycles in the remaining stages of the test. When collected, the lubricant from all six stations was pooled into one container, prior to freezing.

5.3.2.1.2 Particle generation in sterile water

Six CTDR devices were fitted in the spine simulator and tested under standard testing conditions, as per ISO-18192-1:2011. The devices were tested for a total of $1x10^6$ cycles. Sterile water was used as a lubricant, which was collected and stored at -20°C, until required, at every $3.3x10^5$ cycles. When collected, the lubricant from all six stations was pooled into one container, prior to freezing.

5.3.2.2 Chromium nitride and silicon nitride coating particles

One chromium nitride-coated and one silicon nitride-coated CTDR device were fitted in the spine simulator and tested under standard test conditions, as per ISO- ISO-18192-1:2011, with sterile water used as a lubricant. Initially, the devices were tested for $3.6x10^3$ cycles (1 hour) and checked for coating damage.

Following one hour of testing, it was determined that the silicon nitride coating sustained delamination damage and thus no further testing of this coated sample was conducted. The lubricant was collected and stored at -20°C, until required.

The chromium nitride coating did not sustain any damage following one hour of testing and therefore this test was extended to $6.6x10^5$ cycles, in order to maximise the volume of coating particles generated. The lubricant was the then collected and stored at -20°C, until required.

5.3.3 Particle isolation

5.3.3.1 Particle sedimentation

All centrifugation times and speeds were calculated based on the particle sedimentation equations described by Lu et al. [355] and Ohlendieck [356]. As such, the terminal velocity of particles was calculated using Equation 5.1, whilst the terminal velocity was obtained from Equation 5.2.

$$\boldsymbol{V = \frac{g \times D^2 \times (d_p - d_m)}{18 \times \nu}}$$

Equation 5.1

where:

V – terminal velocity
g – gravitational acceleration
D – particle diameter
d_p – particle density
d_m – medium density
v – medium viscosity

$$\boldsymbol{t = \frac{l}{V}}$$

Equation 5.2

where:
t – centrifugation time
l – length of centrifuge tube
V – terminal velocity.

5.3.3.2 Surfasil™ coating

All ultracentrifuge tubes used in particle isolation were coated with Surfacil™ siliconizing fluid, which is a polymeric silicone fluid consisting primarily of dichlorooctamethyltetrasiloxane. The coating reduces sample loss caused by nonspecific interactions with reaction vessels and containers for approximately 5 minutes.

Once placed inside a class II cabinet, tubes were coated using a Surfasil™ soaked cotton wipe handled with a pair of tweezers. Any excess fluid was wiped away with a clean cotton wipe. Subsequently, tubes were rinsed once with methanol and twice with sterile water. After removing the sterile water, the tubes were left to dry in air, inside the class II cabinet for approximately 5 minutes.

5.3.3.3 Preparation of Proteinase-K stock solution

In order to prepare the required proteinase-K stock solution (20 $mg.ml^{-1}$), 500mg of proteinase-K powder was weighed out in a sterile universal tube. Subsequently, 22.35ml of sterile water, 150µl of 0.5M $CaCl_2$ and 2.5ml of 1M HEPES buffer were added and the tube vortexed, until the powder dissolved. The 25ml of stock solution was divided into 1ml aliquots and stored at -20°C.

5.3.3.4 Preparation of Lysozyme stock solution

In order to prepare the required Lysozyme stock solution ($20mg.ml^{-1}$), 140mg of Lysozyme powder was weighed out in a sterile bijou. Subsequently, 7ml of Tris-HCl (pH=8.0) was added and the tube vortexed until the powder has dissolved. The bijou was kept on ice until required.

5.3.3.5 Serum concentration

Frozen foetal bovine serum collected during particle generation tests (section 5.3.2.1.1) was thawed at room temperature for approximately 2 hours. Once defrosted, 180ml of the serum was sonicated for 5 minutes and transferred into six 30ml thin-walled ultracentrifuge tubes. The tubes were placed into swing buckets with lids placed on top of the buckets. Buckets in opposing positions in the rotor (i.e. 1 and 4, 2 and 5, and 3 and 6) were balanced using a microbalance; in instances when buckets required the weight to be adjusted, sterile water was added into the tubes. Once balanced, the buckets were carefully placed in a rotor (SW32), which was placed in the ultracentrifuge (Ultra1). The serum was centrifuged at 125,755g at 25°C, for 3 hours. Following the centrifugation, the tubes were removed from the buckets. A visible pellet of particles and proteins was observed; supernatants were removed and discarded.

5.3.3.6 Protein and bacterial digestion

Immediately after serum concentration and removal of supernatants, 4ml of sterile water was added to each tube. Subsequently, 500µl of 1M HEPES and 250µl of 10% (v/v) SDS was added to each tube. The tubes were then sonicated manually, until the pellets detached from the bottom of the tubes and disintegrated. Subsequently, 250µl of proteinase-K (20mg.ml^{-1} stock concentration) was added to each tube. The tubes were then individually placed in falcon tubes and placed in an incubator set at 50°C on an orbital shaker at 4.83g for 18 hours.

Following 18 hours of incubation at 50°, the particle suspension inside the tubes was semi-transparent. The tubes were topped up with sterile water (up to 30ml), placed in buckets, balanced and placed in a rotor (SW32). The suspension was then centrifuged at 125,755g at 25°C for 1.5 hours. Following centrifugation, the tubes were removed from the buckets. A visible pellet of particles and partially digested proteins was observed; supernatants were removed and discarded.

Using a pipette, 1750µl of STET buffer, containing 100mM NaCl, 10mM Tris-HCl (pH 8.0), 1mM EDTA and 5% (v/v) Triton X-100, was added to each tube. The tubes were then sonicated manually, until the pellets have detached from the bottom of the tubes and disintegrated. Subsequently 1ml of 20mg.ml^{-1} Lysozyme solution was added to each tube. The tubes were individually placed in falcon tubes and placed in the incubator set at 37°C on an orbital shaker at 4.83g for 1 hour. Lysozyme damages bacterial cell walls by catalysing hydrolysis of 1,4-beta-linkages between N-acetylmuramic acid and N-acetyl-D-glucosamine residues in peptidoglycan and between N-acetyl-D-glucosamine residues in chitodextrins, thus destroying bacterial cell walls. Following the bacterial digestion, the tubes were topped up with sterile (up to 30ml), placed in buckets, balanced and placed in a rotor (SW32). The suspension was then centrifuged at 125,755g at 25°C for 1.5 hours. Following centrifugation, the tubes were removed from the buckets. A visible pellet was observed; supernatants were removed and discarded.

Subsequently, 4ml of sterile water were added to each tube. Following this, 500µl of HEPES and 250µl of 10% (w/v) SDS was added to each tube. The tubes were then placed in the ultrasonicating bath, until the pellets detached from the bottom of the tubes and disintegrated. Subsequently, 250µl of proteinase-K (20mg.ml^{-1}) was added to each tube. The tubes were then individually placed in falcon tubes and placed in the incubator set at 50°C on an orbital shaker at 4.83g for 22 hours.

5.3.3.7 Density gradient centrifugation

Six clean 14ml tubes were coated with Surfasil™ (section 5.3.3.1). Filtered sodium polytungstate solution (85%, w/v) was prepared diluted with sterile water into 1.2, 1.6 and 2.0 g/cm^3 density gradients. Subsequently, 2ml of each gradient was added dropwise to each tube, starting from the lowest to highest dilution. Subsequently, tubes containing the digested particle suspension (section 5.3.3.6) were sonicated for 10 minutes. The contents were then layered carefully on top of the polytungstage gradients. Subsequently, the tubes were placed into swing buckets with lids placed on top of the buckets. Buckets in opposing positions in the rotor (i.e. 1 and 4, 2 and 5, and 3 and 6) were balanced; in instances when the buckets required the weight to be adjusted sterile water was added into the tubes. Once balanced, the buckets were carefully placed in a rotor (SW40), which was placed in the ultracentrifuge. The density gradient was centrifuged at 202,048g at 25°C, for 4 hours. Following centrifugation, the tubes were carefully removed from the buckets. The sodium polytungstate and protein bands were removed from the tube leaving behind the particles which had formed a pellet at the bottom of the tube. Subsequently, 2 ml of sterile water was added to each tube and the samples were frozen at -20°C, until required. The particle isolation process is depicted in Figure 5.4.

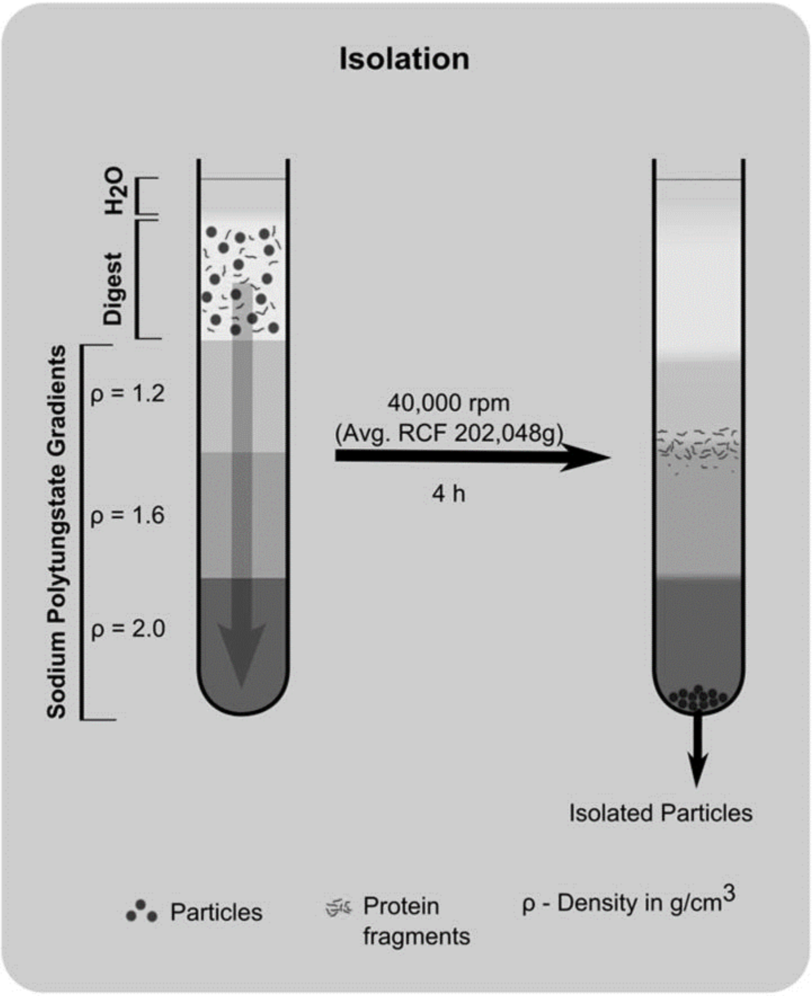
Isolation
H2O
Digest
Sodium Polytungstate Gradients
ρ = 1.2
ρ = 1.6
ρ = 2.0
40,000 rpm
(Avg. RCF 202,048g)
4 h
Isolated Particles
Particles
Protein fragments
ρ - Density in g/cm3

Figure 5.4: Particle isolation process used in this study, based on Lal *et al.* [353]**.**

5.3.3.8 Washes

Samples thawed in room temperature for approximately 2 hours (section 5.3.3.7) were topped up with sterile water, placed in swing buckets and balanced. The buckets were placed in a rotor (SW40) and centrifuged at 202,048g at 25°C, for 1 hours. At this time, a black pellet of particles was visible and supernatants were removed. This step was repeated 3 times; in the final step, after removing supernatants, 2ml of sterile water was added to each tube, which were stored at -20°C until required.

5.3.4 Freeze drying of water generated particle solution

Frozen samples of particles generated in water (sections 5.3.1, 5.3.2.1.2 and 5.3.2.2) were placed in the freeze dryer (-50°C, under vacuum), in order to reduce the volume of water from 500ml to approximately 10ml. The volume-reduced samples were stored at -20°C until required.

5.3.5 Preparation of endotoxin-free wear particles and model silicon nitride particles for cell culture experiments

Ten sterile glass vials, acclimatised for >24 hours in the measurements laboratory (temperature and humidity controlled room) were covered with foil and weighed on the Mettler Toledo XP26 balance (0.001mg readability). An additional glass vial covered with foil was used as a reference. Each vial was weighed at least five times, such that all consecutive measurements were within 0.001mg of each other. Cobalt chromium, chromium nitride and silicon nitride coating wear debris, generated in water (sections 5.3.1, 5.3.2.1.2 and 5.3.2.2) and those generated and isolated from bovine serum (section 5.3.3) were thawed, and a small amount (approx. 5 ml) was pipetted into pre-weighed vials; 2 vials of wear particles for each material were prepared. Similarly, four vials of model silicon nitride particles of each size (section 5.2.4) were prepared. All the vials (covered with foil) were then sterilised for 4 hours at 190°C to evaporate the water and remove and destroy any endotoxin. The bottles were then placed in the measurements laboratory for >24 hours in order to acclimatise to room temperature. The bottles were re-weighed and the mass of the particles was calculated. Particles in each vial were then re-suspended with the appropriate volume of sterile water to produce a stock concentration of 1mg.ml^{-1}, which were stored at -20°C until required.

5.3.6 Characterisation of cobalt chromium, chromium nitride and silicon nitride wear particles and silicon nitride model particles

Small volumes (200μl) of the thawed particle stocks (section 5.3.5) were diluted in 5ml of sterile water and placed in universals vials. The samples were sonicated for 30 minutes, in order to disaggregate the particles. A Millipore glass filtration unit was prepared by washing in soap detergent and rinsing with tap and deionised water, and left to dry inside a class I cabinet. Finally, the particle suspension was filtered through a polycarbonate membranes with 0.015µm pore size. Following filtration, the membranes were dried under an infrared lamp for a duration of 4 hours.

Each polycarbonate membrane was mounted on a 2.5cm aluminium short stub using an adhesive carbon tab. The edges of the membrane were coated with carbon paste. The filter membranes were then sputter coated with Iridium to a thickness of 5nm. Application of iridium coating reduced sample charging by increasing thermal conduction, sample beam penetration by improving edge resolution. The filters were inspected using a Hitachi SU8230 cold field scanning electron microscope at a working distance of 4-15 mm and at 2kV. Images were taken using decelerated backscattered electrons at 1kV, which yielded improved visualisation of topographical detail of the particles. Images were taken at magnifications of 30 K, 40 K, 60 K and 90 K. Particle composition was confirmed using EDX. The images were then analysed using ImageJ software to measure the diameter and area of the particles. A minimum of 150 particles per material were measured, as suggested by ISO-13322-1:2014 – *'Particle size analysis – Image analysis methods. Part 1: Static image analysis methods'* [357].

Table 5.1 shows the summary of all types of particles used in this study, their generation and preparation methods.

Table 5.1: Summary of materials, generation and preparation methods for all particles used.

Material	Generation method	Lubricant used	Storage method	Preparation method	Characterisation
Cobalt chromium	Pin on plate	Sterile water	-20°C	Freeze dried and sterilised	Yes
	Spine Simulator	Sterile water	-20°C	Freeze dried and sterilised	Yes
		Foetal bovine serum	-20°C	Isolated and sterilised	Attempted*
Chromium nitride	Spine simulator	Sterile water	-20°C	Freeze dried and sterilised	Yes
Silicon nitride	Model particles, submicron	NA	Room temperature	Sterilised	Yes
	Model particles, nanoscale	NA	Room temperature	Sterilised	Yes
	Spine simulator	Sterile water	-20°C	Freeze dried and sterilised	Yes

*Particle characterisation attempted, however this was unsuccessful due to high levels of protein contamination

5.3.7 Cell resurrection and cell culture

5.3.7.1 Resurrection of L929 murine fibroblast cell line and primary porcine dural fibroblasts cells

Cell culture medium was prepared using 500 ml of Dulbecco’s Modified Eagle’s Medium (DMEM), supplemented with 10% (v/v) foetal calf serum (FCS), 2mM L-glutamine, 100 U penicillin, and 100µg.ml^{-1} streptomycin. This will subsequently be referred to as cell culture medium (CCM). One cryovial of L929 cells and one of primary porcine dural fibroblasts were removed from liquid nitrogen and thawed at 37°C. The cells were then transferred to separate sterile tubes containing 10ml of fresh cell culture medium. The cell suspensions were centrifuged at 150 RCF for 10 minutes, at room temperature, after which the supernatant was removed from above the cell pellet. The pellets were re-suspended in 5ml of fresh CCM. The cells were added to their respective sterile culture flasks (75cm^3) containing 15ml of fresh CCM and incubated at 37°C in 5% (v/v) CO_2 in air until 80% confluent.

5.3.7.2 Cell culture maintenance of L929 murine fibroblast cell line and primary porcine dural fibroblasts cells

Once approximately 80% confluent, cells were washed with Dulbecco's Phosphate-Buffered Saline (DPBS) (without calcium and magnesium chloride). The cells were treated with 5ml of tripsin-EDTA for 10 minutes at 37°C, to detach cells from the flask. A volume of 10ml of fresh CCM was added to the flask to inhibit the tripsin-EDTA. The contents of the flask were transferred to a universal tube and centrifuged at 150 RCF for 10 minutes, at room temperature, after which the supernatant was removed. The pellet was re-suspended in 10ml of fresh CCM. A total cell count in 1ml of the cell suspension was determined using the method described in section 5.3.8. If cells were needed in further experiments, the remaining cell suspension was added to a 175cm^3 sterile flask containing 20ml of fresh CCM. The cells were incubated at 37°C in 5% (v/v) CO_2 in air until 80% confluent.

5.3.8 Cell count using the trypan blue exclusion assay

The number of viable cells present in 1ml of cell suspension was determined by diluting 80µl of the cell suspension (section 5.3.7.2) with 80µl of trypan blue. From the 160µl of the suspension mixture, 20µl was placed on a Neubauer haemocytometer (Figure 5.5) and viewed under a light microscope. The number of viable cells was counted within the 25 squares, counting at least 100 and maximum of 300 cells. The number of viable cells present in 1ml of cell suspension was calculated using Equation 5.3.

$$\boldsymbol{N = Number\ of\ cells\ counted\ \times\ 2 \times\ 10^4}$$

Equation 5.3

where:

N – number of viable cells present in 1ml of cell suspension

2 - dilution factor of the cell suspension within the 10µl of trypan blue

10^4 – dilution factor per 1ml

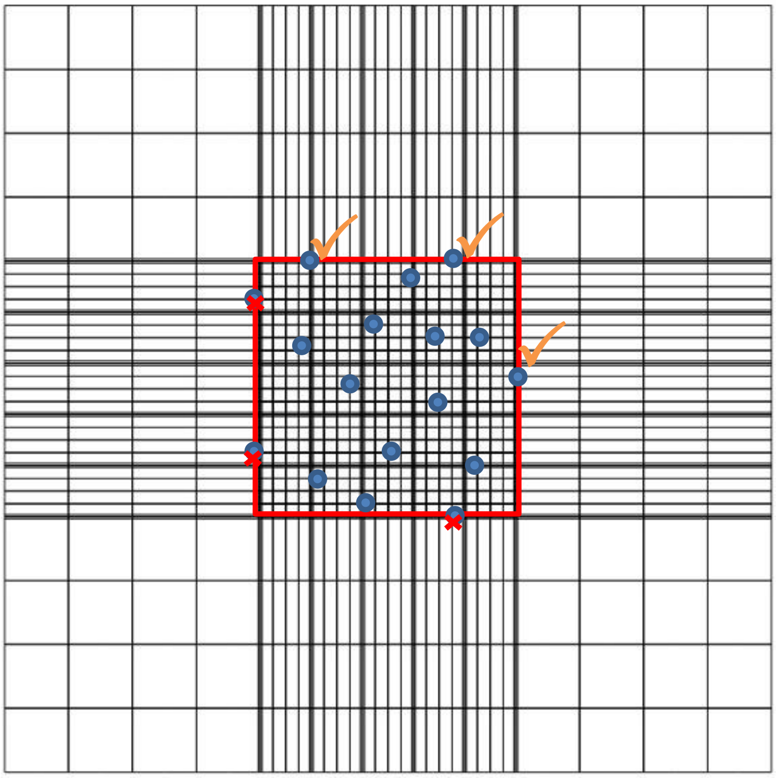

Figure 5.5: Schematic representation of a magnified view the Neubauer haemocytometer grid used in cell counting. At least 100 cells within all 25 squares (selected in red) had to be counted per cell suspension sample. Cells on the left and bottom edge of the grid were not counted; cells on the top and right edge of the grid were counted.

5.3.9 Growth curves for L929 murine fibroblasts and primary porcine dural fibroblasts

5.3.9.1 Seeding 96-well plates

To assess the optimal seeding density for the L929 cell line and primary porcine dural fibroblasts over the duration of experiments, cells were seeded at different seeding densities and the growth followed for up to six days. Following one passage, cells were transferred into 3 larger, (175cm^3) sterile flasks, in order to expand the cell population. Once the cells were confluent (>80% confluence) they were treated with trypsin-EDTA (section 5.3.7.2) and a cell count was performed (section 5.3.8). Cells were seeded at concentrations of 5x10^2.ml^{-1}; 1x10^3.ml^{-1}; 5x10^3.ml^{-1}; 1x10^4.ml^{-1} and 5x10^4.ml^{-1} for each well. Equal volumes (100µl) of fresh CCM were added to each well of a sterile, clear, flat-bottomed 96-well plate. Equal volumes (100µl) of cell suspensions at the required cell concentrations were added to appropriate wells. Each cell seeding density was repeated six times. Four plates, corresponding to four time-points (days 0, 1, 3 and 6), were seeded following the layout described in Figure 5.6. The plates were incubated at 37°C in 5% (v/v) CO_2 in air for at least 2 hours to allow cell attachment.

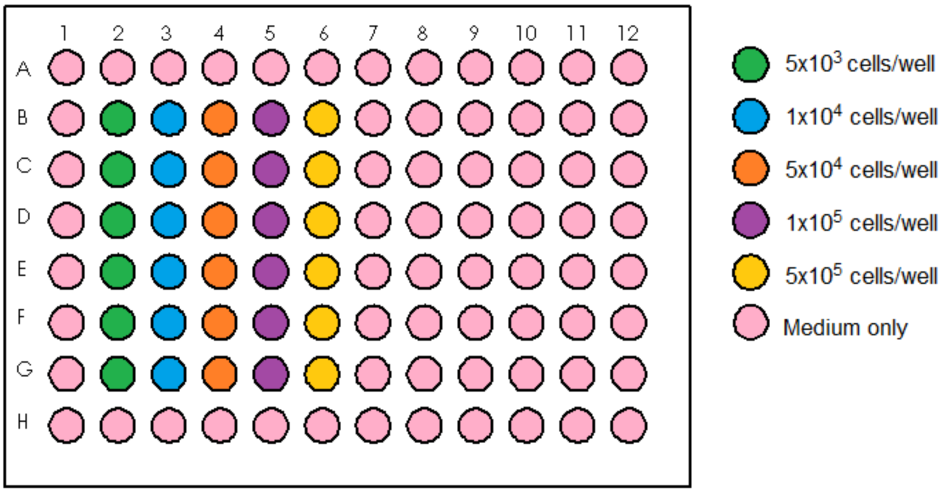

Figure 5.6: Layout of the 96-well plate used in the growth curve studies of L929 murine fibroblasts and primary porcine dural fibroblasts.

5.3.9.2 Determining cell viability using the ATP-Lite assay

Cell viability was determined using the ATP-Lite™ assay. The assay solution consisted of Luciferase and D-Luciferin which interact with adenosine-triphosphate (ATP) released from the cells under investigation to emit light. The luminescence counter detected and measured bioluminescence which was proportional to the ATP concentration within the solution. The amount of ATP produced in a sample was directly proportional to the number of viable cells present; therefore ATP is used as an indicator of cell viability in the ATP-Lite Assay. The principle of the ATP-Lite assay is outlined in the reaction below:

$$ATP + \text{D-Luciferin} + O_2 \xrightarrow{Luciferase+Mg^{2+}} Oxyluciferin + AMP + PP_i + CO_2 + Light$$

The ATP substrate solution was prepared using the contents of the ATP-Lite kit. The contents of a bottle of the lyophilised substrate were mixed with 25ml of substrate buffer solution. The reconstituted ATP substrate solution was then split into small (5ml), sterile glass universal vials and covered with foil. The vials were stored at -20°C until required.

Following the required incubation time, the supernatants (200µl) were removed from each well and replaced with 100µl of fresh CCM. The mammalian cell lysis solution was added to each well (50µl) and the plate was placed on the orbital plate shaker for 4 minutes at 280rpm. Previously thawed, reconstituted lyophilised substrate was then added to each well (50µl) and the plate was covered in foil and placed on the orbital plate shaker for 4 minutes at 280rpm. With the lights switched off in the class II cabinet, 100µl of the contents of each well were transferred to corresponding positions in a 96-well Optiplate® and an adhesive clear film was placed over the plate. The plate was read using the Chameleon™V luminescence reader, following dark-adaptation of the plate for 10 minutes. The luminescence of each well was read for 5 seconds and the output was presented as counts per second (CPS) and exported to Excel.

5.3.10 Culture of L929 and primary dural fibroblasts cells with cobalt chromium wear particles

5.3.10.1 Seeding 96-well plates with L929 fibroblasts

A flask of cells (confluence >80%) was treated with trypsin-EDTA (section 5.3.7.2) and the number of viable cells was determined (section 5.3.8). Cells were seeded in a sterile, clear, flat-bottomed 96-well plate, at the density of $1x10^3$/ml for each well. A volume of 100µl of cell suspension containing required number of cells was added to each well. Plates seeded with cells were incubated at 37°C in 5% (v/v) CO_2 in air for at least 12 hours to allow cell attachment.

5.3.10.2 Seeding 96-well plates with primary porcine dural fibroblasts

Flasks of cells (confluence >80%) were treated with trypsin-EDTA (section 5.3.7.2) and the number of viable cells was determined (section 5.3.8). Cells were seeded in sterile, clear, flat-bottomed 96-well plates at the density of $5x10^2$/ml. A volume of 100µl of cell suspension containing the required number of cells was added to each well. Plates seeded with cells were incubated at 37°C in 5% (v/v) CO_2 in air for at least 12 hours to allow cell attachment.

5.3.10.3 Culturing L929 and primary dural fibroblasts in the presence of cobalt chromium wear particles

The L929 and primary dural fibroblasts cell were cultured with cobalt chromium generated in the six-station pin-on-plate wear simulator (section 5.3.1), six-station spine simulator in water (section 5.3.2.1.2) and foetal bovine serum (5.3.2.1.1). The sterile wear particles (section 5.3.5) were added to the cells at particle volumes per cell of 50µm^3, 5µm^3 and 0.5µm^3 using the 1mg.ml^{-1} particle suspension (section 5.3.5). Each particle suspension was vortexed and sonicated for 30 minutes immediately prior to culturing with the cells. Negative controls consisted of particles only, containing 100µl of the 50µm^3 particles per cell suspension and 100µl of fresh CCM (no cells), cells only, containing 100µl of the cell suspension solution and 100µl of fresh CCM, and the positive control was camptothecin, which induces cell death via apoptosis. The stock solution of the camptothecin was prepared at a concentration of 4µg.ml^{-1}. One hundred microliters of the camptothecin stock was added to corresponding wells and supplemented with 100µl of fresh CCM. Each treatment was repeated six times and the cells were cultured with the particles at 37°C in 5% (v/v) CO_2 in air. The complete layout of the 96-well plates used in this study is shown in Figure 5.7. Cell viability was determined over 6 days using the ATP-Lite assay, at specific time-points (day 0, 1, 3 and 6).

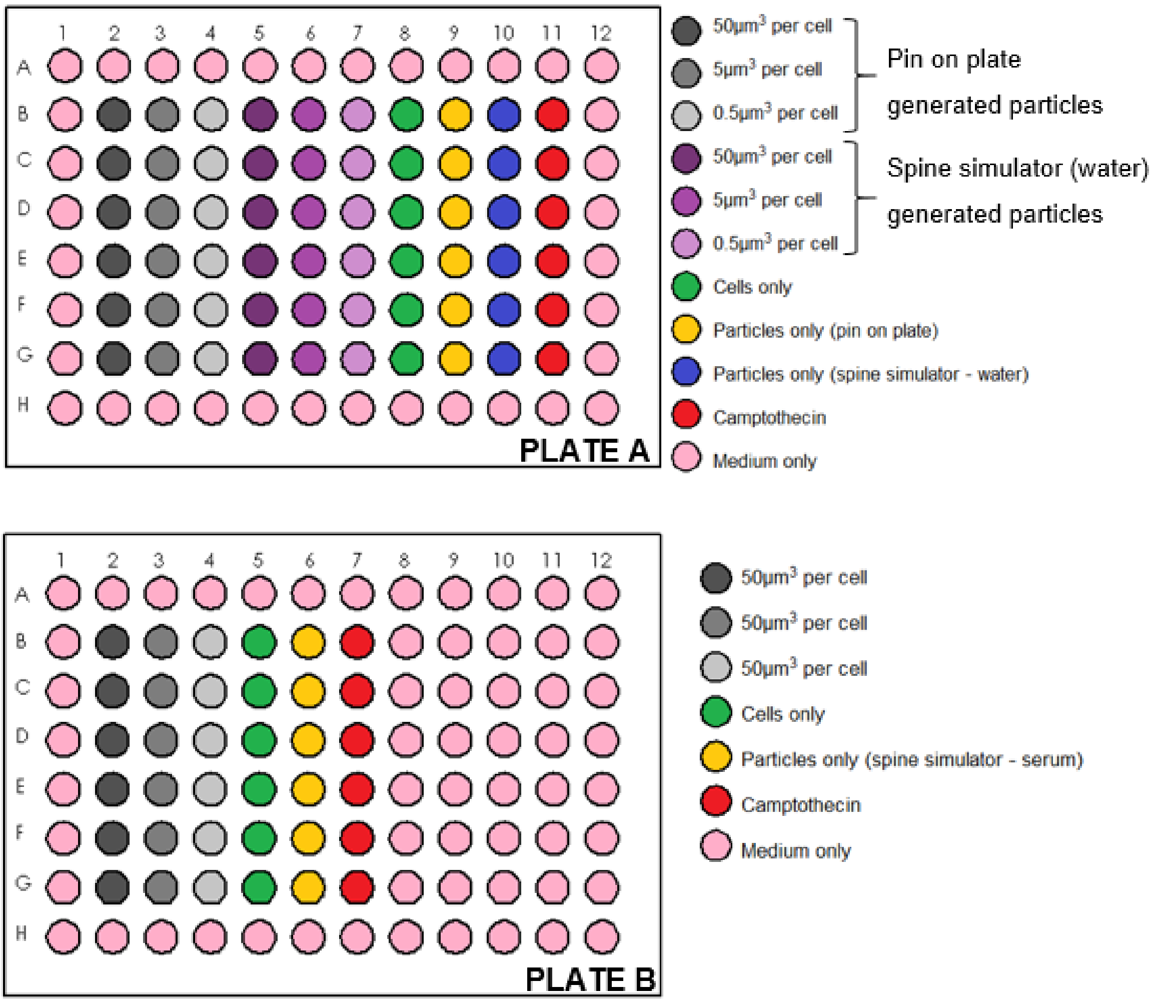
1 2 3 4 5 6 7 8 9 10 11 12
A B C D E F G H
PLATE A
50µm³ per cell
5µm³ per cell
0.5µm³ per cell
Pin on plate generated particles
50µm³ per cell
5µm³ per cell
0.5µm³ per cell
Spine simulator (water) generated particles
Cells only
Particles only (pin on plate)
Particles only (spine simulator - water)
Camptothecin
Medium only
PLATE B
50µm³ per cell
50µm³ per cell
50µm³ per cell
Cells only
Particles only (spine simulator - serum)
Camptothecin
Medium only

Figure 5.7: Layout of 96-well plates used for culturing cells with the cobalt chromium wear particles. Plate A (top) included particles generated in the six-station pin-on-plate wear simulator and the six-station spine simulator in water. Plate B (bottom) included particles generated in the six-station spine simulator in foetal bovine serum. The same plate layouts were used for both L929 and primary dural fibroblasts cells.

5.3.11 Culture of L929 and primary dural fibroblasts cells with model silicon nitride particles and chromium nitride and silicon nitride wear particles

5.3.11.1 Seeding 96-well plate with L929 fibroblasts

The same method of cell seeding was followed as described in section 5.3.10.1.

5.3.11.2 Seeding 96-well plate with primary porcine dural fibroblasts

The same method of cell seeding was followed as described in section 5.3.10.2.

5.3.11.3 Culturing L929 and primary dural fibroblasts in the presence of model silicon nitride model particles (submicron and nanoscale particles)

The L929 and primary dural fibroblasts cells were cultured with the micron- and nanoscale size silicon nitride particles (section 5.2.4). Commercially available model particles of submicron and nanoscale size were used in this experiment. Due to the catastrophic failure of the silicon nitride particles generated in the *in vitro* wear simulation (Chapter 4) were not deemed clinically relevant. For that reason, readily available particles were used in the cytotoxicity studies as a replacement, as well as a comparison to the silicon nitride coating particles collected from the wear study. The model particles of each size (submicron and nanoscale) were added to the cells at particle volumes per cell of 500µm^3, 50µm^3 and 5µm^3 using the 1mg.ml^{-1} particle suspension (section 5.2.4). Each particle suspension was vortexed and sonicated immediately prior to culturing with the cells. A negative control of particles only, containing 100µl of the 500µm^3 particles per cell and 100µl of fresh CCM (no cells), was added to each plate. The particles were investigated following the layout shown in Figure 5.8. The negative control of cells only contained 100µl of the cell suspension solution and 100µl of fresh CCM, and the positive control was camptothecin (4µg.ml^{-1}). The stock solution of the camptothecin was as described in section 5.3.10.3. Each treatment was repeated six times and the cells were cultured with the particles at 37°C in 5% (v/v) CO_2 in air. The cell viability was determined over 6 days at the specific time-points (day 0, 1, 3 and 6).

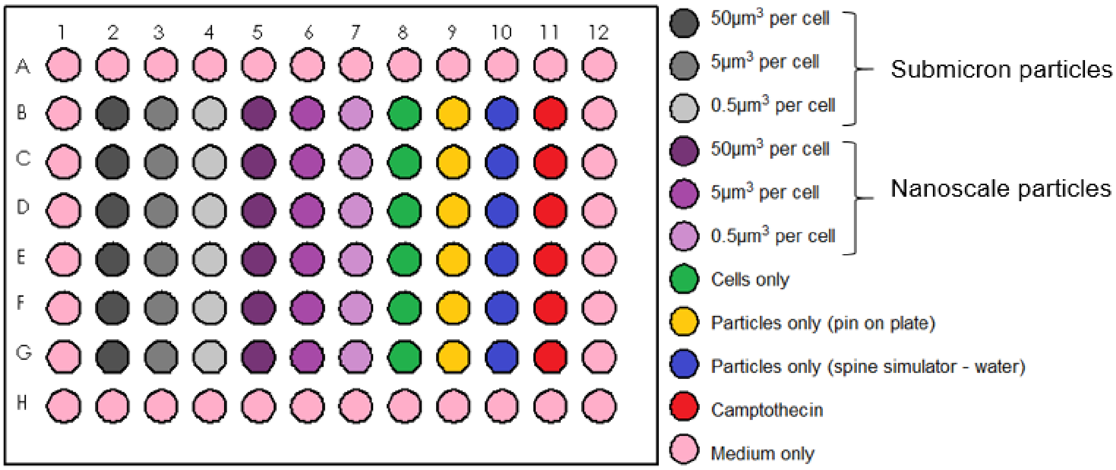
1
2
3
4
5
6
7
8
9
10
11
12
A
B
C
D
E
F
G
H
50µm³ per cell
5µm³ per cell
0.5µm³ per cell
Submicron particles
50µm³ per cell
5µm³ per cell
0.5µm³ per cell
Nanoscale particles
Cells only
Particles only (pin on plate)
Particles only (spine simulator - water)
Camptothecin
Medium only

Figure 5.8: Layout of a 96-well plate used for culturing the L929 cells with the submicron- and nanoscale silicon nitride powder particles.

5.3.11.4 Culturing L929 and primary dural fibroblasts in the presence of ceramic coating wear particles (chromium nitride and silicon nitride)

The L929 and primary dural fibroblasts cells were cultured with chromium nitride and silicon nitride coating wear particles generated in the six-station spine simulator (section5.3.2.2). The particles of each coating were added to the cells at particle volume per cell of 50µm^3, 5µm^3 and 0.5µm^3 using the 1mg.ml^{-1} particle suspension, in the arrangement shown in Figure 5.9. Each particle suspension was vortexed and sonicated immediately prior to culturing with the cells. A negative control of particles only, containing 100µl of the 50µm^3 particles per cell suspension and 100µl of fresh CCM (no cells), was added to each plate. The particles were cultured following the layout shown in Figure 5.8. The negative control with cells only contained 100µl of the cell suspension solution and 100µl of fresh CCM, and the positive control was camptothecin (4µg.ml^{-1}). The stock solution of the camptothecin was as described in section 5.3.10.3. Each treatment was repeated six times and the cells were cultured with the particles at 37°C in 5% (v/v) CO_2 in air. The cell viability was determined over 6 days at specific time-points of day 0, 1, 3 and 6.

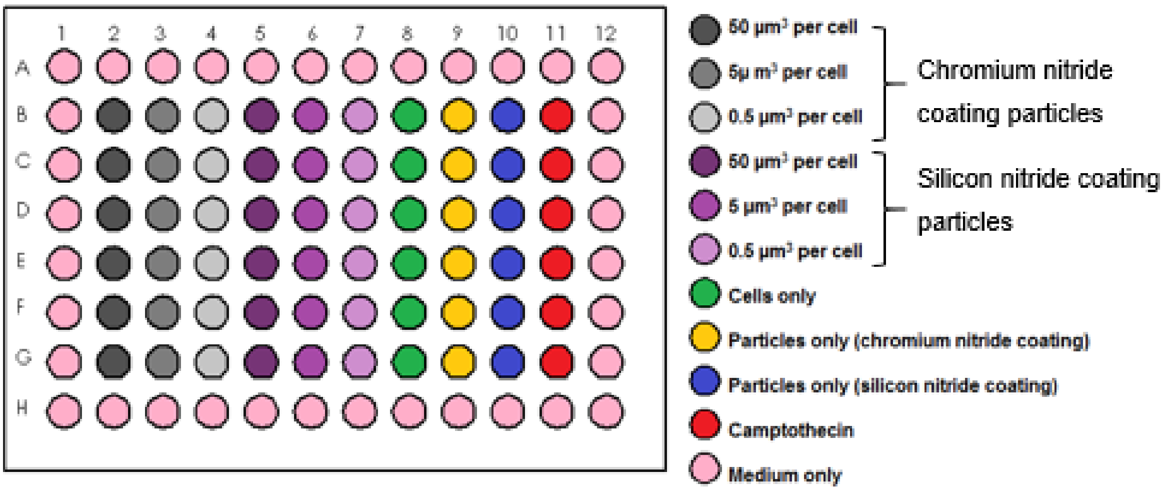
1
2
3
4
5
6
7
8
9
10
11
12
A
B
C
D
E
F
G
H
50 µm³ per cell
5µ m³ per cell
0.5 µm³ per cell
Chromium nitride coating particles
50 µm³ per cell
5 µm³ per cell
0.5 µm³ per cell
Silicon nitride coating particles
Cells only
Particles only (chromium nitride coating)
Particles only (silicon nitride coating)
Camptothecin
Medium only

Figure 5.9: Layout of a 96-well plate used for culturing cells with the chromium nitride and silicon nitride coating particles generated in six-station spine simulator. The same plate layout was used for L929 murine fibroblasts and primary porcine dural fibroblasts.

5.3.12 Determining changes in cell viability using the ATP-Lite assay

The cell viability of the cells seeded with cobalt chrome wear particles (section 5.3.10.3), model silicon nitride particles (section 5.3.11.35.3.11.2) and ceramic coatings wear particles (section 5.3.11.4) was determined using the ATP-Lite assay (section 5.3.9.2). The changes in viability of cells cultured with different particles were determined by assessing changes relative to the cells only control cell viability at each timepoint. The data obtained from the cell viability assay was analysed by one-way analysis of variance (ANOVA, α=0.05) and individual differences between the means were determined using the T-method to calculate the minimum significant difference (MSD).

5.4 Results

5.4.1 Particle generation using a six-station pin-on-plate wear rig

The six-station wear simulator fitted with CoCr pins and plates was stopped following 613,615 cycles. Images of the damage sustained to the surfaces of plates and pins, following the tests are shown in Figure 5.10. Wear debris produced in the test were collected and stored at -20°C. Gravimetric analysis of wear was completed. A summary of the results is shown in Figure 5.11. Results of the gravimetric analysis of wear produced by each component in each station are detailed in Table 5.2. The results showed that the plates produced significantly higher wear volumes ($p<0.05$, CI 95%), when compared to their corresponding pins. The mean wear volume produced by the plates was $2.43\pm0.47mm^3$, whilst the mean wear volume produced by the pins was $0.77\pm0.26mm^3$. The wear factor was derived Equation 5.4 (Archard’s equation [358]) and is defined as a function of the wear volume (V), produced under a given load (W) and over a certain sliding distance (x) travelled by a pin on the surface of a plate:

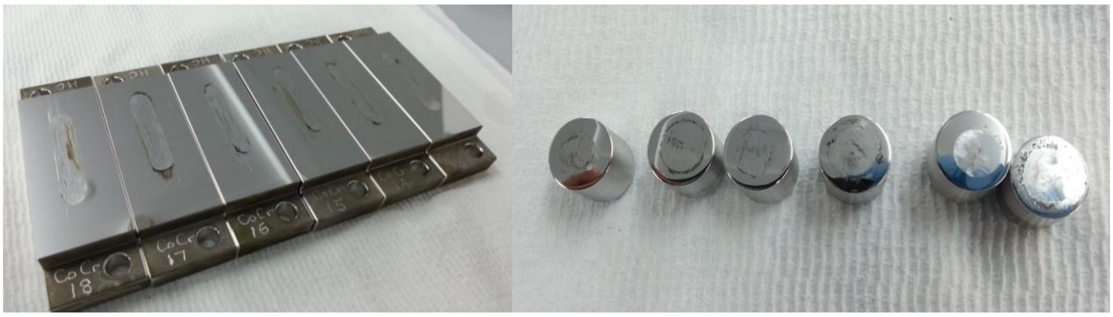

Figure 5.10: Cobalt chrome plates (left) and pins (right) components following 613,615 cycles of testing on the six-station pin-on-plate wear rig. The components shown are arranged in order corresponding to stations 6-1, respectively.

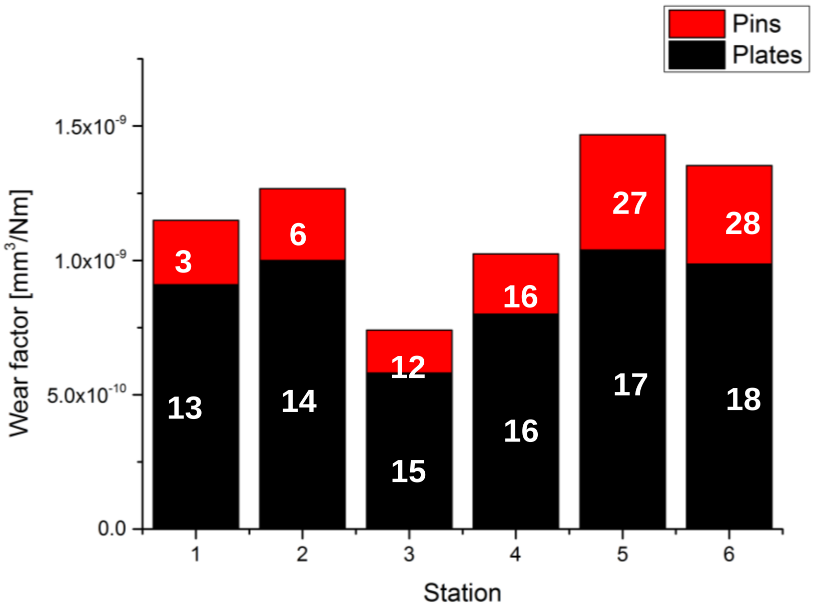

Figure 5.11: Wear factors produced by the cobalt chromium pin and plate by each station, 1-6. Across all the stations, both pins and plates produced relatively similar wear factors, with only station 3 components resulting in a slightly lower wear factors. Identification numbers of pins and plates are marked in each stacked bar.

$$K = \frac{V}{Wx}$$

Equation 5.4

Table 5.2: Summary of wear volumes and factors produced in the 6 station pin on plate wear simulator fitted with cobalt chromium wear test components. Red and black colours distinguish between the pins (red) and plates (black).

Station	**Pin/Plate ID**	**Wear volume [mm^3]**	**Wear factor [mm^3/Nm]**	**Total wear volume per station [mm^3]**
1	**3**	**0.66**	**2.39**	3.16
	13	**2.5**	**9.10**	
2	**6**	**0.73**	**2.67**	3.48
	14	**2.75**	**9.99**	
3	**12**	**0.44**	**1.61**	2.04
	15	**1.6**	**5.81**	
4	**16**	**0.62**	**2.24**	2.82
	16	**2.2**	**7.99**	
5	**27**	**1.18**	**10.03**	4.03
	17	**2.85**	**2.07**	
6	**28**	**1.00**	**9.87**	3.72
	18	**2.71**	**1.97**	

5.4.2 Particle generation using a six-station spine simulator

Six MoM CTDR devices were tested in the six-station spine simulator, under standard ISO testing protocol. The components were tested for 4×10^6 cycles in foetal bovine serum. An additional 1×10^6 cycles in sterile water was also completed. The results of the wear rates exhibited in the spine simulator testing have previously been reported in Chapter 4; a summary of these results is detailed in Table 5.3.

Table 5.3: Summary of wear rates exhibited by different bearing materials of CTDRs tested in the current study.

Bearing	Test protocol	Wear rate±SD
CoCr-CoCr	ISO-18192-1:2011	0.24±0.03 mm^3/MC
CoCr-CoCr	altered ISO-18192-1:2011*	0.08±0.06 mm^3/MC
CrN-CrN	ISO-18192-1:2011	0.03±0.01 mm^3/MC
Si_3N_4- Si_3N_4	ISO-18192-1:2011	2.92±0.88 mm^3/MC**

*for details see Chapter 4 section 4.4.2
**wear rate based on linear extrapolation of results obtained at 71,000 cycles

5.4.3 Characterisation of cobalt chromium wear particles

5.4.3.1 CoCr particles generated in the six-station pin-on-plate wear rig

Particles generated in the six-station pin-on-plate wear rig in water lubricant (section 5.3.1) were investigated using cold field emission SEM. Once collected, the particles were freeze dried (section 5.3.4) and sterilised (section 5.3.5). Subsequently, the particles were filtered through a polycarbonate membranes with 0.015µm pore size. The filter membranes were later mounted onto carbon tabs and sputter coated with iridium, prior to SEM analysis (section 5.3.6). The particles exhibited a tendency to agglomerate, as shown in Figure 5.12. Most particles were round to oval morphology with relatively smooth edges. The particle size distribution showed the mean size to be 51nm, with the sizes of particles ranging from 20 to 120nm, as shown in Figure 5.13. The majority of the particles (~60%) were within the range of 30-60nm. The EDX spectra, as shown in Figure 5.14 confirmed the chemical composition of the particles, detecting chromium and cobalt peaks. Peaks of iridium were also detected in the EDX spectroscopy – prior to imaging each sample was coated with approximately 5nm of iridium coating (section 5.3.6).

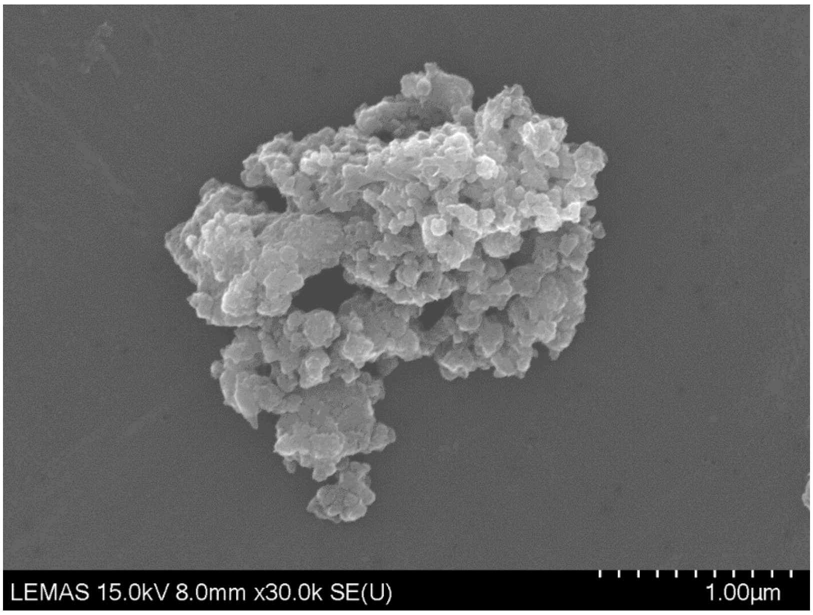

Figure 5.12: Cobalt chromium particles generated in the six-station pin-on-plate wear rig in water. The submicron sized particles showed a tendency to agglomerate.

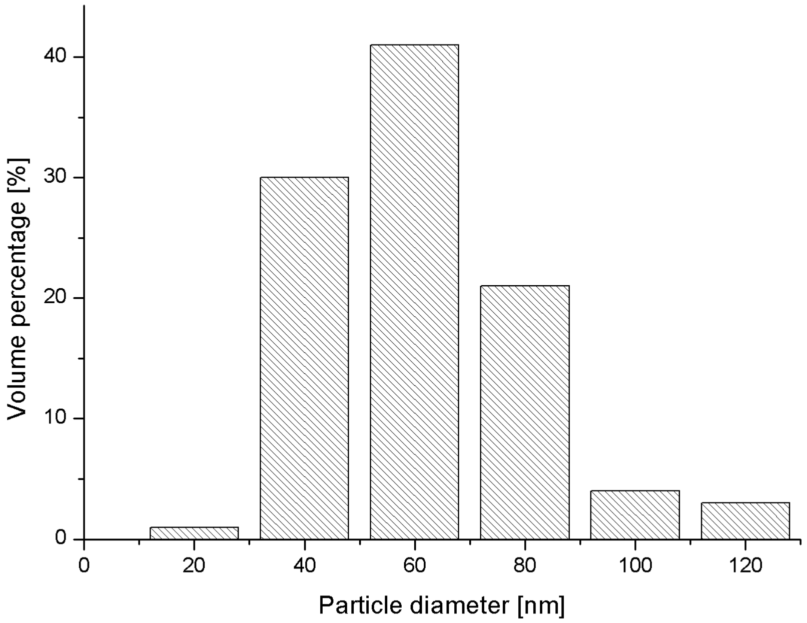

Figure 5.13: Particle volume distribution of cobalt chromium particles generated in a six-station pin-on-plate wear rig in water. The mean particle size was 51nm.

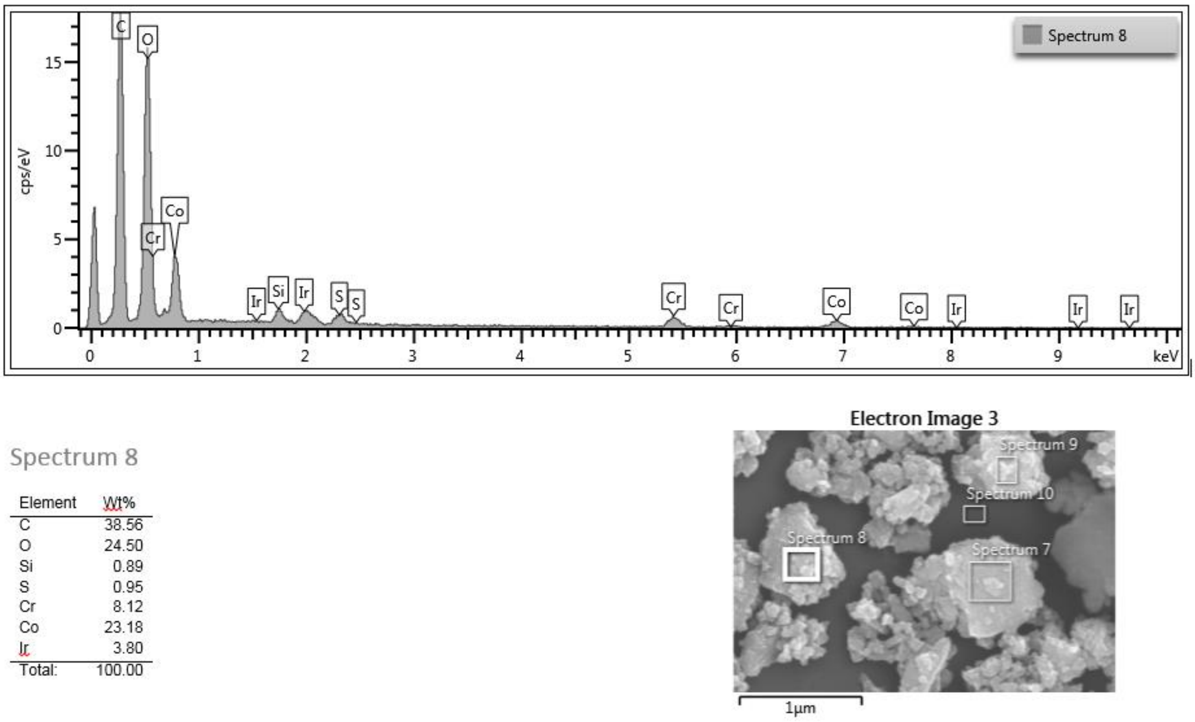

Spectrum 8

Element	Wt%
C	38.56
O	24.50
Si	0.89
S	0.95
Cr	8.12
Co	23.18
Ir	3.80
Total:	100.00

Figure 5.14: EDX spectra of cobalt chromium particles generated in the six-station pin-on-plate wear rig in sterile water. Chromium (Cr) and cobalt (Co) were confirmed in the spectroscopy. Iridium peaks were detected due to the iridium coating the samples were coated with prior to observation.

5.4.3.2 CoCr particles generated in foetal bovine serum

The particles were generated during *in vivo* wear testing of CoCrMo CTDRs (section 5.3.2.1.1). Once collected, the lubricant has undergone protein and bacteria digestion and particles were isolated from the serum (section 5.3.3). Next, particles were freeze dried (section 5.3.4) and sterilised (section 5.3.5). Subsequently, the particles were filtered through a polycarbonate membranes with 0.015µm pore size. The filter membranes were later mounted onto carbon tabs and sputter coated with iridium, prior to SEM analysis (section 5.3.6).

The SEM images of cobalt chromium wear particles isolated from foetal bovine serum highlight the strong agglomeration tendencies of the particles, as shown in Figure 5.15. Moreover, the particles were embedded in proteins and sodium polytungstate residues, which was confirmed by the EDX spectra (Figure 5.16). As a result, particle sizing was not attempted for particles isolated from bovine serum lubricants.

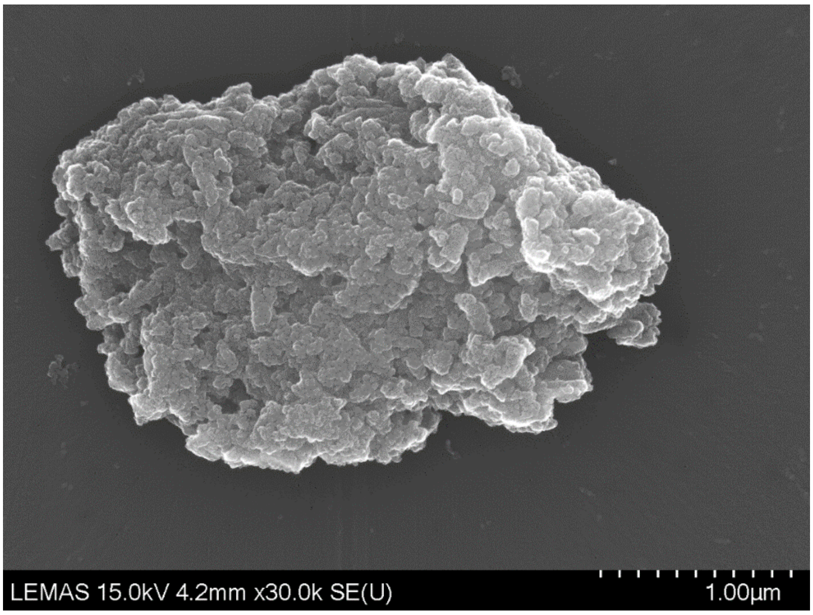

Figure 5.15: Cobalt chromium particles generated in a six-station spine simulator in foetal bovine serum.

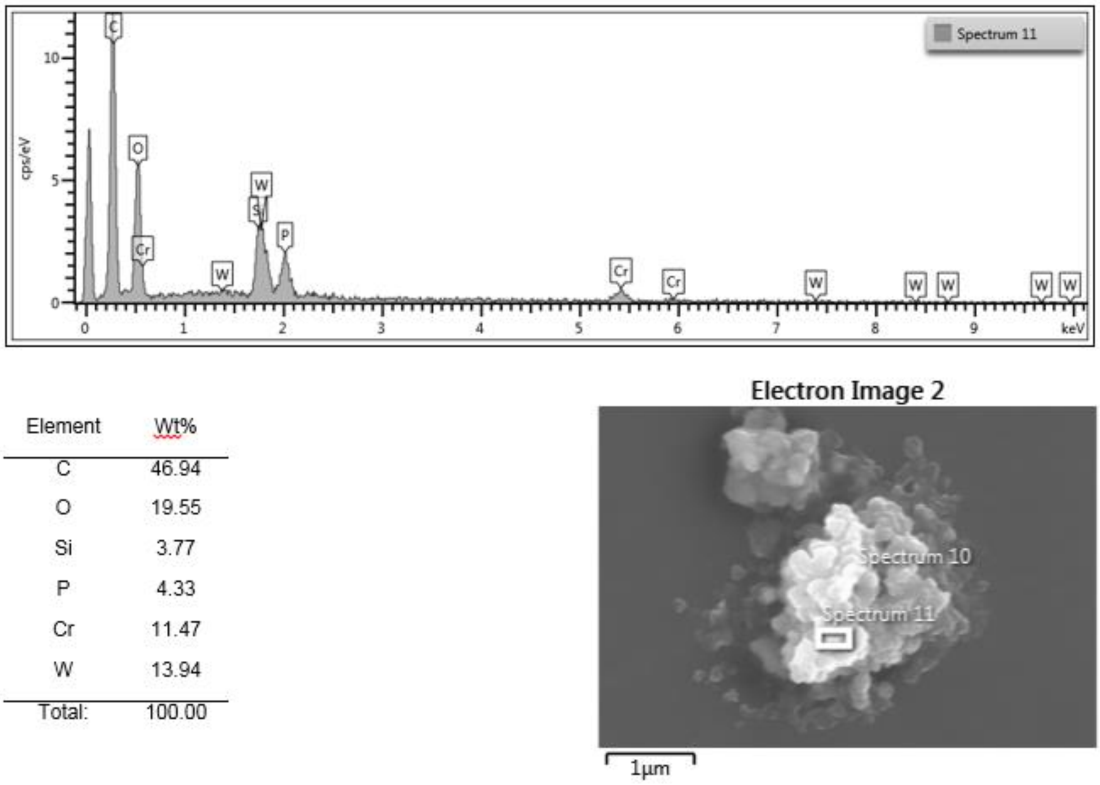

Element	Wt%
C	46.94
O	19.55
Si	3.77
P	4.33
Cr	11.47
W	13.94
Total:	100.00

Figure 5.16: EDX spectra of an agglomerate of cobalt chromium wear particles. Only chromium (Cr) was detected (11.5%wt), alongside a similar amount of tungsten (W) (13.9%wt), which was likely to be a residue from the isolation process. High amounts of carbon (C) and oxygen (O) (46.9%wt and 19.6%wt) suggest protein contamination around the particles.

5.4.3.2.1 CoCr particles generated in sterile water

Particles generated in the *in vitro* wear simulation of the MoM in water lubricant (section 5.3.2.1.2) were investigated using cold field emission SEM. Once collected, the particles were freeze dried (section 5.3.4) and sterilised (section 5.3.5). Subsequently, the particles were filtered through a polycarbonate membranes with 0.015µm pore size. The filter membranes were later mounted onto carbon tabs and sputter coated with iridium, prior to SEM analysis (section 5.3.6). The particles exhibited tendency to agglomerate, as shown in Figure 5.17. Most particles were round with irregular edges. Particle volume distribution shown a mean size of 154nm, with the sizes particles ranging from 50 to 650nm, as shown in Figure 5.18. The majority of the particles (~60%) were within the range of 80-180nm, some particles were as large as 650nm, however these represented a small proportion of all the particles generated (2%). The EDX spectra, as shown in Figure 5.19, confirmed the chemical composition of the particles, detecting chromium and cobalt peaks.

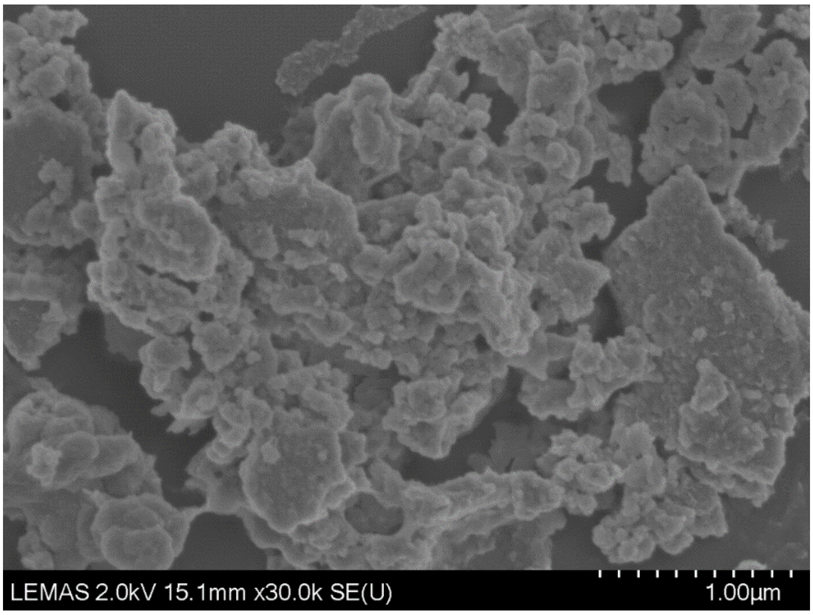

Figure 5.17: Cobalt chromium particles generated in a six-station spine simulator in sterile water.

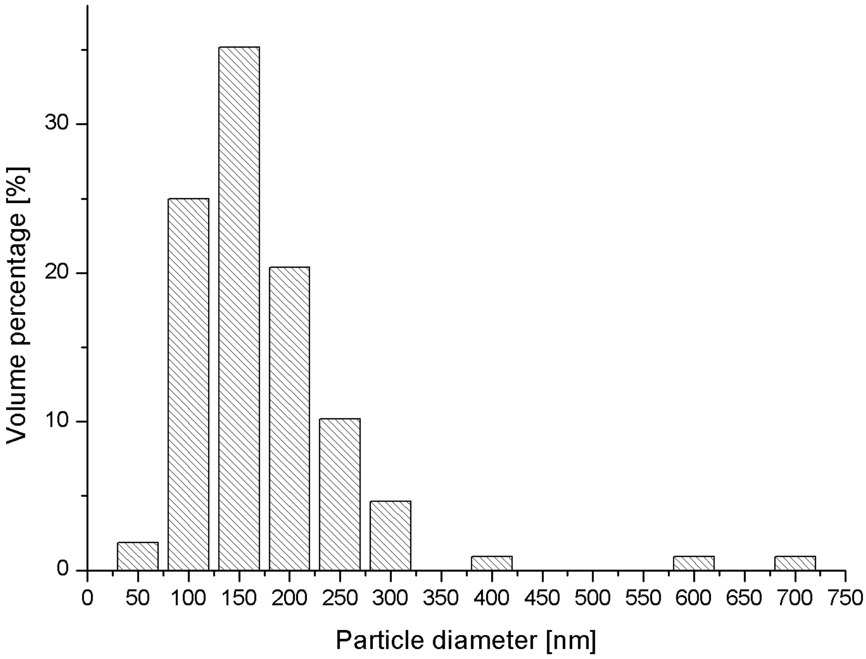

Figure 5.18: Particle volume distribution of cobalt chromium particles generated in a six-station spine simulator in sterile water. The mean particle size was 154nm.

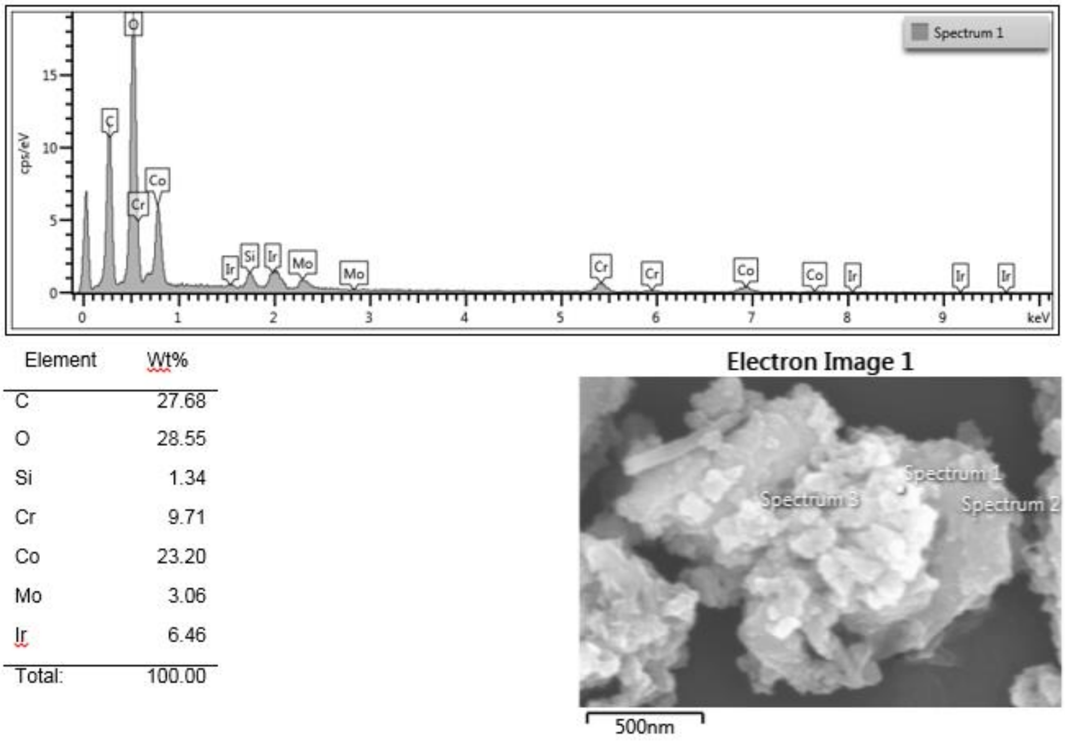

Element	Wt%
C	27.68
O	28.55
Si	1.34
Cr	9.71
Co	23.20
Mo	3.06
Ir	6.46
Total:	100.00

Figure 5.19: EDX spectra of cobalt chromium particles generated in the six-station spine simulator in sterile water. Chromium (Cr), cobalt (Co) and molybdenum (Mo) were confirmed in the spectroscopy. Iridium peaks were detected due to the iridium coating samples were coated with.

5.4.4 Characterisation of ceramic coating wear particles generated in the six-station spine simulator

5.4.4.1 Chromium nitride coating

Particles of the chromium nitride coating generated in the six-station spine simulator in sterile water (section 5.3.2.2) were investigated using the cold field emission SEM. Once collected from the lubricant, the particles were freeze dried (section 5.3.4) and sterilised (section 5.3.5). Subsequently, the particles were filtered through a polycarbonate membranes with 0.015µm pore size. The filter membranes were later mounted onto carbon tabs and sputter coated with iridium, prior to SEM analysis (section 5.3.6). The particles were sporadically found on the polycarbonate filter membrane. Morphologically, the particles were large, and often flake-like and some particles were found to have sharp edges, as shown Figure 5.20. Some of the particles were found to have topographical features such as pitting. The EDX spectra of the chromium nitride coating particle confirmed that the particles detected were of chromium origin, as shown in Figure 5.21.

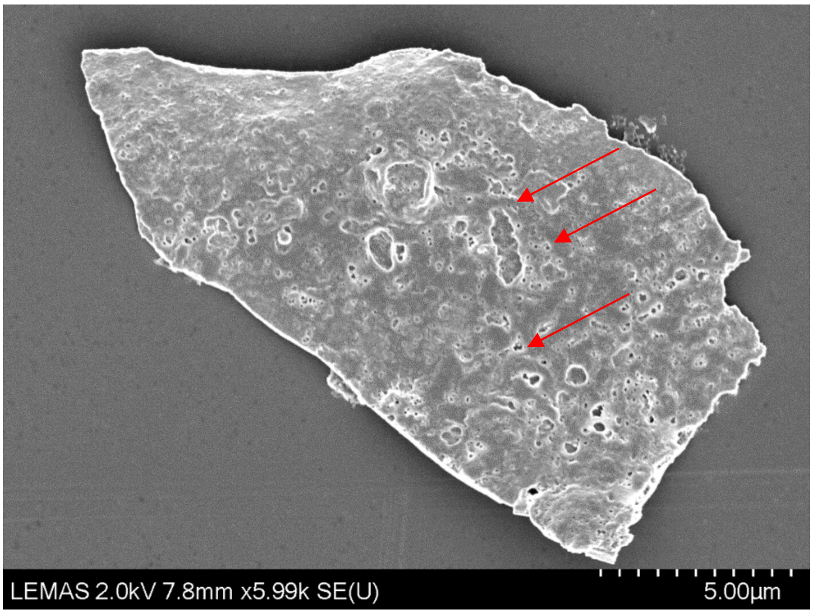

Figure 5.20: A chromium nitride coating particle generated in a six-station spine simulator in sterile water, filtered through a 0.015µm polycarbonate filter membrane. The particles were relatively large with sharp edges and flake-like morphology. Some pitting observed on the surface of the flake-like particles was observed, as indicated by the arrows.

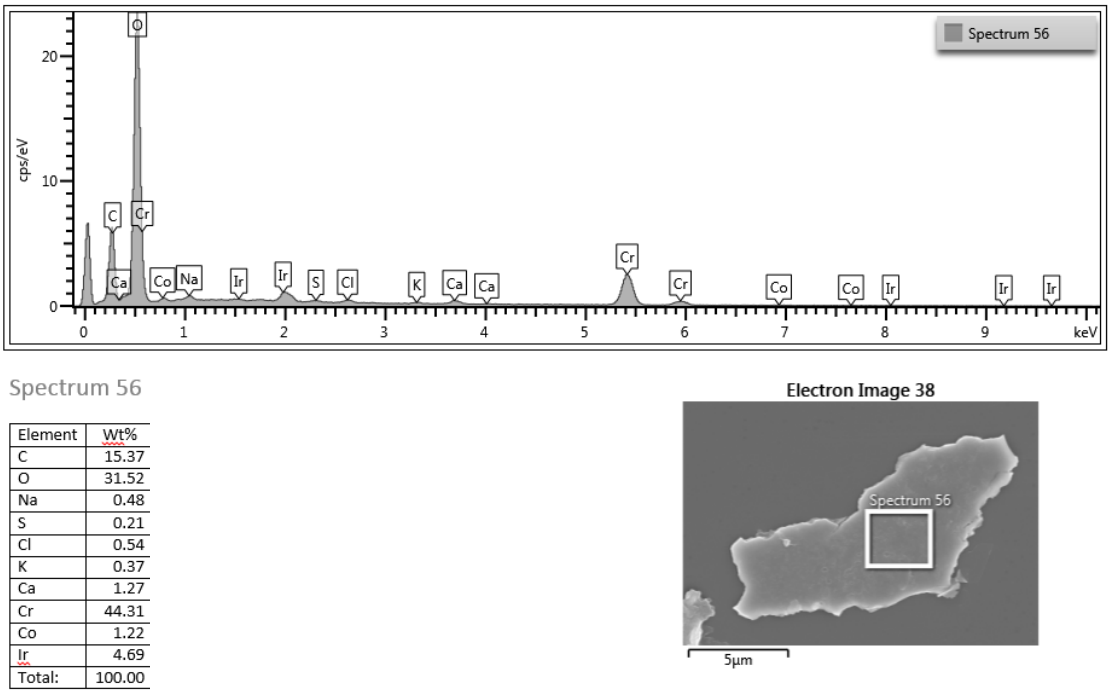

Spectrum 56

Element	Wt%
C	15.37
O	31.52
Na	0.48
S	0.21
Cl	0.54
K	0.37
Ca	1.27
Cr	44.31
Co	1.22
Ir	4.69
Total:	100.00

Figure 5.21: EDX spectra of chromium nitride particle generated in the six-station spine simulator in sterile water. Strong peaks and a large quantity (44.3%) of Chromium (Cr) were confirmed in the spectroscopy.

5.4.4.2 Silicon nitride coating

Particles of the silicon nitride coating generated in the six-station spine simulator in sterile water (section 5.3.2.2) were investigated using the cold field emission SEM. Once collected from the lubricant, the particles were freeze dried (section 5.3.4) and sterilised (section 5.3.5). Subsequently, the particles were filtered through a polycarbonate membranes with 0.015µm pore size. The filter membranes were later mounted onto carbon tabs and sputter coated with iridium, prior to SEM analysis (section 5.3.6). The particles were sporadically found on the polycarbonate filter membrane. Morphologically, the particles were large, flake-like and some particles were found to have sharp edges but a smooth surface, as shown in Figure 5.22. The EDX spectra confirmed that the particles found were of silicon origin (Figure 5.23).

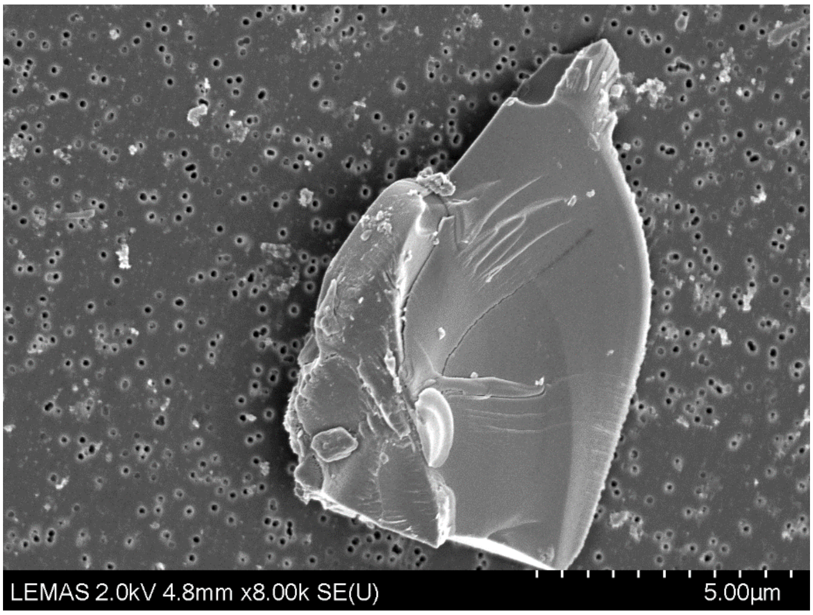

Figure 5.22: Silicon nitride coating particle generated in a six-station spine simulator in sterile water, filtered through a 0.1µm polycarbonate filter membrane. The particles were relatively large with sharp edges and flake-like morphology. Some nano-sized particles can also be observed, however it was not possible to confirm their origin with EDX.

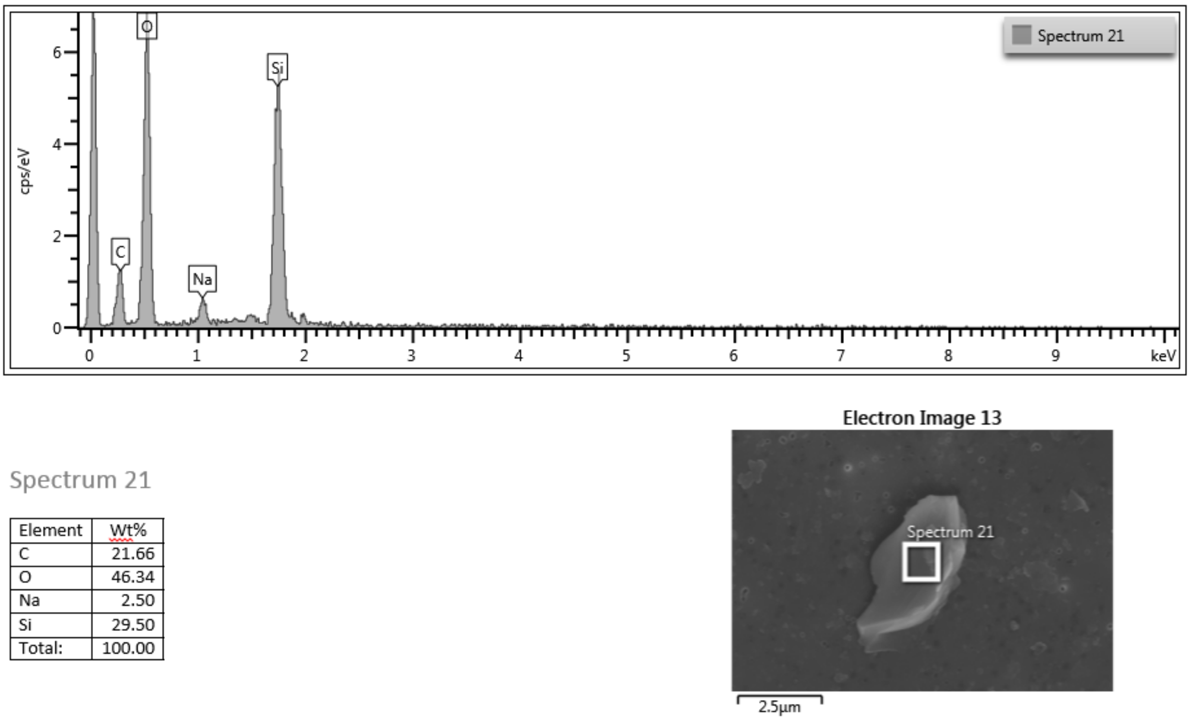

Spectrum 21

Element	Wt%
C	21.66
O	46.34
Na	2.50
Si	29.50
Total:	100.00

Figure 5.23: EDX spectra of a silicon nitride coating particle generated in the six-station spine simulator in sterile water. Strong peaks and large quantity (30%) of Silicon (Si) were confirmed in the spectroscopy.

5.4.5 Characterisation of model silicon nitride particles

5.4.5.1 Submicron silicon nitride particles

Commercially available submicron silicon nitride particles were investigated using cold field emission SEM. The particles sterilised (section 5.3.5) and suspended in sterile water. Next, the particles were filtered through a polycarbonate membranes with 0.015µm pore size. The filter membranes were later mounted onto carbon tabs and sputter coated with iridium, prior to SEM analysis (section 5.3.6). While the majority of the particles were clustered in large aggregates of particles, some, as shown in Figure 5.24, individual particles were irregular but with smooth edges and round in shape. Once sized, it was revealed mean size of the particles was 138nm (Figure 5.25). However, particles as large as 550 nm were also found. The EDX analysis confirmed the chemical composition of the particles, showing strong silicon and nitride peaks (Figure 5.26).

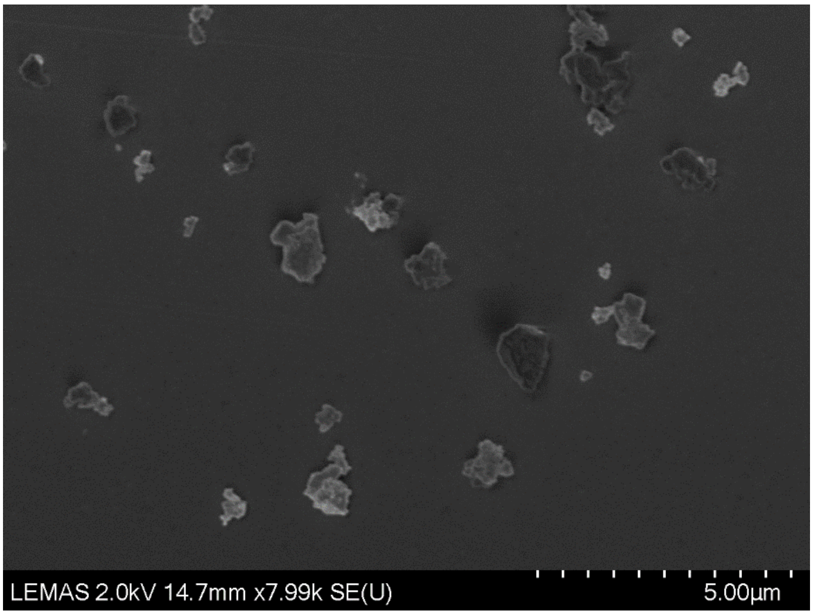

Figure 5.24: Submicron silicon nitride particles aggregated together. The particles were mostly irregular in shape, with some round particles also observed.

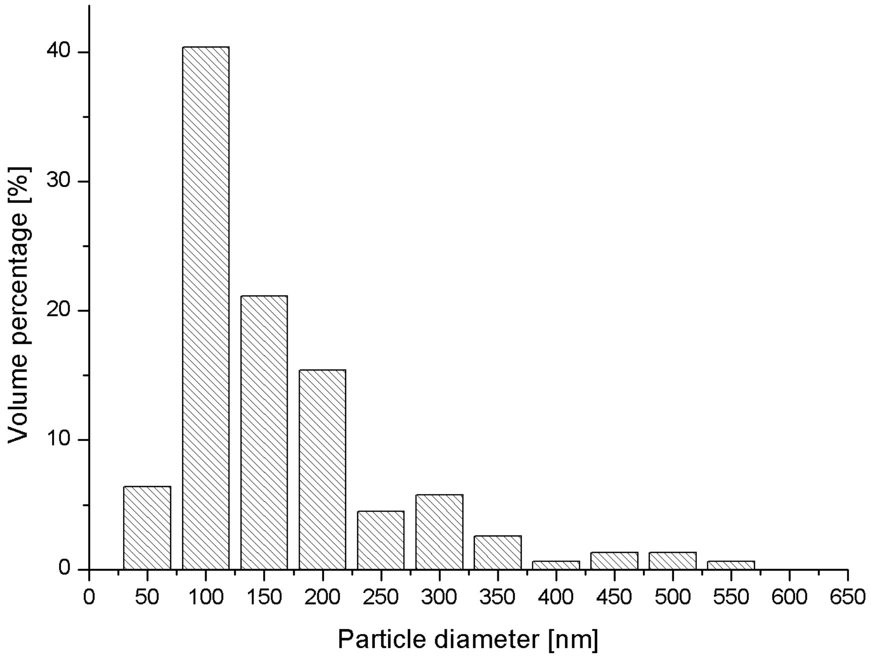

Figure 5.25: Particle size distribution of model silicon nitride particles of submicron size. The mean particle size was 138nm.

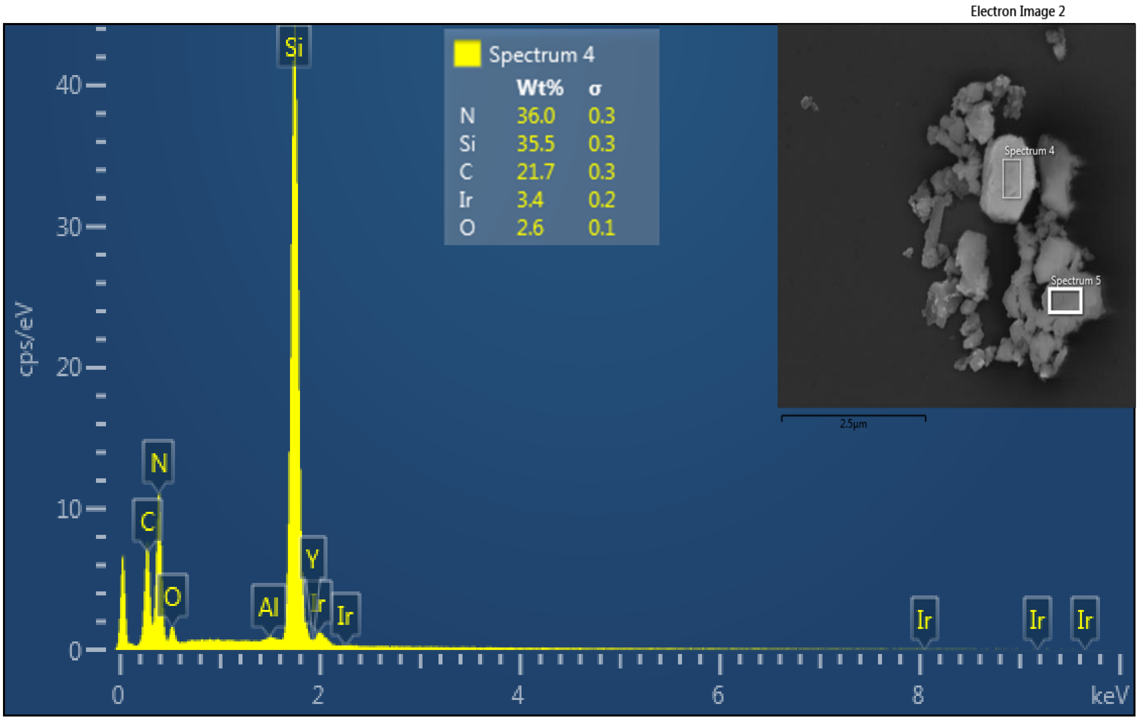
Electron Image 2
cps/eV
0
10
20
30
40
Si
N
C
O
Al
Y
Ir
Ir
Ir
Ir
Ir
0
2
4
6
8
keV
Spectrum 4
Spectrum 5
2.5µm

Spectrum 4

	Wt%	σ
N	36.0	0.3
Si	35.5	0.3
C	21.7	0.3
Ir	3.4	0.2
O	2.6	0.1

Figure 5.26: EDX spectra of the commercially available submicron silicon nitride particles. Strong Silicon (Si) and Nitrogen (N) peaks were detected in the analysis. Iridium peaks were detected due to the iridium coating samples were coated with.

5.4.5.2 Nanoscale silicon nitride particles

Commercially available nanoscale silicon nitride particles were investigated using cold field emission SEM. The particles sterilised (section 5.3.5) and suspended in sterile water. Next, the particles were filtered through a polycarbonate membranes with 0.015µm pore size. The filter membranes were later mounted onto carbon tabs and sputter coated with iridium, prior to SEM analysis (section 5.3.6). The analysis (Figure 5.27) revealed a strong tendency of the particles to agglomerate, as well as their smooth, regular edges and round shape. Sizing of the particles showed a mean particle size of 43nm. Sized particles ranged from 20 to 120 nm, as shown in Figure 5.27. EDX analysis of the nanoscale silicon nitride particles, shown in Figure 5.28, confirmed their chemical composition, showing strong silicon and nitrogen peaks in the spectrum.

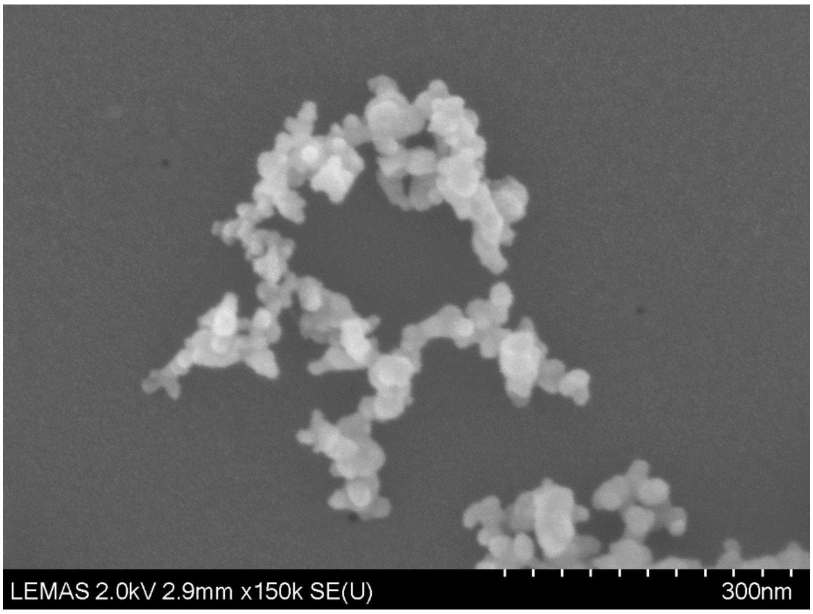

Figure 5.27: Nanoscale silicon nitride model particles agglomerated together. High magnification (x150k) images revealed that the particles were predominantly round and had smooth edges.

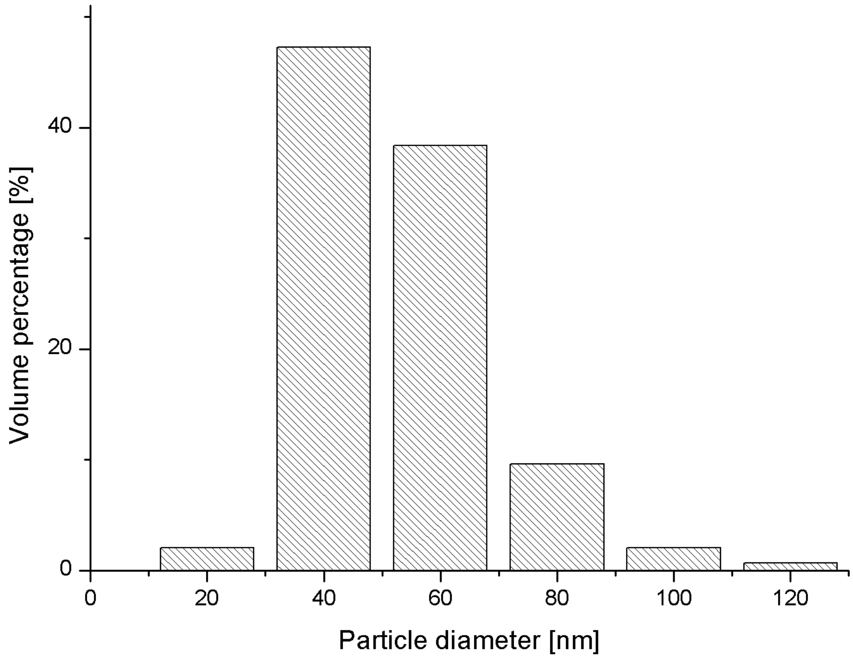

Figure 5.28: Particle size distribution of model silicon nitride particles of nanoscale size. The mean particle size was 43nm.

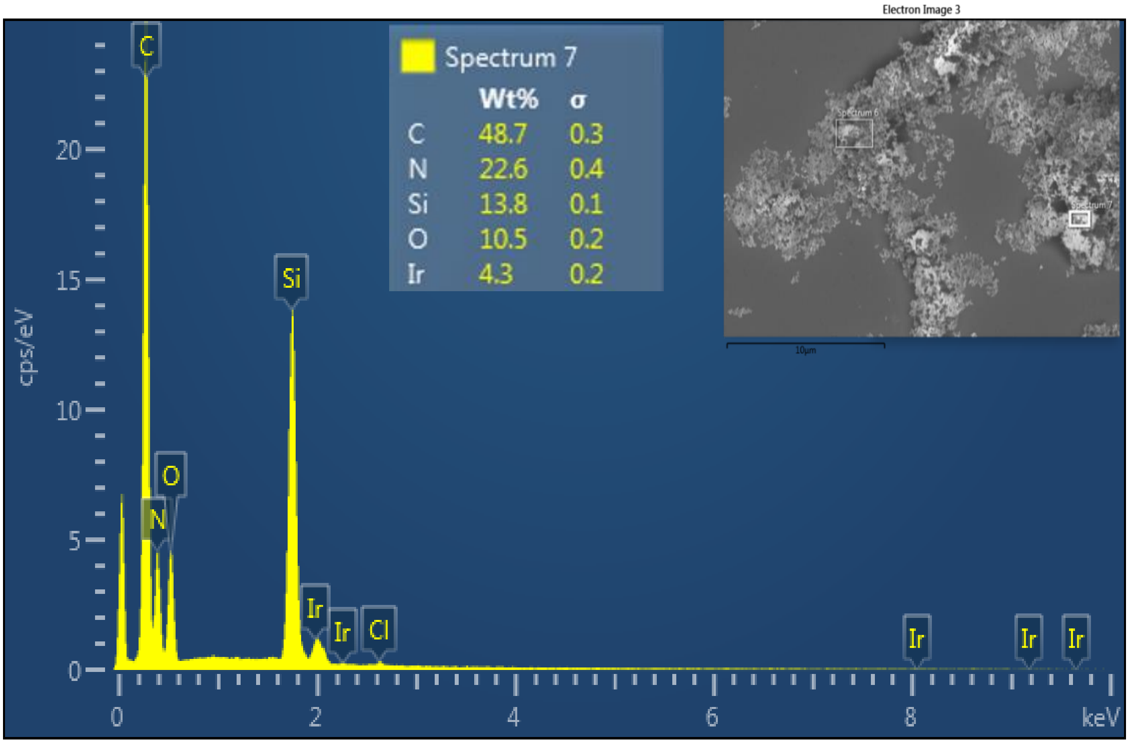

Spectrum 7

	Wt%	σ
C	48.7	0.3
N	22.6	0.4
Si	13.8	0.1
O	10.5	0.2
Ir	4.3	0.2

Figure 5.29: EDX spectra of the commercially available nanoscale silicon nitride particles. Strong Silicon (Si) and Nitrogen (N) peaks were detected in the analysis. Iridium peaks were detected due to the iridium coating samples were coated with.

5.4.6 Growth curve of L929 murine fibroblasts and primary porcine dural fibroblasts

The study assessed viability of the L929 cell line seeded at different densities (section 5.3.9), in order to determine the optimum cell seeding density, to ensure cells remained viable and did not exhaust nutrients present in medium over 6 days of culture. Cell viability was measured at days 0, 1, 3 and 6 using the ATPLite assay. The result were expressed as counts per second.

The ATPLite results demonstrated that the seeding density of L929 cells influenced their viability, when measured over a 6-day period. The highest cell seeding density ($5x10^5$ cells. well^{-1}) showed a steady decrease in cell viability from day 1 onwards. The cells seeded at densities $5x10^3$.ml^{-1}, $1x10^4$.ml^{-1}, $5x10^4$.ml^{-1} and $5x10^4$.ml^{-1} for each well showed a steady exponential increase in cell viability over the duration of the experiment, as shown in Figure 5.30. However, at the day 1 and day 3 timepoints the cell numbers appeared to increase at a slower rate for $5x10^4$ and $1x10^5$ cells.ml^{-1} test groups. As such, it was determined that the most optimum cell seeding density of L929 murine fibroblasts was $1x10^4$ cells per well.

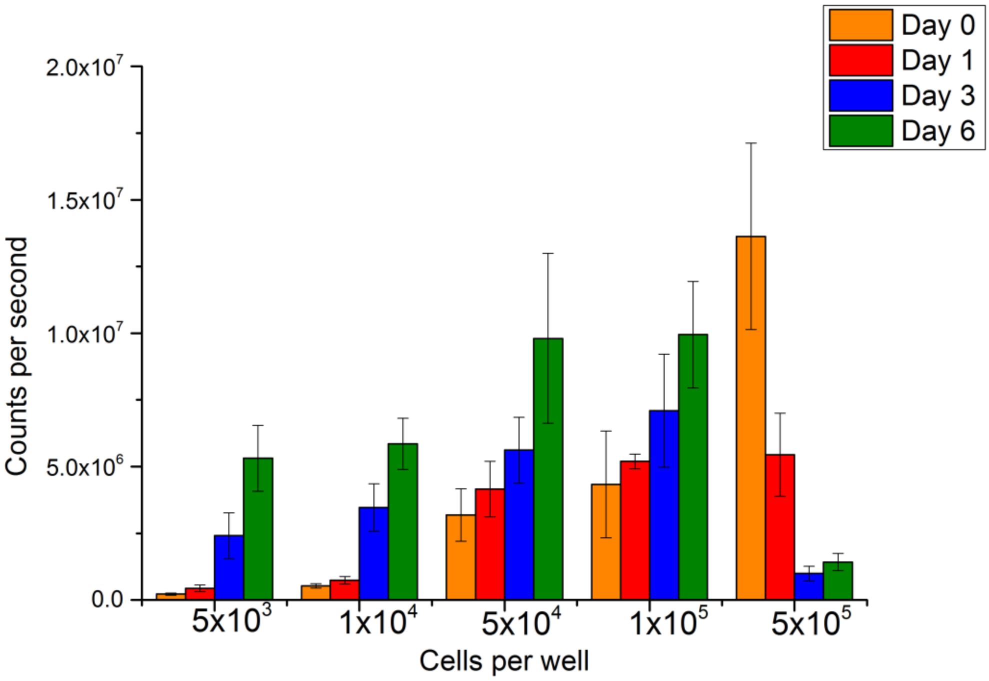

Figure 5.30: Cell viability of L929 murine fibroblasts seeded at different cell seeding densities determined using the ATPLite assay. The error bars represent 95% confidence limits.

Cell viability of primary dural fibroblasts was also affected by the seeding density of cells (Figure 5.31). The two lowest seeding densities – 5x10^2 and 1x10^3 cells.well^{-1} resulted in relatively low counts per second, whilst the two highest seeding densities – 1x10^4 and 5x10^4 cells.well^{-1} showed a plateau in cell growth after day 1 and reduced cell viability at day 6 (relative to the day 3 timepoint), indicating that nutrients were insufficient to sustain cell growth over a 6-day period for these seeding densities. The cell seeding density of 5x10^3 cells.well^{-1} showed a steady increase in cell viability over the 6-day period, and thus was selected as the optimum cell seeding density for further experiments using primary porcine dural fibroblasts.

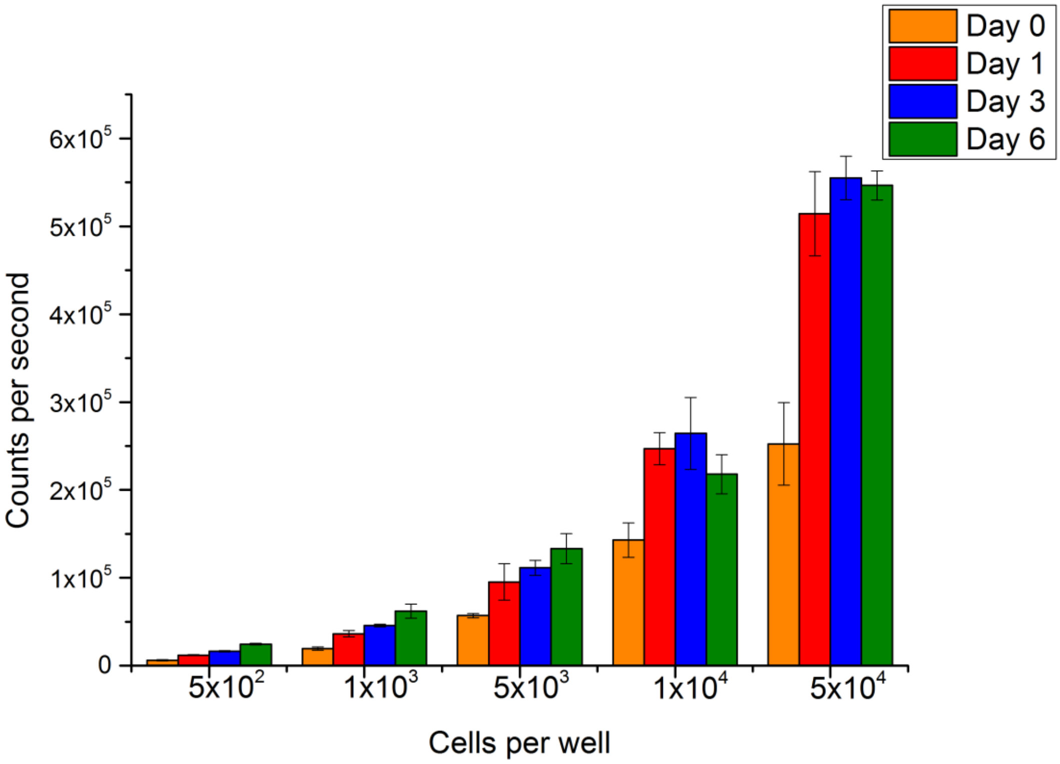

Figure 5.31: Cell viability of primary porcine dural fibroblasts seeded at different cell seeding densities determined using the ATPLite assay. The error bars represent 95% confidence limits.

5.4.7 Investigation of the cytotoxic effects of cobalt chromium wear particles on L929 murine fibroblasts and primary porcine dural fibroblasts

5.4.7.1 L929 murine fibroblasts

The effects of cobalt chromium wear particles generated using a six-station pin-on-plate wear rig and six-station spine simulator on cell viability of L929 murine fibroblasts was investigated using the ATP-Lite assay. The L929 cells were seeded at a concentration of $1x10^4$ $cells.well^{-1}$. For 6 days the cells were cultured in the presence of particle volumes per cell of $50µm^3$ to $0.05µm^3$ (n=6). The results were expressed as a percentage of the cells only negative control. Descriptive statistics were performed on the raw data using the one-way ANOVA ($\alpha=0.05$) and individual differences between the means were determined using the T-method to calculate the MSD. Significant adverse effects on the cell viability were identified ($p<0.05$, CI 95%).

Overall, the ATPLite assay demonstrated that cobalt chromium wear particles significantly reduced the cell viability of L929 murine fibroblasts. The particle only control generated low counts per second and therefore indicated that the particles did not interfere with the assay. The highest volume of particles per cell ($50µm^3$) of the CoCr particles generated in the six-station pin-on-plate wear rig significantly reduced cell viability ($p<0.05$, CI 95%) from day 1 (Figure 5.32), reaching as low as 10% viability relative to the cells-only negative control at day 6. Such reduction of cell viability was on par with the positive control (Camptothecin). Particle volume of $5µm^3$ per cell was also found to significantly reduce cell viability of L929 fibroblasts at days 1 and 6. The lowest dose of pin-on-plate generated particles ($0.5µm^3$ per cell) did not have a significant effect on L929 cell viability.

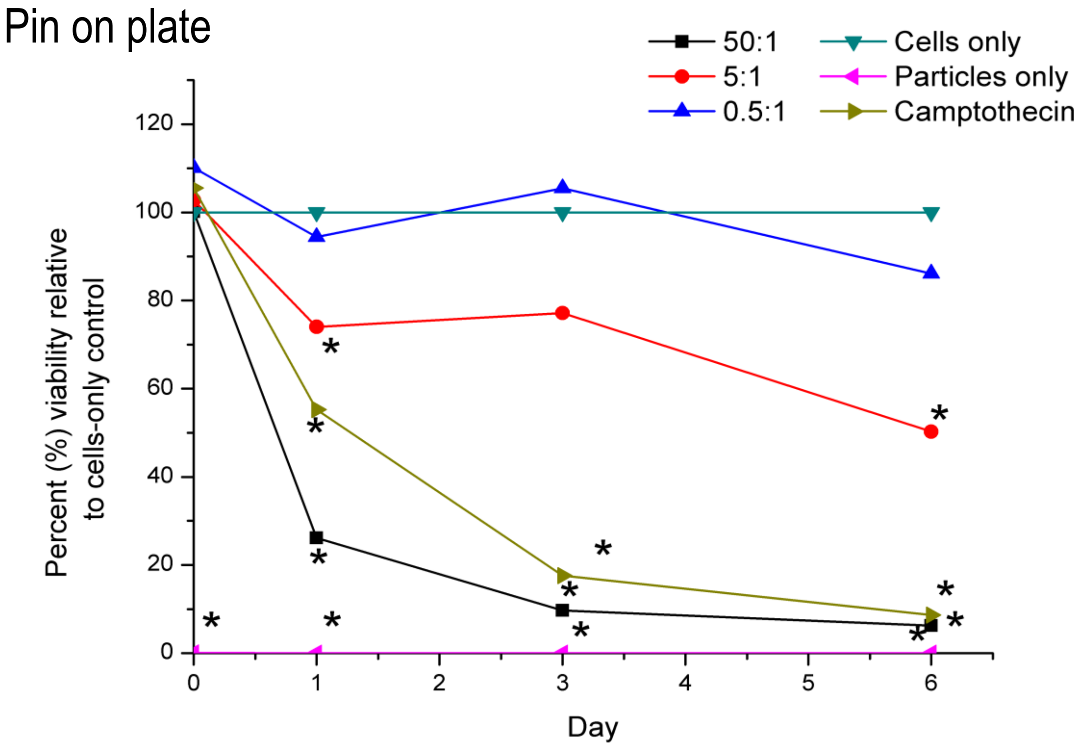

Figure 5.32: Effects of cobalt chromium wear particles generated in the six-station pin-on-plate wear rig on L929 murine fibroblasts cell viability. Data was analysed using ANOVA test (α=0.05) and the T-method. Significantly ($p<0.05$) reduced cell viability was indicated with an asterisk (*)

Similar findings were observed for the L929 fibroblasts cultured with cobalt chromium particles generated in the six-station spine simulator, with sterile water used as a lubricant (Figure 5.33). The two highest particle volumes per cell (50 and 5µm^3) were found to significantly reduce cell viability. The particle dose of 50µm^3 particles per cell significantly decreased the viability of L929 cells from day 1, reaching as low as 30% of the viability relative to the cells only negative control at day 6. The particle volume of 5µm^3 per cell was also found to significantly reduce cell viability of L929 fibroblasts at days 1 and 6. The lowest dose of particles generated in the simulator (0.5µm^3 per cell) did not have a significant effect on the cell viability at point. The particles only control achieved low counts per second results, and indicated that the particles did not interfere with the assay. The positive control (Camptothecin) had the desired effect of significantly reducing the cell viability of L929 fibroblasts from day 1.

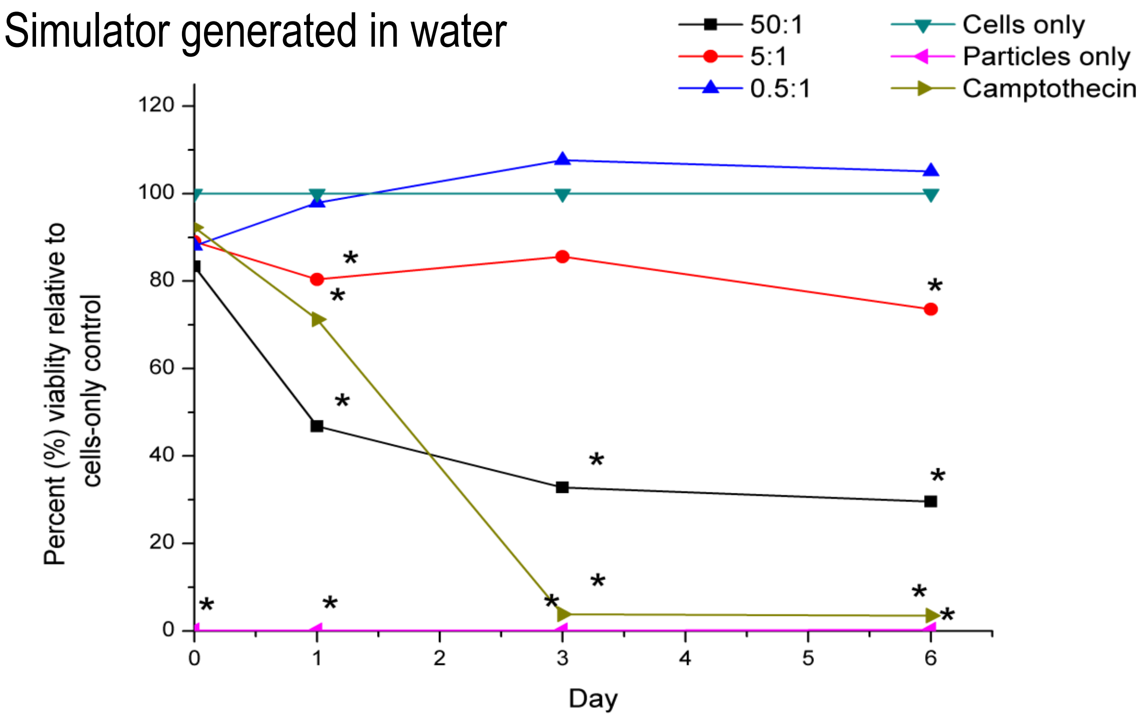

Figure 5.33: Effects of cobalt chromium wear particles generated in the six-station spine simulator in water on L929 murine fibroblasts cell viability. Data was analysed using ANOVA test (α=0.05) and the T-method. Significantly (p<0.05) reduced cell viability was indicated with an asterisk (*)

High doses of cobalt chromium wear particles generated in the six-station spine simulator with foetal bovine serum used as a lubricant showed adverse effects on the cell viability of L929 murine fibroblasts, as shown in Figure 5.34. The highest volume concentration (50µm^3 particles per cell) significantly reduced the cell viability of L929 cells from day 1, reaching 60% viability relative to the cells-only control at day 6. The remaining particle concentrations (5 and 0.5µm^3 particles per cell) also reduced the cell viability from day 1, however these changes were not found to be statistically significant at any timepoint. No interference was detected in the particles only control. The positive control significantly reduced the cell viability of L929 fibroblasts from day 1.

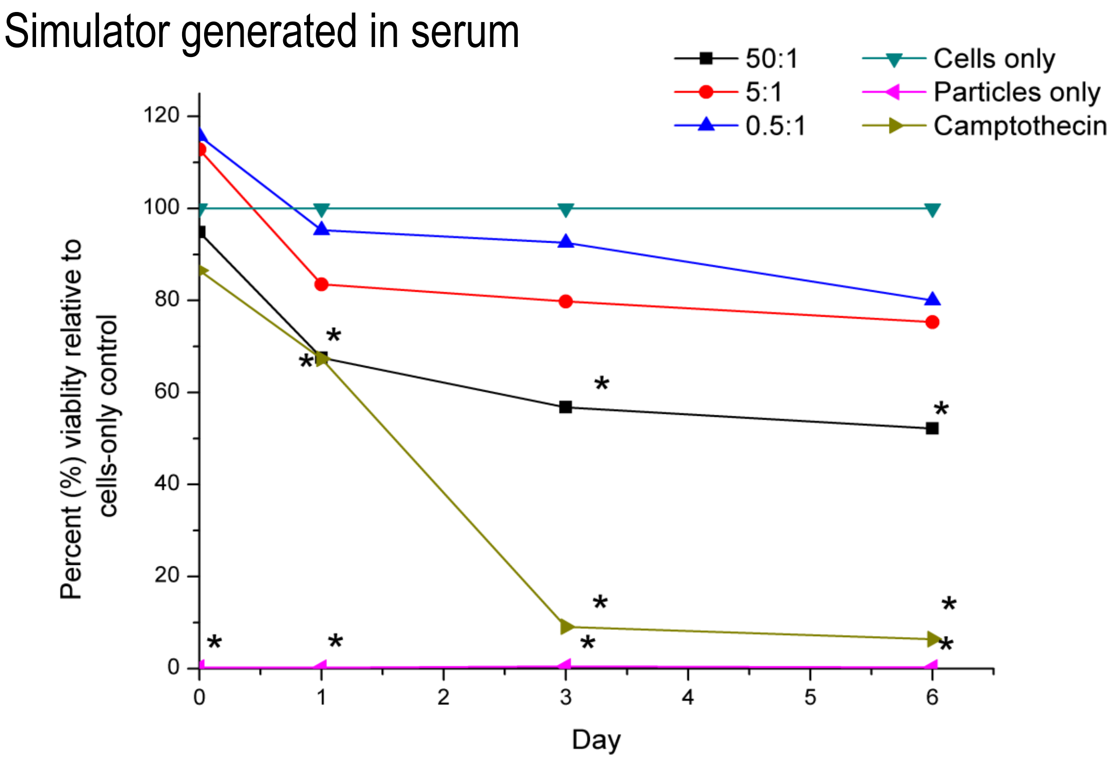

Figure 5.34: Effects of cobalt chromium wear particles generated in the six-station spine simulator in foetal bovine serum on L929 murine fibroblasts cell viability. Data was analysed using ANOVA test (α=0.05) and T-method. Significantly ($p<0.05$) reduced cell viability was indicated with an asterisk (*)

5.4.7.2 Primary porcine dural fibroblasts

The effects of cobalt chromium wear particles generated using the six-station pin-on-plate wear rig and six-station spine simulator on cell viability of primary porcine dural fibroblasts was investigated using the ATP-Lite assay. The dural fibroblast cells were seeded at a concentration of $5x10^3$ cells.well^{-1}. For 6 days, the cells were cultured in the presence of particles volumes per cell of 50μm^3 to 0.05μm^3 (n=6). The results were expressed as a percentage of the cells only negative control. Descriptive statistics were performed on the raw data using the one-way ANOVA and individual differences between the means were determined using the T-method.

In general, the ATPLite assay showed that cobalt chromium wear particles generated in the six-station pin on plate wear rig and the six-station spine simulator had little or no effect on the viability of the primary dural fibroblasts. The particles only control achieved low counts per second results, and therefore indicated that the particles did not interfere with the assay. The positive control significantly reduced the cell viability of the primary porcine dural fibroblasts from day 1.

5.4.7.3 Primary porcine dural fibroblasts

None of the particle concentrations, of particles generated in sterile water in the six-station pin-on-plate wear rig, caused a significant decrease in cell viability of the porcine dural fibroblasts at any of the timepoints tested, as shown in Figure 5.35. On day 6, cells cultured with the lowest particle density per cell (0.5µm^3/cell) achieved a relative cell viability of 110%.

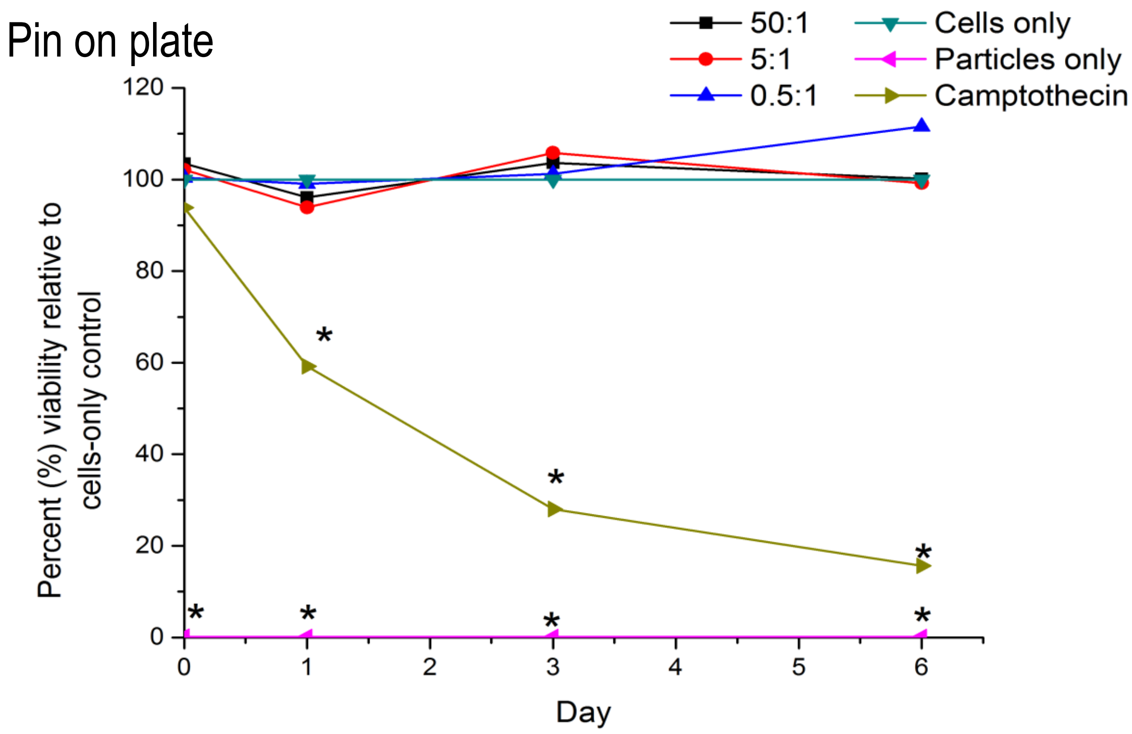

Figure 5.35: Effects of cobalt chromium wear particles generated in sterile water in six-station pin-on-plate wear rig on primary porcine dural fibroblasts cell viability. Data was analysed using ANOVA test (α=0.05) and the T-method. Significantly (p<0.05) reduced cell viability was indicated with an asterisk (*)

Similarly to the pin-on-plate-generated particles, those particles generated in sterile water in the spine simulator had no significant effect on the cell viability of primary dural fibroblasts (Figure 5.36). None of the particle concentrations significantly decreased the cell viability. Throughout the 6 days period the highest particle volume (50µm^3/cell) has slightly reduced the cell viability to 90-95%, relative to the cells-only control, whilst the cells cultured with lower particle doses (0.5-5µm^3/cell) achieved viability between 98% and 110%, relative to the cells-only control.

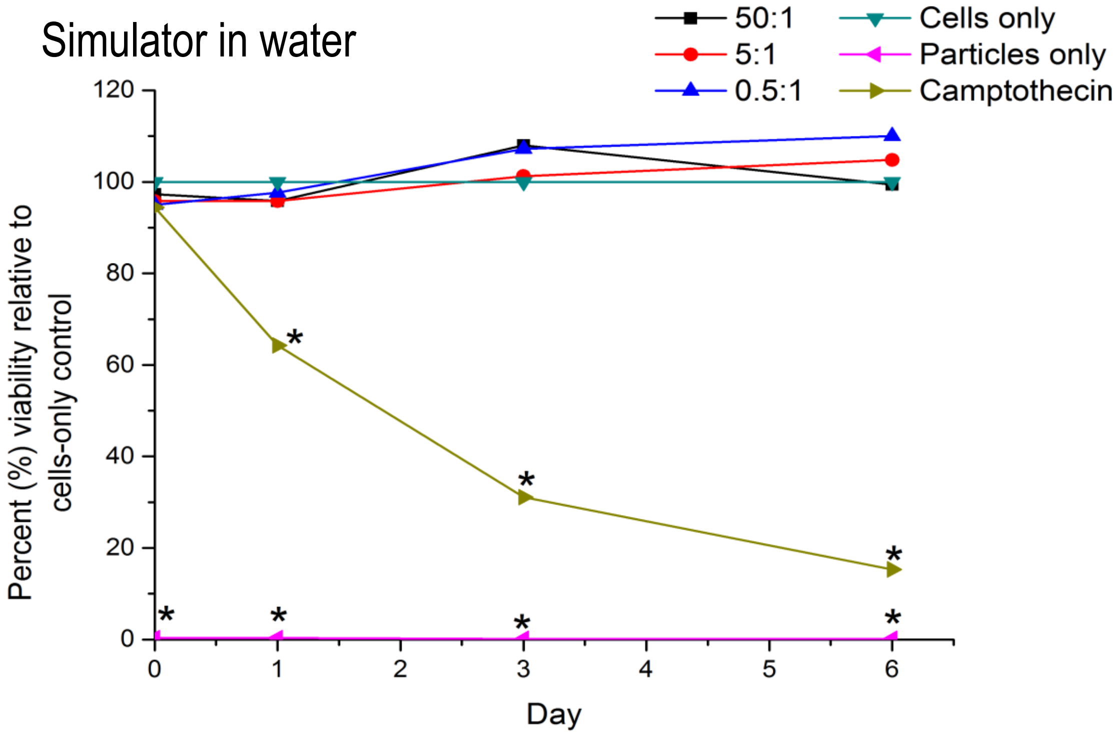

Figure 5.36: Effects of cobalt chromium wear particles generated in sterile water in six-station spine simulator on primary porcine dural fibroblasts cell viability. Data was analysed using ANOVA test (α=0.05) and the T-method. Significantly ($p<0.05$) reduced cell viability was indicated with an asterisk (*)

When cultured with cobalt chromium particles generated in foetal bovine serum in the six-station spine simulator, the viability of primary porcine fibroblasts was not significantly reduced. At all timepoints, relative to the cells-only control, the cells cultured with all particle doses (0.5-50µm^3/cell) ranged between 95% and 110%, as shown in Figure 5.37.

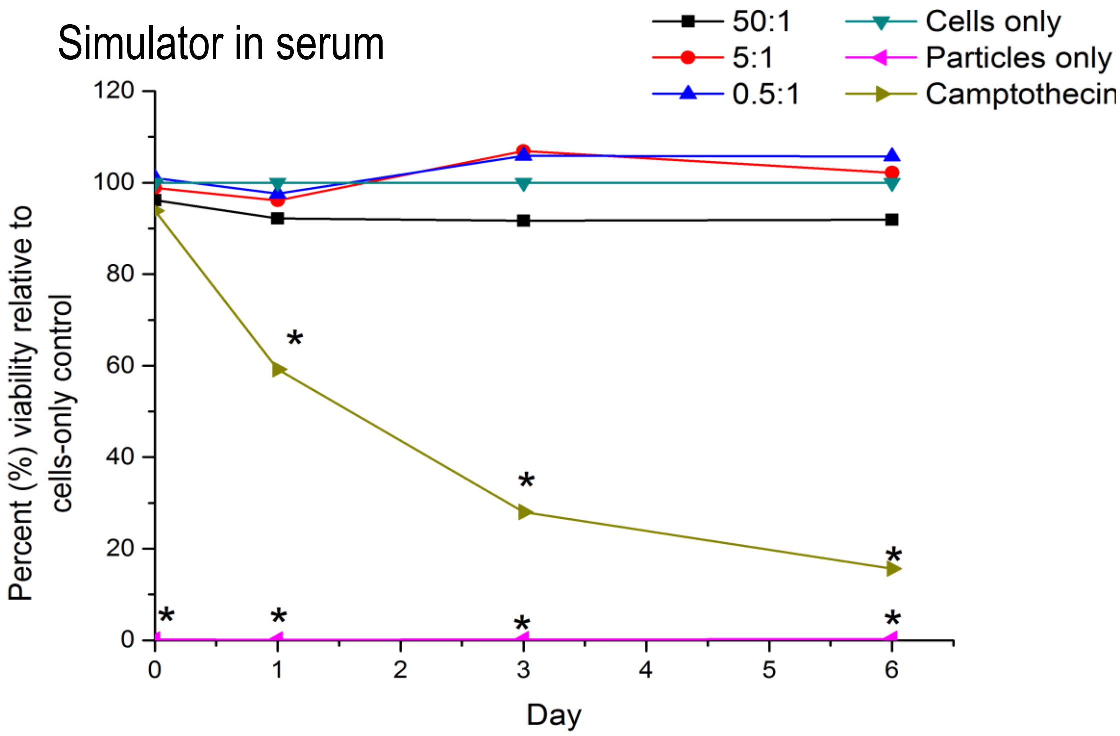

Figure 5.37: Effects of cobalt chromium wear particles generated in foetal bovine serum in the six-station spine simulator on primary porcine dural fibroblasts cell viability. Data was analysed using ANOVA test (α=0.05) and the T-method. Significantly ($p<0.05$) reduced cell viability was indicated with an asterisk (*)

5.4.8 Investigation of the cytotoxic effects of model silicon nitride particles (submicron and nanoscale) on L929 murine fibroblasts and primary porcine dural fibroblasts

5.4.8.1 L929 murine fibroblasts

The effects of commercially available silicon nitride particles (submicron and nanoscale) on cell viability of L929 murine fibroblasts was investigated using ATP-Lite assay. The L929 cells were seeded at a concentration of $1\text{x}10^4$ cells.well^{-1}. For 6 days the cells were cultured in the presence of particles volumes per cell of 500μm^3 to 5μm^3 (n=6). The results were expressed as a percentage of the cells only negative control. Descriptive statistics were performed on the raw data using the one-way ANOVA and individual differences between the means were determined using the T-method.

When cultured with submicron silicon nitride particles, the viability of L929 fibroblasts was not significantly reduced at any timepoint, as shown in Figure 5.38. Up to day 3, the viability of cells cultured with all particle doses (500-5µm^3/cell) was found to be within the range of 100-110%, relative to the cells-only control. At day 6, all test groups were found to have their cell viability reduced to approximately 80%, however, this reduction was not found to be statistically significant (p>0.05, CI 95%). The particles only control achieved low counts per second results, indicating that the particles did not interfere with the assay. The positive control significantly reduced the cell viability of the L929 fibroblasts from day 1.

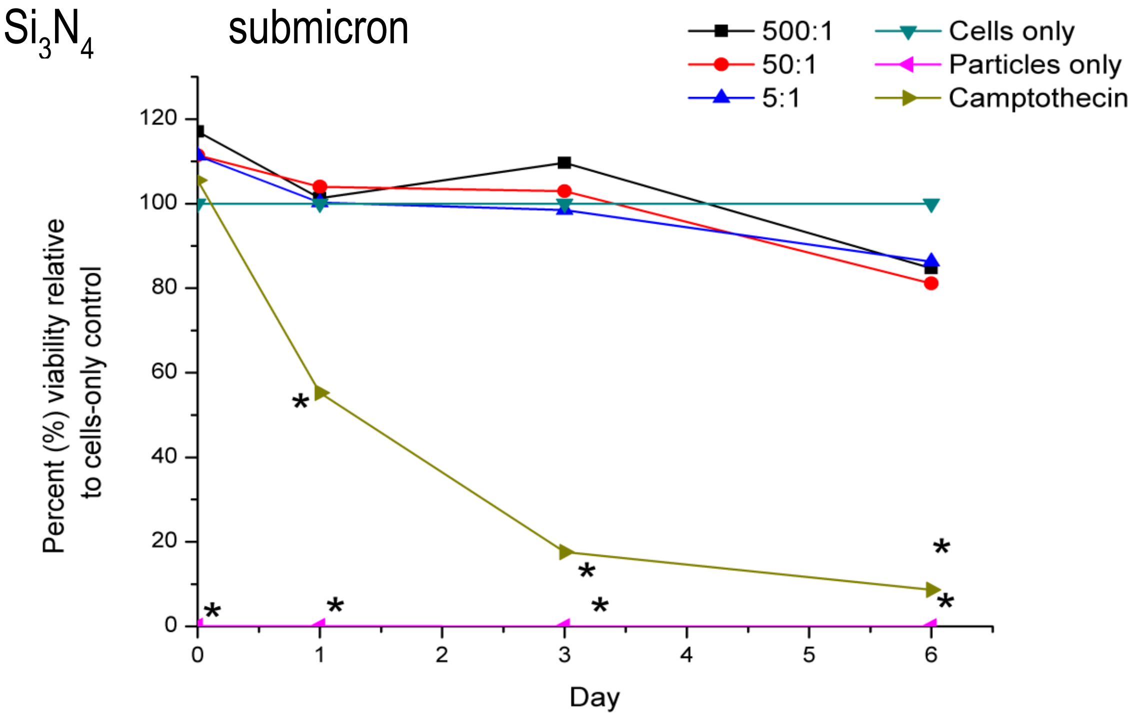

Figure 5.38: Effects of commercially available submicron silicon nitride particles on L929 murine fibroblasts. Data was analysed using ANOVA test (α=0.05) and the T-method. Significantly (p<0.05) reduced cell viability was indicated with an asterisk (*)

The highest dose of nanoscale silicon nitride particles (500µm^3/cell) caused a reduction in the cell viability of the L929 fibroblasts (Figure 5.39). Only on day 1, the reduction in the cell viability was found to be statistically significant (p<0.05, CI 95%); at each subsequent timepoint it was not. Other particle concentrations (5-50µm^3/cell) did not have a significant effect on the cell viability of L929 fibroblasts. In fact, both doses of 5 and 50µm^3 particles per cell resulted in a cell viability between 100% and 110%, relative to cells-only control. No interference between the assay and the particles were detected in the particles-only negative control. The positive control significantly reduced the cell viability of L929 fibroblasts from day 1.

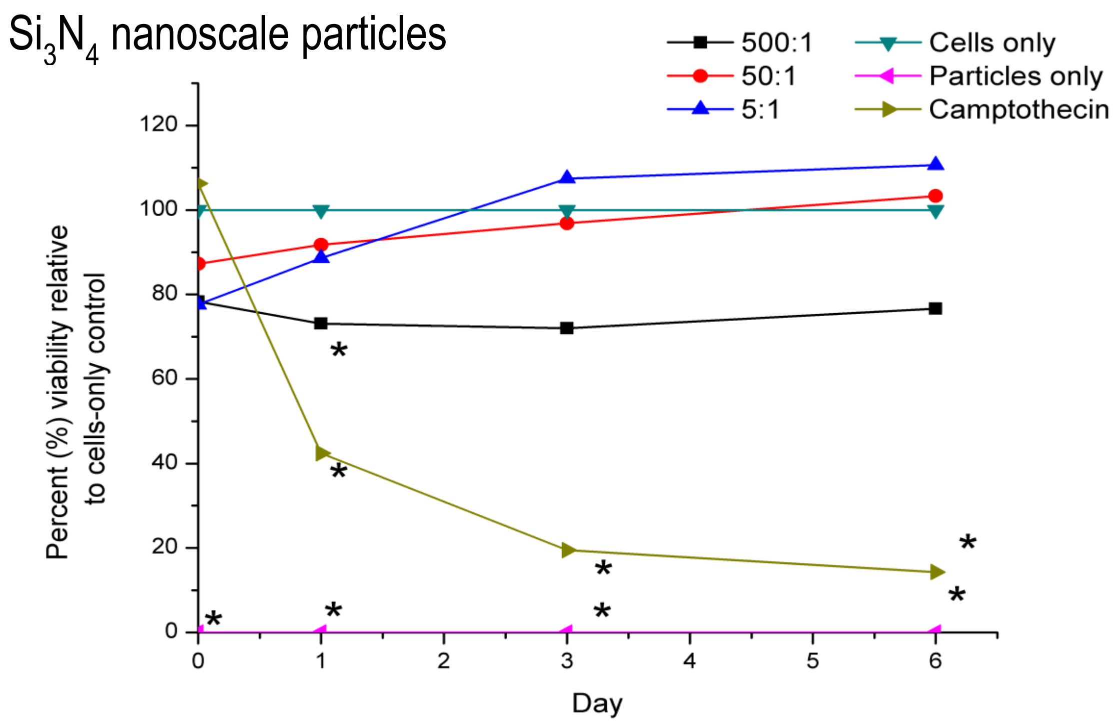

Figure 5.39: Effects of commercially available nanoscale silicon nitride particles on L929 murine fibroblasts. Data was analysed using ANOVA test (α=0.05) the T-method. Significantly ($p<0.05$) reduced cell viability was indicated with an asterisk (*)

5.4.8.2 Primary porcine dural fibroblasts

The effects of commercially available silicon nitride particles (submicron and nanoscale) on the cell viability of primary porcine dural fibroblasts was investigated using the ATP-Lite assay. The dural fibroblast cells were seeded at a concentration of $5x10^3$ cells/well. For 6 days the cells were cultured in the presence of particles volumes per cell of $500µm^3$ to $5µm^3$ (n=6). The results were expressed as a percentage of the cells only negative control. Descriptive statistics were performed on the raw data using the one-way ANOVA and individual differences between the means were determined using the T-method to calculate the MSD. Significant ($p<0.05$, CI 95%) adverse effects on the cell viability were identified.

Only on day 1 the highest particle doses (50-500µm^3/cell) caused a significant reduction in cell viability (p<0.05, CI 95%). At each subsequent timepoint cells cultured with those particle concentrations had higher counts per seconds and have increased the cell viability, relative to cells-only control. The lowest particle dose (5µm^3/cell) did not cause a reduction in cell viability at any timepoint and reached approximately 110% of relative cell viability on day 6. Camptothecin significantly reduced the cell viability of dural fibroblasts from day 1, reaching as low as 35%, relative to cells-only control, on day 6. Measurements of the particles only control group did not detect any interference with the assay.

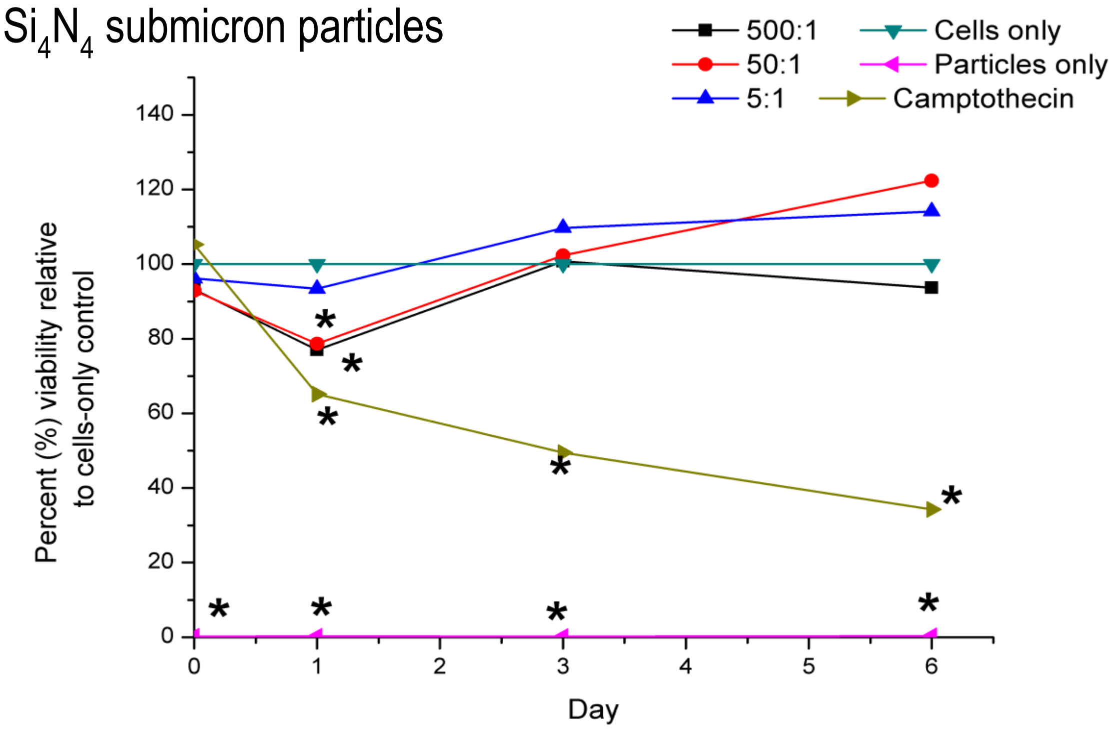

Figure 5.40: Effects of commercially available submicron silicon nitride particles on primary porcine dural fibroblasts. Data was analysed using ANOVA test (α=0.05) and T-method. Significantly (p<0.05) reduced cell viability was indicated with an asterisk (*)

Similar results were observed for the primary dural fibroblasts cultured with nanoscale silicon nitride particles, whereby only the highest dose (500µm^3/cell) caused a significant reduction of cell viability, relative to cells-only control, but only at the day 1 timepoint. As shown in Figure 5.41, cell viability of cells cultured with the remaining particle concentrations, at all timepoints, ranged between 105% and 130%. At all timepoints, a significant reduction in cell viability was observed for the positive control (Camptothecin) and no interference with the assay, caused by the particles-only, was detected.

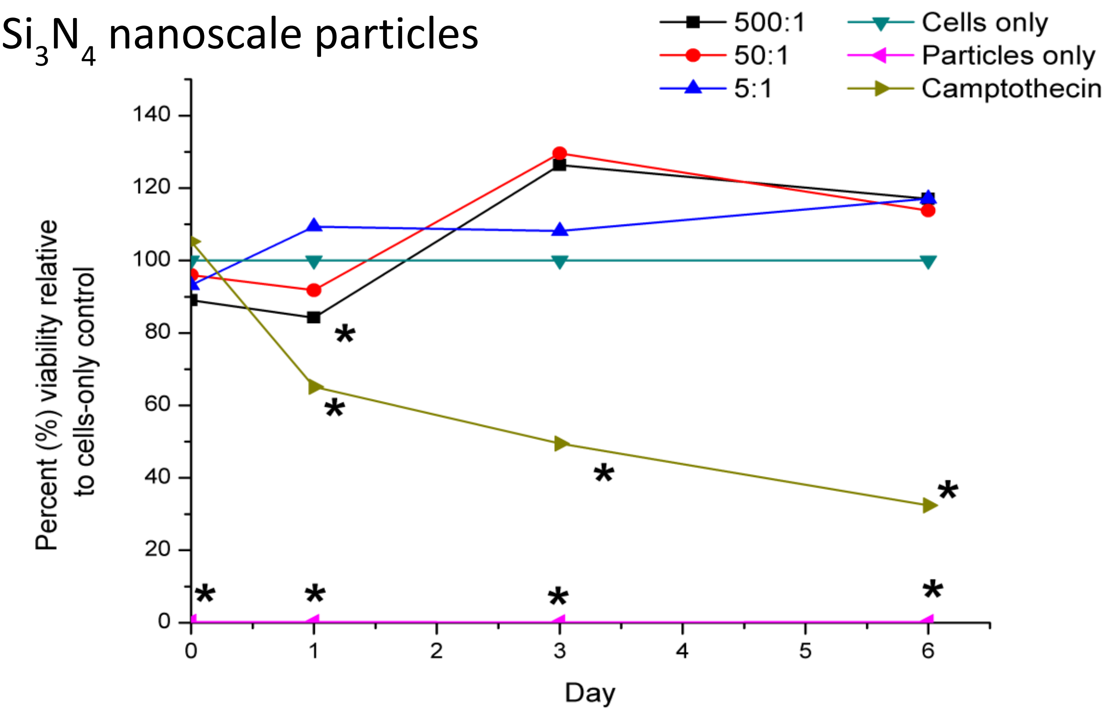

Figure 5.41: Effects of commercially available nanoscale silicon nitride particles on primary porcine dural fibroblasts. Data was analysed using ANOVA test (α=0.05) and the T-method. Significantly ($p<0.05$) reduced cell viability was indicated with an asterisk (*)

5.4.9 Investigation of the cytotoxic effects of ceramic coatings wear particles (chromium nitride and silicon nitride) on L929 murine fibroblasts and primary porcine dural fibroblasts

5.4.9.1 L929 murine fibroblasts

The effects of ceramic coating wear particles – chromium nitride and silicon nitride, generated using the six-station spine simulator on cell viability of L929 murine fibroblasts was investigated using the ATP-Lite assay. The L929 cells were seeded at a concentration of $1x10^4$ cells.well^{-1}. For 6 days the cells were cultured in the presence of particles volumes per cell of 50µm^3 to 0.05µm^3 (n=6). The results were expressed as a percentage of the cells only negative control. Descriptive statistics were performed on the raw data using the one-way ANOVA and individual differences between the means were determined using the T-method. Significant ($p<0.05$, CI 95%) adverse effects on the cell viability were identified.

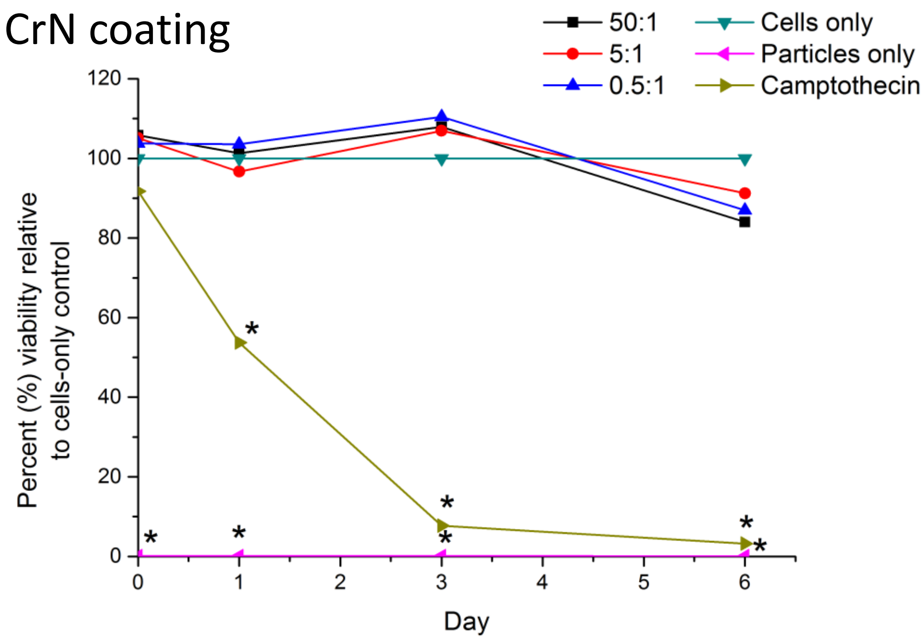

Figure 5.42: Effects of chromium nitride coating particles generated in sterile water in the six-station spine simulator on L929 murine fibroblasts. Data was analysed using ANOVA test (α=0.05) and the T-method. Significantly ($p<0.05$) reduced cell viability was indicated with an asterisk (*).

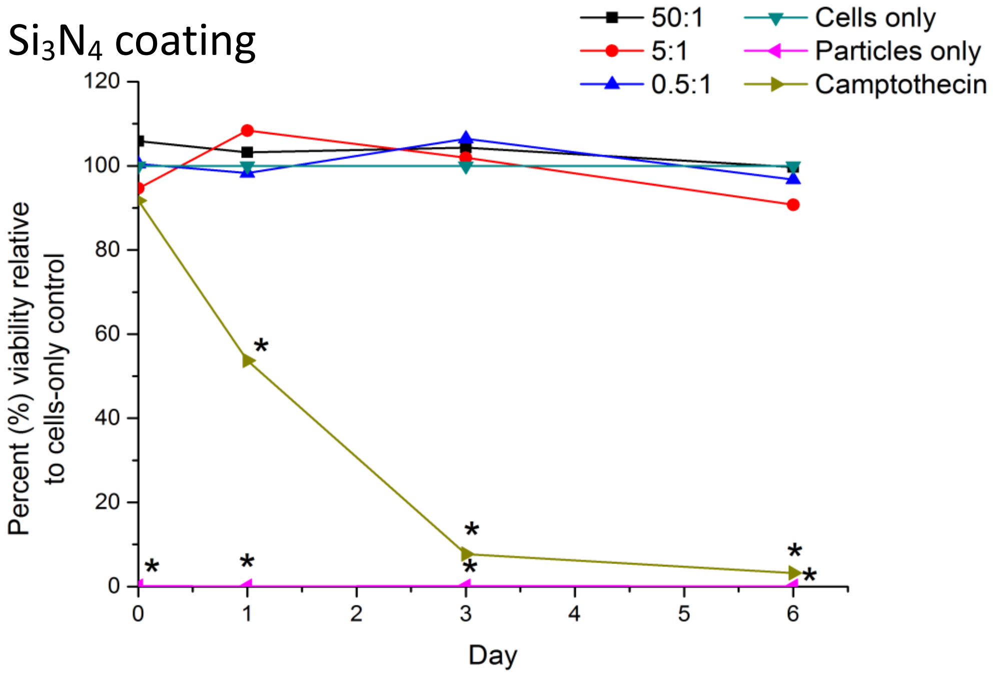

Figure 5.43: Effects of silicon nitride coating particles generated in sterile water in the six-station spine simulator on L929 murine fibroblasts. Data was analysed using ANOVA test (α=0.05) and the T-method. Significantly ($p<0.05$) reduced cell viability was indicated with an asterisk (*).

The study showed that neither chromium nitride (Figure 5.42), nor silicon nitride (Figure 5.43) coating wear particles caused a significant reduction of cell viability of L929 fibroblasts. In both groups, the cell viability, relative to cells-only control, ranged between 90% and 110% across the 6-day duration of the study. At all timepoints, a significant reduction in cell viability was observed for the positive control (Camptothecin) and no interference with the assay, caused by the particles-only negative control, was detected.

5.4.9.2 Primary porcine dural fibroblasts

The effects of ceramic coating (chromium nitride and silicon nitride) wear particles generated using the six-station spine simulator, on cell viability of primary porcine dural fibroblasts was investigated using the ATP-Lite assay. The dural fibroblast cells were seeded at a concentration of $5x10^3$ cells.well^{-1}. For 6-days the cells were cultured in the presence of particles volumes per cell of 50µm^3 to 0.05µm^3 (n=6). The results were expressed as a percentage of the cells only negative control. Descriptive statistics were performed on the raw data using the one-way ANOVA and individual differences between the means were determined using the T-method. Significant ($p<0.05$, CI 95%) adverse effects on the cell viability were identified.

Similarly to L929 cells, primary dural fibroblasts showed resistance to both chromium nitride (**Figure 5.44)** and silicon nitride (Figure 5.45) coating wear particles, and no significant reduction of cell viability of the dural fibroblasts was observed. In both groups, the cell viability, relative to the cells-only negative control, ranged between 90% and 110% across the 6 day duration of the study. At all timepoints, a significant reduction in cell viability was observed for the positive control (Camptothecin) and no interference with the assay, caused by the particles-only negative control, was detected.

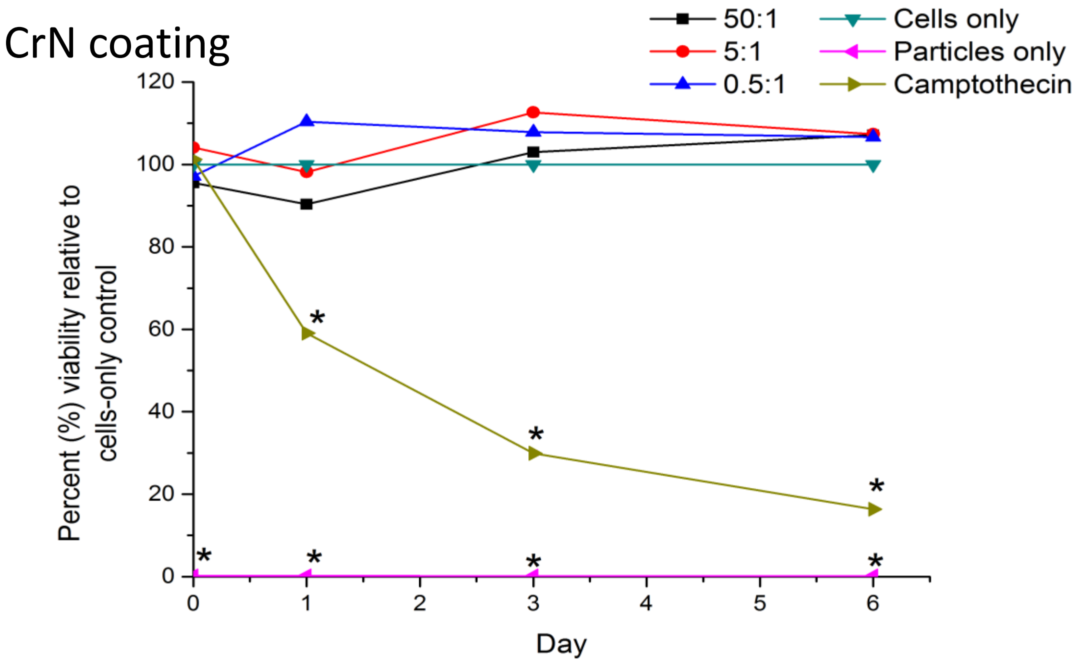

Figure 5.44: Effects of chromium nitride coating particles generated in sterile water in the six-station spine simulator on primary porcine dural fibroblasts. Data was analysed using ANOVA test (α=0.05) and the T-method. Significantly (p<0.05) reduced cell viability was indicated with an asterisk (*).

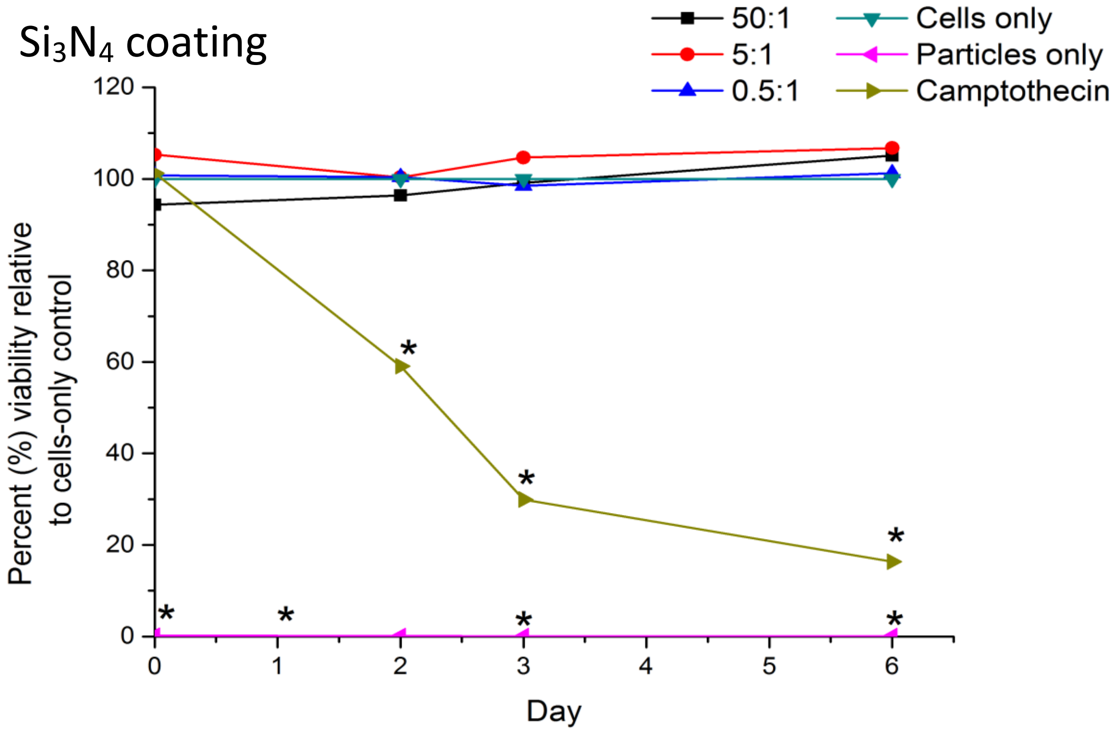

Figure 5.45: Effects of silicon nitride coating particles generated in sterile water in the six-station spine simulator on primary porcine dural fibroblasts. Data was analysed using ANOVA test (α=0.05) **and the T-method. Significantly (p<0.05) reduced cell viability was indicated with an asterisk (*).**

5.5 Discussion

Long term clinical success of TJR is multifactorial and driven not only by how well the device performs mechanically and tribologically, but often more importantly, by how the human body responds to its wear products. Indeed, as indicated by the National Joint Registry, osteolysis and loosening, both directly associated with biological responses to wear, are currently the chief reasons for revision of THR and TKR. A small number of studies have also reported wear-related failure of CTDRs and LTDRs.

The current study characterised the wear particles generated by CoCr MoM CTDRs tested in six-station spine simulator under the kinematics prescribed by the standard ISO-18192-1:2011 protocol. Initially, attempts were made to isolate the particles generated during wear studies, whereby foetal bovine serum was used as lubricant, however the particle isolation method used (adaptation of the method developed by Lal *et al* [353]), was not fully successful in removing serum proteins and sodium polytungsten (SPT) contaminates. As a result, particles contaminated with proteins and SPT were not characterised. It is likely the isolation method requires further development and adjustment to fully digest bovine serum protein adhering to the particles and remove SPT contaminants. The original method [353] has been developed for isolation of ceramic wear particles, which have substantially different surface chemistry. It has been shown that surface chemistry may influence the interaction and adsorption of the bovine serum proteins onto particles [359] and thus the particle isolation method may be different for ceramic and metal particles. Moreover, the mean wear rate generated by the MoM CTDRs was very low (0.24mm^3/MC), thus the number of particles, most of which were nano-size, found in each lubricant sample (500ml collected at each 0.33MC) was likely to be extremely low. As a result, the particle isolation method may not be sensitive enough for this particular application.

To circumvent the issues related to particle isolation method, CTDRs were further tested under the loads and ROMs specified by the ISO-18192-1 standard and with deionised water used as a lubricant, simplifying the particle isolation process. The diameter of particles generated in the six-station spine simulator ranged from 45nm to 658nm, with a mean particle size of 154±88nm.

The particles were mainly round and oval, and had a strong tendency to agglomerate, due to their small size and high surface energy. At the time of writing, no other studies have reported on the characteristics of wear particles generated by MoM CTDRs. The particles generated by the MoM CTDRs were much smaller than polyethylene particles generated by MoP bearings, tested under the same conditions. As previously reported, UHMWPE particles released by MoP CTDRs reached sizes of 0.17-0.33µm [142], 0.22-0.37µm [143] and 0.1-10µm [144]; round and flake-like particle shapes were reported [142–144].

Both the size range and shape of the particles generated in the current study were comparable to previously reported results of particles generated by MoM THRs. Typically, round and oval nanoscale particles were observed both *in vitro* [293,360–362] and *in vivo* [95,363,364]. The mean particle size generated by MoM THRs were typically reported to be ~50nm, thus much smaller than those generated in the current study, however it has previously been indicated by Bowsher *et al*., [365] that larger diameter bearings generate smaller particles. The bearing diameter of CTDRs tested in the current study was 12.6mm and significantly smaller than MoM THRs tested by other authors (28mm-56mm), therefore larger particle size reported by the current study was in line with the hypothesis outlined by Bowsher *et al.* [365]. Moreover, loads and ranges of motion, under which the CTDRs were tested in the current study, were dramatically different to those applied in THR testing, which likely influenced the particle size, as they resulted in different contact stresses exerted on the bearing. Indeed, the current study found that the particles generated in six-station pin-on-plate rig, which has been validated to generate contact stress and operating conditions relevant to THR [351], generated particles of a mean size diameter of 51±21nm and size range of 18-118nm. It has previously been reported for MoM pin-on-plate-generated particles to have a mean diameter of ~40nm [184].

It is not uncommon for nanoparticles to agglomerate in *in vitro* studies and both singular particles and agglomerates have previously been observed *in vivo* [95]. However, due to agglomeration of the particles, the manual sizing method used in the current study was likely to be subjective and may have been associated with a user bias. On the other hand, whist an automated particle sizing method, such as Nanosight, could potentially remove the user bias. The system allows for live tracking of particles, whereby laser beam is shined at a fluid containing particles. The beam is scattered, once it shines over a particle and the scattered light is captured by the camera. The system, however, was unable to distinguish between the single nano-particles and agglomerates studied in the present study.

Commercially available silicon nitride particles of two size ranges (nano- and submicron scale), used in cytotoxicity studies, were also characterised. The nanoscale particles were found to be mainly round and with a strong tendency to agglomerate, due to their high surface energy. The mean particle size was found to be 43±16nm. The submicron particles had a similar morphology to the nano-scale particles and a mean particle size of 137±84µm. It was not possible to compare the commercially available silicon nitride particles generated in the six-station spine simulator due to a catastrophic failure of the coating during the testing. As a result, predominantly large (~1-10µm) flakes of the coating, often with sharp edges, were observed under the SEM. Moreover, only a small number of particles were observed, therefore it was not possible to generate a size distribution for the silicon nitride coating particles. Similarly, only sparse numbers of chromium nitride coating particles were observed using the SEM. The particles were large (~1-10µm) and flake-like. Previously, studies of CrN-coated THR reported the mean size of particles to be in the rage of 40-70nm [180,184]. It was not possible to establish whether there were smaller particles generated by CrN-coated CTDRs, they may have been lost in particle preparation or the current study did not image them suitably under the SEM due to the magnification and resolution limitations.

The use of continuous cell lines, such as the murine fibroblasts (L929), is widely applied in biomedical research. Its main advantage is the ease of cell expansion and ability to propagate continuously in culture. Cell lines are a cost-effective way of conducting research on cells that can serve as a simple model of more complex biological systems or for use in simple screening studies, such as cytotoxicity investigations. Moreover, L929 cell line has been suggested by the ISO-10993-5:2009 for *in vitro* cytotoxicity testing [352].Nevertheless, the adequacy of cell lines, as clinically relevant source of results can be questioned [366–368]. For that reason, primary porcine dural fibroblasts were also used in the current study, as a more clinically relevant cell model for investigating the biological responses to wear particles generated by CTDRs. It has been shown that the pig immune system resembles the one of humans for more than 80% parameters examined, and thus was found suitable for use in the study of human disease processes [369]. Moreover, as the cells have been isolated from porcine meningeal layers, it was considered that for the application of the present study, such cells were highly relevant. Should a CTDR device produce an excessive number of particles, these would likely come in contact with meningeal layers and the ability of the meninges to protect the spinal cord from the particles penetrating thought would be tested.

The current study employed ATP-Lite® assay to quantify the level of cytotoxicity elicited by particles co-cultured with cells. The ATP-detection based assays has been widely used in cytotoxicity studies. The ATP-Lite® assay relies on the reaction of luciferin with the ATP released from lysed cells, which results in the generation of stable form of luciferase, that generates measurable numbers of photos of light. The method can detect as few as 10 cells, however, the results of luminescence can be affected by the mere presence of air bubbles or other contaminants in the wells. For that reason, the current study included a negative control of particles-only, which ensured that the results were not influenced by any artefacts caused by the particles. In none of the experiments reported by the current study the particle-only controls produce counts per second results high enough to be considered as interaction between the particles and the reagents of the assay.

The investigation of potential cytotoxicity of metal particles showed that high doses (5-50µm^3 per cell) of cobalt chrome particles generated in water, regardless of whether six-station pin-on-plate wear rig or six-station spine was used, resulted in significant reduction of cell viability of L929 cells by day 6 of the study. Interestingly, only the highest dose (50µm^3 per cell) of the particles generated in wear assessment of CTDRs (generated in the six-station spine simulator) and isolated from foetal bovine serum caused a significant reduction of the cell viability. As observed in the SEM, the particles isolated from the serum were not completely free adhered proteins. Those proteins may have acted as an additional source of nutrients for the L929 cells, resulting in the reduction of cytotoxic effects elicited by the CoCr particles. At the same time, the proteins may have created a corona around the particles, reducing the cytotoxic potential of the particles. These results indicated a cytotoxic potential of clinically relevant cobalt chrome particles in L929 cells, which has been reported previously [134,180,184,354,370]. It has been observed *in vivo*, that the particles and their degradation products (such as ions) released from MoM joint replacement can cause hypersensitivity, inflammation and pseudotumour formation [128,131,241]. Such reactions are likely a combination of metal ion toxicity and patient-specific reactions, the reasons of which are still not fully understood. The most common oxidation states of chromium observed *in vivo* are Cr(III) and Cr(VI) [371]. Whilst the latter has been classified as group 1 carcinogen by the International Agency for Research on Cancer (IARC), the mechanisms related to cytotoxicity of Cr(III) are still unknown [372]. Cobalt, on the other hand, is mostly observed in its Co(II) and Co(III) oxidation states [373], both of which have been classified as 2B carcinogens (possibly carcinogenic to humans) by the IARD. Indeed, patients who required revision surgeries of MoM THR were found with elevated levels of Cr(III) [374,375] and Co(II) ions [376–378].

The same CoCr particles (generated under the same conditions) did not elicit significant reductions in the cell viability of the primary dural fibroblast cells. In fact, the lower doses of CoCr particles (0.5-5μm^3 per cell), regardless of their generation method, appeared to increase the relative-to-cells-only cell viability. As living organisms require a small amount of Cr and Co microelements to sustain their metabolic functions, it may be that presence of lower doses of CoCr particles played a role in the elevated cell viability of the primary porcine dural fibroblasts. The lack of cytotoxic responses on primary dural fibroblasts, caused by CoCr particles, has previously been reported [354]. Behl *et al.* [354] used a pin-on-plate generated CoCr nano-particles and seeded them with primary porcine dural fibroblasts at seeding densities as high as 121μm^3.cell and evaluated the cytotoxicity over the duration of 4 days using the ATP-Lite assay. The authors showed that only the positive control (Camptothecin) resulted in a significantly reduction of cell viability of the dural fibroblast at day

4. At the time of writing, it was not possible to explain fully the differences in cell responses caused by the same CoCr particles. However, there is a general consensus, that types of cells, depending on their type and source, can present levels of sensitivity and reactivity to different metal particles doses [379].

Potential cytotoxic effects of model silicon nitride particles, available in nano-scale and sub-micron variants, have also been investigated in the current study. At the time of writing, the clinical relevance of the commercially available particles was not known, however, their use allowed the investigator to establish both dose- and size-dependent response profiles for L929 fibroblasts and primary porcine dural fibroblasts. It was found that the submicron silicon nitride particles did not cause reduction of cell viability of neither the L929 fibroblasts nor the primary dural fibroblast cells. Whilst the nano-scale Si_3N_4 particles did not influence the viability of the dural fibroblasts, the highest dose ($500\mu m^3$ per cell) of particles caused reduction of cell viability of the L929 fibroblasts. At the day one of the assay, the reduction was found to be significant ($p<0.05$, CI 95%). On subsequent days, the viability of L929 fibroblasts remained reduced (70-80% relative to cells-only control); however, it was not found to be statistically significant. However, the dose of the particles, which resulted in reduction of the cell viability of L929 fibroblasts ($500\mu m^3$ per cell) was excessively high and unlikely to be observed *in vivo* in low wearing ceramic coatings or bulk ceramics. Silicon nitride, as a ceramic material, has high hardness and abrasive wear resistance, thus very low wear rates of the material should be expected *in vivo.* Whilst the current study observed catastrophic delamination of the silicon nitride coating, it was accepted that, at the time of writing, the coating was at early stages of development and coating adhesion was expected to be subject of further advancement. The results of the current study showed that the responses elicited by the commercially available silicon nitride particles varied with size, dose and type of cells used in the investigation. Previously, Cappi *et al* [380] reported that co-culture of silicon nitride particles with L929 fibroblasts did not cause cytotoxic responses. The authors, however, did not indicate the size and dose of the particles used, and employed a different cell viability assay, therefore direct comparison of the results was not possible. Other authors also reported no cytotoxic effects caused by silicon nitride on the viability of L929 fibroblast cells [381], however, in their study bulk material (1x10mm discs), not particles, was investigated. Overall, it was reported that silicon nitride, as a bulk material, is biocompatible [382–387].

The silicon nitride coating particles generated in six-station spine simulator did not reduce the cell viability of either the L929 fibroblasts, or the primary porcine dural fibroblasts. This was in line with the results achieved by the model particle presented in the current study, however there were some differences in the study setup. Due to limited volumes of particles collected from the six-station simulator, the highest dose of Si_3N_4 coating particles, to which the cells were subjected to, was 50µm^3 per cell. Moreover, it appeared that the majority of the particles generated by the delaminated coating were relatively large (~1-10µm) in comparison to the model particles. There is a general consensus, that particles of sizes 0.1-1µm are the most reactive, therefore large particles, as those generated by the failed coating (generated from a material considered as biocompatible), were unlikely to elicit a cytotoxic response.

The chromium nitride coating particles, produced in the six-station spine simulator, did not impact the cell viability of the L929 murine fibroblasts or primary porcine dural fibroblasts significantly. Previous results reported by Williams *et al.* [180] showed significant reduction of cell viability of L929 cells caused by a high dose (50µm^3 per cell) of CrN coating particles generated by THRs. Similar results were found by another author (Leslie, 2008), whereby the high dose of CrN coating particles caused a 16% reduction in cell viability of L929 fibroblasts [184]. However, the particles used by both Williams *et al.* and Leslie were significantly smaller than the particles generated by the CrN-coated CTDRs (mean size of 40nm and 70nm, respectively vs, 1-10µm), therefore there may be a particle size-dependency in cytotoxic responses of L929 fibroblast cells. Moreover, as with the silicon nitride coating particles, it was expected that such large particles (1-10µm) would not to cause a significant reduction in cell viability. However, it has been previously shown that cytotoxic responses to particles can be multifactorial and dependent on shape and composition [388], size [389–391] and dose [392].

5.6 Conclusions

The particles generated by MoM CTDRs tested in the six-station spine simulator were found to be predominantly round and nanoscale, similarly to those generated by MoM THR. Both chromium nitride and silicon nitride coatings appeared to produce low numbers of large, flake-like particles.

Previously, cell line models, such as L929 fibroblasts, have shown good correlation to in vivo assays, however, they can only be used as initial step in biocompatibility and cytotoxicity testing. The current study used porcine primary cells, as they were considered more clinically relevant in assessing biocompatibility of CTDR-generated wear particles.

High doses (5-50µm^3 per cell) of CoCr particles significantly reduced the cell viability of the L929 fibroblasts, but had no negative effect on the primary dural fibroblasts. It is likely that the cytotoxic effect of the CoCrMo particles was due to the release of Cr ions, previously shown by other authors.

Model particles, of two size groups, were used to determine potential cytotoxicity, as well as size and dose dependency of silicon nitride. Whilst the highest dose (500µm^3 per cell) of the nano-sized particles reduced the cell viability of L929 fibroblasts, it was determined, that the such dose was unlikely to be clinically relevant. No other doses of either sizes of model silicon nitride particles significantly impacted the cell viability of the cells used in the current study. As expected, due to large size of the particles generated by the ceramic coated CTDRs (1-10µm), neither the chromium nitride nor the silicon nitride coating particles caused a significant reduction in cell viability of L929 murine fibroblasts and primary porcine dural fibroblasts. Whilst the silicon nitride has been shown to have good biocompatibility properties in both bulk and particulate forms, conflicting results on nano-scale chromium nitride cytotoxic potential have been published in the past.

Chapter 6 : Summary review

6.1 Overall discussion and main findings

Chronic neck pain, often a result of degenerative disc disease, can be a debilitating condition, which can exert a significant personal and socioeconomic toll. As a result, chronic neck pain is ranked as the fourth leading cause of disability globally [393]. Traditionally, anterior cervical discectomy and fusion (ACDF) have been the gold standard in providing pain relief in patients with chronic degenerative disc disease. However, over the years, it has been discovered that ACDF can be associated with an array of complications such as adjacent segment disease or degeneration and pseudoarthrosis [394]. Fusion of the affected segment often results in increased loads and intradiscal pressure applied on the adjacent levels, leading to degeneration. The principle of motion retention at the affected segment was at the heart of design intent of cervical total disc replacement (CTDR) devices, which is becoming an increasingly popular alternative to ACDF.

The CTDR technology is relatively new – first FDA-approved device entered the commercial market in 2007 (Prestige-ST), and thus the interest in researching potential improvements, causes of failure and general understanding of biomechanical implications of a device, so far has been limited. As such, published literature (Figure 6.1) and FDA approved devices started to emerge only in the last 15 years and the numbers are still sparse, when compared to other joint replacement technologies such as the hip or knee. The limited number of studies, particularly clinical, and the lack of long term follow-up patient data may result in a skewed perception of the benefits presented by the CTDRs and their potential superiority over ACDF. So far it has been established that, statistical noninferiority of CTRDs, when compared to ACDF approach, can be achieved by all of the commercially available devices, however, statistical superiority is met only by some devices and only in certain aspects of establishing clinical success of a devices (Chapter 1). Moreover, in line with other joint replacement device, the MoP CTDRs were found to be associated with failures resulting from excessive wear, such as osteoarthritis [124,128,129] peudoarthrosis have also been reported [395].

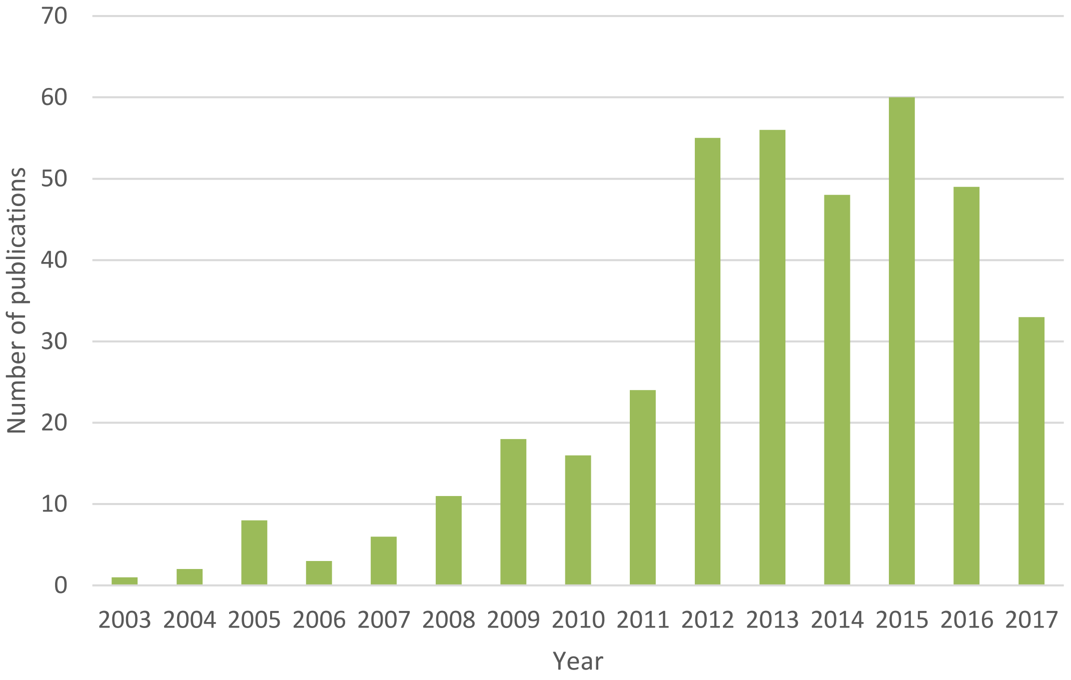

Figure 6.1: Pubmed literature search results for '*cervical total disc replacement*' or '*cervical total disc arthroplasty*' showing the limited numbers of publications around CTDR technology.

This study was initiated following interest in a novel design of CTDR device, which comprised of metal-on-metal (MoM) bearing endplates made from the medical grade cobalt chromium molybdenum (CoCrMo) alloy. The literature review, conducted in Chapter 1 of this thesis, identified lack of availability of a similar device in clinical use. The Prestige ST and the recently launched Prestige LP, whilst comprising of a MoM bearing, are made from a medical grade stainless steel and titanium alloy (Ti6Al4V), respectively. However, titanium, in particular, is more susceptible to wear than CoCrMo when used in TJR applications, and thus represents a less favourable material of choice for bearing surfaces. It has been identified that a lumbar CoCrMo MoM lumbar device has been available commercially for some time (Maverick, Medtronic). Whilst, relatively good 2-10 year patient outcomes of this device were reported [396–399], some complications were also identified and these include focal metalosis and soft tissue necrosis [400], release of metal ions [401] and subsidence [402]. As a result, this study proposed the use of ceramic coatings for potential improved tribological performance and to decrease metal ions generated by the bearing. Ion release, along the wear particles, have previously been associated with necrosis and pseudotumour formation around the hip joint following failed MoM THR [241,287,288,403]. Chromium nitride was selected as one of coatings, as it is relatively well established in various industries, and medical implants applications of the coating have previously been studied [182,183,185].The coating has favourable mechanical and tribological properties. The second coating, silicon nitride, was proposed for this investigation as a novel solution to the potential problem of excessive wear and metal ion release exhibited by MoM CTDRs. Moreover, it has been reported that silicon nitride particles can dissolve in polar solvents [191,193]. Consequently, it has been suggested that wear debris produced by silicon nitride coatings may dissolve over time *in vivo*, and therefore have the potential reduce the adverse biological responses in periprosthetic tissues, increasing the longevity of implants.

To date, there have been no previous data published on the potential wear rates or the potential biological responses elicited by the wear products, generated by a MoM CTDR device. Moreover, no body of work around the proposed use of ceramic coatings in CTDR devices has been published, to date. In order to gather basic but comprehensive data, a series of studies were carried out. The studies in this thesis were divided into themes: theoretical prediction of maximum contact stress and lubrication regime, coating characterisation, wear performance and biological consequences of wear, as it was considered that potential clinical success of the device proposed in this study would be multifactorial and mainly comprise of these four aspects.

The primary aim of this study was to investigate the biotribology of a novel design of cervical total disc replacement device in its pristine form and coated with chromium nitride or silicon nitride, in order to understand the influence of loading conditions upon the tribological performance of the implant, and to investigate biological effects of the wear debris produced by the implants.

The exact design of the proposed novel CTDR device was presented in Chapter 2. Moreover, a Hertzian contact model and Hammrock & Dowson formula were used to establish the theoretical maximum contact stress and operating lubrication regime, respectively. It determined that, compared to previously reported theoretical maximum stress exhibited by PEEK-PEEK CTDR devices [216], the MoM or ceramic coated CTDRs would experience relatively high maximum stress, however the fatigue strength of the materials would not be exceeded. From the three material combinations investigated (CoCr-CoCr, CrN-CrN and Si_3N_4-Si_3N_4) , it was predicted that the chromium nitride coated device would exhibit the lowest maximum contact stress and would operate under the most favourable lubricating conditions. These theoretical models are not a perfect simulation of reality, but they allowed for an initial and simple design verification and comparison of the materials chosen for the device substrate and coatings proposed in this thesis.

Results of physical characterisation of the chromium nitride and silicon nitride coatings were presented out in Chapter 3. Whilst some differences in the mechanical properties (Young’s modulus, hardness) and coating adhesion between the two coatings were identified, they were considered suitable for the CTDR application, as they showed equivalent or better surface finish, coating hardness or bench-tested coating adhesion, than some coatings previously applied onto medical implants.

Wear assessment of the proposed CTDR devices was carried out in Chapter 4. A six-station spine simulator was used to conduct *in vitro* simulation of wear performance of MoM and ceramic-coated CTDR devices and provided new knowledge around the tribological performance of such devices, in comparison to the currently available devices with MoP bearings. It was found that MoM CTDR devices tested under standard ISO-18192-1:2011 protocols produced significantly lower volumetric wear rates than those of various MoP or PEEK-PEEK devices tested under the same conditions [142,143,301,404] . Application of a chromium nitride coating on the CoCrMo substrate reduced the wear rates further to as low as 0.03±0.01mm^3/MC. The silicon nitride coating failed catastrophically resulting in coating delamination. It was suspected that inadequate coating adhesion was the reason for failure. To author's knowledge, this thesis is the first published body of work, which has investigated wear rates of a CoCrMo MoM CTDR device tested under ISO-18192-1:2011. Based on the findings reported by Kurtz *et al.* [119], where explanted devices were found to exhibit substantially less severe surface damage, when compared to *in vitro* tested devices of the same design and supported by further evidence gathered by Cobian *et al.* [49], which showed that the majority or motions executed on daily basis do not exceed a range of motion (ROM) of ±2-3°, the author has challenged the current ISO-18192-1 standard and hypothesised that wear testing conducted as recommended by the current version of the standard may exaggerate wear rates and provide overestimated predictions of wear in CTDRs. Consequently a further 2MC of testing of the MoM CTDRs, with reduced ROMs, showed that the change of the test kinematic inputs resulted in significantly lower wear rates and smaller wear tracks observed on the surface of the devices, which was in line with the findings gathered by Kurtz *et al.* [119] and observations made from explanted MoM TDRs.

As determined from other TJR devices and recent findings from TDRs, wear and wear products can lead to adverse biological reactions and result in implant failure. Particles characterisation and investigation of potential adverse biological reactions to the particles generated by the CTDR devices were carried out in Chapter 5. The particles generated by the MoM CTDRs tested in the six-station spine simulator, under the loading and kinematics regime of ISO-18192-1:2011, were found to be primarily smooth, round and prone to agglomeration. The mean size was significantly smaller (154nm) than those previously reported for MoP

CTDRs (ranging from 0.1 to 10µm) [142–144]. At the time of writing, no previous data on the characteristics of wear particles generated from a MoM CTDR or LTDR devices has been published. Despite the substantial differences in loading and kinematics applied in the testing of CTDRs and THRs, the two types of devices followed the same bearing material-dependent pattern of the sizes of particles generated by different bearings i.e. polyethylene particles are typically significantly larger than those generated from MoM or ceramic-on-ceramic (CoC) bearings. It was found that mean particle size dependent on the conditions under which they were generated; particles generated in a six-station pin-on-plate wear rig were smaller (mean size of 51nm) than those generated in the spine simulator – a likely result of the differences in contact stress applied on the components in the two rigs. Particles generated from the two ceramic coatings were few in numbers and full characterisation was not possible. The particles observed were mainly flake-like, some with sharp edges and were relatively large (approximately 10-15µm). No data on particles generated from silicon nitride coated TJR devices was available at the time of writing, therefore comparison to previously published data was not possible. Chromium nitride coatings for THR applications have previously been tested by Williams *et al.* [405] and Leslie *et al.* [184], who reported particles to be in the nanometre scale, which is was significantly smaller than those observed in the current study. With the information and observations made in the current study, it was not possible to establish the root cause of such differences in particle sizes. It has been hypothesised by the author that different loading and kinematic conditions applied in the testing may have been one of the causes, alongside the potential differences in coating deposition methods.

One of the objectives of this thesis was to apply the modified particle isolation method, originally developed by Lal *et al.* [353], to the wear particles generated in the six-station spine simulator, in foetal bovine serum, and once fully isolated from protein and bacterial contamination, use the particles in biological evaluation of the wear products. Whilst the isolation of wear particles from serum was not fully successful, and a level of protein contamination remained, the particles generated in the *in vitro* wear test were still used in the cytotoxicity assay studies, alongside CoCrMo particles generated in the spine simulator (in sterile water), particles generated in the six-station pin-on-plate wear rig, as well as coating particles generated in the spine simulator, in water. Two types of cells – murine fibroblasts (L929 cell line) and primary porcine dural fibroblasts (DFs) were used in the ATPLite assays. The use of DFs was considered to be more relevant in this application, as they were isolated from meningeal membranes, which *in vivo,* would be in close proximity to the CTDR device and create the natural protective barrier of the spinal cord. It was found that high concentrations (5-50µm^3 per cell) of CoCrMo particles resulted in significant reduction of cell viability of the L929 fibroblast cells, but not the DFs. These findings were in line with previously published data [354], which showed reduction in primary porcine dural fibroblast viability caused by CoCrMo wear particles. No ceramic coating particles, at any concentrations, caused significant reduction of cell viability, which has previously been observed by other authors, whereby ceramic coatings were applied onto joint replacement devices [184,381,384,405].

6.2 Limitations of studies

Some of the studies presented in this thesis were conducted with certain limitations, which may have influenced the interpretation of the results:

- The values of Young's moduli used in theoretical predictions of the lubrication regime and maximum contact stress found in silicon nitride- and chromium nitride-coated CTDR assumed the surfaces were made from bulk silicon nitride and chromium nitride. Instead, the surfaces of ceramic-coated CTDRs should have been assumed as composite materials. However, overall, the values of Young's moduli of the three investigated materials (CoCr, Si_3N_4 and CrN) were not too dissimilar (210GPa, 250GPa and 200GPa, respectively) and thus it was not expected for the simplified calculation approach to skew the results significantly.

- The second part of the spine simulator studies, which investigated the altered ISO-18192-1 protocol, was not conducted on pristine (‘unused’) components, rather the same components, previously used in the first part of the spine simulator studies, were used. Whilst the loss of material experienced by the components was significantly reduced when CTDRs were tested using the altered ISO-181921-1 protocol, it can be argued that following 4MC of standard testing the components have already gone through the bedding-in phase and the surfaces were more conforming when the altered-ISO protocol was investigated. As a result, the reduction of the wear results observed in the second part of simulator testing may have been exaggerated by the use of bedded-in components.
- The results of wear studies conducted on the ceramic-coated CTDRs showed significant reduction in wear rates produced by the CrN-coated CTDRs, when compared to the pristine MoM devices. Whilst the theoretical calculations conducted in Chapter 2, supported the results, showing reduced maximum contract stress and more favourable theoretical lubrication regime exhibited by the CrN-coated implants, the coated devices had smaller radial clearance, in comparison to the MoM components, by approximately 10µm (thickness of the coating). The design of the metal substrate devices (subsequently coated) did not account for coating thickness, as at the time of device design, the coating thickness was not decided upon. As shown by the theoretical lubrication regime calculations, smaller radial clearance can lead to more favourable lubrication between the bearing surfaces, and thus, the reduced wear rates of the CrN device may have been influenced by this reduced radial clearance. It can be argued that a like-for-like comparison between MoM and CrN-coated CTDRs cannot be made, as the design of the devices was not identical. However, considering the magnitude of clearance difference (~10µm) and significant difference in wear rates, it is unlikely that the overall results were substantially affected by this limitation.

- The cytotoxicity studies, employing the ATP Lite assay, were designed so that only one plate, including six repeats of each group, was assessed at each timepoint. Whilst both positive and negative controls were included in each plate, the overall results may have been affected by plate-to-plate variability caused by slight variations in the laboratory techniques applied during the experiment. To fully validate the results, additional plates, at each timepoint, should be added.

6.3 Future work

The current work carried out investigations into a novel MoM CTDR device in its pristine and ceramic-coated variants, and provided comprehensive insight into the wear behaviour of the implants, as well as potential cytotoxic effects of the wear particles generated by these devices. This initial investigative work, whilst answering some of the research questions, opened further avenues of research that have scope for additional investigations. Future work should focus on:

- Machining and polishing of the device used in this research has been carried out in-house at University of Leeds. Improved control and validation of the polishing process could lead to enhanced wear performance, as less variability in the radial clearance and improved surface finish could be ensured.
- There is an obvious need for improvement of coating deposition parameters of the silicon nitride coating on CoCrMo substrate resulting in enhanced coating adhesion, which could withstand the frictional forces applied in *in vitro* wear testing. At the same time, investigation of different substrate materials, such as titanium, which could provide improved adherence between the substrate and the coating.
- Extended duration of wear testing, particularly of coated devices. It has been previously observed for THR devices *in vivo* that coatings fail and wear-through over prolonged period of time, thus extended wear testing is necessary to fully verify the application of ceramic coatings for CTDRs.

The current ISO standard for *in vitro* wear testing of TDR devices suggest a maximum test duration of 1x10^7 cycles, unless otherwise rationalised. Standards for THR and TKR *in vitro* wear testing recommend testing duration of 5x10^6, up to 1x10^7 for TKR designs incorporating thin (<6mm) polyethylene inserts. Therefore extending the testing of CTDRs (coated and uncoated) to at least 5x10^6 seem sensible. This testing should incorporate both the standard and reduced range of motion protocols.

- Adverse biological reactions *in vivo* are not solely caused by metal wear particles, but also by ion release. The ion concentrations in serum can be measured throughout the wear testing using Inductively coupled plasma mass spectroscopy (ICP-MS). Measurements from samples of lubricants from testing of MoM and ceramic coated CTDRs could verify the potential of coatings to reduce the level of toxic ion release.
- New wear testing protocol for lumbar TDRs, including adverse loading conditions and extension impingement inputs (Figure 6.2), have recently been published [406]. The standard suggests an application of a 7.5Nm moment to the device during the impingement. The maximum duration of the impingement protocol testing is specified as 1x10^6 cycles. Similar inputs, adjusted to CTDR kinematics and loadings, could be applied into the *in vitro* wear testing of cervical implants. Assessment of explants made by Kurtz *et al.* [119] reported evidence of impingement found not only in the LTDR devices, but also in the CTDRs.

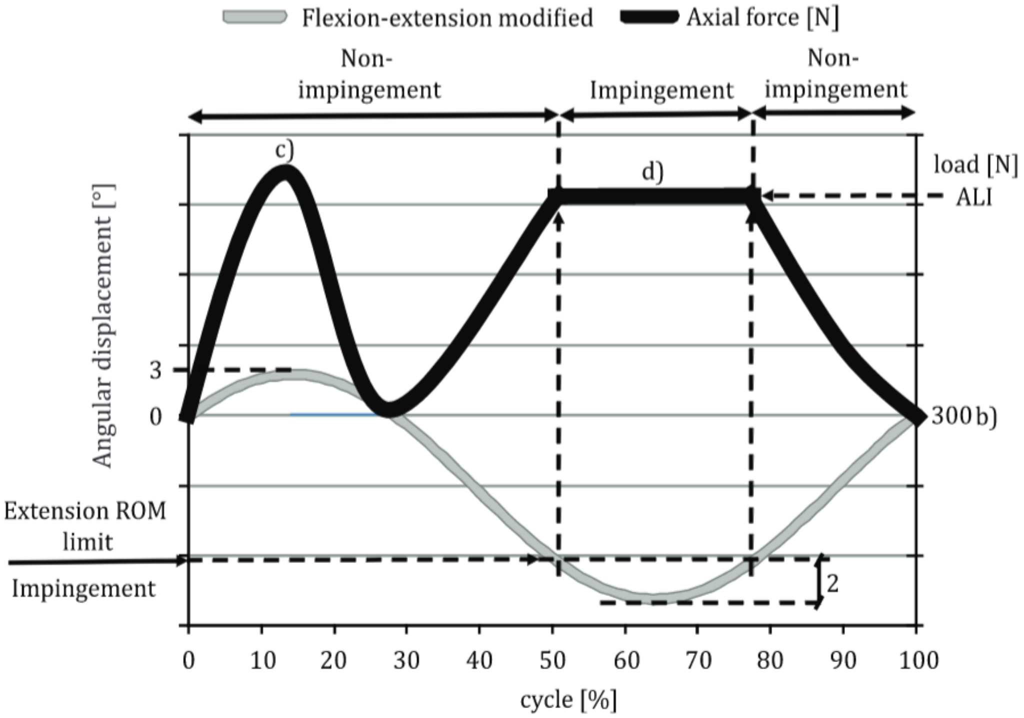

Figure 6.2: Load and displacement profile for lumbar spine extension impingement wear test, as per ISO-18192-3:2017 [406]**.**

6.4 Conclusions

The current version of the ISO-18192-1 (2011) has been challenged in the current study. Unlike the testing protocols for other TJR devices, ISO-18192-1 is available in its second version and it is expected that the standard will continue developing and changing over time. As some of the explanted LTDR were previously reported to provide evidence of impingement [119], a new part to the standard (ISO-18192-3:2017 – 'Wear of total intervertebral spinal disc prostheses -- Part 3: Impingement-wear testing and corresponding environmental conditions for test of lumbar prostheses under adverse kinematic conditions' [406]) has recently developed and published. However, at the time of publication no CTDR counterpart has been developed. Adoption of adverse conditions for testing of TJR devices is considered the way forward, as they often represent more realistic conditions TJR exhibit *in vivo*. As *in vitro* simulation has been considered as one of a key factors in determining the likelihood of clinical success, factoring in adverse loading regimes or potential device malposition allows prediction of implant behaviour in sub-optimal clinical conditions.

Whilst the limitations of the methods employed in the studies presented in the current thesis, the results indicated that whilst the CoCrMo MoM CTDR device exhibited significantly lower wear rates than those of the commercially available MoP devices, the cytotoxic wear particles could potentially lead to adverse biological reactions, particularly in patients with metal hypersensitivity, and lead to devastating consequences similar to those of failed MoM THRs. Currently, the consequences of similar failure, leading to metalosis or pseudotumour formation in the vicinity of the spinal cord are unknown. Whilst it is not known whether metal nanoparticles could potentially cross the blood-brain-barrier (BBB), other nanoparticles, used in drug-delivery, have been shown capable of successfully crossing the BBB [407–409]. Published in 2016 the FDA guidance document on the ISO-10993-1 -*‘Biological evaluation of medical devices - Part 1: Evaluation and testing within a risk management process’*, suggested that, if mechanical failure of a device could alter the biological response to the device (such as production of wear debris), biocompatibility evaluations should be considered. The FDA recommendations show that the awareness of potential cytotoxic effects caused by wear particles is growing. At the same time, it suggests more stringent approval requirements for TJR devices manufacturers may be faced with. During the investigation of the ceramic coatings, it was also found that chromium nitride ceramic coating could not only lower wear rates further, but could potentially lead to reduce the cytotoxic effects caused by wear particles. Whilst the wear results of the silicon nitride coated CTDRs were less than ideal, the cytotoxicity study showed that particles generated from such devices, independent from particle size and concentrations, could potentially reduce the risk of adverse biological reactions. Adding the particle solubility of silicon nitride, the coating could have further advantage of minimising the risk of ion release from particles.

Chapter 7 : Appendices

7.1.1 Appendix I - Summary of the main design features of the CTDR devices cleared by the FDA

Implant	Bryan	Prestige ST	ProDisc-C	Prestige-LP
	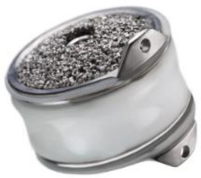	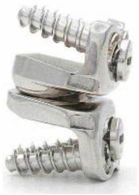	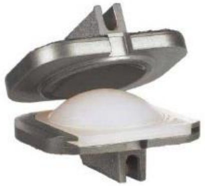	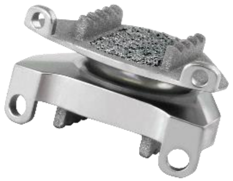
Manufacturer	Medtronic	Medtronic	DePuy Synthes	Medtronic
Bearing surface materials	MoP; titanium endplates, polycarbonate urethane nucleus	MoM; stainless steel	MoP; CoCr, UHMWPE	MoM; Ti ceramic composite
Bearing surface geometry	Biconvex nucleus articulating with upper and lower end plates	Ball-and-through design	Ball-and-socket design, insert fixed to the bottom endplate	Ball-and-through design
Primary fixation	Press fit	Anterior flanges with screws	Keels	Dual serrated keel
Secondary fixation	Titanium porous coating	N/A	Titanium plasma sprayed	Titanium plasma spray coating
Degree of constraint	Unconstrained	Semiconstrained	Semiconstrained	Unconstrained
Implant centre of rotation	Variable; at the centre of the mobile nucleus	Variable; superior to disc space	Fixed; inferior to disc space	Variable; superior to disc space

Implant	Secure-C	PCM	Mobi-C
Manufacturer	Globus Medical	NuVasive	LDR Spine
Bearing surface materials	MoP; CoCr, UHMWPE	MoP; CoCr, UHMWPE	MoP; CoCr, UHMWPE
Bearing surface geometry	Semi-mobile bearing, spherical articulation at the top endplate (rotation), cylindrical articulation at the bottom endplate (translation)	Convex insert fixed to bottom endplate, concave upper endplate articulating with the insert	Mobile bearing; Insert slides and twists on the bottom plate, two keels restrict the movement of the insert, top plate moves over the insert
Primary fixation	Press fit, teethed keel	Press fit and V-teeth	Press fit, teethed keel
Secondary fixation	Titanium plasma spray coating	Titanium Calcium Phosphate porous coating	Hydroxyapatite+titanium porous coating
Degree of constraint	Semiconstrained	Semiconstrained	Semiconstrained
Implant centre of rotation	Variable	Variable; inferior to disc space	Variable

7.1.2 Appendix II – Leeds Spine Simulator

The axial and anterior-posterior loads are applied to each station by the compression of a spring, which is driven by a cam mechanism from the motor (Figure 7.1 and Figure 7.2). This means the two loads (axial and anterior-posterior) are applied via indirect control, which uses Hook's Law principles to allow the application of a load by use of a compressed spring.

The flexion extension, lateral bending, axial rotation and anterior-posterior displacement motions are operated via direct motor control, in which a simple arrangement of connecting rods to the motors is applied, as shown in Figure 7.3, Figure 7.4 and Figure 7.5, respectively. Before carrying out any experimental studies using the wear simulator, it was necessary to calibrate all the motions and loads. Detailed methodology applied in the calibration process of the spine simulator is described in the following section.

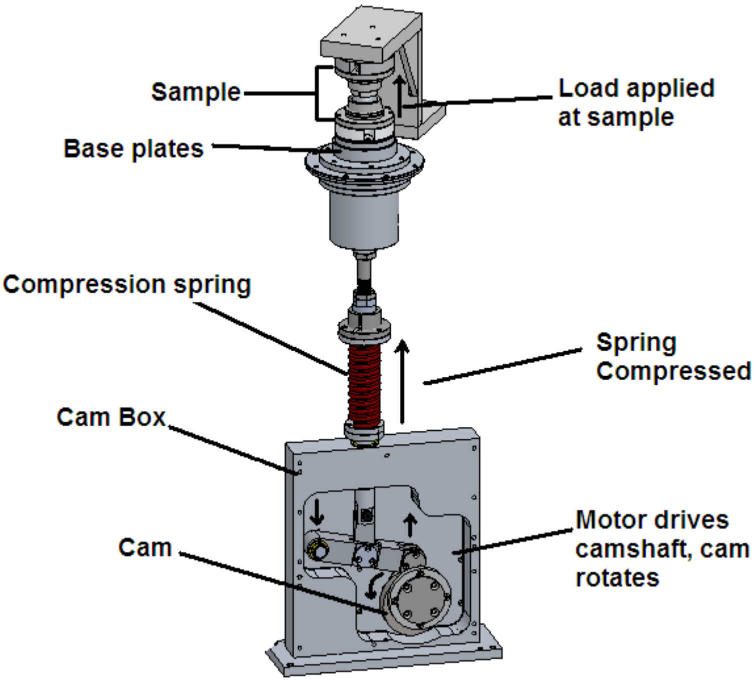
Sample
Load applied at sample
Base plates
Compression spring
Spring Compressed
Cam Box
Cam
Motor drives camshaft, cam rotates

Figure 7.1: Axial loading mechanism showing how the cam compresses the spring, and the load is applied to the sample.

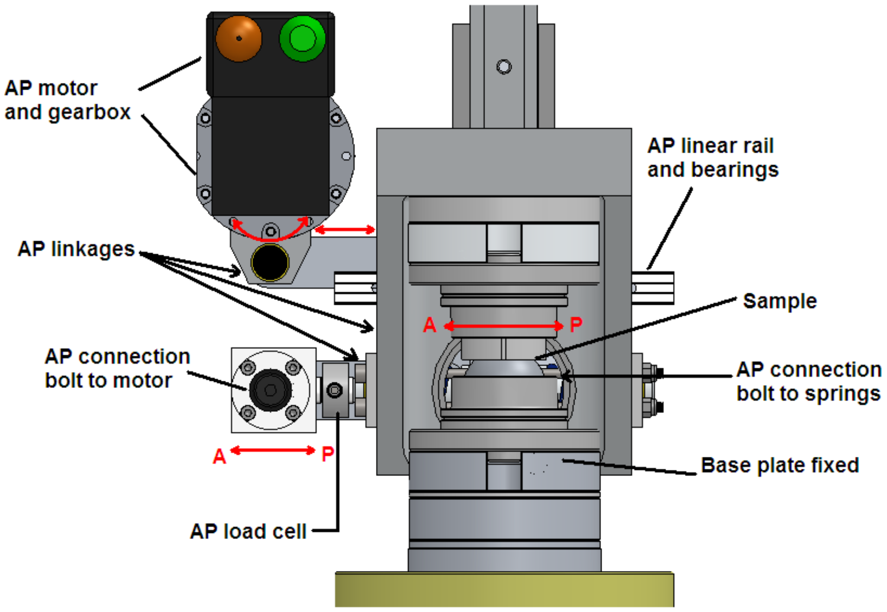
AP motor
and gearbox
AP linkages
AP connection
bolt to motor
A
P
AP load cell
AP linear rail
and bearings
Sample
A
P
AP connection
bolt to springs
Base plate fixed

Figure 7.2: Anterior-posterior shear mechanism, showing the connection of the motor to the individual station, and how this transfers movement to the sample

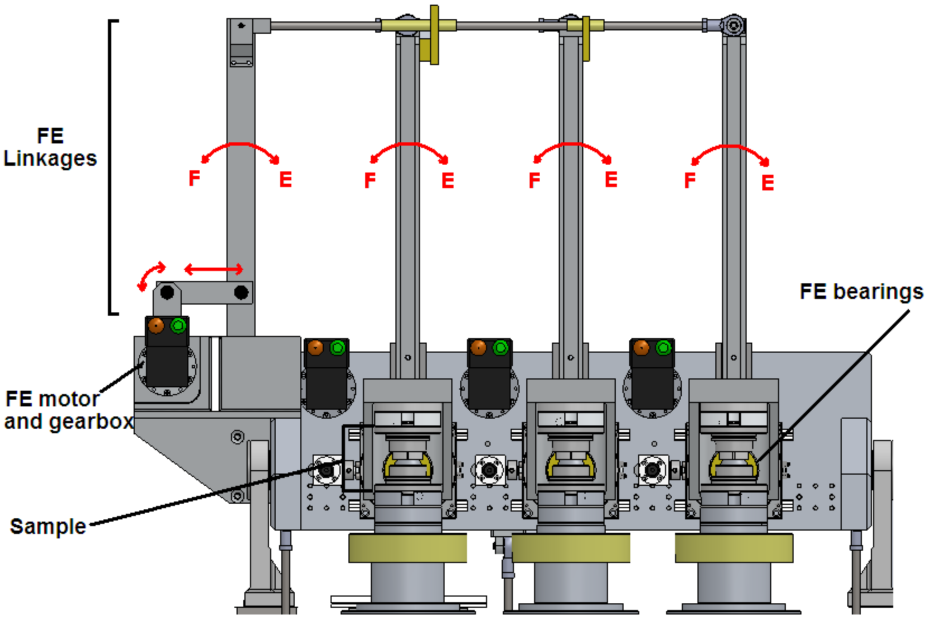
FE
Linkages
F
E
F
E
F
E
F
E
FE bearings
FE motor
and gearbox
Sample

Figure 7.3: Flexion-extension mechanism for one group of three stations, showing application of Flexion (F) and Extension (E)

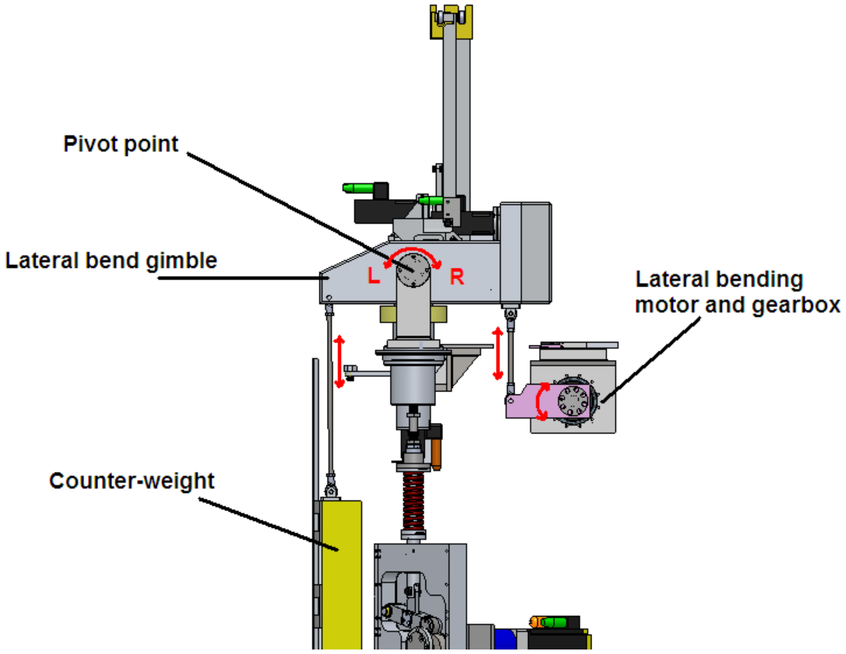
Pivot point
Lateral bend gimble
L
R
Lateral bending motor and gearbox
Counter-weight

Figure 7.4: Lateral bending mechanism showing the lateral bending motor and gearbox, the linkages that attach to the gimbal and the counter-weight needed to stabilise the motion, applying left (L) and right (R) lateral bending

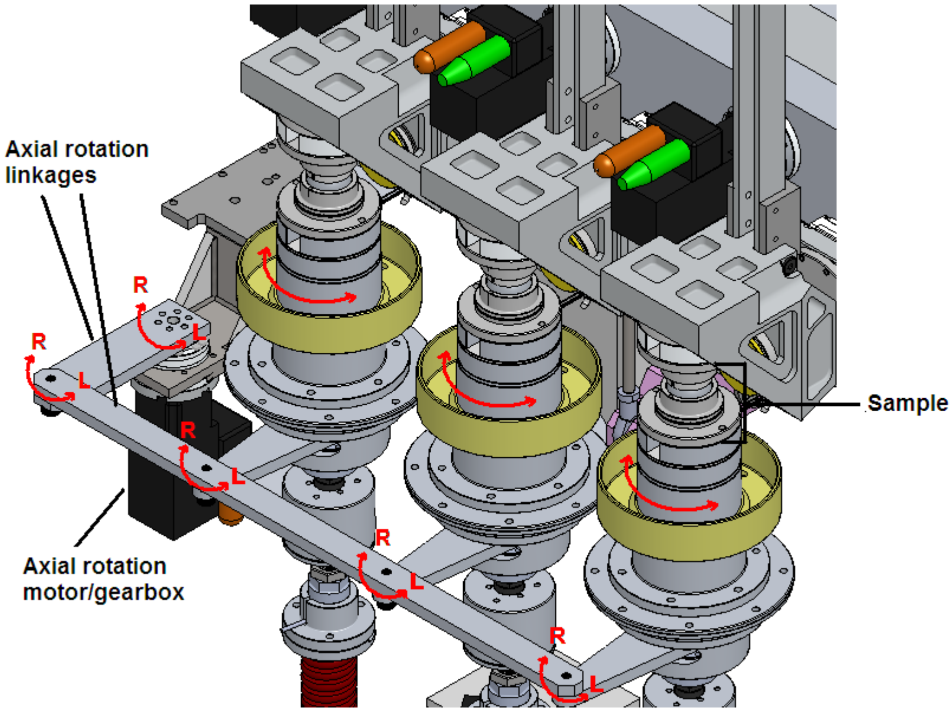
Axial rotation linkages
R
L
R
L
R
L
R
L
R
L
Axial rotation motor/gearbox
Sample

Figure 7.5: Axial rotation mechanism showing right (R) and left (L) axial rotation applied to one group of three stations via linkages

7.1.3 Appendix III – Spine simulator CTDR component fixtures

a) Top fixture holder:

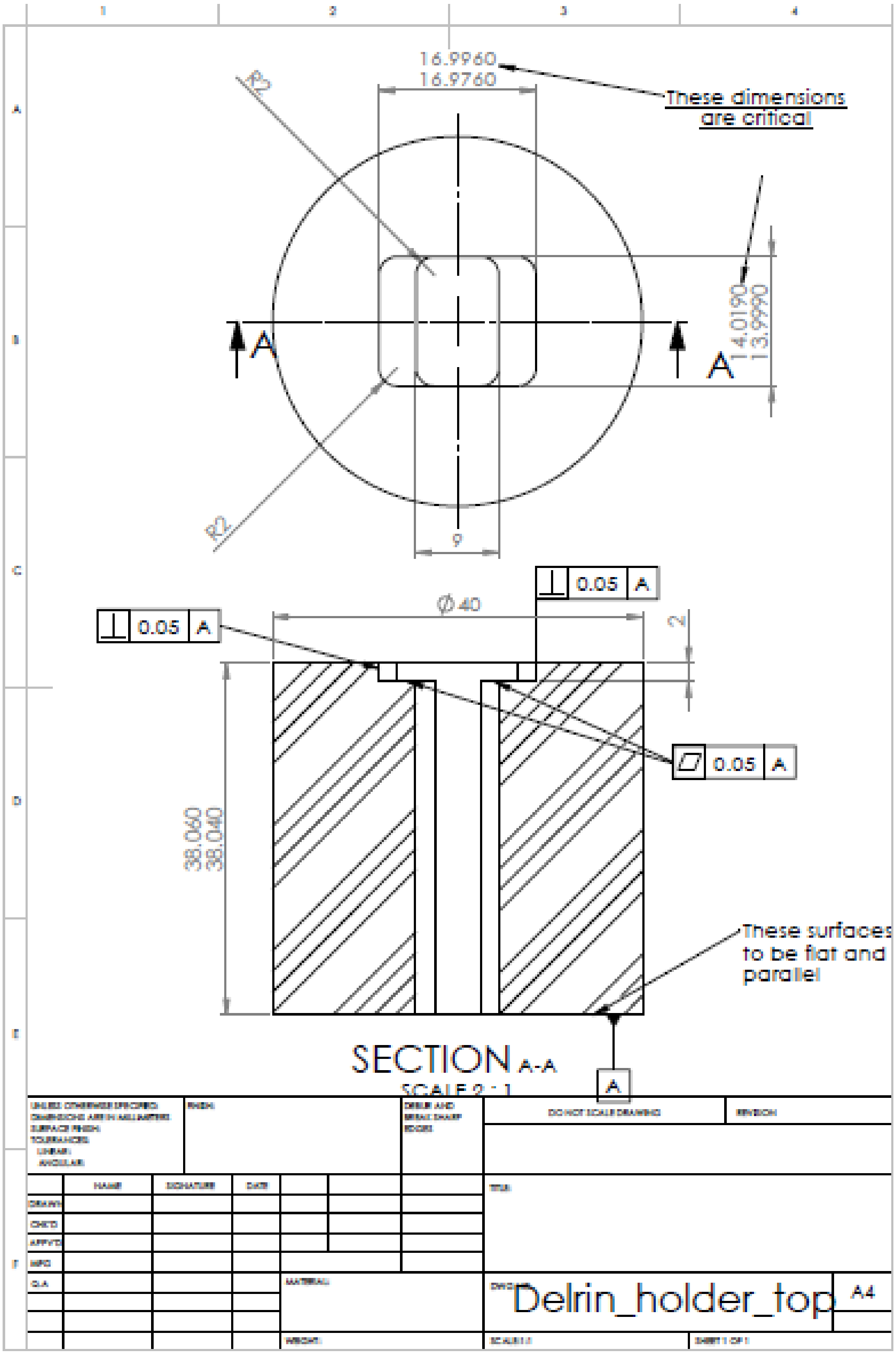
1
2
3
4
A
B
C
D
E
F
16.9960
16.9760
These dimensions are critical
R3
R2
14.0190
13.9990
A
A
9
⊥ 0.05 A
⊥ 0.05 A
Ø 40
2
▱ 0.05 A
38.060
38.040
These surfaces to be flat and parallel
SECTION A-A
SCALE 2 : 1
A
UNLESS OTHERWISE SPECIFIED:
DIMENSIONS ARE IN MILLIMETERS
SURFACE FINISH:
TOLERANCES:
LINEAR:
ANGULAR:
FINISH:
DEBUR AND BREAK SHARP EDGES
DO NOT SCALE DRAWING
REVISION
NAME
SIGNATURE
DATE
DRAWN
CHK'D
APPV'D
MFG
Q.A
MATERIAL:
WEIGHT:
TITLE:
DWG NO.
Delrin_holder_top
A4
SCALE:1:1
SHEET 1 OF 1

b) Bottom fixture holder:

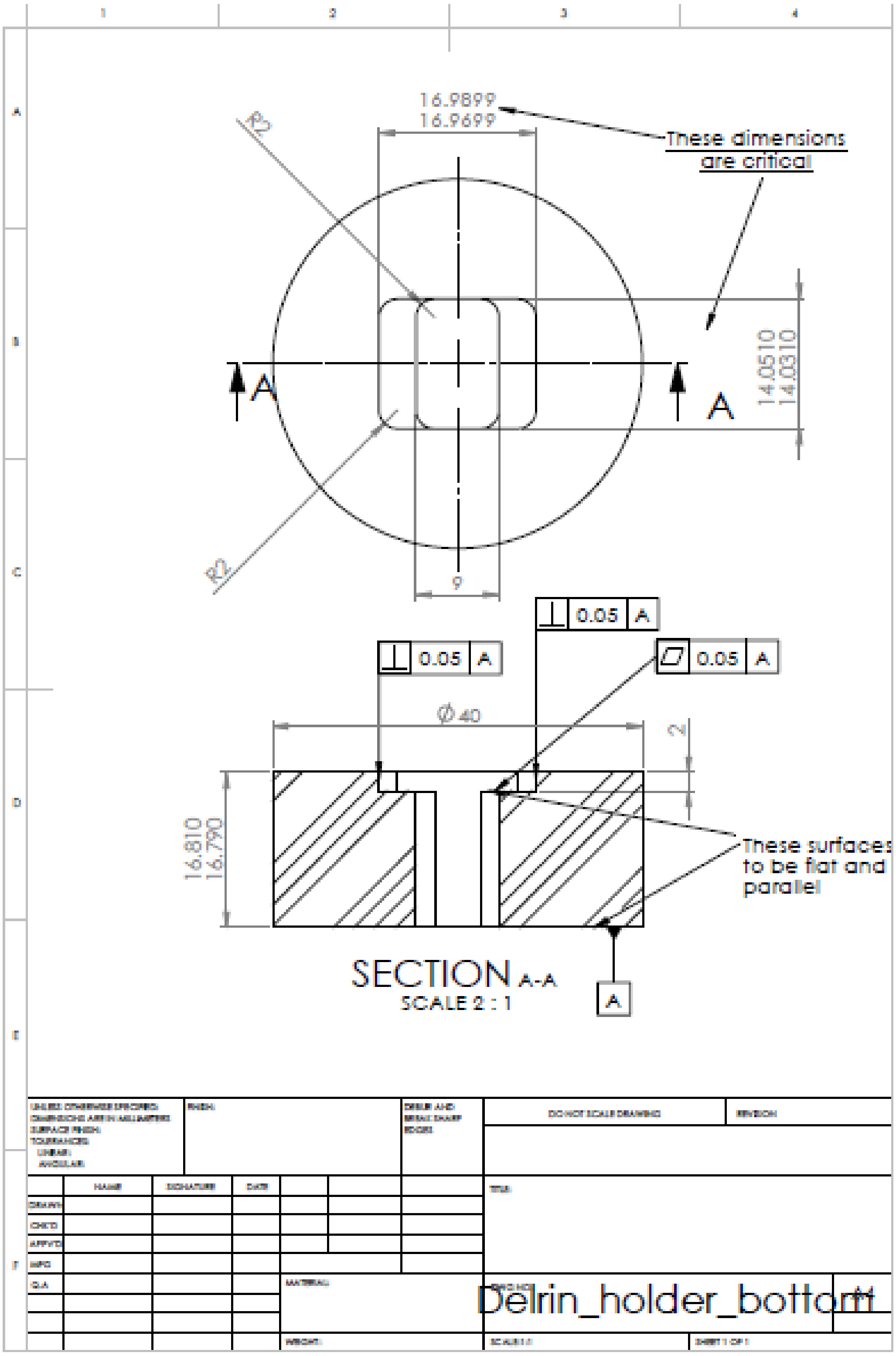
1
2
3
4
A
B
C
D
E
F
16.9899
16.9699
These dimensions are critical
R3
R2
14.0510
14.0310
A
A
9
0.05 A
0.05 A
0.05 A
Ø40
2
16.810
16.790
These surfaces to be flat and parallel
SECTION A-A
SCALE 2 : 1
A
UNLESS OTHERWISE SPECIFIED:
DIMENSIONS ARE IN MILLIMETERS
SURFACE FINISH:
TOLERANCES:
LINEAR:
ANGULAR:
FINISH:
DEBUR AND BREAK SHARP EDGES
DO NOT SCALE DRAWING
REVISION
NAME
SIGNATURE
DATE
TITLE:
DRAWN
CHK'D
APPV'D
MFG
Q.A
MATERIAL:
DWG NO.
Delrin_holder_bottom
A4
WEIGHT:
SCALE:1:1
SHEET 1 OF 1

7.1.4 Appendix IV - Talysurf CTDR component fixture

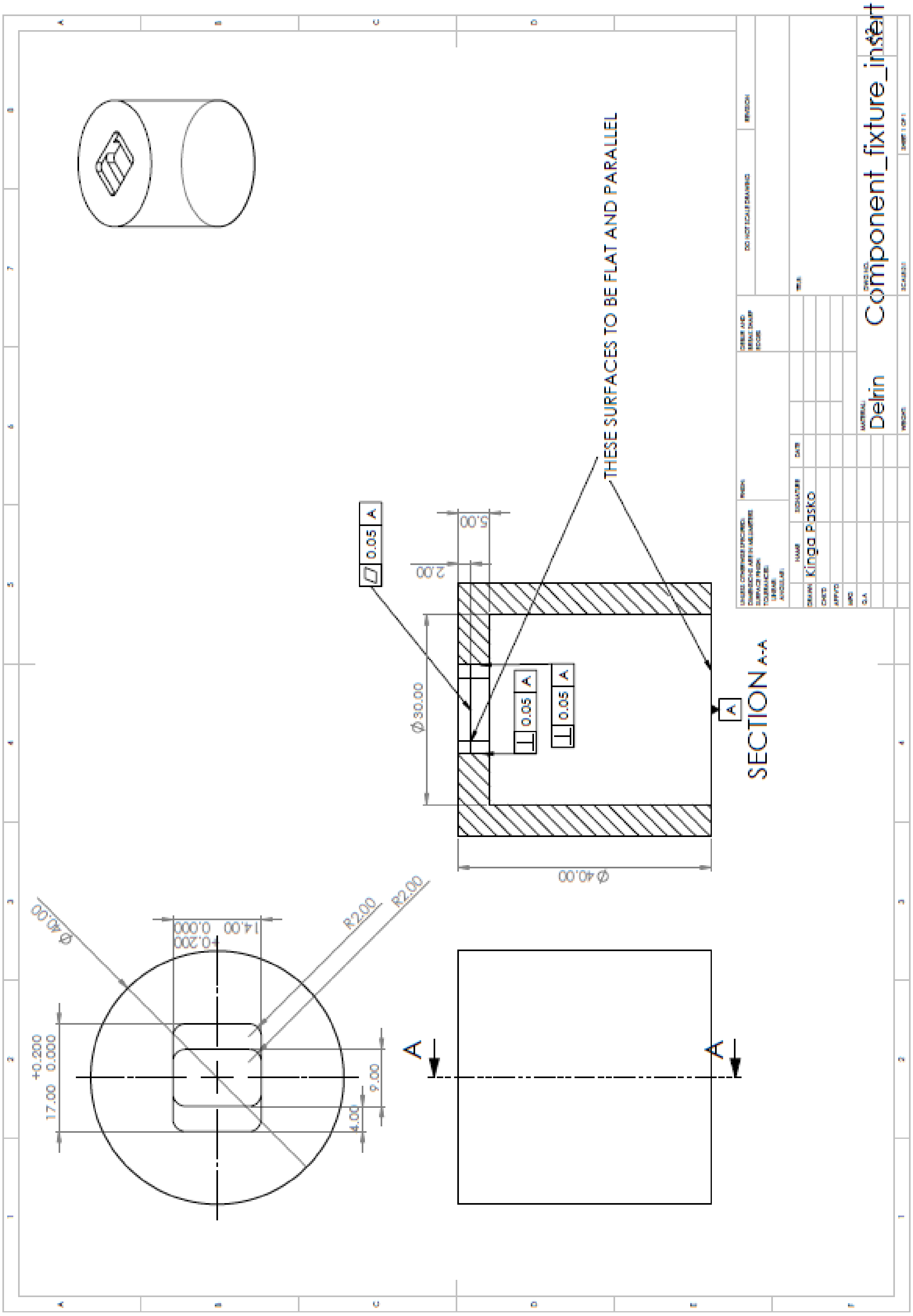
THESE SURFACES TO BE FLAT AND PARALLEL
SECTION A-A
A
A
A
0.05 A
⊥ 0.05 A
⊥ 0.05 A
5.00
2.00
Ø30.00
Ø40.00
Ø40.00
R2.00
R2.00
14.00 +0.200 0.000
17.00 +0.200 0.000
9.00
4.00
Kinga Pasko
Delrin
Component_fixture_insert

7.1.5 Appendix V - SOP 01.03 rev. 6

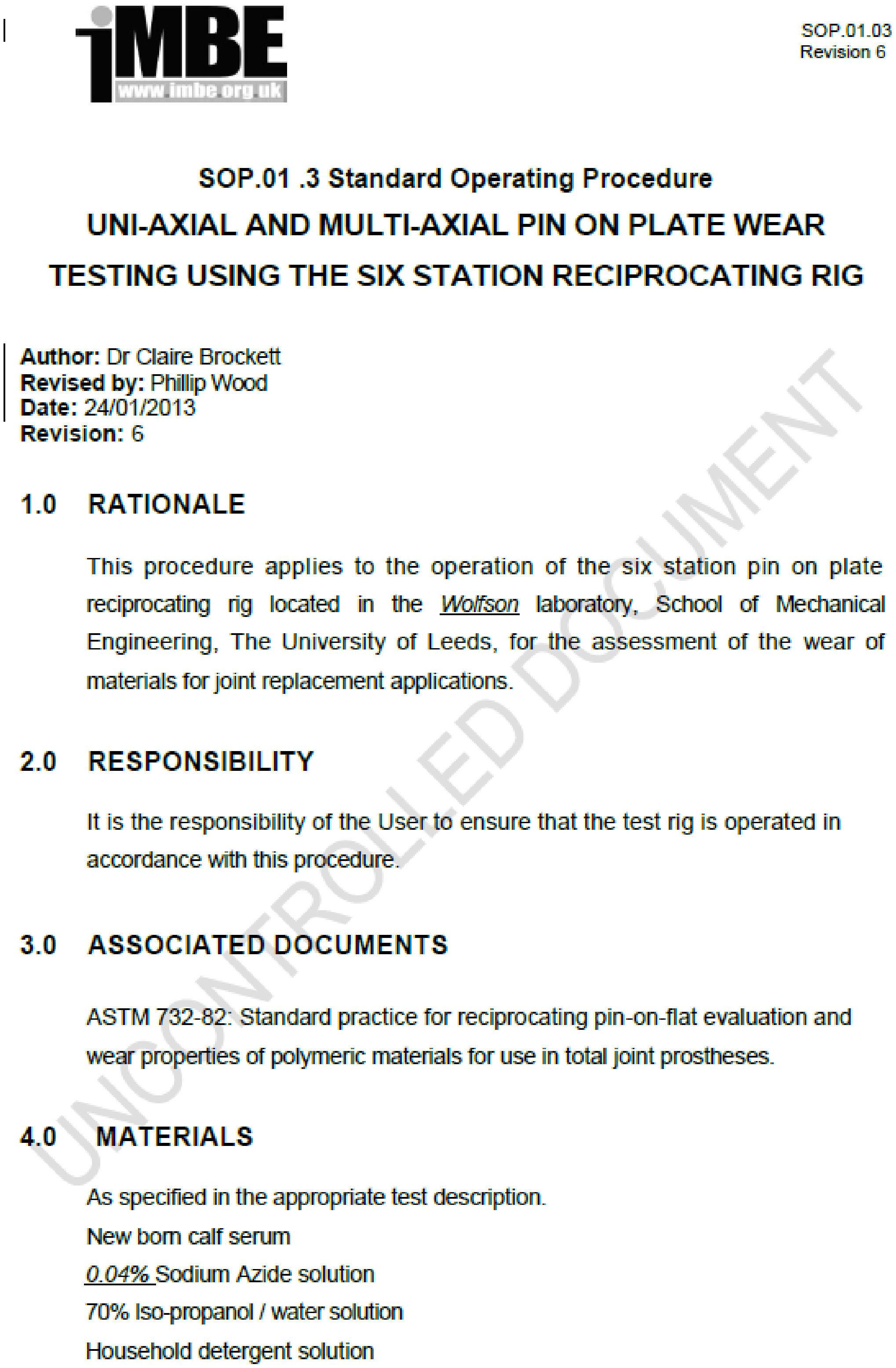

SOP.01.03
Revision 6

SOP.01 .3 Standard Operating Procedure

UNI-AXIAL AND MULTI-AXIAL PIN ON PLATE WEAR TESTING USING THE SIX STATION RECIPROCATING RIG

Author: Dr Claire Brockett
Revised by: Phillip Wood
Date: 24/01/2013
Revision: 6

1.0 RATIONALE

This procedure applies to the operation of the six station pin on plate reciprocating rig located in the *Wolfson* laboratory, School of Mechanical Engineering, The University of Leeds, for the assessment of the wear of materials for joint replacement applications.

2.0 RESPONSIBILITY

It is the responsibility of the User to ensure that the test rig is operated in accordance with this procedure.

3.0 ASSOCIATED DOCUMENTS

ASTM 732-82: Standard practice for reciprocating pin-on-flat evaluation and wear properties of polymeric materials for use in total joint prostheses.

4.0 MATERIALS

As specified in the appropriate test description.
New born calf serum
0.04% Sodium Azide solution
70% Iso-propanol / water solution
Household detergent solution

UNCONTROLLED DOCUMENT

Trigene solution

De-ionised water.

5.0 EQUIPMENT

Six station pin on plate reciprocating wear test rig
Calibrated stopwatch
Calibrated ruler
Calibrated load cell

Balances (Mettler Toledo AT21 digital microbalance & Mettler AT201 digital microbalance)
Ultra sonic cleaner
Form Talysurf

6.0 PROCEDURE

Ensure all specimens and components are visually clean and contaminant free prior to starting this procedure. Lab coats and gloves should be worn at all times.

During operation check the tray lubricant levels and top up as required. Fluid level should *always* be 1-2 mm above the plate wear surface. Also, check the general functioning of the rig. At the beginning and end of each working day fill and operate syringe driver as per section 6.4, *or top up stations as required*.

6.1. Calibration Procedures

The calibration of the load, stroke length and frequency should be checked and adjusted at the beginning of each test.

UNCONTROLLED DOCUMENT

Connect the linear bearings to the scotch yoke mechanism using the connecting rods. For each tray, measure the position of the linear-bearing relative to a fixed point on the bearing base using a calibrated ruler at both ends of sliding. Calculate the stroke length and adjust as required. The actual stroke length should be ±2% of the value required in the test description. Technicians **only** are responsible for altering the stroke lengths.

Insert the bridge sections and cantilever arms, secure with pivot pins. For each station remove spherical ended load screw and replace with flat ended load screw (found in calibration kit). Place the load cell holder in the bridge and under the loading point. Place the calibrated load cell in the holder under the loading point (see Figure 1). Place the weight on the load position on the cantilevered arm required by the test description, gently lower onto the load cell, level with spirit level (see Figure 2), and record the position of the weight. The actual load on the pin shall be ±3% of the value required in the test description.

UNCONTROLLED DOCUMENT

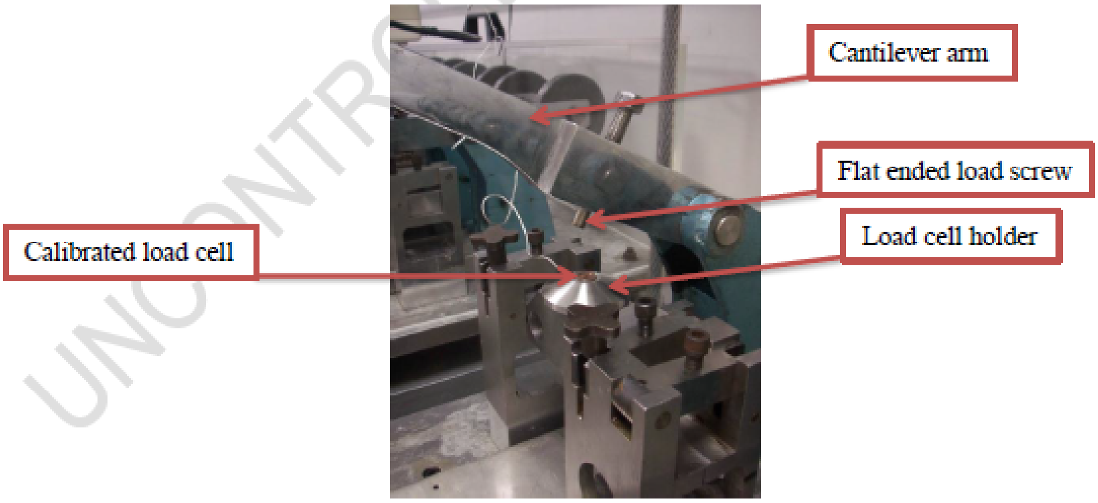

Figure 1

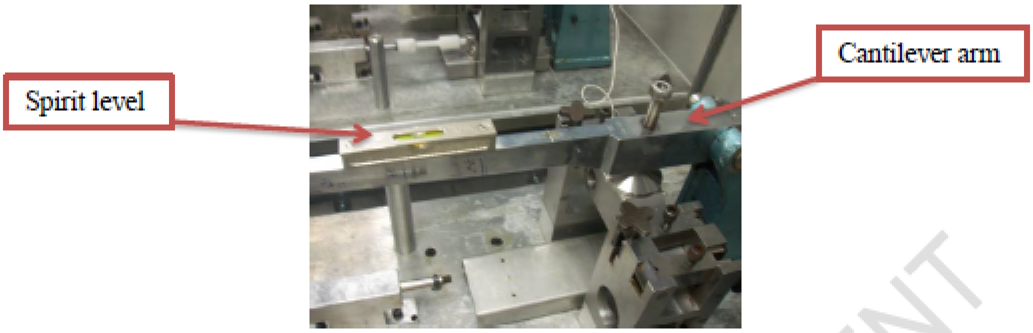

Figure 2

Check that counter is switched on at socket above machine, then check the function of the cycle counter by moving the scotch yoke mechanism ensuring one cycle is counted per pass.

6.2 Preparation of Test Specimens

All specimens should be marked with an identification code and a mark allowing continuity of orientation in the test rig.

Polymer specimens should be pre-soaked in de-ionised water for *at least 14 days* prior to the beginning of a test to ensure any mass change due to moisture absorption has reached a stable level.

Immediately prior to testing, the test specimens should be cleaned ultrasonically with 70% iso-propanol/water solution under the fume hood or on the downdraft table for ten minutes, dried and weighed as per section 6.7 to establish the datum points.

Clean all the metal/ceramic test specimens with 70% iso-propanol/water solution paying particular attention to the wear surface. Characterise the surface topography of the wear surfaces as per section 6.8.
After weighing and characterisation of the surface topography of test specimens, re-clean ultrasonically with 70% iso-propanol/water solution as required prior to

UNCONTROLLED DOCUMENT

setting up the experiment.

6.3 Setting up the Wear Test Rig

Remove the Perspex lid from the wear test rig and ensure all components are present. These should consist of:

- 12 stainless steel screws (large)
- 12 stainless steel screws (small)
- 24 stainless steel screws (small (longer))
- 6 stainless steel wells
- 6 stainless steel bath inserts
- 6 polymer baffles
- 6 stainless steel toothed racks (2 sizes, specify which size) (for multiaxial testing only)
- 6 polymer gear wheels (2 sizes, specify which size) (for multi-axial testing only)
- 4(6) bridge sections (2(0) x double, 2(6) x single spans)
- 6 ball bearing assemblies (12 x grooved racer washers, 6 x bearing inner, 6 x loading washers)
- 6 collets
- 6 pin holder outer sleeves
- 6 threaded nuts
- 6 spacer pins
- 6 connecting rods
- 6 cantilever arms

- 6 weights
- 6 pivot pins
- 12 split pins
- Plastic bearing cover

UNCONTROLLED DOCUMENT

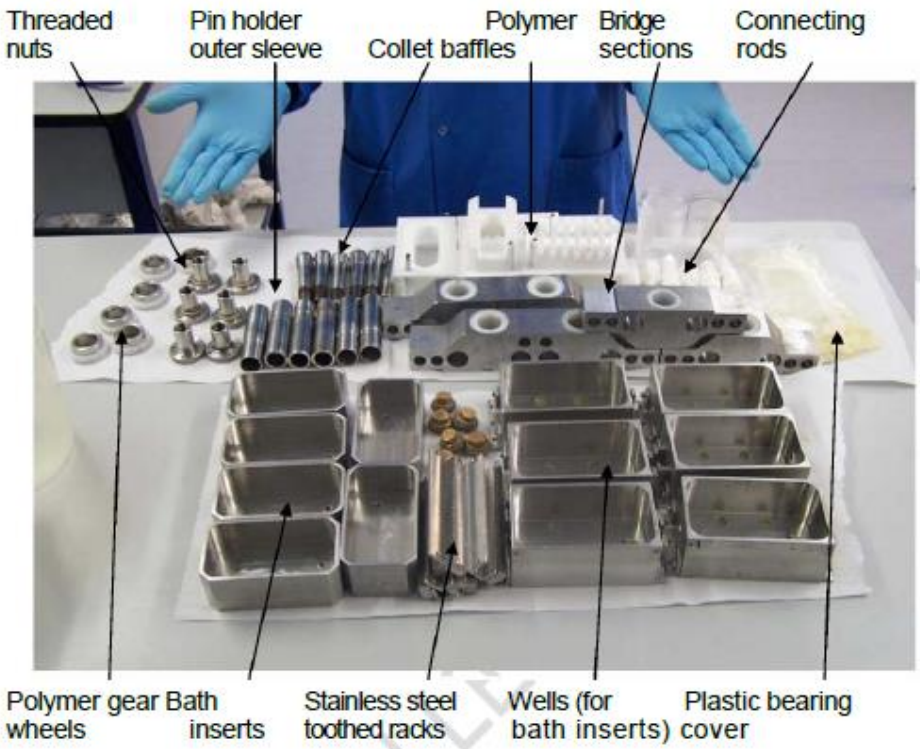
Threaded nuts
Pin holder outer sleeve
Collet baffles
Polymer
Bridge sections
Connecting rods
Polymer gear wheels
Bath inserts
Stainless steel toothed racks
Wells (for bath inserts)
Plastic bearing cover

Figure 3 Components for wear test rig.

6.3.1 Preparation of the Linear Bearing Trays

1. Place the appropriately numbered bath insert into stainless steel well.

2. *Fix* the appropriate plate into the required tray insert using the large screws. Ensure the screw head is not protruding above the wear surface of plate.

3. Note the orientation of the plate and the plate/tray insert numbers. All plates must be replaced into the same tray and in the same orientation after each measurement interval.

4. Select the correct baffle, place over the plate in the tray insert ensuring that

UNCONTROLLED

the small metal pipe is at the back of the tray. Failure to select the correct baffle may cause the fluid inlet pipe to make contact with the bridge during operation.

5. Secure the baffle with PVC tape. Ensure the tape forms a complete seal around the baffle.

6. Connect the fluid inlet pipe (from syringe driver) onto the metal pipe in the baffle, *if required* and secure with PVC tape if necessary.

7. For multi-axial testing, secure the toothed rack onto the left-hand side of the tray using two small screws.

8. Place the bearing tray onto the linear bearing ensuring plastic sheet is underneath. Fasten using 4 of the longer small screws.

Repeat above 8 directions for each tray.

6.3.2 Preparation of the Pin Holders

1. Place a collet into an outer sleeve ensuring correct alignment of keys and tapers (Any collet can be used with any outer sleeve, as there is no number appropriated to them).

2. Loosely screw a threaded nut onto the end of the collet/outer sleeve assembly. Place the required spacer pin into the collet. The face of the test pin must protrude out beyond the collet by approximately 5 mm. Some trial and error may be required to get the appropriate sized spacer pin.

3. Place required pin into collet and tighten the threaded nut to secure the pin in place. If the pin rotates within the collet then it is not seated properly in the pin holder. Loosen the nut, remove the pin and replace it again ensuring it is securely held in place.

UNCONTROLLED DOCUMENT

4. Note the pin/pin holder number. All pins must be replaced into the same station after each measurement interval.

Repeat the above 4 directions for each pin/pin holder.

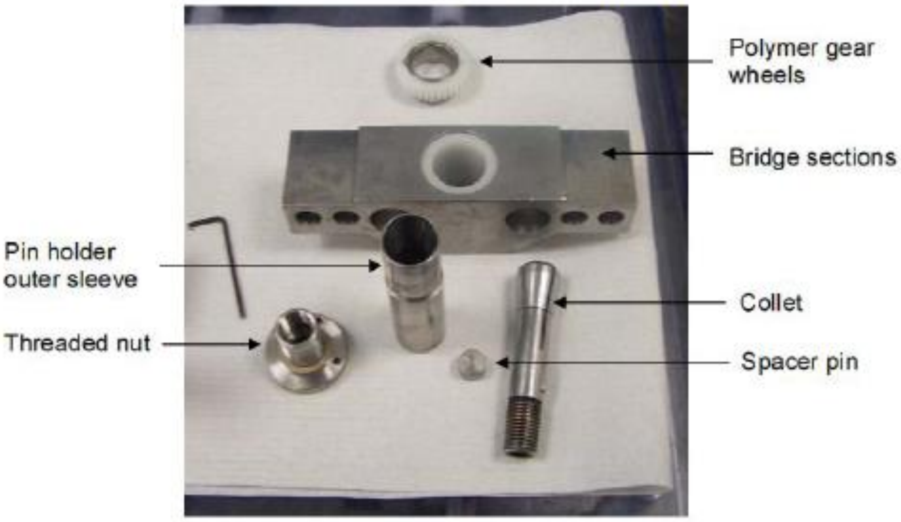

Figure 4 Pin holder components

6.3.3 Final Assembly of the Test Rig

Thread the appropriate pin holder assembly through the required bridge section such that the threaded nut is uppermost.

For multi-axial testing, attach the gear wheel to the top of the pin holder assembly.

Place the bridge sections into the support brackets spanning the trays. Ensure that the number orientation between the tray and the bridge section is correct. Secure using the clamps and ensure that the bridge is correctly located between the support brackets.

Ensure the pins are in contact with the plates and are free to move vertically. Ensure that the threaded nut of the pin holder assembly is not in contact with the

UNCONTROLLED

bridge and that the bottom of the threaded nut remains a couple of millimetres above the bridge.

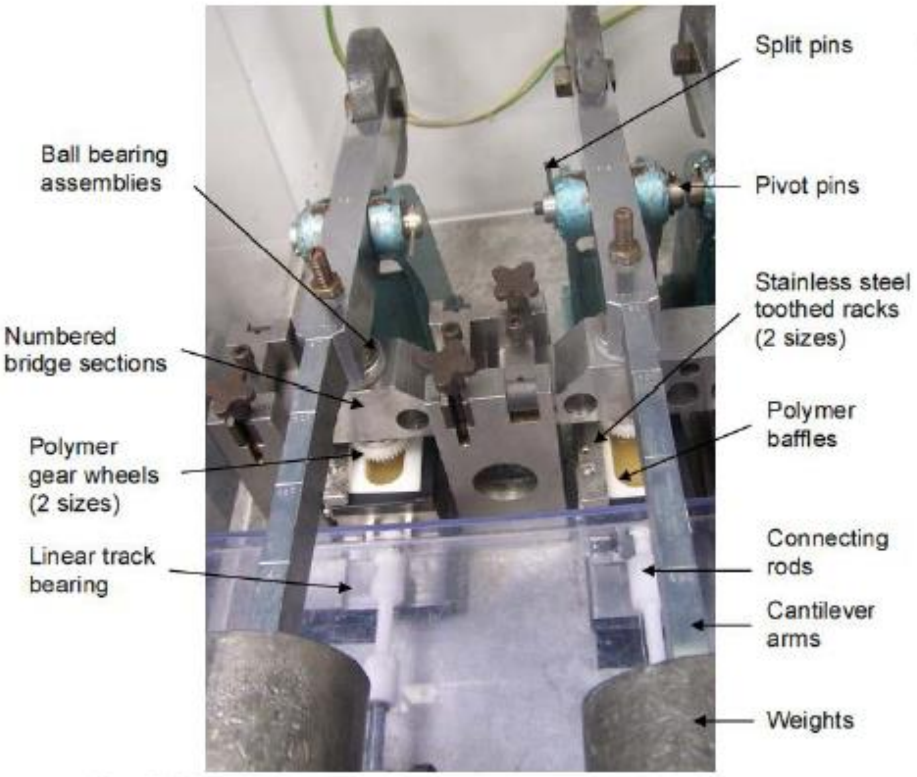
Split pins
Ball bearing assemblies
Pivot pins
Stainless steel toothed racks (2 sizes)
Numbered bridge sections
Polymer baffles
Polymer gear wheels (2 sizes)
Connecting rods
Linear track bearing
Cantilever arms
Weights

UNCO

Figure 5 Fully assembled test rig

Prepare 25% serum lubricant in sodium azide, as per section 6.6.2. Using a syringe place approximately _60_ ml serum solution into each tray. Clean up any spills immediately.

Ensure all linear bearings are functioning.

Connect the scotch yoke mechanism to trays using the connecting rods. Ensure correct sliding distance is set and that the fluid inlet pipes *are not* forced into contact with bridges.

Place the appropriate cantilever arm into bracket and secure the pivot pin with a split pin.

Check that the cantilever arms are level using a spirit level, while either applying a light load by hand or when the actual weights are in position. Adjust the height as necessary until the cantilever arm is level.

If it is the beginning of the study, re-set the cycle counter and start the motor.

Turn the speed controller until the trays are just moving. Adjust the speed to required setting.

Place the appropriately numbered weights onto the cantilever arms and set to the required load position (See calibration of test rig – Section 6.1). The pin on plates rigs must never be started with the weights on.

Check the speed of the test rig using the calibrated stopwatch, the actual speed should be within 10% of the value required as described in the Description of the Test Method.

Replace the rig's Perspex lid.

Fill the syringe driver and operate as per section 6.4, *if required*.

6.4 Setting Up of Syringe Driver Mechanism

Ensure syringe driver motor is turned off (switch should not be lit up).

UNCONTROLLED DOCUMENT

Turn off the valves on all six of the syringes.

Remove the nuts securing the syringe holder.

Loosen the grub screw on the drive shaft; remove syringe holder and place to one side. Detach the threaded shaft from the drive shaft and rewind until all the exposed thread has gone. Reconnect the drive shaft to the threaded shaft ensuring correct alignment. Secure with the grub screw.

Refill all syringes with a similar volume of 0.03 % sodium azide solution made up as per SOP.06.6.

Replace the syringe holder with syringes into the driver and secure with the nuts.

At the beginning of the test flush out the pipes with distilled water, and then prime with 0.03% sodium azide. Re-attach the pipes and turn on all the six valves.

As required, switch on the syringe driver motor and adjust its speed. The quantity of sodium azide solution delivered to the rig will depend on the type of test. For example, metal on metal tests generate a lot of heat and therefore requires additional fluid.

Check the pipes are secure in trays.

To manually top up the pin on plate *rigs whilst the machine is still running* top up each station as required using a syringe and 0.03% sodium azide.

UNCONTROLLED DOCUMENT

6.5 Dismantling the Wear Test Rig

Turn the speed controller down until the machine stops and switch the motor off.

Note the number of cycles.

Switch the syringe driver off.

Remove the counter-weights and cantilever arms.

Remove the ball bearing assemblies from the tops of the pin holders

Disconnect the trays from the scotch yoke mechanisms by removing the connecting rods.

Carefully remove each bridge section.

Where appropriate, remove the gear wheel assembly from the pin holders. Carefully remove each pin holder from the bridge section, loosen the threaded nut and remove the pin (this may require tapping the end of the pin holder to loosen the pin). Remove the pin using a tissue or some other suitable material in order to avoid touching the pin itself.

Place the pin and pin holder assembly components into separate tubs of detergent solution.

Detach the fluid inlet pipes*, as required*.

Using a syringe and tube, transfer all the serum lubricant into a bottle, seal; and label bottle for further analysis or disposal. Flush the syringe and tube before moving onto the next station.
Remove each bearing tray from the linear bearing and place onto the plastic tray holder.

Carefully remove the PVC tape, baffles and bath inserts.

UNCONTROLLED DOCUMENT

Place the baffles and bath inserts into detergent solution.

Remove the plates and place into a separate container with detergent solution.

Wipe the plastic sheets from the top of the linear bearings and dry. Dry the metal cover on linear bearing. Take off metal cover and ensure that there is no corrosion on the bearing.

Clean all rig components (not specimens) in detergent solution until no visible contamination remains. Transfer all components into Trigene solution and allow to soak for a minimum of 20 minutes. Rinse in de-ionised water and *dry the components. Do not leave to drain as this may result in corrosion of the metallic components.*

Clean the plates and pins with detergent solution to remove all visible contamination for 5 minutes in the ultrasonic bath. Rinse well. *Soak plates and pins in Trigene solution for ten minutes. Rinse samples in de-ionised water.* Clean the pins and plates in 70% iso-propanol/water solution in the ultrasonic bath under the fume hood or on the downdraft table for 10 minutes. Remove and wipe clean using tissue.

Once clean and dry always handle the pins and plates with tweezers *or gloves* as any grease deposits from skin contact may affect measurements.

The pins and plates (where appropriate) are ready for measurement.

Visually inspect the plate wear surfaces and check for transfer film. Damaged plates may require replacing or re-surfacing.

Place all rig components into the rig and replace lid.

UNCONTROLLED DOCUMENT

6.6 Making up of Serum Solutions

The Serum/Sodium Azide lubricant, described below, shall be used unless otherwise specified in the Description of the Test Method.

6.6.1 0.03 and 0.04 % Sodium Azide Solution

Mix up sodium azide solution according to SOP.06.6.

6.6.2 Serum/Sodium Azide Solution

The serum is usually supplied frozen and must be totally defrosted before use.

In the fume hood or on the downflow table and wearing the appropriate protective clothing, measure 100 ml of serum into an appropriately sized container.

Measure 300 ml 0.04% sodium azide into a container (*this gives the serum/sodium azide solution a 0.03% composition)*. Mix gently to ensure complete mixture of the solution.

Any excess 25% serum solution should be decanted into a bottle, labelled, dated accordingly and placed in a refrigerator. The serum solution may be used for up to a week after mixing.

Rinse all containers thoroughly to remove all traces of sodium azide solution.

6.7 Weighing of Pin and Plate Specimens

Pin specimens, and where appropriate plates, shall be weighed at the start, end and at regular intervals during the test as described in the test description.

Once clean and dry always handle the pins and plates with tweezers as any grease deposits from skin contact may affect the weight loss.

UNCONTROLLED DOCUMENT

Place the pins/plates into a clean container(s) and transfer the container(s) to the balance room within the measurements laboratory.

Allow the pins/plates to acclimatise: minimum at least 12 hours for metal and ceramic pins and a minimum of 48 hours for polymer pins.

Check the calibration of the balance by measuring the test masses *available within the balance room*.

Weigh pins/plates under 20g on the Mettler Toledo AT21 digital microbalance at least five times such that all measurements are within .5 µg of each other. Weigh pins/plates over 20g on the Mettler AT201 digital microbalance at least five times such that all measurements are within .0.05 mg of each other.

Calculate the average weight loss/gain for each pin/plate, adjusting for moisture uptake using control pins if appropriate (e.g. polyethylene pins). Convert into volume loss/gain by dividing by the density.

6.8 Surface Measurement of Plate Specimens

Where specified in the Description of the Test Method, surface measurement of plate specimens shall occur either at the beginning and end of each test or after they have been repaired.

Ensure the plates are free from contamination paying particular attention to the wear surface.

For the initial measurement, and for plates with a uniform roughness, measure the plate in five places across the middle of the wear surface recording R_a, R_t, R_v, R_p, R_{p1max} ^{and} R_{v1max} at a 5 x 0.8 mm cut-off and using a Gaussian filter. A cut-off of 20 x 0.25 mm may be used if large amounts of waviness are present.
Measure plates with variable surface roughness in sufficient places to

UNCONTROLLED DOCUMENT

characterise all areas. For example, plates with discrete scratches shall be measured in the same manner as uniform plates to identify the background roughness and each scratch shall be measured perpendicular to the scratch direction at the centre of the wear surface. For each scratch R_t, R_{p1max}, R_{v1max} and peak spacing shall be recorded.

6.9 Surface Measurement of Pin Specimens

Where specified in the Description of the Test Method, surface measurement of the pin specimens shall occur either at the beginning and end of each test.

Ensure the pins are free from contamination. Pay particular attention to the wear surface.

For the initial measurement, measure the pin across the centre line of the wear surface in two directions perpendicular to each other. Record R_a, R_t, R_v, R_p, $R_{p1max}{}^{and}{}_{Rv1max}$ at a 5 x 0.8 mm cut-off and using a Gaussian filter, although 20 x 0.25 mm may be used if large amounts of waviness is present or if the wear surface is curved. After testing has begun, for pins with a uniform roughness, repeat the above measurement.

7.0 APPROVAL

Author: Phillip Wood Date:

Laboratory Captain: Dr Louise Jennings Date:

UNCONTROLLED DOCUMENT

Chapter 8 : References

[1] R. Fejer, K.O. Kyvik, J. Hartvigsen, The prevalence of neck pain in the world population: a systematic critical review of the literature, Eur. Spine J. 15 (2006) 834–848. doi:DOI 10.1007/s00586-004-0864-4.

[2] T. Vos, A.D. Flaxman, M. Naghavi, M.A. AlMazroa, Z.A. Memish, Years lived with disability (YLDs) for 1160 sequelae of 289 diseases and injuries 1990-2010: a systematic analysis for the Global Burden of Disease Study 2010 (vol 380, pg 2163, 2012), Lancet. 381 (2013) 628.

[3] D.G. Hoy, M. Protani, R. De, R. Buchbinder, The epidemiology of neck pain, Best Pract. Res. Clin. Rheumatol. 24 (2010) 783–792. doi:DOI 10.1016/j.berh.2011.01.019.

[4] L.J. Carroll, S. Hogg-Johnson, G. van der Velde, S. Haldeman, L.W. Holm, E.J. Carragee, E.L. Hurwitz, P. Cote, M. Nordin, P.M. Peloso, J. Guzman, J.D. Cassidy, Course and prognostic factors for neck pain in the general population - Results of the bone and joint decade 2000-2010 task force on neck pain and its associated disorders, J Manip. Physiol Ther. 32 (2008) S75–S82. doi:DOI 10.1016/j.jmpt.2008.11.013.

[5] J. Hill, M. Lewis, A.C. Papageorgiou, K. Dziedzic, P. Croft, Predicting persistent neck pain - A 1-year follow-up of a population cohort, Spine (Phila Pa 1976). 29 (2004) 1648–1654. doi:Doi 10.1097/01.Brs.0000132307.06321.3c.

[6] P. Cote, G. van der Velde, J.D. Cassidy, L.J. Carroll, S. Hogg-Johnson, L.W. Holm, E.J. Carragee, S. Haldeman, M. Nordin, E.L. Hurwitz, J. Guzman, P.M. Peloso, The burden and determinants of neck pain in workers - Results of the bone and joint decade 2000-2010 task force on neck pain and its associated disorders, J Manip. Physiol Ther. 32 (2008) S60–S74. doi:DOI 10.1016/j.jmpt.2008.11.012.

[7] S.D.M. Bot, J.M. van der Waal, C.B. Terwee, D.A.W.M. van der Windt, F.G. Schellevis, L.M. Bouter, J. Dekker, Incidence and prevalence of complaints of the neck and upper extremity in general practice, Ann Rheum Dis. 64 (2005) 118–123. doi:DOI 10.1136/ard.2003.019349.

[8] P. Cote, J.D. Cassidy, L.J. Carroll, V. Kristman, The annual incidence and course of neck pain in the general population: a population-based cohort study, Pain. 112 (2004) 267–273. doi:DOI 10.1016/j.pain.2004.09.004.

[9] S.D.M. Bot, J.M. van der Waal, C.B. Terwee, D.A.W.M. van der Windt, R.J.P.M. Scholten, L.M. Bouter, J. Dekker, Predictors of outcome in neck and shoulder symptoms - A cohort study in general practice, Spine (Phila Pa 1976). 30 (2005) E459–E470. doi:DOI

10.1097/01.brs.0000174279.44855.02.

[10] A. Berglund, L. Alfredsson, I. Jensen, J.D. Cassidy, A. Nygren, The association between exposure to a rear-end collision and future health complaints, J Clin Epidemiol. 54 (2001) 851–856. doi:Doi 10.1016/S0895-4356(00)00369-3.

[11] E.L. Hurwitz, M.S. Goldstein, H. Morgenstern, L.M. Chiang, The impact of psychosocial factors on neck pain and disability outcomes among primary care patients: Results from the UCLA Neck Pain Study, Disabil Rehabil. 28 (2006) 1319–1329. doi:Doi 10.1080/09638280600641509.

[12] J.L. Kelsey, P.B. Githens, S.D. Walter, W.O. Southwick, U. Weil, T.R. Holford, A.M. Ostfeld, J.A. Calogero, T. Oconnor, A.A. White, An Epidemiological-Study of Acute Prolapsed Cervical Intervertebral-Disk, J. Bone Jt. Surgery-American Vol. 66A (1984) 907–914.

[13] K.T. Palmer, K. Walker-Bone, M.J. Griffin, H. Syddall, B. Pannett, D. Coggon, C. Cooper, Prevalence and occupational associations of neck pain in the British population, Scand J Work Env. Heal. 27 (2001) 49–56. http://www.ncbi.nlm.nih.gov/pubmed/11266146.

[14] J. Guzman, E.L. Hurwitz, L.J. Carroll, S. Haldeman, P. Cote, E.J. Carragee, P.M. Peloso, G. van der Velde, L.W. Holm, S. Hogg-Johnson, M. Nordin, J.D. Cassidy, A new conceptual model of neck pain - Linking onset, course, and care: The bone and joint decade 2000-2010 task force on neck pain and its associated disorders, Spine (Phila Pa 1976). 33 (2008) S14–S23.

[15] L. Manchikanti, V. Singh, S. Datta, S.P. Cohen, J.A. Hirsch, Comprehensive Review of Epidemiology, Scope, and Impact of Spinal Pain, Pain Physician. 12 (2009) E35–E70.

[16] B.I. Martin, R.A. Deyo, S.K. Mirza, J.A. Turner, B.A. Comstock, W. Hollingworth, S.D. Sullivan, Expenditures and health status among adults with back and neck problems, JAMA. 299 (2008) 656–664. doi:10.1001/jama.299.6.656.

[17] S. Haldeman, L.J. Carroll, J.D. Cassidy, The empowerment of people with neck pain: Introduction - The bone and joint decade 2000-2010 task force on neck pain and its associated disorders, Spine (Phila Pa 1976). 33 (2008) S8–S13.

[18] AAOS, Burden of Musculoskeletal Diseases in the United States: Prevalence, Societal and Economic Cost, American Academy of Orthopaedic Surgeons, 2008. http://books.google.co.uk/books?id=Mp0TAQAAMAAJ.

[19] A. Wright, T.G. Mayer, R.J. Gatchel, Outcomes of disabling cervical spine disorders in compensation injuries - A prospective comparison to tertiary rehabilitation response for chronic lumbar spinal disorders, Spine (Phila Pa 1976). 24 (1999) 178–183. doi:Doi 10.1097/00007632-199901150-00020.

[20] W.L. Eckalbar, R.E. Fisher, A. Rawls, K. Kusumi, Scoliosis and segmentation defects of the vertebrae, Wiley Interdiscip. Rev. Dev. Biol. 1 (2012) 401–423. doi:10.1002/wdev.34.

[21] M. Nordin, V.H. Frankel, D. Leger, Basic biomechanics of the musculoskeletal system, 4th ed., Lippincott Williams & Wilkins, Baltimore, MD ; London, 2012.

[22] O.A. Onan, M.H. Heggeness, J.A. Hipp, A motion analysis of the cervical facet joint, Spine (Phila Pa 1976). 23 (1998) 430–439.

[23] C.R. Clark, T.B. Ducker, Cervical Spine Research Society. Editorial Committee., The cervical spine, 3rd ed., Lippincott-Raven, Philadelphia, 1998.

[24] J.D. Bartleson, H.G. Deen, Spine disorders : medical and surgical management, Cambridge University Press, Cambridge, 2009.

[25] V.K. Goel, A. Faizan, V. Palepu, S. Bhattacharya, Parameters that effect spine biomechanics following cervical disc replacement, Eur. Spine J. 21 Suppl 5 (2012) S688-99. doi:10.1007/s00586-011-1816-4.

[26] G.V.K. Faizan A Krishna M, Friesem T, Effects of removal of uncinate process in the cervical disc replacement model: a finite element study, in: 53rd Annu. Meet. Orthop. Res. Soc., San Diego, CA, 2007.

[27] J.T. Snyder, M.N. Tzermiadianos, A.J. Ghanayem, L.I. Voronov, A. Rinella, A. Dooris, G. Carandang, S.M. Renner, R.M. Havey, A.G. Patwardhan, Effect of uncovertebral joint excision on the motion response of the cervical spine after total disc replacement, Spine (Phila Pa 1976). 32 (2007) 2965–2969. doi:10.1097/BRS.0b013e31815cd482.

[28] N. Bogduk, S. Mercer, Biomechanics of the cervical spine. I: Normal kinematics, Clin Biomech (Bristol, Avon). 15 (2000) 633–648. http://www.ncbi.nlm.nih.gov/pubmed/10946096.

[29] M. Muller-Gerbl, S. Weisser, U. Linsenmeier, The distribution of mineral density in the cervical vertebral endplates, Eur. Spine J. 17 (2008) 432–438. doi:10.1007/s00586-008-0601-5.

[30] E.C. Benzel, The cervical spine, 5th ed., Lippincott Williams & Wilkins, Philadelphia, PA, USA, 2012.

[31] P.C. Ivancic, M.P. Coe, A.B. Ndu, Y. Tominaga, E.J. Carlson, W. Rubin, F.H. Dipl-Ing, M.M. Panjabi, Dynamic mechanical properties of intact human cervical spine ligaments, Spine J. 7 (2007) 659–665. doi:http://dx.doi.org/10.1016/j.spinee.2006.10.014.

[32] H.C. Elliott, Cross-sectional diameters and areas of the human spinal cord, Anat Rec. 93 (1945) 287–293. http://www.ncbi.nlm.nih.gov/pubmed/21008200.

[33] A.A. White, M.M. Panjabi, Clinical biomechanics of the spine, 2nd ed., Lippincott, Philadelphia, 1990.

[34] L.T. Twomey, J.R. Taylor, Age-Changes in Lumbar Vertebrae and Intervertebral Disks, Clin. Orthop. Relat. Res. (1987) 97–104.

[35] H.S. An, P.A. Anderson, V.M. Haughton, J.C. Iatridis, J.D. Kang, J.C. Lotz, R.N. Natarajan, T.R. Oegema Jr., P. Roughley, L.A. Setton, J.P. Urban, T. Videman, G.B. Andersson, J.N. Weinstein, Introduction: disc degeneration: summary, Spine (Phila Pa 1976). 29 (2004) 2677–2678. http://www.ncbi.nlm.nih.gov/pubmed/15564916.

[36] J. Yu, P.C. Winlove, S. Roberts, J.P. Urban, Elastic fibre organization in the intervertebral discs of the bovine tail, J Anat. 201 (2002) 465–475. http://www.ncbi.nlm.nih.gov/pubmed/12489758.

[37] J.P.G. Urban, A. Maroudas, M.T. Bayliss, J. Dillon, Swelling Pressures of Proteoglycans at the Concentrations Found in Cartilaginous Tissues, Biorheology. 16 (1979) 447–464.

[38] F. Galbusera, M. van Rijsbergen, K. Ito, J.M. Huyghe, M. Brayda-Bruno, H.-J. Wilke, Ageing and degenerative changes of the intervertebral disc and their impact on spinal flexibility, Eur. Spine J. 23 (2014) 324–332. doi:10.1007/s00586-014-3203-4.

[39] N.A. Ebraheim, A. Hassan, M. Lee, R. Xu, Functional anatomy of the lumbar spine, Semin. Pain Med. 2 (2004) 131–137. doi:http://dx.doi.org/10.1016/j.spmd.2004.08.004.

[40] J. Schroder, M. Herbort, P. Rustemeyer, V. Vieth, H. Wassmann, Mechanical response of cervical vertebral endplates to axial loading, Zentralbl Neurochir. 67 (2006) 188–192. doi:10.1055/s-2006-942279.

[41] T.G. Lowe, S. Hashim, L.A. Wilson, M.F. O'Brien, D.A. Smith, M.J. Diekmann, J. Trommeter, A biomechanical study of regional endplate strength and cage morphology as it relates to structural interbody support, Spine (Phila Pa 1976). 29 (2004) 2389–2394.

[42] R.S. Ochia, A.F. Tencer, R.P. Ching, Effect of loading rate on endplate and vertebral body strength in human lumbar vertebrae, J Biomech. 36 (2003) 1875–1881. doi:http://dx.doi.org/10.1016/S0021-9290(03)00211-2.

[43] S. Roberts, S.M. Eisenstein, J. Menage, E.H. Evans, I.K. Ashton, Mechanoreceptors in intervertebral discs - Morphology, distribution, and neuropeptides, Spine (Phila Pa 1976). 20 (1995) 2645–2651. doi:Doi 10.1097/00007632-199512150-00005.

[44] S.P. Moroney, A.B. Schultz, J.A. Miller, Analysis and measurement of neck loads, J Orthop Res. 6 (1988) 713–720. doi:10.1002/jor.1100060514.

[45] D.A. Winter, Anthropometry, in: Biomech. Mot. Control Hum. Mov., John Wiley & Sons, Inc., 2009: pp. 82–106. doi:10.1002/9780470549148.ch4.

[46] M.M. Panjabi, J. Cholewicki, K. Nibu, J. Grauer, L.B. Babat, J. Dvorak, Critical load of the human cervical spine: an in vitro experimental study, Clin Biomech (Bristol, Avon). 13 (1998) 11–17. http://www.ncbi.nlm.nih.gov/pubmed/11415766.

[47] J.A. Buckwalter, Aging and degeneration of the human intervertebral disc, Spine (Phila Pa 1976). 20 (1995) 1307–1314. http://www.ncbi.nlm.nih.gov/pubmed/7660243.

[48] C. Lansade, S. Laporte, P. Thoreux, M.A. Rousseau, W. Skalli, F. Lavaste, Three-dimensional analysis of the cervical spine kinematics: effect of age and gender in healthy subjects, Spine (Phila Pa 1976). 34 (2009) 2900–2906. doi:10.1097/BRS.0b013e3181b4f667.

[49] D.. H. Cobian B.; Daehn, N.; Anderson, P.A, Comparison of Daily Motion of the Cervical and Lumbar Spine to ASTM F2423-11 and ISO 18192-1.2011 Standard Testing, Static Dyn. Spinal Implant. Are We Eval. Them Appropriately? 1535 (2012) 14. doi:10.1520/JAI103522.

[50] S.E. Bennett, R.J. Schenk, E.D. Simmons, Active range of motion utilized in the cervical spine to perform daily functional tasks, J Spinal Disord Tech. 15 (2002) 307–311.

[51] E. Lysell, Motion in the cervical spine. An experimental study on autopsy specimens, Acta Orthop Scand. (1969) Suppl 123:1+. http://www.ncbi.nlm.nih.gov/pubmed/4907116.

[52] M. Panjabi, J. Dvorak, J. Crisco 3rd, T. Oda, A. Hilibrand, D. Grob, Flexion, extension, and lateral bending of the upper cervical spine in response to alar ligament transections, J Spinal Disord. 4 (1991) 157–167. http://www.ncbi.nlm.nih.gov/pubmed/1806080.

[53] M.P. Steinmetz, T.E. Mroz, E.C. Benzel, Craniovertebral junction: biomechanical considerations, Neurosurgery. 66 (2010) 7–12. doi:10.1227/01.NEU.0000366109.85796.42.

[54] V.K. Goel, C.R. Clark, D. McGowan, S. Goyal, An in-vitro study of the kinematics of the normal, injured and stabilized cervical spine, J Biomech. 17 (1984) 363–376. http://www.ncbi.nlm.nih.gov/pubmed/6736071.

[55] S.P. Cohen, Epidemiology, Diagnosis, and Treatment of Neck Pain, Mayo Clin. Proc. 90 (2015) 284–299. doi:10.1016/j.mayocp.2014.09.008.

[56] K. Fujiwara, M. Fujimoto, H. Owaki, J. Kono, T. Nakase, K. Yonenobu, T. Ochi, Cervical lesions related to the systemic progression in rheumatoid arthritis, Spine (Phila Pa 1976). 23 (1998) 2052–2056. http://www.ncbi.nlm.nih.gov/pubmed/9794048.

[57] W.O. Spitzer, M.L. Skovron, L.R. Salmi, J.D. Cassidy, J. Duranceau, S. Suissa, E. Zeiss, M.L. Skooron, L.R. Salmi, J.D. Cassidy, J. Duranceau, S. Suissa, E. Zeiss, Scientific Monograph of the Quebec Task-Force on Whiplash-Associated Disorders - Redefining Whiplash and Its Management, Spine (Phila Pa 1976). 20 (1995) 2372.

[58] R. Ferrari, Prevention of chronic pain after whiplash, Emerg Med J. 19 (2002) 526–530. http://www.ncbi.nlm.nih.gov/pubmed/12421777.

[59] H.H. Bohlman, S.E. Emery, D.B. Goodfellow, P.K. Jones, Robinson anterior cervical discectomy and arthrodesis for cervical radiculopathy.

Long-term follow-up of one hundred and twenty-two patients, J Bone Jt. Surg Am. 75 (1993) 1298–1307. http://www.ncbi.nlm.nih.gov/pubmed/8408151.

[60] T. Adamson, S.S. Godil, M. Mehrlich, S. Mendenhall, A.L. Asher, M.J. McGirt, Anterior cervical discectomy and fusion in the outpatient ambulatory surgery setting compared with the inpatient hospital setting: analysis of 1000 consecutive cases, J. Neurosurg. Spine. 24 (2016) 878–884. doi:10.3171/2015.8.SPINE14284.

[61] P.S. Saphier, M.S. Arginteanu, F.M. Moore, A.A. Steinberger, M.B. Camins, Stress-shielding compared with load-sharing anterior cervical plate fixation: a clinical and radiographic prospective analysis of 50 patients, J Neurosurg Spine. 6 (2007) 391–397. doi:10.3171/spi.2007.6.5.391.

[62] U.K. Chang, D.H. Kim, M.C. Lee, R. Willenberg, S.H. Kim, J. Lim, Changes in adjacent-level disc pressure and facet joint force after cervical arthroplasty compared with cervical discectomy and fusion, J Neurosurg Spine. 7 (2007) 33–39. doi:10.3171/SPI-07/07/033.

[63] M.P. Kelly, J.M. Mok, R.F. Frisch, B.K. Tay, Adjacent segment motion after anterior cervical discectomy and fusion versus Prodisc-c cervical total disk arthroplasty: analysis from a randomized, controlled trial, Spine (Phila Pa 1976). 36 (2011) 1171–1179. doi:10.1097/BRS.0b013e3181ec5c7d.

[64] J. Goffin, E. Geusens, N. Vantomme, E. Quintens, Y. Waerzeggers, B. Depreitere, F. Van Calenbergh, J. van Loon, Long-term follow-up after interbody fusion of the cervical spine, J Spinal Disord Tech. 17 (2004) 79–85. http://www.ncbi.nlm.nih.gov/pubmed/15260088.

[65] A.S. Hilibrand, G.D. Carlson, M.A. Palumbo, P.K. Jones, H.H. Bohlman, Radiculopathy and myelopathy at segments adjacent to the site of a previous anterior cervical arthrodesis, J. Bone Jt. Surgery-American Vol. 81A (1999) 519–528.

[66] D.-H. Lee, J.H. Cho, C.J. Hwang, C.S. Lee, S.K. Cho, C. Kim, J.-K. Ha, What is the Fate of Pseudarthrosis Detected 1 Year After Anterior Cervical Discectomy and Fusion?, Spine (Phila. Pa. 1976). (2017) 1. doi:10.1097/BRS.0000000000002077.

[67] B. Moatz, P.J. Tortolani, Cervical disc arthroplasty: Pros and cons, Surg Neurol Int. 3 (2012) S216-24. doi:10.4103/2152-7806.98582.

[68] M. Thaler, S. Hartmann, M. Gstottner, R. Lechner, M. Gabl, C. Bach, Footprint mismatch in total cervical disc arthroplasty, Eur. Spine J. 22 (2013) 759–765. doi:10.1007/s00586-012-2594-3.

[69] M. Gstoettner, D. Heider, M. Liebensteiner, C.M. Bach, Footprint mismatch in lumbar total disc arthroplasty, Eur. Spine J. 17 (2008) 1470–1475. doi:10.1007/s00586-008-0780-0.

[70] B.M. Wroblewski, P.D. Siney, P.A. Fleming, The principle of low frictional torque in the Charnley total hip replacement, J Bone Jt. Surg Br. 91 (2009)

855–858. doi:10.1302/0301-620X.91B7.22027.

[71] A. Shaheen, D.E. Shepherd, Lubrication regimes in lumbar total disc arthroplasty, Proc Inst Mech Eng H. 221 (2007) 621–627. http://www.ncbi.nlm.nih.gov/pubmed/17937201.

[72] H. Yao, W.Y. Gu, Physical signals and solute transport in human intervertebral disc during compressive stress relaxation: 3D finite element analysis, Biorheology. 43 (2006) 323–335. http://www.ncbi.nlm.nih.gov/pubmed/16912405.

[73] W. V Dowson. D, Bio-tribology, in: D. T.C (Ed.), Rheol. Lubr., Science Publishers, Barking, 1973: pp. 81–88.

[74] E. Ingham, J. Fisher, Biological reactions to wear debris in total joint replacement, Proc Inst Mech Eng H. 214 (2000) 21–37. http://www.ncbi.nlm.nih.gov/pubmed/10718048.

[75] D.J. Langton, T.J. Joyce, S.S. Jameson, J. Lord, M. Van Orsouw, J.P. Holland, A. V Nargol, K.A. De Smet, Adverse reaction to metal debris following hip resurfacing: the influence of component type, orientation and volumetric wear, J Bone Jt. Surg Br. 93 (2011) 164–171. doi:10.1302/0301-620X.93B2.25099.

[76] Dowson. D, Biotribology of natural and replacement joints, in: V.C. Mow (Ed.), Biomech. Diarthrodial Joints, Springer Verlag, New York, 1990: pp. 303–345.

[77] A. Bennett, Higginso.Gr, Hydrodynamic Lubrication of Soft Solids, J. Mech. Eng. Sci. 12 (1970) 218-.

[78] J.S. Hou, V.C. Mow, W.M. Lai, M.H. Holmes, An analysis of the squeeze-film lubrication mechanism for articular cartilage, J Biomech. 25 (1992) 247–259. http://www.ncbi.nlm.nih.gov/pubmed/1564060.

[79] M. Jagatia, D. Jalali-Vahid, Z.M. Jin, Elastohydrodynamic lubrication analysis of ultra-high molecular weight polyethylene hip joint replacements under squeeze-film motion, Proc Inst Mech Eng H. 215 (2001) 141–152.

[80] P.S. Walker, D. Dowson, M.D. Longfield, V. Wright, “Boosted lubrication” in synovial joints by fluid entrapment and enrichment, Ann Rheum Dis. 27 (1968) 512–520. http://www.ncbi.nlm.nih.gov/pubmed/5728097.

[81] P.R. Lewis, C.W. McCutchen, Experimental evidence for weeping lubrication in mammalian joints, Nature. 184 (1959) 1285.

[82] J.F. Archard, Contact and Rubbing of Flat Surfaces, J. Appl. Phys. 24 (1953) 981–988. doi:10.1063/1.1721448.

[83] R.G. Bayer, Mechanical Wear Fundamentals and Testing, Revised and Expanded, Taylor & Francis, 2004. http://books.google.co.uk/books?id=Q64Kq2HlyucC.

[84] H.C. Amstutz, P. Campbell, N. Kossovsky, I.C. Clarke, Mechanism and clinical significance of wear debris-induced osteolysis, Clin Orthop Relat

Res. (1992) 7–18. http://www.ncbi.nlm.nih.gov/pubmed/1537177.

[85] S.B. Goodman, T. Wright, 2007 AAOS/NIH osteolysis and implant wear: biological, biomedical engineering, and surgical principles. Introduction, J Am Acad Orthop Surg. 16 Suppl 1 (2008) x–xi. doi:16/suppl_1/x [pii].

[86] S.M. Kurtz, A. van Ooij, R. Ross, J. de Waal Malefijt, J. Peloza, L. Ciccarelli, M.L. Villarraga, Polyethylene wear and rim fracture in total disc arthroplasty, Spine J. 7 (2007) 12–21. doi:http://dx.doi.org/10.1016/j.spinee.2006.05.012.

[87] Y. Yan, A. Neville, D. Dowson, Biotribocorrosion—an appraisal of the time dependence of wear and corrosion interactions: II. Surface analysis, J. Phys. D. Appl. Phys. 39 (2006) 3206. http://stacks.iop.org/0022-3727/39/i=15/a=S11.

[88] Y. Yan, A. Neville, D. Dowson, Biotribocorrosion - an appraisal of the time dependence of wear and corrosion interactions: I. The role of corrosion, J. Phys. D. Appl. Phys. 39 (2006) 3200–3205. doi:10.1088/0022-3727/39/15/S10.

[89] S.M. Kurtz, The UHMWPE Handbook: Ultra-High Molecular Weight Polyethylene in Total Joint Replacement, Elsevier Science, 2004. http://books.google.co.uk/books?id=bkuFjppEdMcC.

[90] R. Narayan, Biomedical Materials, Springer Science & Business Media, New York, 2009. http://books.google.co.uk/books?id=wyFYTCus8OgC.

[91] Substech.com, Abrasive wear, (2012). http://www.substech.com/dokuwiki/doku.php?id=mechanisms_of_wear.

[92] B.H. Cummins, J.T. Robertson, S.S. Gill, Surgical experience with an implanted artificial cervical joint, J Neurosurg. 88 (1998) 943–948. doi:10.3171/jns.1998.88.6.0943.

[93] N. Hallab, H.D. Link, P.C. McAfee, Biomaterial optimization in total disc arthroplasty, Spine (Phila Pa 1976). 28 (2003) S139-52. doi:10.1097/01.BRS.0000092214.87225.80.

[94] I. GOTMAN, Characteristics of Metals Used in Implants, J. Endourol. 11 (1997) 383–389. doi:10.1089/end.1997.11.383.

[95] P.F. Doorn, J.M. Mirra, P.A. Campbell, H.C. Amstutz, Tissue reaction to metal on metal total hip prostheses, Clin Orthop Relat Res. (1996) S187-205. http://www.ncbi.nlm.nih.gov/pubmed/8769334.

[96] D. Bitar, J. Parvizi, Biological response to prosthetic debris., World J. Orthop. 6 (2015) 172–89. doi:10.5312/wjo.v6.i2.172.

[97] J.P. Lemaire, H. Carrier, H. Sariali el, W. Skalli, F. Lavaste, Clinical and radiological outcomes with the Charite artificial disc: a 10-year minimum follow-up, J Spinal Disord Tech. 18 (2005) 353–359. http://www.ncbi.nlm.nih.gov/pubmed/16021017.

[98] R.C. Huang, F.P. Girardi, F.P. Cammisa Jr., T.M. Wright, The implications

of constraint in lumbar total disc replacement, J Spinal Disord Tech. 16 (2003) 412–417. http://www.ncbi.nlm.nih.gov/pubmed/12902958.

[99] P. V Mummaneni, J.K. Burkus, R.W. Haid, V.C. Traynelis, T.A. Zdeblick, Clinical and radiographic analysis of cervical disc arthroplasty compared with allograft fusion: a randomized controlled clinical trial, J Neurosurg Spine. 6 (2007) 198–209. doi:10.3171/spi.2007.6.3.198.

[100] J.K. Burkus, R.W. Haid, V.C. Traynelis, P. V Mummaneni, Long-term clinical and radiographic outcomes of cervical disc replacement with the Prestige disc: results from a prospective randomized controlled clinical trial, J Neurosurg Spine. 13 (2010) 308–318. doi:10.3171/2010.3.SPINE09513.

[101] J.K. Burkus, V.C. Traynelis, R.W. Haid, P. V. Mummaneni, Clinical and radiographic analysis of an artificial cervical disc: 7-year follow-up from the Prestige prospective randomized controlled clinical trial, J. Neurosurg. Spine. 21 (2014) 516–528. doi:10.3171/2014.6.SPINE13996.

[102] F. Porchet, N.H. Metcalf, Clinical outcomes with the Prestige II cervical disc: preliminary results from a prospective randomized clinical trial, Neurosurg Focus. 17 (2004) E6. http://www.ncbi.nlm.nih.gov/pubmed/15636562.

[103] D. Murrey, M. Janssen, R. Delamarter, J. Goldstein, J. Zigler, B. Tay, B. Darden, Results of the prospective, randomized, controlled multicenter Food and Drug Administration investigational device exemption study of the ProDisc-C total disc replacement versus anterior discectomy and fusion for the treatment of 1-level symptomatic cervi, Spine J. 9 (2009) 275–286. doi:10.1016/j.spinee.2008.05.006.

[104] R.B. Delamarter, D. Murrey, M.E. Janssen, J.A. Goldstein, J. Zigler, B.K.B. Tay, B. Darden Ii, Results at 24 months from the prospective, randomized, multicenter Investigational Device Exemption trial of ProDisc-C versus anterior cervical discectomy and fusion with 4-year follow-up and continued access patients, SAS J. 4 (2010) 122–128. doi:http://dx.doi.org/10.1016/j.esas.2010.09.001.

[105] J.E. Zigler, R. Delamarter, D. Murrey, J. Spivak, M. Janssen, ProDisc-C and Anterior Cervical Discectomy and Fusion as Surgical Treatment for Single-Level Cervical Symptomatic Degenerative Disc Disease Five-Year Results of a Food and Drug Administration Study, Spine (Phila Pa 1976). 38 (2013) 203–209. doi:Doi 10.1097/Brs.0b013e318278eb38.

[106] R.C. Sasso, P.A. Anderson, K.D. Riew, J.G. Heller, Results of cervical arthroplasty compared with anterior discectomy and fusion: four-year clinical outcomes in a prospective, randomized controlled trial, Orthopedics. 34 (2011) 889. doi:10.3928/01477447-20110922-24.

[107] R.C. Sasso, J.D. Smucker, R.J. Hacker, J.G. Heller, Clinical outcomes of BRYAN cervical disc arthroplasty: a prospective, randomized, controlled, multicenter trial with 24-month follow-up, J Spinal Disord Tech. 20 (2007) 481–491. doi:10.1097/BSD.0b013e3180310534.

[108] J. Marzluff, J. McConnell, C. Tomaras, W. Peppelman, I. Volcan, K. Baker, 2-Year Multicenter Follow-up in a Prospective Randomized Clinical Trial: Comparison of a Cervical Artificial Disc to an ACDF Treatment, Spine J. 10 (2010) S135–S136. doi:http://dx.doi.org/10.1016/j.spinee.2010.07.349.

[109] A. Vaccaro, W. Beutler, W. Peppelman, J.M. Marzluff, J. Highsmith, A. Mugglin, G. DeMuth, M. Gudipally, K.J. Baker, Clinical Outcomes With Selectively Constrained SECURE-C Cervical Disc Arthroplasty, Spine (Phila. Pa. 1976). 38 (2013) 2227–2239. doi:10.1097/BRS.0000000000000031.

[110] F.M. Phillips, J.Y.B. Lee, F.H. Geisler, A. Cappuccino, C.D. Chaput, J.G. DeVine, C. Reah, K.M. Gilder, K.M. Howell, P.C. McAfee, A Prospective, Randomized, Controlled Clinical Investigation Comparing PCM Cervical Disc Arthroplasty With Anterior Cervical Discectomy and Fusion, Spine (Phila. Pa. 1976). 38 (2013) E907–E918. doi:10.1097/BRS.0b013e318296232f.

[111] F.M. Phillips, F.H. Geisler, K.M. Gilder, C. Reah, K.M. Howell, P.C. McAfee, Long-term Outcomes of the US FDA IDE Prospective, Randomized Controlled Clinical Trial Comparing PCM Cervical Disc Arthroplasty With Anterior Cervical Discectomy and Fusion, Spine (Phila. Pa. 1976). 40 (2015) 674–683. doi:10.1097/BRS.0000000000000869.

[112] M. Hisey, H. Bae, R. Davis, S. Gaede, G. Hoffman, K. Kim, P. Nunley, D. Peterson, R. Rashbaum, J. Stokes, Multi-center, Prospective, Randomized, Controlled Investigational Device Exemption Clinical Trial Comparing Mobi?C Cervical Artificial Disc to Anterior Discectomy and Fusion in the Treatment of Symptomatic Degenerative Disc Disease in the Cervical Spine, Int. J. Spine Surg. 8 (2014) 7–7. doi:10.14444/1007.

[113] M.S. Hisey, H.W. Bae, R.J. Davis, S. Gaede, G. Hoffman, K.D. Kim, P.D. Nunley, D. Peterson, R.F. Rashbaum, J. Stokes, D.D. Ohnmeiss, Prospective, Randomized Comparison of Cervical Total Disk Replacement Versus Anterior Cervical Fusion, J. Spinal Disord. Tech. 28 (2015) E237–E243. doi:10.1097/BSD.0000000000000185.

[114] M.S. Hisey, J.E. Zigler, R. Jackson, P.D. Nunley, H.W. Bae, K.D. Kim, D.D. Ohnmeiss, Prospective, Randomized Comparison of One-level Mobi-C Cervical Total Disc Replacement vs. Anterior Cervical Discectomy and Fusion: Results at 5-year Follow-up., Int. J. Spine Surg. 10 (2016) 10. doi:10.14444/3010.

[115] M.F. Gornet, J.K. Burkus, M.E. Shaffrey, P.J. Argires, H. Nian, F.E. Harrell, Cervical disc arthroplasty with PRESTIGE LP disc versus anterior cervical discectomy and fusion: a prospective, multicenter investigational device exemption study, J. Neurosurg. Spine. 23 (2015) 558–573. doi:10.3171/2015.1.SPINE14589.

[116] M. Gornet, J.K. Burkus, M. Shaffrey, H. Nian, F. Harrell, Cervical Disc Arthroplasty with Prestige LP Disc Versus Anterior Cervical Discectomy and Fusion: Seven-Year Outcomes, Int. J. Spine Surg. 10 (2016) 24.

doi:10.14444/3024.

[117] J.G. Heller, R.C. Sasso, S.M. Papadopoulos, P.A. Anderson, R.G. Fessler, R.J. Hacker, D. Coric, J.C. Cauthen, D.K. Riew, Comparison of BRYAN Cervical Disc Arthroplasty With Anterior Cervical Decompression and Fusion, Spine (Phila. Pa. 1976). 34 (2009) 101–107. doi:10.1097/BRS.0b013e31818ee263.

[118] J. Fisher, J. Bell, P.S. Barbour, J.L. Tipper, J.B. Matthews, A.A. Besong, M.H. Stone, E. Ingham, A novel method for the prediction of functional biological activity of polyethylene wear debris, Proc Inst Mech Eng H. 215 (2001) 127–132. http://www.ncbi.nlm.nih.gov/pubmed/11382071.

[119] S.M. Kurtz, J.M. Toth, R. Siskey, L. Ciccarelli, D. MacDonald, J. Isaza, T. Lanman, I. Punt, M. Steinbeck, J. Goffin, A. van Ooij, The Latest Lessons Learned from Retrieval Analyses of Ultra-High Molecular Weight Polyethylene, Metal-on-Metal, and Alternative Bearing Total Disc Replacements, Semin. Spine Surg. 24 (2012) 57–70. doi:http://dx.doi.org/10.1053/j.semss.2011.11.011.

[120] M.A. Wimmer, A. Fischer, R. Buscher, R. Pourzal, C. Sprecher, R. Hauert, J.J. Jacobs, Wear mechanisms in metal-on-metal bearings: the importance of tribochemical reaction layers, J Orthop Res. 28 (2010) 436–443. doi:10.1002/jor.21020.

[121] P.A. Anderson, J.P. Rouleau, J.M. Toth, K.D. Riew, A comparison of simulator-tested and -retrieved cervical disc prostheses. Invited submission from the Joint Section Meeting on Disorders of the Spine and Peripheral Nerves, March 2004, J Neurosurg Spine. 1 (2004) 202–210. doi:10.3171/spi.2004.1.2.0202.

[122] D. Lebl, F. Cammisa, F. Girardi, T. Wright, C. Abjornson, Analysis of Wear, Surface Properties, and Fixation of Explanted Cervical Total Disc Replacements, Spine J. 11 (2011) S45. doi:http://dx.doi.org/10.1016/j.spinee.2011.08.119.

[123] D.R. Lebl, F.P. Cammisa Jr., F.P. Girardi, T. Wright, C. Abjornson, The mechanical performance of cervical total disc replacements in vivo: prospective retrieval analysis of prodisc-C devices, Spine (Phila Pa 1976). 37 (2012) 2151–2160. doi:10.1097/BRS.0b013e31826b3f61.

[124] L.M. Tumialan, W.M. Gluf, Progressive vertebral body osteolysis after cervical disc arthroplasty, Spine (Phila Pa 1976). 36 (2011) E973-8. doi:10.1097/BRS.0b013e3181fd863b.

[125] C.J. Devin, T.G. Myers, J.D. Kang, Chronic failure of a lumbar total disc replacement with osteolysis. Report of a case with nineteen-year follow-up, J Bone Jt. Surg Am. 90 (2008) 2230–2234. doi:10.2106/JBJS.G.01712.

[126] A. van Ooij, S.M. Kurtz, F. Stessels, H. Noten, L. van Rhijn, Polyethylene wear debris and long-term clinical failure of the Charite disc prosthesis: a study of 4 patients, Spine (Phila Pa 1976). 32 (2007) 223–229.

doi:10.1097/01.brs.0000251370.56327.c6.

[127] B.W. Cunningham, C.M. Orbegoso, A.E. Dmitriev, N.J. Hallab, J.C. Sefter, P. Asdourian, P.C. McAfee, The effect of spinal instrumentation particulate wear debris. an in vivo rabbit model and applied clinical study of retrieved instrumentation cases, Spine J. 3 (2003) 19–32. http://www.ncbi.nlm.nih.gov/pubmed/14589241.

[128] R.D. Guyer, J. Shellock, B. MacLennan, D. Hanscom, R.Q. Knight, P. McCombe, J.J. Jacobs, R.M. Urban, D. Bradford, D.D. Ohnmeiss, Early failure of metal-on-metal artificial disc prostheses associated with lymphocytic reaction: diagnosis and treatment experience in four cases, Spine (Phila Pa 1976). 36 (2011) E492-7. doi:10.1097/BRS.0b013e31820ea9a2.

[129] D.A. Cavanaugh, P.D. Nunley, E.J. Kerr 3rd, D.J. Werner, A. Jawahar, Delayed hyper-reactivity to metal ions after cervical disc arthroplasty: a case report and literature review, Spine (Phila Pa 1976). 34 (2009) E262-5. doi:10.1097/BRS.0b013e318195dd60.

[130] M. Lagier, M. Briere, H. Giorgi, S. Fuentes, B. Blondel, P. Tropiano, Delayed hypersensitivity reaction after cervical disc replacement: A case report, Orthop. Traumatol. Surg. Res. 101 (2015) 643–645. doi:10.1016/j.otsr.2015.05.005.

[131] M.R. Berry, B.G. Peterson, D.H. Alander, A granulomatous mass surrounding a Maverick total disc replacement causing iliac vein occlusion and spinal stenosis: a case report, J Bone Jt. Surg Am. 92 (2010) 1242–1245. doi:10.2106/JBJS.H.01625.

[132] J. Francois, R. Coessens, P. Lauweryns, Early removal of a Maverick disc prosthesis: surgical findings and morphological changes, Acta Orthop Belg. 73 (2007) 122–127. http://www.ncbi.nlm.nih.gov/pubmed/17441671.

[133] T.R. Green, J. Fisher, M. Stone, B.M. Wroblewski, E. Ingham, Polyethylene particles of a “critical size” are necessary for the induction of cytokines by macrophages in vitro, Biomaterials. 19 (1998) 2297–2302. http://www.ncbi.nlm.nih.gov/pubmed/9884043.

[134] C. Brown, J. Fisher, E. Ingham, Biological effects of clinically relevant wear particles from metal-on-metal hip prostheses, Proc Inst Mech Eng H. 220 (2006) 355–369. http://www.ncbi.nlm.nih.gov/pubmed/16669401.

[135] International Organization for Standardization, BS ISO-18192-1:2011 - Implants for surgery - Wear of total intervertebral spinal disc prostheses - Part 1: Loading and displacement parameters for wear testing and corresponding environmental conditions for test, (2011).

[136] ASTM, ASTM Standard F2423-11, Stand. Guid. Funct. Kinematic, Wear Assess. Total Disc Prostheses. (2011). doi:10.1520/F2423-11.

[137] P.E. Pare, F.W. Chan, S. Bhattacharya, V.K. Goel, Surface slide track mapping of implants for total disc arthroplasty, J Biomech. 42 (2009) 131–139. doi:10.1016/j.jbiomech.2008.10.025.

[138] S.M. Kurtz, L. Ciccarelli, M.L. Harper, R. Siskey, J. Shorez, F.W. Chan, Comparison of in vivo and simulator-retrieved metal-on-metal cervical disc replacements, Int. J. Spine Surg. 6 (2012) 145–156. doi:http://dx.doi.org/10.1016/j.ijsp.2012.03.002.

[139] S.M.C.F.W. Kurtz Pare P.E, et al., Correlation of in vivo- and simulator-retrieved metal-on-metal cervical disc replacements, 7th Annu. Meet. Spine Arthroplast. Soc. (2007).

[140] R.L.. K. Siskey S.M.; Shah, P.; Ciccarelli, L.; Harper, M.; Chan, F.; White, S., Validation of ISO-Standard Wear Testing with Retrieved Metal-on-Metal Cervical Disc Replacements, 54th Annu. Meet. Orthop. Res. Soc. (2008).

[141] C.J. Kelly N Wright T, Retrieval analysis of ProDisc total disc replacements, 54th Annu. Meet. Orthop. Res. Soc. (2008).

[142] W. Nechtow, M. Bushelow, M. Hintner, A. Ochs, C. Kaddick, Cervical Disc Prosthesis Polyethylene Wear Following The ISO Cervical Test Poster No . 1926 • 54th Annual Meeting of the Orthopaedic Research Society, 1 (2002) 18192. http://www.ors.org/Transactions/54/1926.pdf (accessed April 8, 2017).

[143] M. Bushelow, W. Nechtow, M. Hinter, H. Dressel, C. Kaddick, M.E. Gmbh, W. Chester, Wear Testing of a Cervical Total Disc Replacement : Effect of Motion and Load Parameters on Wear Rate and Particle Morphology 1 EndoLab Materials and Methods : All testing was performed at EndoLab Mechanical Engineering GmbH (Rosenheim , GR). Testing wa, 29 (2006) 2006. http://www.ors.org/Transactions/54/1925.pdf (accessed April 8, 2017).

[144] P.J. Hyde, J. Tipper, J. Fisher, R.M. Hall, Wear and biological effects of a semi-constrained total disc replacement subject to modified ISO standard test conditions, J. Mech. Behav. Biomed. Mater. 44 (2015) 43–52. doi:10.1016/j.jmbbm.2014.12.001.

[145] J.L. Tipper, A.L. Galvin, S. Williams, H.M. McEwen, M.H. Stone, E. Ingham, J. Fisher, Isolation and characterization of UHMWPE wear particles down to ten nanometers in size from in vitro hip and knee joint simulators, J Biomed Mater Res A. 78 (2006) 473–480. doi:10.1002/jbm.a.30824.

[146] T.R. Green, J. Fisher, J.B. Matthews, M.H. Stone, E. Ingham, Effect of size and dose on bone resorption activity of macrophages by in vitro clinically relevant ultra high molecular weight polyethylene particles, J Biomed Mater Res. 53 (2000) 490–497.

[147] K.M. Holmberg A.`, Coatings Tribology: Properties, Mechanisms, Techniques and Applications in Surface Engineering, 2nd ed., Elsevier, Oxford, 2009.

[148] A. Matthews, Advanced surface coatings: a handbook of surface engineering, Blackie, Glasgow, UK, 1991.

[149] C. Christou, Z.H. Barber, Ionization of sputtered material in a planar magnetron discharge, J. Vac. Sci. Technol. A Vacuum, Surfaces Film. 18 (2000) 2897–2907. http://www.scopus.com/inward/record.url?eid=2-s2.0-0034318373&partnerID=40&md5=9bf0568125a1666aa8d200f616960e64.

[150] T. Shimizu, H. Komiya, T. Watanabe, Y. Teranishi, H. Nagasaka, K. Morikawa, M. Yang, HIPIMS deposition of TiAlN films on inner wall of micro-dies and its applicability in micro-sheet metal forming, Surf. Coatings Technol. 250 (2014) 44–51. doi:http://dx.doi.org/10.1016/j.surfcoat.2014.02.008.

[151] V. Kouznetsov, K. MacÁk, J.M. Schneider, U. Helmersson, I. Petrov, A novel pulsed magnetron sputter technique utilizing very high target power densities, Surf. Coatings Technol. 122 (1999) 290–293. http://www.scopus.com/inward/record.url?eid=2-s2.0-0000975178&partnerID=40&md5=997858bd1298305f27622ef858a5185d.

[152] K. Sarakinos, J. Alami, S. Konstantinidis, High power pulsed magnetron sputtering: A review on scientific and engineering state of the art, Surf. Coatings Technol. 204 (2010) 1661–1684. doi:http://dx.doi.org/10.1016/j.surfcoat.2009.11.013.

[153] D.J. Berry, W.S. Harmsen, M.E. Cabanela, B.F. Morrey, Twenty-five-year survivorship of two thousand consecutive primary Charnley total hip replacements: factors affecting survivorship of acetabular and femoral components, J Bone Jt. Surg Am. 84–A (2002) 171–177. http://www.ncbi.nlm.nih.gov/pubmed/11861721.

[154] P.F. Sharkey, W.J. Hozack, R.H. Rothman, S. Shastri, S.M. Jacoby, Insall Award paper. Why are total knee arthroplasties failing today?, Clin Orthop Relat Res. (2002) 7–13. http://www.ncbi.nlm.nih.gov/pubmed/12439231.

[155] S.R.P. Silva, G.A.J. Amaratunga, Doping of rf plasma deposited diamond-like carbon films, Thin Solid Films. 270 (1995) 194–199. http://www.scopus.com/inward/record.url?eid=2-s2.0-0029516498&partnerID=40&md5=0003e753fa6bf960803a73cd8b64c7be.

[156] A.A. Evtukh, V.G. Litovchenko, Y.M. Litvin, D. V Fedin, O.S. Dzyan, Y.N. Pedchenko, A.G. Chakhovskoi, T.E. Felter, Silicon doped diamond-like carbon films as a coating for improvement of electron field emission, J. Vac. Sci. Technol. B Microelectron. Nanom. Struct. 21 (2003) 627–630. http://www.scopus.com/inward/record.url?eid=2-s2.0-0037207783&partnerID=40&md5=86bc0f67a96f8795a579b1f4c2576398.

[157] T. Wehlus, G. Thorwarth, F. Schwarz, M.F. Schneider, B. Saldamli, B. Stritzker, Biocompatible DLC coatings by PBII: Effects of doping and surface roughness, Phys. Status Solidi Curr. Top. Solid State Phys. 5 (2008) 952–955. http://www.scopus.com/inward/record.url?eid=2-s2.0-77951161128&partnerID=40&md5=4665a22f1d9f2fba0aed0eda204cdd8

6.

[158] R. Hauert, A review of modified DLC coatings for biological applications, Diam. Relat. Mater. 12 (2003) 583–589. http://www.scopus.com/inward/record.url?eid=2-s2.0-0037852937&partnerID=40&md5=92c76a7aa72c017d3e2596873471df95.

[159] C. Donnet, Recent progress on the tribology of doped diamond-like and carbon alloy coatings: A review, Surf. Coatings Technol. 100–101 (1998) 180–186. http://www.scopus.com/inward/record.url?eid=2-s2.0-0032026026&partnerID=40&md5=bef4c288e95a27ceb810057aa3792425.

[160] L.A. Thomson, F.C. Law, N. Rushton, J. Franks, Biocompatibility of diamond-like carbon coating, Biomaterials. 12 (1991) 37–40. http://www.ncbi.nlm.nih.gov/pubmed/2009344.

[161] F.Z. Cui, D.J. Li, A review of investigations on biocompatibility of diamond-like carbon and carbon nitride films, Surf. Coatings Technol. 131 (2000) 481–487. http://www.scopus.com/inward/record.url?eid=2-s2.0-0034532526&partnerID=40&md5=aec0c81c6581d564f930f76ed5f3a155.

[162] R.K. Roy, K.R. Lee, Biomedical applications of diamond-like carbon coatings: A review, J. Biomed. Mater. Res. - Part B Appl. Biomater. 83 (2007) 72–84. http://www.scopus.com/inward/record.url?eid=2-s2.0-34648824850&partnerID=40&md5=11bbc5e097fd398dc80cc682ab6f2f01.

[163] C.A. Love, R.B. Cook, T.J. Harvey, P.A. Dearnley, R.J.K. Wood, Diamond like carbon coatings for potential application in biological implants—a review, Tribol. Int. 63 (2013) 141–150. doi:http://dx.doi.org/10.1016/j.triboint.2012.09.006.

[164] R. Lappalainen, M. Selenius, A. Anttila, Y.T. Konttinen, S.S. Santavirta, Reduction of wear in total hip replacement prostheses by amorphous diamond coatings, J Biomed Mater Res B Appl Biomater. 66 (2003) 410–413. doi:10.1002/jbm.b.10026.

[165] S. Affatato, M. Frigo, A. Toni, An in vitro investigation of diamond-like carbon as a femoral head coating, J Biomed Mater Res. 53 (2000) 221–226.

[166] J.I. Oñate, M. Comin, I. Braceras, A. Garcia, J.L. Viviente, M. Brizuela, N. Garagorri, J.L. Peris, J.I. Alava, Wear reduction effect on ultra-high-molecular-weight polyethylene by application of hard coatings and ion implantation on cobalt chromium alloy, as measured in a knee wear simulation machine, Surf. Coatings Technol. 142–144 (2001) 1056–1062. doi:http://dx.doi.org/10.1016/S0257-8972(01)01074-X.

[167] R. Lappalainen, S.S. Santavirta, Potential of coatings in total hip replacement, Clin. Orthop. Relat. Res. (2005) 72–79. http://www.scopus.com/inward/record.url?eid=2-s2.0-

11844275898&partnerID=40&md5=96578c9c52e14919bccd0b8f5727cf56.

[168] G Maestretti, D Noriega, P Otten, P.V. R Srour, BAGUERA® C – A New Cervical Disc Replacement Device, 2008.

[169] M. Benmekhbi, J. Mortada, G. Lungu, D. Eichler, R. Srour, J.M. Vital, Baguera cervical disc prosthesis, Interact. Surg. 3 (2008) 201–204. doi:10.1007/s11610-008-0086-2.

[170] G. Taeger, L.E. Podleska, B. Schmidt, M. Ziegler, D. Nast-Kolb, Comparison of Diamond-Like-Carbon and Alumina-Oxide articulating with Polyethylene in Total Hip Arthroplasty, Materwiss. Werksttech. 34 (2003) 1094–1100. http://www.scopus.com/inward/record.url?eid=2-s2.0-1642488161&partnerID=40&md5=8aa28ada83ec31c9aff7cccdf8a5c7b5.

[171] T.J. Joyce, Examination of failed ex vivo metal-on-metal metatarsophalangeal prosthesis and comparison with theoretically determined lubrication regimes, Wear. 263 (2007) 1050–1054. http://www.scopus.com/inward/record.url?eid=2-s2.0-34548061162&partnerID=40&md5=94df9ad38bd20e554d7c21cd39b3ffb0.

[172] R. Hauert, C. V Falub, G. Thorwarth, K. Thorwarth, C. Affolter, M. Stiefel, L.E. Podleska, G. Taeger, Retrospective lifetime estimation of failed and explanted diamond-like carbon coated hip joint balls, Acta Biomater. 8 (2012) 3170–3176. doi:10.1016/j.actbio.2012.04.016.

[173] R. Hauert, G. Thorwarth, U. Müller, M. Stiefel, C. V Falub, K. Thorwarth, T.J. Joyce, Analysis of the in-vivo failure of the adhesive interlayer for a DLC coated articulating metatarsophalangeal joint, Diam. Relat. Mater. 25 (2012) 34–39. doi:http://dx.doi.org/10.1016/j.diamond.2012.02.001.

[174] M.J. Pappas, G. Makris, F.F. Buechel, Titanium nitride ceramic film against polyethylene. A 48 million cycle wear test, Clin Orthop Relat Res. (1995) 64–70.

[175] M.T. Raimondi, R. Pietrabissa, The in-vivo wear performance of prosthetic femoral heads with titanium nitride coating, Biomaterials. 21 (2000) 907–913.

[176] M.K. Harman, S.A. Banks, W.A. Hodge, Wear analysis of a retrieved hip implant with titanium nitride coating, J Arthroplast. 12 (1997) 938–945.

[177] S.N. Massoud, J.B. Hunter, B.J. Holdsworth, W.A. Wallace, R. Juliusson, EARLY FEMORAL LOOSENING IN ONE DESIGN OF CEMENTED HIP REPLACEMENT, Bone Joint J. 79–B (1997). http://bjj.boneandjoint.org.uk/content/79-B/4/603.short (accessed August 26, 2017).

[178] G.G. Fuentes, R. Rodriguez, J.C. Avelar-Batista, J. Housden, F. Montalá, L.J. Carreras, A.B. Cristóbal, J.J. Damborenea, T.J. Tate, Recent advances in the chromium nitride PVD process for forming and machining surface protection, J. Mater. Process. Technol. 167 (2005) 415–421.

doi:10.1016/j.jmatprotec.2005.06.011.

[179] J. Fisher, X.Q. Hu, J.L. Tipper, T.D. Stewart, S. Williams, M.H. Stone, C. Davies, P. Hatto, J. Bolton, M. Riley, C. Hardaker, G.H. Isaac, G. Berry, E. Ingham, An in vitro study of the reduction in wear of metal-on-metal hip prostheses using surface-engineered femoral heads, Proc Inst Mech Eng H. 216 (2002) 219–230.

[180] S. Williams, G. Isaac, P. Hatto, M.H. Stone, E. Ingham, J. Fisher, Comparative wear under different conditions of surface-engineered metal-on-metal bearings for total hip arthroplasty, J. Arthroplasty. 19 (2004) 112–117. doi:10.1016/j.arth.2004.09.014.

[181] W. Österle, D. Klaffke, M. Griepentrog, U. Gross, I. Kranz, C. Knabe, Potential of wear resistant coatings on Ti–6Al–4V for artificial hip joint bearing surfaces, Wear. 264 (2008) 505–517. doi:http://dx.doi.org/10.1016/j.wear.2007.04.001.

[182] R. Thorkildsen, O. Reigstad, M. R?kkum, Chrome nitride coating reduces wear of small, spherical CrCoMo metal-on-metal articulations in a joint simulator, J. Hand Surg. (European Vol. 42 (2017) 310–315. doi:10.1177/1753193416674161.

[183] I. Leslie, S. Williams, G. Isaac, P. Hatto, E. Ingham, J. Fisher, Wear of surface-engineered metal-on-metal bearings for hip prostheses under adverse conditions with the head loading on the rim of the cup, Proc. Inst. Mech. Eng. Part H J. Eng. Med. 227 (2013) 345–349. doi:10.1177/0954411912468542.

[184] I.J. Leslie, Surface Engineering of Metal-on-Metal Hip Surface Replacements, University of Leeds, 2008.

[185] D. de Villiers, A. Traynor, S.N. Collins, S. Banfield, J. Housden, J.C. Shelton, Chromium nitride coating for large diameter metal-on-polyethylene hip bearings under extreme adverse hip simulator conditions, Wear. 328 (2015) 363–368. doi:10.1016/j.wear.2015.02.060.

[186] M. Mazzocchi, D. Gardini, P.L. Traverso, M.G. Faga, A. Bellosi, On the possibility of silicon nitride as a ceramic for structural orthopaedic implants. Part II: chemical stability and wear resistance in body environment, J Mater Sci Mater Med. 19 (2008) 2889–2901. doi:10.1007/s10856-008-3437-y.

[187] M. Mazzocchi, A. Bellosi, On the possibility of silicon nitride as a ceramic for structural orthopaedic implants. Part I: processing, microstructure, mechanical properties, cytotoxicity, J. Mater. Sci. Mater. Med. 19 (2008) 2881–2887. doi:10.1007/s10856-008-3417-2.

[188] J. Olofsson, M. Pettersson, N. Teuscher, A. Heilmann, K. Larsson, K. Grandfield, C. Persson, S. Jacobson, H. Engqvist, Fabrication and evaluation of SixNy coatings for total joint replacements, J Mater Sci Mater Med. 23 (2012) 1879–1889. doi:10.1007/s10856-012-4625-3.

[189] M. Pettersson, T. Berlind, S. Schmidt, S. Jacobson, L. Hultman, C. Persson, H. Engqvist, Structure and composition of silicon nitride and

silicon carbon nitride coatings for joint replacements, Surf. Coatings Technol. 235 (2013) 827–834. doi:http://dx.doi.org/10.1016/j.surfcoat.2013.09.008.

[190] M. Pettersson, S. Tkachenko, S. Schmidt, T. Berlind, S. Jacobson, L. Hultman, H. Engqvist, C. Persson, Mechanical and tribological behavior of silicon nitride and silicon carbon nitride coatings for total joint replacements, J Mech Behav Biomed Mater. 25 (2013) 41–47. doi:10.1016/j.jmbbm.2013.05.002.

[191] E. Laarz, B. V Zhmud, L. Bergström, Dissolution and Deagglomeration of Silicon Nitride in Aqueous Medium, J. Am. Ceram. Soc. 83 (2000) 2394–2400. doi:10.1111/j.1151-2916.2000.tb01567.x.

[192] B. V Zhmud, L. Bergström, Dissolution Kinetics of Silicon Nitride in Aqueous Suspension, J. Colloid Interface Sci. 218 (1999) 582–584. doi:http://dx.doi.org/10.1006/jcis.1999.6425.

[193] M. Pettersson, M. Bryant, S. Schmidt, H. Engqvist, R.M. Hall, A. Neville, C. Persson, Dissolution behaviour of silicon nitride coatings for joint replacements, Mater. Sci. Eng. C. (2016). doi:10.1016/j.msec.2016.01.049.

[194] N. V Boskitskaya, T.S. Bartnitskaya, G.N. Makarenko, V.A. Lavrenko, N.M. Danilenko, N.P. Tel’nikova, Chemical stability of silicon nitride powders in biochemical media, Powder Metall. Met. Ceram. 35 (1996) 497–500. doi:10.1007/BF01355964.

[195] R.M. Taylor, J.P. Bernero, A.A. Patel, D.S. Brodke, A.C. Khandkar, SILICON NITRIDE: A NEW MATERIAL FOR SPINAL IMPLANTS, J. Bone Jt. Surgery, Br. Vol. 92–B (2010) 133. http://www.bjjprocs.boneandjoint.org.uk/content/92-B/SUPP_I/133.1.abstract.

[196] B.S. Bal, A. Khandkar, R. Lakshminarayanan, I. Clarke, A.A. Hoffman, M.N. Rahaman, Testing of silicon nitride ceramic bearings for total hip arthroplasty, J. Biomed. Mater. Res. Part B Appl. Biomater. 87B (2008) 447–454. doi:10.1002/jbm.b.31123.

[197] A. Neumann, C. Unkel, C. Werry, C.U. Herborn, H.R. Maier, C. Ragoss, K. Jahnke, Prototype of a silicon nitride ceramic-based miniplate osteofixation system for the midface, Otolaryngol Head Neck Surg. 134 (2006) 923–930. doi:10.1016/j.otohns.2006.01.022.

[198] T.G. Ma S.B., Biological Effects of Wear Debris from Joint Arthroplasties, in: P. Ducheyne (Ed.), Compr. Biomater., Elsevier, Oxford, 2011.

[199] M. Navarro, A. Michiardi, O. Castaño, J.A. Planell, Biomaterials in orthopaedics., J. R. Soc. Interface. 5 (2008) 1137–58. doi:10.1098/rsif.2008.0151.

[200] J. Fisher, X.Q. Hu, T.D. Stewart, S. Williams, J.L. Tipper, E. Ingham, M.H. Stone, C. Davies, P. Hatto, J. Bolton, M. Riley, C. Hardaker, G.H. Isaac, G. Berry, Wear of surface engineered metal-on-metal hip prostheses, J.

Mater. Sci. Mater. Med. 15 (2004) 225–235. doi:10.1023/B:JMSM.0000015482.24542.76.

[201] C.Y. Lin, H. Kang, J.P. Rouleau, S.J. Hollister, F.L. Marca, Stress analysis of the interface between cervical vertebrae end plates and the Bryan, Prestige LP, and ProDisc-C cervical disc prostheses: an in vivo image-based finite element study, Spine (Phila Pa 1976). 34 (2009) 1554–1560. doi:10.1097/BRS.0b013e3181aa643b.

[202] International Organization for Standardization, ISO-7206-2:2011 - Implants for surgery -- Partial and total hip joint prostheses -- Part 2: Articulating surfaces made of metallic, ceramic and plastics materials, (2011).

[203] S.A. Wenzel, D.E. Shepherd, Contact stresses in lumbar total disc arthroplasty, Biomed Mater Eng. 17 (2007) 169–173.

[204] J.P. Clewlow, T. Pylios, D.E.T. Shepherd, Soft layer bearing joints for spine arthroplasty, Mater. Des. 29 (2008) 1981–1985. doi:http://dx.doi.org/10.1016/j.matdes.2008.04.008.

[205] I.J. Udofia, Z.M. Jin, Elastohydrodynamic lubrication analysis of metal-on-metal hip-resurfacing prostheses, J Biomech. 36 (2003) 537–544.

[206] T. Pylios, D.E. Shepherd, Soft layered concept in the design of metacarpophalangeal joint replacement implants, Biomed Mater Eng. 18 (2008) 73–82.

[207] ASTM, ASTM Standard F1537-11, Stand. Specif. Wrought Cobalt-28Chromium-6Molybdenum Alloy. Surg. Implant. (UNS R31537, UNS R31538, UNS R31539). (2011). doi:10.1520/F1537-11.

[208] A. Khan, J. Philip, P. Hess, Young's modulus of silicon nitride used in scanning force microscope cantilevers, (n.d.). doi:10.1063/1.1638886.

[209] J. Jagielski, A.S. Khanna, J. Kucinski, D.S. Mishra, P. Racolta, P. Sioshansi, E. Tobin, J. Thereska, V. Uglov, T. Vilaithong, J. Viviente, S.-Z. Yang, A. Zalar, Effect of chromium nitride coating on the corrosion and wear resistance of stainless steel, (n.d.).

[210] L. Mattei, F. Di Puccio, B. Piccigallo, E. Ciulli, Lubrication and wear modelling of artificial hip joints: A review, Tribol. Int. 44 (2011) 532–549. doi:http://dx.doi.org/10.1016/j.triboint.2010.06.010.

[211] S. Williams, D. Jalali-Vahid, C. Brockett, Z. Jin, M.H. Stone, E. Ingham, J. Fisher, Effect of swing phase load on metal-on-metal hip lubrication, friction and wear, J. Biomech. 39 (2006) 2274–2281. doi:10.1016/j.jbiomech.2005.07.011.

[212] J.Q. Yao, M.P. Laurent, T.S. Johnson, C.R. Blanchard, R.D. Crowninshield, The influences of lubricant and material on polymer/CoCr sliding friction, Wear. 255 (2003) 780–784. doi:10.1016/S0043-1648(03)00180-7.

[213] I.G. Goryacheva, Contact Mechanics in Tribology, Springer Netherlands,

2013. https://books.google.co.uk/books?id=G2zuCAAAQBAJ.

[214] G.R. Johnson, 1 - Biomechanics of joints, in: P.A. Revell (Ed.), Jt. Replace. Technol., Woodhead Publishing, 2008: pp. 3–30. doi:http://dx.doi.org/10.1533/9781845694807.1.3.

[215] B.J. Hamrock, D. Dowson, Elastohydrodynamic Lubrication of Elliptical Contacts for Materials of Low Elastic Modulus I—Fully Flooded Conjunction, J. Lubr. Technol. 100 (1978) 236–245. doi:10.1115/1.3453152.

[216] H. Xin, D. Shepherd, K. Dearn, PEEK (Polyether-ether-ketone) Based Cervical Total Disc Arthroplasty: Contact Stress and Lubrication Analysis, Open Biomed Eng J. 6 (2012) 73–79. doi:10.2174/1874230001206010073.

[217] Arcam, ASTM F75 CoCr Alloy, 2015 (n.d.). http://www.arcam.com/wp-content/uploads/Arcam-ASTM-F75-Cobalt-Chrome.pdf.

[218] M.Y.P. Costa, M.L.R. Venditti, M.O.H. Cioffi, H.J.C. Voorwald, V.A. Guimarães, R. Ruas, Fatigue behavior of PVD coated Ti–6Al–4V alloy, Int. J. Fatigue. 33 (2011) 759–765. doi:10.1016/j.ijfatigue.2010.11.007.

[219] K. Ando, M.C. Chu, F. Yao, S. Sato, Fatigue strength of crack-healed Si3N4/SiC composite ceramics, Fatigue <html_ent Glyph="@amp;" ascii="&amp;"/> Fract. Eng. Mater. Struct. 22 (1999) 897–903. doi:10.1046/j.1460-2695.1999.00210.x.

[220] M. Bushelow, W. Nechtow, J. Walker, P8. Metal-on-Metal Lumbar TDR Design: A Theoretical Analysis of the Affect of Diameter Clearance and Surface Finish on Lubrication, Spine J. 8 (2008) 105S. doi:10.1016/j.spinee.2008.06.650.

[221] Z.M. Jin, D. Dowson, A full numerical analysis of hydrodynamic lubrication in artificial hip joint replacements constructed from hard materials, Proc. Inst. Mech. Eng. Part C J. Mech. Eng. Sci. 213 (1999) 355–370. doi:10.1243/0954406991522310.

[222] D. Dowson, C.M. McNie, A.A.J. Goldsmith, Direct experimental evidence of lubrication in a metal-on-metal total hip replacement tested in a joint simulator, Proc. Inst. Mech. Eng. Part C J. Mech. Eng. Sci. 214 (2000) 75–86. doi:10.1243/0954406001522822.

[223] Z.M. Jin, D. Dowson, J. Fisher, Analysis of fluid film lubrication in artificial hip joint replacements with surfaces of high elastic modulus, Proc Inst Mech Eng H. 211 (1997) 247–256.

[224] D. Dowson, Basic Tribology, in: D.W. Dowson V (Ed.), An Introd. to Biomech. Joints Jt. Replace., Mechl Eng Publications Limited, London, 1981: pp. 49–60.

[225] R. Sonntag, J. Reinders, J.S. Rieger, D.W.W. Heitzmann, J.P. Kretzer, Hard-on-Hard Lubrication in the Artificial Hip under Dynamic Loading Conditions, PLoS One. 8 (2013) e71622.

doi:10.1371/journal.pone.0071622.

[226] Z.M. Jin, J. Fisher, E. Ingham, Biotribology: Material Design, Lubrication and Wear in Artificial Hip Joints, in: Handb. Lubr. Tribol. Vol. I Appl. Maint., CRC Press, Boca Raton, FL, 2006.

[227] D. Dowson, Tribological principles in metal-on-metal hip joint design, Proc Inst Mech Eng H. 220 (2006) 161–171.

[228] S.C. Scholes, A. Unsworth, Comparison of friction and lubrication of different hip prostheses, Proc Inst Mech Eng H. 214 (2000) 49–57.

[229] S. Zhang, F. Awaja, N. James, D.R. McKenzie, A.J. Ruys, Autohesion of plasma treated semi-crystalline PEEK: Comparative study of argon, nitrogen and oxygen treatments, Colloids Surfaces A Physicochem. Eng. Asp. 374 (2011) 88–95. doi:10.1016/j.colsurfa.2010.11.013.

[230] C.-C. Sun, S.-C. Lee, W.-C. Hwang, J.-S. Hwang, I.-T. Tang, Y.-S. Fu, Surface Free Energy of Alloy Nitride Coatings Deposited Using Closed Field Unbalanced Magnetron Sputter Ion Plating, Mater. Trans. 47 (2006) 2533–2539. doi:10.2320/matertrans.47.2533.

[231] K. Midtbø, K. Schjølberg-Henriksen, M.M. V Taklo, A. Rønnekleiv, Surface Energy of Fusion Bonded Silicon Nitride to Silicon, (n.d.). http://ma.ecsdl.org/content/MA2005-01/11/519.full.pdf (accessed July 12, 2017).

[232] Y. Yan, H. Yang, Y. Su, L. Qiao, Albumin adsorption on CoCrMo alloy surfaces., Sci. Rep. 5 (2015) 18403. doi:10.1038/srep18403.

[233] M.A. Wimmer, M.T. Mathew, M.P. Laurent, C. Nagelli, Y. Liao, L.D. Marks, R. Pourzal, A. Fischer, J.J. Jacobs, Tribochemical Reactions in Metal-on-Metal Hip Joints Influence Wear and Corrosion, (2012) 1–18. doi:10.1520/STP156020120050.

[234] H. Dong, Y. Nagamatsu, K.-K. Chen, K. Tajima, H. Kakigawa, S. Shi, Y. Kozono, Corrosion behavior of dental alloys in various types of electrolyzed water., Dent. Mater. J. 22 (2003) 482–93. http://www.ncbi.nlm.nih.gov/pubmed/15005226 (accessed February 20, 2017).

[235] M.T. Clarke, P.T.H. Lee, A. Arora, R.N. Villar, Levels of metal ions after small- and large-diameter metal-on-metal hip arthroplasty, Bone Joint J. 85–B (2003).

[236] H.P. Sieber, C.B. Rieker, P. Kottig, Analysis of 118 second-generation metal-on-metal retrieved hip implants, J Bone Jt. Surg Br. 81 (1999) 46–50.

[237] J.L. Gilbert, C.A. Buckley, J.J. Jacobs, In vivo corrosion of modular hip prosthesis components in mixed and similar metal combinations. The effect of crevice, stress, motion, and alloy coupling, J. Biomed. Mater. Res. 27 (1993) 1533–1544. doi:10.1002/jbm.820271210.

[238] G. Manivasagam, D. Dhinasekaran, A. Rajamanickam, Biomedical

Implants: Corrosion and its Prevention -A Review, Recent Patents Corros. Sci. 2 (2010) 40–54.

[239] H. Matusiewicz, Potential release of in vivo trace metals from metallic medical implants in the human body: From ions to nanoparticles – A systematic analytical review, Acta Biomater. 10 (2014) 2379–2403. doi:10.1016/j.actbio.2014.02.027.

[240] D. Ladon, A. Doherty, R. Newson, J. Turner, M. Bhamra, C.P. Case, Changes in metal levels and chromosome aberrations in the peripheral blood of patients after metal-on-metal hip arthroplasty, J Arthroplast. 19 (2004) 78–83.

[241] H. Pandit, S. Glyn-Jones, P. McLardy-Smith, R. Gundle, D. Whitwell, C.L. Gibbons, S. Ostlere, N. Athanasou, H.S. Gill, D.W. Murray, Pseudotumours associated with metal-on-metal hip resurfacings, J Bone Jt. Surg Br. 90 (2008) 847–851. doi:10.1302/0301-620X.90B7.20213.

[242] J. Gallo, S.B. Goodman, Y.T. Konttinen, M. Raska, Particle disease: biologic mechanisms of periprosthetic osteolysis in total hip arthroplasty., Innate Immun. 19 (2013) 213–24. doi:10.1177/1753425912451779.

[243] N. Taki, J.M. Tatro, J.L. Nalepka, D. Togawa, V.M. Goldberg, C.M. Rimnac, E.M. Greenfield, Polyethylene and titanium particles induce osteolysis by similar, lymphocyte-independent, mechanisms, J. Orthop. Res. 23 (2005) 376–383. doi:10.1016/j.orthres.2004.08.023.

[244] R.P. Van Hove, I.N. Sierevelt, B.J. Van Royen, P.A. Nolte, Titanium-Nitride Coating of Orthopaedic Implants: A Review of the Literature, Biomed Res. Int. 2015 (2015) 1–9. doi:10.1155/2015/485975.

[245] J. Olofsson, T.M. Grehk, T. Berlind, C. Persson, S. Jacobson, H. Engqvist, Evaluation of silicon nitride as a wear resistant and resorbable alternative for total hip joint replacement, Biomatter. 2 (2012) 94–102. doi:10.4161/biom.20710.

[246] B.S. Bal, M.N. Rahaman, Orthopedic applications of silicon nitride ceramics, Acta Biomater. 8 (2012) 2889–2898. doi:http://dx.doi.org/10.1016/j.actbio.2012.04.031.

[247] A. Neumann, C. Unkel, C. Werry, C.U. Herborn, H.R. Maier, C. Ragoss, K. Jahnke, [Osteosynthesis in facial bones: silicon nitride ceramic as material], HNO. 54 (2006) 937–942. doi:10.1007/s00106-006-1397-4.

[248] A. Corp, First Silicon Nitride Total Hip Replacement, 2013 (2011). http://www.amedicacorp.com/press_releases/amedica_us_spine_enters_the_reconstructive_surgery_market.

[249] International Organization for Standardization, ISO-4288:1996 - Geometrical Product Specifications (GPS) -- Surface texture: Profile method -- Rules and procedures for the assessment of surface texture, (1996).

[250] International Organization for Standardization, BS EN ISO-3274:1998 -

Geometric product specifications (GPS). Surface texture. Profile method. Nominal characteristics of contact (stylus) instruments, (1998).

[251] International Organization for Standardization, BS EN ISO-26423:2016 - Fine ceramics (advanced ceramics, advanced technical ceramics). Determination of coating thickness by crater-grinding method, (n.d.). http://shop.bsigroup.com/ProductDetail/?pid=000000000030327990 (accessed February 25, 2017).

[252] I.N. Sneddon, The relation between load and penetration in the axisymmetric boussinesq problem for a punch of arbitrary profile, Int. J. Eng. Sci. 3 (1965) 47–57. doi:10.1016/0020-7225(65)90019-4.

[253] W.C. Oliver, G.M. Pharr, An improved technique for determining hardness and elastic modulus using load and displacement sensing indentation experiments, J. Mater. Res. 7 (1992) 1564–1583. doi:doi:10.1557/JMR.1992.1564.

[254] Heavens, O.S., Some factors influencing the adhesion of films produced by vacuum evaporation, J. Phys. Radium. 11 (1950) 355–360. doi:10.1051/jphysrad:01950001107035500.

[255] P. Benjamin, C. Weaver, Measurement of Adhesion of Thin Films, Proc. R. Soc. London. Ser. A. Math. Phys. Sci. 254 (1960) 163 LP-176. http://rspa.royalsocietypublishing.org/content/254/1277/163.abstract.

[256] International Organization for Standardization, BS EN 1071-2:2002 - Advanced technical ceramics. Methods of test for ceramic coatings. Determination of coating thickness by the crater grinding method, (n.d.). http://shop.bsigroup.com/ProductDetail/?pid=000000000030115576 (accessed February 25, 2017).

[257] H.A. Ching, D. Choudhury, M.J. Nine, N.A. Abu Osman, Effects of surface coating on reducing friction and wear of orthopaedic implants, Sci. Technol. Adv. Mater. 15 (2014) 14402. doi:10.1088/1468-6996/15/1/014402.

[258] A.. Ehiasarian, W.-D. Münz, L. Hultman, U. Helmersson, I. Petrov, High power pulsed magnetron sputtered CrNx films, Surf. Coatings Technol. 163–164 (2003) 267–272. doi:10.1016/S0257-8972(02)00479-6.

[259] A.. Ehiasarian, P.E. Hovsepian, L. Hultman, U. Helmersson, Comparison of microstructure and mechanical properties of chromium nitride-based coatings deposited by high power impulse magnetron sputtering and by the combined steered cathodic arc/unbalanced magnetron technique, Thin Solid Films. 457 (2004) 270–277. doi:10.1016/j.tsf.2003.11.113.

[260] A. Anders, Tutorial: Reactive high power impulse magnetron sputtering (R-HiPIMS), J. Appl. Phys. 121 (2017) 171101. doi:10.1063/1.4978350.

[261] P. Hones, R. Sanjines, F. Levy, Characterization of sputter-deposited chromium nitride thin films for hard coatings, Surf. Coatings Technol. 94–95 (1997) 398–402. doi:10.1016/S0257-8972(97)00443-X.

[262] E. Broszeit, C. Friedrich, G. Berg, Deposition, properties and applications of PVD CrxN coatings, Surf. Coatings Technol. 115 (1999) 9–16. doi:10.1016/S0257-8972(99)00021-3.

[263] A. Lippitz, T. Hübert, XPS investigations of chromium nitride thin films, Surf. Coatings Technol. 200 (2005) 250–253. doi:http://dx.doi.org/10.1016/j.surfcoat.2005.02.091.

[264] L. Diéguez, D. Caballero, J. Calderer, M. Moreno, E. Martínez, J. Samitier, Optical Gratings Coated with Thin Si3N4 Layer for Efficient Immunosensing by Optical Waveguide Lightmode Spectroscopy., Biosensors. 2 (2012) 114–26. doi:10.3390/bios2020114.

[265] I.O. for Standarisation, Partial and total hip joint prostheses -- Part 2: Articulating surfaces made of metallic, ceramic and plastics materials, Implant. Surg. 7206–2:201 (2011).

[266] M. Pettersson, Silicon nitride for total hip replacements, 2015. https://uu.diva-portal.org/smash/get/diva2:797505/FULLTEXT01.pdf (accessed June 4, 2017).

[267] F. Zhou, K. Adachi, K. Kato, Influence of deposition parameters on surface roughness and mechanical properties of boron carbon nitride coatings synthesized by ion beam assisted deposition, Thin Solid Films. 497 (2006) 210–217. doi:10.1016/j.tsf.2005.10.070.

[268] D.M. Mattox, Handbook of physical vapor deposition (PVD) processing, Noyes Publications, Westwood, New Jersey, USA, 2010. https://books.google.co.uk/books?id=BZUtFQNuNgMC&pg=PA157&lpg=PA157&dq=physical+vapour+deposition+process+position+in+the+chamber&source=bl&ots=PHFirQn4S5&sig=uM693uVER0aLXTYJR-sqZTCoeW4&hl=en&sa=X&ved=0ahUKEwi1mPf0kqTUAhXsJcAKHZMMCTsQ6AEIYDAJ#v=onepage&q (accessed June 4, 2017).

[269] C. Fabry, C. Zietz, A. Baumann, R. Bader, Wear Performance of Sequentially Cross-Linked Polyethylene Inserts against Ion-Treated CoCr, TiNbN-Coated CoCr and Al2O3 Ceramic Femoral Heads for Total Hip Replacement, Lubricants. 3 (2015) 14–26. doi:10.3390/lubricants3010014.

[270] Aesculap Orthopaedics Columbus ® AS Knee System, (2009). https://www.aesculapimplantsystems.com/assets/base/doc/doc832-askneebrochure.pdf (accessed June 4, 2017).

[271] T. Halim, I.C. Clarke, M.D. Burgett-Moreno, T.K. Donaldson, C. Savisaar, J.G. Bowsher, A simulator study of adverse wear with metal and cement debris contamination in metal-on-metal hip bearings., Bone Joint Res. 4 (2014) 29–37. doi:10.1302/2046-3758.43.2000332.

[272] C.R. Bragdon, M. Jasty, O.K. Muratoglu, W.H. Harris, Third-Body Wear Testing of a Highly Cross-Linked Acetabular Liner, J. Arthroplasty. 20 (2005) 379–385. doi:10.1016/j.arth.2004.09.035.

[273] S.G. Ghalme, A. Mankar, Y. Bhalerao, Biomaterials in Hip Joint

Replacement, Int. J. Mater. Sci. Eng. 4 (2016). doi:10.17706/ijmse.2016.4.2.113-125.

[274] J. Lackner, W. Waldhauser, L. Major, M. Kot, Tribology and Micromechanics of Chromium Nitride Based Multilayer Coatings on Soft and Hard Substrates, Coatings. 4 (2014) 121–138. doi:10.3390/coatings4010121.

[275] L. Cunha, M. Andritschky, K. Pischow, Z. Wang, A. Zarychta, A.S. Miranda, A.M. Cunha, Performance of chromium nitride based coatings under plastic processing conditions, Surf. Coatings Technol. 133 (2000) 61–67. doi:10.1016/S0257-8972(00)00875-6.

[276] A. Leyland, A. Matthews, On the significance of the H/E ratio in wear control: a nanocomposite coating approach to optimised tribological behaviour, Wear. 246 (2000) 1–11. doi:10.1016/S0043-1648(00)00488-9.

[277] A.A.C. Recco, I.C. Oliveira, M. Massi, H.S. Maciel, A.P. Tschiptschin, Adhesion of reactive magnetron sputtered TINx and TICy coatings to AISI H13 tool steel, Surf. Coatings Technol. 202 (2007) 1078–1083. doi:10.1016/j.surfcoat.2007.07.073.

[278] H. Haider, J.N. Weisenburger, F. Namavar, K.L. Garvin, Why We Need Coating Technologies for Hip Replacement Systems, and the Importance of Testing them in Vitro, Oper. Tech. Orthop. (2017). doi:10.1053/j.oto.2017.05.003.

[279] Ł. Łapaj, J. Markuszewski, J. Wendland, A. Mróz, M. Wierusz-Kozłowska, Massive failure of TiNbN coating in surface engineered metal-on-metal hip arthroplasty: Retrieval analysis, J. Biomed. Mater. Res. Part B Appl. Biomater. 104 (2016) 1043–1049. doi:10.1002/jbm.b.33421.

[280] S. Jiang, B. Jiang, Y. Li, Y. Li, G. Yin, C. Zheng, Friction and wear study of diamond-like carbon gradient coatings on Ti6Al4V substrate prepared by plasma source ion implant-ion beam enhanced deposition, Appl. Surf. Sci. 236 (2004) 285–291. doi:10.1016/j.apsusc.2004.04.032.

[281] W. Heinke, A. Leyland, A. Matthews, G. Berg, C. Friedrich, E. Broszeit, Evaluation of PVD nitride coatings, using impact, scratch and Rockwell-C adhesion tests, Thin Solid Films. 270 (1995) 431–438. doi:10.1016/0040-6090(95)06934-8.

[282] H. Ollendorf, D. Schneider, A comparative study of adhesion test methods for hard coatings, Surf. Coatings Technol. 113 (1999) 86–102. doi:10.1016/S0257-8972(98)00827-5.

[283] Z. Wan, T.F. Zhang, H.-B.-R. Lee, J.H. Yang, W.C. Choi, B. Han, K.H. Kim, S.-H. Kwon, Improved Corrosion Resistance and Mechanical Properties of CrN Hard Coatings with an Atomic Layer Deposited Al2O3 Interlayer, ACS Appl. Mater. Interfaces. 7 (2015) 26716–26725. doi:10.1021/acsami.5b08696.

[284] K.-D. Bouzakis, S. Makrimallakis, G. Katirtzoglou, G. Skordaris, S. Gerardis, E. Bouzakis, T. Leyendecker, S. Bolz, W. Koelker, Surface

&amp; coatings technology., Surf. Coatings Technol. 205 (2010) 1564–1570. http://publica.fraunhofer.de/documents/N-171875.html (accessed June 10, 2017).

[285] E. Adoberg, V. Podgurski, P. Peetsalu, L. Lind, V. Mikli, P. Hvizdos, P. Kulu, The effect of surface pre-treatment and coating post-treatment to the properties of TiN coatings, Est. J. Eng. 18 (2012) 185–192. doi:10.3176/eng.2012.3.03.

[286] M. Melancon Paul Hunter, A. Al-Borno, T. Liskiewicz, S. Rao Bassem Salamah Shailesh Dhoke, J. Cortes Xianyi Chen, The Effect of Four Commercially Available Steel Decontamination Processes on the Performance of External Coatings, in: NACE - Int. Corros. Conf. Ser., National Association of Corrosion Engineers International, San Antonio, 2014. http://eprints.whiterose.ac.uk/84172/1/NACE 2014 Paper 4391 External Coatings - Jan 30 2014.pdf (accessed June 10, 2017).

[287] H.-G. Willert, G.H. Buchhorn, A. Fayyazi, R. Flury, M. Windler, G. Köster, C.H. Lohmann, Metal-on-Metal Bearings and Hypersensitivity in Patients with Artificial Hip Joints&lt;sbt aid=&quot;954276&quot;&gt;A Clinical and Histomorphological Study&lt;/sbt&gt;, J. Bone Jt. Surg. 87 (2005) 28. doi:10.2106/JBJS.A.02039pp.

[288] P. Campbell, E. Ebramzadeh, S. Nelson, K. Takamura, K. De Smet, H.C. Amstutz, Histological Features of Pseudotumor-like Tissues From Metal-on-Metal Hips, Clin. Orthop. Relat. Res. 468 (2010) 2321–2327. doi:10.1007/s11999-010-1372-y.

[289] I.J. Leslie, S. Williams, C. Brown, J. Anderson, G. Isaac, P. Hatto, E. Ingham, J. Fisher, Surface engineering: A low wearing solution for metal-on-metal hip surface replacements, J. Biomed. Mater. Res. Part B Appl. Biomater. 90B (2009) 558–565. doi:10.1002/jbm.b.31317.

[290] R. Lappalainen, M. Selenius, P.A. Revell, Joint bearing surfaces and replacement joint design, in: P.A. Revell (Ed.), Jt. Replace. Technol., Woodhead Publishing Limited Cambridge, UK, Cambridge, 2008.

[291] J. Nevelos, E. Ingham, C. Doyle, R. Streicher, A. Nevelos, W. Walter, J. Fisher, Microseparation of the centers of alumina-alumina artificial hip joints during simulator testing produces clinically relevant wear rates and patterns, J Arthroplast. 15 (2000) 7–795. doi:10.1054/arth.2000.8100.

[292] A. Essner, G. Schmidig, A. Wang, The clinical relevance of hip joint simulator testing: In vitro and in vivo comparisons, 2005. doi:10.1016/j.wear.2005.02.105.

[293] P.J. Firkins, J.L. Tipper, M.R. Saadatzadeh, E. Ingham, M.H. Stone, R. Farrar, J. Fisher, Quantitative analysis of wear and wear debris from metal-on-metal hip prostheses tested in a physiological hip joint simulator., Biomed. Mater. Eng. 11 (2001) 143–57. http://www.ncbi.nlm.nih.gov/pubmed/11352113 (accessed March 20, 2017).

[294] J.L. Tipper, A. Hatton, J.E. Nevelos, E. Ingham, C. Doyle, R. Streicher, A.B. Nevelos, J. Fisher, Alumina–alumina artificial hip joints. Part II: Characterisation of the wear debris from in vitro hip joint simulations, Biomaterials. 23 (2002) 3441–3448. doi:10.1016/S0142-9612(02)00048-0.

[295] A. Wang, A. Essner, Three-body wear of UHMWPE acetabular cups by PMMA particles against CoCr, alumina and zirconia heads in a hip joint simulator, Wear. 250 (2001) 212–216. doi:http://dx.doi.org/10.1016/S0043-1648(01)00643-3.

[296] C. Myant, R. Underwood, J. Fan, P.M. Cann, Lubrication of metal-on-metal hip joints: the effect of protein content and load on film formation and wear, J Mech Behav Biomed Mater. 6 (2012) 30–40. doi:10.1016/j.jmbbm.2011.09.008.

[297] J. Lefebvre, Viscosity of concentrated protein solutions, Rheol. Acta. 21 (n.d.) 620–625. doi:10.1007/bf01534361.

[298] S.C. Scholes, A. Unsworth, The effects of proteins on the friction and lubrication of artificial joints, Proc Inst Mech Eng H. 220 (2006) 687–693.

[299] S.M. Kurtz, A.A. Edidin, Spine technology handbook, (2006) xiv, 535 ill. (some col.) 25 cm. http://0-www.engineeringvillage.com.wam.leeds.ac.uk/controller/servlet/OpenURL?genre=book&isbn=9780123693907.

[300] P. Moghadas, A. Mahomed, D.W.L. Hukins, D.E.T. Shepherd, Wear in metal-on-metal total disc arthroplasty., Proc. Inst. Mech. Eng. H. 227 (2013) 356–61. doi:10.1177/0954411912471768.

[301] T.M. Grupp, H.-J. Meisel, J.A. Cotton, J. Schwiesau, B. Fritz, W. Blömer, V. Jansson, Alternative bearing materials for intervertebral disc arthroplasty, Biomaterials. 31 (2010) 523–531. doi:10.1016/j.biomaterials.2009.09.064.

[302] M. Kraft, D. Koch, M. Bushelow, Evaluation of PEEK-on-PEEK as a New Articulation, in: Annu. Meet. Ger. Spine Soc., Hamburg, 2011. http://www.medicalpeek.org/pub_reports/view/143 (accessed April 8, 2017).

[303] R. Vicars, P. Prokopovich, T.D. Brown, J.L. Tipper, E. Ingham, J. Fisher, R.M. Hall, The effect of anterior-posterior shear on the wear of CHARITÉ total disc replacement., Spine (Phila. Pa. 1976). 37 (2012) E528-34. doi:10.1097/BRS.0b013e31823cbd6e.

[304] P. Moghadas, A. Mahomed, D.E. Shepherd, D.W. Hukins, Wear of the Charité ® lumbar intervertebral disc replacement investigated using an electro-mechanical spine simulator, Proc. Inst. Mech. Eng. Part H J. Eng. Med. 229 (2015) 264–268. doi:10.1177/0954411915576537.

[305] P. Prokopovich, S. Perni, J. Fisher, R.M. Hall, Spatial variation of wear on Charité lumbar discs, Acta Biomater. 7 (2011) 3914–3926. doi:10.1016/j.actbio.2011.06.036.

[306] F.W. Chan, J.D. Bobyn, J.B. Medley, J.J. Krygier, M. Tanzer, The Otto Aufranc Award. Wear and lubrication of metal-on-metal hip implants., Clin. Orthop. Relat. Res. (1999) 10–24. http://www.ncbi.nlm.nih.gov/pubmed/10611857 (accessed April 8, 2017).

[307] A.A.J. Goldsmith, D. Dowson, G.H. Isaac, J.G. Lancaster, A comparative joint simulator study of the wear of metal-on-metal and alternative material combinations in hip replacements, Proc. Inst. Mech. Eng. Part H J. Eng. Med. 214 (2000) 39–47. doi:10.1243/0954411001535228.

[308] G.H. Isaac, J. Thompson, S. Williams, J. Fisher, Metal-on-metal bearings surfaces: materials, manufacture, design, optimization, and alternatives, Proc. Inst. Mech. Eng. Part H J. Eng. Med. 220 (2006) 119–133. doi:10.1243/095441105X68953.

[309] C. Duc, P. Salvia, A. Lubansu, V. Feipel, K. Aminian, Objective evaluation of cervical spine mobility after surgery during free-living activity, Clin. Biomech. 28 (2013) 364–369. doi:10.1016/j.clinbiomech.2013.03.006.

[310] M. Al-Hajjar, J. Fisher, S. Williams, J.L. Tipper, L.M. Jennings, Effect of femoral head size on the wear of metal on metal bearings in total hip replacements under adverse edge-loading conditions, J Biomed Mater Res Part B Appl Biomater J Biomed Mater Res Part B. 101101 (2013). doi:10.1002/jbm.b.32824.

[311] C. Klapperich, J. Graham, L. Pruitt, M.D. Ries, Failure of a Metal-on-Metal Total Hip Arthroplasty From Progressive Osteolysis, J. Arthroplasty. 14 (1999). http://www.ewp.rpi.edu/hartford/~ernesto/F2012/FWM/Papers/Klapperich-1999-Total-Hip.pdf (accessed April 9, 2017).

[312] A. Wang, S. Yue, J.. Bobyn, F.. Chan, J.. Medley, Surface characterization of metal-on-metal hip implants tested in a hip simulator, Wear. 225 (1999) 708–715. doi:10.1016/S0043-1648(98)00384-6.

[313] T.J. Joyce, H. Grigg, D.J. Langton, A.V.F. Nargol, Quantification of self-polishing in vivo from explanted metal-on-metal total hip replacements, Tribol. Int. 44 (2011) 513–516. doi:10.1016/j.triboint.2010.04.007.

[314] M.L. Scott, J.I. Partin, Reduced Wear Rates and Tribological Properties of Long-Term Retrieved Metal-on-Metal Tha Bearing Components, in: Proc. 45th Meet. Orthop. Res. Soc., Anaheim, California, 1999: p. 851. http://www.ors.org/Transactions/45/0851.PDF (accessed April 9, 2017).

[315] P.J. Firkins, J.L. Tipper, M.R. Saadatzadeh, E. Ingham, M.H. Stone, R. Farrar, J. Fisher, Quantitative analysis of wear and wear debris from metal-on-metal hip prostheses tested in a physiological hip joint simulator., Biomed. Mater. Eng. 11 (2001) 143–57. http://www.ncbi.nlm.nih.gov/pubmed/11352113 (accessed April 8, 2017).

[316] K. Vassiliou, A.P. D Elfick, S.C. Scholes, A. Unsworth, The effect of “running-in” on the tribology and surface morphology of metal-on-metal Birmingham hip resurfacing device in simulator studies, Proc. Inst. Mech.

Eng. Part H J. Eng. Med. 220 (2006) 269–277. doi:10.1243/09544119JEIM63.

[317] J.L. Tipper, P.J. Firkins, E. Ingham, J. Fisher, M.H. Stone, R. Farrar, Quantitative analysis of the wear and wear debris from low and high carbon content cobalt chrome alloys used in metal on metal total hip replacements., J. Mater. Sci. Mater. Med. 10 (1999) 353–62. http://www.ncbi.nlm.nih.gov/pubmed/15348136 (accessed March 20, 2017).

[318] D.S. Park, S. Danyluk, M.J. McNallan, Influence of Tribochemical Reaction Products on Friction and Wear of Silicon Nitride at Elevated Temperatures in Reactive Environments, J. Am. Ceram. Soc. 75 (1992) 3033–3039. doi:10.1111/j.1151-2916.1992.tb04383.x.

[319] D. Amutha Rani, Y. Yoshizawa, M.I. Jones, H. Hyuga, K. Hirao, Y. Yamauchi, Comparison of Tribological Behavior Between α-Sialon/Si3N4 and Si3N4/Si3N4 Sliding Pairs in Water Lubrication, J. Am. Ceram. Soc. 88 (2005) 1655–1658. doi:10.1111/j.1551-2916.2005.00274.x.

[320] T. Saito, Y. Imada, F. Honda, An analytical observation of the tribochemical reaction of silicon nitride sliding with low friction in aqueous solutions, Wear. 205 (1997) 153–159. doi:http://dx.doi.org/10.1016/S0043-1648(96)07287-0.

[321] J. Xu, K. Kato, Formation of tribochemical layer of ceramics sliding in water and its role for low friction, Wear. 245 (2000) 61–75. doi:http://dx.doi.org/10.1016/S0043-1648(00)00466-X.

[322] H.A. Richardson, I.C. Clarke, P. Williams, T. Donaldson, H. Oonishi, Precision and accuracy in ceramic-on-ceramic wear analyses: influence of simulator test duration, Proc Inst Mech Eng H. 219 (2005) 401–405.

[323] I.C. Clarke, V. Good, P. Williams, D. Schroeder, L. Anissian, A. Stark, H. Oonishi, J. Schuldies, G. Gustafson, Ultra-low wear rates for rigid-on-rigid bearings in total hip replacements, Proc Inst Mech Eng H. 214 (2000) 331–347.

[324] H. Oonishi, I.C. Clarke, V. Good, H. Amino, M. Ueno, Alumina hip joints characterized by run-in wear and steady-state wear to 14 million cycles in hip-simulator model, J Biomed Mater Res A. 70 (2004) 523–532. doi:10.1002/jbm.a.30021.

[325] B.J. McEntire, B.S. Bal, A. Lakshminarayanan, R. Bock, Silicon Nitride Bearings for Total Joint Arthroplasty, Lubricants. 4 (2016) 1–24. doi:10.3390/lubricants4040035.

[326] B.S. Bal, A. Khandkar, R. Lakshminarayanan, I. Clarke, A.A. Hoffman, M.N. Rahaman, Fabrication and Testing of Silicon Nitride Bearings in Total Hip Arthroplasty: Winner of the 2007 “HAP” PAUL Award, J Arthroplast. 24 (2009) 110–116. doi:http://dx.doi.org/10.1016/j.arth.2008.01.300.

[327] F. Liu, I.J. Udofia, Z.M. Jin, F. Hirt, C. Rieker, P. Roberts, P. Grigoris, Comparison of Contact Mechanics between a Total Hip Replacement and

a Hip Resurfacing with a Metal-On-Metal Articulation, Proc. Inst. Mech. Eng. Part C J. Mech. Eng. Sci. 219 (2005) 727–732. doi:10.1243/095440605X31490.

[328] M. Royle, Influence of coatings on ion release from large diameter metal-on-metal hip bearings, Queen Mary, University of London, 2012. http://ethos.bl.uk/OrderDetails.do?uin=uk.bl.ethos.561233 (accessed April 21, 2017).

[329] J.A. Ortega-Saenz, M. Alvarez-Vera, M.A.L. Hernandez-Rodriguez, Biotribological study of multilayer coated metal-on-metal hip prostheses in a hip joint simulator, Wear. 301 (2013) 234–242. doi:10.1016/j.wear.2013.01.024.

[330] A. Mohammed, A. Metcalfe, D. Woodnutt, Medium-term outcome of titanium nitride, mobile bearing total knee replacement., Acta Orthop. Belg. 80 (2014) 269–75. http://www.ncbi.nlm.nih.gov/pubmed/25090802 (accessed April 21, 2017).

[331] D. Woodnutt, K. Hamelynck, Low metal ion release in patients at up to 8 years following titanium niobium nitride (TiNbN) surface treated metal-on-metal hip arthroplasty, Orthop. Proc. 94–B (2012). http://www.bjjprocs.boneandjoint.org.uk/content/94-B/SUPP_XXXIX/6 (accessed April 21, 2017).

[332] D. de Villiers, H. Hothi, H. Khatkar, J. Meswania, G. Blunn, J. Skinner, A. Hart, Lessons from retrievals: Retrievals help understand the reason for revision of coated hip arthroplasties, Proc. Inst. Mech. Eng. Part H J. Eng. Med. 229 (2015) 804–811. doi:10.1177/0954411915611427.

[333] P. Bergschmidt, R. Bader, S. Finze, C. Schulze, G. Kundt, W. Mittelmeier, Comparative Study of Clinical and Radiological Outcomes of Unconstrained Bicondylar Total Knee Endoprostheses with Anti-allergic Coating., Open Orthop. J. 5 (2011) 354–60. doi:10.2174/1874325001105010354.

[334] A. Miletić, P. Terek, L. Kovačević, M. Vilotić, D. Kakaš, B. Škorić, D. Kukuruzović, Influence of substrate roughness on adhesion of TiN coatings, J. Brazilian Soc. Mech. Sci. Eng. 36 (2014) 293–299. doi:10.1007/s40430-013-0102-2.

[335] N. Ravi, R. Markandeya, S. V. Joshi, Effect of substrate roughness on adhesion and tribological properties of nc-TiAlN/a-Si3N4 nanocomposite coatings deposited by cathodic arc PVD process, Surf. Eng. 33 (2017) 7–19. doi:10.1179/1743294415Y.0000000005.

[336] M. Belmonte, A.J.S. Fernandes, F.M. Costa, F.J. Oliveira, R.F. Silva, Adhesion behaviour assessment on diamond coated silicon nitride by acoustic emission, Diam. Relat. Mater. 12 (2003) 733–737. doi:10.1016/S0925-9635(02)00305-9.

[337] N.I. and the I. of M. National Joint Registry for England, Wales, 13th Annual Report - 2016, n.d.

http://www.njrcentre.org.uk/njrcentre/Portals/0/Documents/England/Reports/13th Annual Report/07950 NJR Annual Report 2016 ONLINE REPORT.pdf (accessed March 26, 2017).

[338] P.E. Purdue, P. Koulouvaris, B.J. Nestor, T.P. Sculco, The central role of wear debris in periprosthetic osteolysis., HSS J. 2 (2006) 102–13. doi:10.1007/s11420-006-9003-6.

[339] W.J. Maloney, R.L. Smith, Periprosthetic osteolysis in total hip arthroplasty: the role of particulate wear debris., Instr. Course Lect. 45 (1996) 171–82. http://www.ncbi.nlm.nih.gov/pubmed/8727736 (accessed March 26, 2017).

[340] S.-Y. Yang, W. Ren, Y. Park, A. Sieving, S. Hsu, S. Nasser, P.H. Wooley, Diverse cellular and apoptotic responses to variant shapes of UHMWPE particles in a murine model of inflammation., Biomaterials. 23 (2002) 3535–43. http://www.ncbi.nlm.nih.gov/pubmed/12109677 (accessed March 26, 2017).

[341] M. Nine, D. Choudhury, A. Hee, R. Mootanah, N. Osman, Wear Debris Characterization and Corresponding Biological Response: Artificial Hip and Knee Joints, Materials (Basel). 7 (2014) 980–1016. doi:10.3390/ma7020980.

[342] M.S. Caicedo, L. Samelko, K. McAllister, J.J. Jacobs, N.J. Hallab, Increasing both CoCrMo-alloy particle size and surface irregularity induces increased macrophage inflammasome activation in vitro potentially through lysosomal destabilization mechanisms, J. Orthop. Res. 31 (2013) 1633–1642. doi:10.1002/jor.22411.

[343] R.S. Tuan, F.Y.-I. Lee, Y. T Konttinen, J.M. Wilkinson, R.L. Smith, Implant Wear Symposium 2007 Biologic Work Group, What are the local and systemic biologic reactions and mediators to wear debris, and what host factors determine or modulate the biologic response to wear particles?, J. Am. Acad. Orthop. Surg. 16 Suppl 1 (2008) S42-8. http://www.ncbi.nlm.nih.gov/pubmed/18612013 (accessed March 28, 2017).

[344] V. Sansone, D. Pagani, M. Melato, The effects on bone cells of metal ions released from orthopaedic implants. A review., Clin. Cases Miner. Bone Metab. 10 (2013) 34–40. doi:10.11138/ccmbm/2013.10.1.034.

[345] N.J. Hallab, J.J. Jacobs, Biologic effects of implant debris., Bull. NYU Hosp. Jt. Dis. 67 (2009) 182–8. http://www.ncbi.nlm.nih.gov/pubmed/19583551 (accessed March 26, 2017).

[346] I. Catelas, J.J. Jacobs, Biologic activity of wear particles., Instr. Course Lect. 59 (2010) 3–16. http://www.ncbi.nlm.nih.gov/pubmed/20415362 (accessed March 28, 2017).

[347] T.S. Watters, D.M. Cardona, K.S. Menon, E.N. Vinson, M.P. Bolognesi, L.G. Dodd, Aseptic Lymphocyte-Dominated Vasculitis-Associated Lesion,

Am. J. Clin. Pathol. 134 (2010) 886–893. doi:10.1309/AJCPLTNEUAH8XI4W.

[348] H.S. Gill, G. Grammatopoulos, S. Adshead, E. Tsialogiannis, E. Tsiridis, Molecular and immune toxicity of CoCr nanoparticles in MoM hip arthroplasty, Trends Mol Med. 18 (2012) 145–155. doi:10.1016/j.molmed.2011.12.002.

[349] J.A. D'Antonio, W.N. Capello, M. Naughton, Ceramic bearings for total hip arthroplasty have high survivorship at 10 years, Clin Orthop Relat Res. 470 (2012) 373–381. doi:10.1007/s11999-011-2076-7.

[350] D.G. Kang, S.C. Wagner, R.A. Lehman, Osteolysis in the setting of metal-on-metal cervical disc arthroplasty, Spine J. 14 (2014) 1362–1365. doi:10.1016/j.spinee.2014.02.034.

[351] S.C. Scholes, A. Unsworth, Pin-on-plate studies on the effect of rotation on the wear of metal-on-metal samples, J. Mater. Sci. Mater. Med. 12 (2001) 299–303. doi:10.1023/A:1011238902803.

[352] International Organization for Standardization, ISO-10993-5:2009 - Biological evaluation of medical devices - Part 5: Tests for in vitro cytotoxicity., (2009).

[353] S. Lal, R.M. Hall, J.L. Tipper, A novel method for isolation and recovery of ceramic nanoparticles and metal wear debris from serum lubricants at ultra-low wear rates, Acta Biomater. 42 (2016) 420–428. doi:10.1016/j.actbio.2016.07.004.

[354] B. Behl, I. Papageorgiou, C. Brown, R. Hall, J.L. Tipper, J. Fisher, E. Ingham, Biological effects of cobalt-chromium nanoparticles and ions on dural fibroblasts and dural epithelial cells, Biomaterials. 34 (2013) 3547–3558. doi:10.1016/j.biomaterials.2013.01.023.

[355] F. Lu, M. Royle, F. V Lali, A.J. Hart, S. Collins, J. Housden, J.C. Shelton, Simple isolation method for the bulk isolation of wear particles from metal on metal bearing surfaces generated in a hip simulator test, J. Mater. Sci. Mater. Med. 23 (2012) 891–901. doi:10.1007/s10856-012-4573-y.

[356] K. Ohlendieck, Centrifugation, in: J. Walker (Ed.), Princ. Tech. Biochem. Mol. Biol., Cambridge University Press, Cambridge, 2005: pp. 76–80.

[357] International Organization for Standardization, ISO-13322-1:2014 – "Particle size analysis – Image analysis methods. Part 1: Static image analysis methods.," (2014).

[358] J.F. Archard, W. Hirst, The Wear of Metals under Unlubricated Conditions, Proc. R. Soc. A Math. Phys. Eng. Sci. 236 (1956) 397–410. doi:10.1098/rspa.1956.0144.

[359] F. Meder, T. Daberkow, L. Treccani, M. Wilhelm, M. Schowalter, A. Rosenauer, L. Mädler, K. Rezwan, Protein adsorption on colloidal alumina particles functionalized with amino, carboxyl, sulfonate and phosphate groups, Acta Biomater. 8 (2012) 1221–1229.

doi:10.1016/j.actbio.2011.09.014.

[360] C. Brown, S. Williams, J.L. Tipper, J. Fisher, E. Ingham, Characterisation of wear particles produced by metal on metal and ceramic on metal hip prostheses under standard and microseparation simulation, J Mater Sci Mater Med. 18 (2007) 819–827. doi:10.1007/s10856-006-0015-z.

[361] I. Catelas, J.D. Bobyn, J.B. Medley, J.J. Krygier, D.J. Zukor, O.L. Huk, Size, shape, and composition of wear particles from metal-metal hip simulator testing: Effects of alloy and number of loading cycles, J. Biomed. Mater. Res. 67A (2003) 312–327. doi:10.1002/jbm.a.10088.

[362] R. Büscher, G. Täger, W. Dudzinski, B. Gleising, M.A. Wimmer, A. Fischer, Subsurface microstructure of metal-on-metal hip joints and its relationship to wear particle generation, J. Biomed. Mater. Res. Part B Appl. Biomater. 72B (2005) 206–214. doi:10.1002/jbm.b.30132.

[363] I. Catelas, J.B. Medley, P.A. Campbell, O.L. Huk, J.D. Bobyn, Comparison ofin vitro within vivo characteristics of wear particles from metal-metal hip implants, J. Biomed. Mater. Res. 70B (2004) 167–178. doi:10.1002/jbm.b.20036.

[364] Z. Xia, Y.-M. Kwon, S. Mehmood, C. Downing, K. Jurkschat, D.W. Murray, Characterization of metal-wear nanoparticles in pseudotumor following metal-on-metal hip resurfacing, 2011. doi:10.1016/j.nano.2011.08.002.

[365] J.G. Bowsher, A. Hussain, J. Nevelos, Williams, J.C. Shelton, LARGE HEAD DIAMETERS HAVE THE POTENTIAL TO REDUCE ION RELEASE IN METAL-ON-METAL HIP WEAR SIMULATIONS, (n.d.). http://www.ors.org/Transactions/51/1626.pdf (accessed April 29, 2017).

[366] M. Boerma, G.R. Burton, J. Wang, L.M. Fink, R.E. McGehee, M. Hauer-Jensen, Comparative expression profiling in primary and immortalized endothelial cells: changes in gene expression in response to hydroxy methylglutaryl-coenzyme A reductase inhibition, Blood Coagul. Fibrinolysis. 17 (2006) 173–180. doi:10.1097/01.mbc.0000220237.99843.a1.

[367] E. Lidington, D. Moyes, A. McCormack, M. Rose, A comparison of primary endothelial cells and endothelial cell lines for studies of immune interactions, Transpl. Immunol. 7 (1999) 239–246. doi:10.1016/S0966-3274(99)80008-2.

[368] C. Pan, C. Kumar, S. Bohl, U. Klingmueller, M. Mann, Comparative Proteomic Phenotyping of Cell Lines and Primary Cells to Assess Preservation of Cell Type-specific Functions, Mol. Cell. Proteomics. 8 (2009) 443–450. doi:10.1074/mcp.M800258-MCP200.

[369] L. Fairbairn, R. Kapetanovic, D.P. Sester, D.A. Hume, The mononuclear phagocyte system of the pig as a model for understanding human innate immunity and disease., J. Leukoc. Biol. 89 (2011) 855–71. doi:10.1189/jlb.1110607.

[370] M.A. Germain, A. Hatton, S. Williams, J.B. Matthews, M.H. Stone, J.

Fisher, E. Ingham, Comparison of the cytotoxicity of clinically relevant cobalt-chromium and alumina ceramic wear particles in vitro, Biomaterials. 24 (2003) 469–479.

[371] B. Scharf, C.C. Clement, V. Zolla, G. Perino, B. Yan, S.G. Elci, E. Purdue, S. Goldring, F. Macaluso, N. Cobelli, R.W. Vachet, L. Santambrogio, Molecular analysis of chromium and cobalt-related toxicity, Sci. Rep. 4 (2015) 5729. doi:10.1038/srep05729.

[372] D. Beyersmann, A. Hartwig, Carcinogenic metal compounds: recent insight into molecular and cellular mechanisms, Arch. Toxicol. 82 (2008) 493–512. doi:10.1007/s00204-008-0313-y.

[373] D.G. Barceloux, Cobalt., J. Toxicol. Clin. Toxicol. 37 (1999) 201–6. http://www.ncbi.nlm.nih.gov/pubmed/10382556 (accessed May 1, 2017).

[374] A.J. Hart, S.A. Sabah, A.S. Bandi, P. Maggiore, P. Tarassoli, B. Sampson, J. A. Skinner, Sensitivity and specificity of blood cobalt and chromium metal ions for predicting failure of metal-on-metal hip replacement, Bone Joint J. 93–B (2011) 1308–1313. doi:10.1302/0301-620X.93B10.26249.

[375] K. De Smet, R. De Haan, A. Calistri, P. Campbell, E. Ebramzadeh, C. Pattyn, H. Gill, Metal Ion Measurement as a Diagnostic Tool to Identify Problems with Metal-on-Metal Hip Resurfacing, J. Bone Jt. Surgery-American Vol. 90 (2008) 202–208. doi:10.2106/JBJS.H.00672.

[376] J. Daniel, H. Ziaee, C. Pradhan, D.J.W. McMinn, Six-year results of a prospective study of metal ion levels in young patients with metal-on-metal hip resurfacings, J. Bone Jt. Surg. - Br. Vol. 91–B (2009) 176–179. doi:10.1302/0301-620X.91B2.21654.

[377] E. Dunstan, A.P. Sanghrajka, S. Tilley, P. Unwin, G. Blunn, S.R. Cannon, T.W.R. Briggs, Metal ion levels after metal-on-metal proximal femoral replacements: A 30-YEAR FOLLOW-UP, J. Bone Jt. Surg. - Br. Vol. 87–B (2005) 628–631. doi:10.1302/0301-620X.87B5.15384.

[378] A.W. Schaffer, A. Pilger, C. Engelhardt, K. Zweymueller, H.W. Ruediger, Increased blood cobalt and chromium after total hip replacement., J. Toxicol. Clin. Toxicol. 37 (1999) 839–44. http://www.ncbi.nlm.nih.gov/pubmed/10630267 (accessed May 1, 2017).

[379] O. Posada, R. Tate, R.M. Meek, M. Grant, In Vitro Analyses of the Toxicity, Immunological, and Gene Expression Effects of Cobalt-Chromium Alloy Wear Debris and Co Ions Derived from Metal-on-Metal Hip Implants, Lubricants. 3 (2015) 539–568. doi:10.3390/lubricants3030539.

[380] B. Cappi, S. Neuss, J. Salber, R. Telle, R. Knuchel, H. Fischer, Cytocompatibility of high strength non-oxide ceramics, J Biomed Mater Res A. 93 (2010) 67–76. doi:10.1002/jbm.a.32527.

[381] A. Neumann, T. Reske, M. Held, K. Jahnke, C. Ragoß, H.R. Maier, Comparative investigation of the biocompatibility of various silicon nitride ceramic qualities in vitro, J. Mater. Sci. Mater. Med. 15 (2004) 1135–1140. doi:10.1023/B:JMSM.0000046396.14073.92.

[382] G. Kotzar, M. Freas, P. Abel, A. Fleischman, S. Roy, C. Zorman, J.M. Moran, J. Melzak, Evaluation of MEMS materials of construction for implantable medical devices, Biomaterials. 23 (2002) 2737–2750. doi:http://dx.doi.org/10.1016/S0142-9612(02)00007-8.

[383] R. Kue, A. Sohrabi, D. Nagle, C. Frondoza, D. Hungerford, Enhanced proliferation and osteocalcin production by human osteoblast-like MG63 cells on silicon nitride ceramic discs, Biomaterials. 20 (1999) 1195–1201. doi:http://dx.doi.org/10.1016/S0142-9612(99)00007-1.

[384] C.C. Guedes e Silva, O.Z. Higa, J.C. Bressiani, Cytotoxic evaluation of silicon nitride-based ceramics, Mater. Sci. Eng. C. 24 (2004) 643–646. doi:http://dx.doi.org/10.1016/j.msec.2004.08.007.

[385] A. Neumann, M. Kramps, C. Ragoß, H.R. Maier, K. Jahnke, Histological and microradiographic appearances of Silicon Nitride and Aluminum Oxide in a rabbit femur implantation model*, Materwiss. Werksttech. 35 (2004) 569–573. doi:10.1002/mawe.200400778.

[386] C.R. Howlett, E. McCartney, W. Ching, The effect of silicon nitride ceramic on rabbit skeletal cells and tissue. An in vitro and in vivo investigation, Clin Orthop Relat Res. (1989) 293–304.

[387] T.J. Webster, A.A. Patel, M.N. Rahaman, B. Sonny Bal, Anti-infective and osteointegration properties of silicon nitride, poly(ether ether ketone), and titanium implants, Acta Biomater. 8 (2012) 4447–4454. doi:10.1016/j.actbio.2012.07.038.

[388] S. Yang, X. Wu, Y. Hu, J. Li, G. Liu, W. Xu, C. Yang, S. Ye, Early and intermediate follow-up results after treatment of degenerative disc disease with the Bryan cervical disc prosthesis: single- and multiple-level, Spine (Phila Pa 1976). 33 (2008) E371-7. doi:10.1097/BRS.0b013e31817343a6.

[389] H.L. Karlsson, J. Gustafsson, P. Cronholm, L. Möller, Size-dependent toxicity of metal oxide particles—A comparison between nano- and micrometer size, Toxicol. Lett. 188 (2009) 112–118. doi:10.1016/j.toxlet.2009.03.014.

[390] T.T. Liao, Q.Y. Deng, S.S. Li, X. Li, L. Ji, Q. Wang, Y.X. Leng, N. Huang, Evaluation of the Size-Dependent Cytotoxicity of DLC (Diamondlike Carbon) Wear Debris in Arthroplasty Applications, ACS Biomater. Sci. Eng. 3 (2017) 530–539. doi:10.1021/acsbiomaterials.6b00618.

[391] I. Papageorgiou, C. Brown, R. Schins, S. Singh, R. Newson, S. Davis, J. Fisher, E. Ingham, C.P. Case, The effect of nano- and micron-sized particles of cobalt-chromium alloy on human fibroblasts in vitro, Biomaterials. 28 (2007) 2946–2958. doi:10.1016/j.biomaterials.2007.02.034.

[392] Y.-M. Kwon, Z. Xia, S. Glyn-Jones, D. Beard, H.S. Gill, D.W. Murray, Dose-dependent cytotoxicity of clinically relevant cobalt nanoparticles and ions on macrophages *in vitro*, Biomed. Mater. 4 (2009) 25018. doi:10.1088/1748-6041/4/2/025018.

[393] R. Liu, C. Kurihara, H. Tsai, P.J. Silvestri, M.I. Bennett, P.F. Pasquina, S.P. Cohen, Classification and Treatment of Chronic Neck Pain, Reg. Anesth. Pain Med. 42 (2017) 52–61. doi:10.1097/AAP.0000000000000505.

[394] M.F. Shriver, D.J. Lewis, V.R. Kshettry, B.P. Rosenbaum, E.C. Benzel, T.E. Mroz, Pseudoarthrosis rates in anterior cervical discectomy and fusion: A meta-analysis, Spine J. 15 (2015). doi:10.1016/j.spinee.2015.05.010.

[395] M.F. Shriver, D. Lubelski, A.M. Sharma, M.P. Steinmetz, E.C. Benzel, T.E. Mroz, Adjacent segment degeneration and disease following cervical arthroplasty: a systematic review and meta-analysis, Spine J. 16 (2016) 168–181. doi:10.1016/j.spinee.2015.10.032.

[396] R. Assaker, K. Ritter-Lang, D. Vardon, S. Litrico, S. Fuentes, M. Putzier, J. Franke, P. Jarzem, P. Guigui, G. Nakach, J.-C. Le Huec, Maverick total disc replacement in a real-world patient population: a prospective, multicentre, observational study, Eur. Spine J. 24 (2015) 2047–2055. doi:10.1007/s00586-015-3918-x.

[397] M.F. Gornet, J.K. Burkus, R.F. Dryer, J.H. Peloza, Lumbar Disc Arthroplasty With MAVERICK Disc Versus Stand-Alone Interbody Fusion, Spine (Phila. Pa. 1976). 36 (2011) E1600–E1611. doi:10.1097/BRS.0b013e318217668f.

[398] R.D. Guyer, K. Pettine, J.S. Roh, T.A. Dimmig, D. Coric, P.C. McAfee, D.D. Ohnmeiss, Comparison of 2 Lumbar Total Disc Replacements, Spine (Phila. Pa. 1976). 39 (2014) 925–931. doi:10.1097/BRS.0000000000000319.

[399] N. Plais, X. Thevenot, A. Cogniet, J. Rigal, J.C. Le Huec, Maverick total disc arthroplasty performs well at 10 years follow-up: a prospective study with HRQL and balance analysis, Eur. Spine J. (2017). doi:10.1007/s00586-017-5065-z.

[400] S. Green, Chapter 3 - Compounds and Composite Materials A2 - Kurtz, Steven M, in: PEEK Biomater. Handb., William Andrew Publishing, Oxford, 2012: pp. 23–48. doi:http://dx.doi.org/10.1016/B978-1-4377-4463-7.10003-X.

[401] A. Zeh, M. Planert, G. Siegert, P. Lattke, A. Held, W. Hein, Release of Cobalt and Chromium Ions Into the Serum Following Implantation of the Metal-on-Metal Maverick-Type Artificial Lumbar Disc (Medtronic Sofamor Danek), Spine (Phila. Pa. 1976). 32 (2007) 348–352. doi:10.1097/01.brs.0000253599.89694.c0.

[402] L.A.G. Marshman, T. Friesem, Y.R. Rampersaud, J.-C. Le Huec, M. Krishna, Subsidence and malplacement with the Oblique Maverick Lumbar Disc Arthroplasty: technical note, Spine J. 8 (2008) 650–655. doi:10.1016/j.spinee.2007.03.010.

[403] R. Vanos, L.L. Lildhar, E.A. Lehoux, P.E. Beaulé, I. Catelas, In vitro macrophage response to nanometer-size chromium oxide particles, J.

Biomed. Mater. Res. - Part B Appl. Biomater. 102 (2014). doi:10.1002/jbm.b.32991.

[404] M. Kraft, Wear Performance of a Peek-on-Peek Bearing under Cervical Loading Conditions and at Different Test Frequencies, Glob. Spine J. 2 (2012) s-0032-1319995-s-0032-1319995. doi:10.1055/s-0032-1319995.

[405] S. Williams, J.L. Tipper, E. Ingham, M.H. Stone, J. Fisher, In vitro analysis of the wear, wear debris and biological activity of surface-engineered coatings for use in metal-on-metal total hip replacements, Proc. Inst. Mech. Eng. Part H J. Eng. Med. 217 (2003) 155–163. doi:10.1243/095441103765212659.

[406] International Organization for Standardization, BS ISO-18192-3:2017 - Implants for surgery - Wear of total intervertebral spinal disc prostheses - Part 3: Impingement-wear testing and corresponding environmental conditions for test of lumbar prostheses under adverse kinematic conditions, (2017) 21.

[407] S. Wohlfart, S. Gelperina, J. Kreuter, Transport of drugs across the blood–brain barrier by nanoparticles, J. Control. Release. 161 (2012) 264–273. doi:10.1016/j.jconrel.2011.08.017.

[408] C. Saraiva, C. Praça, R. Ferreira, T. Santos, L. Ferreira, L. Bernardino, Nanoparticle-mediated brain drug delivery: Overcoming blood–brain barrier to treat neurodegenerative diseases, J. Control. Release. 235 (2016) 34–47. doi:10.1016/j.jconrel.2016.05.044.

[409] P.R. Lockman, R.J. Mumper, M.A. Khan, D.D. Allen, Nanoparticle Technology for Drug Delivery Across the Blood-Brain Barrier, Drug Dev. Ind. Pharm. 28 (2002) 1–13. doi:10.1081/DDC-120001481.